44th Course
The Power of Powder Diffraction

Erice, Italy 2-12 June 2011

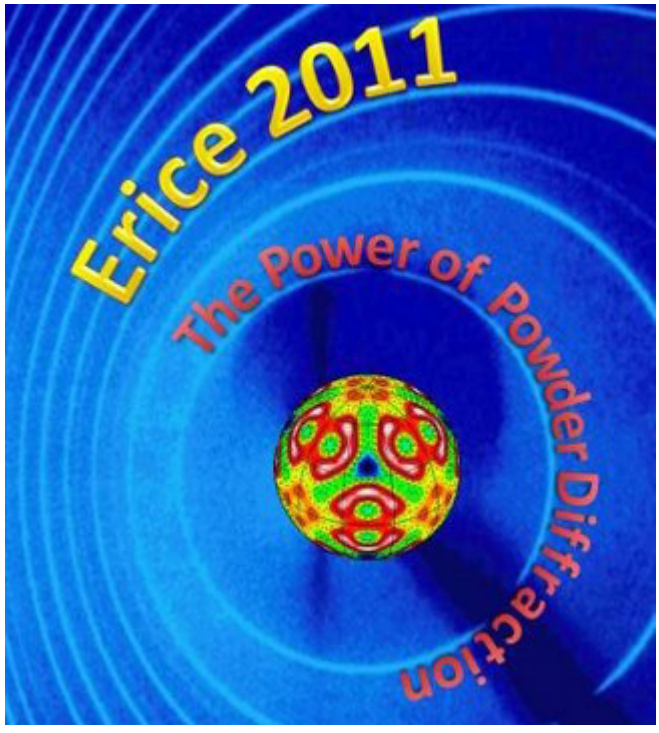

Acknowledgements

This Nato Advanced Study Institute is supported through the Nato Science for Peace and Security Programme.

It is also sponsored by:

European Crystallographic Association
International Union of Crystallography
OPCW

and generously financed by:

Bruker
ICDD
PANalytical

Organisers

Course Directors

Bill David

Kenneth Shankland

Local Organisers

Paola Spadon

Annalisa Guerri

John Irwin

Organisers

Orange scarves

Erin Bolstad

Elvira Fantechi

Gianni Grassi

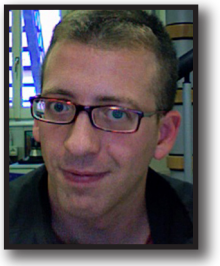

Giulio Isacco Lampronti

Matteo Lusi

Fabio Nicoli

Elena Papinutto

Mattia Rocco

Giovanna Scapin

Programme

Friday, 3 June Fundamentals

9:00 **Opening Remarks (Joint session with EC Course)**

9:15 **Bill David and Ute Kolb (Joint session with EC Course)**
Powder and Electron diffraction - by decades

10:40 **Coffee break**

11:00 **Kenneth Shankland**
Data Collection – Good Practices

11:50 **Peter Stephens**
Indexing

12:40 **Lunch**

14:30 **Peter Stephens**
Rietveld Refinement

15.20 **Lynne McCusker**
Structure solution overview

16:10 **Coffee break**

16:30 **Radovan Cerny**
Inorganic Materials

17:20 **Kenneth Shankland**
Organic Materials

18:10 **Meeting tutors**

19:30 **Celebrating Lodovico (S. Domenico)**

20:00 **Welcome Buffet Dinner & Sicilian Evening (S. Francesco)**

Saturday, 4 June — Instrumentation at the Frontiers

9:00 **Pamela Whitfield**
Laboratory X-ray Diffraction

9:50 **Fabia Gozzo**
Synchrotron X-ray Diffraction

10:40 **Coffee break**

11:00 **Laurent Chapon**
Neutron Powder Diffraction

11:50 **Andy Fitch**
Ultrafast Powder Diffraction

12:40 **Lunch while "watching" Poster Session 1**

14:30 **Colin Pulham**
Taking it to extremes

15:20 **DEMO**
Laurent Chapon
Introduction to FullProf

16:10 **Coffee break**

16:30 **DEMO**
Bob VonDreele
Introduction to GSAS

17:20 **WORKSHOP**
Laurent Chapon: FullProf

WORKSHOP
Bob VonDreele: GSAS

20:00 **Dinner**

Sunday, 5 June — Structure Solution

9:00 **Carmelo Giacovazzo (Joint session with EC Course)**
Structure solution using direct methods

9:50 **Chris Gilmore (Joint session with EC Course)**
Structure solution using maximum entropy methods

10:40 **Coffee break**

11:00 **Lukas Palatinus (Joint session with EC Course)**
Structure solution using charge flipping

11:50 **Kenneth Shankland (Joint session with EC Course)**
Structure solution via global optimisation methods

12:40 **Lunch**

14:30 **DEMO**
Angela Altomare
Introduction to EXPO

15:20 **DEMO**
Radovan Cerny
FOX

16:10 **Coffee break**

16:30 **WORKSHOP**
Angela Altomare: EXPO

WORKSHOP
Radovan Cerny: FOX

18:30 **Poster Session 1 (odd numbers) in San Francesco Court**

20:00 **Pasta Party (at S. Francesco)**

Monday, 6 June — Big Challenges

9:00 **Jon Wright**
Proteins and Powders – Technical Developments

9:50 **Irene Margiolaki**
Proteins and Powders – An Overview

10:40 **Coffee break**

11:00 **Joel Bernstein**
Pharmaceuticals and Powders – An Overview

11:50 **Bill David**
Parametric Powder Diffraction

12:40 **EXCURSION to Mothia Island (alternatively: Trapani sand beach)**
(Lunch during excursion)

19:00 **Return to Erice**

20:00 **Dinner**

Tuesday, 7 June Powder Plus

8:45 **Christian Baerlocher (Joint session with EC Course)**
Combination of X-ray powder diffraction,
electron diffraction and HRTEM data

9:50 **Yaroslav Filinchuk**
In-situ Powder Diffraction

10:40 **Coffee break**

11:00 **Laurent Chapon**
Powder Diffraction and Magnetism

11:50 **Lubo Smrcok**
Powder diffraction and Computational Methods

12:40 **Lunch while watching Poster Session 2**

14:30 **DEMO**
Kenneth Shankland / Bill David
DASH

15:20 **DEMO**
Lukas Palatinus
Introduction to SUPERFLIP

16:10 **Coffee break**

16:30 **WORKSHOP**
Kenneth Shankland / Bill David: DASH

WORKSHOP
Lukas Palatinus: SUPERFLIP

18:10 **DEMO**
Arnt Kern / Robert Dinnebier
Introduction to TOPAS

20:00 **Dinner**

Wednesday, 8 June Less than Perfect

9:00 **Matteo Leoni**
Information on Imperfections

9:50 **Tamas Ungar**
Whose Fault is it?

10:40 **Coffee break**

11:00 **Simon Billinge**
Pair Distribution Function Analysis

11:50 **Yuri Andreev**
Debye Analysis

12:40 **Lunch**

14:30 **DEMO**
Simon Billinge
PDFgetX2

15:20 **DEMO**
Matteo Leoni
WPPM

16:10 **Coffee break**

16:30 **WORKSHOP**
Arnt Kern / Robert Dinnebier: TOPAS

WORKSHOP
Simon Billinge: PDFgetX2

WORKSHOP
Matteo Leoni: WPPM

18:30 **Poster Session 2 (even numbers) in San Francesco Court**

20:00 **Pizza Party (at S. Francesco)**

Thursday, 9 June Quantitative

9:00 **Ian Madsen**
Quantitative phase analysis: introduction and standards

9:50 **Arnt Kern**
Quantifying Amorphous Phases

10:40 **Coffee break**

11:00 **Luca Lutterotti**
Quantitative phase analysis: method developments

11:50 **EXCURSION to Selinunte and Segesta (alternatively to S. Vito lo Capo beach)**
(Lunch during excursion)

20:00 **Buffet dinner in front of the Segesta Temple**

Friday, 10 June Texture Friend and Foe

9:00 **Bob von Dreele**
Texture – An Overview

9:50 **Christian Baerlocher**
Using Texture for Structure Solution

10:40 **Coffee break**

11:00 **Gilberto Artioli**
Cultural Heritage

11:50 **Xun-Li Wang**
From railway lines to Airbus wings

12:40 **Lunch**

14:30 **DEMO**
Luca Lutterotti
Introduction to MAUD

15:20 **Student corner**

16:10 **Coffee break**

16:30 **WORKSHOP**
Luca Lutterotti: MAUD (texture & size/strain)

WORKSHOP
Ian Madsen: QPA using TOPAS

WORKSHOP
Bob VonDreele: Texture in GSAS

20:00 **Dinner**

Saturday, 11 June Crystal-ball- gazing

9:00 **Selected contributions**
Hot topics

10:40 **Coffee break**

11:00 **Selected contributions**
Hot topics

12:40 **Lunch**

14:30 **Lynne McCusker**
Old ideas – new opportunities

15:20 **Robert Dinnibier**
The Future of Laboratory Powder Diffraction

16:10 **Coffee break**

16:30 **Kenneth Shankland**
The Future Role of Computing – from Prediction to Automation

17:20 **Bill David**
What does the future hold?

20:00 **Goodbye Buffet Dinner**

Invited Speakers' Contributions

Powder Diffraction: by decades

William I. F. David
ISIS Facility, Science and Technology Facilities Council, Rutherford Appleton Laboratory, Harwell Science and Innovation Campus, Didcot, OX11 0QX, UK

Abstract This introductory lecture reviews the first one hundred years of powder diffraction, decade by decade, from the earliest X-ray powder diffraction measurements of the crystal structure of graphite through to the diversity and complexity of 21st century powder diffraction. Carbon features as an illustrative example throughout the discussion of these ten decades from graphite and the disorder of carbon black through to lonsdaleite, the elusive hexagonal polymorph of diamond, and C_{60}, the most symmetrical of molecules. Electronics and computing have played a leading role in the development of powder diffraction, particularly over the past sixty years, and the Moore's Law decade-by-decade rise in computing power is clear in the increasing complexity of powder diffraction experiments and material systems that can be studied. The lecture concludes with a final discussion of decades – the four decades of length-scale from the ångstrom to the micron that not only represent the domain of powder diffraction but are also the distances that will dominate 21st century science and technology.

1. Powder diffraction – the first 100 years

1.1 A brief preamble

The origins of X-ray diffraction can be traced back to the discovery of X-rays by Wilhelm Conrad Roentgen in the University of Wurzburg in the summer of 1895 [1]. The dramatic early images of the bones of living hands (initially, those of his wife!) created an immediate sensation and, even before the turn of the century, medical applications were quickly developed. Perhaps less well-known was Roentgen's repeated attempts to observe the phenomenon of X-ray diffraction – and he was most likely successful, as his Third Communication on X-rays in March 1897 suggests, in observing diffraction on a few fleeting occasions. Roentgen moved from Wurzburg to Munich in 1900 and in 1901 was accordingly awarded the first Nobel Prize in Physics. The University of Munich was one of the leading universities in the world in the "new physics" and rapidly became the centre of the development of X-rays physics with a roll call of names such as Sommerfeld, Groth, Debye, Ewald and Laue that would define much of the early years of the subject. Laue arrived in Munich in 1909 with interests that ranged across the whole of physics from special relativity and optics to thermodynamics and the theory of radiation. Prompted by Ewald, Laue's intuition led him to an analysis of the first diffraction data collected by his

assistants, Friedrich and Knipping. The first diffraction pattern (Fig. 1a) was essentially uninterpretable but within weeks the improvement in data quality was not only remarkable but, crucially, also led to an interpretable solution [2] (Figs. 1b and 1c) and the 1914 Nobel Prize in Physics – but only to Laue! The first crystal structure is, however, attributed to the father and son team, W.H. and W.L. Bragg.

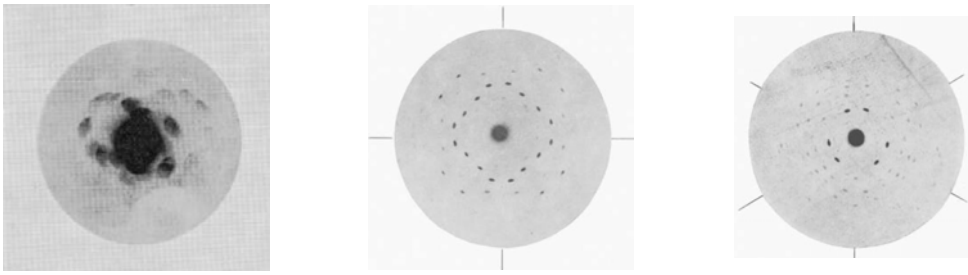

Fig.1. (a) Friedrich and Knipping's first successful X-ray diffraction photograph – the crystal was copper sulphate; (b) and (c) zinc-blende Laue photographs along the 4-fold (b) and 3-fold (c) axes from Laue, Friedrich and Knipping, *Sitz. Ger. Bayer. Akademie d. Wiss*, 8 June 1912.

On October 18, 1912, only a few months after the first diffraction patterns had been successfully collected, the elder Bragg published his first paper [3] offering an interpretation of the zinc-blended diffraction data published by Laue, Friedrich and Knipping. It was, however, the younger Bragg who, while still a student at Cambridge, came up with a correct analysis of the origins of the diffraction data [4]. Shortly afterwards, the Braggs collected single crystal data and solved the crystal structures of NaCl, KCl, KBr and KI [5] – four crystal structures in the first paper and the Nobel Prize in Physics within two years in 1915! Powder diffraction, with its lower intensities, had to wait only a little longer. Some of the first clues are to be found in the 1914 Nobel Prize lecture delivered by Max von Laue on December 12, 1915 who said "Since 1912 much has been done in both fields, and in both sectors W. L. Bragg and W. H. Bragg have taken the first important step beyond the investigations carried out at Munich. It would range far too wide if I were, at this juncture, to compile a fairly comprehensive list of all the researchers who have gained distinction in that research work. I can mention here only the transformation of the process, which proved to be of great importance for the further conduct of the experiments and in which Debye transferred the examination of beautiful, well-formed crystal fragments - which sometimes are obtainable only with considerable difficulty - to research into the finest possible crystal powder."

1.2 The first powder diffraction measurements

X-ray powder diffraction has two separate beginnings in Germany, again in Munich, and almost simultaneously in the United States. In Munich, Peter Debye determined that not only powders but also liquids should exhibit distinctive diffraction patterns [7]. Along with Paul Scherrer, Debye performed the first powder diffraction meas-

urements [8] discovering, inter alia, the crystal structure of graphite. The first measurements in the United States happened in very different circumstances – not in a university but in the General Electric Research Laboratory (GERL) in Schenectady, New York by Albert Hull [9]. A chance comment about the unsolved structure of iron by W.H. Bragg, who visited GERL in 1914, drew Hull into the field of X-ray structural analysis and rapidly, although World War 1 interrupted his efforts, he developed many of the essentials of the powder diffraction technique using photographic techniques (see Fig. 2) and discussed multi-phase analysis, preferred orientation, the need for sample rotation, wavelength filters, absorption, the importance of sample preparation and the concept of a "lattice constant". The three principal papers [10-12] that Hull published are significant tours-de-force – his first paper alone described the correct crystal structures of iron, silicon, aluminium, magnesium, sodium, lithium, nickel, diamond and graphite. While Debye and Scherrer reported the 3R structure of graphite (space group *R-3m* with hexagonal lattice constants, a= 2.516Å and c=10.206Å), Hull reported the more familiar 2H structure which adopts space group $P6_3/mmc$ with a= 2.47Å and c=6.80Å.

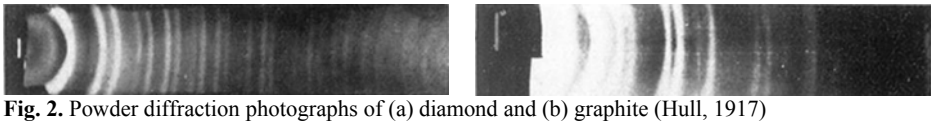

Fig. 2. Powder diffraction photographs of (a) diamond and (b) graphite (Hull, 1917)

Hull, like Debye, did not stay long in powder diffraction research (indeed, his short time in powder diffraction was essentially a diversion from his research on thermionic valves) but moved on in GERL to invent, among other things, the magnetron which was later used not only to create the microwave oven but also by the British military in the development of radar.

1.3 Towards disorder

Crystallography developed rapidly in the 1920s and 1930s with an increasing awareness of the power of the technique, particularly when single crystals were available. Powder diffraction, although a powerful tool for fingerprinting and phase identification, suffered (and still does) from a paucity of information compared with what is available from single crystal data. One person deserves a special mention in the development of the powder diffraction technique over the next thirty years and he took the technique in the direction of disorder. Carbon, again, is the principal element of the story; Bertram Warren [13, 14] was the scientist. The Fourier Inversion Method, which provides the pair distribution function, had applied to the diffraction patterns of glass, and Warren was keen to apply the method to other forms of amorphous matter. Carbon black was presumed to be amorphous and Warren collected data from a sample that happened to be in the laboratory. Knowing that carbon black diffracted poorly, he discovered, to his surprise, that the diffraction pattern, when Fourier inverted to provide the atom-atom separations, resulted in a

distribution that was remarkably similar to graphite (Figure 3). He concluded, in his first paper on the subject published in 1934 [15], that carbon black was not a truly amorphous form of carbon stating that "the existence of single graphite layers is very definite and therefore the material is at least mesomorphic. The diffraction data indicate a heterogeneous mixture containing particles which range from single graphite layers up to graphite crystals several layers thick." It was a topic that he returned to throughout his career [16-18] – his last carbon-black paper was published in 1965.

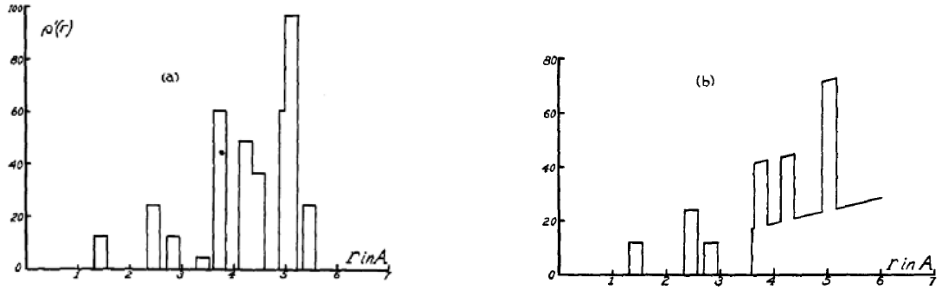

Fig. 3. (a) Atom distribution in a graphite crystal and (b) Atom distribution in carbon black, "a mesomorphic form of carbon, consisting of single graphite layers stacked roughly parallel to one another" [15]. It is noteworthy that while the data are not of the quality obtained with modern instrumentation, the experimental, mathematical and analytical rigour are all of a standard to aspire!

Very significantly, Warren discovered that materials did not fit into neatly defined categories of crystalline and amorphous. Powder diffraction is not simply the domain of crystalline systems – or should not be – and a major objective of this school is to remove the artificial boundaries in the solid-state between crystalline, poorly crystalline and amorphous. Powder diffraction is not synonymous with the Rietveld method – but we are ahead of ourselves – that is the next topic!

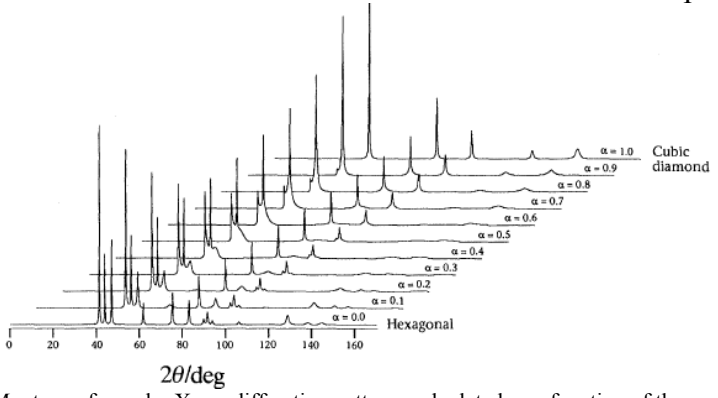

Fig. 4. Montage of powder X-ray diffraction patterns calculated as a function of the probability that layers in a diamond crystal will stack in the cubic diamond sequence. Thus α=0 corresponds to pure lonsdaleite and α=1 corresponds to pure diamond. [19]

As a postscript to this section, it is worth noting that there has been significant subsequent development in the analysis of disordered and partially ordered systems. Deem, Newsam and Treacy (1991) [19] produced an elegant program for calculating the diffraction patterns of faulted and strained crystals. Figure 4 continues the theme of carbon and illustrates the continuous variation of diffraction pattern from diamond to lonsdaleite, the hexagonal variant of diamond. The peak broadening and appearance and disappearance of peaks are particularly noteworthy. Other major developments have been reviewed by Egami and Billinge [20] and Scardi and Leoni [21].

1.4 Neutron powder diffraction and the Rietveld method

The first neutron diffraction experiments were performed in 1945 by Ernest O. Wollan using the Graphite Reactor at Oak Ridge National Laboratory, USA. He was joined shortly afterwards (June 1946) by Clifford Shull, and together they established the basic principles of the technique and applied it successfully to many different materials, addressing problems such as the structure of ice and the microscopic arrangements of magnetic moments in materials [22]. For this achievement, Shull was awarded one half of the 1994 Nobel Prize in Physics with Bertram Brockhouse (who received the reward for his research on neutron triple-axis spectrometers and inelastic neutron scattering). Wollan died in 1984 and did not receive the prize that was rightfully his. It is said that the unusually long delay in awarding the prize was due to the politically incorrect association of neutron diffraction analysis with nuclear power!

While Shull and Wollan performed the first neutron powder diffraction measurements, the most significant contribution from neutron diffraction is almost certainly the development of the structure refinement using the full diffraction profile by Hugo Rietveld in the late 1960s [23, 24]. Fame is assured when one's name becomes an adjective and the technique that is ubiquitous today and has enabled the development of the full power of the powder diffraction method is, of course, now called the Rietveld method [25]. Rietveld's two principal papers [23, 24] are elegantly written and the abstract of his 1969 paper succinctly describes the challenge and his solution.

"A structure refinement method is described which does not use integrated neutron powder intensities, single or overlapping, but employs directly the profile intensities obtained from step-scanning measurements of the powder diagram. Nuclear as well as magnetic structures can be refined, the latter only when their magnetic unit cell is equal to, or a multiple of, the nuclear cell. The least-squares refinement procedure allows, with a simple code, the introduction of linear or quadratic constraints between the parameters."

Rietveld's original program not only enabled the refinement of chemical and magnetic structures but also contained constraints, preferred orientation, peak asymmetry, essentially all the current definitions of R-factors, and the generally used formu-

lation of F_{obs}. He even stated that the method can, in principle, also be extended to X-ray powder diagrams, if a satisfactory function can be found to describe the peak profiles. This had to wait a further decade and then, as with the beginnings of powder diffraction, two groups [26, 27] independently adapted the technique to X-ray data. Malmros and Thomas in the University of Uppsala, Sweden applied the Rietveld method to Guinier-Hagg film data while Khattak and Cox at Brookhaven National Laboratory, USA, demonstrated its feasibility with a conventional focussing X-ray powder diffractometer.

1.5 Back to carbon

The principal purpose of this introductory talk has been to present a short – and very selective – history of the development of powder diffraction. Modern powder diffraction – the topic of this 44th International School of Crystallography – spans an enormous breadth of topics [28-31] from archaeology and applied engineering through to pharmaceutical science and protein crystallography. Given this range of modern powder diffraction, it is probably best to finish the story a few years ago. Carbon, in the form of graphite, carbon black, diamond and lonsdaleite have all featured in the decades of powder diffraction and so it is appropriate to finish with the crystal structure of C_{60}, buckminsterfullerene, the most symmetrical of all molecules.

C_{60} was first identified in a molecular beam in 1985 by Kroto and colleagues [32] who confirmed its truncated dodecahedral shape and icosahedral symmetry. However, it was the discovery of a synthesis route for bulk C_{60} [33] that led to the dramatic development of fullerenes and subsequently carbon nanotubes. The crystal structure was soon identified to adopt a face-centred cubic lattice [34-36] that contained orientationally disordered molecules at room temperature which ordered below 249K to a primitive cubic *Pa3* symmetry. Neutron powder diffraction measurements [37] not only determined the subtle deviations from spherical behaviour in the high temperature phase (Figure 5a) but also revealed an orientational glass transition which was explained by the presence of two crystallographically distinct orientations (Figures 5b and c).

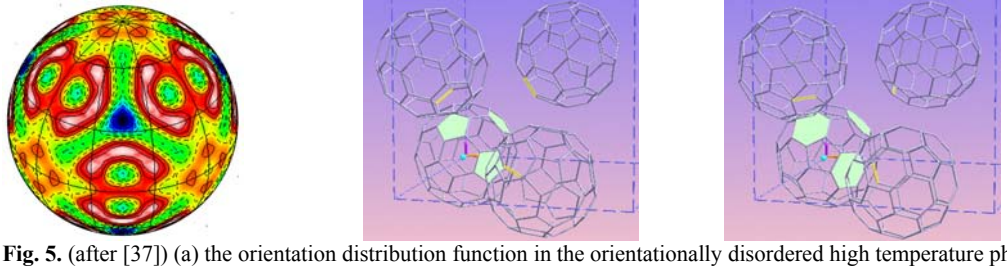

Fig. 5. (after [37]) (a) the orientation distribution function in the orientationally disordered high temperature phase. White represents excess density and blue low density – the overall deviation from spherical symmetry is only *ca.*10%; (b) and (c) the two distinct C_{60} orientations in the low-temperature phase. The orientation with pentagons (b) aligned along ~110 directions pointing towards the C=C bonds are lower in energy than the "hexagon" orientation (c). This energy difference is calculated from powder diffraction data alone.

The most symmetrical of molecules is itself two-fold disordered in the ordered low-temperature phase and this disorder is paradoxically a consequence of the very high molecular symmetry. More recent neutron powder diffraction analysis [38] has not only obtained very precise measurements of these orientations at 4K but has also determined the single and double bond lengths to an extreme precision (see Table 1) and modelled the orientational single-particle diffuse scattering (Figure 6). These latest results would not have been possible without substantial developments in instrumentation, driven in significant part by advances in electronics (see Section 2), but also by progress in powder diffraction software – in this case, specifically the implementation of computer algebra in TOPAS [39] (see Table 2).

Table 1 Structural data for C_{60} obtained from HRPD, ISIS in 1991 and 2007. a, b_d and b_d are the 4K lattice constant and double and single bond lengths while ϕ_p, ϕ_h and n_p are the rotation angles along 111 for "pentagon" and "hexagon" orientation and the fraction of "pentagon" orientation at 5K. The increase in 2007 precision is a consequence of the larger Q range and also the refinement parameterisation.

year	a (Å)	b_d(Å)	b_s(Å)	ϕ_p (°)	ϕ_h (°)	n_p
1991	14.04212(4)	1.391(18)	1.455(12)	98 (fixed)	38 (fixed)	0.838(2)
2007	14.04225(2)	1.39745 (30)	1.44953 (15)	99.751 (3)	41.915 (15)	0.8276 (9)

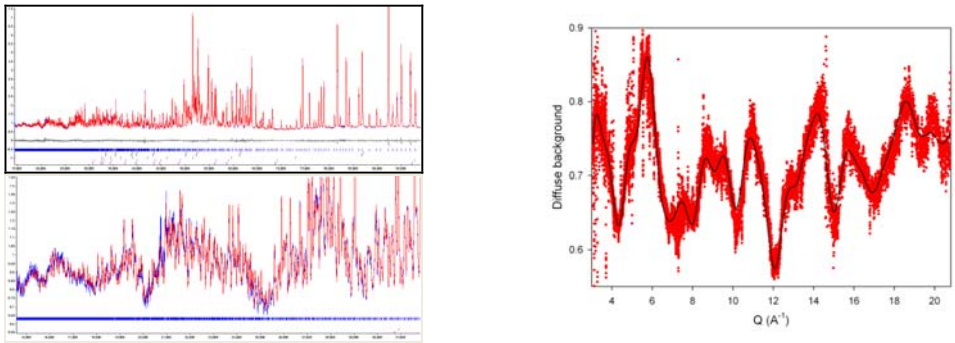

Fig. 6. (a) Observed and calculated 2007 HRPD neutron powder diffraction of C_{60} at 4K (top) the full range of data from 0.3Å to 2.0Å and (bottom) the new range available in 2007 from 0.3Å to 0.6Å containing ~1500 new reflections, (b) the background fitted in TOPAS as part of a Rietveld refinement using a single molecule diffuse scattering model to a Q_{max} of 21Å^{-1}. [38]

Table 2 Part of the TOPAS input file for the 4K refinement of C_{60} that defines all atomic positions in the standard orientation based solely on C-C and C=C bond lengths. A single rotation angle C_{60} is required to define the atomic coorindates of each of the "pentagon" and "hexagon" orientations. The script highlights the power of computer algebra in TOPAS to define the refinement in terms of the appropriate parameters. [38]

```
prm bsing  1.45022`_0.00014 .
prm bdoub  1.39646`_0.00025.
prm !b0  =  (2.*bsing + bdoub)/(3.*acel) ; :  0.10200`_0.00001
prm !eps = (bsing - bdoub)/(2.*bsing + bdoub);        .
prm !tau 1.6180339887498948482045868343656.
.
prm !xx01 = 0.;.
prm !yy01 = b0*(0.5-eps); :  0.04972`_0.00000.
prm !zz01 = 1.5*b0*tau; :  0.24756`_0.00002.
prm !xx02 = -0.5*b0*tau*(1.+eps); : -0.08355`_0.00001.
prm !yy02 =  0.5*b0*(2.-eps); :  0.10136`_0.00001.
prm !zz02 =  0.5*b0*((1.+eps)*(1.-tau)+3.*tau); :  0.21564`_0.00002.
prm !xx03 = -xx02; :  0.08355`_0.00001.
prm !yy03 =  yy02; :  0.10136`_0.00000.
prm !zz03 =  zz02; :  0.21564`_0.00000.
prm !xx04 = -0.5*b0*(1.+eps);  : -0.05164`_0.00000.
prm !yy04 =  0.5*b0*((1.+eps)*(tau-1.)+3.); :  0.18491`_0.00002.
prm !zz04 =  0.5*b0*tau*(2.-eps);  :  0.16401`_0.00001.
prm !xx05 = -xx04; :  0.05164`_0.00000.
prm !yy05 =  yy04; :  0.18491`_0.00000.
prm !zz05 =  zz04; :  0.16401`_0.00000.
```

2. Powder diffraction – the power of Moore's Law

The previous section noted the importance of advances in computing power in the development of the powder diffraction method. It would have been impossible to utilise the Rietveld method without computers and early measurements were restricted by both the computer speed and also the extremely small computer memories compared with modern-day machines. Initially, a single cycle of Rietveld analysis could be measured in hours and diffraction data collection was limited to a few thousand datapoints per day. Figure 7 shows the increase in data collection rates for neutron powder diffraction instruments since 1947. The graph follows an exponential Moore's Law growth suggesting that computer memory is the limiting factor, rather than neutron sources, at the frontiers of neutron scattering. Time-of-flight instruments such as GEM and WISH require massive raw files for collecting data as a function of both scattering angle and time of flight. These instruments would be impossible to build and operate without massive data storage and rapid data reduction facilities. The ability to store and collate data rapidly is also crucial in the development of ultra-fast X-ray powder diffraction measurements.

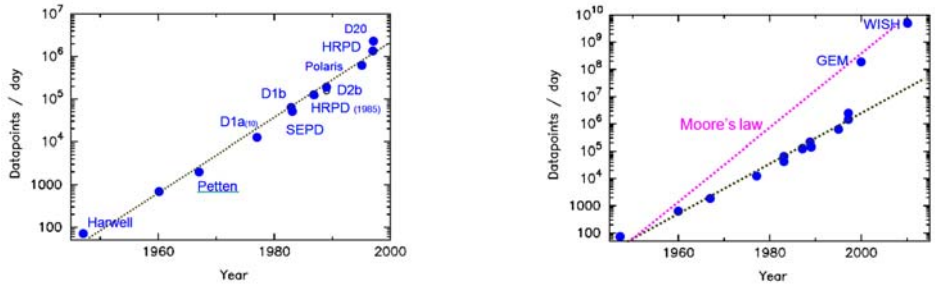

Fig.7. The exponential rise in raw data collection rates for neutron powder diffraction. The early measurements at Harwell by George Bacon were written down by hand – around 100 data points were collected each day. The Petten measurements are attributed to Hugo Rietveld and mark the beginning of the Rietveld method.

3. The four most important decades – from the Ångstrom to the micron – the domain of powder diffraction

In the previous sections, we have discussed the development of powder diffraction over the decades of the 20th century and emphasised the central importance of the decades of growth in computer speed and memory. However, the decades of the 20th century have not only transformed powder diffraction but all of science and this has been fuelled by the growth in electronics that has taken us, within the span of a single scientific career, from kilobytes to megabytes, gigabytes, terabytes and, just over the horizon, petabytes. But there is another set of decades, the decades of length scales that are also worthy of mention. The shortest length-scale that has meaning in our universe is the Planck length, $\ell_P = \sqrt{(\hbar G/c^3)}$, which represents the granularity of space itself. Coming in at around 1.6×10^{-35}m., it is unbelievably small and, of course, at present is a conjecture and not proven. The smallest distance that has been measured and probed comes in at $\sim10^{-20}$m., around 10^{-5} of the diameter of a proton. This is, of course, the domain of particle physics which represents our quest to understand the fundamental particles and interactions and the underlying laws that govern our universe. At the other length of the length spectrum is the dimension of the visible universe itself. Multiplying the estimated age of the universe, 13.75±0.11 billion years, by the speed of light leads to a massive 1.3×10^{26}m. This is domain of astronomy and cosmology where we can observe and understand but cannot touch nor change. Within the 61 orders of magnitude from the Planck length to the size of the visible universe, there are four decades from the ångstrom to the micron that already dominate the science of the 21st century and will continue to define our future technological developments. The ability to synthesise, visualise, understand and modify objects on these length-scales place powder diffraction, along with other techniques such as electron microscopy, at the centre of the discovery and development of 21st century science and technology.

References

1. http://www.iucr.org/publ/50yearsofxraydiffraction
2. W. Friedrich, P. Knipping and M. v. Laue, *Sitz. Ger. Bayer. Akademie d. Wiss*. (1912).
3. W.H. Bragg "The Specular Reflexion of X-rays". *Nature* **90** 410 (1912)
4. W.L. Bragg "The Diffraction of Short Electromagnetic Waves by a Crystal". *Proc. Cam. Phil. Soc.* **17** 43 (1913)
5. W.H. Bragg "The Reflection of X-rays by Crystals. (II)" *Proc. Roy. Soc. Lond.* **A89** 246-248; W.L. Bragg "The Structure of Some Crystals as Indicated by their Diffraction of X-rays". *Proc. Roy. Soc. Lond.* **A89** 248-277; W. H. Bragg and W. L. Bragg "The structure of the diamond" *Proc. Roy. Soc. Lond.* **A89** 277-291 (1913)
6. M. v. Laue "Concerning the detection of X-ray interferences" Nobel Lecture, November 12, 1915, http://nobelprize.org/nobel_prizes/physics/laureates/1914/laue-lecture.pdf
7. P. Debye *Ann. Physik* **46** 809 (1915)
8. P. Debye and P. Scherrer, *Physik. Z.,* **17** 277 (1916)
9. http://www.iucr.org/__data/assets/pdf_file/0015/771/hull.pdf
10. A.W. Hull, "A New Method of X-Ray Crystal Analysis" *Phys. Rev*. **10**, 661-96 (1917).
11. A.W. Hull, "A New Method of Chemical Analysis" *J. Am. Chem. Soc.* **41**, 1168-75 (1919).
12. A.W. Hull, "The X-Ray Crystal Analysis of Thirteen Common Metals" *Phys. Rev.* **17**, 571-88 (1921).
13. http://ww1.iucr.org/people/warren.htm; http://www.iucr.org/__data/assets/pdf_file/0020/785/warren.pdf
14. B.E. Warren, "X-ray diffraction" Addison-Wesley, Reading MA/Dover, Mineola NY (1969/1990)
15. B.E. Warren, "X-ray powder diffraction study of carbon black", *J. Chem. Phys.* **2** 551-555 (1934)
16. J. Biscoe and B.E. Warren, "An X-Ray Study of Carbon Black", *J. Appl. Phys.* **13** 364-371 (1942)
17. C. R. Houska and B.E. Warren, "X-Ray Study of the Graphitization of Carbon Black" *J. Appl. Phys.* **25** 1503-1509 (1954)
18. B.E. Warren and P. Bodenstein "The Shape of Two-Dimensional Carbon Black Reflections" *Acta Cryst.* **20**, 602-604 (1966)
19. M.M.J. Treacy, J.M. Newsam & M.W. Deem "A General Recursion Method for Calculating Diffracted Intensities From Crystals Containing Planar Faults" *Proc. Roy. Soc. Lond.* **A433**, 499–520 (1991) ; http://www.public.asu.edu/~mtreacy/DIFFaX_manual.pdf
20. T. Egami and S. J. L. Billinge, Underneath the Bragg peaks: structural analysis of complex materials, Pergamon Press Elsevier, Oxford England (2003)
21. P. Scardi, M. Ortolani and M. Leoni, "WPPM: microstructural analysis beyond the Rietveld method" *Materials Science Forum* **651**, 155-171 (2010); M. Leoni, J. Martinez-Garcia and P. Scardi, *Materials Science Forum* **651**, 173-186 (2010);
22. C.G. Shull: Early development of neutron scattering" *Rev. Mod. Phys.* **67** 753–757 (1995)
23. H.M. Rietveld "Line Profiles of Neutron Powder-Diffraction Peaks for Structure Refinement" *Acta Cryst.* **22** 151-152 (1967)
24. H.M. Rietveld "A profile refinement method for nuclear and magnetic structures", *J. Appl. Crystallogr.* **2** 65–71 (1969).
25. R.A. Young, ed., "The Rietveld Method" Oxford University Press & International Union of Crystallography. ISBN 0-19-855577-6 (1993)
26. G. Malmros and J.O. Thomas, "Least-squares structure refinement based on profile analysis of powder film intensity data measured on an automatic microdensitometer" *J. Appl. Crystallogr*. **10** 7-11 (1977)
27. C.P. Khattak and D.E. Cox, "Profile analysis of X-ray powder diffractometer data: structural refinement of $La_{0.75}Sr_{0.25}CrO_3$" *J. Appl. Crystallogr.* **10** 405-11 (1977)
28. W.I.F. David, K. Shankland, L.B. McCusker and C. Baerlocher, eds., "Structure determination form powder diffraction data" Oxford University Press & International Union of Crystallography. ISBN 0-19-850091-2 (2002)
29. V. Pecharsky and P. Zavalij, "Fundamentals of Powder Diffraction and Structural Characterization of Materials" Springer. ISBN 0-387-09578-0 (2008).
30. E.H. Kisi and C.J. Howard, "Applications of neutron powder diffraction" Oxford University Press & International Union of Crystallography. ISBN 0198515944 (2008)
31. R.E. Dinnebier and S.J.L. Billinge, eds., "Powder Diffraction: Theory and Practice" RSC Publishing. ISBN: 978-1-84755-823-7 (2008)
32. H.W. Kroto, J.R. Heath, S.C. O'Brien, R.F. Curl and R.E. Smalley, "C_{60}: buckminsterfullerene", *Nature* **318**, 162-3 (1985)
33. W. Krätschmer, D. Lowell, D. Lamb, K. Fostiropoulos & D.R. Huffman, "Solid C_{60}: a new form of carbon", *Nature* **347**, 354-358 (1990)

34. P.A. Heiney, J.E. Fischer, A.R. McGhie, W.J. Romanow, A.M. Denenstein, J.P. McCauley Jr., A.B. Smith III, and D.E. Cox, "Orientational Ordering Transition in Solid C_{60}," *Phys. Rev. Lett.* **66**, 2911-2914 (1991).
35. R. Sachidanandam and A.B. Harris, "Comment on 'Orientational ordering transition in solid C_{60}'" *Phys. Rev. Lett.* **67**, 1467–1467 (1991)
36. W.I.F. David, R.M. Ibberson, J.C. Matthewman, K. Prassides, T.J.S. Dennis, J.P. Hare, H.W. Kroto, R. Taylor and D.R.M. Walton "Crystal Structure and Bonding of Ordered C_{60}" *Nature* **353** 147-149 (1991)
37. W.I.F. David, R.M. Ibberson and T. Matsuo, "High resolution neutron powder diffraction - a case study of the structure of C_{60}." *Proc. Roy. Soc. Lond. A - Mathematical Physical and Engineering Sciences,* **442** 129-146 (1993)
38. W.I.F. David and R.M. Ibberson (in preparation) (2011)
39. A.A. Coelho, TOPAS Academic; http://www.topas-academic.net/

Electron Crystallography – New methods to explore structure and properties of the nano world

Ute Kolb
Institute of Physical Chemistry, Johannes-Gutenberg University Mainz, Mainz Germany

Introduction

Structural elucidation of materials is a key step in the characterization of their physical properties, and therefore of particular interest to both academics and industry. The majority of spectroscopic methods are used to investigate the molecular structure whereas diffraction experiments allow as well analysis of the crystal structure. Quantitative crystallography dates back to 1780, when Carangeot invented the contact goniometer in order to measure the angles between the faces of a crystal [1]. Already in 1850 Bravais introduced the concept of polar axes describing a unit cell but only when Wilhelm Conrad Röntgen (University of Würzburg and Munich, first Nobel Prize in physics 1901) discovered X-rays in 1895 Bravais's concept could be featured by scaling these axes, called reciprocal axes [1]. First diffraction experiments on zinc-blende by Max von Laue (University of Munich, Nobel Prize in physics 1914) and co-workers Friedrich and Knipping [2] together with the interpretation of the data by William Lawrence Bragg in 1912 (University of Cambridge, Nobel Prize in physics 1915 together with W.H. Bragg) started the era of crystal structure analysis [3]. In the next decades crystallography and especially single crystal structure analysis developed rapidly. Severe technical improvement (x-ray sources, goniometers, detectors and automation) reduced the accessible crystal size, to about 1 mm^3 for standard laboratory sources down to a few μm^3 using synchrotron radiation [4], but beyond this X-ray data collection needs to be extended to measure crystal ensembles, i.e. crystal powder.

The first X-ray powder diffraction data (XRPD) was collected by Peter Debye and Paul Scherrer [5] and in parallel by Albert Hull in 1914 [6] but the sparsity of achievable data in comparison to single crystal measurements hampered the development of XRPD analysis. An important step was performed by Bertram Warren with the analysis of carbon black in 1934 [7]. Using the Fourier Inversion Method to calculate the pair distribution function (PDF) he discovered that carbon black is not amorphous but consists of single or multiple graphite layers. Structure solution using XRPD developed rapidly in the following years being accelerated by the development of a method by Ernest O. Rietveld in the field of neutron diffraction in 1945 [8]. The Rietveld method allows the usage of the full diffraction profile for structure refinement. XRPD, for which well consolidated structure analysis routines exist, utilizes the diffraction of X-rays on samples consisting of many small crystallites. Exactly this circumstance provides one of the strongest advantages of XRPD namely

that the data is collected from the bulk sample and not from a selected crystal which may not be representative for the material. On the other hand the simultaneous measurement of many crystallites leads to the reduction of three dimensional diffraction data to one dimensional data. The resulting reflection overlap, apart from the mere multiplicity, can happen systematically in the case of high symmetric space groups (e.g. cubic case (511)/(333)) or accidentally dependent on cell dimensions and space group. This prevents the direct analysis of many peaks and enforces an estimation of the underlying intensities. Additionally, peak profile shapes may be strongly biased by broadening due to small crystallite size in the nano regime and asymmetry due to strain effects, which both may appear even in an anisotropic manner. The uncertainties in intensity determination hamper structure solution significantly. Even cell parameter determination and thus indexation of the diffraction pattern can be problematic or impossible and is enhanced for samples consisting of multiple phases or containing impurities. XRPD typically uses crystals of 1-10 μm but can utilize smaller crystals as well. The borderline caused by crystal-size driven peak broadening (Scherrer equation [9]) is about 100nm for inorganic structures and approx. 300nm for organics.

Electron microscopy

1924 Louis de Broglie postulated that to every particle with matter and speed a wavelength can be assigned. Inspired by this, the first diffraction experiments using electrons were performed by Clinton Joseph Davisson and Lester Germer in the low-energy range [10] and by George Paget Thomson and A. Reid in the high-energy range [11] both in 1927. Thomson (University of Cambridge) shared with Davisson (Bell-Laboratories, New York City) the Nobel Prize in 1937. 1931 Ernst August Friedrich Ruska (University of Berlin, Nobel Prize 1986) and Max Knoll build the first electron microscope prototype based on electron lenses and Ruska succeeded to beat the resolution of an optical microscope in 1933 [12]. The advantage of using electron radiation is that structural information can be collected from areas of a few tens of nanometres [13]. This is possible because the charged electron undergoes coulombic interaction and has therefore a stronger interaction with matter. In addition, electron microscopy is the only method where imaging and diffraction can be performed on the same sample volume.

A few crystal structures containing light elements were solved by single crystal electron diffraction data [14-16] but due to problems related to dynamical scattering in electron diffraction, as described by the theory of multibeam dynamical scattering developed by Cowley and Moodie 1957 [17] the main attention focused on high-resolution transmission electron microscopy (HRTEM) and only a few scientists continued to use quantitative electron diffraction data for structure analysis. HRTEM proved to be successful in solving heavy atom positions in inorganic structures, and also some of the more radiation resistant organic molecules after the necessary point-to-point resolution of less than 4 Å has been surpassed in the late 1960's. Later

imaging by scanning transmission electron microscopy (STEM) gained increasing importance [18], especially after highly sensitive high angular annular dark field detectors (HAADF) were developed. Substantial efforts were dedicated to the construction of field emission guns, delivering a highly coherent and bright electron source. Additionally, elemental analysis methods such as energy dispersive X-ray spectroscopy (EDX) or electron energy loss spectroscopy (EELS) were implemented. In parallel, various preparation methods have been invented in order to optimize the production of electron transparent samples.

With increasing interest in synthesis and characterization of nano particles high resolution transmission electron microscopy (HRTEM) gained more and more importance. Unfortunately, based on lens aberrations of axially symmetric electromagnetic lenses the resolution is limited to about 100 times the used wavelength (Scherzer theorem [19]) and is coupled to the spherical aberration of the microscope. The only chance to achieve higher resolution was to use higher acceleration voltages thus increasing beam damage. High resolution imaging in general requires a relatively strong illumination and thus a large electron dose on the sample. Under these conditions, nearly all organic and most of inorganic materials suffer a fast deterioration due to beam damage. This leads to a modification of the crystalline structure or to complete amorphization or sublimation of the sample [20, 21]. Therefore one of the biggest improvements of TEMs, developed recently, is the design of non-axial symmetric lenses that can correct these lens aberrations [22] thus allowing the usage of low-voltage for imaging purposes. Nowadays, aberration correctors for STEM and HRTEM are available in order to achieve sub-Ångstrom resolved images [23].

Electron diffraction, which provides 3D sub-Ångstrom structural information with good signal-to-noise ratio in reciprocal space, is usually performed using a parallel illumination (Bragg diffraction) of the specimen and selecting the area of interest by insertion of a selected area aperture in the image plane of the objective lens. Illumination of the sample with a higher beam convergence leads to diffraction discs rather than focused spot patterns. Electron diffraction in high-convergence mode (convergent-beam electron diffraction – CBED also referred to as nano-beam diffraction (NBD) or micro-diffraction) traditionally uses the disc patterns to extract cell parameters and space group information including the existence of inversion symmetry [24-26]. CBED recently showed its potential for “ab-initio” structure solution of materials based on extracted intensities [27]. This technique almost has no applications to beam sensitive materials since high convergence of the beam introduces high electron dose at the sample which many materials cannot tolerate. Furthermore, long crystallographic axes cause overlap of the diffraction disks and limit the useful information in CBED patterns.

In order to utilize electron diffraction for structure solution dynamical scattering had to be reduced or taken into account. In the attempt to avoid these effects a group in Moscow used texture patterns and solved several inorganic and organic structures

successfully [28-31]. Textured samples are large aggregates of regularly oriented small crystals. These are achieved by different techniques, for instance by use of orienting supports, mechanical action or application of an electrical field. Other scientists focused on organic or biological samples since for these materials dynamical effects are small and in a first approximation kinematic [32-34]. A third approach is the preparation of thin samples and the combination of information from HRTEM imaging with electron diffraction patterns [35-37]. In 1994, the precession electron diffraction (PED) technique was developed by Vincent and Midgley as another approach to reduce dynamical effects in electron diffraction patterns [38-41]. This method is based on the precession of the incident primary electron beam which is inclined away from the optical axis of the TEM. A diffraction pattern recorded in this mode is the sum of patterns produced by the precessing beam sequentially. The intensities of the reflections are integrated throughout the reciprocal volume covered by the precessing Ewald sphere and show reduced dynamic diffraction effects. Having the ability to access more kinematic diffraction data the use of two and three dimensional PED for structural investigations dramatically increased in recent years [42-46]

Other attempts for structure solution, were performed in combination with imaging, or focused on weak scatterer such as organic [47, 48] or biological samples [49-51] which were expected to deliver nearly kinematical diffraction data. A further approach to reduce dynamical effects was the use of very thin crystals (e.g. less than 50 Å) so that intensities can be estimated proportional to F^2 and will be sufficient for structure solution [52-54] was applied.

Scope of the school

The first day of this school is dedicated to provide the basic knowledge of electron diffraction and crystallography. Here symmetry considerations in direct space are connected to reciprocal space, ranging from the discussion of phase transformations to lattice defects and twinning. The theory of kinematical and dynamical diffraction is covered as well as the basic mechanism of TEM image formation. Finally an introduction to structure solution strategies is provided.

The next sequence discusses the combination of HRTEM images and diffraction data taken with parallel illumination for structure solution; followed by a comparison of reflections appearing in “in-zone” (oriented) and “off-zone” (non-oriented) diffraction patterns. Subsequently, the concept of electron beam precession and automated diffraction tomography, two methods collecting diffraction “off-zone” and their use for structure solution will be described.

A broad range of powerful and robust structure solution methods have been developed in the X-ray world already and many of the approaches can be adapted to electron diffraction data as well. This covered by the lectures joined with the XRPD school. Direct methods, i.e. “ab-initio” structure solution methods, relying only on

diffraction data will be covered as well as the principles of global optimization methods.
Structure solution depends mainly on data quantity and needs only a certain amount of intensity accuracy. When it comes to structure refinement the quality of the intensities becomes more and more important. In the following sequence the improvement of intensity determination using different approaches is discussed.
In addition to the above described structure solution path special possibilities concerning the optimization of data acquisition, - processing and –analysis are discussed.
The next sequence will cover several convergent beam electron diffraction techniques which can be used in various ways to carry out precise analysis of cell parameters, symmetry and intensities. Advantages and optimal usage of these methods will be discussed.
Protein crystallography is an outstanding topic and one day is dedicated to it, because these samples need to be treated in a special ways according to sample preparation, data collection and structure analysis methods.
Beside dedicated diffraction methods high resolution imaging is an important tool to investigate crystals. Many specialities like defects, stress, superstructures and incommensurate structures can be investigated in such a way. In addition, the new development of aberration corrected TEMs and STEMs will be described.
The last day is dedicated to a selection of properties which can be measured directly or derived from crystal structures of certain classes of materials.

Conclusion

Based on new technical developments electron diffraction is an upcoming method for structural investigation of matter on the nano scale. The possibility to computer control data acquisition as well as the vast improvement of computer performance for data processing supports new methods. These methods deliver improved data quantity and quality for “ab-initio” structure solution and increase the amount of accessible crystal structures significant. Moreover, new developments like aberration correction, open up imaging to beam sensitive materials. The topics covered in this school are hoped to connect the above mentioned methods in order to provide a substantial overview.

References

[1] http://www.iucr.org/publ/50yearsofxraydiffraction

[2] W. Friedrich, P. Knipping and M.v.Laue, *Sitzung der Bayerischen Akademie der Wissenschaften* (1912).

[3] W.H. Bragg, "The Specular Reflexion of X-rays" *Nature* **90** 410 (1912); W.L. Bragg "The diffraction of short Electromagnetic Waves by a crystal", Proc. Cam. Phil. Soc. 17 43 (1913); W.H. Bragg, "The reflections of X-rays by Crystals (II)" *Proc. Roy. Soc. Lond.* **A89** 246-248; W.L. Bragg "The structure of some Crystals as indicated by their Diffraction of X-rays" *Proc. Roy. Soc. Lond.* **A89** 248-277

[4] Holton, J.M. and Frankel, K.A., "The minimum crystal size needed for a complete diffraction data set", *Acta Cryst.* **D66**, 393-408 (2010)

[5] P. Debye *Ann. Physik* **46** 809 (1915); P. Debye and P. Scherrer, *Physik. Zeitschrift*, **17** 277 (1916)

[6] A.W. Hull „A new method of X-ray crsytal analysis" *Phys. Rev.* **10** 661-96 (1917); A.W. Hull "A new method for chemical analysis" *J. Am. Chem. Soc.* **41** 1168-75 (1919); A.W. Hull "The C-ray Crystal Analysis of thirteen Common Metals", *Phys. Rev.* **17** 571-588 (1921)

[7] B.E. Warren "An X-ray powder diffraction study of Carbon Black" *J. Chem. Phys* **2** 551-555 (1934)

[8] H.M. Rietveld "A profile refinement method for nuclear and magnetic structures" *J. Appl Crystallogr.* **2** 65-71 (1969)

[9] P. Scherrer, *Göttinger Nachrichten Gesell.*, **2** 98 (1918)

[10] C.J. Davisson and L.H. Germer, *Nature* **119** 558-560 (1927) and *Phys. Rev.* **30** 705 (1927)

[11] G.P. Thomson and A. Reid, *Nature* **119** 890 (1927)

[12] E. Ruska und M. Knoll, „Die magnetische Sammelspule für schnelle Elektronenstrahlen, *Z. techn. Physik.* **12** 389–400 und 448 (1931); M. Knoll und E. Ruska, „Das Elektronenmikroskop", *Zeitschrift für Physik* **78** 318–339 (1932); E. Ruska, „The Electron Microscope as Ultra-Microscope, *Research and Progress* **1** 18–19 (1935)

[13] Cowley, J.M., Goodman, P., Vainshtein, B.K., Zvyagin, B.B., Dorset, D.L., 2001 in *International tables for crystallography*, edited by Shmueli U., Volume B, Reciprocal space, 2nd edn. (Dordrecht: Kluwer Academic Publishers)

[14] Cowley, J. M., Structure analysis of single crystals by electron diffraction. II. Disordered boric acid structure 1953, *Acta Cryst.* 6, 522–529.

[15] Cowley, J. M., Structure analysis of single crystals by electron diffraction. III. Modification of alumina, 1953, *Acta Cryst.* 6, 846–853.

[16] Rigamonti R., La struttura della catena paraffinica studiata mediante i raggi di elettroni, Gazzetta Chimica Italiana 1936, 66, 174-182.

[17] Cowley, J. M. and Moodie, A. F. The scattering of electrons by atoms and crystals. I. A new theoretical approach, *Acta Cryst*. **10**, 609–619 (1957); II. The effects of finite source size, 1959, *Acta Cryst*. **12**, 353–359 (1959); III. Single-crystal diffraction patterns 1959, *Acta Cryst*. **12**, 360–367 (1959).

[18] Pennycook, S.J., *Z*-contrast transmission electronmicroscopy-direct atomic imaging of materials *Annu. Rev. Mater. Sci.* **22**, 171–195 (1992).

[19] O. Scherzer, Z- Phys. **101** (1936) p593.

[20] Spence, J.C.H., 2003, *High-Resolution Electron Microscopy*, 3rd edn. (New York: Oxford University Press).

[21] Reimer, L., Kohl, H., 2008, *Transmission Electron Microscopy*, Physics of Image Formation, 5th edn. (New York: Springer).

[22] H. Rose Optik **85** (1990) p19.

[23] M. A. O'Keefe, Seeing Atoms at Sub-Ångstrom Resolution with Aberration-Corrected TEM, Microscopy and Microanalysis 2004, 10 (Suppl 2), 972.

[24] Tanaka, M., Terauchi, M., Kaneyama, T., Tsuda, M. and Saitoh, K. (1985) Convergent Beam Electron Diffraction, vol I-IV, JEOL, Tokyo.

[25] Sung, C. M. and Williams, D. B. (1991). A bibliography of CBED papers from 1939-1990, *J. Elect. Microsc. Tech.*, 17, pp. 95-118.

[26] Buxton, B.F., Eades, J.A., Steeds, J.W. and Rackham, G.M., The symmetry of electron diffraction zone-axis patterns. *Phil. Trans. Roy. Soc. London* 1976, A281, 181–184.

[27] Nakashima, P.N.H., Moodie, A.F., Etheridge, J., Structural phase and amplitude measurement from distances in convergent-beam electron diffraction patterns, Acta Cryst. 2007, A63, 387-390.

[28] Pinsker, Z. G. (1949). Diffraktsiya Elektronov. Moscow/Leningrad: Akad. Nauk SSSR Press. Engl. transl: Electron Diffraction (1953). London: Butterworths.

[29] Zvyagin, B. B. (1967). Electron Diffraction Analysis of Clay Mineral Structures. New York: Plenum Press.

[30] Vainshtein, B. K. (1956). Strukturnaya Elektronographiya. Moscow: Izd'vo Akad. Nauk SSSR. Engl. transl: Structure Analysis by Electron Diffraction (1964). Oxford: Pergamon Press.

[31] Vainshtein, B. K., Zvyagin, B. B. & Avilov, A. S. (1992). Electron Diffraction Techniques, Vol. 1, edited by J. M. Cowley, p. 216. Oxford University Press.
[32] Geil, P.H., Nylon single crystals. *J. Polymer Sci.* 1960, 44, 449–458.
[33] Dorset D.L. Structural electron crystallography,(1995) Plenum. New York
[34] Dorset, D., Gilmore, C., Prospects for kinematical least-squares refinement in polymer electron crystallography, *Acta Cryst.* 2000, A56, 62-67.
[35] Hovmöller, S., Sjogren, A., Farrants, G., Sundberg, M. and Marinder, B.-O., Accurate atomic positions from electron microscopy. *Nature* 1984, 311, 238–241.
[36] Voigt-Martin, I. G., Yan, D. H., Wortmann, R., Elich, K., The use of simulation methods to obtain the structure and conformation of 10-cyano-9,9'-bianthryl by electron diffraction and high-resolution imaging, *Ultramicroscopy* 1995, 57, 29-43.
[37] Weirich, T. E., Ramlau, R., Simon, A., Hovmöller, S. & Zou, X. D. *Nature* (London), 1996, 382, 144–146.
[38] Vincent,R.and Midgley, P. A., *Ultramicroscopy* 1994, 53, 271.
[39] A. Avilov, K. Kuligin, S. Nicolopoulos, M. Nickolskiy, K. Boulahya, J. Portillo, G. Lepeshov, B. Sobolev, J. P. Collette, N. Martin, A. C. Robins, P. Fischione, Ultramicroscopy 107, 431 (2007).
[40] M. Gemmi, S. Nicolopoulos, *Ultramicroscopy* 2007, 107, 483.
[41] Own, C.S., System design and verification of the precession electron diffraction technique, Ph.D. Thesis, http://www.numis.northwestern.edu/Research/ Current/precessions, Northwestern University Evanston Illinois 2005
[42] Gjønnes J., Hansen V., Berg B.S., Runde P., Cheng Y.F., Gjønnes K., Dorset D.L., Gilmore C.J.: Structure Model for the Phase Al_mFe Derived from Three-Dimensional Electron Diffraction Intensity Data Collected by a Precession Technique. Comparison with Convergent-Beam Diffraction, *Acta Crystallographica A* 1998, 54, 306-319.
[43] Gemmi M., Zou X., Hovmöller S., Migliori A., Vennström M., Andersson Y.: Structure of Ti_2P solved by three-dimensional electron diffraction data collected with the precession technique and high-resolution electron microscopy, *Acta Crystallographica A* 2003, 59, 117-126.
[44] Gjønnes J., Hansen V., Kverneland A.: The Precession Technique in Electron Diffraction and Its Application to Structure Determination of Nano-Size Precipitates in Alloys, *Microscopy and Microanalysis* 2004, 10, 16-20.
[45] Weirich T.E., Portillo J., Cox G., Hibst H., Nicolopoulos S.: Ab initio determination of the framework structure of the heavy-metal oxide $Cs_xNb_{2.54}W_{2.46}O_{14}$ from 100 kV precession electron diffraction data, *Ultramicroscopy* 2006, **106**, 164-175.
[46] Gemmi M., Nicolopoulos S.: Structure solution with three-dimensional sets of precessed electron diffraction intensities, *Ultramicroscopy* 2007, 107, 483-494.
[47] Dorset, D.L., Hauptman, H.A., 1976, *Ultramicroscopy*, **1**, 195.
[48] Dorset, D.L., 1995, *Structural Electron Crystallography,* (New York: Plenum Press).
[49] Dorset, D.L., 1995, *Proc. Natl. Acad. Sci.*, **92(22)**, 10074.
[50] Kühlbrandt, W., Wang, D. N., Fujiyoshi, Y., 1997, *Nature*, **367**, 614.
[51] Unwin, P.N.T., Henderson, R., 1976, *J. Mol. Biol.*, **94**, 425.
[52] Nicolopoulos, S., González-Calbet, J.M., Vallet-Regí, M., Corma, A., Corell, C., Guil, J.M., Pérez-Pariente, J., 1995, *J. Am. Chem. Soc.*, **117**, 8947.
[53] Weirich, T.E., Ramlau, R., Simon, A., Hovmöller, S., Zou, X., 1996, *Nature,* **382**, 144.
[54] Wagner, P., Terasaki, O., Ritsch, S., Nery, J.G., Zones, S.I., Davis, M.E., Hiraga, K., 1999, *J. Phys. Chem.*, **B103**, 8245.

Data collection: good practices

Kenneth Shankland
School of Pharmacy, University of Reading, Whiteknights, PO Box 224, Reading, UK

Abstract. The diffraction data collection stage is arguably the single most important one in determining the success or otherwise of a crystallography experiment. Choosing the right instrument for the task in hand is one major factor, but how that instrument is setup and how the sample is presented are just some of the many others. Many of the problems associated with data analysis are mitigated if the correct data collection schemes are employed.
Data collection in powder diffraction is often seen as a routine step that is merely a stepping stone to the more important structure elucidation / interpretation stage. Whilst there is an element of truth in this view, the reflection overlap problem in powder diffraction has always meant that it is a stage that should not be taken for granted. In particular, the way in which data are collected should reflect the intended outcome of the diffraction experiment. If, for example, one merely wishes to confirm the presence of some known crystalline phase within a sample, then a rapid scan over some limited 'diagnostic' region of 2θ will be sufficient. If, on the other hand, a full Rietveld refinement of an unknown phase is required, then data extending to high values of 2θ will be required. The following is a non-exhaustive list of factors that should be taken into consideration when attempting to match experiment to outcome.

Radiation source: The most obvious division here is the choice between laboratory X-rays and synchrotron X-rays. The former have the advantage of ease-of-access and experiments that are less constrained in time than those performed at a synchrotron, and modern diffractometers can accommodate a wide variety of sample environment equipment to allow control of, for example, temperature and humidity. The limited flux available from a conventional sealed-tube source is mitigated to some extent by advances in detector technology, with 1D detectors collecting several degrees of diffracted data simultaneously and 2D detectors collecting entire diffraction rings, albeit at lower resolution. As such, a great many experiments that used to be candidates for synchrotron time can now be performed in-house. Nevertheless, tuneable wavelengths and the flux attainable at synchrotron sources offers some significant advantages, including the use of crystal analyser detectors for very high resolution and complex sample environments. One downside of the intense incident beam is the possibility of radiation damage to the sample, which in extreme cases can limit data collection times to a few seconds or less [1]. In such cases, large

curved detectors such as the MYTHEN [2] can be used to compensate and robotic sample changers can be used to ensure that fresh sample is always available for exposure to the beam.

Neutron diffraction experiments are confined to central facilities, but neutrons may be the radiation of choice for particular classes of samples or experiment e.g. sample that exhibit very strong X-ray absorption or experiments with bulky and complex sample environment. Recent source and instrumental developments have also challenged the traditional view that hydrogenous materials are not good candidates for powder neutron diffraction [3,4]. In particular, the use of long wavelength neutrons from cold sources and large detector arrays can be used to improve the level of discrimination between coherent Bragg diffraction and the incoherent background associated with the presence of hydrogen atoms. This can obviate the need to deuterate organic samples, conferring an obvious advantage, given that deuteration is often non-trivial and frequently expensive.

For simplicity, subsequent sections in this report will assume that one is working with laboratory-based PXRD and that the incident radiation is monochromatic Cu $K\alpha_1$, bearing in mind that non-monochromated tubes offer significantly greater incident flux and that some diffractometers are now shipped with Mo-based tubes ($\lambda \sim$ half that of Cu) and others with Ag-based tubes [5] ($\lambda \sim$ one third that of Cu). We will also assume that the diffractometer has been well aligned such that reflection positions are recorded accurately.

Reflection versus transmission: Figure 1 shows schematic views two commonly-used geometries for laboratory-based X-ray diffraction.

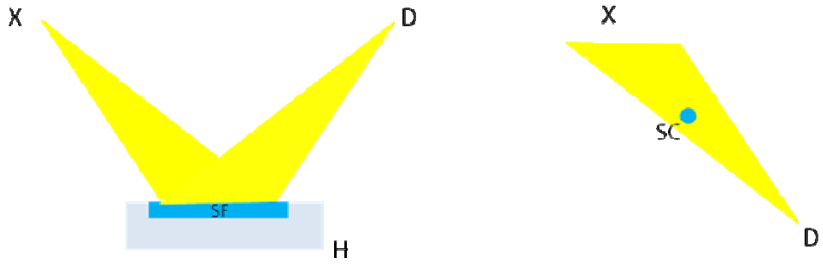

Fig. 1. Schematic view of two laboratory-based powder X-ray diffraction experiments. In the reflection setup (left) the beam from the X-ray tube (X) is divergent onto the flat sample (SF) held in the sample holder (H). Reflection from the surface of the sample focusses the beam on the detector (D), giving high resolution and high count rates. In the transmission setup (right) the beam from the X-ray tube is convergent on the sample, which is contained in a capillary (SC, perpendicular to the plane of the paper.

The reflection mode has the advantage of combining high resolution with good count rates. Material is typically packed into the depression of a plastic sample holder and a coupled scan (i.e. one in which the sample stage and the detector are moved in sync, in order to enable access to high values of 2θ within the confines of

a relatively small radiation safety cabinet) performed to collect the data. If only limited amounts of powder are available, good results can still be achieved by sprinkling a thin layer of powder onto a 'zero-background' plate. Indeed, this may be the preferred mode for indexing of materials containing only light atoms, as it avoids the problem of sample transparency (where diffraction peaks are shifted to lower values of 2θ) when thick layers of sample are present in normal sample holders. Preferred orientation, where sample crystallites arrange in some non-random fashion on the reflection plate, is a common problem, resulting in reflection intensities that deviate in some systematic manner from those obtained from a random distribution of crystallites. Transmission geometry, in which the X-rays pass *through* the sample contained in a rotating glass capillary, is extremely effective in mitigating the effect of preferred orientation, and is the preferred mode for collecting accurate reflection intensity data from samples that do not contain strongly absorbing elements. The glass capillaries are *typically* 0.7mm in diameter: this represents a good compromise between the amount of sample required, exposing a representative number of crystallites in the beam and the resulting recorded diffraction peak widths. Smaller capillaries may give narrower peaks, but they may also prove very difficult to fill and the reduced number of crystallites in the beam can lead to long count times. If the diffraction peak width is sample limited, as opposed to instrument limited, then decreasing capillary size offers only disadvantages. If only small very amounts of sample are available, then the sample can be presented as a thin layer, held between two sheets of kapton or mylar film, at 90° to the incident beam. The detector is then scanned in 2θ to record the diffraction pattern. This mode offers high resolution, at a cost of increased count times and the presence of a significant 'bump' in the diffraction pattern between 4 and 5° if kapton film is used [6]. Regardless of the diffraction geometry, the use of some collimation device (such as a knife edge) is essential to reduce the background scattering that is visible at low angle, close to the path of the straight through beam.

As mentioned above, capillary geometry is the preferred mode for the collection of data that most accurately reflects the 'true' distribution of intensities. Recently, however, systems that aim to reduce the presence of preferred orientation in non-capillary setups have been introduced. For example, the InXitu benchtop XRD system uses a piezo-electric transducer to induce powder 'flow' inside the sample holder, through which the X-rays are shone. The system is highly effective and provides a useful alternative geometry, particularly for use in field conditions when coupled with a low-power microfocus X-ray source [7].

Sample preparation: There are no hard and fast rules as to the best way to prepare a powder sample for optimal data collection. If the crystallite size is too large, then there will be an insufficient number of crystallites exposed to the incident beam to provide good particle averaging. Furthermore, there may be difficulties filling a

capillary. Particle size reduction (typically light grinding) will correct these problems, but carries the dual risk of (a) pressure or temperature induced phase transformation and (b) increased peak widths due to crystallite size / strain changes. The latter, of course, may not actually be noticeable, if the limiting factor in the diffraction experiment is the instrumental resolution. As such, some level of experimentation will almost certainly be required in order to achieve the best overall diffraction pattern. Hill and Madsen have summarised some useful guidelines for overcoming sample-related problems [8].

Count time schemes: The majority of powder diffraction patterns are still collected in the simplest way possible, with a detector being scanned at some constant rate across the 2θ range of interest. This, despite the fact that it has been reported for many years by many authors that *variable* count time (VCT) schemes provide significant advantages when it comes to (in particular) the structure refinement stage [9, 10]. The idea is simple - match the time spent counting at any particular point in the diffraction pattern to the expected diffraction intensity at that point. The average drop in intensity across a pattern, attributable to the Lorentz-polarisation effect and the form-factor fall off, can easily be calculated. From this, for example, it is easy to obtain a count time scheme needed to collect the same number of photons for any given E magnitude, irrespective of its position in the pattern:

$$t(\theta) \propto (\sin\theta \sin 2\theta) / [f_{av}(\theta) \exp(-2B_{av} \sin^2\theta / \lambda^2)]$$

where θ is the diffraction angle, f_{av} is a representative atomic scattering factor, B_{av} is an estimated overall temperature factor, λ is the incident wavelength and $t(\theta)$ is the calculated detector dwell time. The resultant continuous scheme is usually approximated as a series of ranges (Figure 2) and the introduction of diffractometer control software (e.g. XRD Commander [11]) that directly supports the use of such schemes should see their increasing adoption.

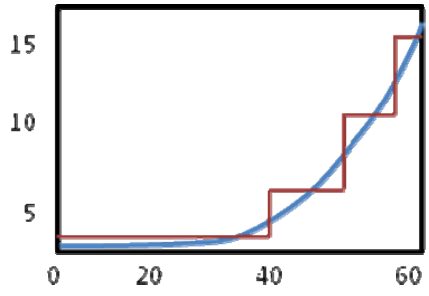

Fig. 2. An example of a variable count time scheme, with detector dwell time in seconds plotted (blue line) against diffraction angle in two theta. The continuous scheme is approximated, for simplicity of implementation, as a series of four ranges of different count times (red line).

Variable temperature: Data collection at low temperatures can provide significant benefits in the case of materials that do not scatter strongly at high angle; decreased thermal vibration leads to increased intensity. Data collection at multiple temperatures provides a further benefit for materials that exhibit anisotropic thermal expansion i.e. materials whose unit cell dimensions vary differently in response to changes in temperature [12, 13]. Such dimension changes result in changes in the reflection positions in the diffraction pattern, with reflections that are overlapping at one temperature often well resolved at another (Figure 3).

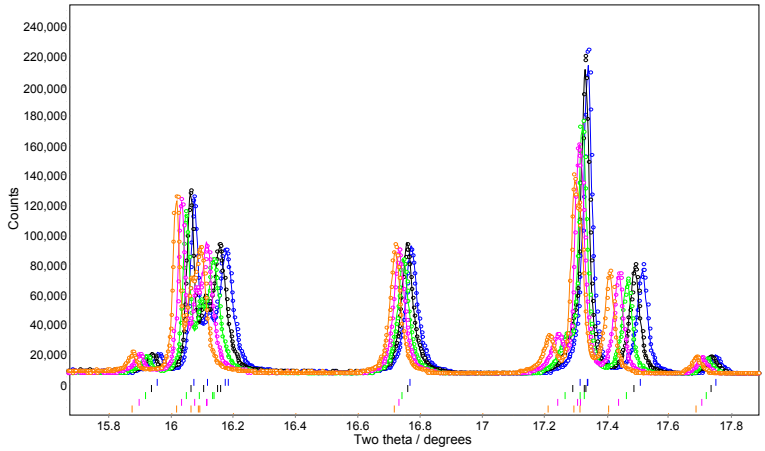

Fig. 3. A section of the final observed and calculated plot for the Pawley fit to five datasets collected from the molecular organic compound chlorothiazide (R_{wp} = 5.04): 90 K=blue, 120 K=black, 150 K=green, 180 K=pink, 210 K=orange. Note in particular the tickmarks at (a) ~16.1°, showing reflections (0 2 2) and (1 2 1) split at 90 K, completely overlapping by 180 K and crossed-over at 210 K ; (b) ~17.3°, showing reflections (1 1 -2) and (0 -2 1) splitting as the temperature is increased from 90 K to 210 K [13].

With appropriate processing, a composite data set, which is more single-crystal like in terms of its information content, can be constructed from multiple sets collected over a range of temperatures. Typically, four or five data sets, collected with $\Delta T \approx$ 30K between sets, is required to make a useful gain for structure solution purposes. For indexing, a similar approach may well prove useful in resolving overlapping reflections. Similar improvements in the accuracy of individual measured intensities can be achieved by deliberately exploiting texture in samples [14], though the temperature based method has the advantage of simplicity of implementation. It is even possible to exploit radiation-damage-induced lattice changes to aid with the intensity extraction process [15].

Summary: Problems encountered in sample preparation for PXRD experiments can usually be overcome with a little foresight and appropriate use of geometry and sample presentation equipment. Problems that exist for one class of compounds may be absent for another and it is always wise to consult specific literature (e.g. [16]) to learn from the experiences of others. For a general overview of sample

preparation and data collection in powder diffraction, one could do much worse than to consult the chapter of Hill and Madsen [8].

Acknowledgements

I am grateful to my many collaborators in experimental powder diffraction and in particular to Bill David, Alastair Florence, Norman Shankland and the staff of BM16/ID31 of the ESRF.

References

1. http://en.wikibooks.org/wiki/Xray_Crystallography/Radiation_Damage
2. A. Bergamaschi, A. Cervellino, R. Dinapoli, F. Gozzo, B. Henrich, I. Johnson, P. Kraft, A. Mozzanica, B. Schmitt & X. Shi. "The MYTHEN detector for X-ray powder diffraction experiments at the Swiss Light Source". *Journal of synchrotron radiation*, (2010). 17(5), 653.
3. P. F. Henry, M. T. Weller and C. C. Wilson. "Neutron powder diffraction in materials with incoherent scattering: an illustration of Rietveld refinement quality from nondeuterated gypsum " J. Appl. Cryst. (2009). 42, 1176-1188
4. http://www.isis.stfc.ac.uk/instruments/wish/science/wish-science6445.html
5. The Philips X'Pert PRO MPD system and the Bruker D8 Advance can both be equipped with Cu, Mo or Ag sources.
6. A. J. Florence, B. Baumgartner, C. Weston, N. Shankland, A. R. Kennedy, K. Shankland & W. I. F. David, Indexing powder patterns in physical form screening: Instrumentation and data quality. *Journal of Pharmaceutical Sciences*, (2003), 92,1930.
7. http://www.inxitu.com/html/BTX.html
8. R. J. Hill and I. C. Madsen in "Structure Determination from Powder Diffraction Data", OUP (2002).
9. I. C. Madsen & R. J. Hill, "Collection and analysis of powder diffraction data with near-constant counting statistics". *Journal of Applied Crystallography*, (1994), 27,385.
10. K. Shankland, W. I. F. David & D. S. Sivia, Routine ab initio structure determination of chlorothiazide by X-ray powder diffraction using optimised data collection and analysis strategies. *Journal of Materials Chemistry*, (1997), 7,569.
11. http://www.bruker-axs.com/index.php?id=basicmeasurementpa
12. M. Brunelli, J. P. Wright, G. B. M. Vaughan, A. J. Mora, A. N. Fitch "Solving Larger Molecular Crystal Structures from Powder Diffraction Data by Exploiting Anisotropic Thermal Expansion" *Angew. Chemie Int. Ed.* (2003) 42, 2029–2032.
13. P. Fernandes, K. Shankland, W. I. F. David, A. J. Markvardsen, A. J. Florence, N. Shankland & C. K. Leech, A differential thermal expansion approach to crystal structure determination from powder diffraction data. *Journal of Applied Crystallography*, (2008), 41,1089.
14. C. Baerlocher, L. B. McCusker, S. Prokic & T. Wessels, Exploiting texture to estimate the relative intensities of overlapping reflections. *Z. Kristall.*, (2004), 219,803.
15. C. Besnard, F. Camus, M. Fleurant, A. Dahlström, J. P. Wright, I. Margiolaki, P. Pattison and M. Schiltz (2007). "Exploiting X-ray induced anisotropic lattice changes to improve intensity extraction in protein powder diffraction: Application to heavy atom detection". Zeitschrift für Kristallographie Supplements: Vol. 2007, No. suppl_26, pp. 39-44.
16. I. Margiolaki, J. P. Wright, A. N. Fitch, G. C. Fox, A. Labrador, R. B. Von Dreele, K. Miura, F. Gozzo, M. Schiltz, C. Besnard, F. Camus, P. Pattison, D. Beckers & T. Degen. "Powder diffraction studies on proteins: An overview of data collection approaches". *Z. Kristall.*, (2007), 1.

Rietveld refinement

Peter W. Stephens
Dept Physics & Astronomy, SUNY Stony Brook, Stony Brook, NY, USA

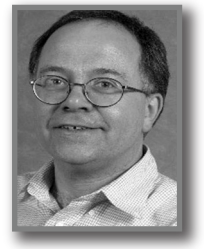

Preface

Rietveld refinement is generally the last stage of structure determination. The determination of unknown structures generally proceeds through a series of hypotheses of lattice, space group, atomic structure, each of which is subject to subsequent verification, so Rietveld refinement is the final test of the correctness of a structure. Unfortunately, there are not such clear tests of the veracity of a Rietveld refinement as there are of single crystal structures, and so a clear understanding of the process is required to judge a correct solution. This talk will not directly address another frequent use of the technique, quantitative phase analysis, although many of the principles discussed here are relevant.

There are any number of widely used programs, several of which will be discussed in subsequent talks at this school. I will therefore emphasize general features of the process over specific implementations. All of us who use the technique owe a great debt to people who have worked hard to write software, provide useful documentation and tutorials, and assist others in its use.

Introduction

In powder diffraction, unlike a single crystal experiment, the 3D diffraction pattern is compressed into one dimension. While each (*hkl*) diffraction peak occupies a specific position, the density of peaks rapidly rises with increasing diffraction angle 2θ (or decreasing time of flight in a pulsed neutron experiment) that most peaks are overlapped, and it is a non-trivial task to separate their intensities.* A nice example of a pre-Rietveld structure determination from powder x-ray data is Zachariasen's (1951) solution of cubic Pu_2C_3.[1] The structure was solved by determining the intensity of a set of diffraction peaks, and then choosing space group and coordinate(s) to fit. This works well for reasonably high symmetry, for relatively simple structures (only the Pu atom was considered in matching intensities, and the number and location of C atoms was inferred), and for people as ingenious as Zachariasen.

* For notational convenience I will restrict this discussion to angle-dispersive experiments, with absolutely no prejudice against pulsed neutron techniques.

The Rietveld method, in use since 1969, goes the other direction.[2] From a hypothesized structure, one calculates the diffraction pattern to compare with the measured diffraction profile, i.e., intensity as a function of 2θ in a step scan. That allows a treatment of overlapping peaks which, we will see, allows the maximum amount of information to be extracted from an experimental pattern. This was originally done for relatively low resolution CW neutron data from a reactor, for which it was possible to give a fairly accurate model lineshape. In general, one imagines that the lineshape, which depends on a convolution of instrumental parameters and sample microstructure, can be specified more or less independently of the crystal structure (peak positions and intensities), so that a simultaneous refinement of lineshape and structure can be factored into reliable information about each, separately. We will return to this point subsequently.

For the purpose of this discussion, we assume that an approximate structural model (lattice parameters, space group, atom positions) is at hand. Our task is to optimize those various parameters, while keeping a close watch for any symptoms that the starting point was incorrect and needs to be revisited. The information in a powder diffraction pattern consists of:

- Peak positions, which depend on lattice dimensions and space group,
- Peak intensities, which depend on the distribution of atoms within the unit cell,
- Peak shapes, which are a convolution of instrumental parameters and the microstructure of the sample.

Crystallographic structure starts with the unit cell, defined by translation vectors $\boldsymbol{a}$, $\boldsymbol{b}$, $\boldsymbol{c}$. Diffraction peaks form a reciprocal lattice spanned by vectors $\boldsymbol{a}^*$, $\boldsymbol{b}^*$, $\boldsymbol{c}^*$ such that any diffraction peak can be specified as $\boldsymbol{Q}=h\boldsymbol{a}^*+k\boldsymbol{b}^*+l\boldsymbol{c}^*$, defined as $\boldsymbol{a}^*=2\pi(\boldsymbol{b}\times\boldsymbol{c})/\boldsymbol{a}\cdot(\boldsymbol{b}\times\boldsymbol{c})$, *etc*. The diffracting planes for each reflection are separated by $d=2\pi/|\boldsymbol{Q}|$, and the diffraction condition that the vector difference between incident and diffracted radiation wave vectors $\boldsymbol{k_i}$ and $\boldsymbol{k_f}$ (of equal magnitude $2\pi/\lambda$) is $\boldsymbol{Q}=\boldsymbol{k_f}-\boldsymbol{k_i}$ is equivalent to Bragg's law, $\lambda=2d\sin\theta$. The above definitions are those commonly used in the physics community; others frequently drop all of the factors of 2π in the equations and definitions in the foregoing paragraph. The position of a peak in a powder pattern can be obtained from the magnitude of $\boldsymbol{Q}$, and the equations above can be put in the convenient form $\sin^2\theta=(\lambda^2/4d^2)=(\lambda^2/4)(Ah^2+Bk^2+Cl^2+Dkl+Ehl+Fhk)$, where the metric parameters A, …, F depend only on the real (or reciprocal) lattice parameters.

In a powder pattern, the integrated intensity of a given peak is

$$I(hkl) = cM_{hkl}\left|\sum_{\text{atoms } j} f_j \exp 2\pi i\left[hx+ky+lz\right]\exp -2W\right|^2 \mathrm{g}LP(\theta)$$

Here c is an overall scale factor, M_{hkl} is the multiplicity of the given peak, LP is the Lorentz-Polarization factor, *e.g.*, $LP(\theta)=1/(\sin\theta\sin 2\theta)$ for x-rays polarized perpendicular to the scattering plane and a detector scanning 2θ with constant solid

angle. f_j is the atomic scattering factor of the j^{th} atom, including consideration of partial or mixed occupancy, and $\exp{-2W}$ is the Debye-Waller factor. The sum runs over all atoms in the unit cell, including symmetry equivalent positions generated by the space group. Details of the derivation and implementation of this equation are given in any comprehensive crystallography text, e.g., Giacovazzo *et al.*[3]

Lineshape

In order to obtain a computed powder pattern, $Y^{calc}(2\theta)$, one must model the peak shape, taking into account contributions both of the sample microstructure and the diffractometer. Treatment of all of these effects is well beyond the scope of this paper, but we can briefly summarize the usual approach to Rietveld refinement. The comprehensive text edited by Dinnebier and Billinge contains much more detail.[4]

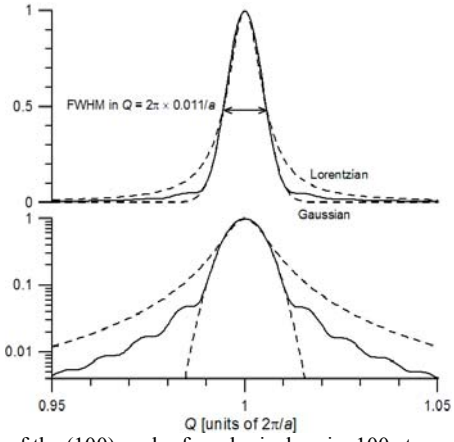

Fig.1. Computed powder lineshape of the (100) peak of a spherical grain, 100 atoms in diameter.

Size: Consider the case of an ideal lattice, truncated to spherical shape. Figure 1 shows the powder-averaged lineshape, computed from the Debye equation, for a sphere with a diameter of one hundred lattice spacings. The full width at half maximum of this peak is $\Gamma = 0.011 \times 2\pi/a$ in Q. The Scherrer equation, $L = K\lambda/\Gamma_{2\theta}\cos\theta$, is frequently used to estimate crystallite size L, where K is a numerical constant having something to do with the (assumed) shape of the grains and $\Gamma_{2\theta}$ is the diffraction peak FWHM in radians. The numerical computation that led to Fig. 1 gives $K \approx 1.10$ for a particle of spherical shape. Powder samples with a single grain size are rare in practice; a distribution of grain sizes will wash out the observed peak shape function and further obscure the relationship between peak width and grain size.

For almost all Rietveld refinements of crystal structures, the microstructural details that could be extracted from the lineshape are secondary to the desire to have a simple analytical model, and so one can imagine that the ideal lineshape function might be modeled as a Gaussian or Lorentzian. Figure 1 shows Gaussian and

Lorentzian lineshapes of the same full width at half maximum, from which it is obvious that the one has tails that are too weak, and the other, too strong. It is generally satisfactory to use an interpolation of the two, for example, a pseudo-Voigt centered at $2\theta_0$,

$$f(2\theta) = \eta \frac{\Gamma/4\pi}{(2\theta - 2\theta_0)^2 + \Gamma^2/4} + (1-\eta)\frac{\sqrt{4\ln 2}}{\Gamma\sqrt{\pi}} \exp - \left(\frac{(2\theta - 2\theta_0)^2}{\Gamma^2} 4\ln 2 \right),$$

normalized to unit integrated intensity, with full width at half maximum Γ, and interpolation parameter η.

Strain: Another sample dependent effect frequently encountered is microstrain, whereby the peak width in Q is proportional to the diffraction order, *i.e.*, the width in 2θ grows in proportion to tanθ. One could rationalize that effect by imagining that some form of disorder causes each crystallite to have a slightly different lattice parameter. A more microscopically satisfying description would come from considering the internal strains within each individual crystallite caused by lattice defects, and then computing the diffraction pattern so produced. However, this requires a lot more effort than is usually justified for a crystal structure analysis. Especially in high resolution measurements, it is frequently found that fitting experimental lineshapes require more elaborate models of size or strain, *e.g.*, to take account of anisotropic broadening; these are available in most Rietveld software, and are beyond the scope of the current treatment.

Combining the effects of size and strain, and imagining that contributions to the width of a diffraction peak can be modeled as a convolution, it is plausible that the observed width in diffraction angle 2θ could be written as $\Gamma_{2\theta} = X/\cos\theta + Y\tan\theta$, where X and Y are parameters that represent the size and strain contributions. (This expression is justified if both contributions are regarded as Lorentzians, whose widths add directly in convolution. For Gaussians, the widths would add in quadrature.)

The first application of the Rietveld method was to powder neutron diffraction at a CW source, where the instrumental lineshape is essentially a Gaussian whose variance depends on the diffraction angle as $\sigma^2 = U\tan^2\theta + V\tan\theta + W$, where the parameters U, V, and W depend on the width of the collimators, and d-spacings and mosaics of the monochromator.[5] X-ray spectral lines are combinations of several Lorentzians in wavelength, and in high resolution diffractometers with perfect crystals as monochromators and/or analyzers, the intrinsic reflection curves have long ($\Delta\theta^{-2}$) tails. The approach of convoluting the contribution of each optical element, known as fundamental parameters, was described in detail by Klug and Alexander.[6] The utility of fundamental parameters approach has greatly expanded with modern computational techniques, exemplified by Cleary & Coelho.[7] While such methods are extremely powerful, they are generally beyond the scope of this

chapter, and so we will restrict our attention to the more widely used empirical lineshape models.

One important aberration in most powder diffractometers is axial divergence. This produces asymmetric peaks, especially at low diffraction angles. The effect may be visualized as shown in Figure 2, where the diffracted radiation from a given order radiates from the sample as a cone. The edges of the detector slit intercept part of that cone below the nominal diffraction angle, and so there is a tail extending to the low angle side of the peak, which is especially pronounced for low diffraction angles. Several analytical treatments of this effect have been published, and it is incorporated in modern Rietveld programs. In the opinion of this author, unsubstantiated numerical approaches to this effect, such as the split-Pearson VII lineshape, should be avoided.

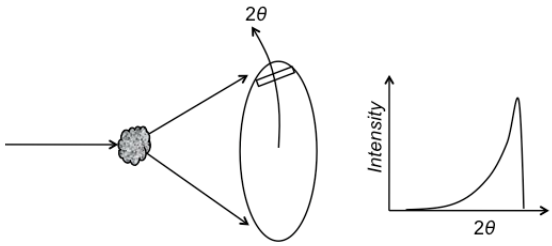

Fig. 2. Sketch illustrating the origin of low-angle tails on diffraction peaks due to axial divergence.

A good point of reference is the lineshape function used in GSAS,[8] which is an approximate (pseudo-Voigt) convolution of a Gaussian with variance $\sigma^2 = U\tan^2\theta + V\tan\theta + W + P/\cos^2\theta$ with a Lorentzian of full width at half maximum (FWHM) $\Gamma = X/\cos\theta + Y\tan\theta$ and an asymmetric function to describe axial divergence of the diffracted beam. The origin of these parameters can be traced to elements of the discussion above, although it is not at all clear how to unravel information about sample microstructure from their converged values. Rietveld codes usually incorporate other parameters for instrumental corrections such as detector offset angle, sample displacement, etc.

Since the purpose of Rietveld refinement is to adjust various structural and lineshape parameters to obtain the best agreement between model and data, it is important to be clear on the figure of merit used. Suppose that the data consists of x-ray intensities collected in a step scan of 2θ, so that the observed intensity and standard error at each point are $Y^{obs}(2\theta)$ and $\sigma_{2\theta}$ respectively. (Here we are regarding 2θ as an index spanning the discrete set of measured data points.) If $Y^{obs}(2\theta)$ is the number of counts detected, $\sigma_{2\theta}$ is simply $(Y^{obs}(2\theta))^{1/2}$, but it is frequently the case that the intensity is not constant through the scan, *e.g.*, for a synchrotron or pulsed neutron source, or if a variable counting time data collection strategy is in use. In that case, $Y^{obs}(2\theta)$ must be normalized to the dose of radiation reaching the sample while the

data point at 2θ was being integrated, and $\sigma_{2\theta}$ scaled by the same factor. If the computed profile is given by $Y^{calc}(2\theta)$, the familiar reduced χ^2 parameter is given by

$$\chi^2 = (N-P)^{-1}\sum_{2\theta}^{N}\left(\frac{Y^{obs}(2\theta)-Y^{calc}(2\theta)}{\sigma_{2\theta}}\right)^2,$$

where N is the number of points in the data set and P is the number of parameters adjusted in the fit. If the deviation between model and observed data is due to the counting statistics alone, one expects χ^2 to be very close to unity. Another parameter frequently used is the weighted profile R-factor, defined as

$$R_{wp} = \sum_{2\theta}\left(\frac{Y^{obs}(2\theta)-Y^{calc}(2\theta)}{\sigma_{2\theta}}\right)^2 \Bigg/ \sum_{2\theta}\left(\frac{Y^{obs}(2\theta)}{\sigma_{2\theta}}\right)^2$$

Again, if differences between model and data are purely due to counting statistics, R_{wp} should approach the expected R-factor, R_{exp}, which is given by

$$R_{exp} = (N-P)\Bigg/\sum_{2\theta}\left(\frac{Y^{obs}(2\theta)}{\sigma_{2\theta}}\right)^2.$$

It is evident $R_{wp} / R_{exp} = \sqrt{\chi^2}$, a number which is also referred to as the "goodness of fit" (GOF).

An obvious question is whether there is some threshold χ^2 or R_{wp} which indicates a correct solution. The answer is no, and this is a source of consternation to people who try to publish refinements, as well as journal editors and referees, who are usually used to the clearer diagnostic signatures of a valid structure from single crystal data. Indeed, in comparing two different Rietveld refinements, even of the same sample, it is not necessarily the case that a better figure of merit indicates superior structural results. This arises partly because the quality of a Rietveld fit depends on details of the data that have little to do with the structure, and partly because most of the information content in a diffraction pattern is at the higher angles where peaks are generally weaker and more strongly overlapped, but likely have less effect on the refinement statistics than a few strong low angle peaks. For this reason, it is recommended to spend more data collection time on the high angle peaks for the refinement of any complicated material. These issues are discussed in greater detail in several useful papers, *e.g.*, references [9] and [10].

In refining a structure, one must be prepared to examine both the fit and the reasonableness of the result in detail. A paper entitled "Rietveld refinement of a wrong crystal structure" provides a cautionary example, although there are significant danger signals in the example discussed there.[11]

Intensity estimation and extraction from powder diffraction patterns

The Rietveld method offers an approximate technique to estimate intensities of partially overlapping peaks from the recorded profile, based in part on the structural

model. Imagine that the computed, normalized profile function of the *n*th diffraction peak is given by $f_n(2\theta)$, so that the computed profile at a given point of the profile is given by

$$Y^{calc}(2\theta) = \sum_{2\theta} I_n f_n(2\theta) + B(2\theta),$$

where B is the background function, and I_n is the integrated intensity of the n^{th} diffraction peak. Measured intensity at a given profile point is attributed to all diffraction peaks in proportion to their calculated contribution at that point, i.e.,

$$I_n^{obs} = \sum_{2\theta} \left(Y_i^{obs}(2\theta) - B(2\theta) \right) \frac{I_n^{calc} f_n(2\theta)}{\sum_m I_m^{calc} f_m(2\theta)}$$

One can then compute the standard crystallographic Bragg R factor comparing "observed" and computed intensities, $R_B = \sum_n | I_n^{obs} - I_n^{calc} | \Big/ \sum_n I_n^{obs}$.

Of course, the estimated intensities are obviously biased by the optimistic model-based division of intensity of unresolved peaks.

It is frequently desired to "deconstruct" a powder diffraction profile into a set of integrated intensities of the diffraction peaks present. Armel Le Bail noted that the Rietveld intensity estimation can be used in an iterative fashion to obtain estimates of the integrated intensities of all peaks in a powder pattern.[12] Cycles of refinement of profile, lattice, and background parameters alternate with reassignments of the set of integrated intensities, and the process is repeated until it converges. Computationally, this is very convenient because most of the work is already performed in the Rietveld program. The method is widely used and has had a tremendous impact on the techniques of structure determination from powder data.

Another method of intensity extraction was pioneered by Pawley, who treated the set of diffraction peak intensities $\{I^{obs}\}$ as parameters in a least squares fit, along side of the profile, lattice, and background parameters.[13] This idea faces the technical obstacle of instability of the refinement when poorly peaks are present. Indeed, the usual Hessian matrix is singular if two peaks have the same position, as occurs, for example, with cubic (333) and (511) reflections. Until relatively recently (~10y), the Pawley method was less used than the Le Bail method, but it is now incorporated into several widely-used Rietveld codes. One direct advantage of the Pawley method is that it provides estimates of the correlation between extracted intensities. This can be used to compare the quality of a structural model much more rapidly than by computing an entire profile R_{wp}.[14] Indeed, it has been shown that no information is lost in reducing a powder diffraction pattern to Pawley intensities and covariance matrix $\boldsymbol{A}$, so that a quality of fit parameter

$$\chi^2 = \sum_{n,m} (I_n^{obs} - I_n^{calc})(A^{-1})_{nm}(I_m^{obs} - I_m^{calc})$$

is just as good as a full pattern Rietveld fit to refine a model (with some subtleties associated with the background.[15] A similar method has been applied to intensities obtained from a Le Bail fit.[16]

Whether the Le Bail or the Pawley method is used, a lineshape fit to an experimental data set is an important intermediate step in determining a crystal structure from powder data. It generally allows accurate refinement of lattice parameters, and a visual inspection can reveal whether a proposed lattice and space group are correct, as well as the presence of impurities. R_{wp} of a Pawley or Le Bail fit can be regarded as the target of a correct structural refinement, insofar as the difference between such a fit and the structural Rietveld refinement lie in the integrated intensities of the diffraction lines.

Example: RB_3C_{60}

We now briefly illustrate some of the preceeding points by analysis of a sample of Rb_3C_{60}.[17] Fig. 3a shows the data, collected at a wavelength of 0.69970Å at beamline X3B1 at the National Synchrotron Light Source, in 2002. The experimental conditions were a double crystal Si(111) monochromator and a Ge(111) analyzer, with no focusing optics. The sample was in a 1 mm diameter capillary, spun about its axis to improve the powder statistics. The illuminated area extended about 8 mm along the capillary, and the horizontal (out of scattering plane) slits before the detector were also 8mm wide, about 300 mm from the sample. Visual inspection of the data reveals that it has face-centered cubic structure, and shows clearly the aforementioned low angle asymmetry.

Fig. 3a actually shows a Pawley fit to the data, with axial divergence refined to a value consistent with the known diffractometer geometry, no observable size broadening, and diffraction FWHM proportional to $\tan\theta$ with roughly equal Gaussian and Lorentzian components. Actually, the strain broadening is slightly anisotropic, with peaks about 30% broader along the {100} directions than along {111}. This can be modeled phenomenologically, and, at least in the case of cubic materials, qualitatively understood as arising from the elastic response to random internal stresses.[18] The background is a quadratic polynomial plus a term in $1/\theta$, plus a broad (pseudo-Voigt) peak centered at 11.5°. This Pawley fit has R_{wp} = 3.61%, $\chi^2 = 2.12$, which, frankly, is about as good as it gets.

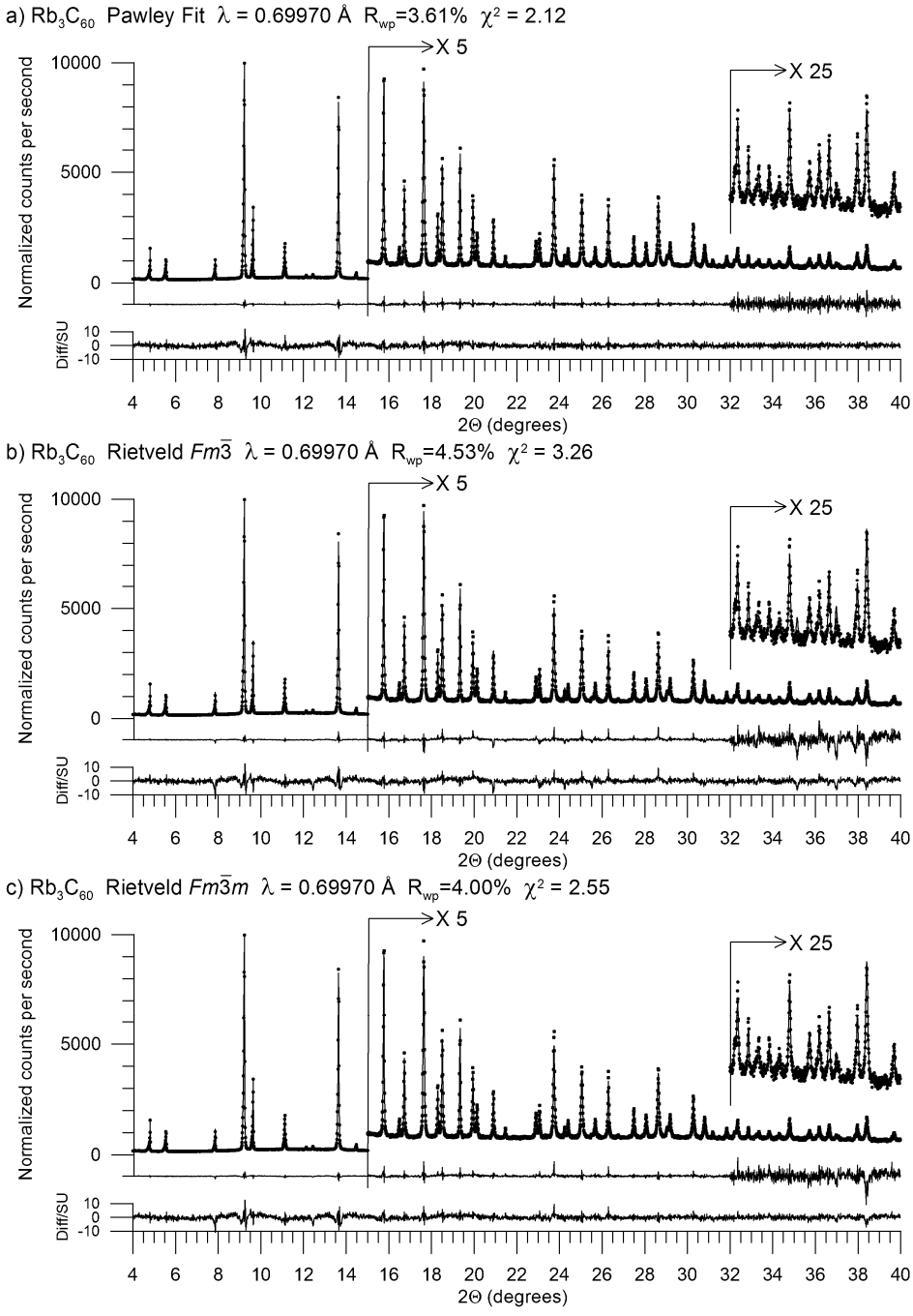

Fig. 3. a) Pawley fit to synchrotron powder x-ray data on Rb_3C_{60}, based on the model described in the text. Note the breaks in vertical scale. Difference curves are shown both in measured intensity (with the same vertical scale changes as the data and model) and as difference divided by the standard uncertainty of each data point (from counting statistics). b) Rietveld refinement in space group $Fm\bar{3}$. c) Rietveld refinement in space group $Fm\bar{3}m$.Ï

With the benefit of hindsight, we can immediately solve the structure. The lattice parameter (14.424 Å) is slightly larger than that of an fcc crystal of C_{60}, and a moment's consideration of the cubic close packing of spheres shows that there are two tetrahedral and one octahedral spaces per sphere, which are clearly the sites of the Rb cations, with fractional coordinates (¼,¼,¼) and (½,0,0) respectively. Examination of a soccer ball leads to the conclusion that it fits naturally into a site of cubic point symmetry, with three-fold axes at the centers of hexagons pointing in the [111] directions, and two-fold axes, at the center of the stitching between two hexagons, pointing in [100] directions. That leads to three crystallographically distinct sites for C atoms: two in general positions (*x, y, z*), and one on the coordinate plane (0*, y, z*). Space group $Fm\bar{3}$ seems the obvious choice, with a multiplicity of 96 in the general position and 48 in the *y*-*z* plane, for a total of 4×60 carbon atoms. Throwing three carbon atoms at random positions, along with the two fixed cations, into a Rietveld program (here, TOPAS, ref. [19]), quickly converges to the decent-looking solution shown in Fig. 3b.

It was previously noted that even subtle problems in a Rietveld refinement can reveal fundamentally incorrect assumptions. As it happens, Fig. 3b is based on an incorrect space group. The fullerene molecule can be rotated by 90° without changing any of the Rb-C distances, which suggests that it could be disordered. Indeed, going to space group $Fm\bar{3}m$ with 50% occupancy of each C position embodies this disorder, and produces the significantly better fit shown in Fig. 3c. Despite the small change in refinement statistics, the better fit is clearly evident, especially at high angles. (Note to skeptics – this disorder appears much more clearly in neutron refinements of Rb_3C_{60}, as well as in the isostructural K_3C_{60}.) The refined bond distances, shown along with refinement statistics in Table I, are also somewhat more plausible in the disordered model. We will stop short of considering further improvements in the model, such as cation vacancies and anisotropic thermal parameters, illustrating the maxim that no Rietveld refinement is ever entirely finished, merely abandoned.

Table 1. Refinement statistics and derived bond lengths of Rb_3C_{60} fits shown in Fig. 3.

	Pawley	$Fm\bar{3}$	$Fm\bar{3}m$
R_{wp} (%)	3.61	4.53	4.00
χ^2	2.12	3.26	2.55
R_B (%)	0.43	2.31	1.26
double bond (Å)		1.346(5)	1.389(8)
double bond (Å)		1.347(7)	1.405(6)
single bond (Å)		1.418(5)	1.442(5)
single bond (Å)		1.494(5)	1.443(5)
single bond (Å)		1.504(5)	1.467(7)
pentagon (deg)		105.0(3)	103.0(4)
pentagon (deg)		109.9(4)	107.1(2)
pentagon (deg)		110.0(2)	111.4(4)
hexagon (deg)		118.2(2)	117.7(3)
hexagon (deg)		118.4(3)	119.2(4)
hexagon (deg)		119.9(2)	120.4(2)
hexagon (deg)		121.6(3)	120.8(4)
hexagon (deg)		121.9(4)	121.9(2)

References

1. W.H. Zachariasen, "The crystal structure of plutonium sesquicarbide," Argonne National Laboratory report #ANL-4631 (1951).
2. H.M. Rietveld, "A Profile Refinement Method for Nuclear and Magnetic Structures," *J. Appl. Cryst.* **2**, 65 (1969).
3. C. Giacovazzo *et al.*, *Fundamentals of Crystallography, 2nd ed.*, Oxford University Press, (2002).
4. R.E. Dinnebier and S.J.L. Billinge, *Powder Diffraction Theory and Practice,* Royal Society of Chemistry, (2008).
5. G. Caglioti, A. Paoletti, and R.P. Ricci, "Choice of Collimators for a Crystal Spectrometer for Neutron Diffraction," *Nuclear Instruments* **3**, 223-228 (1958).
6. H.P. Klug and L.E. Alexander, *X-ray Diffraction Procedures for Polycrystalline and Amorphous Materials*. (Wiley, New York, 1974)
7. R.W. Cheary and A. Coelho, "A fundamental parameters approach to x-ray line-profile fitting," *J. Appl. Cryst.* **25**, 109 (1992).
8. A.C. Larsen and R.B. Von Dreele (1985), "GSAS: General Structure Analysis System," Los Alamos National Laboratory report MS-H805.
9. L.B. McCusker *et al.*, "Rietveld refinement guidelines," *J. Appl. Cryst.* **32** 36 (1999).
10. B.H. Toby, "*R* factors in Rietveld analysis: How good is good enough?" *Powder Diffraction* **21**, 67 (2006).
11. C. Buchsbaum and M.U. Schmidt, "Rietveld refinement of a wrong crystal structure," *Acta Cryst.* B**63**, 926 (2007).
12. A. Le Bail, "Whole Powder Pattern Decomposition Methods and Applications: A Retrospection," *Powder Diffraction* **20**, 316-326 (2005).
13. G.S. Pawley, "Unit-Cell Refinement from Powder Diffraction Scans," *J. Appl. Cryst.* **14**, 357-361 (1981).
14. W.I.F. David, K. Shankland, and N. Shankland, "Routine determination of molecular crystal structures from powder diffraction data," *Chem. Comm.* **1998**, 931.
15. W.I.F. David, "On the equivalence of the Rietveld method and the correlated integrated intensities method in powder diffraction," *J. Appl. Cryst.* B**37,** 621 (2004).
16. S. Pagola *et al.*, "The Structure of Malaria Pigment β-Hematin," *Nature* **404**, 307 (2000); S. Pagola and P.W. Stephens, "*PSSP,* a computer program for the crystal structure solution of molecular materials from X-ray powder diffraction data," *J. Appl. Cryst.* **43**, 370-376 (2010).
17. A. Huq and P. Stephens, "Transition Temperatures and Vacancies in Superconducting Rb_3C_{60}," *Phys. Rev. B* **72**, 092511 (2005).
18. P.W. Stephens, "Phenomenological model of anisotropic peak broadening in powder diffraction," *J. Appl. Cryst.* **32**, 281 (1999); A.R. Stokes and A.J.C. Wilson, "The diffraction of x-rays by distorted crystal aggregates," *Proc. Phys. Soc. London* **56**, 174 (1944).
19. Bruker AXS. "Topas V3: General profile and structure analysis software for powder diffraction data – User's manual," Bruker AXS, Karlsruhe, Germany (2005); A.A. Coehlo, "TOPAS Academic," Coelho Software: Brisbane, Australia. http://www.topas-academic.net (2007)

Structure Solution - an Overview

Lynne B. McCusker and Christian Baerlocher
Laboratory of Crystallography, ETH Zurich, Zurich, Switzerland

Abstract. The structure solution process consists of a series of steps, each requiring decisions and each depending upon the previous ones having been performed correctly. The preliminary steps involve selecting the best sample, choosing the most appropriate radiation, collecting the data, indexing the pattern, determining the most probable space group(s), and estimating the profile parameters. If extracted intensities are to be used for structure solution, something must be done about the overlapping reflections. They can be equipartitioned, or, if necessary, more sophisticated approaches can be applied to improve the partitioning. At this point, the structure solution algorithm most appropriate for the material and the data must be chosen and applied. Finally, the (partial) structural model has to be completed and refined. The art of structure determination from powder diffraction data lies in finding a viable path through the maze of possibilities.

1. Introduction

There has been a veritable explosion in the development of structure determination methodology for powder diffraction data in the last 25 years. What used to be considered a fairly reliable technique for phase identification and perhaps unit cell determination, has become an almost standard one for complete structure analysis: from the determination of a unit cell and space group, to the generation of an approximate structure, to the refinement of that structure. What has caused this modest technique to emerge from the shadow of its immensely superior single-crystal cousin? Certainly, the advances in instrumentation (from radiation sources to detectors and everything in between) and the phenomenal increase in readily available computing power have made many of the developments possible. However, the driving force has come from scientists from disciplines as diverse as physics, chemistry, biology, materials science and geology, who need to know the structures of their polycrystalline materials.

Perhaps the beginning can be traced back to the introduction of the Rietveld method of structure refinement in 1969 [1]. It was soon realized that the structural information hidden in a powder diffraction pattern was not only substantial, but retrievable. Then it was only a small step to ask if there was enough, not only to refine an approximate structure, but also to determine one. The fact that the Rietveld method could be adapted from neutrons to X-rays also played a key role here, because X-ray

powder diffraction patterns are much easier to come by [2]. Once the first few structure solutions were reported, an increasing number of crystallographers took up the challenge. Even today, they continue to push the limits of powder structure analysis to address increasingly complex problems. Three rich sources of information on this topic, besides this conference, can be found in the book entitled *Structure Determination from Powder Diffraction Data*, first published in 2002 [3], a special issue of *Z. Kristallogr*. devoted to the same topic, published in 2004 [4], and a recent review by David and Shankland [5].

The problems to be overcome in structure determination from powder diffraction data are twofold: (1) the basic phase problem, which is central to all crystallographic structure analyses, whether the data be from a single-crystal or a powder diffraction experiment, and (2) the reflection overlap problem, which is specific to powder diffraction data. No single approach to these two problems has emerged as the optimal one. The best approach always depends upon the nature and complexity of the material under investigation, and the quality of the diffraction data. The whole process can be viewed as finding a viable path through a maze of possibilities (Figure 1). Selecting the best path to take is part of the art of structure solution from powder diffraction data. In the following sections, we will wend our way through this maze.

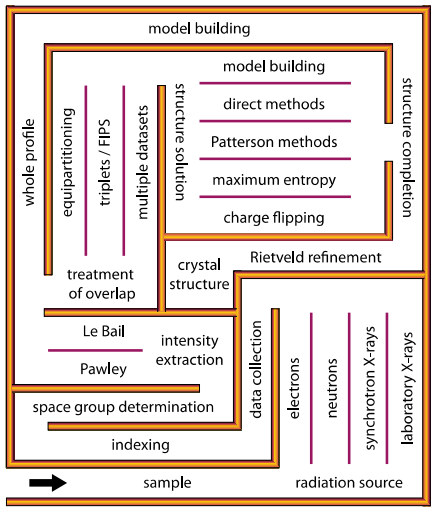

Fig. 1. The structure determination maze.

2. The initial steps

The structure determination process is a sequential one. That is, each step depends upon the previous one being correct. A mistake made early on in the procedure can make all subsequent steps useless, so a careful approach is usually better than a quick one. It may sound trivial, but structure solution begins with the sample. If the

sample is poorly crystallized or contains impurities, structure solution is severly hindered and may become impossible. It is essential that the best sample available be used for the data collection, because all of the following steps are based on these data. It is well worth spending some time on optimizing synthesis conditions to obtain the best possible material.

The first decision to be made is which radiation is best suited to the problem and what parameters should be used for data collection [6]. Are laboratory X-rays sufficient [7] or is the high resolution and/or tunability of a synchrotron source necessary [8]? Would the nature of the sample make a neutron [9] source more appropriate? Is the sample perhaps suited for (nanometer scale) single-crystal electron crystallography?

Once the data have been collected, the pattern has to be indexed and the most probable space group(s) determined [10]. At this point, the positions of the reflections are known and their intensities can be estimated. This is best done with a whole-profile fit, where a peak shape, which can vary as a function of diffraction angle, is assigned to each reflection and its intensity is either refined (Pawley method [11]) or adjusted in an iterative procedure (Le Bail method [12]) to fit the measured data. Fine adjustments to the reflection positions can be made by refining the lattice parameters. This approach to the determination of the reflection intensities can be described as a model-free Rietveld refinement, where the intensities of the reflections rather than the atomic coordinates are optimized [13]. Even if the whole profile rather than the individual reflection intensities are to be used for structure solution, this step is needed to determine the profile parameters (peak width, peak asymmetry, peak shape, peak range, sample displacement, 2θ zero correction, background) and the optimal unit cell. This information is used each time the diffraction pattern of a structural model is calculated, so that it can be compared directly with the measured pattern.

3. Treating overlapping reflections

If the extracted intensities are to be used as input to the structure solution program, something has to be done about the overlapping reflections. The better these are estimated, the closer one comes to single-crystal data and the better the chances of solving the structure. Usually, however, the intensity of a peak resulting from several (overlapping) reflections is simply divided equally over the contributing reflections. This is known as equipartitioning. Although this approach necessarily yields a number incorrect intensties, it has proven to be sufficient for structure solution in many cases.

For the more difficult cases, more sophisticated approaches can be used. Two ways of using the information from non-overlapping reflections in conjunction with simple assumptions such as atomicity and positivity to get a rough estimate of the relative intensities of overlapping reflections have been developed [13].

Should these computational approaches fail, an alternative is to attack the problem experimentally. By collecting multiple datasets on a single sample under different, but controlled conditions, additional information about the relative intensities of overlapping reflections can be obtained. For example, if a sample exhibits anisotropic thermal expansion without undergoing a phase transition (i.e. the reflection intensities remain the same), the overlap pattern in a series of diffraction patterns measured at different temperatures will change as the cell parameters change. Reflections that overlap at one temperature may not at another. By combining the information from the different patterns, better estimates of the individual reflection intensities can be derived [14]. A related approach was used by Von Dreele on a protein sample, whose lattice parameters had changed as a result of solvent-induced and radiation-damage induced strains [15]. Another possibility is to exploit (an induced) preferred orientation of the crystallites. If the crystallites are oriented, the differences in the diffraction patterns measured for different sample orientations can be used in a similar way [16].
Whichever approach is used to treat the overlapping reflections, the final result is a list of reflections with their *hkl* indices and their intensities, from which their structure factor amplitudes |**F**| can be calculated. That is, the list looks like a single-crystal dataset. The |**F**|'s are just not as reliable.

4. Structure solution

There are several algorithms to choose from for structure solution, and the best choice will depend upon the problem at hand. In the early days of structure solution from powder diffraction data, the extracted structure factor amplitudes were simply used as input to one of the single-crystal programs (e.g. direct methods, Patterson or maximum entropy algorithms). These all attempt to solve the phase problem from the diffraction data (i.e. in reciprocal space). Today, several algorithms that take the ambiguity in the intensities of overlapping reflections into account are available. Perhaps the most commonly used structure-solution programs that work in reciprocal space are *EXPO* [17] or *XLENS* [18] for direct methods [19] and *MICE* for maximum entropy [20]. Recently, Rius reported the development of a Patterson-function direct methods program that is particularly well-suited to dealing with powder diffraction data [21].
If reciprocal space methods do not work, structure solution in direct or real space can be tried. This is how single-crystal structures were solved in the days before Patterson and direct methods. That is, a structural model that was consistent with all known information about the material (both diffraction and non-diffraction experimental results) was built, and then its diffraction pattern calculated and compared with the measured one. This is an extremely powerful method, limited only by the imagination of the model builder, and can be used very well with powder diffraction data. The only drawback is that it takes time and patience to build such models and

to check them. It also requires considerable experience and chemical intuition to build the correct model. Fortunately, computers have come along, and algorithms for generating chemically sensible models and checking them have been written. These are generally global optimization methods, most commonly based on either simulated annealing or evolutionary algorithms [5]. The two most commonly used programs for this approach are *Fox* [22] and *DASH* [23].

A few algorithms that exploit the advantages of both reciprocal and real space have also been developed for powder diffraction data. The first of these was the zeolite-specific *Focus* algorithm [24], where the reflection intensities are used in conjunction with starting (usually random) phases to generate an electron density map. This map is interpreted in real space using a framework search routine. The largest fragment from this search is then used to generate a new set of phases and these are combined with the extracted intensities to generate a new electron density map. By going back and forth between real and reciprocal space, information in both realms (e.g. the diffraction intensities and the chemical information about zeolite framework structures) are used actively in the structure determination procedure. Similarly, simulated annealing has been combined with direct methods in the newer versions of *EXPO* [19,25]. The newest algorithm on the scene, charge flipping, is also a hybrid method. It was introduced for single crystals by Oszlányi and Sütő in 2004 [26] and then adapted to powder diffraction data by two separate groups just a few years later [27]. The algorithm combines electron density map generation (generally starting with random phases) in reciprocal space with a density modification in real space (flipping the sign of all densities below a very small positive threshold value). The modified map is then used to calculate new phases, and, as in *Focus*, these are combined with the observed amplitudes to produce a new electron density map for the next cycle. For powder data, an additional loop for the repartitioning of overlapping reflections is added. In the program *Superflip* [28], this repartitioning is coupled to a second density modification in real space involving histogram matching [29]. Coelho has also combined the charge-flipping algorithm with the tangent formula in his program *Topas* [30].

5. Structure completion and refinement

Whichever method is used to solve the structure, the resulting structural model is usually only approximate and may be incomplete. The final, and often most difficult step of the structure solution procedure, is to complete the model and to refine the structure. Before the atomic coordinates can be refined reliably, all atoms have to be found. To do this, the approximate model is used, not only to calculate the phases of the reflections, but also to partition the intensities of the overlapping ones. Then a difference electron density map (measured structure factor amplitudes partitioned according to the model minus those calculated from the model, combined with phases from the model) can be calculated. This is usually good enough to find the

missing atoms and/or to identify problem areas in the model. Finally, the structural parameters are refined using the whole-profile Rietveld method [31].

References

[1] Rietveld, H. M. 1969, A profile refinement method for nuclear and magnetic structures, *Acta Crystallogr.* **2**, 65-71.

[2] Snyder, R.L. 1993, Analytical profile fitting of X-ray powder diffraction profiles in Rietveld analysis, in *The Rietveld Method* R.A. Young, ed., Oxford University Press, Oxford, pp. 111-131.

[3] David, W.I.F., Shankland, K., McCusker, L.B. and Baerlocher, Ch., eds. 2002, *Structure Determination from Powder Diffraction Data*, Oxford University Press, Oxford.

[4] Baerlocher, Ch. and McCusker, L.B., eds. 2004, Structure determination from powder diffraction data, *Z. Kristallogr*. **219**, 782-901.

[5] David, W.I.F. and Shankland, K. 2008, Structure determination from powder diffraction data, *Acta Crystallogr. A***64**, 52-64.

[6] Shankland, K. 2011, this conference.

[7] Whitfield, P. 2011, this conference.

[8] Gozzo, F. 2011, this conference

[9] Chapon, L. 2011, this conference.

[10] Stephens, P. 2011a, this conference.

[11] Pawley, G.S. 1981, Unit cell refinement from powder diffraction scans, *J. Appl. Crystallogr*., **14**, 357-361.

[12] Le Bail, A., Duroy, H. and Fourquet, J.L. 1988, *Ab-initio* structure determination of $LiSbWO_4$ by X-ray powder diffraction, *Mater. Res. Bull*., **23**, 447-452.

[13] David, W.I.F. and Sivia, D.S.2002, Extracting integrated intensities from powder diffraction patterns, in *Structure Determination from Powder Diffraction Data*, W.I.F. David, K. Shankland, L.B. McCusker and Ch. Baerlocher, eds., Oxford University Press, Oxford, pp. 136-161.

[14] (a) Fernandes, P., Shankland, K., David, W.I.F., Markvardsen, A.J., Florence, A.J., Shankland, N. and Leech, C.K. 2008, A differential thermal expansion approach to crystal structure determination from powder diffraction data, *J. Appl. Crystallogr*. **41**, 1089-1094.
(b) Wright, J.P. 2004, Extraction and use of correlated integrated intensities with powder diffraction data, *Z. Kristallogr*. **219**, 791-802.

[15] Von Dreele, R.B. 2007, Multipattern Rietveld refinement of protein powder data: an approach to higher resolution, *J. Appl. Crystallogr*. **40**, 133-143.

[16] (a) Baerlocher, Ch. 2011, this conference.
(b) Baerlocher, Ch., McCusker, L.B., Prokic, S. and Wessels, T. 2004, Exploiting texture to estimate the relative intensities of overlapping reflections, *Z. Kristallogr*. **219**, 803-812.

[17] Altomare, A., Caliandro, R., Camalli, M., Cuocci, C., Giacovazzo, C., Moliterni, A.G.G. and Rizzi, R. 2004, Automatic structure determination from powder data with EXPO2004, *J. Appl. Crystallogr*. **37**, 1025-1028.

[18] Rius, J. and Frontera, C. 2007, Application of the constrained S-FFT direct-phasing method to powder diffraction data. XIII, *J. Appl. Crystallogr*. **40**, 1035-1038.

[19] Giacovazzo, C. 2011, this conference.

[20] (a) Gilmore, C. 2011, this conference.
(b) Gilmore, C., Dong, W. and Bricogne, G. 1999, A multisolution method of phase determination by combined maximization of entropy and likelihood. VI. The use of error-correcting codes as a source of phase permutation and thier application to the phase problem in powder, electron and macromolecular crystallography, *Acta Crystallogr. A***55**, 70-83.

[21] Rius, J. 2011, Patterson-function direct methods for structure determination of organic compounds from powder diffraction data. XVI, *Acta Crystallogr. A***67**, 63-67.

[22] Favre-Nicolin, V. and Cerny, R. 2004, A better FOX: using flexible modelling and maximum likelihood to improve direct-space *ab initio* structure determination from powder diffraction, *Z. Kristallogr*. **219**, 847-856.

[23] David, W.I.F., Shankland, K., van de Streek, J., Pidcock, E., Motherwell, W.D.S. and Cole, J.C. 2006, DASH: a program for crystal structure determination from powder diffraction data, *J. Appl. Crystallogr*. **39**, 910-915.

[24] Grosse-Kunstleve, R.W., McCusker, L.B. and Baerlocher, Ch. 1997, Powder diffraction data and crystal chemical information combined in an automated structure determination procedure for zeolites, *J. Appl. Crystallogr.* **30**, 985-995.
[25] Altomare, A., Caliandro, R., Cuocci, C., Giacovazzo, C., Moliterni, A.G.G., Rizzi, R. and Platteau, C. 2008, Direct methods and simulated annealing: a hybrid approach for powder diffraction data, *J. Appl. Crystallogr*. **41**, 56-61.
[26] Oszlányi, G. and Sütő, A. 2004, *Ab initio* structure solution by charge flipping, *Acta Crystallogr. A***60**, 134-141.
[27] (a) Wu, J., Leinenweber, K., Spence, J.C.H. and O'Keeffe, M. 2006, *Ab initio* phasing of X-ray powder diffraction patterns by charge flipping, *Nature Mater*. **5**, 647-652.
(b) Baerlocher, Ch., McCusker, L.B. and Palatinus, L. 2007, Charge flipping combined with histogram matching to solve complex crystal structures from powder diffraction data, *Z. Kristallogr*. **222**, 47-53.
[28] Palatinus, L. and Chapuis, G. 2007, SUPERFLIP - a computer program for the solution of crystal structures by charge flipping in arbitrary dimensions, *J. Appl. Cryst.* **40**, 786-790.
[29] Zhang, K.Y.J. and Main, P. 1990, Histogram matching as a new density modification technique for phase refinement and extension of protein molecules, *Acta Crystallogr*. *A***46**, 41-46.
[30] Coelho, A.A. 2007, A charge-flipping algorithm incorporating the tangent formula for solving difficult structures, *Acta Crystallogr. A***63**, 400-406.
[31] (a) Stephens, P. 2011b, this conference .
(b) Young, R.A., ed. 1993, *The Rietveld Method*, Oxford University Press, Oxford.

Inorganic Materials

Radovan Černý
Laboratory of Crystallography, University of Geneva, Switzerland

Ab initio structure determination - polyhedral description

Inorganic compounds usually do not contain isolated molecules. This does not mean a particular difficulty for the *ab initio* structure solution methods working entirely in the reciprocal space (RSM). However, it becomes a difficulty for the methods working entirely (global optimization methods) in the direct space (DSM) and using the chemical knowledge in this space (for a comprehensive review on the methods see [1]). The structure solution algorithm working in the direct space has to know how to define basic structural blocks of the crystal which are then manipulated (optimized) by the algorithm.

The choice of the structural blocks is easy when isolated molecules are present in the crystal like in organic or coordination compounds where the molecules are easily described by a finite number of the internal molecular coordinates (bonding distances, angles and dihedral angles). A molecule is naturally an isolated structural block that can be moved in the unit cell, and deformed from its planar form. No sharing of atoms between the molecules occurs. The situation becomes rather unclear when one tries to model the crystal structure of a non-molecular compound. The definition of a finite structural block for a crystal like iron or sodium chloride is not unambiguous; should it be one atom, first coordination sphere of each atom, structural sheet of finite thickness, the asymmetric unit?

Coordination polyhedra, typically the first coordination spheres, of selected atoms, which will generate the whole inorganic crystal structure, can always be identified. These polyhedra will share corners, edges or faces. A wide range of polyhedra can be defined, and these are naturally described using again bond distances, angles and dihedral angles. Sharing of atoms between the polyhedra is either evident (for example exclusive corner sharing of SiO_4 tetrahedra in alumino-silicates [2]), or can be better described generally with an automatic, adaptive routine, the Dynamical Occupancy Correction (DOC) which handles also the special Wyckoff positions as it is used in the program Fox [3]. The optimization algorithm of DSM must be able to move smoothly the building blocks to the positions when they share atoms or to move an atom on the special position, while also allowing separation of the building blocks or moving the atom *away* from the special position, without *any* intervention from the user.

The polyhedra are typically described using Z-matrices as for the molecules [3]. The restraint-based description [4] of the polyhedra then solved some pitfalls of Z-matrices, however, with less benefit for the non-molecular compounds. A careful choice of the structural blocks may significantly improve the convergence of the DSM as illustrated on the example of AlMePO-γ phosponate [5] where the modelling by two free Al atoms converges faster than the modelling by AlO_4 tetrahedron and AlO_5 trigonal bipyramid.

Direct- or Reciprocal- space method?

The principal difference between DSM and RSM and an advantage of the former is that DSM does not require the extraction of integrated intensities of individual reflections which are needed for RSM. In the case of powder patterns of inorganic compounds showing often broad peaks, because of particular sample synthesis like mechanochemistry (ball-milling) or in situ studies of phase transformations and non ambient studies the DSM are the only option as no reliable integrated intensities can be extracted.

An excellent example that has been solved *ab initio* by both DSM and RSM, and shows effectiveness of both approaches when well crystallized samples are available, is $Mg(BH_4)_2$ (Fig. 1). With 55 atoms in the asymmetric unit it represents one of the most complex atomic arrangements ever solved from powder diffraction data. The correct structure was found independently by DSM [6] and by RSM [7]. In both cases high resolution synchrotron data were required for indexing. In the DSM approach, the structure was modelled by five free Mg atoms and ten rigid tetrahedral BD_4 groups, and optimized jointly with synchrotron and neutron data by using the program Fox [3]. The correct structure was recognized after several hours of optimization (guidelines for efficient use of Fox can be found in [8]). In the RSM approach, the structure was solved with the aid of the program EXPO [9] using only synchrotron data. The positions of Mg and B atoms were recognized in electron density maps. In both cases the structure was refined by Rietveld refinement keeping the borohydride groups rigid.

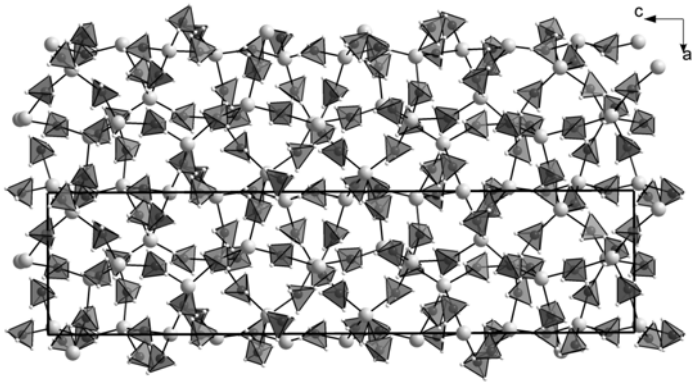

Fig.1. Structure of $Mg(BH_4)_2$ viewed along the hexagonal *b* axis, showing two unit cells. Dark grey (partially transparent) tetrahedra are BH_4 units; Mg atoms in light grey.

Need for accurate unit cell content

Knowledge of the chemical composition and estimation of the unit cell content are the necessary information for most structure solution algorithms. The DSM may successfully work with overestimated cell content as the DOC can simply merge excess atoms (but does not create missing atoms!).

The recently discovered borohydrides $AZn_2(BH_4)_5$ (A=Li, Na) [10] are an example how important is the correct estimation of the unit cell content for an unknown phase. In a parallel study [11] the chemical composition of the ball milled product was wrongly estimated as $AZn(BH_4)_3$, and led to structural models that have shortcomings in Rietveld plots (Fig. 2.) which are not easily detectable from the powder diffraction data. Such a structural model can have balanced interatomic forces as shown by the DFT optimization, but does not correspond to a stable polymorph at given conditions.

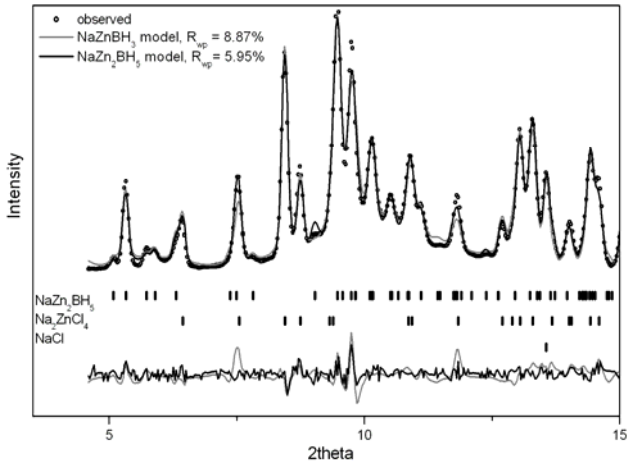

Fig.2. Comparison of Rietveld plots for wrong, $NaZn(BH_4)_3$, and correct, $NaZn_2(BH_4)_5$, structural models, both in the same monoclinic cell (s.g. $P2_1/c$, a=9.440(4), b=16.573(4), c =9.110(2) Å, β=112.99(3) °).

Only warning about the wrong structural model came from the significant increase of the cell volume (+5.2 %) in the DFT optimized structure, because of higher cell content (16 cations and 24 anions) compared to the correct model (12 cations and 20 anions). It means also that the wrong model is more packed (34.52 $Å^3$/ion) than the correct one (40.81 $Å^3$/ion) as calculated on DFT optimized cells. Another warning about the wrong model could have been certainly obtained from the measured density, a difficult experiment for a relatively reactive powder. In the case of multiphase samples containing new phase with unknown exact chemical composition it is therefore crucial to perform the synthesis of starting mixtures in several different ratios of the starting compounds. This procedure allows deducing the chemical composition of the new phase from molar fractions of known phases in different mixtures.

Structure validation and verification

A post-experimental DFT-optimization helps to validate new structures, locate light atoms (hydrogen), especially when using high-pressure diffraction data [12], and even correct the symmetry and some structural details as shown on following examples:

The difficulty in finding the correct orientation of BH_4 tetrahedra led to the overlooked 2-fold axes in the $Mg(BH_4)_2$ space group symmetry originally identified as $P6_1$ [6, 7]. The DFT optimization of the structural model [13] has suggested the true symmetry as $P6_122$, which was then unambiguously confirmed by the single crystal X-ray diffraction [14]. The fact that the structural solution has been found independently by DSM and RSM in the lower Laue symmetry 6/*m* of the space groups $P6_1$ rather than in the true Laue symmetry 6/*mmm* of the true space groups $P6_122$ can be also understood by more degree of freedom (*hkl* and *khl* are independent) in 6/*m* allowing to correct the systematic errors of the powder diffraction data (grain statistics) having the symmetry 6/*mmm*.

In the case of $Li_4Al_3(BH_4)_{13}$ (*P*-43*n*) the DFT optimization [15] of the experimental structure has corrected the orientation of the complex anion $[Al(BH_4)_4]^-$ and modified so the bonding scheme in the structure from isolated complex ions $[(BH_4)Li_4]^{3+}$ and $[Al(BH_4)_4]^-$ rather to a 3D-framework structure (Fig. 3). The corrected model was indeed confirmed by the Rietveld refinement. A similar situation occurred for a nanocrystalline inorganic-organic hybrid compound $VO(C_6H_5COO)_2$ [16] where the correct orientation of the VO_6 octahedron was revealed by the DFT calculation.

The post-experimental DFT-optimization of the crystal structures allows achieving the global minimum in the Rietveld refinement which is not easily visible from the diffraction data only, and can be thus highly recommended.

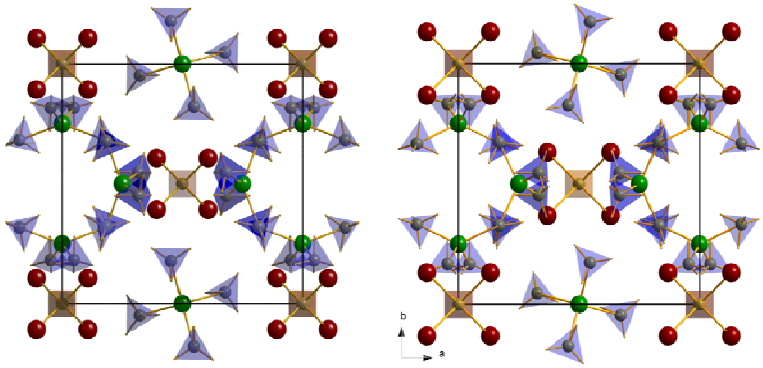

Fig.3. Unit cell of $Al_3Li_4(BH_4)_{13}$ as solved from SR-XPD (left) and as corrected by DFT optimization (right). Complex cation $[(BH_4)Li_4]^{3+}$ centred by BH_4 tetrahedron in brown (light grey), complex anion $[Al(BH_4)_4]^-$ centred by Al atom in green (dark grey).

Symmetry guided refinement, phase transitions

The analysis of crystal symmetry plays an important role in the structure solution/refinement of inorganic compounds. The most complex inorganic structures were solved from powder diffraction data by the symmetry analysis of superstructures based on a well described average structure. Good example is α-$Bi_2Sn_2O_7$, a 176 atom crystal structure based on a pyrochlore structure [17]. Other example of symmetry guided refinement is the parametric Rietveld refinement [18], *i.e.* constraining the crystallographic parameters by set of equations which may have a physical basis, and follow the crystal symmetry. Structural phase transitions are one of the examples [19].

Multiphase samples, impurities

Solid state route synthesis is a method often used for the preparation of inorganic compounds. The resulting products may contain more than one phase like unreacted starting components and side reactions products. As the bottle-neck of the *ab initio* structural studies is still indexing of the powder data, multiphase samples introduce an additional complication.

A successful strategy consists of the so-called 'decomposition-aided indexing', which utilizes *in situ* diffraction as a function of the temperature (*T*-ramping) up to the decomposition/melting temperature of different phases. This procedure allows to separate diffraction peaks of individual phases as illustrated in Fig. 4 by synchrotron powder diffraction data for a ball milled KBH_4-$ScCl_3$ mixture [20].

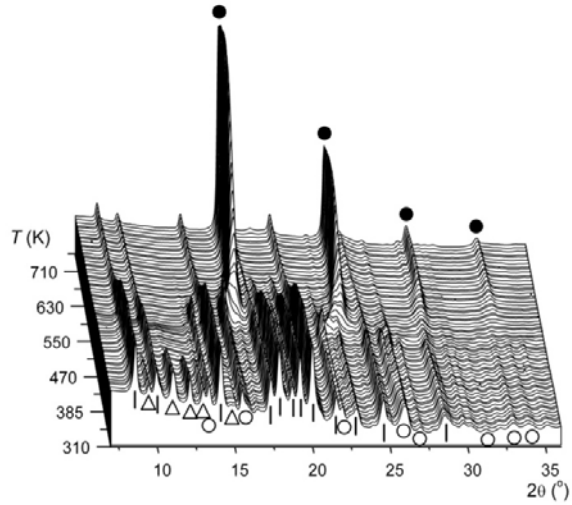

Fig.4. *In situ* synchrotron radiation X-ray powder diffraction data for a ball milled sample of KBH_4-$ScCl_3$ (2:1) (*RT* to 580 K, $\Delta T/\Delta t$ = 5 K/min, λ = 0.9707 Å). Only utilization of T-ramping allowed for determination of attribution of observed peaks to individual phases, $KSc(BH_4)_4$ and K_3ScCl_6, and led to a successful indexing of the RT-powder pattern. Symbols: Δ $KSc(BH_4)_4$, | K_3ScCl_6, O KBH_4 and ● KCl.

The T-ramps (as well as any set of powder patterns collected as a function of external stimuli like pressure, excitation by a light) play an important role in the analysis of multiphase samples, as already mentioned. The studies of physical properties (thermal dilatation, compressibility), and of phase transitions are of course the original reason of the non-ambient diffraction studies.

Weak superstructures and lattice pseudo-symmetry

The arrangement of atoms in the lattice of an inorganic compound may show a small deviation from an arrangement with higher symmetry or shorter periodicity. A typical example are metal hydrides where this deviation is created by positioning H atoms in the matrix of metal atoms which becomes then only slightly deformed or by positioning a lower symmetry structural block like BH_4 tetrahedron on a high symmetry Wyckoff site. Because of a small deformation of the metal matrix and the low scattering power of hydrogen for X-rays, the splitting of peaks caused by lowering the symmetry is not very strong and the superstructures peaks are very weak in X-ray patterns as was the case of $Mg_6Co_2H_{11}$ [21] or $Y(BH_4)_3$ [22,23].

Chemical and positional disorder - local structures

Chemical disorder is often observed in metal alloys where metal sites may have mixed occupation. When the occupation of individual sites by different metals is not statistically random, it can be analyzed provided the scattering contrast between the metals is strong enough. It can be achieved either using the X-ray and neutron data jointly or by resonant X-ray scattering. Note that for the case of *n* atomic species (including vacancies) on one Wyckoff site, one needs *n*-1 diffraction patterns with

different contrast between the scatterers under the question. An example of the analysis of the multi-substituted $LaNi_5$ alloy is given in [24].
Positional atomic disorder may show a local order (short range order) which can be studied from the diffuse intensity of the scattered radiation. The diffuse scattering from polycrystalline samples may be studied by using the Pair Distribution Function (see [25] for more details) like local hydrogen ordering in Laves phases [26].

Powder vs. Single crystal

Independent studies of the orthorhombic (*Cmca*) $Mg_{1+x}Ir_{1-x}$ by single-crystal and powder diffraction methods [27] have allowed a comparison of the structural results obtained by two different methods on a compound having rather a complex crystal structure with 304 atoms in the unit cell. The investigated volume in the reciprocal space was approximately the same in both experiments, but with more than 4000 unique reflections and redundancy factor of 7 for single crystal experiment and 754 unique non-overlapped reflections for the powder data. The atomic positional parameters from both methods are identical within 3-4 times standard uncertainties (s.u.) of the powder diffraction with the s.u. of the powder diffraction by one order of magnitude higher than corresponding s.u. of single crystal results. On the contrary the s.u. of the lattice parameters were by more than one order lower in favour of the powder diffraction.
It is sometimes possible to find a single grain of sufficient size for X-ray single crystal diffraction in an apparently powder sample, as was the case for $Li_4BN_3H_{10}$ [28] or $LiBH_4$ [29]. Even a multi-domain single crystal obtained by a low temperature annealing of an air- and moisture-sensitive $Mg(BH_4)_2$ has produced more accurate structural results than powder diffraction [14].

Conclusions

The powder diffraction on inorganic compounds is not a routine work. A crystallographer has to face numerous crystallographic challenges: complex structures, superstructures, pseudo-symmetries, twinning, chemical and positional disorder, local order, and structural solution from low quality data. On the other hand many powerful tools are available: resonant scattering, total scattering analysis, fast in-situ data collection. The good knowledge of basic crystallographic concepts like symmetry analysis, theory of scattering including diffuse effects, aperiodic crystals, and knowledge of limits and accuracy of powder data helps to avoid erroneous conclusions. The final cut should be always left to the crystal chemistry analysis.

Acknowledgments

The author wants to thank to all users of Fox, and especially to them who have kindly provided the details of their work when solving the crystal structures.

References

[1] David, W.I.F. ; Shankland, K. ; McCusker, L.B. ; Baerlocher, Ch.: *Structure Determination from Powder Diffraction Data*. Editors. Oxford University Press, **2002**.
[2] Deem, M.W. and Newsam, J.M. *Nature* **1989**, *342*, 260-262.
[3] Favre-Nicolin, V. and Černý, R. *J. Appl. Cryst*. **2002**, *35*, 734-743.
[4] Favre-Nicolin, V. and Černý, R. *Z. Kristallogr*. **2004**, *219*, 847-856.
[5] Edgar, M.; Carter, V.J.; Tunstall, D.P.; Grewal, P.; Favre-Nicolin, V.; Cox, P.A.; Lightfoot, P. and Wright, P.A. *Chem. Commun.* **2002**, *8*, 808-809.
[6] Černý, R.; Filinchuk, Y.; Hagemann, H.; Yvon, K. *Angew. Chem. Int. Ed.* **2007**, *46*, 5765-5767.
[7] Her, J.-H.; Stephens, P.W.; Gao, Y.; Soloveichik, G.L.; Rijssenbeek, J.; Andrus, M.; Zhao, J.-C. *Acta Cryst. B* **2007**, *63*, 561-568.
[8] Černý, R.; Favre-Nicolin, V. *Z. Kristallogr.* **2007**, *222*, 105-113.
[9] Altomare, A.; Caliandro, R.; Camalli, M.; Cuocci, C.; Giacovazzo, C.; Moliternia, A.G.G.; Rizzi, R. *J. Appl. Crystallography* **2004**, *37*, 1025-1028.
[10] Ravnsbæk, D.; Filinchuk, Y.; Cerenius, Y.; Jakobsen, H. J.; Besenbacher, F.; Skibsted, J.; Jensen T. R. *Angew. Chem. Int. Ed.* **2009**, *48*, 6659-6663.
[11] Černý, R.; Kim, K.Ch.; Penin, N.; D'Anna, V.; Hagemann, H.; Sholl, D.S. *J. Phys. Chem. C* **2010**, *114*, 19127-19133.
[12] Filinchuk, Y.; Chernyshov, D.; Nevidomskyy, A.; Dmitriev, V. *Angew. Chem. Int. Ed*. **2008**, *47*, 529-532.
[13] Dai, B.; Sholl, D. S.; Johnson, J. K. *J. Phys. Chem. C* **2008**, *112*, 4391-4395.
[14] Filinchuk, Y.; Černý, R.; Hagemann, H. *Chem. Mater.* **2009**, *21*, 925-933.
[15] Lindemann, I.; Ferrer, R. D.; Dunsch, L.; Filinchuk, Y.; Černý, R.; Hagemann, H.; D'Anna, V.; Lawson Daku, L. M., Latevi M.; Schultz, L.; Gutfleisch, O. *Chem. Eur. J.* **2010**, *16*, 8707-8712.
[16] Djerdj, I.; Cao, M.; Rocquefelte, X.; Černý, R.; Jagličič, Z.; Arčon, D.; Potočnik, A.; Gozzo, F.; Niederberger, M.: *Chem. Mater.* **2009**, *21*, 3356-3369.
[17] Evans, I.R.; Howard, J.A.K.; Evans, J.S.O. *J. Mater. Chem.* **2003**, *13*, 2098-2103.
[18] Stinton, G.W.; Evans, J.S.O. *J. Appl. Cryst*. **2007**, *40*, 87-95.
[19] Müller, M.; Dinnebier, R.E.; Ali Naveed, Z.; Campbell, B.J.; Jansen, M. Materials Sci. Forum **2010**, *651*, 79-95.
[20] Černý, R.; Ravnsbæk, D. B.; Severa, G.; Filinchuk, Y.; D'Anna, V.; Hagemann, H.; Haase, D.; Jensen, C.M.; Jensen, T.R. *J. Phys. Chem. C* **2010**, *114*, 19540-19549.
[21] Černý, R.; Bonhomme, F.; Yvon, K.; Fischer, P.; Zolliker, P.; Cox, D.E.; Hewat, A. *J. Alloys and Compounds* **1992**, *187*, 233-241.
[22] Ravnsbæk, D. B.; Filinchuk, Y.; Černý, R.; Ley, M. B.; Haase, D.; Jakobsen, H. J.; Skibsted, J.; Jensen, T. R. *Inorg. Chem*. **2010**, *49*, 3801-3809.
[23] Frommen, C.; Aliouane, N.; Daledda, S.; Fonneløp, J. E.; Grove, H.; Lieutenant, K.; Llamas-Jansa, I.; Sartori, S.; Sørby, M. H.; Hauback, B. C. *J. Alloys Compd.* **2010**, *496*, 710–716.
[24] Joubert, J.-M.; Černý, R.; Latroche, M.; Percheron-Guégan, A.; Yvon, K. *J. Appl. Crystallography* **1998**, *31*, 327-332.
[25] Egami, T.; Billinge, S.J.L.: *Underneath the Bragg-Peaks: Structural Analysis of Complex Materials.* Pergamon Press, Oxford **2003**.
[26] Ropka, J; Černý, R.; Paul-Boncour, V. *J. Solid State Chem*. **2011**, in press.
[27] Černý, R.; Renaudin, G. ; Favre-Nicolin, V. ; Hlukhyy, V. and Pöttgen R. *Acta Cryst. B* **2004**, *60*, 272-281.
[28] Filinchuk, Y.E.; Yvon, K.; Meisner, G.P.; Pinkerton, F.E.; Balogh, M.P. *Inorg. Chem.* **2006**, *45*, 1433-1435.
[29] Filinchuk, Y.; Chernyshov, D.; Černý, R. *J. Phys. Chem. C* **2008**, *112*, 10579-10584.

Organic compounds

Kenneth Shankland
School of Pharmacy, University of Reading, Whiteknights, Reading, UK

Abstract. For many years, powder X-ray diffraction was used primarily as a fingerprinting method for phase identification in the context of molecular organic materials. In the early 1990s, with only a few notable exceptions, structures of even moderate complexity were not solvable from PXRD data alone. Global optimisation methods and highly-modified direct methods have transformed this situation by specifically exploiting some well-known properties of molecular compounds. This presentation will consider some of these properties.

Molecular organic materials tend to crystallise in low-symmetry space groups (some 80% crystallise in one of five space group, $P2_1/c$, $P\text{-}1$, $P2_12_12_1$, $P2_1$ and $C2/c$ [1, with % updated for Nov 2010 release of the CSD]) and as such exhibit substantial accidental reflection overlap, particularly at high values of 2θ. This, coupled with the fact that molecular materials do not, in general, have strongly scattering elements present to boost measurable intensities at high angle means that it is particularly difficult to extract accurate reflection intensities. As such, the application of unmodified direct methods of crystal structure determination is generally unsuccessful. Spurred on by this failing, numerous groups have developed global optimisation based methods of structure determination, where the position, orientation and conformation of a molecule are adjusted in such a way as to maximise the agreement between observed and calculated diffraction data [2]. Clearly, to be able to perform such an optimisation, one must have a fairly accurate model of the molecule being studied. The vast number of previously determined organic crystal structures provides a rich source of prior information that can be used in the construction of such models ready for optimisation. This is discussed in more detail below.

Molecular connectivity: In single-crystal diffraction, it is not generally necessary to know the molecular connectivity in advance of the diffraction experiment, as the wealth of diffraction data, coupled with the power of direct (and other) methods of structure determination / completion means that the molecular structure usually emerges directly from the Fourier maps. In the case of powder diffraction, this is not normally the case and when applying global optimisation methods, it is necessary to know the molecular connectivity (or at least, a large part of it) in advance of structure determination. This is a significant constraint, but is not as restrictive as it seems at first sight; analytical techniques such as mass spectrometry and NMR can be used to determine 2D connectivity quickly and accurately and many diffraction

problems consist of solving the structures of new crystalline forms of previously well-characterised molecules. That said, if the 2D connectivity supplied is wrong in any significant regard, it is unlikely that the structure determination will succeed and the crystallographer should always be alert to this possibility. For example, should the chemist tell the crystallographer that he has systhesised a *cis* isomer and structure solution with a *cis* model fails, then the *trans* isomer should be checked, or the bond about which the *cis*/*trans* isomerism occurs could be treated as flexible.
If a new structure is being studied, one can frequently find significant molecular 'chunks' of the structure in existing crystal structures. In this regard, the Cambridge Structural Database (CSD) and its associated search interface ConQuest (Figure 1) are essential tools [3], as is a good molecular modelling program with which one can edit retrieved structures to delete unwanted atoms or add new ones.

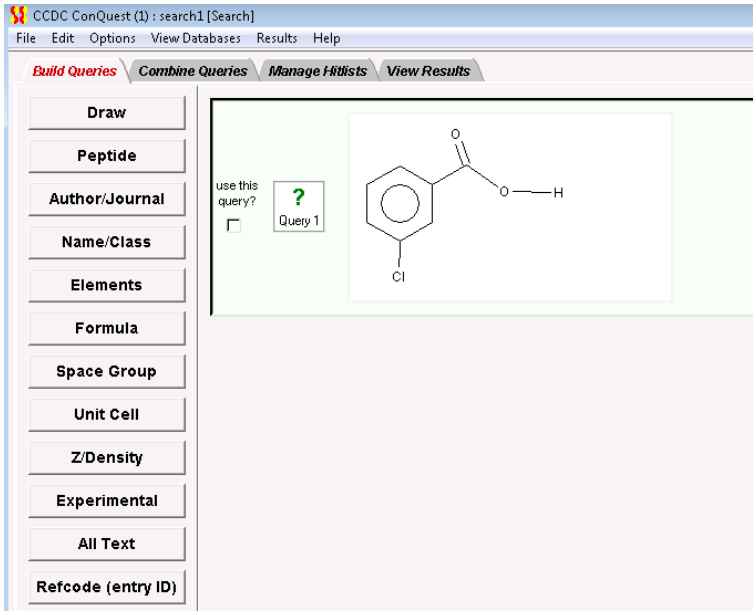

Fig. 1. Search options in the ConQuest program, with the 'Draw' option being used to search for all crystal structures containing the sketched substructure. This particular fragment matches 92 structures in the November 2010 version of the CSD.

In the construction of a molecular model, one generally does not have to worry about the *exact* positions of hydrogen atoms, as their individual contribution to the scattering from any given point of the unit cell is relatively small. However, collectively, their contribution to the overall scattering can be significant and they should be included in the molecular model whenever possible.
Once a model of the molecule being studied has been constructed, it should be carefully checked for chemical sense - this is discussed in more detail in a separate section below.

Molecular volume: Many molecular modelling programs (e.g. Marvin [4]) will quickly calculate a volume for any given isolated molecule. These values can be extremely useful as the powder pattern indexing stages, as the experimentally determined unit cell volume should be able to accommodate a crystallographically sensible number of molecular units. If the value of V_{cell}/V_{mol} makes crystallographic sense, this is a very good indicator of the correctness of the solution, above and beyond whatever the indexing figures of merit suggest. In considering the calculation of V_{cell}/V_{mol}, it should be remembered that the V_{mol} obtained for an isolated molecule cannot be used "as is", as it does not take into account the crystal packing index. Fortunately, this is easily corrected by the use of an average crystal packing index of 0.7 i.e. $V_{cell}/(V_{mol} \div 0.7)$.
The 18Å rule [5], where the estimated molecular volume of an organic material is obtained by counting all the non-hydrogen atoms in the structure and multiplying this number by $18Å^3$, is commonly used on account of its speed and simplicity. The figure of $18Å^3$ per atom is an average value derived from a survey of crystal structures in the Cambridge Structural Database. In 2002, Hofmann introduced a more specific formula [6], again based on observed crystal structures, but with individual volume terms for each atom type present in the structure. The formula is given in simplified form below:

$$V_{mol} = \sum_{i=1}^{x} n_i v_i$$

where the summation is over the x different atom types in the molecule, n_i is the number of atoms of the i^{th} type in the structure and v_i is a volume contribution (in $Å^3$, derived from the CSD) for the i^{th} atom type. This method is very accurate and should be used in preference to the $18Å^3$ rule.

Molecular description: The 2D connectivity of a molecule has to be translated into a 3D description for use in global optimization. This is generally a two-stage process: (1) perform the 2D to 3D conversion (if required), and (2) convert the 3D description into a format suitable for the optimisation program. The 2D to 3D conversion can be performed in a variety of ways but is generally done with a molecular modeling program. The specifics of such programs lie outside the scope of this summary, but regardless of the method used, the output structure should be checked carefully against the expectation values before use (see Structure Checking). The output structure will have atomic coordinates in a Cartesian frame and may or may not retain the explicit connectivity information. For global optimisation, were this collection of N atoms to be optimised as freely moving objects, there would be $3N$ parameters. However, to do so would neglect the fact that we actually know a great deal about the molecular geometry [7]. Any two directly bonded atoms in a molecu-

lar structure sit at well-defined distances from one another, and these distances are not greatly influenced by the environment of the crystal structure. As such, a bond length may generally be considered to be a fixed entity and not one that requires to be optimised. Bond angles created by three connected atoms are similarly well-defined, mainly by the molecular environment as opposed to the crystallographic one. They are 'softer' than bond lengths (in that it takes considerably less energy to induce a deviation from the value found in an isolated molecule) but may generally be considered to be fixed entities that do not require to be optimised. Bond torsion angles (defined as the angle between two bonds A-B and C-D, viewed along a common bond B-C), are extremely 'soft' in comparison to bond lengths and angles, as changing the bond torsion changes only non-bonded contact distances. As such, they are considered to be flexible entities whose values cannot (in general) be assigned in advance and that must be parameters in the global optimisation.
Using an internal coordinate description of the molecule [7,8] is a convenient way of encoding this prior molecular knowledge and serves to reduce considerably the number of parameters that needs to be determined. A very simple example is shown in Figure 2.

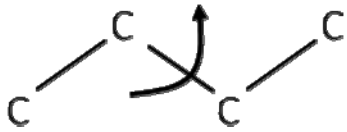

Fig. 2. A simplified molecular model for butane, with H atoms omitted. The bond lengths are known to be 1.54Å and the bond angles are known to be 109.5°. The arrow shows a torsion angle whose exact value cannot be specified in advance of the optimisation. The 12 degrees of freedom associated with the use of independent atoms are reduced to 7 (six positional, one torsional) when an internal coordinate description is used.

It is worth mentioning, however, that in some cases, it may be advantageous to allow some variation in bond lengths and angles during the optimisation process [9].

Other sources of prior information: Although the values of flexible torsion angles in a structure cannot, in general, be specified in advance, that is not to say that one cannot infer probable values in advance of an optimisation. It should come as no surprise that molecular conformations within crystal structures populate low-lying areas of an energy surface and as such, it is possible to either (a) attempt to calculate in advance likely molecular conformations based on isolated molecule calculations [1], or (b) examine ensembles of existing crystal structures in order to determine energetically favorable confirmations; see, for example [10]. The latter is conveniently achieved through the Conquest or Mogul [11] front ends to the Cambridge Structural

[1] Carrying such calculations to their logical periodic conclusion brings us to the domain of crystal structure prediction.

Database and Figure 3 shows the result obtained for the facile example of the amide bond.

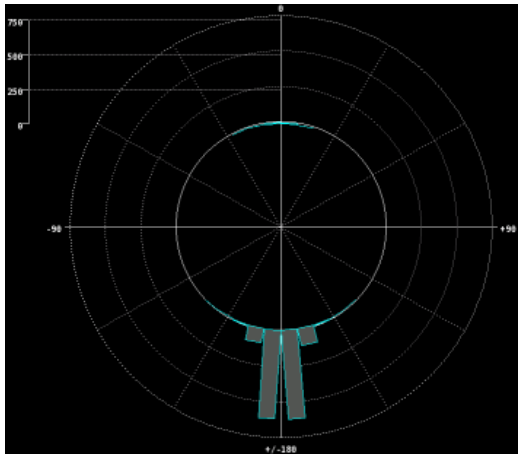

Fig. 3. A polar plot of the torsion angle associated with the amide bond (-C(=O)-NH-) in crystal structures in the Nov 2010 CSD release. The plot summarises some 1573 observations and shows clearly that the amide bond is *trans* planar.

Few distributions are as well defined as the one shown in Figure 3, but it still possible to use the distributions to influence the way in which torsional parameters in the optimization are varied. For problems involving multiple torsion angles, significant reductions in the search space can be achieve, with consequent benefits for both speed of solution and frequency of success [12].

For problems involving more than one fragment in the asymmetric unit, information about non-bonded contacts can also be also derived from the CSD using either the Conquest or Isostar front ends. Both distance and direction information can be obtained quickly and easily. Such information can be incorporated into the internal coordinate description of the fragments in order to reduce the degrees of freedom in the search. For the case shown in Figure 3, the distance information can be included in the form of a virtual bond and the angle information (not shown) in the form of a virtual angle. Only one degree of freedom is saved (i.e. three positional for the Cl-ion are reduced to two internal) but the resultant internal degrees of freedom are very highly restrained, leading to a significant reduction in the search space [13].

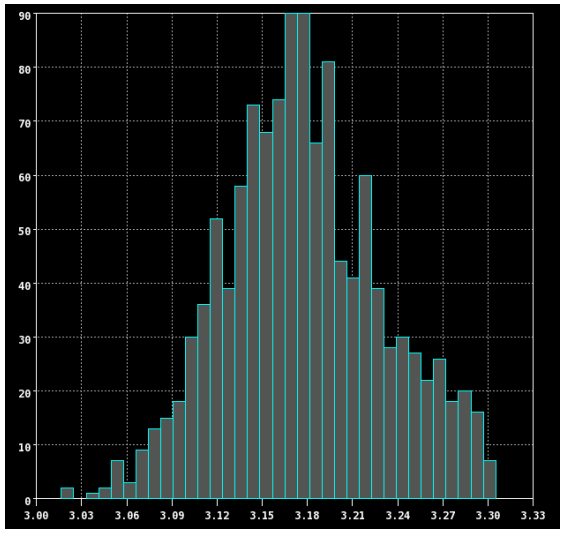

Fig. 3. A histogram of the distance (Å) associated with the intermolecular contact $N^{+}\cdots Cl^{-}$ in crystal structures containing the motif $R\text{-}NH_3^{+}\cdots Cl^{-}$. Only structures with an *R* factor less than 5% were included in the search of the Nov 2010 CSD release. The plot summarises some 1200 observations and shows clearly that the chloride ion is consistently located at a distance of 3.18 ± 0.05Å from the positively-charged nitrogen atom.

Structure checking: As mentioned earlier, when a model is constructed and ready for global optimisation against the measured diffraction data, it is wise to check to make sure that the model does not contain any bond lengths or angles that deviate too far from expected (previously observed) values. In this regard, the Mogul [14] front end to the CSD is an extremely valuable tool that makes this process straightforward. Figure 4 shows the results of a check performed on the molecular structure of carbamazepine as recorded in CSD refcode CBMZPN01. These results make it easy to identify any length, angle or torsion that deviates significantly from expectation values and that might need modification in the input model.

Summary: There are many different ways of constructing molecular models ready for global optimisation and this document has concentrated on arriving at the most accurate internal coordinate description. As highly accurate computational methods (such as DFT) become more widely used on the desktop, they will form an extremely valuable addition to the range of tools than can be brought to bear on this problem.

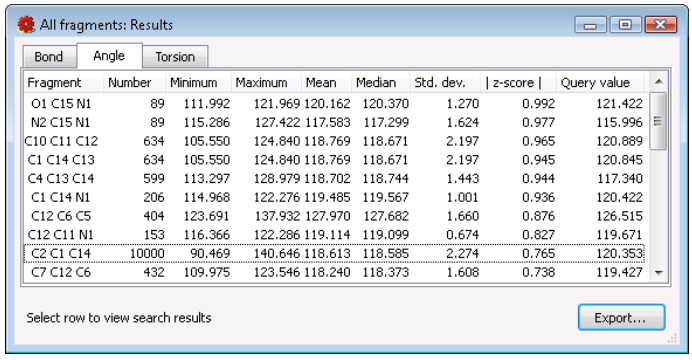

Fig. 4. The Mogul summary output of bond angles in CBMZPN01. Bong angle values in the input structure ("Query value" column) can be quickly compared with the observed distribution of similar angles present in structures in the CSD.

Acknowledgements

I am especially grateful to the staff of the CCDC in Cambridge, with whom we have explored the applicability to powder diffraction of many of the tools mentioned here.

References

1. A. D. Mighell, V. L. Himes & J. R. Rodgers, "Space-group frequencies for organic-compounds". *Acta Crystallogr. Sect. A*, (1983), **39**,737.
2. K. Shankland and W. I. F. David in "Structure Determination from Powder Diffraction Data", OUP (2002).
3. F. H. Allen. "The Cambridge Structural Database: a quarter of a million crystal structures and rising" *Acta Cryst*., **B58**, 380-388, 2002
4. http://www.chemaxon.com/products/marvin/
5. C. J. Kempster & H. Lipson, "Rapid method of assessing number of molecules in unit-cell of an organic crystal". *Acta Crystallogr. Sect. B-Struct. Commun.*, (1972), **28**,3674.
6. D. W. M. Hofmann, "Fast estimation of crystal densities". *Acta Cryst*, (2002), **B58**,489.
7. K. Shankland, "Whole molecular constraints - the Z-matrix unravelled", IUCR Commission on Crystallographic Computing, August 2004.
8. A. R. Leach "Molecular Modelling: Principles and Applications 2nd Ed.", Prentice-Hall (2001).
9. V. Favre-Nicolin & R. Cerny, "A better FOX: using flexible modelling and maximum likelihood to improve direct-space ab initio structure determination from powder diffraction". *Z. Kristall.*, (2004), 219,847.
10. N. Shankland, A. J. Florence, P. J. Cox, C. C. Wilson & K. Shankland, "Conformational analysis of Ibuprofen by crystallographic database searching and potential energy calculation". *Int. J. Pharm.*, (1998), **165**,107.
11 I. J. Bruno, J. C. Cole, J. P. M. Lommerse, R. S. Rowland, R. Taylor and M. L. Verdonk, " Isostar: A library of information about non-bonded interactions". *J. Comput.-Aided Mol. Des*., (1997), **11**, 525-537.
12. A. J. Florence, N. Shankland, K. Shankland, W. I. F. David, E. Pidcock, X. L. Xu, A. Johnston, A. R. Kennedy, P. J. Cox, J. S. O. Evans, G. Steele, S. D. Cosgrove & C. S. Frampton, "Solving molecular crystal structures from laboratory X-ray powder diffraction data with DASH: the state of the art and challenges". *Journal of Applied Crystallography*, (2005), 38,249.
13. H. Nowell, J. P. Attfield, J. C. Cole, P. J. Cox, K. Shankland, S. J. Maginn & W. D. S. Motherwell, "Structure solution and refinement of tetracaine hydrochloride from X-ray powder diffraction data". *New J. Chem.*, (2002), **26**,469.
14. I. J. Bruno, J. C. Cole, M. Kessler, Jie Luo, W. D. S. Motherwell, L. H. Purkis, B. R. Smith, R. Taylor, R. I. Cooper, S. E. Harris and A. G. Orpen, *J. Chem. Inf. Comput. Sci*. (2004), **44**, 2133-2144.

Laboratory X-ray Diffraction

Pamela Whitfield
National Research Council Canada, Ottawa, Canada

Abstract. Laboratory diffractometers form the introduction to powder diffraction for most researchers. On a basic level for phase ID, etc, one diffractometer is very much like another. However when configuring a system for more challenging and advanced experiments, a variety of options and choices confront the experimentalist. Rather than cover the basics of diffractometer operation and geometry we will discover how a good understanding of the concepts behind laboratory diffractometers and their components is vital to getting the best from a system and pushing the limits of what can be achieved with lab instrumentation. Laboratory instrumentation will never compete with the sheer power and resolution of a synchrotron beamline. However, by departing from the conventional setups, it can be surprising what may be achieved in-house without resorting to the delay and inconvenience of synchrotron beamtime proposals.

1. Introduction

Although there have been many recent developments in software and instrumentation, the most basic Bragg-Brentano geometry used by many laboratory instruments is unchanged. It is a parafocussing geometry with a X-ray tube source and scintillation detector, with or without a monochromator. The biggest change has been the increasing use of position sensitive detectors, although in many instances the underlying parafocusing geometry is unchanged. This is not the forum to describe the basic geometry of diffractometers, and the reader is referred to the classical book by Jenkins and Snyder [1] or more recent texts [2-4] for further details.

2. Challenges in Everyday Powder Diffraction

Some researchers during their career are fortunate enough to be in the position to purchase one or more new powder diffractometers and write the specifications themselves. In many instances the standard system with a copper tube is not the best configuration. In order to obtain the best instrument for the job a few basic questions need to be answered.

The instrument should be matched to the type of sample to be analyzed - there is no laboratory configuration that will be good for every conceivable sample. This can be a challenge in a multi-user environment with a wide variety of sample types, where certain compromises may be necessary. The first question should always be “what are my samples?” Organic samples with low X-ray absorption and inorganic samples with high X-ray absorption tend to require different configurations to obtain

high quality data. Organic samples are usually best served with a transmission geometry, while inorganics tend to require reflection geometry. The second question should be "how much sample do I have?" Very small samples may require capillary geometry or a specialist microdiffractometer to obtain the best results. The third question should be what elements do I have? The experienced analyst will come to regard sample fluorescence as one of their biggest enemies. Avoidance is much preferable to dealing with fluorescence after the fact.

2.1. Fluorescence

Fluorescence occurs when elements in a sample absorb a portion of the incident radiation and re-emit it at different energies (inelastic scattering). Effectively intensity is taken from the Bragg peaks and distributed into the background, producing a poor quality diffraction pattern. The most problematic elements (most often transition metal elements) for each type of X-ray tube are known, so it can often be avoided by selecting a suitable X-ray energy. The different X-ray tubes, both common and uncommon are shown in Table 2. Unfortunately, in a multiuser/multisample environment it may not be possible to avoid generating fluorescence. This can be problematic where high-speed position sensitive detectors are used, as secondary X-ray optics to remove fluorescence often can't be used.

Table 1. Problematic transition metal elements for Cu and Co X-ray tubes

X-ray Tube	Problematic transition metal elements
Cu	Co, Fe, Mn
Co	Mn, Cr, Ti

Scintillation detectors can easily be fitted with a graphite secondary monochromator which is very effective at removing the background due to fluorescence. There is an additional penalty in terms of peak intensity but the improvement in data quality is usually more than worth it. If a secondary monochromator isn't available, the peak-to-background ratio (P/B) can be improved somewhat by optimizing the electronic discriminators of the detector. P/B is important in structure analysis - the Rietveld round robin showed that a P/B of 50 or better is needed for accurate atomic positions in a structure refinement to remove uncertainty in the background fitting [5]. The discriminators determine the X-ray energies that the detector will 'throw away' and ignore. The degree of discrimination for scintillation detectors and PSDs is limited compared to energy-discriminating Si(Li) detectors but can go some way to improving the P/B of the data collected.

Table 2. Different X-ray tubes available for laboratory X-ray diffractometers listed by increasing $K\alpha_1$ energy

Anode	Energy (KeV)	Wavelength (Å)	Uses
Cr	5.4	2.290	Lowest energy. Used for stress analysis, SAXS and samples with large d-spacings (clays)
Fe	6.4	1.936	Rare tube, low power, used by some groups for Mn-containing samples
Co	6.9	1.789	Fe-containing samples to reduce fluorescence. Common in analysis of steel and minerals
Cu	8.0	1.541	Most common energy. Well matched to distances in lattice planes. X-ray detectors often optimized for CuKα.
Mo	17.5	0.709	Small unit cell samples, highly absorbing samples, in-situ work. Common in single crystal.
Ag	22.2	0.559	Very rare tube. Highest practical energy available. Very penetrating, best for PDF work

3. Beyond the Sales Brochure

The sales brochures tell you what vendor can guarantee the instrument will do. To find out what a lab diffractometer is *really* capable of requires an understanding of the different concepts behind diffractometer geometry and the different components (radiation properties, optics, detectors, software, etc). Customized sample environments benefit greatly from a good design/fabrication shop due to the precision required. Integration with diffractometer systems and control software can require some fore-thought in terms of controllers and computer I/O systems.

3.1. High-energy radiation with lab diffractometers

MoKα is commonly used in single crystal diffractometers, but has recently become quite rare in powder diffraction. Older systems with scintillation detectors are perfectly capable of operating with higher energies, but many of the modern generation PSD detectors are much more limited in their wavelength capabilities, and in some instances will only operate with CuKα.

Even if your detector will operate with higher energies there are some potential issues when using MoKα or AgKα. In the absence of a monochromator it is custom-

ary to use a Kβ filter. With CuKα this does induce some subtle and hardly noticeable artefacts in the background. However, with MoKα and AgKα they are very noticeable and may cause serious problems in data analysis. Attempting to fit these artefacts with a conventional background in a Rietveld analysis fails miserably. However, modifying the emission profile either empirically or using a function written for the purpose can do a reasonable job as shown in Figure 1. The calculated profile in Figure 1 shows the low-angle step and high-angle tail present on all the intense reflections.

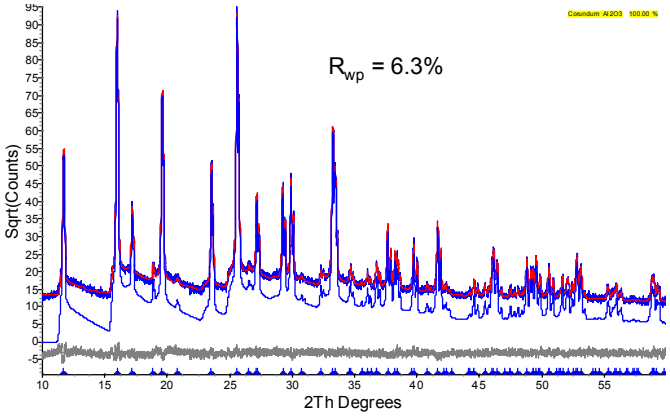

Fig. 1. (a) Rietveld fit to data from SRM1976 corundum collected using MoKα and a Zr Kβ filter using a modified emission profile. The calculated profile includes the low-angle step and high angle tail caused by the Kβ filter.

3.1.1. Laboratory Pressure Cells

One of the obvious applications for high energy X-rays is for laboratory-based pressure cells. Here the attraction of higher energies is the improved penetration through the cell windows and sample. The key to obtaining a reasonable time resolution is sufficient transmission of X-rays reaching a detector that ideally has good detection efficiency at higher X-ray energies.

3.1.1.1. Gas Pressure Cell at the National Research Council

A 1st generation 125 bar, 200ºC pressure cell was constructed [6] for studying crystallization of polymers under CO_2 pressure (Figure 2a). The design was a modification of a literature design [7] to meet the ASME Boiler and Pressure Vessel Code [8]. The use of high energy X-rays was dictated by the transmission through the 1/8" beryllium windows and the pressurized CO_2. The theoretical transmission with different X-ray energies is shown in Figure 2b.

This cell was used with MoKα and a Vantec-1 PSD detector with a 8º window. This configuration was capable of producing good data with reasonable time resolution either in scanning or snapshot mode. The reaction kinetics of the carbonation of

wollastonite ($CaSiO_3$) was studied using quantitative Rietveld analysis with this cell [9]. Data from different pressures and temperatures such as that showed in Figure 3 allowed an activation energy for the carbonation of wollastonite to be calculated.

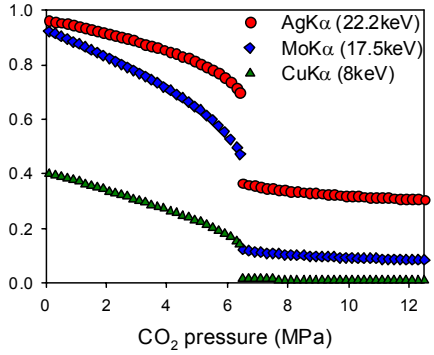

(a) (b)

Fig. 2. (a) 125 bar CO_2 laboratory pressure cell and (b) the theoretical X-ray transmission through the cell with different X-ray energies.

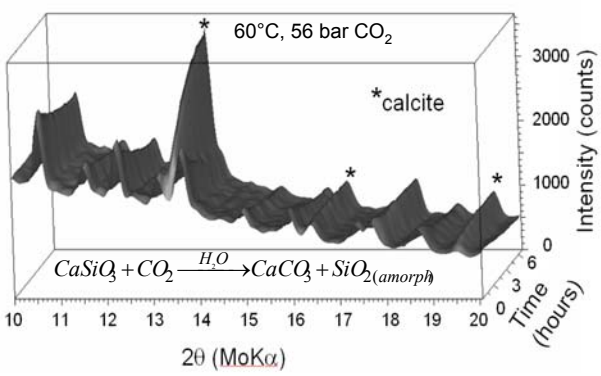

Fig. 3. In-situ data showing the carbonation of $CaSiO_3$ over a period of 6 hours at 60ºC and under 56 bar CO_2 pressure

3.1.1.2. High Pressure Acid Leaching Studies at CSIRO

The group of Ian Madsen and Nikki Scarlett at CSIRO have been studying reaction processes occurring during high pressure acid leaching of nickel laterite ores [10-11]. Industrially this process takes place in an autoclave to stop the acid boiling. Studying the reaction *in-situ* requires penetrating a mixture of a solid and an acidic solution, leading to use of MoKα radiation to reduce attenuation. To reduce absorption a thick-walled 1mm quartz capillary is used as shown in Figure 4, and mounted in an Inel diffractometer with a 120º PSD detector. A hot air heater was used to heat the sample and the capillary was oscillated as opposed to fully rotated due to the

connection of the pressure line. Maximizing the counting efficiency of this detector with MoKα required the use of a custom counting gas mixture.

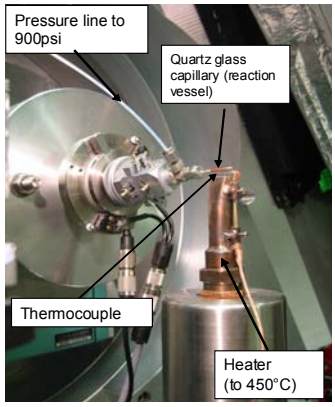

Fig. 4. Capillary cell used for the high pressure acid leaching experiments. This setup was used both in laboratory and synchrotron experiments.

The sample was either a slurry or powder. For powdered samples the acid solution is forced into the powder by pressure. The lack of delay between fluid injection and data collection allows a long series of 2 minute datasets to be collected from the exact moment of acid injection. An example dataset from the leaching experiments is shown in Figure 5.

3.1.2. Highly Absorbing Capillary Samples

Capillary samples in a laboratory setting are usually restricted to samples with low linear absorption with CuKα - often organics. When a small quantity of a new mineral with the composition PbF_2 appeared, the use of a laboratory instrument is not the first thing that comes to mind. The use of MoKα with a 0.3mm capillary

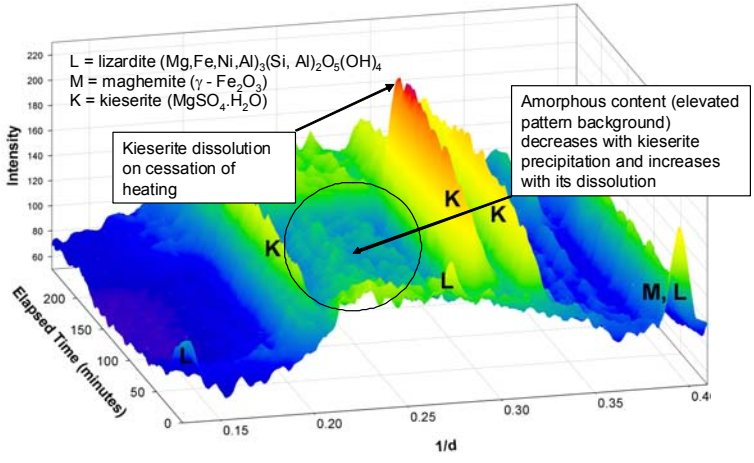

Fig. 5. Example dataset from high pressure acid leaching experiments.

produced decent looking data but had an excessive absorption for a publication-quality Rietveld refinement. Rather than use synchrotron radiation, AgKα radiation with a focusing primary mirror optic was used to obtain data with an acceptable absorption of μR <3. The data was of sufficient quality for a multi-phase refinement (Figure 6) of the new mineral that has the same cubic structure as synthetic β-PbF_2. This structure refinement was used in a submission to the International Mineralogical Association [12] and corresponding journal submission.

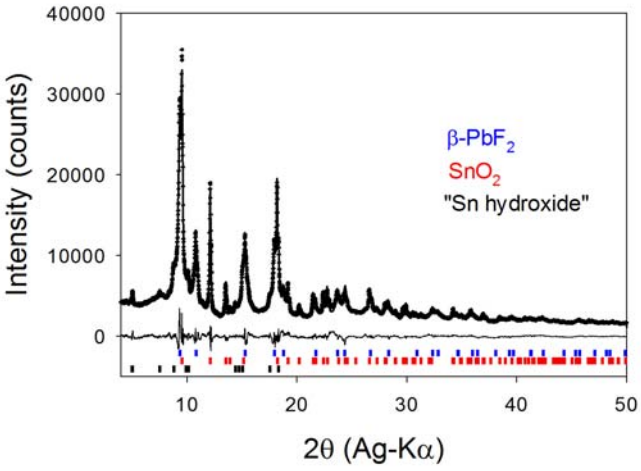

Fig. 6. Rietveld refinement of the β-PbF_2 mineral with the intimately associated phases SnO_2 and a new, uncharacterized "Sn hydroxide" mineral.

3.2. Low Temperature Capillary Experiments

Liquid nitrogen cryostream systems are standard equipment in single crystal instruments. However, the upright goniometer of most powder diffractometers conspires to reduce the space in front the doors, and no easy access is available for the semi-flexible vacuum insulated transfer line. A customized setup was assembled using different supplied components that integrated with the diffractometer control software. The laminar flow of nitrogen gas co-axial along the capillary cools samples to 80K without icing either the capillary or the goniometer head.

This setup allowed for very rapid quenching of samples including liquid solvents. Combined with an optimized diffractometer configuration of a CuKα tube, focusing primary mirror and a Vantec-1 detector with a 10º window, very rapid data collection was possible. Very satisfactory data could be collected between 10-60º 2θ in 4 minutes to the extent that crystal structures could be determined *ab-intio* from some datasets using simulated annealing. Refinements of the structures were carried out using Variable Count Time (VCT) data [13] to rebalance the loss of intensity in the peak-rich high angle region.

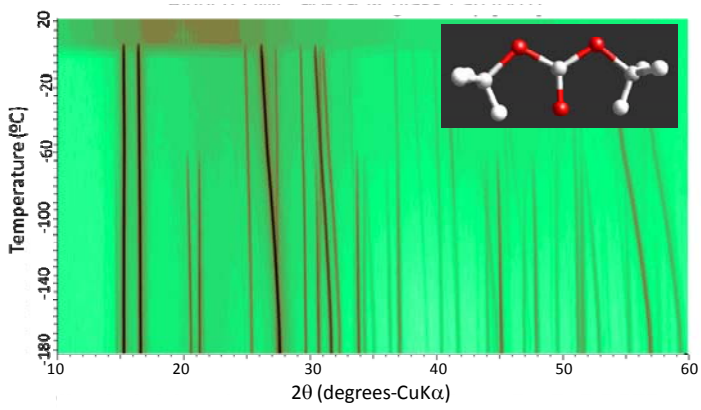

Fig. 7. Diffraction data from the solvent dimethyl carbonate between -180 and +20ºC. Repeated rapid quenching to 82K was used to determine reproducibility and improve particle statistics. The data were collected every 5ºC and each dataset was collected in approximately 4 minutes.

3.3 Modified Relative Humidity (RH) Stage (Queens University)

Not every problem needs the design and construction of equipment from scratch. In many instances modification of an existing stage can extend its capabilities. Ron Peterson at Queens University has taken a commercial Anton Paar THC stage and modified it to better control the RH and collect data from thin layers of sample [14]. Accurate control of RH is problematic as any cold-points in the gas-circuit will lead to condensation and a drop in the RH of the gas stream. This has been tackled by using the water from a recirculating bath to make the system isothermal from the initial gas-mixing, along jacketed gas-lines and a water jacket around the chamber. Accurate RH readings from the chamber are taken using a chilled mirror hygrometer mounted as shown in Figure 8. Kapton film windows and a PANalytical X'Celerator PSD detector allow for rapid data collection with CoKα to reduce fluorescence in the iron-containing samples. An example dataset from this system can be seen in Figure 9, showing the phase behavior between $FeSO_4 \cdot 4H_2O$ and $FeSO_4 \cdot 7H_2O$ at a fixed temperature of 40ºC but varying the RH.

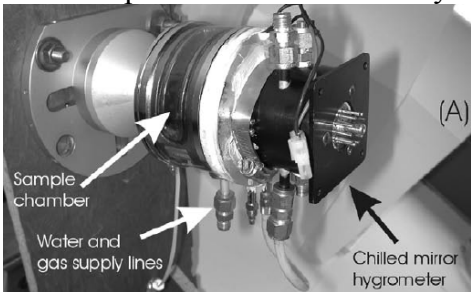

Fig. 8. Photo of the modified relative humidity cell showing the chilled mirror hygrometer and some of the water-jacketed gas lines.

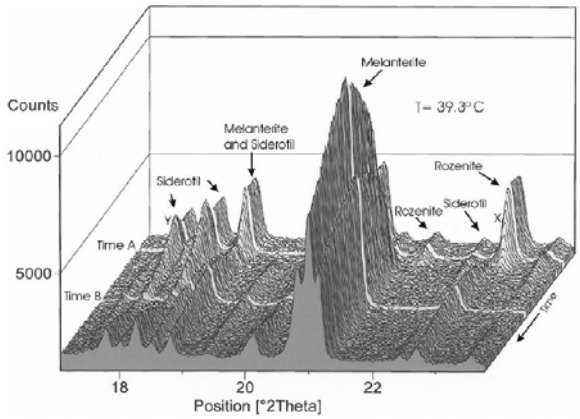

Fig. 9. Data showing phase behaviour between $FeSO_4 \cdot 4H_2O$ (rozenite) and $FeSO_4 \cdot 7H_2O$ (melanterite) at 40ºC while varying the RH. The experiment started with RH = 57%, increased to 76% at Time A and reduced to 68% at Time B.

4. Conclusions

A good understanding of the concepts and components of a laboratory diffractometer allows for effective design for advanced experimental setups. Being open to the possibilities of non-standard configurations allows the researcher to push the limits of what is possible in the laboratory. This may involve the use of more exotic X-ray tubes, different instrument optics, customized sample environments or a combination of these. Although the time and effort required to yield results may be considerable, the potentially unique capabilities can open up new areas of research that could be very productive over an extended period.

Acknowledgments The author would like to thank Ian Madsen and Nikki Scarlett of CSIRO, Melbourne, Australia and Ron Peterson of Queens University, Kingston, Canada for kindly allowing their work to be used as examples.

References

1. R. Jenkins, R. Snyder: Introduction to X-ray Diffractometry (Wiley-Interscience New York 1996)
2. A. Clearfield, J. Riebenspies, N, Bhuvanesh (eds): Principles and Applications of Powder Diffraction (Wiley-Blackwell 2008)
3. V. Pecharsky, P. Zavalij: Fundamentals of Powder Diffraction and Structural Characterization of Materials (2nd edition) (Springer 2008)
4. R.E. Dinnebier, S.J.L Billinge (eds): Powder Diffraction: Theory and Practice (Royal Society of Chemistry London 2008)
5. L.B. McCusker, R.B. Von Dreele, D.E. Cox, D. Louër, P. Scardi: J. Appl. Cryst. 32, 36 (1999)
6. P.S. Whitfield, A.V. Nawaby, B. Blak, J. Ross: J. Appl. Cryst. 41, 350 (2008)
7. A.F. Koster van Groos, S. Guggenheim, C. Cornell: Rev. Sci. Instr. 74, 273 (2003)
8. Boiler and Pressure Vessel Code, American Society of Mechanical Engineers (2004)
9. P.S. Whitfield, L.D. Mitchell: Appl. Geochem. 24, 1635 (2010)
10. I.C. Madsen, N.V.Y. Scarlett, B.I. Whittingham: J. Appl. Cryst. 38, 927 (2005)
11. N.V.Y. Scarlett, I.C. Madsen, B.I. Whittingham: J. Appl. Cryst. 41, 572 (2008)
12. S.J. Mills, P.M. Kartashov, G.N. Gamyanin, P.S. Whitfield, A. Kern, H. Guerault, M. Raudsepp: Fluorocronite, IMA 2010-023. International Mineralogical Association
13. I.C. Madsen, R.J. Hill: J. Appl. Cryst. 27, 385 (1994)
14. R.C. Peterson, A.H. Grant: Can. Mineral. 43, 1305 (2005)

Synchrotron X-Ray Powder Diffraction

Fabia Gozzo
Swiss Light Source, Paul Scherrer Institut, Villigen, Switzerland

Abstract The large breadth of the Synchrotron Radiation X-ray Powder Diffraction (SR-XRPD) technique inevitably requires that we make a certain number of choices in its discussion. Assuming you already have some knowledge of SR and XRPD, we explore the peculiar features that arise from combining them. From the perspective of a beamline scientist, we discuss aspects influencing the beamline optics, diffractometer, detectors and sample environments with attention to details important to perform outstanding SR-XRPD experiments. We begin with a brief overview of SR characteristics and properties and finish with a few SR-XRPD highlights. An extensive literature citation is provided for those who want to delve deeper into those topics that are inevitably not completely covered here.

1. Properties of Synchrotron Radiation

When a charged particle is accelerated or decelerated it emits electromagnetic (e.m.) radiation. This is what happens, for example when an electron moves along a curved trajectory. If the speed v of the electron is much smaller than the speed of light c ($v<<c$) the emitted e.m. radiation (called ***cyclotron radiation***) is uniformly distributed around the moving electron. When the electron's speed reaches values close to the speed of light ($v\sim c$), relativistic effects dramatically change the properties of the emitted radiation making it a very attractive source of radiation for a large variety of experiments. The emitted radiation is called ***synchrotron radiation*** from the specific type of particle accelerator (the electron synchrotron) in which it was first observed in 1947 [1]. Figure 1 is a pictorial representation of cyclotron and synchrotron radiation. Today it is hard to believe that SR has not been always perceived as a precious good. Initially considered only a side negative effect in high-energy physics accelerators that needed to be investigated and minimized, it took almost 20 years for SR to become a fundamental tool in physics, chemistry, biology and medical science.

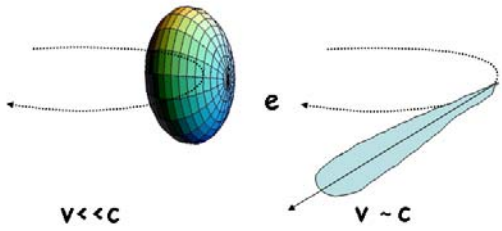

Fig.1. Pictorial representation of the radiation emitted by an electron moving along a curved trajectory: when its speed **v** is much smaller than the speed of light (left) and **v~c** (right)

The history of synchrotron radiation is truly fascinating and the interested reader can find a few dedicated reviews in [2-4].

The main characteristics of synchrotron radiation are here summarized [5-7]:

1. **Tunable photon energy** (or wavelength) over a wide spectral range.
2. **Spectral Brightness** (or brilliance) defined as the flux per unit area of the radiation source per unit solid angle of the radiation cone per unit spectral bandwidth: **[Brightness]=[photons/s/0.1% BW/mm²/mrad²]** that tells us how collimated and intense the emitted photon beam is per unit spectral bandwidth. Relativistic effects ($v \sim c$) alter the angular distribution of the emitted SR, which is then concentrated around a direction tangential to the storage ring orbit (see Fig.1). The divergence of the SR emitted by the single particle is approximately given by $1/\gamma$, where γ is the particle (typically electrons) energy E_e in units of its rest energy: $\gamma = \frac{E_e}{m_0 c^2} = \frac{1}{\sqrt{1-\left(v/c\right)^2}}$.
3. **Polarization**: the emitted radiation is linearly polarized with the electric vector parallel to the plane of the orbit. Above and below the plane of the orbit, it is elliptically polarized.
4. **Pulsed time structure** of the source, defined by the duration (order of psec) and the separation between pulses (order of nsec or longer if requested). It depends on the size of the ring (a fixed parameter) and the number of circulating bunches that can be changed by changing the electron current I, usually measured in mA.
5. **Coherence**: *transverse* (or *spatial* or *lateral*) and *longitudinal* (or *temporal*) coherence, the former depending on the size and angular spread of the source, the latter on its wavelength bandwidth $\Delta\lambda$.

Although these properties qualitatively characterize all SR facilities, the detailed characteristics of a given facility determine its specific numbers [5-7]. For example, the Swiss light Source is a 2.4 GeV facility, where 2.4 GeV refers to the electron energy E_e defined before. The value of E_e and the average magnetic field B produced

by the storage ring dipoles (also called *bending magnets*) influence the effective radius of curvature ρ of the storage ring (i.e. the radius of curvature that the ring would have without the straight sections that host wigglers and undulators): $\rho = cte\, E_e[GeV]/B[T]$. The value of E_e and B also affects the critical photon energy: $h\nu_c = {3hc\gamma^3}/{4\pi\rho} \Rightarrow h\nu_c\,[keV] \approx 0.67\, E_e^2[GeV]\, B[T]$, i.e. the value that divides the spectral distribution of the emitted radiation into two parts of equal total power. The critical energy obviously sets a limit to the maximum photon energy that the given facility would be able to provide out of its bending magnets.

The SR characteristics can be further tuned and enhanced if the radiation is extracted from the so-called *insertion devices* (wigglers and undulators, accommodated in the straight sections of the storage ring). Wigglers and undulators characterize 3rd generation synchrotron sources. They are **multiple magnets** that force the electrons to perform a *slalom course* instead of going along a straight line when they traverse them and, therefore, emit e.m. radiation at each oscillation. What makes multiple magnets wigglers or undulators is essentially the amount of deviation from a straight path (i.e. the size of the excursions inside the device) that they force the electrons to undergo, large for wigglers and small for undulators. This in turn depends on the spatial period λ_u of the magnet array (smaller for undulators) and the amplitude of the oscillating magnetic field B (larger for wigglers), the latter essentially defined by the magnetic properties of the materials. Figure 2 shows how the electron oscillations differ for wigglers and undulators.

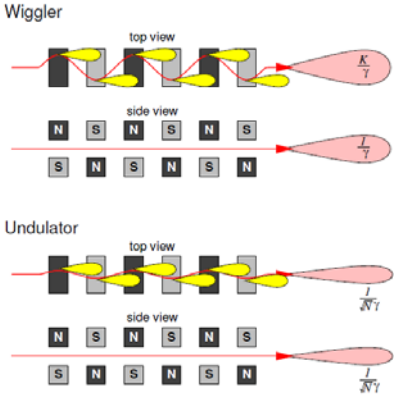

Fig. 2. . Schematic representation of the electron beam behavior in a wiggler or an undulator (Courtesy P.Willmott [7]).

Since λ_u and B define the wiggler- or undulator-like character of a multiple magnet (wiggler: longer λ_u, stronger B; undulator: shorter λ_u , weaker B), the best parameter to define if a periodic insertion device behaves like a wiggler or an undulator is

the dimensionless K parameter, $K \approx 0.934\, B[T]\lambda_u[cm]$ whose value is ~ 1 for undulators and >> 1 for wigglers.

It should be clear that without relativistic effects, the SR wavelength would not be in the desired short-wavelength range. For example, an undulator with period λ_u=1.4 cm would produce radiation of the order of its period, that is in the radio frequency range. Relativistic effects (Lorentz contraction and Doppler effect) shorten the λ of the emitted radiation in the laboratory reference system by the relativistic factor $2\gamma^2$:

$$\lambda_1 \approx \frac{\lambda_u}{2\gamma^2}\left(1+\frac{K^2}{2}+\gamma^2\theta^2\right) \overset{\text{for collection angles } \theta \text{ close to zero}}{\approx} \frac{\lambda_u}{2\gamma^2}\left(1+\frac{K^2}{2}\right).$$

For K small (<0.4) the emitted intensity is mostly concentrated at the fundamental wavelength λ_1. As K increases by applying higher B values, however, the motion of the electrons inside the multiple magnets is no longer a pure sinusoidal transverse motion and not negligible intensity is also emitted corresponding to higher harmonics λ_n [5-7]:

$$n\lambda_n \approx \frac{\lambda_u}{2\gamma^2}\left(1+\frac{K^2}{2}\right) \approx \frac{13.056\,\lambda_u[cm]}{E_e^2[GeV]}\left(1+\frac{K^2}{2}\right).$$

The energy of the emitted radiation depends, therefore, on K but how close in energy are the harmonics and how the intensity is distributed among the fundamental wavelength and its harmonics also depends on K[1]. Tuning K, therefore, allows us to change the intrinsically discrete character of the undulator emission spectrum (spectrum with well separated emission lines) into a sort of continuous-like spectrum by smoothly swap from the fundamental λ_1 to the higher harmonics while tuning the K parameter. It remains intrinsically different from the continuous emission spectrum of the bending magnet and wiggler radiation, but it allows covering uninterruptedly a wide energy range.

Another important figure of merit characterizing SR is its angular spread in both the direction perpendicular θ_v and parallel θ_h to the storage ring plane. Referring to [6] for a derivation, we find that:

Wigglers: $\theta_v \approx 1/\gamma; \quad \theta_h \approx K/\gamma$

[1] The higher is the value of K, the closer are to each other the generated harmonics. Therefore, a wiggler can be thought as an undulator with an extremely high number of harmonics so close to each other to generate a continuous bending magnet-like spectrum. The wiggler continuous spectrum is also characterized by the critical photon energy $h\nu_c \propto E_c^2, B$, where B is now the amplitude of the "local" magnetic field. Because wigglers are characterized by higher B value, they shift the maximum emitted photon energy towards values higher than those of bending magnets.

Undulators: $\theta_v = \theta_h \approx 1/\gamma\sqrt{nN}$ (n: harmonic number, N:number of periods)

Bending magnets: $\theta_v \approx 1/\gamma$; $\theta_h \approx$ no intrinsic limitation

The *unlimited* horizontal angular spread characterizing bending magnets is due to the fact that here the emission direction of the radiation changes as the electrons move inside the storage ring and, therefore, the SR is emitted in the horizontal plane as a search light. In practice, the value of θ_h is limited by the obviously limited acceptance of the beamline optics and explains why one single bending magnet occasionally serves more than one bending magnet beamline.

2. SR-XRPD beamline optics

Once SR is extracted, depending on the planned experiments, the SR beam will be ad-hoc *conditioned* by appropriate beamline optics. Beamline optics together with the choice of a given magnetic device allow the same synchrotron facility to host beamlines operating over very different energy ranges (e.g. from the infra-red up to the hard X-rays in a medium energy facility like the SLS[2]).

In the case of powder diffraction, the ultimate achievable overall angular (FWHM) resolution depends on (but not only) the energy resolution $\Delta\lambda/\lambda$ and the degree of collimation of the photon beam. Therefore, the beamline optics for a high-resolution PD station should provide a highly monochromatic and collimated beam. On the other hand, for experiments requiring fast acquisition times (e.g. time-resolved XRPD) and/or "photon-hungry" experiments (e.g. Pair Distribution Function data collection), the ability to focus the X-ray beam is very important. The beamline optics should, therefore, ideally provide dynamic focusing capabilities.

Beamline optics for SR-XRPD usually consists of a monochromator (typically a double crystal monochromator DCM) and one or two mirrors [8-12]. A channel cut can replace or follow the DCM to further improve the energy resolution [13]. As a representative example of SR-XRPD beamline optics, we discuss the optics characterizing the Swiss Light Source Materials Science (SLS-MS) beamline before and after its upgrade to an undulator beamline, started in October 2010.

The SLS-MS beamline started being operative in 2001 and for ~10 years it has been the only wiggler beamline at the SLS and the one delivering the hardest X-rays (5-40 keV) [8]. Back in 2001, in medium energy facilities, a wiggler was in fact the only option to reach photon energies as high as 40 keV with usable intensities. The maximum achievable photon energy that the 2001 undulator technology was able to achieve was ~25 keV with a U19, a prototype at that time [14].

[2] Since the optics needs to be optimized for the specific working energy range and the specific experiment, each beamline covers only a portion of the entire range covered by the given facility.

The discovery of stronger magnetic materials (i.e. with higher B) and the improvement of the *in-vacuum* undulator technology have made it possible to design and construct a new *in-vacuum* undulator with a shorter λ_u=14mm period (therefore called U14 [14]). A shorter λ_u allows the energy of the fundamental and higher harmonics to be shifted towards higher values, whereas higher B values allow one to keep the K value essentially constant ($K \propto B \cdot \lambda_u$).With the prototype U14 therefore, the SLS-MS beamline still covers the 5-40 keV energy range, but with all the advantages of an undulator beamline, namely enhanced brilliance and intrinsic collimation of the beam.

Figure 3 shows a schematic view of the SLS-MS beamline optics based on a wiggler (2001-2010) and an undulator source (2010-on). With the wiggler source, the first optical element is a vertically collimating Rh-coated Si mirror followed by a Si(111) DCM and a second Rh-coated Si refocusing mirror. The DCM main axis of rotation defines the selected wavelength via Bragg's law: $2d_{Si(111)} \sin\theta = n\lambda$. In a DCM, however, the energy resolution totally relies on the degree of collimation of the incoming photon beam (see Fig. 4).

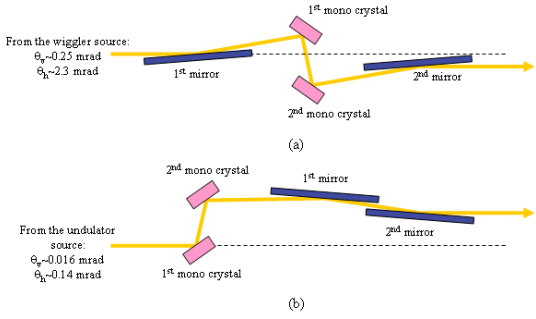

Fig. 3. Schematic representation of the SLS-MS beamline optics based on a wiggler (a) and on an undulator (b) source

We have seen that the intrinsic divergence of a photon beam generated by a wiggler source is relatively large (~0.25 x 2.3 mrad^2 at the SLS-MS) and, therefore, it imperatively requires the use of a collimating mirror placed before the DCM. The second crystal of the DCM is a bendable crystal which provides a collimated or a focused beam in the sagittal (horizontal) plane and guarantees a fixed beam exit height. Finally, the beam is reflected onto the second mirror, which can either be bent, and deliver a focused beam or kept flat and deliver a collimated beam (high-angular resolution set up).

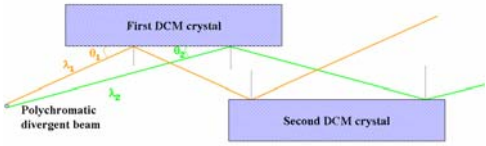

Fig. 4. Schematic view of a DCM: λ_1 and λ_2 are two discrete wavelengths belonging to the polychromatic divergent incident beam satisfying Bragg law for the same interplanar distance d of the DCM crystal and a combination (λ_i,θ_i) of photon wavelength and Bragg angles.

The SLS-MS beamline optics based on an undulator source is also schematically described in Fig.3. The photon beam can now directly be sent on the DCM being the fairly small undulator beam residual divergence in the vertical (diffraction) plane comparable with that of the wiggler beam after collimation from the first mirror. Why still having two mirrors? For essentially two reasons:

- The ability to focus the beam down to approximately 200 x 9 μm^2 (unfocused beam size 2.9 x 0.34 mm^2) for all photon energies, but to this purpose one single mirror would have been enough.
- To get an horizontal and fixed beam exit.
- Higher harmonics suppression to better than 10^{-7} that can only be achieved with two mirrors working close to the critical angle α_c for total external reflection [15].

For the purpose of the efficient suppression of the higher harmonics, whether the mirrors are placed before or after the DCM does not play any role. Placing them after the DCM, however, allows us to preserve the beam coherence when working with only one or no mirrors.

3. Powder Diffractometer

The mechanical properties of SR powder diffractometers need to be consistent with ultra-high-resolution requirements. Mechanical accuracy and precision (reproducibility) of ±1-2 and resolution of 1 arcsec usually characterize SR powder diffractometers [8-13, 16].
Figure 5 (left) shows the SLS-MS powder diffractometer as an example. If you are used to laboratory diffractometers, what probably immediately strikes you is the size and weight and the vertical plane of diffraction.

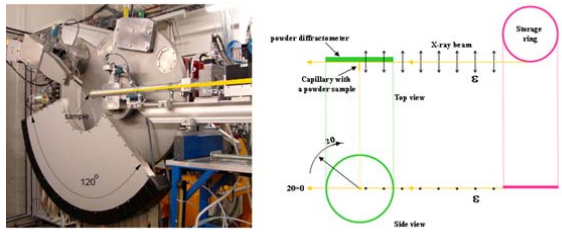

Fig. 5 . The SLS-MS powder diffractometer (left). A pictorial description explaining why the diffraction plane is vertical (right).

The considerable size and weight guarantee high mechanical stability, whereas the choice of the vertical plane as diffraction plane is related to the linear polarization property of the SR beam in the plane of the electron orbit. As pictorially described by Fig.5, if the diffraction plane is perpendicular to the electron orbit (storage ring plane), the electric field **ε** associated with the incoming e.m. radiation will always be at 90° with respect to the scattered beam for all 2θ values. In other words, there will not be a 2θ dependence of the scattered intensity from the 2θ and the polarization factor P=1.

The SLS-MS powder diffractometer consists of three coaxial independent rotary tables and it is the result of a joint SLS and Rotary Precision Instrument® development project. The central table (ω-axis) hosts the sample or sample environment. The other two tables host two independent detection systems: a multi-crystal analyzer detector [17] and a wide-angle (120°) silicon solid state microstrip 1-D position sensitive detector (MYTHEN II) [18] that we discuss later.

4. Detectors

A comprehensive overview of detectors is beyond the scope of this lecture. Through examples of detectors widely used at synchrotron facilities, however, we define and discuss a few relevant detector-related concepts, namely ***angular selectivity***, ***position sensitivity***, ***point-***, ***1D-*** or ***2D-***detectors, ***direct*** or ***indirect conversion***, ***single-photon-counting*** or ***integrated*** detectors.

Angular selectivity refers to the selection of the diffracted beam by means of a crystal (called, therefore***, crystal analyzer***) oriented at the appropriate Bragg angle, before reaching the detector. Without a crystal in the secondary beam, the diffracted rays are assigned an angular value based on the position at which they hit the detector, therefore called ***position-sensitive*** detector. Intensity that arrives at the analyzer crystal from inelastic scattering (i.e. fluorescence emission, Compton scattering), air scattering is suppressed providing an ultra-high angular (FWHM) resolution, a high signal-to-noise (S/N) and a high signal-to-background (S/B). In addition to that, the angular selectivity makes the angular (FWHM) resolution independent of the sample

dimension (capillary diameter in transmission measurements) and its accurate positioning at the center of the diffractometer.

Analyzer detectors – These are detectors (typically point-detectors) that include a crystal analyzer in the secondary beam. Angular selectivity is very costly in terms of diffracted intensity and a smart solution to recover some of the lost intensity was found by Hodeau et al. in 1998 [17] with their ***multicrystal analyzer detector*** design. Their idea consisted in placing n independent analyzer crystals as a fan at a fixed offset and simultaneously collecting the diffracted signal with the detector following each crystal. The counting statistics are, then, increased by n but the counting time still remains of the order of min or hours.

Position sensitive detectors - These are 1- or 2-D detectors that identify the value of the 2θ scattering angle from the position at which the diffracted ray reaches the detector. 2-D detectors record the full Debye-Scherrer rings whereas the 1-D detectors only one section of them, whose width is defined by the detector aperture and make, therefore, the implicit assumption that the selected sections are representative of the whole rings. The MYTHEN detector is a 1-D position silicon solid state detector. It is an *in-house* development at the Paul Scherrer Institut conceived for time-resolved powder diffraction experiments. [18] It is a modular 1-D detector with over 30'000 elements covering an angular range of 120° in 2θ (24 modules, each covering 5°). Depending on the dynamic range (4-24 bits), the read out time ranges between 90 and 250 μsec whereas its frame rate (1 frame = 1 diffraction pattern) ranges from 10 Hz (24 modules, 24 bits) to 600 Hz (1 module, 4 bits). Figure 6 explains the principle of operation of solid state detectors. MYTHEN performances in terms of high angular (FWHM) and d-spacing resolution, S/N and S/B are comparable with those of analyzer detectors with a counting efficiency at least two orders of magnitude higher and acquisition times several orders of magnitude shorter. These outstanding characteristics make MYTHEN also ideal for the structural analysis of radiation-sensitive materials, such as organic compounds, and for applications to total scattering techniques for which high real space resolution data (i.e. high values of the momentum transfer $Q=2\pi\sin\theta/\lambda$), high S/B, high S/N ratios and a remarkable counting statistics over the entire angular range are of paramount importance.

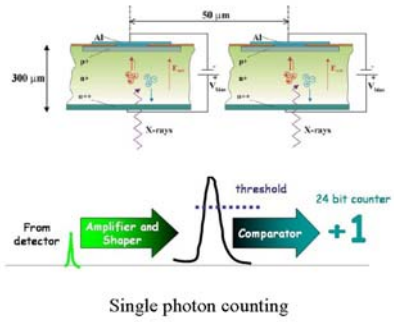

Fig. 6. Principle of operation of a solid state detector like MYTHEN.

As all position-sensitive detectors, MYTHEN does not perform an angular selection of the diffracted beam and is, therefore, sensitive to inelastic scattering signals and its intrinsic angular resolution (~ 0.004° in 2θ) is relaxed by the sample dimension. What makes MYTHEN very special among conventional position sensitive detectors, however, is connected to the fact of being a ***direct conversion single photon counting*** detector. When X-ray photons arrive on the silicon sensor (see Fig.6), they are absorbed and produce free charge (electron-hole pairs) whose number is proportional to the energy of the X-ray photon. The created charge is, then, separated by a voltage V_{bias} applied to the junction and travels to the electrodes where it results in a pulse. The pulse is then amplified, shaped and compared to a user-defined threshold. Only the signal whose amplitude is above this threshold is counted. Properly chosen for the given experiment, the threshold rejects, therefore, all unwanted signal (e.g. electronic noise, fluorescence signal).

Solid state detectors are, therefore, based on the production of charge directly from the X-ray photons without the intermediate conversion into visible light in a phosphor screen (which normally poses limitations on the spatial resolution because of light diffusion). Their efficiency depend on the photon energy and for Si and 300 µm sensor thickness (as for MYTHEN) is 100% at 7keV but already 15% at 25 keV, making them not ideal for photon energies above 40 keV. The PSI detector group is presently working on thicker Si sensors and detectors made with different absorbing materials.

For powder diffraction, 2-D detectors (e.g. **I**mage **P**late, **C**harged **C**oupled **D**evices, amorphous-Si **F**lat **P**late, **P**ixel **D**etectors) are also often employed. They simultaneously collect full Debye-Scherrer rings and their direct-space resolution is directly proportional to their size and inversely proportional to the angular (FWHM) resolution. With MYTHEN, the FWHM and d-spacing resolutions are instead decoupled. In Image Plate (IP) detectors [19], the core of the detector is a storage phosphor screen and the creation of an image requires illuminating the plate twice: the first exposure, to the radiation of interest, "writes" the image, and the second, to a visi-

ble-laser, "reads" the image. After the initial exposure, excited electrons in the phosphor material remain "trapped" in color centers (so-called F-centers) in the crystal lattice that constitutes the image plate until stimulated by a second illumination. The emitted visible light is, then, recorded by a photomultiplier. In terms of efficiency, dynamic range and read-out times the IP detectors are not very competitive and CCD or amorphous-Si Flat Plate detectors are often preferred.
At the APS 1-ID beamline [20], a high-sensitivity (quantum efficiency > 65%), fast-readout (up to 30 Hz) a-Si Flat Plate (FP) detector has been installed for in-situ fast PDF acquisitions at high Q values (Qmax > 35Å-1). FP detectors are based on amorphous-silicon thin-film-transistor (TNT)/photodiode arrays coupled to X-ray scintillators. The coupling with scintillators that convert the X-rays into visible light makes them very efficient even with the hard X-ray photon beams.
Charged Coupled Devices (CCD) detectors performances are, to some extend, in between the IP and the a-Si FP detectors. Reference [20, Table 1] provides a suitable comparison among these three different detector technologies. CCDs consist of a photoactive region (usually epitaxial p+-Si) and a transmission region (the CCD, properly speaking). As for the IP and the a-Si FP, it is based on the conversion of the X-rays into visible light by means of scintillators.
All the 2-D detectors discussed above are ***integrating detectors***. They collect the totality (elastically and inelastically scattered plus noise) of the signal reaching the detector without setting a discriminating threshold, as MYTHEN does.
The 2-D version of MYTHEN is the PILATUS pixel detector [21]. Apart from all the advantages of the single photon counting mode discussed for MYTHEN, PILATUS has a readout time of 5ms, a dynamic range of 20 bits and a pixel size of 172 μm x 172 μm. Pixel 2D detectors have, however, quite small area/pixel ratio, which often make IPs and CCDs a preferred choice for XRPD [18] MYTHEN and PILATUS are now commercialized by the spin-off company DECTRIS [22].

6.1 .SR-XRPD highlights

The remarkable developments of instrumentation, computer technology, experimental techniques (e.g. anisotropic thermal expansion and texture methods by Brunelli et al [23] and Wessels et al [24] and methodologies [e.g. global optimization techniques by David & Shankland [25]; resolution bias algorithm by Altomare et al [26]; charge flipping by Oszlanyi et al [27]) that have characterized the powder diffraction technique of the last 10-15 years, have made it an undoubtedly powerful tool for both structural solution and refinement and microstructural analysis of a large variety of materials. Not only is powder diffraction a valuable alternative to single crystal diffraction when appropriate single crystals cannot be obtained, but it is often the preferable choice for *in-situ*, non-ambient and time-resolved analyses and for the analysis of materials at the nanoscale [28,29].

We discuss here a few experiments performed at synchrotron facilities as examples of recent SR-XRPD applications. They do not constitute an overview of outstanding SR-XRPD applications, but a restricted choice due to the limited available time and space. Not discussed but of special note are SR-XRPD applications to the structural analysis of proteins that will be the subject of two lectures by Irene Margiolaki and Jonathan Wright, pioneers in this field with their co-workers at the ESRF [30]; the *in-situ* studies of polymorphism of chocolate where polymorphic transformation in coca butter have been studied *in-situ* and in real time as a function of temperature and in parallel to the rheological properties of fats [31]; the study of the dependence of the photocatalytic activity of TiO_2 nanocrystals (a *smart textile* material of industrial interest) on the nanocrystals size and shape by means of a combination of SR-XRPD and total scattering methods based on the Debye function [32].

5.1 Structural solution of small organic molecules

Ab-initio structural solution and refinement of small organic molecular compounds (e.g. pharmaceuticals) is one of the fields where advanced SR-XRPD instrumentation and new methodologies are perfectly married to each other. Although successful structural solutions from powders have been achieved using laboratory data [33], for increased complexity of the system under investigation the outstanding quality of SR-XRPD data is often the key for the success of their structural solution. Small organic molecular compounds, however, are often strongly affected by radiation damage, a normally unavoidable side effect of SR [34]. Therefore, the combination of SR properties with the very high counting efficiency of the SR detectors discussed before, allows collecting data of outstanding quality before irreversible changes in the compound occur. At the SLS-MS powder beamline we have devoted considerable efforts to optimizing the beamline optics, the calibration of the 1-D single-photon counting detector MYTHEN II, the experimental set up and the data collection strategy. Furthermore, the remarkable counting statistics of MYTHEN II even at subsec acquisition times allows us to study *in-situ* the details of structural transformations. Figure 7 shows as an example the diffraction patterns of S-bupivacaine hydrochloride, a long-acting anesthetic drug of the amide type used for local anesthesia [35], recorded at the SLS-MS powder station using the Si(111) multicrystal analyzer detector and MYTHEN II at 50% reduced beam intensity.

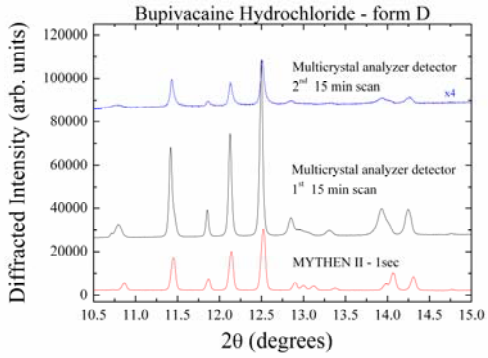

Fig.7. Detail of the SR-XRPD pattern of form D of S-bupivacaine recorded at 12 keV with the multicrystal detector for 15 min and with MYTHEN II in 1 sec.

The first and second powder diffraction patterns recorded by the multicrystal analyzer detector were acquired for 15 min by continuously moving the detector arm between 0° and 50° in 2θ, whereas several 1 sec diffraction patterns were collected with MYTHEN covering simultaneously 120° in 2θ. A comparison of the first and second multicrystal analyzer diffraction patterns clearly shows that the first 15 min of measurements already damaged the sample and that the damage was already not negligible after the acquisition of the first 10°. The structures at 13° and 14° are strongly compromised by the radiation damage. Successive multiple 1 s data acquisition with MYTHEN, always at reduced intensity, showed that the powder was stable for at least 2-3 min (Fig.7 shows one of these 1s runs). While the analyzer detector data were not usable for indexation and structural solution, MYTHEN data delivered a successful structural solution of form D of bupivacaine in $P2_12_12_1$ space group type [36].

Another example of structural solution and refinement achieved with MYTHEN II data is the study of the polymorphism of carprofen, which undergoes a subtle isostructural transformation as a function of temperature and whose structure was not accessible with analysis of laboratory data [37]. Figure 8 shows the molecular packing of the metastable form of carprofen (left) and its molecular scheme (right) indicating the internal degrees of freedom of the molecule. It was found that the main difference between polymorph I and II structures was the rotation of the propane skeleton about the C-C bond (torsion 1 in Fig.8) and that form II was characterized by configurational disorder**.**

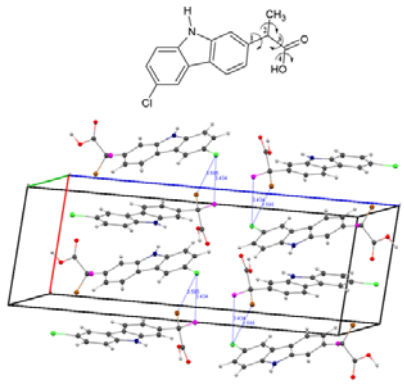

Fig.8. Molecular packing diagram of polymorph II of carprofen showing the predominant (C atom in brown) and the disordered (carbon atom in magenta) configurations. The H atoms of the methyl group directly involved in the configurational disorder have been omitted for clarity. A complete discussion of the structure of carprofen can be found in [37]

5.2 Microwave-assisted heating

Microwaves can be efficiently used as source of heating during the chemical synthesis of materials. Due to its low energy consumption and ultrafast heating and cooling rates, the latter essential for the preservation of nanoscale features in bulk nanostructured solids, microwave-assisted heating has recently received a lot of attention as a valid alternative to conventional methods [38,39]. Its development and scaling up to industrial applications depends, however, on the understanding of the mechanisms behind it, which in turn is related to the ability to follow in-situ and in real time the evolution of materials during heating and cooling. In 2007, Vaucher, Nicula and coworkers [39] have performed at the SLS-MS powder station the first in-situ microwave heating experiments using synchrotron radiation and MYTHEN I detector (Fig 9).

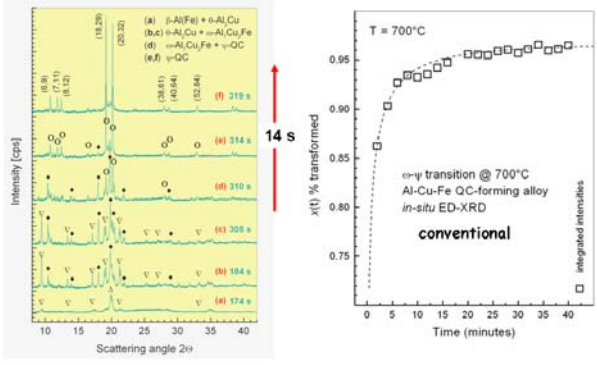

Fig.9. Left: sequence of solid-state transitions leading to the formation of single-phase quasicrystals [37]. Up-triangles β-Fe(Al); down-triangles θ-Al2Cu; diamonds ω-Al7Cu2Fe; open circles ψ-phase. Right: rate of transformation of θ→ψ phases at 700 C with conventional heating. Courtesy Sebastian Vaucher.

Figure 9 (left) shows the evolution in time of the solid state phase transformations during microwave heating of metallic nanopowders of Al, Cu and Fe to form single phase quasicrystals. The comparison of the transformation rate between microwave assisted and conventional heating (Fig. 9, right) shows for the former an exceptional rate enhancement. After 40 min at 700° C only 96% of the sample is transformed into the QC phase with conventional heating, whereas the same transition is fully completed in less than 10 s if microwaves are employed**.**

5.3 Self-Propagating Exothermic Reactions

Ultra-fast SR-XRPD experiments were performed by Fadenberger and co-workers to study *in-situ* the dynamics of structural transformations occurring in Self-Propagating Exothermic Reactions (SPER). For the first time this was performed with the angular (FWHM) resolution necessary to identify and follow the formation and evolution of phases [40]. Self-Propagating Exothermic Reaction (SPER) are self-sustained thermal processes that interest industry for their reduced energy consumption via targeted delivery of the heat in the desired area. The understanding of the mechanisms driving self-propagating reactions requires monitoring the reactions and the induced phase transformations as they occur. The high flame front velocities (1-20 m/s) characterizing SPER require, therefore, diffraction analysis at the submilliseconds scale with angular resolutions and statistics appropriate for phase identification.

Figure 10 shows the experimental set up of an *in-situ* SPER experiment performed on nanoscale foils of $Ni_{0.9}V_{0.1}$-Al multilayers at the SLS-MS beamline using MYTHEN II detector, in combination with high-speed (HS) optical and infrared (IR) imaging [38].The experiment starts with the foil ignition via a high-voltage electric spark generated by a central trigger system, which simultaneously triggers the HS and thermal cameras and the MYTHEN II detector.

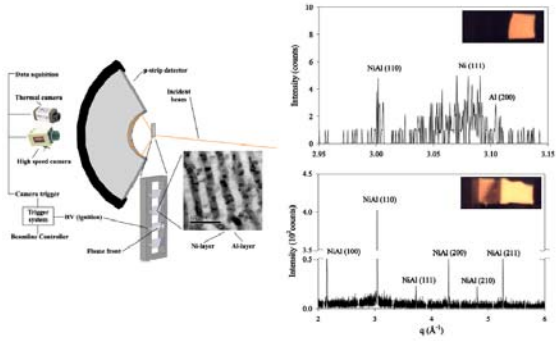

Fig. 10. Left: SPER experimental set-up for *in-situ* SR-XRPD with MYTHEN II. Right above: 1 to 1.125 msec after ignition (acquisition time of 0.125 msec) showing superimposed peaks of reactants and the formed NiAl. Right, below: identification of NiAl phase 8 to 9 ms after ignition (acquisition time of 1 msec)**.**

The HS and thermal cameras start recording optical and thermal images while MYTHEN starts recording successive XRPD patterns. XRPD frames were recorded using 0.125, 0.25, 1 and 5 msec acquisition times with dead times between successive frames of 0.125 or 20 msec, depending on the acquisition time. Figure 10 shows the complex SPER experimental set up and two of the multiple XRPD frames recorded by MYTHEN II at 0.125 msec (above) and 1 msec (below) acquisition time at 1msec and 8 msec from ignition, respectively. The patterns remarkably show the change in composition of the films occurring over extremely short times.

Acknowlwdgements

Behind successful SR beamlines there is always a team of people (always smaller than necessary) working enthusiastically together and sharing the many heavy tasks. At the SLS-MS we are, in alphabetic order: Antonio Cervellino, Fabia Gozzo, Michael Lange, Dominik Meister, and Philip Willmott. At the MS, we also have the chance to closely work with a fantastic detector group at PSI, which has delivered at PSI and worldwide outstanding new detector technology. MS is particularly grateful to Bernd Schmitt and Anna Bergamaschi.

References

[1] F. R. Elder, A. M. Gurewitsch, R. V. Langmuir, H. C. Pollock, Phys. Rev. **71**, 829-830 (1947).
[2] J. Blewett, J. Synchrotron Rad. (1998). **5**, 135-139.
[3] G. C. Baldwin, Physics Today (1975), 9.
[4] J. R. Helliwell, Acta Cryst. (1998). **A54**, 738-749.
[5] *Introduction to Synchrotron Radiation*, Giorgio Margaritondo, Oxford University Press 1988.
[6] *Elements of Synchrotron Light*, Giorgio Margaritordo, Oxford University Press 2002.
[7] *An Introduction to Synchrotron Radiation: Techniques and Applications*, Philip Willmott. John Wiley and Sons, Chichester, GB, July 2011
[8] B.D Patterson, R. Abela, H. Auderset, Q. Chen, F. Fauth, F. Gozzo, G. Ingold, H. Kuehne, M. Lange, D. Maden, D. Meister, P. Pattison, Th. Schmidt, B. Schmitt, C. Schulze-Briese, X. Shi, M. Stampanoni & P. R. Willmott, Nucl. Instrum. Meth. (2005). **A540**, 42-67.
[9] B. H. Toby, Y. Huang, D. Dohan, D. Carroll, X. Jiao, L. Ribaud, J. A.. Doebbler, M. R. Suchomel, J. Wang, C. Preissner, D. Klinea and T. M. Mooneya, J. Appl. Cryst. (2009). **42**, 990-993.
[10] K. S. Wallwork, B.J. Kennedy, and D. Wang, AIP Conf. Proc.(2007). **879**(1), 879-882.
[11] C.C. Tang, M.A. Roberts, F. Azough, C. Leach & R. Freer (2002), J. Materials Research **17**, 675-682.
[12] O. Masson, E. Dooryhee, R.W. Cheary, and A.N. Fitch,Mater. Sci. Forum, (2001) **300**, 378–381. See also: http://www.esrf.eu/UsersAndScience/Experiments/StructMaterials/ID31.
[13] Technical information and a complete list of the Swiss Norwegian beamline publications can be found at: http://www.esrf.eu/UsersAndScience/Experiments/CRG/BM01/bm01b
[14]Th. Schmidt, G. Ingold, private Communication.
[15]Thin Film Analysis by X-ray Scattering, Mario Birkholz, John Wiley-VCH 2006, p.161-165.
[16] F. Gozzo, B. Schmitt, Th. Bortolamedi, C. Giannini, A. Guagliardi, M. Lange, D. Meister, D. Maden, P.R. Willmott and B.D. Patterson, J. Alloy Compd. (2004), **362**, 206-217.
[17] J.-L. Hodeau, P. Bordet, M. Anne, A. Prat, A..N. Fitch, E. Dooryhee, E., G. Vaughan and A.K. Freund, Proc. SPIE (1998). **3448**, 353–361.
[18] A. Bergamaschi, A. Cervellino, R. Dinapoli, F. Gozzo, B. Henrich, I. Johnson, P. Kraft, A. Mozzanica, B. Schmitt and X. Shi, Nucl. Instrum. Methods (2010)**17**(5):653-68.
[19] P. J. Chupas, X. Qiu, J. C. Hanson, P. L. Lee, C. P. Grey and S. Billinge, J. Appl. Cryst. (2003). **36**, 1342-1347.
[20] P.J.Chupas, K.W.Chapman and P.L.Lee, C. P. Grey, J. Appl. Cryst. (2007). 40, 463-470.
[21] C.M. Schlepuetz, R. Herger, P.R. Willmott, B.D. Patterson, O. Bunk, C. Broennimann, B. Henrich, G. Huelsen, and E.F. Eikenberry, Acta Crystal. (2005). **A61**, 418.
[22] See extensive technical information on the company web site at: http://www.dectris.com

[23] Brunelli, M., Wright, J. P., Vaughan, G. B. M., Mora, A. J. & Fitch, A. N. (2003). Angew. Chem. **115**, 2075–2078.
[24] Wessels, T., Baerlocher, C. & McCusker, L. B. (1999). Science, **284**, 477–479
[25] David, W. I. F. & Shankland, K. (2008). Acta Cryst. **A64**, 52–64.
[26] Altomare, A., Cuocci, C., Giacovazzo, C., Maggi, S., Moliterni, A. & Rizzi, R. (2009). Acta Cryst. **A65**, 183–189
[27] Oszlanyi, G.,Suto, A.,Czugler, M. & Parkanyi,L. (2006). J. Am. Chem. Soc.**128**,8392–8393.
[28] *Structure Determination from Powder Diffraction Data*, Ed. W.I.F. David, K. Shankland, L.B.McCusker and Ch. Baerlocher, Oxford University Press, 2002.
[29] *Diffraction at the Nanoscale: Nanocrystals, Defective & Amorphous Materials*, Ed. A. Guagliardi & N.Masciocchi, Insubria University Press, 2010.
[30] Margiolaki, I., Wright, J. P., Fitch, A. N., Fox, G. C. & Von Dreele, R. B. (2005). Acta Cryst. **D61**, 423–432. See also: Margiolaki, I. & Wright, J. P. (2008). Acta Cryst. **A64**, 169–180.
[31] S. Padar, Y. E. Merhle and E. J. Windhab, Cryst. Growth Des.(2009), 9,4023-4031. See also: ESRF highlights at www.esrf.eu/UsersAndScience/Publications/Highlights.
[32] G. Cernuto, N. Masciocchi, A. Cervellino, G.M.Colonna and A. Guagliardi, J. Am. Chem. Soc. 2011, **133**,3114-3119.
[33] K. D. M. Harris**,** Current Opinion in Solid State and Materials Science 6 (2002) 125–130
[34] Niederwanger, V., Gozzo, F. & Griesser, U. (2009). J. Pharm. Sci. **98**, 1064–1074.
[35] Holton, J. M. (2009). J. Synchrotron Rad. **16**, 133–142.
[36] Gozzo, F., Masciocchi, N., Olieric, V., Wang, M., Griesser, U. & Niederwanger, V. (2010). Personal communication.
[37] G. Bruni, F. Gozzo, D. Capsoni, M. Bini, P. Macchi, P. Simoncic, V. Berbenni, C. Milanese, A. Girella, S. Ferrari and A. Marini, J. Pharm. Sci. 2011 Jan 18. doi: 10.1002/jps.22470
[38]S. Vaucher & R. Nicula, Chemistry Today **26**(3) 2008, 38-39.
[39]S. Vaucher, R. Nicula, J.M.Catala-Civera, B. Schmitt and B. Patterson, J. Mater. Res., **23**(1), 2008, 170-175.
[40]K. Fadenberger, I. E. Gunduz, C. Tsotsos, M. Kokonou, S. Gravani, S. Brandstetter, A. Bergamaschi, B. Schmitt, P. H. Mayrhofer, C. C. Doumanidis and C. Rebholz, Appl. Phys. Lett. **97**, 144101 (2010).

Ultrafast Powder Diffraction

Andy Fitch and Caroline Curfs
ESRF, BP 220, F-38043 Grenoble, France

Introduction

An important use of powder diffraction is in the study of samples that are undergoing some sort of structural modification of a physical or chemical nature. Such experiments are often designed to investigate the kinetics and the mechanism of the process, which can be a phase transition caused by a change of the temperature, pressure or other external condition, or a chemical reaction taking place in the sample. Modern powder instruments, particularly at sources of penetrating radiation such as neutrons or high-energy synchrotron X-rays, allow sophisticated sample environments to be exploited, with great flexibility in the design of *in-situ* experiments to study evolving systems. The question naturally arises as to just how fast a process can be usefully measured.

For measuring rapidly there are several technical issues to consider. For example, rapid processes require powder diffraction patterns to be recorded with appropriate time resolution – on the timescale of s, ms, μs, or faster still? – needing a detector system that can acquire data and be read out fast enough. However, simply registering patterns at enormous speed is of little use if the quality of the data is not sufficient to reveal the relevant details of the sample on that time scale. For the fastest, irreversible processes therefore, both high flux at the sample and efficient detectors are required. A high flux at the sample can be obtained by appropriate design of the source and instrumental optics, possibly focusing, and maximizing the energy spread of the radiation used to probe the sample.

For reversible processes, the stroboscopic approach can be used, in which the process under investigation is cycled and diffraction patterns registered during a small time window are accumulated over a number of cycles, progressively building up the statistical quality of the pattern. During the course of the experiment, the time window probes different parts of the cycle so as to cover it as required.

As a general rule, speed has to be traded against *d*-spacing or angular resolution. High resolution involves selecting only those neutrons or X-rays with an energy lying in a narrow range and whose trajectory from the source to the detector via the sample follows a stringently defined path (i.e. with a low divergence for the radiation incident on the sample and a tightly defined angular acceptance range for the detector, so as to have an exact measure of the Bragg angle θ). This necessarily excludes a large fraction of the photons or neutrons from the source or scattered by the

sample which do not fulfill the criteria and so is a relatively inefficient process. Rapidly acquiring data of adequate statistical quality for meaningful analysis requires the maximum number of photons or neutrons to contribute to the diffraction pattern. Thus the selection criteria on the recorded radiation need to be relaxed by increasing the energy spread of the radiation and by allowing more pathways through the instrument (greater divergence), thus reducing the overall resolution.

Instrumentation

Fast data collection requires a fixed multi-channel detector system that can record the whole of the diffraction pattern essentially in one cycle. Scanning a detector system through the *d*-spacing range of interest necessarily takes a few seconds so is too slow to measure the fastest processes.

If working with monochromatic radiation and an angular-dispersive instrument then a fast-readout two-dimensional area detector or a one-dimensional position sensitive detector is the system of choice. 2-D detectors that have been found suitable for use with hard X-rays include the Frelon camera, based on CCD technology, and developed at the ESRF [1], and commercially available large flat-panel detectors, developed primarily for medical imaging at hard energies, which have been exploited at speeds of up to 30 Hz [2–4]. A 1-D detector can be emulated by applying a mask to an area detector and only reading out the region of interest. Using the Frelon camera at beamline ID11 at ESRF, a time resolution of 10 ms has been achieved in this way with a 64 × 1 rebin of the data on the CCD chip [1]. Other read-out modes exist, such as rapidly transferring the electronic image to the masked part of the plate, which is read while the plate is re-exposed.

The best one-dimensional curved PSD for X-rays is the modular Mythen detector developed at the Paul-Scherrer Institute in Switzerland [5]. These detectors can be found on the powder diffraction beamlines at the Swiss Light Source, the Australian synchrotron, and Diamond in the UK. Based on Si technology, (at the time of writing), the detector is limited to detecting X-rays of up to ≈25 keV (0.5 Å wavelength). At SLS the detector covers 120° in 2θ, 30720 channels, that can be read in parallel in 250 μs, with plans to be able to read even faster.

At ILL Grenoble, the angular-dispersive powder neutron diffractometer D20 [6] is equipped with a large curved microstrip PSD covering 153.6° in 2θ in 0.1° steps. The detector can be read in around 160 ms so giving a maximum time resolution of about 6 Hz. At ANSTO in Sydney, the high intensity powder diffractometer Wombat [7] is equipped with a similar curved PSD, covering 120° in steps of 0.125°. The detectors of both instruments can be used in stroboscopic mode.

With polychromatic radiation - which automatically exploits a greater fraction of the radiation from the source - the neutron time-of-flight approach is ideal, or for synchrotron radiation an energy-dispersive solid-state detector is required. Both methods work with detectors positioned at known 2θ angles that record the diffraction

pattern by discriminating the wavelength or energy of each detected neutron or photon. For the fastest measuring rates multiple detectors are required. Examples of neutron powder diffractometers with extensive detector coverage are GEM [8] at ISIS, and the recently opened POWGEN [9] at the SNS (Oak Ridge). The former has a detector area of 7.27 m^2 covering scattering angles from 1.2° to 171.4°, and the latter, when completed, will have more than 40 m^2 of detectors from 10° – 170° 2θ (about 4 steradians of detector coverage, some 240,000 individual elements).
With energy-dispersive measurements the detector consists of a liquid-nitrogen-cooled semiconducting Ge crystal. The energy of an absorbed X-ray photon, typically within the range 10–150 keV depending on the source, promotes electrons to the conduction band in proportion to its energy. By analyzing the amplitude of the charge pulses arriving from the crystal, the energy of the absorbed photon is determined with a multi-channel analyzer. The conversion from photon energy (in keV) to wavelength (in Å) is $E = 12.398 / \lambda$ (where $12.398 \approx hc/e \times 10^7$). The energy resolution of such a detector is modest, around 2%. Owing to the need to take into account several energy-dependent effects, e.g. absorption and scattering factors, the shape of the incident X-ray spectrum, and the detector response, modeling the intensities of the powder diffraction pattern in a Rietveld refinement is generally difficult.

Examples
For the fastest processes, synchrotron radiation is generally expected to have the best performance, because of the very high flux from the source. However, neutrons, because of their penetrating power, can be used with larger samples, which can compensate to some extent.

Combustion synthesis
This is a technique for synthesizing materials that exploits the high exothermic heat of reaction to promote a self-sustaining reaction, either by propagation from a point of ignition, or by heating the whole sample volume to a point where reaction occurs essentially simultaneously throughout. A number of advantages are cited for such an approach including reduced energy requirements, rapid reaction rates, and combined synthesis and sintering of the final product.
D20 at ILL was used at its peak-flux wavelength of 1.3 Å to investigate a number of systems by heating pre-pressed pellets of the starting products, 10 – 20 g, in a standard furnace for powder neutron diffraction until reaction was initiated [10–14]. Patterns were collected for 200 – 500 ms with readout of the detector requiring 80 – 400 ms. For the formation of Ti_3SiC_2 from a stoichiometric mixture of Ti, SiC and C five stages of the process were identified, including the transformation of α-Ti to β-Ti, the pre-ignition exothermic formation of intermediate TiC_x phases, the very rapid (sub-second) formation of a single intermediate phase, corresponding to a solid solution of Si in TiC. After an incubation period of a few seconds the product Ti_3SiC_2

nucleates and precipitates out as the temperature falls. Lattice parameter variations were used to estimate the bulk temperature and indicated that ≈2600 K was attained. Rietveld analysis allowed the amount of each phase present to be determined, from which kinetic parameters were derived via a non-isothermal form of the Avrami equation. An activation energy of ≈45 kJ mol^{-1} was estimated for the nucleation and growth of the product phase. During cooling, the temperature deviated positively from an exponential decrease over a part of the range because of the release of latent heat correlated with the precipitation of the product phase. Analogous to differential thermal analysis, it was possible from this to estimate the enthalpy of formation of Ti_3SiC_2 as -76 kJ mol^{-1} [15].

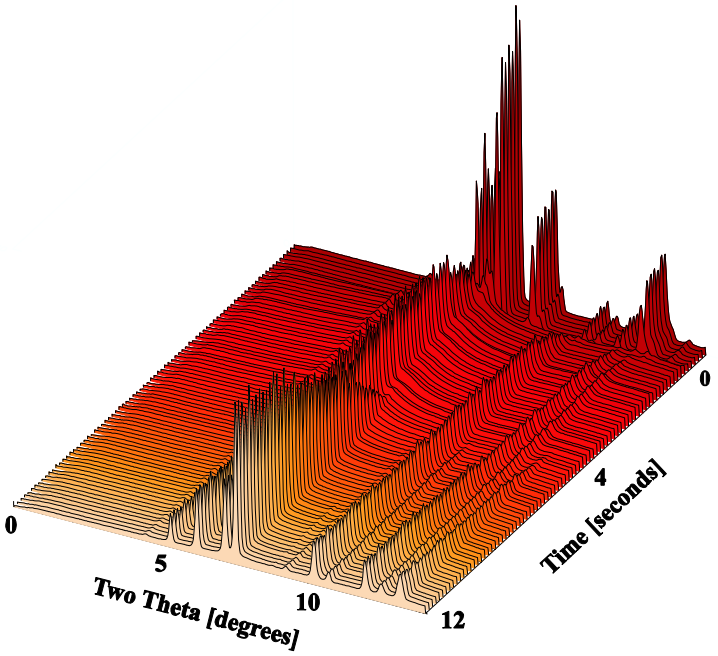

Fig. 1. Powder diffraction patterns of the Al-Ni-Ti-C system during self-propagating combustion synthesis measured on ID11 [17].

On beamline ID11 at ESRF several systems have been studied in the self-propagating mode. [1,16–21]. Discs of the reactants were pressed, 20 mm in diameter × ≈2 mm thick, which were mounted in transmission with a 200 × 200 μm^2 monochromatic beam in the range 40 – 50 keV. The beam characteristics were chosen to obtain a balance between incident flux, penetration through the sample, the size of the combustion front, the grain size, and the angular resolution. Ignition via an electrically heated wire led to the propagation of the reaction through the sample at speeds of up to 100 mm s^{-1}, monitored with the 2-D Frelon camera with the temperature estimated via a pyrometer. The time resolution was typically in the range 65 – 135 ms when exploiting the whole area of the detector and 20 ms when masking

and rebinning on the chip as in the synthesis of Jacobsite, Fe_2MnO_4 [1]. Systems studied included the synthesis of TiC-NiAl, TiC-WC and TiC-TiB_2 composites, Al-Ni intermetallics, TiC-FeTi cermets. For the TiC-NiAl system, for example, the formation of TiC accompanies the melting of Al then Ni and the formation of a (probably) ternary phase before the final formation of NiAl during cooling. The final product has small TiC particles embedded in a matrix of NiAl.
On beamline X11A at the NSLS Brookhaven the formation of several refractory carbides and diborides (of Ti, Zr, Nb, Hf or Ta) was studied in a specially built reaction chamber allowing operation under vacuum or in the presence of different reactive or inert gasses [22]. The chamber is equipped with a 2048-channel 50-mm photodiode array covering 30° in 2θ, and a pyrometer. Data were collected in 50 – 200 ms at an energy of 8 keV in reflection mode.
Energy-dispersive measurements of the formation of barium, lithium and magnesium zinc ferrites were made on station 16.4 at the SRS Daresbury [23]. The reaction is driven by the oxidation of iron which is highly exothermic. Reaction was carried out in oxygen, and with the addition of sodium perchlorate as an internal oxidizing agent. Three energy-dispersive detectors were set at low 2θ angles of 1.8°, 4.7° and 7.5° and measurements were made in reflection with a 100 μm diameter white beam from the wiggler source. The time resolution was 100 ms. Measurements were also made under an applied magnetic field using a 1.1 T permanent magnet with a cylindrical bore of 20 mm diameter. The X-ray beam direction was parallel to the axis of the bore and the fixed scattering geometry made the measurements possible. The magnetic field was seen to induce a transient phase identified as magnetite in the synthesis of barium ferrite.

Metallurgy

Processing of metals is an area where rapid changes of state are involved, such as during welding [24–28], heat treatment [29–32], and quenching [33,34], etc. To understand the effects induced by these actions, detailed microscopic structural information is required.
At BL-10-2 at SSRL (Stamford), (beamline based on a multipole wiggler), rapid, *in-situ* powder diffraction patterns were recorded as gas tungsten arc spot welds were made on carbon-manganese steel bars [24,25]. To prevent oxidation the experiments were performed under a helium atmosphere, and used a 50-mm photodiode array covering 24 – 54° 2θ with a time resolution of 100 ms (260 μm X-ray spot) or 50 ms (730 μm spot size) at an X-ray energy of 12.0 keV. The fcc-to-bcc ($\gamma \rightarrow \alpha$) transition on cooling happened twice as fast as the bcc-to-fcc ($\alpha \rightarrow \gamma$) transition on heating reflecting, most probably, differences in the heating and cooling rates. Subtle changes in *d*-spacings indicated the precipitation of carbide or the relief of residual stress during heating. Detailed analysis indicated that there were differences in microstructure between the weld fusion zone and the nearby heat-affected zone (HAZ). The

same experimental arrangement was also used to study welding of stainless steel at two positions in the HAZ, 0.2 mm and 0.7 mm from the fusion zone boundary, to investigate the transformation of austenite (γ phase) to ferrite (δ phase) on heating, and back on cooling [26]. Volume fractions, peak positions and widths were tracked and correlated with the temperature calculated via a numerical heat transfer and fluid flow model.

Time resolution of down to 10 ms was exploited at Spring-8 (Japan) using undulator beamline 46XU to study solidification during welding of martensitic steel using X-rays of energies 18 keV or 30 keV and a large area pixel detector [28]. In a further development, fast diffraction measurements during heat treatment of mild steel and low-temperature transformation steel were combined with concurrent fast laser scanning confocal microscopy, allowing insight into the origin and morphology of the observed microstructural changes accompanying phase transitions on cooling [29].

NiTi shape memory alloy wires must be annealed, modifying the cold-worked deformed microstructure, and mechanically constrained to set the wire, to give the shape-memory properties. Practically, heating can be done via an electrical pulse. ID11 was used to study the transformation of a wire under rapid electrical heating with applied tensile force and simultaneous electrical resistivity measurements [32]. By masking the detector and rebinning on the chip, a time resolution of 10 ms was obtained. Marked changes in microstructure and strain were apparent from monitoring the evolution of the 011 reflection of the austenitic phase present, depending on the power dissipated during the thermal treatment.

Catalysis

Many chemical processes are catalyzed by metallic nanoparticles such as platinum or gold. Studying such systems by conventional diffraction is hampered because of the effect of particle-size broadening on the diffraction pattern. Nevertheless the structure of such systems can be studied by measuring to high Q values (where $Q = 4\pi \sin\theta / \lambda$), then Fourier transforming to give the pair distribution function (PDF). Measuring to high Q requires hard X-ray energies and, if not scanning to high 2θ, a large 2-D detector such as the GE medical imaging detector [3,4] installed at the APS (Illinois), which moreover has a time resolution of 30 Hz. Thus the reduction of PtO_2 to Pt metal by hydrogen at 200°C was studied at an energy of 77 keV (just below the Pt K edge to minimize fluorescence) while recording data up to ≈ 25 Å^{-1}. The individual patterns collected in 130 ms could be suitably converted to yield a PDF showing the overall course of the reaction. In a similar experiment, catalytic Pt nanoparticles were prepared in situ by reducing with hydrogen a deposit of H_2PtCl_6 on a TiO_2 support [35]. The support forms the bulk of the system, but nevertheless sensitivity to the Pt particles is achieved by adopting the differential PDF approach whereby the PDF of the bare support (measured under equivalent conditions) is sub-

tracted from the total PDFs obtained from the individual patterns. It is evident that the reduction follows pseudo-zero-order kinetics, and by performing the measurements at different temperatures (100, 150 and 200°C) an Arrhenius plot allows an activation energy for the reduction of a nanoparticle to be estimated at about 50 kJ mol^{-1}, a quantity very difficult to obtain by any other means.
At ESRF beamline ID15B diffraction patterns from 2% of Pd nanoparticles (≈3 nm diameter) supported on alumina were recorded using high energy (86.8 keV) X-rays with a time resolution of 2 Hz [36]. During the measurements the atmosphere was cycled between CO and NO, in simulation of a working car exhaust catalyst. The reactions were also monitored by diffuse reflectance infrared spectroscopy (DRIFTS) and mass spectroscopy (MS) of the effluent gas. A complementary experiment applied time resolved dispersive EXAFS at the Pd K edge in combination with DRIFTS and MS. During the CO cycle the Pd cell parameter was seen to increase linearly with time accompanied by the production of CO_2 then reverse when switched to NO flow. The studies show that CO dissociates on the surface of the nanoparticles to produce CO_2 and PdC_x (lattice expansion consistent with $x \leq 0.06$). Under NO, the PdC_x is converted back to Pd, with the emission of CO_2 and nitrogen gas. The IR spectroscopic measurements indicate moreover that the formation of the PdC_x also promotes the adsorption of CO in a linear configuration (PdCO) compared to a bridging (Pd_2CO) arrangement.

Stroboscopic measurements
Commercial, doped, polycrystalline lead zirconate titanate (PZT) piezoelectric ceramics were measured in a cyclic electric field of ±400 V mm^{-1} at frequencies up to 500 Hz via the stroboscopic approach using WOMBAT [37]. Each detected neutron is time stamped and subsequently binned together with others that have been scattered from the sample at the equivalent time in the electrical cycle. The data resulting from the sum of many cycles can be represented relative to just a single cycle. An effective time resolution of 30 μs is available using this approach. Shifts in peak positions indicate the level of piezoelectric strain generated by the field and showed no dependence on frequency. Time-of-flight neutron diffraction studies performed at ISIS on a related system using ENGIN-X [38] showed time and orientation dependence of the lattice strains [39]. Possible mechanisms for the observed behavior were discussed.
Rather than using the detector to time the arrival of the scattered radiation, the source can be pulsed to give the time frame for stroboscopic measurements. This is particularly appropriate at a synchrotron where tight bunches of electrons are in fact circulating in the storage ring. Specific ring-filling modes can be exploited to enhance the possibilities for time-resolved studies. Thus at ESRF, when operating in 16-bunch mode, an intense pulse (70 ps duration) of X-rays is emitted from the ring every 180 ns as each bunch of electrons flashes past the entrance to a beamline. A

high-speed chopper in the X-ray beam can be used to select the source frequency desired for any particular experiment. Of particular note are pump-probe experiments, whereby a very short laser pulse (of the order 100 fs) excites the sample, which is then probed with an X-ray pulse a chosen delay time later. The diffraction pattern can be simply accumulated over a number of cycles on a passive 2-D detector like an image plate, because of the intrinsic low dark current for these devices. Accurate electronics are required to synchronize the laser and chopper with the bunch clock tracking the electron bunches in the storage ring.

Two examples studied at the ESRF on beamline ID09B are 4-(dimethylamino) benzonitrile and 4-(diisopropylamino)benzonitrile [40,41], whose fluorescence properties indicate that photo-excitation leads to the formation of an intramolecular charge-transfer state. Powder diffraction patterns were collected over 10 minutes at a frequency of 897 Hz at delay times ranging from -150 ps (i.e. as a reference before the laser excitation) to 2500 ps after excitation. Only about 5% of the molecules are excited by the laser, so the diffraction pattern is from a structure containing both excited and ground-state molecules. Rietveld refinement of the structure from the diffraction patterns gave the number of excited (distorted) molecules as a function of delay time, and the nature of the molecular change induced by the photo-excitation. For the isopropyl analogue, an exponential decay time of 6.3 (±2.8) ns was observed for the excited molecules (compared to 3.28 ns seen spectroscopically). The main distortion to the molecules was a change in the torsion angle between the diisopropylamino group and the benzene ring from 13–14° determined from the pre-excitation patterns (14.3° in the single-crystal structure) to 10 (±1–2)°. Such experiments give the highest time resolution currently possible for powder diffraction experiments, though future experiments using free-electron lasers are being considered [42].

Data analysis

Measuring data at high speed produces a large number of powder patterns that need to be analyzed, to extract lattice parameters, phase fractions, structural parameters, etc. as required to understand the behavior of the system. Modern Rietveld refinement programs (e.g. GSAS, Fulprof, Topas) allow a series of patterns to be processed. One approach takes the output from pattern n as the input to pattern n+1, sequentially progressing through the series, (but watch out for abrupt changes as the system evolves). Another way is to analyze several datasets simultaneously in a single refinement, tying together chosen parameters between patterns so as to vary according to an underlying theoretical model or to follow an empirical evolution, i.e. essentially fitting to a data surface rather than to the individual patterns [43]. For example, instead of refining the lattice parameters for each pattern, the thermal expansion coefficients can be refined, defining how the lattice parameters vary over the series. Care is required in analyzing patterns from time-resolved measurements as

they are necessarily compromised by the need to measure rapidly. However you choose to analyze your data, good luck.

References

1. J.-C. Labiche, *et al*., "The fast readout low noise camera as a versatile X-ray detector for time resolved dispersive EXAFS and diffraction studies of dynamic problems in materials science, chemistry and catalysis", Rev. Sci. Instr., 78, 091301, (2007).
2. J.E. Daniels and M. Drakopoulos, "High-energy X-ray diffraction using the Pixium 4700 flat-panel detector", J. Sync. Rad., 16, 463–468, (2009).
3. P.J. Chupas, K.W. Chapman and P.L. Lee, "Applications of an amorphous silicon-based area detector for high-resolution, high-sensitivity and fast time-resolved pair distribution function measurements", J. Appl. Cryst., 40, 463–470, (2007).
4. J.H. Lee *et al*., "Synchrotron applications of an amorphous silicon flat-panel detector", J. Sync. Rad., 15, 477–488, (2008).
5. A. Bergamaschi, *et al*., The MYTHEN detector for X-ray powder diffraction experiments at the Swiss Light Source", J. Sync. Rad., 17, 653–668, (2010).
6. T.C. Hansen, P.F. Henry, H.E. Fischer, J. Torregrossa and P. Convert, "The D20 instrument at the ILL: a versatile high-intensity two-axis neutron diffractometer", Meas. Sci. Technol., 19, 034001, (2008).
7. A. J. Studer, M. E. Hagen and T. J. Noakes, "Wombat: The high-intensity powder diffractometer at the OPAL reactor", Physica B, 385-386, 1013–1015, (2006).
8. A.C. Hannon, "Results on disordered materials from the GEneral Materials diffractometer, GEM, at ISIS", Nucl. Inst. Meth. A, 551, 88–107, (2005).
9. http://www.jcns.info/POWGEN
10. D.P. Riley, E.H. Kisi, E. Wu, T. Hansen and P. Henry, "Applications of in situ neutron diffraction to optimization of novel materials synthesis", in "Studying Kinetics with Neutrons", Springer Series in Solid State Sciences, 161, 123–148, (2010).
11. E.H. Kisi and D.P. Riley, "Neutron diffraction studies of self-propagating high-temperature synthesis", IUCr Commission on Powder Diffraction Newsletter, 29, 18–20, (2003).
12. D.P. Riley, E.H. Kisi, T.C. Hansen and A.W. Hewat, "Self-propagating high-temperature synthesis of Ti_3SiC_2: I, ultra-high-speed neutron diffraction study of the reaction mechanism", J. Am. Ceram. Soc., 85, 2417–2424, (2002).
13. E.H. Kisi, D.P. Riley and C. Curfs, "Ultra-high speed neutron diffraction studies of combustion synthesis", Physica B, 385–386, 487–492, (2006).
14. D.P. Riley, E.H. Kisi and T.C. Hansen, "Self-propagating high-temperature synthesis of Ti_3SiC_2: II. Kinetics of ultra-high-speed reactions from *in situ* neutron diffraction", J. Am. Ceram. Soc., 91, 3207–3210, (2008).
15. E.H. Kisi and D.P. Riley, "Diffraction thermometry and differential thermal analysis", J. Appl. Cryst., 35, 664–668, (2002).
16. C. Curfs, I.G. Cano, G.B.M. Vaughan, M.A. Rodríguez, X. Turillas and Å. Kvick, "Intermetallic-ceramic composites synthesis by SHS. Time-resolved studies using synchrotron radiation X-rays", Int. J. SHS, 9, 331–339, (2000).
17. C. Curfs, I.G. Cano, G.B.M. Vaughan, X. Turillas, Å. Kvick and M.A. Rodríguez, "TiC-NiAl composites obtained by SHS: a time-resolved XRD study", J. Eur. Ceram. Soc., 22, 1039–1044, (2002).
18. L. Contreras, X. Turillas, G.B.M. Vaughan, Å. Kvick and M.A. Rodríguez, "Time-resolved XRD study of TiC-TiB_2 composites by SHS", Acta Materialia, 52, 4783–4790, (2004).
19. L. Contreras, X. Turillas, M.J. Mas-Guindal, G.B.M. Vaughan, Å. Kvick and M.A. Rodríguez, "Synchrotron diffraction studies of TiC/FeTi cermets obtained by SHS", J. Solid State Chem., 178, 1595–1600, (2005).
20. M.J. Mas-Guindal, L. Contreras, X. Turillas, G.B.M. Vaughan, Å. Kvick and M.A. Rodríguez, "Selg-propagating high-temperature synthesis of TiC-WC composite materials", J. Alloys and Compounds, 419, 227–233, (2006).
21. C. Curfs, X. Turillas, G.B.M. Vaughan, A.E. Terry, Å. Kvick and M.A. Rodríguez, "Al-Ni intermetallics obtained by SHS; A time-resolved X-ray diffraction study", Intermetallics, 15, 1163–1171, (2007).
22. J. Wong, E.M. Larson, P.A. Waide and R. Frahm, "Combustion front dynamics in the combustion synthesis of refractory metal carbides and di-borides using time-resolved X-ray diffraction", J. Sync. Rad., 13, 326–335, (2006).
23. I.P Parkin, Q.A. Pankhurst, L. Affleck, M.D. Aguas and M.V. Kuznetsov, "Self-propagating high temperature synthesis of $BaFe_{12}O_{19}$, $Mg_{0.5}Zn_{0.5}Fe_2O_4$ and $Li_{0.5}Fe_{2.5}O_4$; time resolved X-ray diffraction studies (TRXRD)", J. Mater. Chem., 11, 193–199, (2001).

24. J. Wong, “Phase mapping and transformation dynamics in fusion welds”, IUCr Commission on Powder Diffraction Newsletter, 29, 26–30, (2003).
25. J. Wong, T. Ressler and J.W. Elmer, “Dynamics of phase transformations and microstructure evolution in carbon-manganese steel arc welds using time-resolved synchrotron X-ray diffraction”, J. Sync. Rad., 10, 154–167, (2003).
26. T.A. Palmer, J.W. Elmer and S.S. Babu, “Observation of ferrite/austenite transformations in the heat affected zone of 2205 duplex stainless steel spot welds using time resolved X-ray diffraction”, Mat. Sci. Eng. A, 374, 307–321, (2004).
27. H.J. Stone, H.K.D.H. Bhadeshia and P.J. Withers, “In situ monitoring of weld transformations to control weld residual stresses”, Mat. Sci. Forum, 571–572, 393–398, (2008).
28. Y. Komizo, and H. Terasaki, “In-situ observation of solidification behavior during welding”, Mat. Sci. Forum, 638–642, 3722–3726, (2010).
29. H. Terasaki and Y. Komizo, “Diffusional and displacive transformation behavior in low carbon-low alloy steels studied by a hybrid in situ observation system”, Scripta Mater., 64, 29–32, (2011).
30. J.W. Elmer, T.A. Palmer and E.D. Specht, “In situ observation of sigma phase dissolution in 2205 duplex stainless steel using synchrotron X-ray diffraction”, Mat. Sci. Eng. A, 459, 151–155, (2007).
31. D. Zhang, H. Terasaki and Y. Komizo, “In situ observation of phase transformation in Fe-0.15C binary alloy”, J. Alloys and Compounds, 484, 929–933, (2009).
32. B. Malard, J. Pilch, P. Sittner, R. Delville and C. Curfs, “In situ investigation of the fast microstructure evolution during electropulse treatment of cold drawn NiTi wires”, Acta Mater., 59, 1542–1556, (2011).
33. J. Epp, T.Hirsch and C.Curfs, “In situ X-Ray Diffraction analysis of unexpected carbon partitioning during quenching of low carbon steel”, xyzzy in press.
34. J. Epp, T.Hirsch, A.Kuznetsov and C. Curfs, “Martensite self-tempering in a ball bearing steel: in situ X-ray diffraction analysis during quenching”, pqrst in press
35. P.J. Chupas, K.W. Chapman, G. Jennings, P.L. Lee and C.P. Grey, “Watching nanoparticles grow: The mechanism and kinetics for the formation of TiO_2-supported platinum nanoparticles”, J. Am. Chem. Soc., 129, 13822–13824, (2007).
36. M.A. Newton, M. Di Michiel, A. Kubacka and M. Fernández-García, “Combining time-resolved hard X-ray diffraction and diffuse reflectance infrared spectroscopy to illuminate CO dissociation and transient carbon storage by supported Pd nanoparticles during CO/NO cycling”, J. Am. Chem. Soc., 132, 4540–4541, (2010).
37. A. Pramanick, *et al*., “In situ neutron diffraction studies of a commercial, soft lead zirconate titanate ceramic: response to electric fields and mechanical stress”, Appl. Phys. A, 99, 557–564, (2010).
38. J.R. Santisteban, M.R. Daymond, J.A. James and L. Edwards, “ENGIN-X: a third-generation neutron strain scanner”, J. Appl. Cryst. (2006). 39, 812–825, (2006).
39. J.L. Jones *et al*., “Time-resolved and orientation-dependent electric-field-induced strains in lead zirconate titanate ceramics”, Appl. Phys. Lett., 90, 172909, (2007).
40. J. Davaasambuu, P. Durand and S. Techert, “Experimental requirements for light-induced reactions in powders investigated by time-resolved X-ray diffraction”, J. Sync. Rad., 11, 483–489, (2004).
41. S. Techert and K.A. Zachariasse, “Structure determination of the intramolecular charge transfer state in crystalline 4-(diisopropylamino)benzonitrile from picoseconds X-ray diffraction”, J. Am. Chem. Soc., 126, 5593–5600, (2004).
42. C. Blome, Th. Tschentscher, J. Davaasambuu, P. Durand and S. Techert, “Femtosecond time-resolved powder diffraction experiments using hard X-ray free-electron lasers”, J. Sync. Rad., 12, 812–819, (2005).
43. G.W. Stinton and J.S.O. Evans, “Parametric Rietveld refinement”, J. Appl. Cryst., 40, 87–95, (2007).

Taking it to Extremes – Powder Diffraction at Elevated Pressures

David I. A. Millar and Colin R. Pulham
School of Chemistry and Centre for Science at Extreme Conditions, The University of Edinburgh, King's Buildings, Edinburgh, UK

Abstract. Structural studies of materials under elevated pressures provide a fascinating insight into the physical and chemical behaviour of matter under the wide range of conditions experienced throughout the Universe. Both x-ray and neutron powder diffraction techniques play a crucial role in structural studies and are therefore at the forefront of high-pressure research. These notes provide a short introduction to the principles and experimental practice of high-pressure powder diffraction techniques.

1. Introduction

Although on the surface of the Earth we rarely experience pressures that deviate significantly from 1 atmosphere, much of the Universe experiences a much wider range of pressures that span the near vacuum of outer space to the pressure at the centre of a neutron star (estimated to be 10^{30} atmospheres). Even on Earth there is a significant variation – at the bottom of the Mariana Trench in the Pacific Ocean at a depth of 11,000 metres, the pressure is over 1000 atmospheres, and the pressure at the centre of the Earth is 3.5 million atmospheres. Under this range of extreme conditions, structural and chemical changes in materials can be dramatic - proteins are denatured; pathogenic bacteria are destroyed; ice melts above 100 °C; graphite turns to diamond; and non-metals become metallic. Such conditions also provide a rich regime for geochemical synthesis – diamonds, garnets, and perovskites are just a few of the many minerals produced under extreme conditions within the Earth. The domain of pressure therefore provides an exciting additional dimension to explore structure, chemical reactivity, and physical properties. At the same time it provides a powerful way to test computational models, with a particular focus on the validation of the efficacy of intermolecular potentials.

It is for these reasons that high-pressure research attracts such interest across a wide range of disciplines that includes: geosciences; physics; chemistry; materials science; biology; engineering; and astronomy. Since physical properties are intrinsically linked to structure, structural studies are key to understanding how matter behaves under extreme conditions. Both x-ray and neutron powder diffraction techniques therefore play a crucial role in such structural studies. These notes will therefore provide a short introduction to high-pressure powder diffraction techniques. The associated lecture at the Erice School will then present a selection of examples where high-pressure powder diffraction studies have provided fascinating insight into the behaviour of matter under extreme conditions.

2. Techniques

High-pressure structural science is a particularly good example of an area that relies upon the complementarity of various techniques to achieve the final aim of the structural characterisation of novel materials. The advances in this field are intertwined with the evolution of complex sample environments for experiments at elevated temperatures and/or pressures, as well as the development of techniques for the collection and analysis of spectroscopic and diffraction data under extreme conditions. In particular, developments of high brightness x-ray and neutron sources, coupled with the enhancement of associated detectors, have played a major part in advancing powder diffraction studies at extreme conditions [1].

2.1. The Diamond-Anvil Cell

High-pressure X-ray diffraction measurements are generally performed using a gasketed diamond-anvil cell (DAC). The premise for this device is relatively simple; the sample is placed between two diamond faces (culets) and is subjected to high pressures when a force pushes the opposed anvils together (see Figure 1). The DAC utilised in this work was based on developments by Merrill and Bassett in 1974 [2]. The small size (~5 cm diameter) and relative ease of use make these cells extremely versatile and perfectly suited for high-pressure X-ray diffraction studies. Depending on the size of the culets and the gasket hole, pressures beyond 100 GPa can be obtained. Note that in high-pressure research it is common to find various units used, sometimes interchangeably, as a measure of pressure. Gigapascals (GPa) may be related to other units as follows:

1 GPa = 10 kbar = 9869.2 atm.

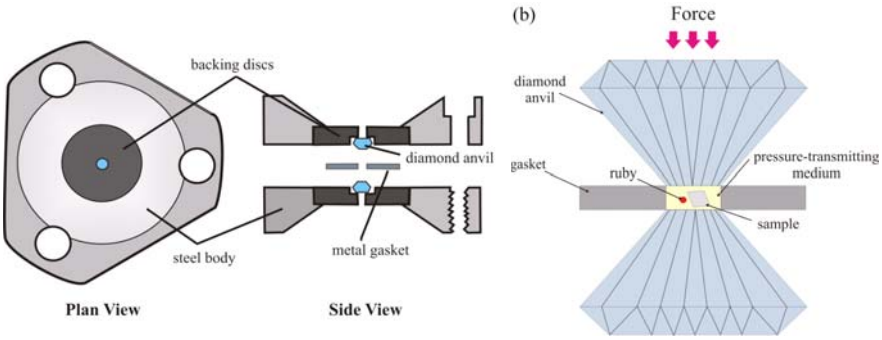

Fig. 1. Schematic representation of Merrill-Bassett diamond-anvil cell.

The experimental set-up for a typical high-pressure X-ray powder diffraction experiment is represented in Figure 2(a). Data are collected on an image plate detector and are generally processed according to the procedure outlined for ambient-pressure powder diffraction, although in some cases it may also be necessary to

mask out intense single-crystal reflections arising from the diamond anvils to ensure no anomalies occur in the I_{obs} vs 2θ profile. The image can then be integrated to provide the one-dimensional powder diffraction

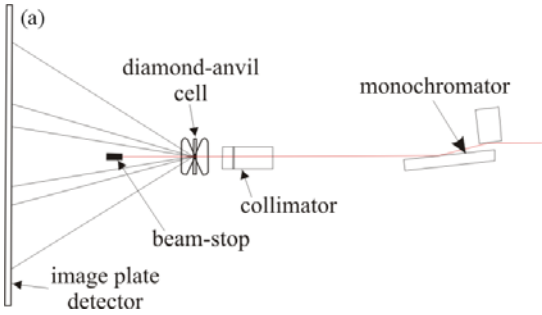

Fig. 2a. Schematic illustrating the key components of a high-pressure X-ray powder diffraction experiment.

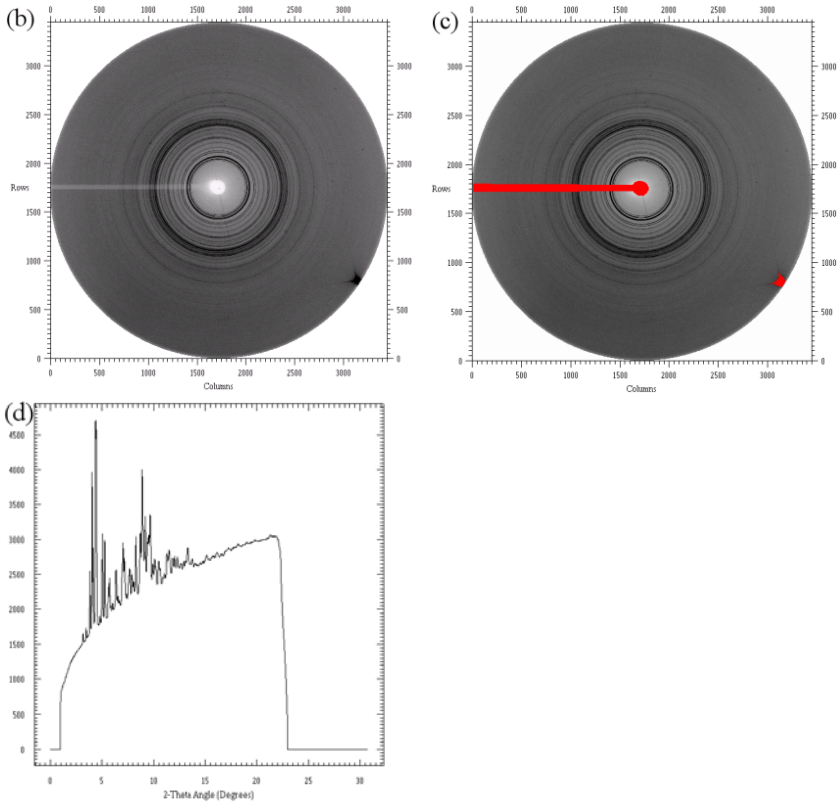

Fig. 2(b)-(d). Schematic illustrating the stages of data reduction. The raw image is shown in (b). The concentric rings correspond to the diffracted intensities from the sample; the dark spot at the edge of the image is an intense diamond reflection.

pattern using programs such as Fit2D [3]. It is also possible to mask intense powder diffraction rings due to the tungsten gasket, although should this interfere with sample peaks it is also possible to perform Rietveld refinements in which the tungsten diffraction pattern is incorporated. Finally the data can be integrated to give a plot of diffraction intensity against scattering angle. The large background common to such data collections is due to Compton (inelastic) scattering from the diamonds and can be subtracted prior to data refinement.

2.2. Radiation sources

Whilst in principle it is possible to record powder diffraction patterns on laboratory instruments using conventional sealed sources (e.g. Mo-K_α), far superior results can be obtained using synchrotron sources that combine high flux with tuneable wavelength and low divergence. Beam diameters of less than 30 μm are easily obtained and hence allow one to record diffraction patterns for heterogeneous samples and without contamination from the DAC components. In such studies, however, great care must be taken to ensure effective powder averaging of such a small sample volume. This is typically achieved by ensuring that the DAC is loaded with a very finely ground powder and rocking the DAC through an angle of 5-20°.

2.3. Pressure Measurement in the DAC

Direct pressure measurement from the applied force is both inaccurate and impractical. Instead, Piermarini *et al.* demonstrated that a small chip or sphere of ruby (Al_2O_3:Cr^{3+}) could serve as a continuous pressure sensor within the DAC by utilising its laser-induced fluorescence [4]. Indeed the simplicity of the ruby fluorescence method for *in situ* pressure calibration is without question a contributing factor to the widespread application of diamond-anvil cell techniques and, as such, was the subject of an extensive review by Syassen in 2008 [5]. The spectral lines of ruby undergo a pronounced red-shift with applied pressure; the R_1 electronic transition shows a linear dependence with pressure up to at least 20 GPa at ambient temperature [4].

2.4. The Paris-Edinburgh Cell

Neutron diffraction experiments (see Section **Errore. L'origine riferimento non è stata trovata.**) require sample volumes *ca* 10^6 times larger than those required for X-ray powder diffraction, thus precluding the use of diamond-anvil cells. High-pressure neutron diffraction experiments were therefore severely limited until the advent of the Paris-Edinburgh cell (P-E Cell), developed in 1992, which extended the pressure range to 10 – 20 GPa [6]. The popularity of the P-E Cell arose from its (relatively) light-weight design and its portability – the Paris-Edinburgh cell weighs ~ 50 kg, in contrast to other commercial devices of the time with comparable sample volume that weighed close to 1 tonne. This portability, coupled with the fact that loads can be applied to the cell by a hydraulic ram while it remains *in situ* on the beamline, greatly simplified high-pressure experiments. The P-E Cell is also an op-

posed-anvil device, like the diamond-anvil cell and the Bridgman cell. In this construction, however, the sample is compressed between anvils made of either tungsten carbide (WC) or sintered diamond, see Figure 3(a). Early designs utilised null-scattering TiZr toroidal gaskets located into corresponding grooves machined into the anvil faces to confine the sample and, generally, a solid pressure-transmitting medium. Compression studies using the preferred fluid pressure-transmitting media (methanol:ethanol and iso:n-pentane) were limited to *ca* 2.0 GPa before anvil failure. It was realised that complete encapsulation of the sample and pressure-transmitting medium in two flanged hemispherical caps (TiZr) would prevent the fluid media coming into direct contact with the anvil surface [7]. In this way the anvils were shown to be protected and the available pressure range for hydrostatic studies were extended up to the freezing pressure of methanol:ethanol (*i.e.* ~10 GPa). The encapsulated gasket is compared to the 'standard' TiZr toroidal gasket in Figure 3(b).

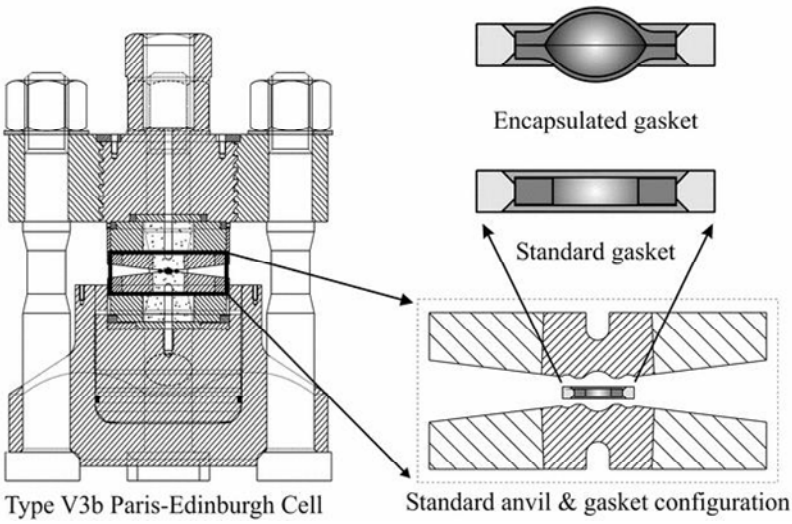

Fig. 3(a). Cross-section of the Paris-Edinburgh cell (V3b) and (b) a comparison of the standard and encapsulated gaskets [7].

2.5. Pressure Measurement in the Paris-Edinburgh cell

Unlike the diamond-anvil cell, the Paris-Edinburgh cell does not allow optical access to the sample chamber and therefore a method for pressure calibration other than the ruby fluorescence method had to be developed. Instead small quantities of internal pressure calibrants are used, typically either NaCl(s) or Pb(s). Both materials have clearly defined equations of state which means that the unit cell volume of the chosen calibrant (as determined by Rietveld refinement of the powder diffraction patterns) is directly related to the pressure within the gasket.

3. Pressure-transmitting media

In most powder diffraction experiments it is desirable to ensure that the stress applied to the sample is homogeneous and that the sample is free of any differential stress or induced shear strain over the entire pressure range of the experiment. In order to achieve these conditions, the powder must be immersed in a medium that displays hydrostatic behaviour. The consequences of a non-hydrostaticity include: inhomogeneous strain in the crystallites leading to broadening of Bragg peaks with associated loss of resolution and signal-to-noise; modification of the relative evolution of unit cell parameters; and difficulties in measuring the pressure using the ruby-fluorescence technique. Non-hydrostatic stresses may therefore adversely affect results from equation of state and elasticity studies, especially those aimed at obtaining accurate pressure derivatives of elastic moduli. Non-hydrostatic stresses can also promote or suppress phase transitions [8, 9] and they can promote the amorphisation of crystalline samples [10, 11]. Table 1 shows the nominal hydrostatic limits of some common pressure-transmitting media. There is considerable variation within the literature about the precise values of hydrostatic limits - this arises because of the different ways that loss of hydrostaticity can be assessed. The onset of line-broadening of the fluorescence spectra of ruby chips immersed in the medium has often been used, but ruby is a relatively stiff material with a bulk modulus of about 254 GPa and is thus intrinsically less sensitive to non-hydrostatic stresses than most minerals or molecular compounds. Furthermore, the fluorescence spectra are intrinsically broad as a result of defects and strains within the ruby crystals, unless the crystallites have been very carefully annealed. More recently a systematic, more sensitive, ruby-fluorescence study has been performed, which monitored values of the pressure gradients across the sample chamber for the pressure-solidified medium [12]. An alternative method for monitoring non-hydrostatic stresses is to measure the widths of the diffraction peaks of quartz single crystals [13]. Quartz is available as gem-quality samples that have intrinsically sharp diffraction peaks and it has a low bulk modulus, which make the peak positions and widths sensitive to small non-hydrostatic stresses. Gigahertz ultrasonic interferometry has also been used to detect the onset of the pressure-induced glass transition in methanol:ethanol mixtures [13].

Table 1. Nominal hydrostatic limits of pressure-transmitting media (from refs. 12 and 13).

Medium	Hydrostatic limit /GPa
4:1 methanol:ethanol	9.8-10.5
16:3:1 methanol:ethanol:water,	10.5
Anhydrous 2-propanol (isopropanol)	4.2
Glycerol	1.4
1:1 Pentane:iso-pentane	7.4
Silicone oil (various viscosities)	0.9
Fluorinert	2.0
Argon	1.9
Nitrogen	3.0
Neon	15
Helium	23

It should also be noted that neutron experiments require the use of fully deuterated pressure-transmitting media since hydrogen-containing material produces a strong background due to the large incoherent cross section of hydrogen.

4. Further reading

References 14 and 15, which represent proceedings of previous Erice Schools, give a flavour of research in the field of high-pressure crystallography. Reference 16 is an informative review of high-pressure chemistry that highlights some of the fascinating structural changes induced by elevated pressures. References 17-21 provide a combination of tutorial and critical reviews that cover a range of high-pressure research from simple metals through molecular compounds to ceramic materials.

Acknowledgments

We thank Dstl and EPSRC for contributions toward a studentship, and the Diamond Light Source and the ISIS Neutron and Muon Facility for the provision of beamtime. We are extremely grateful to Dr Bill Marshall (ISIS) for a longstanding and fruitful collaboration.

References

[1] Miniature diamond anvil pressure cell for single crystal x-ray diffraction studies. L. Merrill and W.A. Bassett, *Rev. Sci. Instrum.*, 1974, **45**, 290.

[2] Powder diffraction under non-ambient conditions, P. Norby and U. Schwarz, in Powder Diffraction Theory and Practice (eds. R.E. Dinnebier and S.J.L. Billinge), Royal Society of Chemistry, Cambridge, UK, 2008.

[3] Two-dimensional detector software: From real detector to idealised image or two-theta scan. A.P. Hammersley, S.O. Svensson, M. Hanfland, A.N. Fitch, and D. Hausermann, *High Press. Res.*, 1996, **14**, 235.

[4] Calibration of the pressure dependence of the R1 ruby fluorescence line to 195 kbar. G. J. Piermarini, S. Block, J.D. Barnett, and R.A. Forman, *J. Appl. Phys.*, 1975, **46**, 2774.

[5] Ruby under pressure. K. Syassen, *High Pressure Res.*, 2008, **28**, 75.

[6] Neutron powder diffraction above 10 GPa. J.M. Besson, R.J. Nelmes, G. Hamel, J.S. Loveday, G. Weill, and S. Hull, *Physica B*, 1992, **180-181**, 907.

[7] Attainment of near-hydrostatic compression conditions using the Paris-Edinburgh cell W.G. Marshall and D.J. Francis, *J. Appl. Crystallogr.*, 2002, **35**, 122.

[8] Pressure-induced ferroelastic phase transition in $Pb_3(PO_4)_2$: A neutron-diffraction study. D.L. Decker, S. Petersen, D. Debray and M. Lambert, *Phys. Rev. B*, 1979, **19**, 3552.

[9] On the phase-transition in anthracene induced by high pressure. R. Resel, M. Oehzelt, K. Shimizu, A. Nakayama and K. Takemura, *Solid State Commun.*, 2004, **129**, 103.

[10] Crystalline post-quartz phase in silica at high pressure. J. Haines, J.M. Léger, F. Gorelli, M. Hanfland, *Phys. Rev.Lett.*, 2001, **87**, 15503.

[11] Pseudoamorphization of Cs_2HgBr_4. D. Machon, V. P., Dmitriev, P. Bouvier, P. N. Timonin, V. B. Shirokov and H.-P. Weber, *Phys. Rev. B*, 2003, **68**, 144104.

[12] Hydrostatic limits of 11 pressure transmitting media. *J. Phys. D: Appl. Phys.*, 2009, **42**, 075413.

[13] Effective hydrostatic limits of pressure media for high-pressure crystallographic studies R.J. Angel, M. Bujak, J. Zhao, G.D. Gatta, and S.D. Jacobsen, *J. Appl. Crystallogr.*, 2007, **40**, 26.

[14] High-Pressure Crystallography, E. Boldyreva and P. Dera, Editors, 2010, Springer Netherlands.

[15] High-pressure Crystallography, ed. A. Katrusiak and P. McMillan, NATO Science Series 2, 2003, vol. 140.

[16] The chemical imagination at work in very tight places. W. Grochala, R. Hoffmann, J. Feng, and N. W. Ashcroft, *Angew. Chem. Int. Ed.* 2007, **46**, 3620.

[17] Probing hydrogen-rich molecular systems at high pressures and temperatures. A. F. Goncharov and R. J. Hemley, *Chem. Soc. Rev.*, 2006, **35**, 899.

[18] High pressure solid state chemistry of carbon dioxide. M. Santoro and F. A. Gorelli, *Chem. Soc. Rev.*, 2006, **35**, 918.

[19] High-pressure studies of pharmaceutical compounds and energetic materials F.P. A. Fabbiani and C.R. Pulham, *Chem. Soc. Rev.*, 2006, **35**, 932.

[20] High-pressure structures and phase transformations in elemental metals M.I. McMahon and R. J. Nelmes, *Chem. Soc. Rev.*, 2006, **35**, 943.

[21] High-pressure chemistry of nitride-based materials. E. Horvath-Bordon, R. Riedel, A. Zerr, P. F. McMillan, G. Auffermann, Y. Prots, W. Bronger, R. Kniep and P. Kroll, *Chem. Soc. Rev.*, 2006, **35**, 987.

Structure solution by Direct Methods

Carmelo Giacovazzo
Istituto di Cristallografia, CNR,
Bari University, Italy

carmelo.giacovazzo@ic.cnr.it

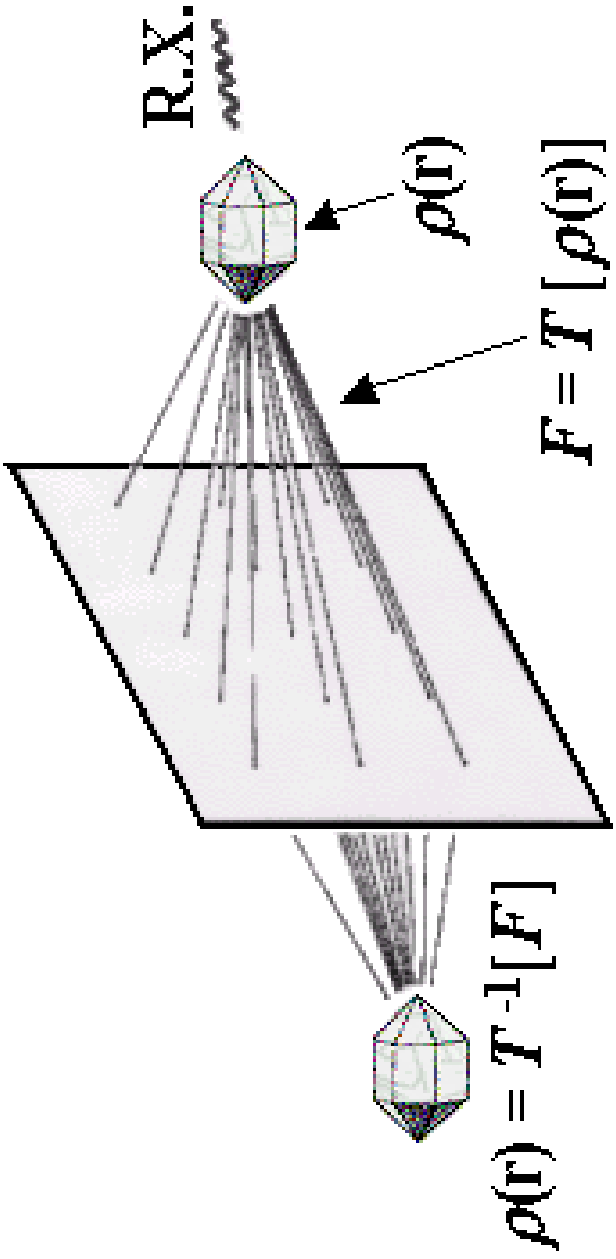
R.X.
ρ(r)
F = T [ρ(r)]
ρ(r) = T -1[F]

Let us answer the following questions:

crystal structure $\Rightarrow$ $\{|F|^2\}$?

$\{|F|^2\} \Rightarrow$ crystal structure ?

$$|F_{\boldsymbol{h}}|^2 = \sum_{j=1}^{N} f_j \exp(2\pi i \boldsymbol{h}\boldsymbol{r}_j) \sum_{j=1}^{N} f_j \exp(-2\pi i \boldsymbol{h}\boldsymbol{r}_j)$$

$$= \sum_{i,j=1}^{N} f_i f_j \exp[2\pi i \boldsymbol{h}(\boldsymbol{r}_i - \boldsymbol{r}_j)]$$

$$= \sum_{j=1}^{N} f_j^2 + \sum_{i \neq j=1}^{N} f_i f_j \exp[2\pi\, i \boldsymbol{h}(\boldsymbol{r}_i - \boldsymbol{r}_j)]$$

As a consequence: $\{|F|^2\} \Leftrightarrow \rho(\boldsymbol{r})$

A third question: *structure* $\Leftrightarrow \{\varphi\}$?

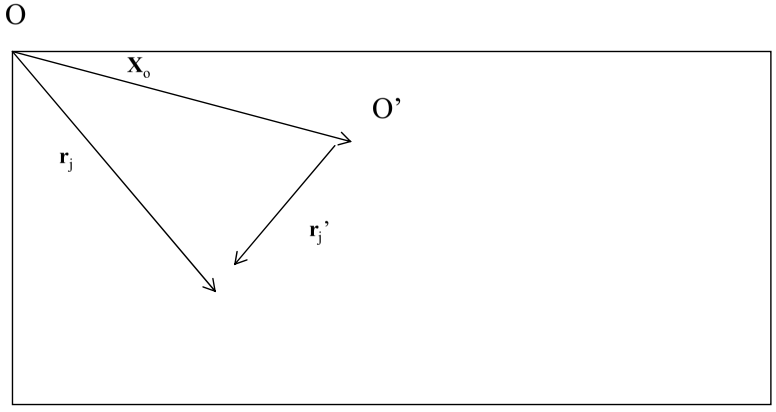

$$F_{\boldsymbol{h}} = \sum_{j=1}^{N} f_j \exp\left(2\pi i \boldsymbol{h}\boldsymbol{r}_j\right) = \sum_{j=1}^{N} f_j \exp\left(2\pi i \boldsymbol{h}(\boldsymbol{X}_0 + \boldsymbol{r}_j')\right)$$

$$= \exp\left(2\pi i \boldsymbol{h}\boldsymbol{X}_0\right) \sum_{j=1}^{N} f_j \exp\left(2\pi i \boldsymbol{h}\boldsymbol{r}_j'\right)$$

$$= \exp\left(2\pi i \boldsymbol{h}\boldsymbol{X}_0\right) F_{\boldsymbol{h}}'$$

$$\rightarrow F_{\boldsymbol{h}}' = F_{\boldsymbol{h}} \exp\left(-2\pi i \boldsymbol{h}\boldsymbol{X}_0\right) = \left|F_{\boldsymbol{h}}\right| \exp\, i\left(\varphi_h - 2\pi \boldsymbol{h}\boldsymbol{X}_0\right)$$

A fourth basic question

How can we derive phases from diffraction moduli?
This seems contradictory: indeed
Phase values depend on the origin chosen by the user, moduli are independent of the user .

The moduli are *structure invariants* ,
the phases are not structure invariants.

Evidently, from the moduli we can derive information only on those combinations of phases (if they exist) which are structure invariants.

The simplest invariant : *the triplet invariant*

***U*se the relation**

$$F'_{\mathbf{h}} = F_{\mathbf{h}} \exp(-2\pi i \mathbf{h} \mathbf{X}_0)$$

to check that the invariant $F_h F_k F_{-h-k}$ does not depend on the origin.

$$F'_{\boldsymbol{h}} F'_{\boldsymbol{k}} F'_{-\boldsymbol{h}-\boldsymbol{k}} = |F_{\boldsymbol{h}}| \exp i(\phi_{\boldsymbol{h}} - 2\pi \boldsymbol{h} \boldsymbol{X}_0) |F_{\boldsymbol{k}}| \exp i(\phi_{\boldsymbol{h}} - 2\pi \boldsymbol{k} \boldsymbol{X}_0)$$
$$|F_{-\boldsymbol{h}-\boldsymbol{k}}| \exp i[\varphi_{-\boldsymbol{h}-\boldsymbol{k}} + 2\pi(\boldsymbol{h}+\boldsymbol{k}) \boldsymbol{X}_0]$$
$$= |F_{\boldsymbol{h}}| |F_{\boldsymbol{k}}| |F_{-\boldsymbol{h}-\boldsymbol{k}}| \exp i(\varphi_{\boldsymbol{h}} + \varphi_{\boldsymbol{k}} + \varphi_{-\boldsymbol{h}-\boldsymbol{k}})$$

The sum ($\varphi_{\mathbf{h}} + \varphi_{\mathbf{k}} + \varphi_{\mathbf{-h-k}}$) is called ***triplet phase invariant***

Structure invariants

Any invariant satisfies the condition that the sum of the indices is zero:

doublet invariant : $F_h F_{-h} = |F_h|^2$

triplet invariant : $F_h F_k F_{-h-k}$

quartet invariant : $F_h F_k F_l F_{-h-k-l}$

quintet invariant : $F_h F_k F_l F_m F_{-h-k-l-m}$

The prior information we can use for deriving the phase estimates may be so summarised:

1) ***atomicity***: the electron density is concentrated in atoms:

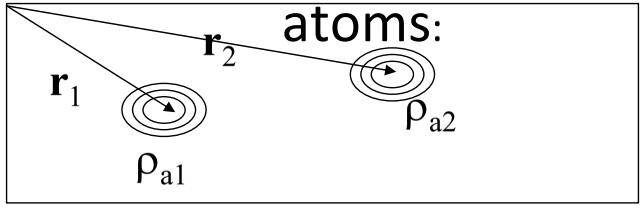

$$\rho(\boldsymbol{r}) = \sum_{j=1}^{N} \rho_{aj}(\boldsymbol{r} - \boldsymbol{r}_j)$$

2) ***positivity*** of the electron density:

$\rho(\mathbf{r}) > 0 \Rightarrow f > 0$

3) ***uniform distribution of the atoms in the unit cell.***

The Wilson statistics

- Under the above conditions Wilson (1942,1949) derived the structure factor statistics. The main results where:
- $$<|F_{\mathbf{h}}|^2>=\sum_{j=1}^{N} f_j^2 \qquad (1)$$
- Eq.(1) is :
- a) resolution dependent (f_j varies with θ),
- b) temperature dependent: $f_j = f_j^0 \exp(-B_j \sin^2\theta/\lambda^2)$
- From eq.(1) the concept of normalized structure factor arises:

$$E_{\mathbf{h}} = F_{\mathbf{h}} / (\sum_{j=1}^{N} f_j^2)^{1/2}$$

The Wilson Statistics

- **|E|-distributions:**

$$P_1(|E|) = 2|E|\exp(-|E|^2)$$

$$P_{\bar{1}}(|E|) = \sqrt{\frac{2}{\pi}}\exp(-|E|^2/2)$$

and $<|E|^2>=1$

in both the cases.
The statistics may be used to evaluate the average themel factor and the absolute scale factor.

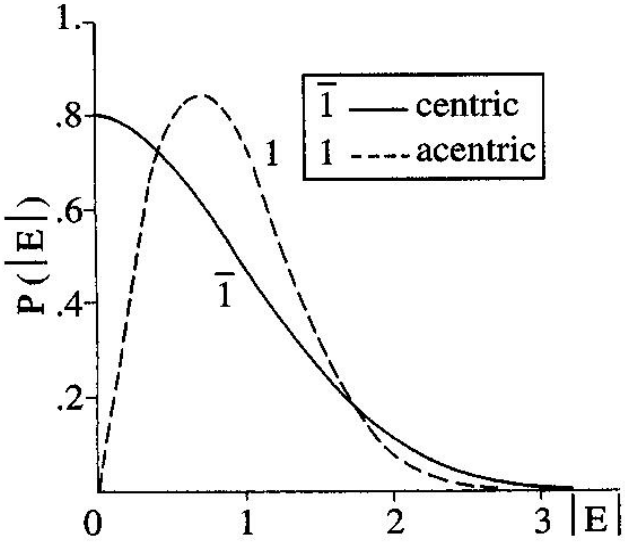

The Wilson plot

$$F_{\mathbf{h}} = \sum_{j=1}^{N} f_j \exp 2\pi i \mathbf{hr}_j = \sum f_j^0 \exp\left(-B_j \frac{\sin^2\theta}{\lambda^2}\right) \exp 2\pi i \mathbf{hr}_j$$

A

$$\exp\left(-B \underbrace{\frac{\sin^2\theta}{\lambda^2}}_{s^2}\right) \underbrace{\sum f_j^0 \exp 2\pi i \mathbf{hr}_j}_{F_h^0}$$

$$|F_h|^2_{obs} = K|F_h|^2 = K\left|F_h^0\right|^2 \exp\left(-2Bs^2\right)$$

A

$$<|F_h|^2_{obs}> = K<\left|F_h^0\right|^2> \exp\left(-2Bs^2\right) = K\Sigma_s^0 \exp\left(-2Bs^2\right)$$

$$\underbrace{\ln\left(\frac{<|F_h|^2_{obs}}{\Sigma_s^0}\right)}_{y} = \ln K - 2Bs^2$$

s^2 = x

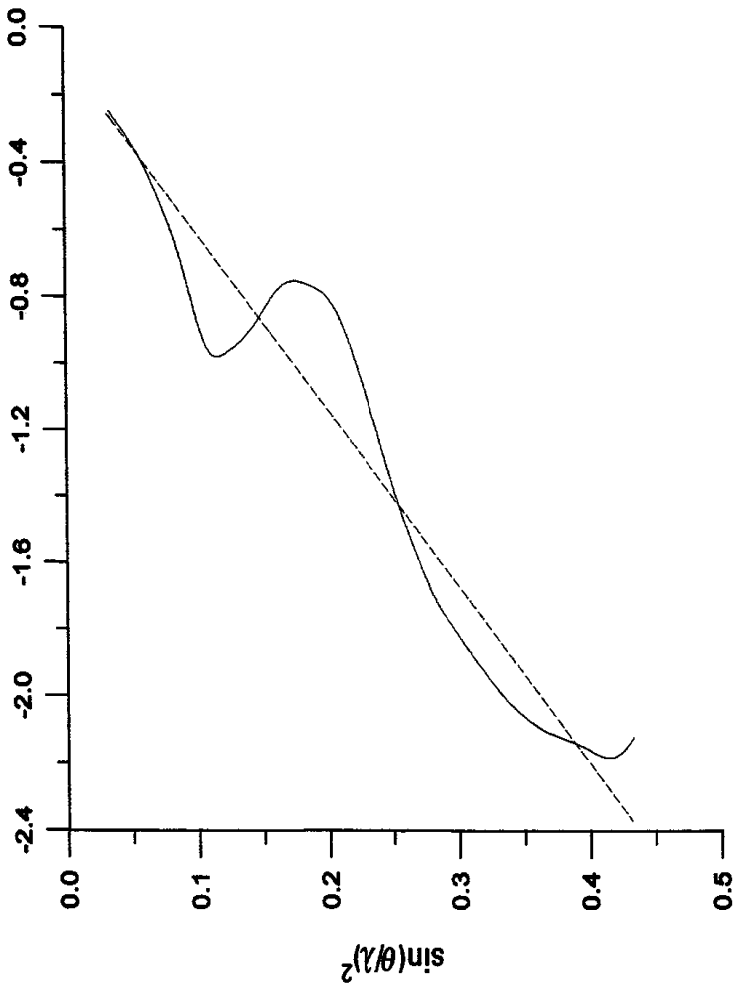
0.0
-0.4
-0.8
-1.2
-1.6
-2.0
-2.4
0.0
0.1
0.2
0.3
0.4
0.5
sin(θ/λ)²

The Cochran formula

$\Phi_{h,k} = \varphi_h + \varphi_k + \varphi_{-h-k} = \varphi_h + \varphi_k - \varphi_{h-}$

$P(\Phi_{hk}) \approx [2\pi I_0]^{-1} \exp(G \cos \Phi_{hk})$

where $G = 2 \mid E_h E_k E_{h+k} \mid / N^{1/2}$

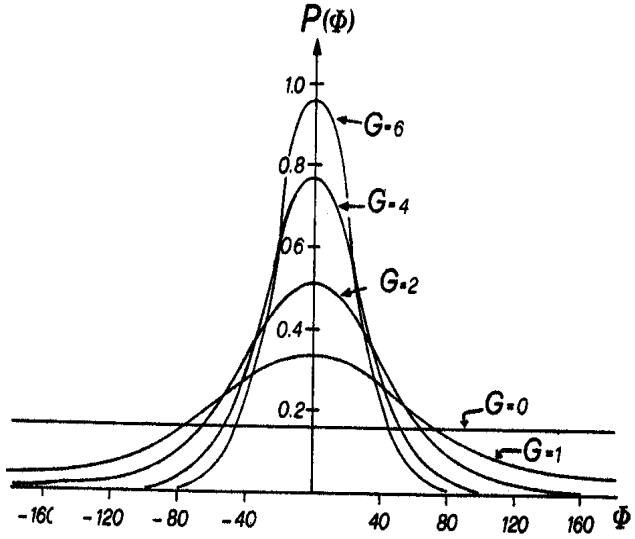

Accordingly:

$\varphi_h + \varphi_k - \varphi_{h+k} \approx 0$	$\propto$	$G = 2 \mid E_h E_k E_{h+k} \mid / N^{1/2}$
$\varphi_h - \varphi_k - \varphi_{h-k} \approx 0$	$\propto$	$G = 2 \mid E_h E_k E_{h-k} \mid / N^{1/2}$
$\varphi_h \approx \varphi_k - \varphi_{h-k}$	$\propto$	$G = 2 \mid E_h E_k E_{h-k} \mid / N^{1/2}$

The tangent formula

A reflection can enter into several triplets.Accordingly

$\varphi_h \approx \varphi_{k1} + \varphi_{h-k1} = \theta_1$ with $P_1(\varphi_h) \propto G_1 = 2|\, E_h\, E_{k1}\, E_{h-k1}\,|/N^{1/2}$

$\varphi_h \approx \varphi_{k2} + \varphi_{h-k2} = \theta_2$ with $P_2(\varphi_h) \propto G_2 = 2|\, E_h\, E_{k2}\, E_{h-k2}\,|/N^{1/2}$

.....

$\varphi_h \approx \varphi_{kn} + \varphi_{h-kn} = \theta_n$ with $P_n(\varphi_h) \propto G_n = 2|\, E_h\, E_{kn}\, E_{h-kn}\,|/N^{1/2}$

Then

$P(\varphi_h) \approx \prod_j P_j(\varphi_h) \approx L^{-1} \prod_j \exp\,[G_j \cos\,(\varphi_h - \theta_j)]$

$= L^{-1} \exp\,[\alpha \cos\,(\varphi_h - \theta_h)]$

where

$$\tan\,\theta_h = \frac{\sum G_j \sin\,\theta_j}{\sum G_j \cos\,\theta_j} = \frac{T}{B}, \qquad \alpha_h = \left(T^2 + B^2\right)^{1/2}$$

A geometric interpretation of α

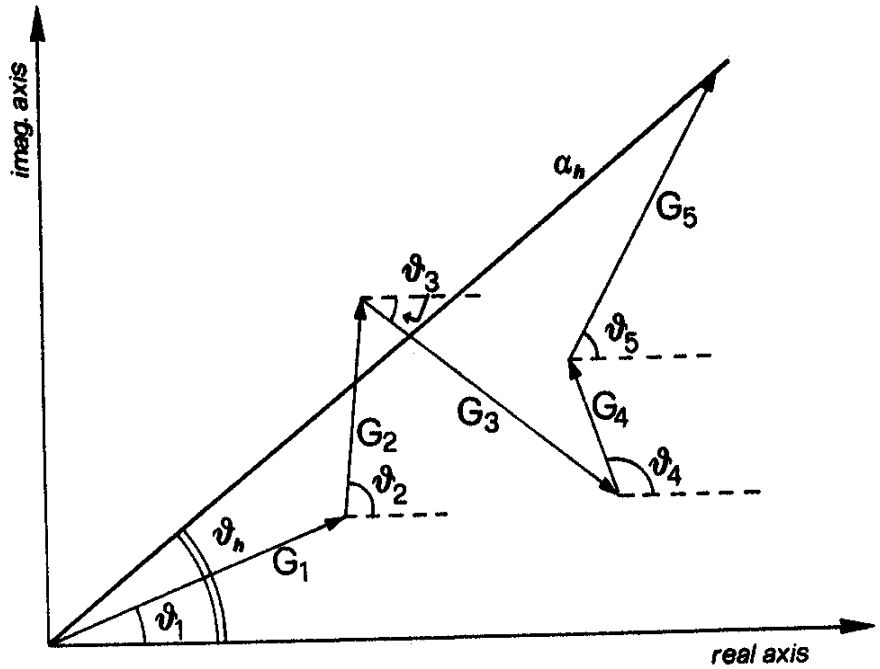

The random starting approach

To apply the tangent formula we need to know one or more pairs ($\varphi_k + \varphi_{h-k}$). *Where to find such an information?*

The most simple approach is the ***random starting approach***. Random phases are associated to a *chosen* set of reflections. The tangent formula should drive these phases to the correct values. The procedure is cyclic (up to ***convergence***).

How to recognize the correct solution?
Figures of merit can or cannot be applied

Tangent cycles

- ϕ_1 ϕ'_1 ϕ''_1 ..... ϕ^c_1
- ϕ_2 ϕ'_2 ϕ''_2 ..... ϕ^c_2
- ϕ_3 ϕ'_3 ϕ''_3 ..... ϕ^c_3
- .....
- ϕ_n ϕ'_n ϕ''_n..... ϕ^c_n
-

- ***Ab initio* phasing**
- **SIR2009** is able to solve

-small size structures (up to 80 atoms in the a.u.);

-medium-size structures (up to 200);

-large size (no upper limit)

- It uses
- **Patterson deconvolution techniques**
- (***multiple implication transformations***)
- as well as
- **Direct methods**
- to obtain a starting set of phases. They are extended and refined *via*
- ***electron density modification techniques***
-

- **Direct methods limits for proteins**:

- 1) the large size (proteins range from300 atoms in the asymmetric unit to several thousands). The G factor in the Cochran formula are very small.

- 2) data resolution

- To overcome the limits one is obliged to :
- -increase the **number of direct methods trials** . The cost to pay concerns the computing time.
- - **improve and extend the the poor phases** available by DM by exploiting some specific features of the proteins (e.g., the solvent , etc.).

About the data resolution limit

Atomic resolution at length was considered a necessary (and not sufficient) condition for **ab initio phasing** (Sheldrick rule) , condition relaxed later on (up to 1.2 Å). If it is not satisfied:

- - the atomicity condition is violated;
- - the number of reliable triplet invariants exploitable by the tangent procedure is small.
- - Patterson and EDM procedures are less effective;
- - the small ratio
- ***number of observations/ number of parameters***
- make least squares unreliable.

The Maximum Entropy Method
Theory and applications to electron and powder diffraction data

Chris J.Gilmore
School of Chemistry, University of Glasgow, Glasgow, Scotland, UK

Abstract The maximum entropy for solving crystal structures from electron and powder diffraction data is described. The basic theory is supplemented by density histogram methods, the use of error correcting codes and the charge flipping method.

Introduction

This chapter will illustrate the process of solving crystal structures using the maximum entropy (ME) method. In the first section the theory is described; this is followed by a practical examples of the method in action for both electron and powder diffraction data

Bayesian Statistics

Maximum entropy (ME) is a tool of Bayesian statistics, and thus is built around Bayes' Theorem. Since, as crystallographers, we are interested in maps and particularly in obtaining an optimum map from measured data, we can state this theorem in the following way

$$p(map|data) \propto p(map)\, p(data|map) \qquad (1)$$

posterior prior likelihood

where *p(.)* means 'probability of'. In Bayesian statistics we define a map with our current knowledge to give the *prior*; we then consult the data with *likelihood* and the use of Bayes' theorem gives us an updated *posterior map*. The whole process can be repeated in a cyclical way. There is, however, a problem: bias in our prior belief about the map; we need to minimize this, and the ME method is a way of obtaining maps with a minimum bias.

The Maximum Entropy Principle

Consider a situation for which we know a set of N probabilities about something, $P=\{p_1, p_2 \ldots\ldots p_N\}$. We can represent this by a probability distribution, and this distribution has an entropy, S, given by:

$$S = -\sum_{i=1}^{N} p_i \log p_i \qquad (2)$$

This equation was first defined and used in a non-thermodynamic context by Shannon [1] when working with problems of the capacity of communication channels, and the transmission of signals down noisy lines. Suppose we have m constraints, expressed as expectation values, $\langle A_r \rangle$, which represent our knowledge derived from experiment. These constraints can be written:

$$\sum_{j=1}^{N} A_{ri} p_i = \langle A_r \rangle \qquad r = 1, 2 \ldots\ldots\ldots m \qquad (3)$$

and from these we wish to derive the set of probabilities {P}. Often the situation under study is a mathematically indeterminate one in which $N >> m$ and it is here that the method can be especially powerful. The ME approach consists of maximizing the entropy subject to the constraints to determine {P}.

The Brandeis Dice Problem

This classical (although controversial!) problem may help to illuminate this idea. Consider a die. When it is thrown there are six possible results, *i,* where $1 \leq i \leq 6$. If it is thrown N times, an "honest" dice will give all $p_i = 1/6$, and an average throw of 3.5 when thrown repeatedly. Suppose, however, we have a biased one for which the mean is 4.5 *i.e.*

$$\sum_{i=1}^{6} i p_i = 4.5 \qquad (4)$$

Given this information *and nothing else* what probability, $p_{i,i=1,6}$ should we assign to the *i* spots on the next throw?

Clearly the problem is indeterminate, and it is possible to devise an infinity of solutions. (*e.g.* the die only gives *i=5* or *i=4* with equal probabilities). The ME principle, however, generates a unique solution which, in the jargon of the subject, is *maximally unbiased*, has a *minimum information content*, and is declared *maximally non-committal with respect to missing information:*

In this case, there are two constraints: the value of the mean and the normalization condition:

$$\sum_{i=1}^{6} p_i = 1 \qquad (5)$$

We maximize *S* subject to these constraints. This is a standard variation problem solved by the use of Lagrangian multipliers. A numerical solution using standard variation methods gives $\{p_1 \ldots . p_6\} = \{0.05435, 0.07877, 0.11416, 0.16545, 0.23977,$

0.34749}, with an entropy of 1.61358 natural units. (S depends on the base of the logarithms.)
Now what does this result mean? To quote Jaynes [2] " *..our result as it stands is only a means of describing a state of knowledge about the outcome of a single trial. It represents a state of knowledge in which one has only (1) the enumeration of the six possibilities, and (2) the mean value constraint...and no other information. The distribution is maximally noncommittal with respect to all other matters; it is as uniform ... as it can get without violating the given constraint."*

Crystallography: maps
A map has entropy. Take a map and partition it into pixels. Let the *i-th* pixel be p_i then we can normalize each pixel to get

$$p_i^{'} = p_i \Big/ \sum p_i \qquad (6)$$

and the map has an entropy

$$S = -\sum_i p_i^{'} \log p_i^{'} \qquad (7)$$

The maximum entropy principle: To produce an image or map which is maximally non-committal or minimally biased with respect to missing data, maximize the entropy of the map subject to the constraint that this map must reproduce the data which generated it within experimental error.

Applications to Crystallography
The theory of the application of the ME formalism was derived by Bricogne [3], and later by Bricogne and Gilmore [4, 5]. We start with a set of unitary structure factors $|U_{\mathbf{h}}|^{obs}$ which are derived from the intensity data by standard normalization procedures.

$$\left(|U_{\mathbf{h}}|^{obs}\right)^2 = k\sigma_2 \left(|F_{\mathbf{h}}|^{obs}\right)^2 \Big/ \sigma_1 \exp\left(-2B\sin^2\theta/\lambda^2\right)\varepsilon_{\mathbf{h}} \sum_{j=1}^{N} f_j^2 \quad (8)$$

where B is an overall, isotropic temperature factor, k a scale factor (both obtained by a Wilson plot), f_j is the electron scattering factor for atom j, the summation spans the N atoms in the unit cell, θ is the Bragg angle , $\varepsilon_{\mathbf{h}}$ is the statistical weight for reflection **h** and:

$$\sigma_n = \sum_{j=1}^{N} f_j^n \qquad (9)$$

(For N point atoms of unit weight in space group P1: $|U_{\mathbf{h}}|^{obs} = 1/\sqrt{N}\,|E_{\mathbf{h}}|^{obs}$.) We also have a set of phase angles $\varphi_{\mathbf{h}}$ most of which are either unknown (the *ab initio* case), or obtained from image data (phase extension) often at low resolution. For *ab initio* structure solution, because of rules of origin and enantiomorph definition, some phases can usually, but not always (it depends on the space group) be assigned subject to certain well known rules.

Those reflections which are phased comprise the *basis set* {H}; the disjoint set, the non-basis set, of unphased amplitudes is {K}; the phase problem is one of phasing $|U_{\mathbf{h}\in K}|^{obs}$ from $U_{\mathbf{h}\in H}$. In electron diffraction the unmeasured set {U} may also be important. This is shown diagrammatically in Figure 1.

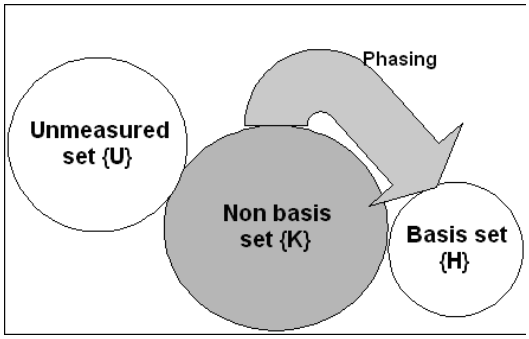

Fig 1: Partitioning the data into disjoint basis, non-basis, and unmeasured sets.

A set of reflections is chosen to form the basis set. These reflections are used as constraints in an entropy maximization to generate a maximum entropy map $q^{ME}(\underline{x})$. Because it has maximum entropy $q^{ME}(\underline{x})$ satisfies the following conditions:

1. It is optimally unbiased.
2. Its Fourier transform reproduces the constraints to within experimental error.
3. The Fourier transform of $q^{ME}(\underline{x})$ generates estimates of amplitudes and phases for reflections in {K} and {U}. This process is called *extrapolation.*

This is shown diagrammatically in Figure 2.

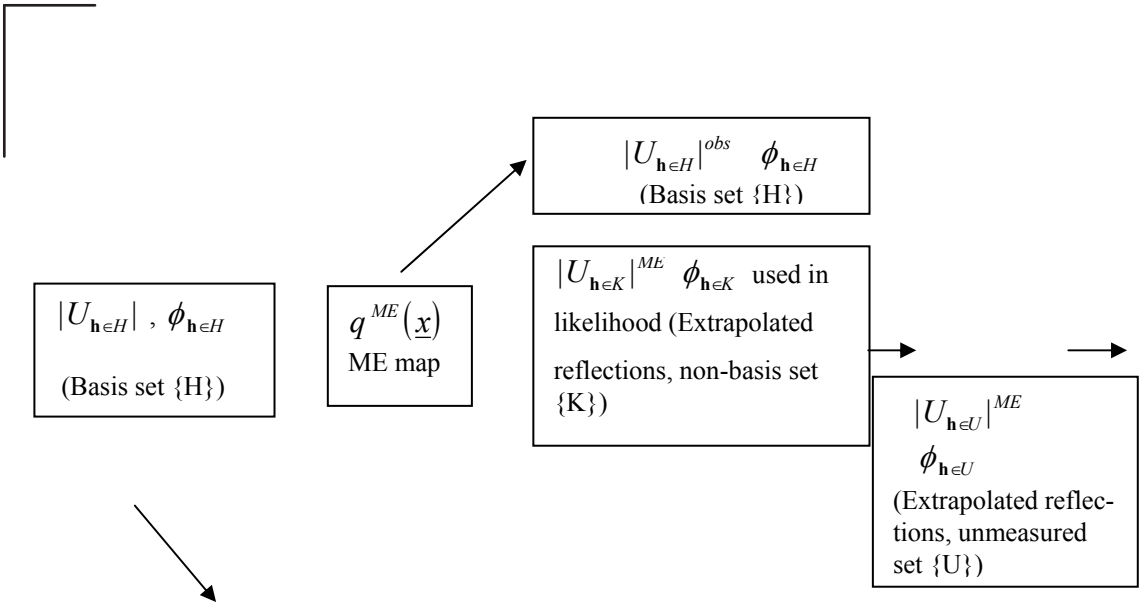

Fig. 2. Phase extrapolation

At early stages of phase determination with small basis sets the extrapolation is very weak, and the structure is usually not visible in any map one cares to generate. So what can be done? The most obvious answer is to examine the most strongly extrapolated reflections in {K}, and use the phase information from them coupled with the observed U magnitudes, and add them into the basis set {H}. This usually leads to disaster: the ME solution gets trapped in a local maximum, whole subsets of reflections become wrongly phased, and the structure remains unsolved. This is a manifestation of the *branching problem* where phases are being selected without exploring the relevant space in sufficient detail, so that what appears to be an unambiguous choice of new phase is, in reality, no such thing. To overcome this, extra unphased reflections must be added to the starting set with permuted phases giving rise to a multisolution environment just as in conventional direct methods, and the reflections we choose should be those which are very weakly extrapolated, so that their inclusion in a new basis set offers maximum surprise to the calculations.

Using Error Correcting Codes to Permute Phases

First we need to define the concept of degrees of freedom: a centric reflection has two possible phase choices (*e.g. 0, π; ±π/2*) and therefore has 1 degree of freedom. We define the total number of degrees of freedom arising from n_c centric reflections as n_c. For acentric reflections there are no phase restrictions. If you just fix the quadrant then there are 4 possible choices, and 2 degrees of freedom: 1 to fix the real part, and 1 to fix the imaginary part of the structure factor, so if you have n_a acentric

phases there is a total of $2n_a$ degrees of freedom. A set of n_a acentric phases and from n_c centric reflections has a total number of degrees of freedom $n = 2n_a + n_c$. This has serious consequences if you wish to explore the phase space of a set of reflections having n total degrees of freedom: you need, at minimum, to explore 2^n phase combinations; this means that for 24 of degrees of freedom you have 16,777,216 choices, and each one needs to be subjected to entropy maximization. There is an alternative using error correcting codes as a source of phase permutation [6]. The MICE computer program offers 6 choices (plus incomplete factorial designs) as shown in Table 1.

Code	n	No of nodes	No of nodes for a full factorial design
Hadamard [15,113,3] or [16,11,4]		2048	65536 / 32768
Nordström-Robinson (16,256,5) or (16,256,6)	15/16	256	16384 / 32768
Golay [23,12,7] or [24,12,8]	23/24	4096	8388608 / 16777216
Extended Golay	47/48	32768	$1407 / 2814\times10^{14}$
	96/97	262144	$3961 / 7922\times10^{28}$

Table 1: The use of error correcting codes to explore phase space.

With a set of possible solutions, how then do you select the correct one? Can you choose those which give maps of maximum entropy? The answer to this is *'no'*, but likelihood functions can help.

Likelihood

We split our reflections into two groups: the centric ones which have phase restrictions such as 0,π and acentric one which are unrestricted. For each acentric extrapolated, non-basis set reflection **k** the likelihood measure, in its diagonal approximation, can be written [3, 4, 5]

$$\Lambda_{\mathbf{k}} = \frac{|U_{\mathbf{k}}|^{obs}}{\varepsilon_{\mathbf{k}}\Sigma+\sigma_{\mathbf{k}}^2}\exp\left\{-\frac{1}{2}\frac{\left(|U_{\mathbf{k}}|^{obs}\right)^2+|U_{\mathbf{k}}^{ME}|^2}{\varepsilon_{\mathbf{k}}\Sigma+\sigma_{\mathbf{k}}^2}\right\}I_0\left(\frac{|U_{\mathbf{k}}|^{obs}|U_{\mathbf{k}}^{ME}|}{\varepsilon_{\mathbf{k}}\Sigma+\sigma_{\mathbf{k}}^2}\right) \quad (10)$$

where $\sigma_{\mathbf{k}}^2$ is the variance of $|U_{\mathbf{k}}|^{obs}$ and Σ a (refinable) measure of unit cell contents $\Sigma \approx 1/(2N)$ for N point atoms in the unit cell. Note that this expression is a measure of agreement between $|U_{\mathbf{k}}|^{obs}$ and $|U_{\mathbf{k}}^{ME}|$, indeed it has a maximum where $|U_{\mathbf{k}}|^{obs} = |U_{\mathbf{k}}^{ME}|$. For the centric case the Bessel function is replaced by a cosh term:

$$\Lambda_{\mathbf{k}} = \frac{2|U_{\mathbf{k}}|^{obs}}{\pi\left(2\varepsilon_{\mathbf{k}}\Sigma+\sigma_{\mathbf{k}}^2\right)}\exp\left\{-\frac{1}{2}\frac{\left(|U_{\mathbf{k}}|^{obs}\right)^2+|U_{\mathbf{k}}^{ME}|^2}{2\varepsilon_{\mathbf{k}}\Sigma+\sigma_{\mathbf{k}}^2}\right\}\cosh\left(\frac{|U_{\mathbf{k}}|^{obs}|U_{\mathbf{k}}^{ME}|}{2\varepsilon_{\mathbf{k}}\Sigma+\sigma_{\mathbf{k}}^2}\right) \quad (11)$$

In the spirit of traditional

likelihood analysis, we define a null hypothesis for the situation where $\left|U_{\mathbf{k}}^{ME}\right| = 0$. This gives the Gaussian distribution of Wilson statistics. For acentric reflections:

$$\Lambda_{\mathbf{k}}^{0} = \frac{\left|U_{\mathbf{k}}\right|^{obs}}{\varepsilon_{\mathbf{k}}\Sigma + \sigma_{\mathbf{k}}^{2}} \exp\left\{ -\frac{1}{2} \frac{\left(\left|U_{\mathbf{k}}\right|^{obs} \right)^{2}}{\varepsilon_{\mathbf{k}}\Sigma + \sigma_{\mathbf{k}}^{2}} \right\} \quad (12)$$

The extension to centric reflections is obvious. Define:

$$L_{\mathbf{k}} = \log \frac{\Lambda_{\mathbf{k}}}{\Lambda_{\mathbf{k}}^{0}} \quad (13)$$

Then the global log-likelihood gain (LLG) is derived by summing over all the extrapolates:

$$LLG = \sum_{\mathbf{k}} L_{\mathbf{k}} \quad (14)$$

The LLG will be largest when the phase assumptions for the basis set lead to predictions of deviations from Wilson statistics for the unphased reflections, and in this context it is used as a powerful figure of merit.
However, rather than just choose those phase sets with high associated LLG, which is a somewhat subjective process, the Student t-test is used [7] in which the LLGs are analyzed for phase indications. The simplest example involves the detection of the sign (corresponding to the 0,π or ±π/2 choices) of a single centric phase. The LLG average, μ^{+}, and its associated variance V^{+} is computed for those sets in which the sign of this permuted phase under test is + (*i.e.* 0 phase). The calculation is then repeated for those sets in which the same sign is - (π) to give the corresponding μ^{-}, and variance V^{-}. The t-statistic is then:

$$t = \frac{\left|\mu^{+} - \mu^{-}\right|}{\sqrt{V^{+} + V^{-}}} \quad (15)$$

The use of the t-test enables a sign choice to be derived with an associated significance level. This calculation is repeated for all the single-phase indications, and is then extended to combinations of two and three phases. An extension to acentric phases is straightforward by employing two signs to define the phase quadrant *(i.e.* ±π/4, ±3π/4) both in permutation and in the subsequent analysis. In general, only relationships with associated significance levels <2% are used, but this is sometimes relaxed. Each of the *m* phase relationships, *i*, so generated is given an associated weight w_i

$$w_i = \left(1 - \frac{I_1(s_i)}{I_0(s_i)}\right) \qquad (16)$$

where I_1 and I_0 are the appropriate Bessel functions and s_i is the significance level of the *i-th* relationship from the t-test. This weighting function reflects the need for a scheme in which the absolute values of the significance levels are not given undue emphasis since they are themselves subject to errors arising from the diagonal nature of the likelihood function used and the lack of error estimates for the LLGs themselves. Each node n is now given a score, s_n

$$s_n = LLG_n \sum_{j=1}^{m} w_j \qquad (17)$$

where the summation spans only those phase relationships where there is agreement between the basis set phases and the t-test derived phase relationships. The scores are sorted and only the top nodes are kept; the rest are discarded. New reflections are then permuted and a corresponding set of ME solutions is generated. In this way we build a *phasing tree* in which each set of phase permutations is represented as a *node*, and has a score as described above. The root node of the tree is defined by the origin defining reflections. The first set of phase permutations defines the second level. Those which do not pass the analysis of likelihood are discarded, then further phase permutations are used to generate the third level, and this continues until a recognizable structure or structural fragment appears. Figure 3 shows an outline of a three-level phasing tree.

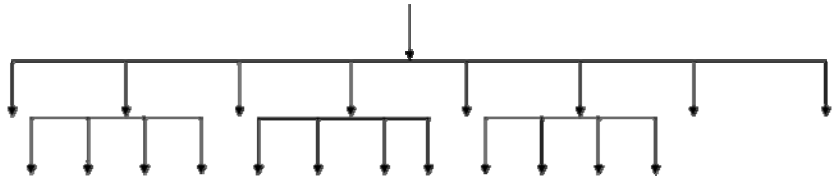

Fig. 3. A three-level, 21 node phasing tree

Centroid Maps

Now $q^{ME}(\underline{x})$ is a probability distribution, and not a map in the traditional sense (although its peaks do correspond to atom positions), and thus it needs conversion to a more conventional one. The trial electron density maps generated in this approach are called *centroid maps*, and can be visualized as Sim-filtered maximum entropy maps [4, 5]. For **k** acentric, the Fourier coefficients are:

$$\left|U_{\mathbf{k}}\right|^{obs}\left[I_1\left(X_{\mathbf{k}}\right)/I_0\left(X_{\mathbf{k}}\right)\right]\exp\left(i\varphi_{\mathbf{k}}^{ME}\right) \qquad (18)$$

where:

$$X_{\mathbf{k}}=\left(2N/\varepsilon_{\mathbf{k}}\right)\left|U_{\mathbf{k}}\right|^{obs}\left|U_{\mathbf{k}}^{ME}\right| \qquad (19)$$

For **k** centric, these coefficients become:

$$\left|U_{\mathbf{k}}\right|^{obs}\tanh\left(X_{\mathbf{k}}\right)\exp\left(i\varphi_{\mathbf{k}}^{ME}\right) \qquad (20)$$

with:

$$X_{\mathbf{k}}=\left(N/\varepsilon_{\mathbf{k}}\right)\left|U_{\mathbf{k}}\right|^{obs}\left|U_{\mathbf{k}}^{ME}\right| \qquad (21)$$

Fitting

One final practical point needs to be made here concerning the tightness with which one fits the constraints in the entropy maximization which can be very important in a phasing environment. If the fit between $\left|U_{\mathbf{h}}\right|^{obs}$ and $\left|U_{\mathbf{h}}^{ME}\right|$ is very slack, the ME extrapolation is weaker than it can be, and the phasing power and the discriminating power of likelihood is correspondingly reduced. If however there is over fitting, spurious details (often looking like small stones) appear in $q^{ME}(x)$ which give false phase indications. The latter situation can often be detected by the use of likelihood: if the LLG is monitored through the iterative cycles of entropy maximization, a maximum is often reached and this can be used as a place to stop. Alternatively, the χ^2 statistic can be used with a default choice of unity as a place to stop.

$$\chi^2=\frac{1}{n}\sum_{h\in H}\frac{1}{\sigma_h^2}\left(\left|U_{\mathbf{h}}\right|^{obs}-\left|U_{\mathbf{h}}^{ME}\right|\right)^2 \qquad (22)$$

In practice, for small basis sets either method works well, but for large basis sets maximum LLG is preferred.

The MICE computer program is a practical implementation of the ME formalism [8] a simple flowchart is shown in Figure 3

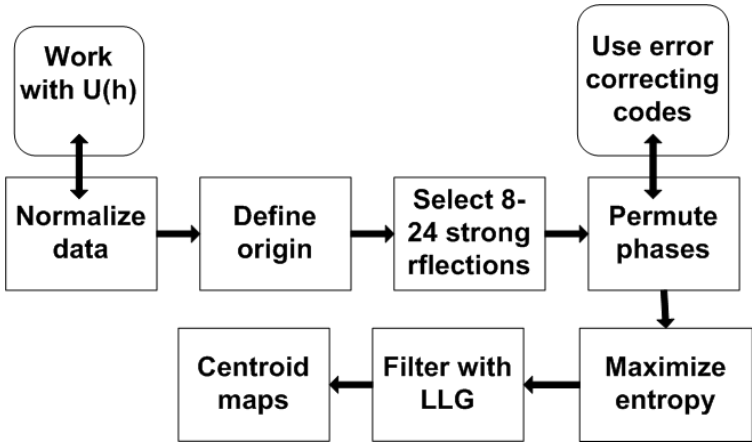

Fig. 3. Flow chart for the MICE program in default mode.

Using Density Histograms

Although successful the ME procedure has some problems:

1. It can necessary to scan a large number of maps. In these circumstances identifying a correct or near-correct solution can be difficult.
2. Is a usable solution present in the phase set that is not being considered?

The problem arises from difficulties with LLG estimates as figures of merit. In electron diffraction the data are sparse with systematic errors especially involving kinematically weak reflections whose magnitudes are consistently overestimated.. Although the LLG estimates are robust, the nature of ED data perturbed by multiple scattering weakens their power to discriminate phase sets. In powder diffraction overlapped reflections can also weaken the discriminating power of LLG.
Density histograms and histogram matching [9, 10] are now a routine tool in macromolecular crystallography for improving phases. Baerlocher *et al.* [11] have shown that histogram matching also can be a powerful technique for solving zeolite structures from powder diffraction data, and it is an obvious extension to these arguments to supplement the use of ME and LLG estimates with potential map histograms from electron and powder diffraction data.
To generate idealized electron potential histograms from ED data, centroid potential maps were generated for several structures at different resolutions using experimental intensity data. The phases were taken from solved structures, the entropy maximized, and the corresponding centroid map calculated. A typical histogram for a zeolite is shown below:

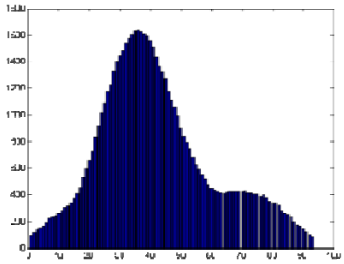

Fig. 4. A typical zeolite density histogram derived from centroid maps using known phases.

To use this information, the standard ME method is modified as follows:

1. The ME process is carried out to the point where a set of 32-64 maps are selected using LLG criteria.
2. Each map generates the corresponding density histogram. Let x_i be the counts in bin i for the idealized histogram, and y_i the counts in the corresponding experimental density from the ME generated centroid maps. To compare to the two, two correlation coefficients are used: the Pearson (r_P)

$$r_P = \frac{\sum_{i=1}^{n}\left(x_i - \bar{x}\right)\left(y_i - \bar{y}\right)}{\left[\sum_{i=1}^{n}\left(x_i - \bar{x}\right)^2 \sum_{i=1}^{n}\left(y_i - \bar{y}\right)^2\right]^{1/2}} \quad (23)$$

and the Spearman, r_S

$$r_S = \frac{\sum_{i=1}^{n} R(x_i)R(y_i) - n\left(\frac{n+1}{2}\right)^2}{\left(\sum_{i=1}^{n} R(x_i)^2 - n\left(\frac{n+1}{2}\right)^2\right)^{1/2}\left(\sum_{i=1}^{n} R(y_i)^2 - n\left(\frac{n+1}{2}\right)^2\right)^{1/2}} \quad (24)$$

where n is the number of bins (always set to 100 in this work). $R(x_i)$ and $R(y_i)$ are the ranks of the sorted histogram bins rather than their values.
The use of two correlation coefficients stems from our work in pattern matching using powder diffraction data [12]. The Spearman coefficient is less susceptible to outliers, and the Pearson coefficient less susceptible to scaling issues and we have found that the use of these coefficients both separately and together to be optimal. Furthermore, the Spearman test does not assume that the data are normally distributed, and this is clearly the case for the ideal histogram. This also helps to make the histogram independent of data resolution. The following maps are examined:

1. Those with the 5 top scores from LLG analysis.
2. Those with the 5 maximum values of r_P.

3. Those with the 5 maximum values of r_S.
4. Those with the 5 maximum values of $(r_P+r_S)/2$.

These four sets are not usually disjoint, and one often examines only approximately 10 maps. These rules are wholly heuristic and derived from the experience of density matching, but, as shown in the next sections, they have proved to be wholly effective in solving zeolite structures from ED data [13, 14]. A flowchart of the procedure is shown below in Figure 5.

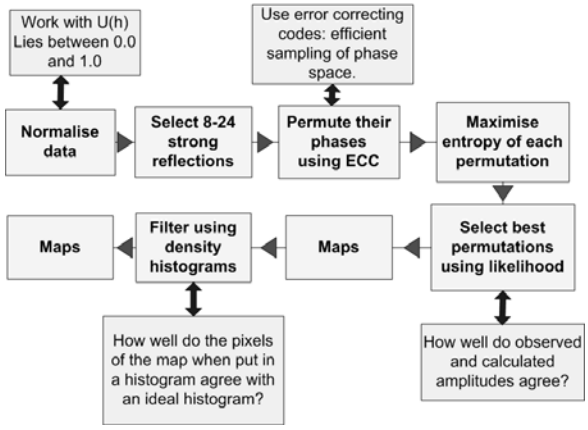

Fig. 5. A flowchart of the ME procedure using density histograms as figures of merit.

Example Using Electron Diffraction Data

Three-dimensional data were obtained at 300 kV for the MWW zeolite by tilting microcrystals around the a*-axis [15]. There are 155 unique reflections with a maximum resolution of 1.3Å. The space group is P6/mmm with a = 14.21 and c = 24.94Å.The origin was defined *via* a single reflection (52-3) with U magnitude 0.16. Sixteen reflections were given permuted phases via the Nördstrom-Robinson code to give 257 nodes all of which were subjected to entropy maximization. Figure 6 gives a view down both the c- and a-axes using the node ranked 4th in LLG analysis, 24th, by the Pearson, 35th by the Spearman coefficients using the mean density histogram correlation coefficients.

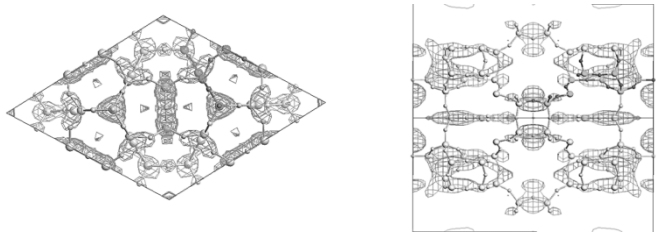

Fig. 6. Best solution for MWW.

Density Building Functions

Density building functions take a low resolution molecular envelope and attempt to build atomic level detail inside the envelope. The method we use works as follows [14]:

1. A starting map is defined. This can come from a number of possible sources: it can be an origin map defined from 1-3 reflections (up to 4 if the enantiomorph is to be defined) in the usual way (See Rogers [16] for a summary of the method and the necessary rules for origin definition) or an image derived map from electron microscopy.
2. A maximum entropy map, $q^{ME}(\boldsymbol{x})$, is generated by maximizing the map entropy subject to the constraints of the phase and intensities of the reflections used to generate the starting map.
3. A set of reflections is now chosen which optimally enlarges the second neighbourhood of the origin, and their phases are permuted using a full factorial design (*i.e.* every possible combination of phases is explored). Each permutation gives rise to a map δq(**x**) which is Fourier transform of

$$|U_{\mathbf{h}}|^{obs} e^{i\phi_{\mathbf{h}}^{perm}} - |U_{\mathbf{h}}|^{ME} e^{i\phi_{\mathbf{h}}^{ME}} \qquad (25)$$

where $\phi_{\mathbf{h}}^{perm}$ is the phase angle for reflection **h** generate by phase permutation and $\phi_{\mathbf{h}}^{ME}$ is the equivalent extrapolated phase from the current $q^{ME}(\underline{x})$.

4. We now compute

$$P(\delta q) = \int_V \frac{\delta q(\mathbf{x})^2}{q^{ME}(\mathbf{x})} d\mathbf{x} \qquad (26)$$

for each phase permutation. A minimum value of $P(\delta q)$ is expected for the correct phase set. In practice the 50-100 phase sets with the minimum values of $P(\delta q)$ are retained, and these sets are subjected to constrained entropy maximization in the usual way with associated likelihood estimation. The *EXTEND* module in the *MICE* computer program performs the necessary calculations. Centroid maps are then generated for the 64 nodes with the largest LLG. They are further filtered using histograms and the top 8 inspected.

This technique has several important features:

1. Each phase permutation requires only one Fourier synthesis and a map division and so density building is very fast.
2. It acts as a filter to exponential modeling; the reflections to be permuted are first subjected to this filter and only those with a certain minimum $P(\delta q)$ are passed to the maximum entropy step.

3. The likelihood function uses only moduli, but $P(\delta q)$ incorporates phases into the calculation. It therefore acts as a useful tool in exploring structure-factor space from the current state of knowledge before moving to various P minima.

Figure 7 shows a flowchart for the procedure.
$P(\delta q)$ cannot be used indiscriminately, there are certain necessary conditions for its successful implementation:

1. $q^{ME}(\boldsymbol{x})$ must have developed sufficient detail. Thus maps based on a very small basis set or utilizing only small U magnitudes may have insufficient contrast for its successful use. This is made manifest by a set of $P(\delta q)$ values that are virtually constant through phase permutation. In addition, division by $q^{ME}(x)$ is inherently unstable because of very low values of q and constraints in division must be employed.
2. The reflections which act as coefficients for permutation should be chosen using the same criteria of optimum second-neighbourhood extension used in regular entropy maximization. It is also advantageous to choose reflections for which there is a small but finite extrapolated magnitude from the current $q^{ME}(\boldsymbol{x})$.
3. Situations where there is no clear minima or where all the $P(\delta q)$ values are constant are clear indications that either $q^{ME}(x)$ has insufficient contrast or that unsuitable reflections have been chosen as coefficients.

The technique preferentially selects those phases that build density where it is already well defined. This is very appropriate in this situation where we have a clear envelope.

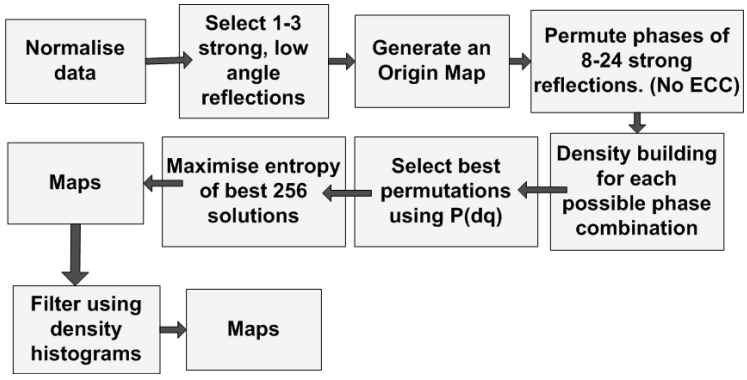

Fig. 7. A flowchart for density building procedures.

An Example with Electron Data

MCM-68 [17] crystallizes in space group $P4_2/mnm$ and this data set comprises 42 hk0 reflections with a maximum resolution of *ca.* 1.8Å (Figure 8(a)). Figure 8(b)

shows the origin centroid map for based on one reflection (520) with $|U_{\mathbf{h}}|^{obs}$=0.19, $\phi_{\mathbf{h}}$=0

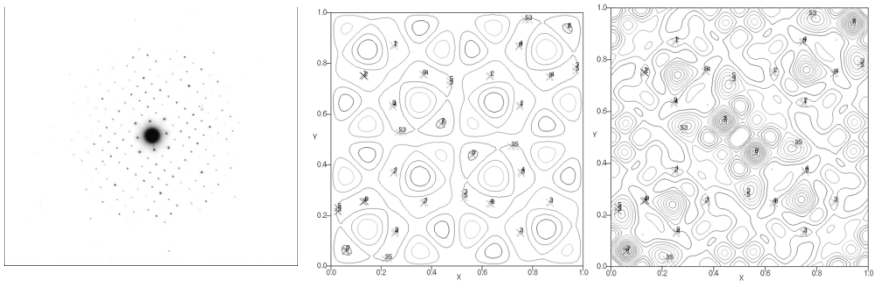

(a) (b) (c)

Fig. 8. Using density building function on MCM-68: (a) The intensity data; (b) The origin map based on the single (520) reflection and (c) the best centroid map.

Figure 8(c) shows the centroid map based on the origin defining reflections and 8 reflections with permuted reflections filtered via the *P(δq)* function. This is the map with the highest associated likelihood estimate. Two of the T-sites are not clearly defined, and the problem in which a single elongated peak represents two Si atoms is evident here, and is a consequence of data resolution and sparsity.

Extension to Powder Diffraction

The ME method needs to be adapted for powder diffraction to deal with the overlap problem. This is relatively straightforward. To do this we split the data into sets of overlaps Let a given overlap comprise $R_{i,\ i=1,m}$ observed intensities, $|U_{\mathbf{h}}|^{obs}$, and $r_{i,\ i=1,m}$ calculated intensities produced as a result of extrapolation from a maximum entropy optimization $\left|U_{\mathbf{h}}^{ME}\right|$. For each overlap or single reflection (in which case $m=1$), define

$$R=\sum_{i=1}^{m} p_i R_i^2 \qquad (27)$$

and

$$r=\sum_{i=1}^{m} p_i r_i^2 \qquad (28)$$

where p is the reflection multiplicity. Define

$$z=Rr/\Sigma \qquad (29)$$

Further define

$$X_n(z)=e^{-z}\,{}_0F_1\left(-;n/2;z^2/4\right) \qquad (30)$$

where ${}_0F_1$ is a confluent hypergeometric function. The log likelihood, LH, is written

$$LH = \sum_{\substack{all \\ extrapolates}} \left[-n/2 \log \Sigma - \left(R - r\right)^2 / 2\Sigma + \log X_n\left(z\right) \right] \quad (31)$$

For the null hypothesis, LH_0, we set r, and hence z =0. The log-likelihood gain (LLG) is then, as usual

$$LLG = LH - LH_0 \qquad (32)$$

We then proceed in the usual way, including the optional use of histograms. We also need to deal with centroid maps where there are overlaps. In this case we use Sim-type weights *w* computed *via*

$$w = \frac{R^2 \, {}_0F_1\left(-; n/2+1; z^2/4\right)}{n\Sigma \, {}_0F_1\left(-; n/2; z^2/4\right)} \qquad (33)$$

Example of Powder Diffraction Structure Solution

The example is the zeolite EMM-8 [18], ($Al_{32}P_{32}O_{128}$) which crystalizes in space group C2/c with a cell a = 22.5541, b = 13.7357, c = 14.0756, β = 98.617°. The channels are apertures formed by 6-rings only. We used 305 unique reflections of which 83% overlapped and worked at 1.5Å resolution. Using 16 non-overlapped reflections and permuting them using a Nordström-Robinson code gave 256 possible solutions. These were filtered using LLG (with overlap data) and histograms. The best map is shown in Figure 9; the channels are clearly defined.

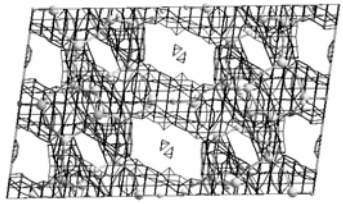

Fig. 9. Centroid map for EMM-8. The channels are clearly defined.

Interfacing Superflip

Superflip [19] is a computer program that implements the charge flipping algorithm devised by Oszlányi and Süto [20]. There is a section on this method elsewhere in this book, and so it is not described here.

The method needs complete, high resolution (1.1Å) data to work. However, it may be that the solution is sometimes present and not detected by the figures of merit used. The technique is easily interface to MICE and can be used as a source of phase

sets: 100 sets of phases are generated by Superflip and these are input as nodes into MICE. Each node is subjected to constrained entropy maximization and the solutions filtered using LLG and histograms in the usual way. The method is surprisingly successful and the next section gives an example.

Example with powder data

Here is an example from the database of powder data for structure solution devised by David *et al.* [21]. The is N,N'-Bis-[1-pyridin-4-yl-meth-(E)-ylidene]-hydrazine shown in Figure 11.

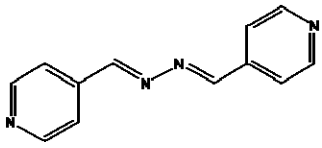

Fig. 11. Chemical structure of N,N'-Bis-[1-pyridin-4-yl-meth-(E)-ylidene]-hydrazine.

The space group is $P2_1/c$ with unit cell of dimensions a = 3.848, b = 11.005, c = 12.727, $\beta = 92.38°$; Z=4. A total of 198 non-overlapped reflections at 1.42Å resolution were input into Superflip and 100 phase sets generated. Most of these had not converged after 10000 cycles or had high figures of merit. The solutions were passed into MICE; each phase set node was subjected to constrained entropy maximization and the solutions filtered using LLG and histograms in the usual way. Only one solution had LLG > 1.0 and the corresponding centroid map is shown in Figure 12. The molecular envelope is clear.

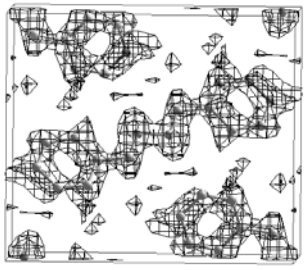

Fig. 12. The centroid map for N,N'-Bis-[1-pyridin-4-yl-meth-(E)-ylidene]-hydrazine with the highest LLG. The phase sets were generated by Superflip.

Acknowledgments

The zeolite work was carried out with Doug Dorset at ExxonMobil. I wish to thank them for their support. The Superflip research was carried out at the Technical University, Delft with Henny Zhandbergen and Jouk Jansen. The author thanks the University for a visiting professorship. I also wish to thank Lukas Palatinus at the University of Lausanne for assistance with Superflip developments. Kenneth Shankland at the University of Reading was the collaborator in the project involving Superflip, MICE and powder diffraction data. I also acknowledge support from the University of Glasgow.

References

[1] Shannon, C.E. & Weaver, W. (1949). *The Mathematical Theory of Communication*. University of Illinois Press, Urbana, USA.
[2] Jaynes, E.T. (1986) in J.H.Justice (ed.), *Maximum Entropy and Bayesian Methods in Applied Statistics,* Cambridge University Press, Cambridge, pp 26-58.
[3] Bricogne, G. (1984). *Acta Cryst*. **A40**, 410-445.
[4] Bricogne, G. & Gilmore, C.J. (1990). *Acta Cryst.* **A46**, 284-297.
[5] Gilmore, C.J., Bricogne, G. & Bannister, C. (1990). *Acta Cryst.* **A46**, 297-308.
[6] Gilmore, C.J., Dong, W. and Bricogne, G. (1999). *Acta Cryst*, **A55,** 70-83.
[7] Shankland, K., Gilmore, C.J., Bricogne G. & Hashizume, H. (1993). *Acta Cryst.* **A49**, 493-501.
[8] Gilmore, C.J. & Bricogne, G. (1997). The MICE Computer Program in *Methods in Enzymology vol. 277* C.W.C. Carter Jnr.(ed.) Academic Press, New York 65-78.
[9] Zhang, K.Y.J. & Main, P. (1990). *Acta Cryst*. **A45**, 41-46.
[10] Main, P. (1990). *Acta Cryst.* A**46**, 507-509.
[11] Baerlocher, Ch., McCuster, L.B. & Palatinus, L. (2007). *Z. Kristallogr*. **222**, 47-53.
[12] Barr, G., Dong, W. & Gilmore, C.J. (2009). *J. Appl. Cryst.,* **42**, 965-974.
[13] Gilmore, C.J., Dong, W &Dorset, D.L. (2005). *Acta Cryst.* **A64,** 284-294.
[14] Gilmore, C.J., Dong, W &Dorset, D.L. (2005). *Acta Cryst.* **A64,** 295-302.
[15] Dorset, D.L., Roth, W.J. & Gilmore, C.J. (2005). Acta Cryst. **A61**, 516 -527.
[16] Rogers, D. (1980) *Theory and Practice of Direct Methods in Crystallography* edited by M.F.C. Ladd & R.A. Palmer pp. 23-92. New York: Plenum Press.
[17] Dorset, D. L. (2006) Z. Kristallogr. 221, 260-265.
[18] Cao, G., Afeworki,M., Kennedy, G.J., Strohmaier, K.G. & Dorset, D.L. (2007). *Acta Cryst.* **B63**, 52-56.
[19] Palatinus, L. & Chapuis, G. (2007). *J. Appl. Cryst.* **40**, 786-790.
[20] Oszlányi, G. & Süto, A. (2008). *Acta Cryst.* **A64**, 123-134.
[21] See: www.powderdata.info

Structure solution by charge flipping

Lukáš Palatinus
Institute of Physics of the AS CR, v.v.i., Prague, Czech Republic

Abstract. Charge flipping is an iterative structure solution method based on the alternating modification of an electron density in direct space and structure factors in reciprocal space. It has been successfully applied to a range of crystallographic problems, including structure solution from powder difraction data and from electron diffraction data obtained by the precession electron diffraction method. For electron diffraction no modification of the basic algorithm is neccessary. For the structure solution from powder diffraction the histogram matching technique proved to be a powerful method to improve the quality of the solutions and use the algorithm to to solve quite complex structures.

1. Introduction

The phase problem in crystallography is almost as old as structural crystallography itself. For a long time, the approaches to this problem have been driven by the attempts to reduce the computational complexity of the solution methods because of the limited (or non-existent) access to powerful computers. Lots of effort has been invested in the development of Patterson and direct methods in order to make them as computationally efficient as possible.

The advent of cheap computer power available on almost everyone's desk has allowed the development of methods that are conceptually simpler than the classical methods at the expense of higher requirements for computing power. Among these techniques are direct-space methods (simulated annealing, genetic algorithms...) and extensions of the classical direct methods, like Shake-and-Bake. Recently, a new class of methods based neither on the direct methods nor on direct-space approaches have emerged. These methods are based on an iterative modification of an image in both direct and reciprocal (Fourier) space, and can therefore be referred to as dual-space iterative methods.

2. Dual-space iterative methods

The diffraction experiment provides information about the amplitudes of the Fourier coefficients of the scattering density, but the phases of the structure factors are lost. In the case of X-ray diffraction by a crystal, the scattering density is the electron density in the unit cell of the crystal. For diffraction by electrons the scattering density is the electrostatic potential. The knowledge of the Fourier amplitudes imposes constraints on possible electron densities (the *amplitude constraints*), but these constraints alone are not sufficient for the solution of the phase problem. To solve the phase problem without serious ambiguities, we have to define additional constraints

that allow us to discriminate between physically meaningful and meaningless electron densities. The weakest and most general constraint is the requirement for the electron density to remain positive (*positivity constraint*). Another obvious constraint follows from the fact that crystals consist of individual atoms. We could thus require that the electron density contains only a limited number of significant peaks, and the rest of the unit cell is filled by almost zero density. A weaker variant of this constraint is the mere requirement that only a small part of the unit cell has significant density, with the rest being zero. In this weaker formulation there is no explicit assumption that the significant density is grouped into separated point-like peaks. We can call this condition a *sparseness constraint*. All these constraints are defined with respect to the electron density rather than its Fourier coefficients, and they are therefore direct-space constraints in contrast to the amplitude constraint, which is defined in reciprocal space.

Whatever constraint we choose, we can now reformulate the solution of the phase problem from a different perspective. In the space that contains all possible electron densities, we seek the subset of densities that fulfill both the amplitude constraint and some of the direct space constraints. This subset is an intersection of the subsets fitting the amplitude constraint and the direct-space constraint. We are therefore looking for an intersection of two subsets in the space of electron densities. The sets of densities that fulfill the constraints are termed constraint sets.

The problem of finding an element from the intersection of two (or more) constraint sets has been treated by mathematicians since long time ago. In the special case of *convex feasibility* or *convex optimization* problems, where all sets are convex, well-defined iterative procedures exist with proven convergence properties. For instance, the intersection between two convex constraint sets is always reached simply by alternating projections onto the first and the second set (Figure 1a). In crystallography, the set associated with the amplitude constraint is unfortunately non-convex. In such case the algorithms developed for convex sets are not guaranteed to work, because they can get trapped in local minima (Figure 1b). It is nevertheless useful to use the terminology and approaches developed for the convex feasibility problem. The two main elements constituting the basis of the algorithms are the constraint sets and the projections onto them. We have already discussed the constraints. Now let us consider the projections. For the purposes of this chapter a projection P is a mapping from an arbitrary point ρ in the image space onto the nearest point of the constraint set C:

$$P : P_\rho \in C \text{ and } \left\| P_\rho - \rho \right\| = \min$$

Applying a projection to an arbitrary density results in a new density that belongs to the constraint set. A projection P_F that projects an arbitrary density ρ on the amplitude constraint C_A can be written as:

$$P_F = \Phi^{-1} A \Phi$$

where Φ represents a Fourier transform, and A an operation on the Fourier coefficients such that the phases remain intact, and the amplitudes are replaced with the experimental amplitudes.

It is obvious from Figure 1b that "naively" alternating the projections onto the first and second constraint set can only be successful sometimes, but it is prone to stagnation at local minima. This drawback can be overcome by replacing simple projections by relaxed projections (overprojections), or combining these relaxed projections in more elaborate schemes. A relaxed projection R is defined as:

$$R = P + \gamma(P - I)$$

Thus, a relaxed projection is obtained by a "prolongation" of the vector from ρ to P_ρ by a factor γ. The special case $\gamma = 1$ is called a reflection. Figure 1c illustrates that using relaxed projections may allow the iteration to escape from a local minimum.

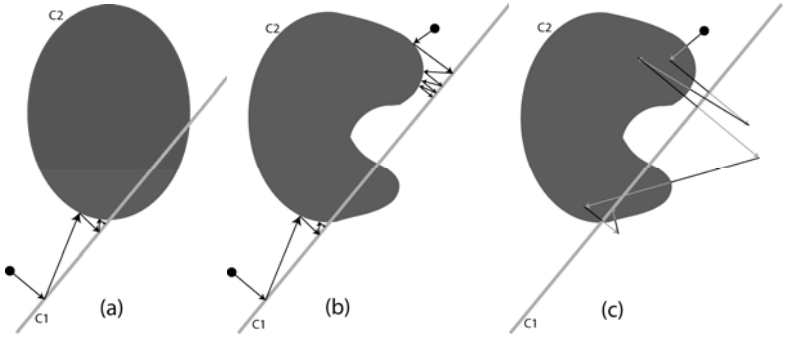

Fig. 1. Finding the inter-section of two constraint sets. (a) Convex constraint sets and repeated projections. (b) Non-convex constraint sets and repeated projections. (c) Non-convex constraint sets and repeated overprojections.

Multiple different combinations of projections have been suggested in the literature (see Thibault 2007 for overview), but it must be emphasized that not all possible combinations are useful. A good algorithm must be designed in such a way that it searches the image space efficiently, *i.e.* it does not get trapped in local minima, and explores large parts of the image space. On the other hand, if the iteration approaches the true solution, it must converge close to the solution, and not diverge again. Clearly, the algorithm must be a balance between the perturbing aspect necessary to explore the search space, and the stabilizing aspect needed for the stability at the solution.

3. The Charge-Flipping Algorithm

Several dual space algorithms can be described in the frame-work of repeated (over)projections onto the constraint sets. Among them the charge flipping algorithm has gained the widest attention, and is currently the main dual-space iterative method used to solve structures in practical crystallogra-phy. The basic algorithm can be briefly described as an alternation of a simple projection onto the amplitude

constraint set followed by an overprojection onto the positivity constraint set. However, the exact implementation deviates somewhat from this general scheme, and we will discuss these deviations later.

Figure 2 shows the flow chart of the basic algorithm. The electron density ρ is sampled on a grid with $N_{pix} = N_1 \times N_2 \times N_3$ pixels. The density values ρ_i are evaluated in each pixel $i = 1,\ldots,N_{pix}$ of the grid. $|F^{obs}(\mathbf{h})|$ are the experimental amplitudes of the structure factors. The algorithm is initiated in the zeroth cycle by assigning random starting phases $\varphi_{rand}(\mathbf{h})$ to all experimental amplitudes and making all unobserved amplitudes equal to zero:

$$F^{(0)}(\mathbf{h}) = \begin{cases} \left|F^{obs}(\mathbf{h})\right| \exp(i\varphi_{rand}(\mathbf{h})) & \text{if } \left|F^{obs}(\mathbf{h})\right| \text{ is known} \\ 0 & \text{otherwise} \end{cases}$$

The iteration cycle then proceeds as follows:

1. The density $\rho^{(n)}$ is calculated by inverse Fourier transform of $F^{(n)}$.
2. The modified density $g^{(n)}$ is obtained by flipping the density of all pixels with density values below a small positive threshold δ and keeping the rest of the pixels unchanged:

$$g_i^{(n)} = \begin{cases} \rho_i^{(n)} & \text{if } \rho_i^{(n)} > \delta \\ -\rho_i^{(n)} & \text{if } \rho_i^{(n)} \le \delta \end{cases}$$

3. Temporary structure factors $G^{(n)}(\mathbf{h}) = \left|G^{(n)}(\mathbf{h})\right| \exp(i\varphi_G^{(n)}(\mathbf{h}))$ are calculated by Fourier transform of $g^{(n)}$.
4. New structure factors $F^{(n+1)}$ are obtained by combining the experimental amplitudes with the phases of $G^{(n)}$ and setting all non-measured structure factors to zero:

$$F^{(n+1)}(\mathbf{h}) = \begin{cases} \left|F^{obs}(\mathbf{h})\right| \exp(i\varphi_G^{(n)}(\mathbf{h})) & \text{if } \left|F^{obs}(\mathbf{h})\right| \text{ is known} \\ 0 & \text{otherwise} \end{cases}$$

These structure factors then enter the next iteration cycle.

Let us analyze the steps in detail. Steps 1 and 3 are just Fourier transforms that transform the quantities between direct and reciprocal space. Steps 2 and 4 are the actual modifications. Step 4 is a standard projection onto the amplitude constraint set, as described in the previous section. To understand the meaning of step 2 let us first define a *significance pseudoprojection* as an operation that sets all density values below the (small, but positive) threshold δ to zero. This operation can be understood as a combination of the positivity projection (all negative densities are set to zero), and the sparseness projection (small density values are considered insignificant and set to zero). If we combine the definition of the significance pseudoprojection and the definition of an overprojection, we see that the charge flipping operation is an overprojection with $\gamma = 1$ associated with the significance pseudoprojection. But why do

we call the significance pseudoprojection a pseudoprojection, and not simply a projection? Because this operation does not minimize the distance between the original and modified density, and therefore it does not match the definition of projection introduced above. For example, for the value of δ equal to 0.5, the constraint set consists of all densities with density values either exactly zero or larger than 0.5. Consider now a density value 0.4. The minimum change of this value to bring it onto the constraint set is to increase it by 0.1 to 0.5. However, the significance pseudoprojection is defined so that this value becomes zero, i.e. a change by -0.4. As a result, the charge flipping operation cannot be understood as an overprojection in the strict sense. The difference might seem unimportant, but tests show that replacing the charge flipping operation by a true overprojection visibly decreases the efficiency of the algorithm.

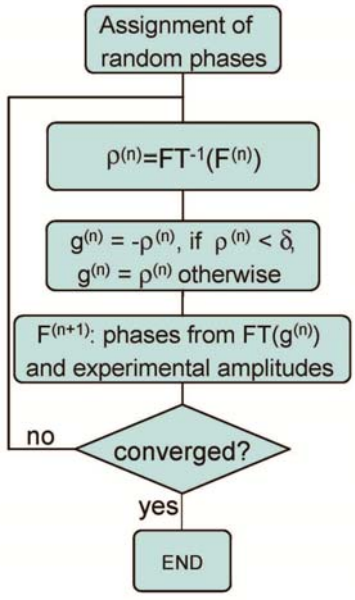

Fig. 2. The flow chart of the basic charge flipping algorithm.

The basic algorithm has been extended several times to improve the efficiency and to widen its applicability. One improvement involves the replacement of the amplitude projection by the corresponding overprojection. This simple extension significantly improves the ability of the algorithm to solve complex structures. Another improvement has been obtained by introducing a so-called π-half variant of the amplitude projection. In this variant, the amplitudes of the weak reflections are not modified in step 4 of the algorithm, but their phase is shifted by π/2:

$$F^{(n+1)}(\mathbf{h}) = \begin{cases} |F^{obs}(\mathbf{h})| \exp(i\varphi_G^{(n)}(\mathbf{h})) & \text{if } |F^{obs}(\mathbf{h})| \text{ is known and strong} \\ |G^{(n)}(\mathbf{h})| \exp(i\varphi_G^{(n)}(\mathbf{h}) + \frac{\pi}{2}) & \text{if } |F^{obs}(\mathbf{h})| \text{ is known and weak} \\ 0 & \text{otherwise} \end{cases}$$

Typically around 20% weakest reflections are treated as weak.
An extension of the algorithm towards scattering densities that are not strictly positive (like neutron scattering densities in presence of isotopes of some elements) is possible by a modification of the flipping operation. In this so-called *band flipping* variant only densities between $+\delta$ and $-\delta$ are multiplied by -1. This operation leaves large negative densities intact, and allows the development of negative peaks.

4. Practical considerations

The charge flipping algorithm has many practical aspects that are not fundamental, but are important for application of the algorithm to real problems. Let us comment on the two most important aspects.

4.1. Data completeness

Charge flipping requires atomic resolution to work. That means that the resolution should be better than 1.2 Å for organic structures. The limit can be relaxed to 1.6 Å or even more for structures containing heavier atoms. Being a method based on Fourier transform, charge flipping is more sensitive to data completeness than direct methods. It is especially harmful to remove strong reflections from the data set. This, unfortunately, happens in practice, if strong reflections are saturated during the exposure, and then removed from the data set as unreliable. It is recommended to include the strong reflections in the data set for solution, even if their intensity is less reliable. These reflections should, however, be removed before the structure refinement procedure.

4.2. Symmetry determination

An important aspect of the algorithm is the handling of symmetry. During the iteration no symmetry is imposed on the density. The algorithm is said to "solve the structures in *P*1". Any attempt to use the symmetry information during the iteration has so far resulted in a decreased or at least unchanged efficiency of the algorithm. The symmetry is, of course, indirectly encoded in the diffraction intensities, and therefore the reconstructed electron density contains the proper symmetry. As a result the symmetry can be estimated from the electron density. This is an important advantage, because the symmetry analysis can be based both on the experimental amplitudes and reconstructed phases rather than only on the amplitudes (Palatinus and van der Lee 2008). Consequently, the symmetry analysis does not suffer from ambiguities between centrosymmetric and noncentrosymmetric space groups. It is also less sensitive to the noise in the data. In the analysis of systematic absences a handful of false strong reflections (arising for example due to diffuse scattering) can obscure the detection of the corresponding symmetry element. The analysis of the density, on the other hand, relies on the full density in the unit cell, and is therefore much more robust.
Sometimes, however, the solution is not sufficiently accurate to detect small deviations from a higher symmetry. This can happen for example, if large parts of the

structure (say all heavy atoms) match a higher symmetry, and only a few light atoms break the symmetry. The best practice in symmetry determination is therefore combining both standard symmetry analysis based on the distribution of diffraction intensities, and the symmetry analysis of the electron density reconstructed by charge flipping in $P1$.

5. Applications of charge flipping to powder diffraction data

A powder diffraction diagram can be considered as a projection of the 3D diffraction pattern onto one dimension. Such projection inevitably results in the overlap of reflections in the pattern and consequently in the loss of information about the intensity of individual reflections.

Using some of the decomposition procedures (Le Bail or Pawley decomposition) it is possible to extract approximate reflection intensities from the powder diagram. Some of these intensities can be very accurate, but those exhibiting heavy overlap will be estimated with a significant inaccuracy. Nevertheless, such a set of intensities can be considered as a noisy single crystal data set.

If the reflection overlap is not too severe, the charge flipping algorithm can solve structures directly from the extracted intensities. In such case the structure solution process is not different from the structure solution from single crystal data. Such solutions are especially successful if synchrotron radiation data are available (Baerlocher et al. 2007a, Le Bail et al. 2009).

However, as the reflection overlap increases, the quality of the data set decreases to the point when the density map reconstructed by charge flipping becomes uninterpretable, although not completely wrong. We then stand in front of the following problem: we have a partial solution, and we would like to modify the solution in such a way that with the help of the modified solution we can obtain a better guess for the individual intensities that are overlapped in the diffraction pattern.

The first attempt to make such modification was to use the ratio of $|G^{(n)}(\mathbf{h})|$ of the overlapped reflections, and modify their $|F(\mathbf{h})|$ to have the same ratio while keeping the total intensity of the overlapped group of reflections equal to the experimentally determined value (Wu et al. 2006). However, this approach does not bring any really new information in the iteration process, and it has so far not gained wider application.

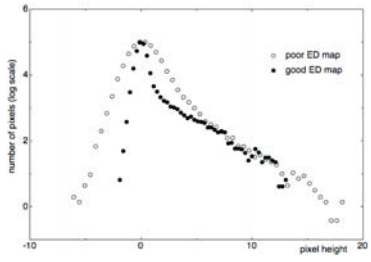

Fig. 3. Density histogram of a partial solution obtained by charge flipping from powder diffraction data, and a histogram of a good solution From Baerlocher et al. (2007a)

An alternative approach has been developed by Baerlocher et al. (2007a). It was noted that the partial solution from the original, noisy data exhibited typical distributions of the density values (density histograms), which were different from the density histograms of the correct solutions (Figure 3). The technique called histogram matching is used successfully in protein crystallography to improve the estimated reflection phases by modifying a partial solution so that its histogram matches the expected histogram. For powder diffraction this idea was modified, and the histogram matching is used to improve the estimates of *intensities* rather than phases.

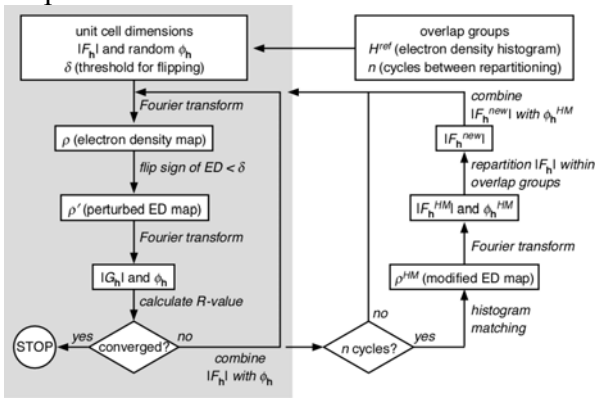

Fig. 4. The flowchart of the charge flipping algorithm with histogram matching. From Baerlocher et al. (2007a)

The flowchart of the complete algorithm is shown in Figure 4. The heart of the algorithm is the original charge flipping algorithm. However, after every n cycles (n being typically between 20 and 100), the current density $\rho^{(n)}$ is submitted to a histogram matching procedure, which modifies the density values so that histogram of the modified density matches the expected histogram. Structure factors calculated from such modified density are different from the original structure factors. Because it can be assumed that the density was improved by the histogram matching procedure, the calculated structure factors should also be improved, and in particular the ratios of the structure factor amplitudes are probably closer to the correct values than in the original dataset extracted from the powder pattern. These ratios can thus be used to repartition the intensities in overlapped reflection groups. The charge flipping algorithm then continues with the improved data set, and the whole metacycle of n cycles of charge flipping followed by histogram matching is repeated until convergence.

This algorithm proved to be successful in solution of several complex structures (Baerlocher et al. 2007a). For extremely difficult problems the algorithm can be combined with additional information obtained from high-resolution electron microscopy, and such combination then resulted in solution of some of the most complex zeolite structures known to date (Baerlocher et al. 2007b, Baerlocher et al. 2008).

6. Structure solution from electron diffraction data

Electron diffraction data have long been deemed generally unsuitable for *ab initio* solution of crystal structures. This is because the dynamical effects present in the electron diffraction scramble the intensities to such an extent that the structure-solution techniques, which are based on the kinematical theory of diffraction, do not work anymore. The situation has changed a few years ago, when the precession electron diffraction method gained more attention. With this method the electron beam precesses with high frequency along the surface of a cone with the vertex on the sample. The motion of the beam is compensated under the sample so that the resulting diffraction pattern is still point-like. The intensities in such pattern are then integrals over all orientations of the incident beam. As a result, some of the dynamical effects are averaged out, and the intensities are closer to intensities predicted by kinematical theory.

Despite of this important advance the PED intensities are not perfectly kinematical, and they exhibit non-negligible dynamical effects. Therefore, from the point of view of the structure solution, the intensity data from PED can be considered a very noisy kinematical data set.

Charge flipping does not make any use of atomic scattering factors, because it operates only with the scattering density. Therefore, charge flipping can be, in principle, applied without any modifications to precession electron diffraction data.

Practical applications of charge flipping can be hindered by the incompleteness of the data set. Traditionally the intensity data are recorded as a set of oriented zone-axis patterns. Such a data set can have severe gaps and relatively low completeness even at low diffraction angles. As mentioned in Section 4.3, such incomplete data set is not suitable for charge flipping. Recently, however, 3D diffraction tomography technique is becoming more and more popular (Kolb et al. 2007, Zhang et al. 2010). In this technique the sample is rotated in small steps, and a diffraction pattern is recorded in each step. The intensities are then extracted from the collected images analogically to the standard procedure used in X-ray crystallography, and the data set is complete within the limits of the tilt of the sample holder.

The application of charge flipping to solution of crystal structures from precession electron diffraction data is still in its very beginning. The first demonstration on a structure of barium sulphate has been made by Mugnaioli et al. (2009). Eggeman et al. (2009) showed a solution of the structure of erbium pyrogermanate by charge flipping, and proposed a special treatment of symmetry to enhance the quality of the structure solution from sparse intensity data. Recently charge flipping was successfully applied to a structure solution of a complex aperiodic structure of copper silicogermanate $Cu_{3+x}(Si,Ge)$ (Palatinus et al. 2011). The latter example illustrates the potential of charge flipping for the solution of complex structures. The full potential and limitation of the application still remains to be explored.

Baerlocher, C., McCusker, L., Palatinus, L.: Charge flipping combined with histogram matching to solve complex crystal structures from powder diffraction data. Z. Kristalogr. **222**, 47–53 (2007a)
Baerlocher, C., Gramm, F., Massuger, L., McCusker, L.B., He, Z.B., Hovmoller, S., Zou, X.D.: Structure of the polycrystalline zeolite catalyst IM-5 solved by enhanced charge flipping. Science **315**, 1113–1116 (2007b)
Baerlocher, C., Xie, D., McCusker, L.B., Hwang, S.J., Chan, I.Y., Ong, K., Burton, A.W., Zones, S.I.: Ordered silicon vacancies in the framework structure of the zeolite catalyst SSZ-74. Nature Materials **7**, 631–635 (2008)
Eggeman, A.; White, T.; Midgley, P.: Symmetry-modified charge flipping. Acta Cryst. A**65**, 120–127 (2009)
Kolb, U., Gorelik, T., Kuebel, C., Otten, M. T., Hubert, D.: Towards automated diffraction tomography: Part I – Data acquisition. Ultramicroscopy **107**, 507–513 (2007)
Le Bail, A., Cranswick, L. et al.: Third structure determination by powder diffractometry round robin (SDPDRR-3). Powder Diffraction **24**, 254–262 (2009)
Mugnaioli, E., Gorelik, T., Kolb, U.: *Ab initio* structure solution from electron diffraction data obtained by a combination of automated diffraction tomography and precession technique. Ultramicroscopy **109**, 758–765 (2009)
Palatinus, L., van der Lee, A.: Symmetry determination following structure solution in *P*1. J. Appl. Cryst. **41**, 975–984 (2008)
Palatinus, L., Klementová, M., Dřínek, V., Jarošová, M., Petříček, V.: An incommensurately modulated structure of η'-phase of $Cu_{3+x}Si$ determined by quantitative electron diffraction tomography. Inorg. Chem., in press (2011)
Oszlányi, G., Sütő, A.: *Ab initio* structure solution by charge flipping. Acta Cryst. A**60**, 134–141 (2004)
Oszlányi, G., Sütő, A.: *Ab initio* structure solution by charge flipping. II. Use of weak reflections. Acta Cryst. A**61**, 147–152 (2005)
Oszlányi, G., Sütő, A.: The charge flipping algorithm. Acta Cryst. A**63**, 156–163 (2008)
Thibault, P.: Algorithmic methods in diffraction microscopy (PhD dissertation), Cornell University (2007)
Wu, J.S., Leinweber, K., Spence, J.C.H., O'Keefe, M.: Ab initio phasing of X-ray powder diffraction patterns by charge flipping. Nature Materials **5**, 647–652 (2006)
Zhang, D., Oleynikov, P., Hovmoller, S., Zou, X.: Collecting 3D electron diffraction data by the rotation method. Z. Krist. **225**, 94–102 (2010)

Structure solution: global optimisation methods

Kenneth Shankland
School of Pharmacy, University of Reading, Whiteknights, Reading, UK

Abstract. The direct location of atomic positions from electron density maps generated using conventional direct methods solutions is a far more difficult exercise when using powder data as opposed to single crystal data. Global optimisation methods that involve the assessment of trial crystal structures in real space offer a powerful alternative method of structure solution that circumvents the map interpretation stage by directly maximising the agreement between calculated and observed diffraction intensities.

Given a known unit cell, space group, and a set of atomic coordinates with corresponding atom types, the structure factors for a trial crystal structure may be easily calculated. The agreement between these structure factors and a set of experimentally determined structure factor intensities (obtained from, for example, a Pawley or LeBail refinement against a powder pattern) can be easily quantified using a measure such as the |F| R-factor:

$$R = \sum_{\mathbf{h}} \left\| F_{\mathbf{h}}^{o} \right| - K \left| F_{\mathbf{h}}^{c} \right\| \Big/ \sum_{\mathbf{h}} \left| F_{\mathbf{h}}^{o} \right|$$

where the summation is over the list of observed intensities [1].

The chances of guessing all of the atomic positions in a crystal structure correctly in a single step are negligible, even if significant amounts of prior chemical information are incorporated into the formulation of those positions (see, for example the 'Organic Compounds' presentation). As such, the coordinates of the trial structure must be adjusted in order to explore the function that describes the agreement between the calculated and measured diffraction data, with a view to maximising the level of agreement, which equates to minimizing the R-factor (or some equivalent fit criterion, such as χ^2). This function has N-dimensions, where N is the number of structural parameters associated with the formulation of the model being optimised. The process of structure solution is therefore equivalent to searching for, and locating the position of, the minimum value of an N-dimensional agreement hypersurface. Though the exact topology of the surfaces varies from problem to problem, it is the topology (as opposed to the number of dimensions) that determines how difficult it is to locate the global minimum - were it everywhere convex, for example, containing just one minimum, local minimisation from any point would always locate the global minimum. In fact, a typical hypersurface in the context of structure solu-

tion exhibits multiple stationary points - this is easily verified by employing multiple local minimisations, starting from random trial structures each time. Figure 1 shows the results of such a verification exercise, for the relatively simple 13 dimensional problem of solving the crystal structure of famotidine form B from powder data fitted to 1.75Å resolution [2].

χ^2 range	No. of χ^2 values
$0 < \chi^2 \leq 200$	10
$200 < \chi^2 \leq 400$	453
$400 < \chi^2 \leq 600$	138,491
$600 < \chi^2 \leq 800$	74,208
$800 < \chi^2 \leq 1,100$	1085
Total	214,527

Fig. 1. The number of stationary point χ^2 values located on the χ^2 hypersurface of FFB. The χ^2 agreement factor is as defined in [3]. A total of one million minimisations was run in order to locate the ca. quarter of a million stationary points.

These stationary points may be divided into two sets: (a) the *global* minimum that corresponds to the fully determined crystal structure and (b) *local* minima and saddle points that correspond to incorrectly determined crystal structures. In a structure *refinement*, it is assumed that the starting model is sufficiently close to the true crystal structure that the agreement function value lies within the radius of convergence of the *N*-dimensional well that surrounds the global minimum. In these circumstances, least-squares can quickly locate the precise global minimum. In structure solution, this is unlikely to be the case and so global optimisation algorithms, that possess the ability to escape from local minima, are employed. Figure 2 shows a block outline of a generic global optimisation strategy for powder difraction.

Search methods A wide range of search methods, designed to locate the global minimum in a structure solution context, have been employed. Any 'Monte-Carlo' method involves some element of random sampling; the term 'Reverse Monte-Carlo' is sometime used in the context of the solution of disordered crystal structures. Here, we use the term 'global optimisation' to represent both *search* and *optimisation* algorithms, bearing in mind that 'global search' and 'global optimisation' are normally used interchangeably in the literature [5].
The global optimisation problem in powder diffraction is analogous to the conformational search problem in molecular modelling [6], with the

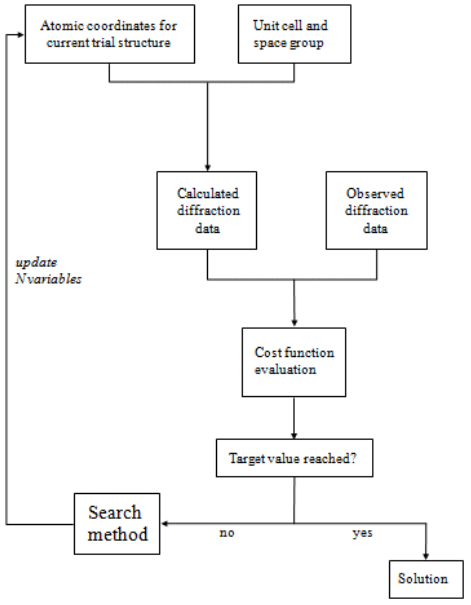

Fig. 2. A generic flowchart for implementing a global optimisation approach to crystal structure solution. The target value is usually some small multiple of the best R_{wp} or χ^2 obtained from a Pawley or LeBail fit to the data.

additional complication that the position and orientation of the molecule in the unit cell must also be identified. It is therefore unsurprising that many of the optimisation methods employed in molecular modelling are transferable to the crystal structure solution problem.

The simplest approach is to perform an exhaustive grid search over the parameter space of interest, and this has been applied successfully to some problems in powder diffraction [7,8]. However, the 'combinatorial explosion' that arises when dealing with large numbers of parameters renders the approach somewhat limited in applicability.

Simulated annealing (SA) is the most widely used optimisation method for SDPD. References 9 to 14 all describe SA-based approaches and associated computer programs. It is effective and requires only a limited number of control parameters. A single SA run is only *guaranteed* to find the global minimum after an infinite number of steps, but in practice, the global minimum is normally located in a finite number of steps. There are many variants on the basic SA algorithm. For example, rather than simply reduce the temperature of the system at a preset rate [11], the rate of cooling can be linked to function value fluctuations [3]. Parallel tempering, has also been used to good effect [14]. SA is intrinsically a sequential process but is easily adapted to parallel computing environments in the context of *parametric execution*. For example, multiple SA runs can be started in parallel, in order to ensure that the same function minimum can be located several times from different random starting points [15,16]. SA has been responsible for the vast majority of crystal

structures from powder data solved using the global optimisation approach and has even been combined with direct methods of structure solution to provide an additional powerful tool [17].

Genetic algorithms (GAs) are an approach to global optimisation that borrow heavily from the Darwinian theory of evolution and been widely applied to optimisation problems such as molecular docking [18]. In structure solution, each trial crystal structure is treated as an individual defined by a collection ('chromosome') of variables ('genes'). The fitness of an individual is (generally) nothing more than the figure of merit that describes how well calculated and observed diffraction data agree. The genetic operators of crossover and mutation are applied to generate new structures from a population of individuals, with the fittest members having the highest probability of surviving into subsequent generations. Applied to the powder diffraction problem [19-21] they have proven effective, but are not as widely used as SA. Closely-related evolutionary algorithms have also been applied to the powder problem [22] though they have not found wide adoption. As with SA, there are a great many variants on the basic theme. For example, Lamarkian evolution assumes that an individual is not a fixed-fitness entity, but rather one that improves during its lifetime and that such improvements are coded back into the chromosome. This notion can be incorporated into computer code by use of a *local* optimiser, which quickly pulls each candidate GA solution to location of the closest function minimum before the genetic operators are applied. Unsurprisingly, this can improve the convergence rate of a GA significantly [23].

Both SA and GAs are examples of *stochastic* algorithms, but *deterministic* algorithms can also be employed in the context of global optimization. An excellent example is the hybrid Monte Carlo (HMC) approach [24] - the algorithm combines the key components of molecular dynamics (MD) and Monte Carlo (MC) simulations to achieve efficient sampling of phase space, allowing a crystal structure to be solved more effectively than using a SA-based approach. Put simply, the trial crystal structure can be considered to be a hypothetical particle moving over a hypersurface, following a trajectory determined by its initial momentum and the local gradient of the hypersurface. As the total "energy" of the system must be conserved throughout a particular particle trajectory, a promising structure (i.e. one lying on a low point of the hypersurface) is said to have low potential energy and high kinetic energy. It is this high kinetic energy component that allows the particle to subsequently move uphill and thus escape local minima. Figure 3 shows how the algorithm explores the potential energy surface and how the finite step size in the MD component results in an accumulation of errors in the total energy. It is here, at the end of a single MD trajectory, that the MC component is invoked to decide whether or not the trajectory should be accepted or rejected, in a way similar to the move accept / reject step in SA.

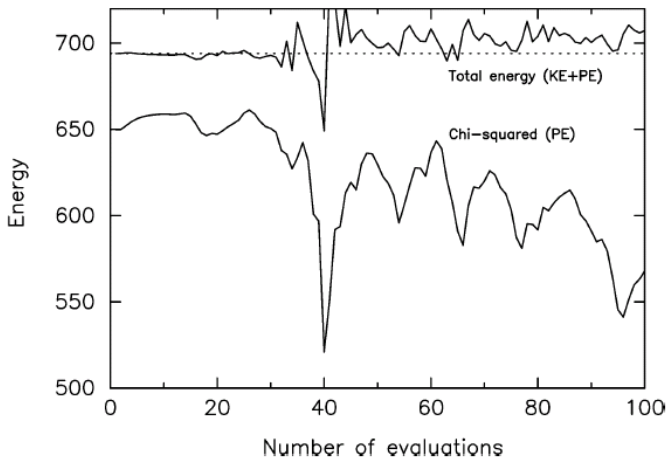

Fig. 3. The potential energy (FOM for fit to the data) and total energy (kinetic energy plus potential energy) evaluated over a single MD trajectory during the crystal structure solution of capsaicin. The initial total energy is shown as a dotted line in order to highlight the total energy fluctuations arising from the finite MD step size

Other approaches have been investigated and sometimes incorporated into SDPD schemes. For example, the downhill simplex can be employed towards the end of a global optimisation as a robust method for quickly and efficiently descending to the lowest point on the hypersurface from the lowest point located by the global optimisation method [25]. Recently, it has been shown (somewhat unexpectedly) that simple local minimizers can in fact locate the global minimum from a completely random start point [2]. Furthermore, they do so with a frequency higher than that expected if one assumes that all stationary points have an equal probability of location. Figure 4 shows the trajectory of one successful quasi-Newton Raphson minimisation for the structure of famotidine form B (13 degrees of freedom). Whilst this plot appears similar to the 'ridge-and-cliff'-type plots sometimes used to illustrate the progress of global optimisation algorithms, there is an important distinction; the latter show *only* the lowest hypersurface values encountered as a function of time, whereas Fig. 4 shows *all* hypersurface values encountered, confirming the monotonically decreasing nature of the path. The starting structure is clearly randomised and a recognisable structure appears after only 30 iterations, with the structure clearly solved by iteration 50. Significantly, minimisation takes less than 50 μs to execute on a single core of a 2.5 GHz Xeon E5420 CPU.

The contribution of global optimisation methods to structure solution has been, and continues to be, highly important but there is clearly still significant room for development in the coming years.

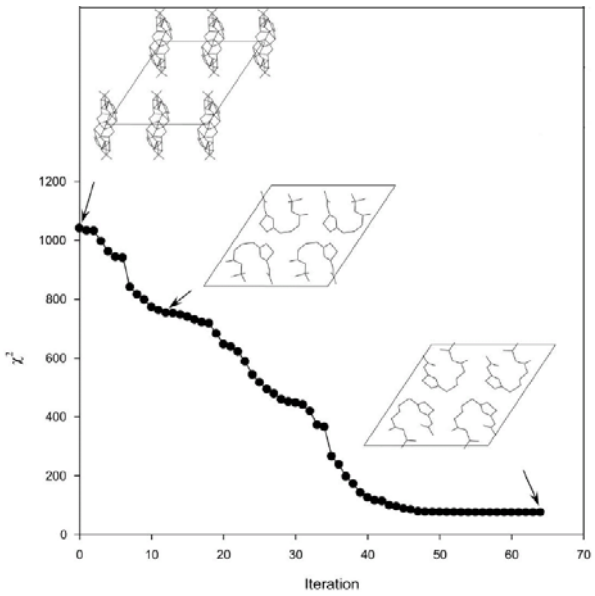

Fig. 4. χ^2 (hypersurface FOM) values at each of the 64 iterations of a single successful quasi-Newton Raphson minimisation of the structure of famotidine form B i.e. one that reaches the global minimum of $\chi^2 = 75.3333$. The unit cell contents (viewed down the *b*-axis) of the structure are shown at 3 points along the path.

Acknowledgements

I am extremely grateful to my collaborators Bill David, Tony Csoka, Anders Markvardsen, John Johnston, Gareth Didlick and Chris Rowlatt, all of whom have played crucial roles in helping me explore the global optimisation landscape.

References

1. K. Shankland and W. I. F. David in "Structure Determination from Powder Diffraction Data", OUP (2002).
2. K. Shankland, A. J. Markvardsen, C. Rowlatt, N. Shankland & W. I. F. David, "A benchmark method for global optimization problems in structure determination from powder diffraction data". *Journal of Applied Crystallography*, (2010) **43**,401.
3. W. I. F. David, K. Shankland & N. Shankland, "Routine determination of molecular crystal structures from powder diffraction data". *Chem. Commun.*, (1998), 931.
4. D. A. Keen, in "*Local Structure From Diffraction"* (1998) (ed. S. J. L Billinge and M. F. Thorpe). Plenum Press, New York.
5. G. A. Hazelrigg "Systems Engineering : An approach to information based design" (1996). Prentice-Hall International
6. A. R. Leach "Molecular Modelling: Principles and Applications 2nd Ed.", Prentice-Hall (2001).
7. R. B. Hammond, K. J. Roberts, R. Docherty & M. Edmondson, "Computationally assisted structure determination for molecular materials from X-ray powder diffraction data". *Journal of Physical Chemistry B*, (1997), **101**,6532
8. E. Dova, K. Goubitz, R. Driessen, E. Sonneveld, V. Chernyshev & H. Schenk, "Structure determination of two organometallic complexes from powder data using grid-search techniques". *Epdic 7: European Powder Diffraction, Pts 1 and 2*, (2001), 378-3,798.
9. Y. G. Andreev, G. S. MacGlashan & P. G. Bruce, "Ab initio solution of a complex crystal structure from powder-diffraction data using simulated-annealing method and a high degree of molecular flexibility". *Physical Review B*, (1997), **55**,12011
10. G. E. Engel, S. Wilke, O. Konig, K. D. M. Harris & F. J. J. Leusen, "PowderSolve - a complete package for crystal structure solution from powder diffraction patterns". *Journal of Applied Crystallography*, (1999), **32**,1169.

11. H. Putz, J. C. Schon & M. Jansen, "Combined method for ab initio structure solution from powder diffraction data". *Journal of Applied Crystallography*, (1999), **32**,864.
12. S. Pagola, P. W. Stephens, D. S. Bohle, A. D. Kosar & S. K. Madsen, "The structure of malaria pigment beta-haematin". *Nature*, (2000), 404,307.
13. A. A. Coelho, "Whole-profile structure solution from powder diffraction data using simulated annealing". *Journal of Applied Crystallography*, (2000), **33**,899.
14. V. Favre-Nicolin & R. Cerny (2004). "FOX: Modular approach to crystal structure determination from powder diffraction", Vol. 443-4, European Powder Diffraction Epdic 8, edited by Y. Andersson, E. J. Mittemeijer & U. Welzel, pp. 35. Zurich-Uetikon: Trans Tech Publications Ltd.
15. T. A. N. Griffin, K. Shankland, J. V. van de Streek & J. Cole, "GDASH: a grid-enabled program for structure solution from powder diffraction data". *Journal of Applied Crystallography*, (2009), **42**,356.
16. J. Rohlíček, M. Husák and V. Favre-Nicolin "FOX.Grid - a grid computing extension of the Fox program for ab initio structure determination from powder diffraction"
Journal of Applied Crystallography, (2011) in press.
17. A. Altomare, R. Caliandro, C. Giacovazzo, A. G. G. Moliterni & R. Rizzi, "Solution of organic crystal structures from powder diffraction by combining simulated annealing and direct methods". *Journal of Applied Crystallography*, (2003), 36,230.
18. G. Jones, P. Willett, R. C. Glen, A. R. Leach & R. Taylor, "Development and validation of a genetic algorithm for flexible docking". *Journal of Molecular Biology*, (1997), **267**,727
19. B. M. Kariuki, H. Serrano-Gonzalez, R. L. Johnston & K. D. M. Harris, "The application of a genetic algorithm for solving crystal structures from powder diffraction data". *Chemical Physics Letters*, (1997), **280**,189
20. K. Shankland, W. I. F. David & T. Csoka, "Crystal structure determination from powder diffraction data by the application of a genetic algorithm". *Z. Kristall.*, (1997), **212**,550.
21. X. D. Deng & C. Dong, "EPCryst: a computer program for solving crystal structures from powder diffraction dat"a. *Journal of Applied Crystallography*, (2011) **44**, 230.
22. S. Y. Chong & M. Tremayne, "Combined optimization using cultural and differential evolution: application to crystal structure solution from powder diffraction data". *Chem. Commun.*, (2006), 4078.
23. G. W. Turner, E. Tedesco, K. D. M. Harris, R. L. Johnston & B. M. Kariuki, "Implementation of Lamarckian concepts in a Genetic Algorithm for structure solution from powder diffraction data". *Chemical Physics Letters*, (2000), **321**,183
24. J. C. Johnston, W. I. F. David, A. J. Markvardsen & K. Shankland, "A hybrid Monte Carlo method for crystal structure determination from powder diffraction data". *Acta Crystallogr. Sect. A*, (2002), **58**,441.
25. W. I. F. David, K. Shankland, J. van de Streek, E. Pidcock, W. D. S. Motherwell & J. C. Cole, "DASH: a program for crystal structure determination from powder diffraction data". *Journal of Applied Crystallography*, (2006), **39**,910.

Proteins and Powders: Technical Developments

Jonathan P. Wright
European Synchrotron Radiation Facility, Grenoble, France

Abstract. Protein powder samples offer many technical challenges for powder diffraction experiments and data analysis. Samples are sensitive to radiation damage and the large unit cells lead to severe peak overlaps, creating interesting challenges. Powder diffraction remains as the unique tool to characterize certain polymorphic forms of crystalline proteins.

Some 12 years ago Von Dreele published a Rietveld refinement of the structure of the protein myoglobin from powder diffraction data [1]. For many crystallographers this came as a surprise; could it be possible to refine a 1261 atom structure using only a powder diagram? This landmark achievement was the result of a system of stereochemical restraints which keeps the local atomic geometry correct while the secondary and tertiary structures of the molecule were determined by the powder data. This work generalizes to many different protein structures, almost all proteins mainly consist of a folded polymeric chain of amino acids, so that the same restraint macros can be re-used. By making his work available to the community in the GSAS software package [2] Von Dreele has helped many of us to join him in working at an exciting new frontier in powder diffraction.

Since that breakthrough there has been good deal of progress and other reviews are already available [3, 4]. This chapter focuses mainly on technical aspects and should be complementary to previous reviews, and also to the chapter from Irene Margiolaki which gives more scientific results.

Technical developments come about when we address difficult challenges. A few proteins, such as lysozyme, offer highly crystalline samples with huge unit cells so that we can obtain stunning diffraction patterns and really push our instrumentation to the limits [5]. Making a complete analysis of such a rich dataset then encourages progress on software and algorithms too. With these new methods in hand, proteins provide a rich source of poorly crystalline samples and difficult problems which motivate us to optimize our strategies as far as possible.

Protein structures are unlike small molecule or inorganic crystal structures in a couple of important ways; we rarely have “atomic resolution” in the data and so we cannot resolve individual atomic positions, also, large regions of the unit cell may be filled with liquid water. The “structural resolution” is usually quoted in Ångstroms and corresponds to the real space resolution for which the data can provide an electron density map. A “high resolution” crystal structure is one where we can actually

see the atoms, and would be somewhat better than 2 Å. If we can obtain a structural resolution of around 3 Å we may expect to see how the protein chain is folded and packed into the crystal. At resolutions lower than about 10 Å the peak intensities are strongly affected by the disordered solvent in the structure, but still give information about how the molecules pack into the unit cell. Many of the technical developments have been motivated to increase the structural resolution we can obtain as far as possible.

The structural resolution we can obtain for a powder depends on the sample and instrumentation, as for a single crystal. However, quite unlike single crystal data, the numerical resolution is strongly affected by the size of the unit cell of the sample. In a powder pattern the density of overlapping peaks gets worse as we go further out into the reciprocal lattice. Even with high resolution instrumentation it is rare to get more than about 1000 peaks out of a powder diagram. This leads to a conclusion that the structural resolution we may obtain for a sample is on the order of the size of the asymmetric unit divided by 10, or in other words, 10x10x10 independent voxels. This limit may be too cautious if there is high solvent content or other favorable effects, but nevertheless, it gives a useful guide as to what can be expected for structural resolution from powder data. For a small protein with a unit cell of 20-30 Å we may resolve amino acid side chains (2-3 Å), but for a large macromolecular complex, we will probably remain limited to seeing only the tertiary structures from powder data.

The strong contribution of the liquid water in a protein crystal structure causes large changes in the low angle peak intensities. These differences may be modeled by a Babinet model where all atoms are assumed to be embedded in a continuous electron density from which they displace a local volume. This model modifies the atomic scattering factors according to:

$$F = F_0 - A \exp\{-8\pi^2 U \sin^2\theta/\lambda^2\}$$

This Babinet model was originally implemented for powder data in the GSAS software package [2]. “A” represents the average electron density of the solvent and takes values of 3-6 and “U” is a thermal parameter falling in the range 1-10. The equivalent model is also now available in Topas; see reference [6] for details on how to use Topas with protein data. An alternative approach which is more common in protein crystallography is to fill the empty parts of the unit cell with a uniform density. Then a fourier transform is carried out to get the structure factor of these solvent regions. An advantage of this method is that empty regions of the unit cell which are too small to contain water can be excluded. This method has been implemented in the protpow software [7]. Until recently the main drawback of the map based methods were that they were not differentiable for least squares fitting, but this too has been addressed in a recent publication [8]. We may hope that this new differentiable model will improve the fitting of low resolution powder data, as soon as it can be implemented into the various software packages.

In order to solve or refine any complex structure from a powder sample we should try to get the best possible data. More time spent on the sample preparation and experiment will make any analysis easier. We want to get data with good counting statistics and very sharp diffraction peaks, but these two goals lead to a conflict, when we improve the peak resolution, we tend to cut down the count rate. Proteins present a problem as the counts we can collect are limited by radiation damage in the sample.

Cooling the sample to cryogenic temperatures reduces the rate of radiation damage by a factor of about 80 in most protein samples. Protocols for cryoprotection of single crystal samples are almost universally used nowadays and many single crystal synchrotron beamlines allow samples to be delivered and loaded onto the diffractometer while remaining always at low temperatures. For powder diffraction, cryocooling turns out to be more difficult than expected. The problem is avoiding the formation of crystalline ice, which causes large strains and damage to the protein crystals. By cooling a sample very quickly we can avoid ice formation and instead obtain amorphous ice. Typically this process can be favoured by adding a cryoprotectant chemical to the mother liquor which disrupts the formation of crystalline ice. We compared the effects of a series of different cryoprotectant molecules in a systematic study [9] where we found that higher concentrations of cryoprotectants worked better. We also found that the peak broadening due to strain is proportional to the unit cell change which occurred when the sample was frozen. Since then, Yves Watier [10] has further developed cryoprotection strategies for powders at ESRF by using annular samples and kapton capillaries. A thin annular sample can be prepared by inserting an empty capillary up the centre of a previous filled capillary sample. The thin sample can then be cooled much more rapidly and uniformly when plunging into liquid nitrogen, in comparison to the regular capillary sample, where the core of the sample is insulated from the outside. This procedure is also helped by the relatively high thermal conductivity of kapton at low temperatures. Unfortunately, some small amounts of peak broadening are still induced by cryocooling a sample, so that the data are not as sharp as can be obtained at room temperature. While a cryocooled sample will last for many hours in the X-ray beam, even at an undulator beamline at the ESRF, at room temperature the lifetime is around 10 minutes. When a large sample is available, radiation damage problems may be avoided at ID31 at the ESRF due to the invention of a translating capillary spinner. A series of short scans are collected and then the capillary is translated to give a fresh area of sample for the next scan. By coupling this spinner with a sample changing robot one can continuously replenish the sample as it is destroyed by the X-ray radiation. In this way, the data which can be obtained at ID31 are usually limited by the quantity of sample that is available. Small samples are unfortunately very common, especially when the protein has to be expressed from bacteria. This forces us to turn to area detectors or cryocooling to improve the counting statistics.

By using a 1D strip [11] or 2D area detector [12], we may record many more of the photons scattered by the sample in comparison to the use of a scanning bank of point detectors. The instrumental resolution we can obtain in this case is given mainly by the sample dimensions and the point spread function (typically similar to the pixel size) of the detector system. Many single crystal diffraction beamlines are available at synchrotrons for protein crystallography, and these too may be used for powder diffraction. Getting a good powder diagram requires that the rings recorded on the detector are as narrow as possible, which is helped by focusing the X-ray beam at the detector surface. To overcome the point spread of the detector, it is better to have a very large area detector with many pixels. A cost effective way to make a modest sized are detector appear larger is to place it on a translation stage and scan it. Then the powder diagram can be reconstructed in software by calibrating the detector position and integrating each image separately. The peak width that can be obtained with an area detector is limited by several contributions other than the intrinsic sample broadening:

- Detector pixel size (point spread)
- X-ray beam size at the detector surface
- X-ray band pass and divergence
- Projected sample thickness

The beam size and point spread contributions give an angular broadening which is reduced when the detector distance is increased. The sample thickness broading (figure 1) depends on tan2θ as well as the sample to detector distance, so that this contribution is reduced for peaks at lower 2θ angles, e.g., it is less problematic for very large unit cells as in proteins. While most of the broadening effects are reduced by moving the detector further back, this does reduce the overall 2θ range. The range can be recovered by scanning the detector, or purchasing one with more pixels. Finally, the bandpass contribution is determined by the X-ray source and optics and contributes as cotθ dθ, so is typically unimportant for proteins at small θ.

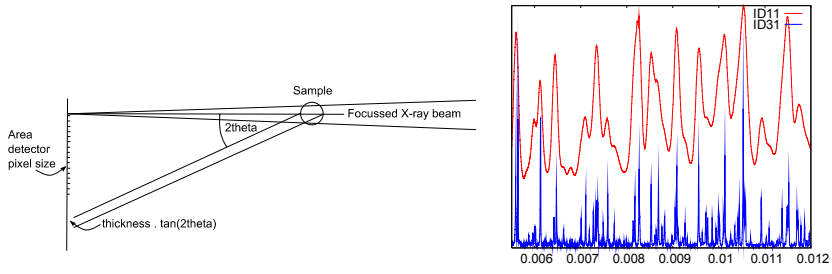

Fig. 1. Left, geometrical contributions to the peak width in area detector powder diffraction. Right, comparison of data for Typsin plotted versus 1/resolution^2 for an analyser crystal instrument (ID31) and an area detector (ID11).

By using a lens focusing system at beamline ID11 at the ESRF [13] we are able to focus the X-ray beamsize to less than 10 microns at the detector surface, making this

contribution negligible. The band pass of our Laue-Laue monochromator is about $3x10^{-3}$ and the pixel size is about 50 microns. If the sample to detector distance is around 1.5 m and the wavelength is 0.3-0.4 Å then we have sufficient resolution to index even very large unit cells [14]. The resolution can be improved by using a thinner sample, or by moving the detector even further back. A similar system at Spring8 uses an image plate and gives a peak width resolution of 0.028 degrees [15].

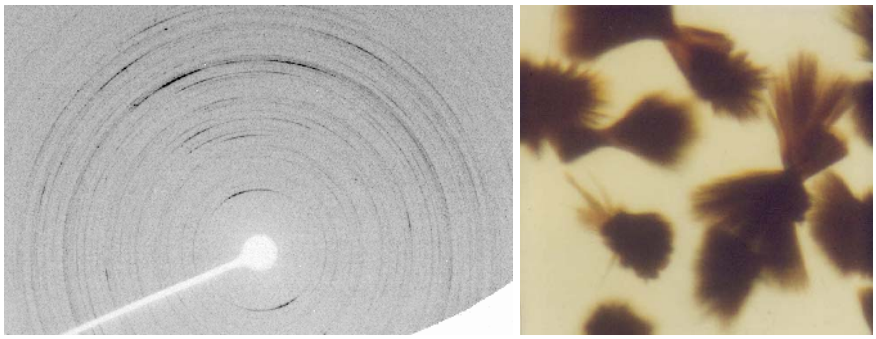

Fig. 2. Powder data for myoglobin and the bundles of needles which give rise to these strong preferred orientation effects.

A great advantage of area detector data, especially for screening samples, is that you get an extra dimension of information about the sample, in comparison to a traditional 1D powder diagram. If the sample shows strong preferred orientation, this is immediately obvious in the area detector images as the rings do not show a uniform intensity around the azimuth. This is explored in greater detail in the chapter by Christian Baerlocher. We have observed strong preferred orientation effects in a number of proteins. While such images offer strong encouragement for obtaining more "single crystal" like data from powder samples, we still struggle to get strong data at high scattering angles with such samples. This is mainly the technical difficulty of obtaining a large sample while preserving the preferred orientation effect, and also keeping the crystallites wet and immobilised. Ideally a series of images should be collected as the sample rotates, which means overcoming radiation damage problems.

Occasionally, single crystals can be found in a sample which appears to be a powder when viewed in an optical microscope. When data are collected using an area detector and a small beam size we often observe spots superimposed on the powder rings. Then we can perform the same experiment as for single crystal diffraction, record a series of pictures as the sample is rotated. Indeed, any powder sample is just a collection of individual single crystals, and if we can make the beam size small enough we may always hope to resolve the individual diffraction spots on the rings. The challenge is then to assign each individual diffraction spot to an individual crystallite in the sample. A good deal of progress has been made in this area thanks to the "TotalCrystallograpy" project [16].

An outline of an algorithm that was developed specifically for indexing protein multi-crystal data is given here. Peak positions the detector are converted into scattering vectors in reciprocal space using the ImageD11 software package [17]. Then the observed peaks are treated as indexed peaks in an arbitrary, but very large sized unit cell. If we make a Patterson map using the data indexed in such a large cell, we will find origin Patterson peaks at the lattice positions of the individual crystallites in the sample. Choosing one of the origin peaks out of this Patterson map will give one of the lattice vectors of one of the crystallites in the sample. We may attempt to group the lattice vectors together by observing which peaks are indexed by multiple Patterson vectors, or simply by a brute force method which picks triplets of vectors from the map. Once the peaks have been assigned to crystals they may be integrated as usual. Figure 3 shows a set of 5 superposed lattices which have been indexed using this procedure as implemented in the index_unknown.py script in the ImageD11 software package [17]. The script has also been successful in indexing a number of small molecule crystal samples, as well as the protein multicrystal samples for which it was designed [18].

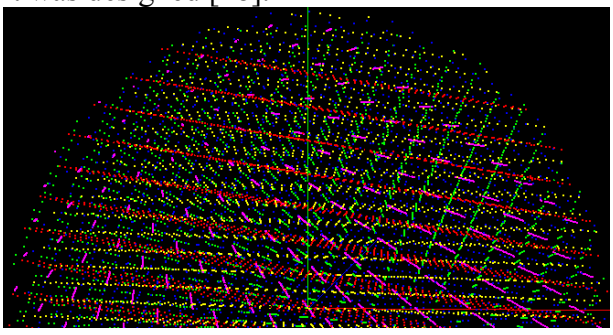

Fig. 3. Simulation of 5 overlapping 3D lattices from a multi-crystal sample of triclinic lysozyme to 3 Å resolution. The peaks were indexed to individual grains in the sample automatically using the index_unknown.py script.

When we cannot induce crystallographic texture or resolve diffraction spots from individual crystallites, we are faced with the powder overlap problem. One of the ways we can try to alleviate this problem is to persuade the peaks to move a little with respect to each other, so that the pattern of peak overlaps changes. Then by fitting the various patterns to a single set of integrated intensities we can unravel the intensities of the individual contributions. This method has been used for structure solution of several small molecules [19, 20] and is now often exploited for protein data collections. Many external variables can be used to perturb the unit cell, including; temperature, pressure, pH, humidity, salt concentration and radiation damage. A multipattern fit using such data can be used to enhance the estimation of overlapped peaks in an intensity extraction. These peaks can then be used for molecular replacement structure solution [21, 22] and typically enhance the signal to noise ratio compared to a single pattern fit. Alternatively the multiple datasets can be combined for a Rietveld refinement of the crystal structure [23, 24]. The multiple histo-

gram approach for Rietveld refinement leads to more stable fits than with a single pattern.

In order to attack the crystallographic phase problem we have also exploited anisotropic variations in the unit cell [25] to improve the data. Currently the majority of software for solving the phase problem is only available for single crystal data, and so we need to extract integrated intensities from the powder profiles. By using likelihood based criteria we are able to improve the estimation of overlapped peaks in intensity extractions, especially in space groups where symmetry systematically enhances certain peaks [26]. Using very heavy atoms, Gadolinium with lysozyme, uranium with elastase, we were able to measure significant changes in peak intensities in the heavy atom derivatives [27]. These intensity changes were sufficient to unambiguously locate the heavy atoms in the unit cell and the find the shapes of the solvent channels in the structure. By adding data from another heavy atom derivative, based on Holmium, to the lysozyme data, it was possible to find shown the shape of a protein molecule [28]. Electron density maps showing the backbone of the protein molecule were of sufficient quality to be interpreted by automatic software.

Suppression of radiation damage has been critical to being able to collect powder data for proteins at elemental absorption edges. In order to detect small differences due to anomalous scattering good counting statistics are required. In the study of $PtBr_6$ binding to lysozyme [29] data were recorded at the f' dip wavelength which corresponds to the inflection point on the absorption edge. This is in contrast to single crystal MAD experiments where a wavelength at the top of the absorption edge will be selected. The reasoning for this is as follows; atomic scattering factors near and absorption edge are given by:

$f = f_0 + f' + if''$

For any reflection (hkl) there will always be another reflection (-h-k-l) which overlaps it exactly. The contribution of f' to the structure factor summation is the same for both of these reflections, however, the contribution of the f'' part has a phase shift which is opposite for the two reflections in the Friedel pair. Therefore we should experimentally maximize the f' variation. This has been explored in detail by Prandl [30, 31]. Figure 4 shows how the contributions add up:

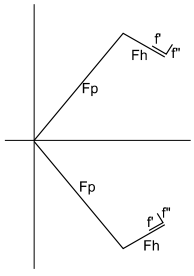

Fig. 4. Protein (Fp) and heavy atom (Fh) contributions to the structure factor for a Friedel pair. At the absorbtion edge f' and f'' modify the Fh contribution.

By using a cryocooled sample and collecting data at both the Br and Pt edges Helliwell et al [29] were able to recover the positions of the heavy elements in the unit cell. These show up clearly in difference Fourier maps. Once the heavy atom substructure has been obtained, the next step is to compute an electron density map for the protein. While a range of single crystal software packages are available, more optimized methods are have recently been developed for MAD phasing of powder data [32, 33].

When we refine complex structures we are often not sure that the changes we make to a model offer a genuine improvement, or whether we are merely fitting the noise which is present in the data. One useful figure of merit that has been developed for protein crystallography is the free R-factor. The idea is exclude a fraction of the dataset from the refinement and then watch how the model predicts these excluded peaks as the fitting progresses. One can think of this procedure as hiding some data from our refinement software which we can use to monitor progress. In a powder diagram it does not work to remove some individual data points for this computation, as they can easily be interpolated based on their neighbors. A method was proposed by the author in terms of a refinement based on extracted correlated integrated intensities [34]. To apply the same idea in a Rietveld refinement one would need to allow the free-R reflections to vary so that they fit the pattern as well as possible, and then compare them to the computed values from the model. In practice this could be achieved either by including their intensities as free variables (as in a Pawley refinement) or, perhaps with less programming effort, by using Lebail extraction for these peaks. One just needs to replace Icalc by Iobs from the previous cycle only for free-R flagged reflections, and then compute the R-factors as usual.

The future outlook for protein powder diffraction is bright and there are still many opportunities for cross fertilization of ideas. By combining powder diffraction data with NMR and molecular dynamics simulations we may expect to go further in the size and complexity of powder structures that can be tackled. Moreover, as our knowledge of protein structure becomes more and more detailed, based on the results of the many single crystal structures that are produced in the PDB databank, we may get better at producing restraints for low resolution crystallography. A recent development of DEN refinement [35] added a new restraint which was highly effective for low resolution single crystal structures; we may hope it will be equally useful for powder data.

Powder diffraction as a technique has many applications outside of structure solution, and continues to play an important industrial role in phase identification. Recent developments at the free electron laser would seem to suggest that the size limitation for single crystal diffraction no longer exists [36], and so that one day there might be fewer structural problems which are only amenable to powder diffraction, but probably not for a few more years. Nevertheless, for polymorph characterization

and in-situ experiments, powder diffraction will continue to offer unique insights to the structural behavior of macromolecular crystals.

Acknowledgements

I am especially grateful to my collaborators in this adventure into protein powder diffraction; Irene Margiolaki, Yves Watier and Andy Fitch and all of the students and colleagues who have carried the work that was summarized here. We thank the ESRF for provision of synchrotron beamtime.

References

1. R. B. Von Dreele. "Combined Rietveld and stereochemical restraint refinement of a protein crystal structure" J. Appl. Cryst. (1999). 32, 1084-1089. doi:10.1107/S002188989901064X
2. A.C. Larson and R.B. Von Dreele, "General Structure Analysis System (GSAS)", Los Alamos National Laboratory Report LAUR 86-748 (1994).
3. I. Margiolaki and J. P. Wright. "Powder crystallography on macromolecules" Acta Cryst. (2008). A64, 169-180. doi:10.1107/S0108767307043735
4. Von Dreele, R. B. "Protein Crystal Structure Analysis from High-Resolution X-Ray Powder-Diffraction Data" Methods in Enzymology, Volume 368, 2003, Pages 254-267. doi:10.1016/S0076-6879(03)68014-6
5. I. Margiolaki, J. P. Wright, A. N. Fitch, G. C. Fox, A. Labrador, R. B. Von Dreele, K. Miura, F. Gozzo, M. Schiltz, C. Besnard, F. Camus, P. Pattison, D. Beckers and T. Degen (2007). Powder diffraction studies on proteins: An overview of data collection approaches. Zeitschrift für Kristallographie Supplements: Vol. 2007, No. suppl_26, pp. 1-13. doi: 10.1524/zksu.2007.2007.suppl_26.1
6. Y. Watier, A. N. Fitch "Protein Powder Diffraction with Topas" Materials Science Forum (2010) 651, 117-129, doi: 10.4028/www.scientific.net/MSF.651.117
7. C. G. Hartmann, O. F. Nielsen, K. Ståhl and P. Harris "In-house characterization of protein powder" J. Appl. Cryst. (2010). 43, 876-882. doi:10.1107/S0021889810019576
8. T. D. Fenn, M. J. Schnieders and A. T. Brunger. "A smooth and differentiable bulk-solvent model for macromolecular diffraction" Acta Cryst. (2010). D66, 1024-1031 doi:10.1107/S0907444910031045
9. M. J. Jenner, J. P. Wright, I. Margiolaki and A. N. Fitch "Successful protein cryocooling for powder diffraction", J. Appl. Cryst. (2007). 40, 121-124 doi:10.1107/S0021889806044943
10. Yves Watier, PhD Thesis, University Joseph Fourier, Grenoble, 2011.
11. A. Bergamaschi, A. Cervellino, R. Dinapoli, F. Gozzo, B. Henrich, I. Johnson, P. Kraft, A. Mozzanica, B. Schmitt and X. Shi "The MYTHEN detector for X-ray powder diffraction experiments at the Swiss Light Source" J. Synchrotron Rad. (2010). 17, 653-668 doi:10.1107/S0909049510026051
12. J. A. Doebbler and R. B. Von Dreele "Application of molecular replacement to protein powder data from image plates" Acta Cryst. (2009). D65, 348-355
doi:10.1107/S0907444909003783
13. G. B. M. Vaughan, J. P. Wright, A. Bytchkov, M. Rossat, H. Gleyzolle, I. Snigireva and A. Snigirev, X-ray transfocators: focusing devices based on compound refractive lenses, J. Synchrotron Rad. (2011). 18, 125-133. doi:10.1107/S0909049510044365
14. Nicolas Papageorgiou, Yves Watier, Lucy Saunders, Bruno Coutard, Violaine Lantez, Ernest A. Gould, Andrew N. Fitch, J. P. Wright, Bruno Canard and Irene Margiolaki (2010). "Preliminary insights into the non structural protein 3 macro domain of the Mayaro virus by powder diffraction". Zeitschrift für Kristallographie: Vol. 225, 12th European Powder Diffraction Conference, pp. 576-580. doi: 10.1524/zkri.2010.1348
15. T. Oka, K. Miura, K. Inoue, T. Ueki and N. Yagi "High-resolution powder diffraction study of purple membrane with a large Guinier-type camera" J. Synchrotron Rad. (2006). 13, 281-284. doi:10.1107/S0909049506004766
16. See http://www.totalcryst.dk/
17. J. P. Wright, http://sourceforge.net/apps/trac/fable/wiki/imaged11
18. K. S. Paithankar, H. O. Sorensen, J. P. Wright, S. Schmidt, H. F. Poulsen and E. F. Garman. "Simultaneous X-ray diffraction from multiple single crystals of macromolecules" Acta Cryst D, in preparation.
19. William I. F. David, Kenneth Shankland, Kenneth Shankland and Norman Shankland, "Routine determination of molecular crystal structures from powder diffraction data" Chem. Commun., 1998, 931. DOI: 10.1039/a800855h
20. M. Brunelli, J. P. Wright, G. B. M. Vaughan, A. J. Mora, A. N. Fitch "Solving Larger Molecular Crystal Structures from Powder Diffraction Data by Exploiting Anisotropic Thermal Expansion" Angew. Chemie Int. Ed. (2003) 42, 2029–2032, DOI: 10.1002/anie.200250607

21. I. Margiolaki, J. P. Wright, M. Wilmanns, A. N. Fitch, and N. Pinotsis. “Second SH3 Domain of Ponsin Solved from Powder Diffraction” J. Am. Chem. Soc., 2007, 129, 11865–11871. DOI: 10.1021/ja073846c
22. J. A. Doebbler and R. B. Von “Application of molecular replacement to protein powder data from image plates” Dreele Acta Cryst. (2009). D65, 348-355 doi:10.1107/S0907444909003783
23. S. Basso, A. N. Fitch, G. C. Fox, I. Margiolaki and J. P. Wright, “High-throughput phase-diagram mapping via powder diffraction: a case study of HEWL versus pH” Acta Cryst. (2005). D61, 1612-1625. doi:10.1107/S0907444905031963
24. R. B. Von Dreele “Multipattern Rietveld refinement of protein powder data: an approach to higher resolution” J. Appl. Cryst. (2007). 40, 133-143. doi:10.1107/S0021889806045493
25. C. Besnard, F. Camus, M. Fleurant, A. Dahlström, J. P. Wright, I. Margiolaki, P. Pattison and M. Schiltz (2007). “Exploiting X-ray induced anisotropic lattice changes to improve intensity extraction in protein powder diffraction: Application to heavy atom detection”. Zeitschrift für Kristallographie Supplements: Vol. 2007, No. suppl_26, pp. 39-44. doi: 10.1524/zksu.2007.2007.suppl_26.39
26. J. P. Wright,, A. J. Markvardsen and I. Margiolaki, “Likelihood methods with protein powder diffraction data”, Z. Kristallogr. Suppl. 26 (2007) 27-32. Doi: 10.1524/zksu.2007.2007.suppl_26.27
27. J. P. Wright, C. Besnard, I. Margiolaki, S. Basso, F. Camus, A. N. Fitch, G. C. Fox, P. Pattison and M. Schiltz. “Molecular envelopes derived from protein powder diffraction data” J. Appl. Cryst. (2008). 41, 329-339. doi:10.1107/S0021889808002732
28. Basso, S., Besnard, C., Wright, J. P., Margiolaki, I., Fitch, A., Pattison, P. & Schiltz, M. “Features of the secondary structure of a protein molecule from powder diffraction data” Acta Cryst. (2010) D66, 756-761. doi:10.1107/S0907444910010723
29. J. R. Helliwell, A. M. T. Bell, P. Bryant, S. Fisher, J. Habash, Madeleine Helliwell, Irene Margiolaki, S. Kaenket, Yves Watier, J. P. Wright and S. Yalamanchilli (2010). Time-dependent analysis of K2PtBr6 binding to lysozyme studied by protein powder and single crystal X-ray analysis. Zeitschrift für Kristallographie: Vol. 225, 12th European Powder Diffraction Conference, pp. 570-575. doi: 10.1524/zkri.2010.1349
30. W. Prandl “Phase determination and Patterson maps from multiwave powder data” Acta Cryst. (1990). A46, 988-992. doi:10.1107/S0108767390008819
31. W. Prandl “Phase determination from X-ray powder diffraction data. II. Partial Patterson maps and the localization of anomalously scattering atoms” Acta Cryst. (1994). A50, 52-55 doi:10.1107/S0108767393005793
32. A. Altomare, M. C. Burla, C. Cuocci, C. Giacovazzo, F. Gozzo, A. Moliterni, G. Polidori and R. Rizzi, “MAD techniques applied to powder data: finding the structure given the substructure” Acta Cryst. (2009). A65, 291-299. doi:10.1107/S0108767309016304
33. A. Altomare, B. D. Belviso, M. C. Burla, G. Campi, C. Cuocci, C. Giacovazzo, F. Gozzo, A. Moliterni, G. Polidori and R. Rizzi, “Multiple-wavelength anomalous dispersion techniques applied to powder data: a probabilistic method for finding the substructure via joint probability distribution functions”. J. Appl. Cryst. (2009). 42, 30-35 doi:10.1107/S0021889808039538
34. J. P. Wright (2004). Extraction and use of correlated integrated intensities with powder diffraction data. Zeitschrift für Kristallographie: Vol. 219, Issue 12 Structure Determination from Powder Diffraction Data, pp. 791-802. doi: 10.1524/zkri.219.12.791.55857
35. G.F.Schroeder, M.Levitt, A.T.Brunger “Super-resolution biomolecular crystallography with low-resolution data” Nature 464, 1218–1222 (22 April 2010) doi:10.1038/nature08892
36. H. N. Chapman, P. Fromme, A. Barty, T. A. White, R. A. Kirian, A. Aquila, M. S. Hunter, J. Schulz, D. P. DePonte, U. Weierstall, et al. “Femtosecond X-ray protein nanocrystallography” Nature 470, 73-77 (2011) doi:10.1038/nature09750

Proteins and Powders: An Overview

Irene Margiolaki
Department of Biology, Section of Genetics, Cell Biology and Development, University of Patras, Greece & European Synchrotron Radiation Facility, Grenoble, France

Abstract. Following the seminal work of Von Dreele, powder X-ray diffraction studies on proteins are being established as a valuable complementary technique to single crystal measurements. A wide range of small proteins have been found to give synchrotron powder diffraction profiles where the peak widths are essentially limited only by the instrumental resolution. The rich information contained in these profiles, combined with developments in data analysis, has stimulated research and development to apply the powder technique to microcrystalline protein samples. In this chapter, progress in using powder diffraction for macromolecular crystallography is reported.

1. Introduction

In recent years, modern powder diffraction techniques have been applied to several microcrystalline proteins. The use of high-resolution synchrotron data, together with new analysis procedures, has stimulated exciting progress which is showing that powders can offer unique opportunities for the structural characterization of proteins and are complementary to existing methods. The developments in experimental methods and instrumentation have been absolutely essential, and they have been discussed recently in another article [1] as well as in the chapter from Jonathan Wright which describes various technical aspects. Perhaps the most enticing goal for any crystallographer is to solve new structures, and §2 discusses the progress and prospects for powder diffraction data in this area. We then describe in §3 some of the structural refinements which have been carried out for powders using single or multiple pattern fitting and the Rietveld method. The application of the powder diffraction method to phase identification in mixtures and crystal screening is discussed in §4.

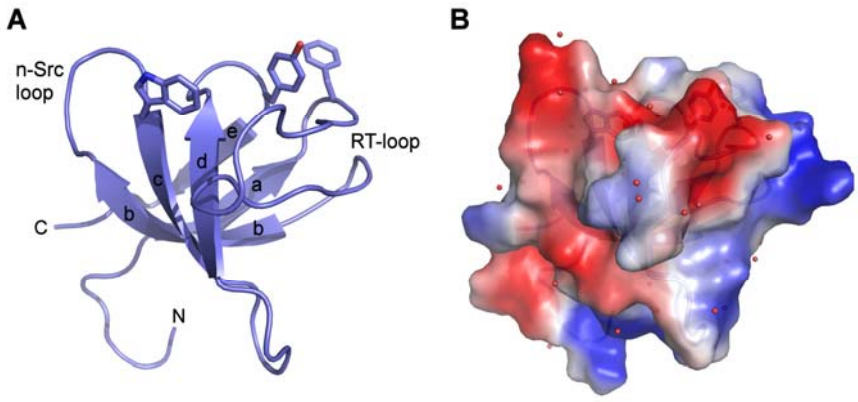

Figure 1. Powder-diffraction structure of the ponsin SH3.2 domain. (A) Ribbon representation of the SH3.2 indicating the secondary structure elements of the domain. The main hydrophobic residues of the binding interface as well as the positions of the n-Src and RT loops are indicated. (B) Electrostatic potential representation of domain identifying additionally the water molecules as red spheres [1]. This figure was generated using PYMOL (http://pymol.sourceforge.net/).

2. Structure solution

If powder data contain enough information to refine the structure of a small protein, then it follows that the structure might also be solved from the same data. We are choosing an inclusive definition of 'solving' a protein structure in this context. The use of stereochemical restraints and introduction of prior knowledge, such as the amino acid sequence, will be used to fill in missing information at high resolution. Powder data can certainly be used to uncover new structural information at low or even modest resolution, and we expect to see this becoming a more common approach in the future. As water molecules have been seen in at least two refinements already [1,2], we can be confident that powder data will be sufficient to unravel new structural information.

2.1. The molecular replacement method

In the molecular replacement method [3], a model for a protein molecule is proposed based on other known structures of proteins which have similar amino acid sequences. This model is then oriented and positioned in the unit cell to match the experimental data for the unknown structure. In this era of structural genomics [4], the quality of the search models is expected to improve dramatically so that molecular replacement using a powder diagram may be sufficient to confirm that a new protein is indeed similar to one that is previously known. Proteins are often found in a variety of different organisms with very similar amino acid sequences, or are expressed with a few modified residues to investigate the effects these changes have on the protein. There are only six degrees of freedom to be determined per molecule in solving a structure by molecular replacement. The first three give the orientation and

the second three give the position of the molecule with respect to the symmetry elements of the space group. Relatively low resolution data can often be used for molecular replacement problems. A resolution of 6 Å can be sufficient and a cut-off of 3 Å is often applied. Typically, even with single-crystal data, the highest resolution data are not so useful as the details of the model structure will not be correct at high resolution anyway. The solution of the structure of T3R3 insulin by Von Dreele et al. [5] is the first example of the molecular replacement method at work. In our own laboratory, we have been able to successfully use the MOLREP software [6] together with powder data for a variety of small proteins. Integrated intensities are extracted [7] from the powder profile and then treated as if they came from a single crystal, ignoring the overlap problem. Fortunately, the molecular replacement method tolerates errors in the input data as if they were due to errors in the model for the structure. In the cases of turkey [8] and hen [9] egg white lysozymes, there was a clear distinction of the correct structure which was proposed by MOLREP from the second best, and in both cases these were the correct positions and orientations for the molecule in the unit cell. After determining the position and orientation of a model for the protein molecule in the unit cell, it is of critical importance to be able to go through the structure and identify the regions that are different in the new protein compared to the initial model. A more recent example is the structure solution of the second SH3 domain (SH3.2) of ponsin via molecular replacement. The high-quality extracted intensities from the measured profiles led to the unique determination of an unknown 544-atom protein structure from powder data. The search model had a moderate similarity (38% sequence identity) and was sufficient for molecular replacement and model building based on electron-density maps. Fig. 1 illustrates the structure of the SH3.2 domain derived from powders [1]. Another example of a molecular replacement style approach is the use of phase angle or structural information from another technique, combined with data collected using powder methods. Oka et al. [10] have investigated the structure of purple membranes, which comprise two-dimensional crystals of bacteriorhodopsin trimers. They collected high-resolution synchrotron powder diffraction data using a 1 m path length Guinier-type camera at beamline BL40B2 at SPring-8. By combining extracted intensities up to a resolution of 4.2 Å with phases from cryoelectron microscopy, they were able to produce an electron-density map. The data from the synchrotron improved the resolution for purple membrane compared to that attained previously with laboratory X-rays (intensities extracted up to ~7 Å) and opens up the possibility of studying these systems under a wider range of conditions.

Recently, we have extended our studies on the 160 amino-acid nsP3 protein macro domain of the Mayaro virus (MAYV), an emerging virus of South American tropic regions, by means of powder diffraction on microcrystalline precipitants. These results correspond to the first structural data existing in the literature since 1954 when the virus was isolated in Trinidad [11, 12]. Comparison with known structures of

sequence-homologous Chikungunya virus (CHIKV) macro domains [13] indicate that MAYV adopts a trigonal/hexagonal structure associated with a looser molecular packing. The cell dimensions of MAYV are significantly altered in comparison to CHIKV and the unit cell is composed of 6 molecules and 58% solvent. Structure solution via the molecular replacement technique and refinement of MAYV are currently in progress. [14].

2.2. The isomorphous replacement method

When there is no starting model available for a protein molecule, then we face the crystallographic phase problem. The isomorphous replacement method [15] determines the phases of X-ray reflections by comparing data from a series of crystals which contain different additive heavy atoms. This method was already in common use prior to the application to proteins for the determination of organic structures by comparing crystalline salts with differing cations or anions. The first application to proteins [16] was used to determine the signs of centric reflections in haemoglobin. In order to use the isomorphous replacement method, one needs to collect data for a protein with and without the added heavy atom and to be able to measure and interpret the differences in the data due to the added atoms. Difficulties arise when the addition of the heavy atom perturbs the structure leading to non-isomorphism and differences that can no longer be simply interpreted by a few atoms. With powder data, we can determine whether or not a particular heavy atom has formed a derivative by comparing the unit-cell parameters, which are normally perturbed by the addition of a heavy atom. In the case of a gadolinium derivative of hen egg white lysozyme (HEWL) [17], we prepared derivatives using different concentrations of Gd and also different pH values in order to alleviate the peak-overlap problem. Extracted intensities were then used to solve for the atomic positions of the Gd atoms using SHELXD [18] and then refinement of the heavy-atom substructure and phasing were carried out using Sharp [19]. Similarly, in the case of a uranium derivative of elastase [20], the peak-overlap problem was reduced by comparing data sets that had been exposed to the X-ray beam for different amounts of time. The gradual changes in unit-cell parameters due to radiation damage changed the pattern of peak overlaps sufficiently to deconvolute the overlapping peaks. The U atom is clearly visible in a difference Patterson map from native and derivative data sets and phasing using Sharp proceeds to give a solvent mask which clearly and correctly delineates the protein and solvent regions [17]. Recently, two heavy-atom derivatives of tetragonal HEWL (a gadolinium derivative and a holmium derivative) were crystallized at room temperature. Using synchrotron radiation, high-quality powder patterns were collected in which pH-induced anisotropic lattice-parameter changes were exploited in order to reduce the problem of overlapping reflections. The phasing power of two heavy atom derivatives in a multiple isomorphous replacement (MIR) analysis enabled molecular structural information to be obtained up to approximately 5.3 Å resolution. At such a resolution, features of the secondary struc-

ture of the lysozyme molecule could be accurately located using programs dedicated to that effect. In addition, the quoted resolution was sufficient to determine the correct hand of the heavy-atom substructure which leads to an electron-density map representing the
protein molecule of proper chirality [21].

3. Rietveld fits to high-resolution synchrotron powder data

In 1999, the first protein structure refinement using powder data was reported [22] for metmyoglobin. High-angular resolution synchrotron data from beamline X3B1 (λ = 1.14991 Å) at the National Synchrotron Light Source (NSLS), Brookhaven National Laboratory, USA, were used for the refinement. A key characteristic of the powder profile was the observation of very sharp reflections associated with the highly crystalline protein sample. By combining a suite of stereochemical restraints with the measured diffraction profile, a successful refinement of the atomic positions of the 1260-atom protein was achieved (pdb code 1f6h). In order to carry out this refinement, Von Dreele upgraded the GSAS [23] software package in several ways. A suite of stereochemical restraints, as are normally used in low-resolution refinements with single crystal data, were implemented with automatic recognition of atom and bond types for the standard amino acid residues. A novel restraint was introduced to describe the two-dimensional pseudo-potential surface of a Ramachandran plot [24]. Also, a Babinet's principle solvent correction was used to account for the disordered solvent within the crystal structure. The excellent Rietveld fit obtained was a breakthrough, showing for the first time that a crystal structure refinement could be carried out for a protein molecule from powder data. The following year, the structure of a new variant of the T3R3 human insulin–Zn complex, produced by mechanical grinding of a polycrystalline sample, was solved and refined from a powder [5]. It was determined that the reversible grinding-induced phase change is accompanied by 9.5 and 17.2° rotations of the two T3R3 complexes that comprise the crystal structure. These results were later born out by a single-crystal study [25] at cryogenic temperatures (100 K). The possibility of using powder diffraction data on microcrystalline protein samples for detection of ligands in protein–ligand complexes was illustrated by the studies of HEWL complexes with N-acetylglucosamine (NAGn, n = 1–6) oligosaccharides [26, 27]. The location of each NAGn could be found from difference Fourier maps generated from structure factors extracted during preliminary Rietveld refinements. Full NAGn–protein structures were subjected to combined Rietveld and stereochemical restraint refinements and revealed binding modes for NAGn that depended on the length of the NAG oligosaccharide. The series of refined powder structures are available in the pdb database via access codes 1ja2, 1ja4, 1ja6, 1ja7, 1sf4, 1sf6, 1sf7, 1sfb and 1sfg. These studies showed that powder diagrams can give useful electron density maps for protein samples and show unambiguously that a powder sample can be sufficient for structural analysis. Following the tradition in the powder diffraction community, Von Dreele has made

the GSAS software package freely available, including the most recent features for refinements of protein structures. We were able to benefit from this generous philanthropy to use the package in our laboratory to carry out a Rietveld refinement of the structure of turkey egg white lysozyme [8]. By carefully balancing the restraint weights with a highly resolved powder diagram collected at beamline ID31 at the ESRF, we were able to produce an excellent fit and refined model (pdb code: 1xft). In the course of refining this structure using GSAS, we also became convinced that powder methods can indeed be applied to such large structures.

Structure refinements can be improved by the use of multiple datasets, provided there are not significant changes in structure factors between the different data sets. Two independent investigations of HEWL showed that the use of multiple patterns associated with slightly different lattice parameters leads to enhanced extracted intensities and more robust structure refinements [9, 28] using a modified version of GSAS which could account for small lattice strains in different patterns. In our laboratory, we prepared a total of 44 different polycrystalline HEWL precipitates at 277 K and room temperature and in the pH range between 6.56 and 3.33 [9]. High resolution powder diffraction data were collected at room temperature (λ = 1.249826 Å , ID31, ESRF). The anisotropic effect of pH of crystallization on the lattice dimensions of tetragonal HEWL shifts the peaks significantly and alleviates the peak-overlap problem. We selected four patterns across the range of pH for use in a multi-pattern Rietveld refinement [29] in order to extract an average structural model for tetragonal HEWL using the GSAS software. Some differences between diffraction patterns could be accounted for by allowing the solvent-scattering coefficients to differ for each one of the four histograms following the observation that the largest observed differences in peak intensities were mainly at low angles. A more detailed description of this refinement can be found elsewhere [9] and the model is deposited in the pdb database with access code 2a6u. We found that this approach resulted in a much smoother and more robust refinement than previously experienced with single-pattern fits and produced a structural model with excellent stereochemistry. Von Dreele has also applied a multi-pattern approach to HEWL but using data sets obtained from an image plate and approaching single-crystal resolution limits (dmin ≈ 2 Å). The patterns differ due to changes in salt concentration and radiation-induced lattice strains. Anisotropic changes in the unit cell are taken into account in all of these refinements using a special profile function implemented in GSAS (No. 5). Using this function, only one set of unit-cell parameters is refined and those corresponding to the other patterns are related via a strain ($\Delta d/d$) of the reciprocal metric tensor elements. By selecting different combinations of data sets, Von Dreele refined three structural models and was able to add water molecules in each case (pdb codes 2hs7, 2hs9 and 2hso). Many of these water molecules are conserved between the three models and have also been found in single-crystal structures. The stereochemistries of the resulting multi-dataset models show significant improvements in com-

parison to previous single-pattern powder refinements. In one of our most recent studies of the second SH3 domain of ponsin [1], we exploited radiation-induced anisotropic lattice strains in a specially modified multi-pattern Pawley refinement taking into consideration likelihood criteria for partitioning overlapped peaks [30]. The outcome of this analysis was a set of improved extracted intensities, in excellent agreement with single-crystal intensities later obtained by an independent experiment. The powder extracted data were sufficient for the structure solution of the domain via the molecular replacement method.

Maximum-likelihood refinement improved the phases to a level where we could trace the main-chain alterations, build additional residues where needed and eventually place the correct side chains along the sequence; a substantial result from powder diffraction data. The protein conformation was refined in a multiple-data-set stereochemically restrained Rietveld analysis taking advantage of sample-induced anisotropic lattice strains. We further benefited from an approach combining multiple-data-set Rietveld analysis and periodical OMIT map [31] computation, to reduce the bias of the final model, extending the resolution limits to levels comparable to single-crystal measurements, and even detecting several water molecules bound to the protein [1]. The refined model is deposited in the pdb database with access code 2O31 and is illustrated in Figure 1.

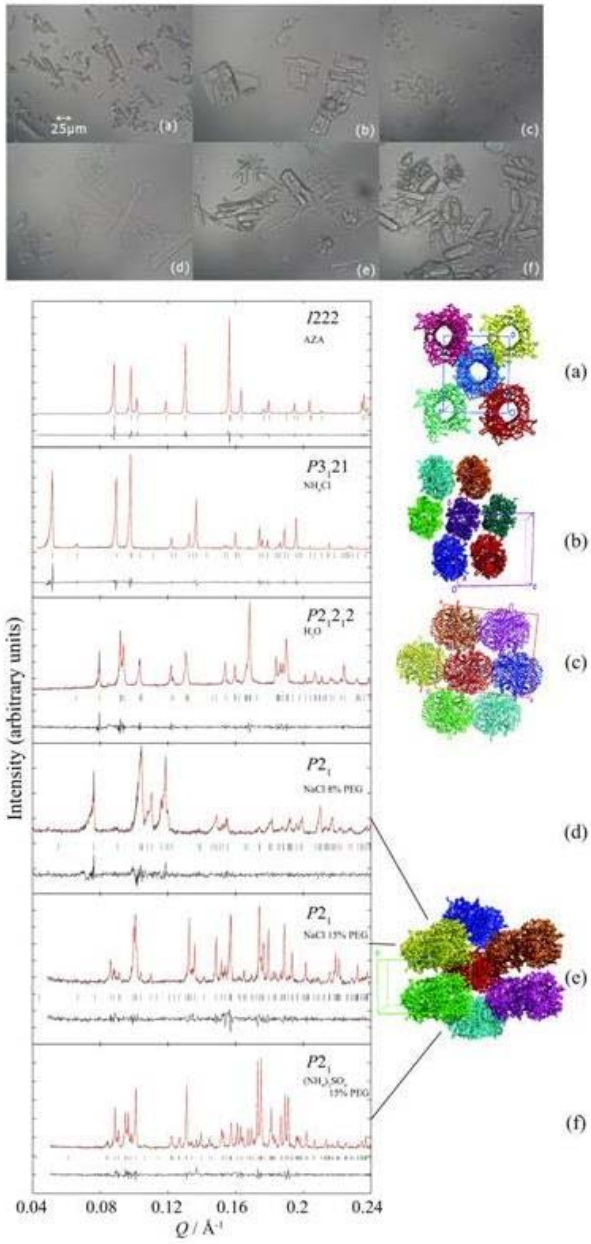

Figure 2. ***Upper panel***: Optical microscopy images of Uox micro-crystals prepared at different con-ditions. (a) Uox ligand-free with NH4Cl and 15 % PEG 8000, (b) Uox ligand-free with NaCl and 15 % PEG 8000, (c) Uox ligand-free with (NH4)2SO4 and 15 % PEG 8000, (d) Uox ligand-free with 10 % PEG, (e) Uox ligand-free with KCl and 10 % PEG 8000, (f) Uox complexed to AZA with NaCl and 10 % PEG 8000. ***Lower panel***: Selected Q-region of the LeBail fits for six distinct phases of Uox [41]. Projection in the *ab* plane of candidate structure models available in the pdb (a) 1R51 [45], (b) 1WS3 [46], (c) 1XXJ [46], (d), (e), and (f) 1XY3 [46].

4. Crystal screening

Powder diffraction has been exploited as a technique for fingerprinting different crystalline substances and allows rapid phase identification and quantification of mixtures. High-resolution powder instrumentation is designed to obtain the sharpest possible peaks in reciprocal space and also to determine accurate peak positions. These features are complementary to area-detector single-crystal experiments, where the aim is normally to measure diffraction peaks at the highest possible scattering angles, to improve the direct-space resolution in an electron-density map. By exploiting the excellent reciprocal-space resolution of powder instruments, a variety of complementary studies can be carried out which are typically more difficult to do with single crystals. Powder samples contain many millions of individual crystallites and give information about the bulk properties of a material; there is no question of whether a particular crystallite is representative of the whole sample.

Wherever microcrystalline proteins come into use as biomaterials or medicines, there will be an increasingly important role for powder diffraction to play. There are many added benefits from using a crystalline form of an already existing drug: it permits better control over the release rate into the system by an optimisation of the crystals size and polymorphism, and it should also offer an extended shelf -life and a reduction in production costs [32, 33, 34, 35, 36, 37, 38]. Microcrystalline forms of protein-based drugs tend to be slower acting as the crystallites must dissolve before acting. Crystallite size and polymorphism both affect dissolution rates and so they are important factors in understanding formulations.

To date, our studies on microcrystalline Human Insulin (HI) [39,40] and Urate oxidase/ Rasburicase (Uox) [41] suspensions using the powder diffraction method have revealed a high degree of polymorphism upon variation of their physicochemical environment (i.e. pH, ligand binding etc.). Even more important was our discovery of 2 new biologically active Insulin-phenol complexes which were later on characterized via single crystal methods [42]. In the case of Uox, a key protein component of currently existing drugs (i.e. Fasturtec) helping body to eliminate uric acid [43,44], a previously unknown, biologically active polymorph was discovered when crystallization was performed in the absence of any chemical additives. The structure solution of the latter Uox form is currently in progress. Part of the current research within our group is devoted to the structural characterization of an extensive series of Insulin-ligand complexes and Uox polymorphs, prepared at different crystallization conditions (pH, ionic strength, crystallization agent) which are potential drug targets. Figure 2 shows crystalline Uox samples, Le Bail fits for six distinct phases of Uox identified from powders and the corresponding candidate structure models available in the PDB.

5. Conclusions

In the last 10 years, the use of powder data with macromolecules has gone from being an ambitious suggestion to a respectable practice. A series of demonstration ex-

periments and data analyses has been carried out which establishes the validity of the methodology. Although developments are still in progress for phasing methods and structure solution, there are already molecular-replacement and structure-refinement methods that are now mature enough for consumption by the more adventurous protein crystallographer. The solution of the structure of the SH3 domain of ponsin shows how powder diffraction is already moving 'beyond lysozyme' and is a technique ready to tackle genuine biological problems.

Acknowledgments I am grateful to Dr A. N. Fitch & Dr. J. P. Wright for their continuous input, advice and support during this project. I would like to thank 6 undergraduate students from the University of Bath who have worked with us one year each: S. Basso, L. Knight, S. Dagogo, M. Jenner, I. Collings, L. Saunders as well as our PhD student, Y. Watier. Many thanks to my 3 M.Sc. students at the department of biology of the University of Patras (UPAT): Miss Evdokia-Anastasia Giannopoulou, Foteini Karavasili & Eleni Kotsiliti. Special thanks go to Drs R. B. Von Dreele, M. Norrman, G. Schluckebier, M. El Hajji, F. Bonnete, M. Giffard, N. Papageorgiou, B. Canard, B. Coutard, M. Wilmanns and N. Pinotsis, and also Dr M. Schiltz and his group, for the provision of interesting samples, their help and collaboration. I am grateful to the UNESCO and L'OREAL foundations for the international fellowship for women in science (2010). Finally, we thank the ESRF for provision of synchrotron beam time and UPAT for provision of facilities and financial resources.

References

[1] Margiolaki, I. et al. (2007). J. Am. Chem. Soc., 2007, 129, 11865–11871.
[2] Von Dreele, R. B. (2007). J. Appl. Cryst. 40, 133–143.
[3] Rossmann, M. G. (1990). Acta Cryst. A46, 73–82.
[4] Stevens, R. C. et al. (2001). Science, 294, 89–92.
[5] Von Dreele, R. B. (2000). Acta Cryst. D56, 1549-1553.
[6] Vagin, A. & Teplyakov, A. (1997). J. Appl. Cryst. 30, 1022–1025.
[7] Wright, J. P. (2004). Z. Kristallogr. 219, 791–802.
[8] Margiolaki, I. et al. (2005). Acta Cryst. D61, 423–432.
[9] Basso, S. et al. (2005). Acta Cryst. D61, 1612–1625.
[10] Oka, T. et al. (2006). J. Synchrotron Rad. 13, 281–284.
[11] Anderson, C. R. et al. (1957). 6, 1012.
[12] Causey O. R. & Maroja O. M. (1957). Am. J. Trop. Med. Hyg. 6, 1017.
[13] Malet, H. et al. (2009). J. Virol., 83, 6534.
[14] Papageorgiou, N. et al. (2010), Z. Kristallogr. 225, 576.
[15] Perutz, M. F. (1956). Acta Cryst. 9, 867–873.
[16] Green, D. W. et al. (1954). Proc. R. Soc. London Ser. A, 225, 287.
[17] Wright, J. P. Et al. (2007). J. Appl. Cryst. 41, 329-339.
[18] Uson, I. & Sheldrick, G. M. (1999). Curr. Opin. Struct. Biol. 9, 643–648.
[19] La Fortelle, E. & Bricogne, G. (1997). Methods Enzymol. 276, 472–494.
[20] Besnard, C. et al. (2007). Z. Kristallogr. Suppl. 26, 39-44.
[21] Basso, S. et al. (2010). Acta Cryst. D66, 756-761.
[22] Von Dreele, R. B. (1999). J. Appl. Cryst. 32, 1084–1089.
[23] Larson, A. C. & Von Dreele, R. B. (2004). General Structure Analysis System (GSAS), Los Alamos National Laboratory Report LAUR 86-748, Los Alamos, USA.
[24] Ramachandran, G. N. et al. (1963). J. Mol. Biol. 7, 95–99.

[25] Smith, G. D. et al. (2001). Acta Cryst. D57, 1091–1100.
[26] Von Dreele, R. B. (2001). Acta Cryst. D57, 1836–1842.
[27] Von Dreele, R. B. (2005). Acta Cryst. D61, 22–32.
[28] Von Dreele, R. B. (2007). J. Appl. Cryst. 40, 133–143.
[29] Rietveld, H. M. (1969). J. Appl. Cryst. 2, 65–71.
[30] Wright, J. P. Et al. (2007). Z. Kristallogr. 26, 27-32
[31] Bhat, T. N. (1988). J. Appl. Cryst. 21, 279–281.
[32] Yang, M. X. et al. (2003). Proc. Natl Acad. Sci. USA, 100, 6934–6939.
[33] Basu, S. et al. (2004). Expert Opin. Biol. Ther. 4, 301–317.
[34] Havelund, S. (2009). US Patent 2009/0010854A9.
[35] Brader, M. L. & Sukumar, M. (2005). US Patent 2005/0054818A1.
[36] Rabinow, B. E. (2004). Nature Rev. Drug Discov. 3, 785–796.
[37] Aguiar, A. J. Et al. (1967). J. Pharm. Sci. 56, 847–853.
[38] Bauer, J. et al. (2001). Pharm. Res. 18, 859–866.
[39] Knight L. et al. (2007). Acta Cryst. A63, s243.
[40] Watier, Y. et al. (2009). Acta Cryst. A65, s320.
[41] Collings, I. et al. (2010). Acta Cryst. D 66, 539-548.
[42] Norrman M. & Schluckebier G. (2007). BMC Structural Biology, 7, 83.
[43] McGrath, B. M. &Walsh, G. (2005). Editors. Directory of Therapeutic Enzymes. Boca Raton: CRC Press.
[44] Wu, X. et al. (1992). J. Mol. Evol.34, 78–84.
[45] Retailleau, P. et al. (2004). Acta. Cryst. D, 60(3), 453–462.
[46] Retailleau, P. et al. (2005). Acta. Cryst. D, 61(3), 218–229.

Pharmaceuticals and Powders – An Overview

Joel Bernstein
Faculty of Natural Sciences, NYU Abu Dhabi, Abu Dhabi UAE

Abstract
The vast majority of pharmaceutically active ingredients, as well as the excipients employed in formulating pills, tablets and capsules, are solids. The generally preferred analytical technique for characterization and identification of those solids is x-ray powder diffraction (XRPD). XRPD is employed in virtually every stage of the life cycle of pharmaceutical products, from the early crystal form screening to monitoring pilot plant and full production scaleup. It often plays a crucial role in monitoring production batches and stability with shelf life. XRPD data are used to characterize the solid state forms for purposes of defining patent claims on crystal forms and are also used in monitoring and litigating alleged patent infringements. XRPD is also playing an important role in detecting and monitoring counterfeit drug products as well as in the characterization of amorphous and crystalline character of a solid form.
Literature examples of these various aspects of powders in pharmaceuticals are given.

Introduction
X-ray powder diffraction plays an important, if not crucial, role in the pharmaceutical industry. In much of the western world, the vast majority of pharmaceutical products are administered as solids in various forms – generally as capsules, tablets or pills, but even in many cases when administered via inhalation, as suppositories, by parenteral injection or topically the characterization and control of solid sate properties of the active pharmaceutical ingredient (API) are of prime importance in the formulation of the final product. As demonstrated in Figure 1, solid state technology is applicable to virtually every aspect of the pharmaceutical industry. X-ray powder diffraction is usually considered the "gold standard" for the identification and characterization of those solid materials. This lecture/chapter will briefly describe and provide examples of some of the important applications of powder diffraction in various stages of a pharmaceutical product, from initial identification of a potential API through the lifetime of a marketed product.

Fig 1 A diagram of the role of solid state studies in the pharmaceutical industry.

These are notes intended to accompany a formal lecture and are meant to provide an entry to the relevant literature. The cited works here were specifically chosen because they contain descriptions and appropriate figures to demonstrate the principles and/or the phenomena described and those references should be consulted for further detail and specific examples.

Some basic background and references

Because it has long been recognized as an important analytical tool for the identification and characterization of solids, a great deal has been written about the applications of X-ray powder diffraction in the pharmaceutical industry. The fundamentals of modern powder diffraction may be found in other sections of these lecture notes, as well as in classic texts by Jenkins and Snyder (1996). Applications to the pharmaceutical industry are discussed, for instance, by Byrn et al. (1999), as a chapter topic (e.g. Bernstein and Henck 2000) or by examples in many of the chapters of the multi-authored volumes authored or edited by Hilfiker (2006) and Brittain (1999, 2009) (Erice 2004). The annual summaries by Brittain (e.g. Brittain, 2011) provide many examples of the application of X-ray powder diffraction to polymorphic and solvatomorphic pharmaceutical materials, either as a single analytical techniques, or increasingly more often in combination with other analytical techniques – a strategy which is definitely to be encouraged.

The utility of powder diffraction in the pharmaceutical industry can be demonstrated by examining examples from the various stages of drug development, manufacturing and marketing.

What solid form should be chosen for the lead compound?

Even upon identification and choice of a lead compound for further pharmaceutical development it is usually advisable to survey the crystal form landscape to get some idea of the number and characteristics of the polymorphs, solvates and hydrates that might exist for that compound. Such a survey can never be considered complete, especially in the early stages of development since new crystal forms are often discovered, even serendipitously, well into development or even after launch (hilfiker 2006), but it can often provide very useful information about the ultimate choice of

crystal form and the difficulties that might be encountered in obtaining that form consistently and robustly (Bernstein 2002, (Braga and Bernstein 2007, Morris 1999, Griesser 2006, Byrn et al. 1999).

Traditional crystallization methods such as solution crystallization, with variations in solvent(s) (including solvent mixtures), temperature, stirring, cooling rate, seeding, antisolvent, slurrying are still, of course, in common use, but a variety of newer techniques are being developed and refined in the attempt to prepare new crystal forms. A number of excellent reviews of these techniques have appeared recently, and offer the potential for developing exciting strategies for searching for new forms (Stahly 2007, Llinàs and Goodman 2008).

Other conventional (although not as widely used) methods of crystallization (with typical variable parameters) include the following: sublimation (pressure, temperature gradient), crystallization from melt (temperature program), freeze drying, spray drying.

Some (but by no means all) of the additional methods of crystallization that have been added recently to the armory of crystallization tools (Llinàs and Goodman (2008)): confinement crystallizations (capillary, contact line, nano), electrochemical crystallizations, gel crystallizations, vapor diffusion crystallizations, use of ("tailor made") additives, use of templates (polymers, inert surfaces etc.), mechanical grinding (co-crystals), solvent drop grinding (co-crystals), microporous membranes, sonocrystallizations.

In this regard the continuing development of high-throughput crystallization methods is particularly noteworthy (Morissette et al. 2004, Kumar et al. 2007), and the availability of automatic sampling and measuring systems for X-ray powder diffraction (e.g. Beckers 2008) of the large number of samples prepared by this method are making it increasingly feasible as a routine screening technique.

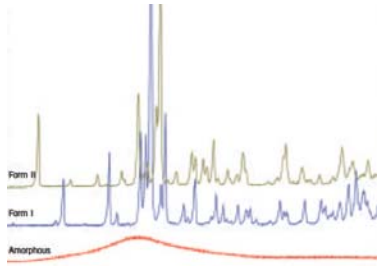

Fig 2 X-ray diffraction patterns of two polymorphic foms and one amorphous form of a single substance (From Beckers 2008)

Figure 2 illustrates the differences between the XRPD's of crystalline polymorphic forms and amorphous material (*vide infra*).

Making the chosen form consistently and robustly

Many pharmaceutical companies seek to identify and then develop the most stable form of an API (Wieckhusen 2010), but there are sometimes reasons – i.e. material handling properties or intellectual property issues - to identify and occasionally use less stable forms, provided they can be stabilized to prevent conversion to the stable form (Capes et al. (2007, Singhal and Curatolo 2004).

Once the most desired crystal form has been chosen for further development, the crystallization must be scaled up from laboratory bench quantities (~1-100g) through pilot plant (~1-30kg) to production scale (~50-500kg) (Marti 1988, Giron 2003, Yu et al. 2004, Birch et al. 2005). The resulting process must not only lead consistently to the desired crystal form; it must also exhibit desired physical properties such as particle size, habit, bulk density, flowability, filterability, etc. While practitioners of industrial crystallizations are familiar with the problems of scaleup (e.g. Mangin et al. 2009, Wirth and Stephenson 1997) for industrial proprietary reasons very few of the problems encountered and solved are documented in the literature. One of the techniques used to assure the reproducibility of the crystal form is intentional seeding, which also requires detailed understanding of the crystallization process at the desired scale (Beckman et al. (1998), Beckmann (2000), Beckmann et al. 2001, Meyerson 2002, Wieckhusen 2010).

X-ray powder methods are being widely utilized in monitoring the crystal form that is obtained as these scaleup and manufacturing processes are developed, refined, and adopted as standard practice in the drug production.

Quality control of production and stability monitoring

Once the manufacturing and production protocols for an API have been established, each production batch must be monitored for quality control and long term stability. Whereas the earlier stages of product development of crystal form utilize X-ray methods for crystal form identification, once those protocols have been established the role of X-ray analysis – if applied to a particular system – is more in determining *crystal form purity* (as distinguished from *chemical purity)*. In many cases the determination of crystal form purity requires the application of methods of quantitative analysis methods of X-ray powder diffraction. Many of the basics of modern quantitative X-ray diffractometry are given by Zevin and Kimmel (1995), following the early pioneering work of Klug and Alexander (1954).

For the purposes of quantitative analysis of an API, one is most often working in the realm of small concentrations of production generated impurities or degradation products due to lack of long term stability. The detection of these small amounts is indeed a challenge to the methods of quantitative analysis that have been improving along with increasingly powerful laboratory and synchrotron X-ray sources, instrumentation and software (e.g. Chipera and Bish 2002). A number of illustrative examples (of which there are many more) may be found in Suryanaruyanan 1990,

Tanninen and Yliruusi 1992, Yamamura and Momoe 2001 and Iyengar et al. 2001. It is worthy of note that Giron et al. (2007) carried out a comparative study of the relative merits of a number of analytical techniques for analyzing mixtures of pharmaceutical compounds and found that XRPD is usually the preferred method.

The general preference for application of quantitative XRPD in analyzing solid mixtures has led to the application of these methods to other challenging regulatory and intellectual property problems in the pharmaceutical industry, as we discuss below.

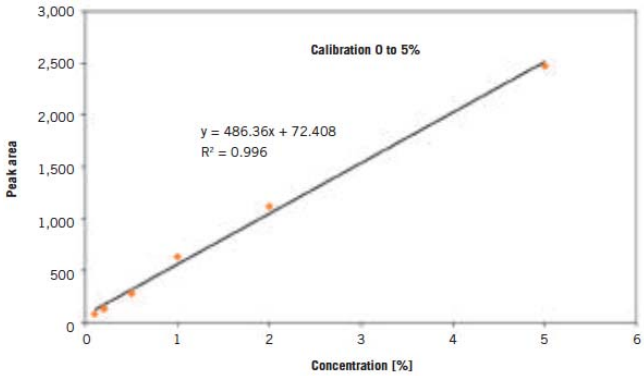

Fig 3 Calibration plot for mixtures of two polymorphs with different concentrations obtained from XRPD data showing a detection limit of LoD=3.3, S=0.082% and a quantification limit of LoQ=10, S=0.23% (From Beckers 2008)

Regulatory issues

The FDA has published guidelines (2007) for dealing with polymorphic substances in APIs of ANDAs (Abbreviated New Drug Applications), both in initial preparations and as the result of changes that may take place in storage. These can be, and in many cases indeed are, monitored by quantitative XRPD methods. Since these are guidelines they still leave the method of choice to the discretion of the applicant, but as above, XRPD will likely be the first method of choice. For obvious reasons, there are no published data of specific APIs to provide relevant examples, but those who are potentially involved in regulatory matters of solid state APIs should be aware of these guidelines and how to adhere to them.

Establishing and protecting intellectual property

In principle, patents are granted for inventions and give the grantee exclusive rights over that invention – that is, the right to prevent others from making it, using it or selling it. Two of the fundamental criteria for the granting of a patent are that the invention must be *novel* and it must be *non-obvious* to the hypothetical person "skilled in the art" – someone with competence but without imagination. Novelty and obviousness are terms that are debated in virtually every legal confrontation on crystal forms. As pointed out earlier (Bernstein 2002, Bernstein 2006) by definition, essentially every new crystal form is novel. Furthermore, for any compound it is not ob-

vious - and not possible to predict - how many different crystal forms can be prepared, how to prepare any, as yet unknown, crystal forms, or to predict the properties of any, as yet unknown, crystal forms. It is virtually impossible to provide specifics beyond that general statement since every compound is a new situation and every legal jurisdiction has its own rules, regulations, legal framework and case law, but the novelty and non-obviousness of crystal forms means that virtually every new crystal form is potentially a patentable entity.

Because of the (albeit limited-term) market exclusivity they provide, the patents on crystal forms for many drugs are the lynchpins of commercial success. The role of XRPD in defining the inventions for the preparation of a patent application and in the subsequent protection of the patent against alleged infringement is often crucial. The XRPD of a solid material is generally viewed as a fingerprint and is often considered the "gold standard" for characterizing solid materials. Therefore many patents on crystal forms contain XRPDs of the claimed form(s).

The invention in a patent (for the present discussion, a crystal form) is defined by the claim(s) that are listed separately from the general description of the invention. Proof of infringement requires proving that the alleged infringer has made, used or sold the invention as defined in the claim. Hence the framing and interpretation of claims on crystal forms is often a crucial issue in patent litigations.

There is considerable debate on how to present and define the XRPD of a crystal form in a patent. Should the claim contain a graphical representation of the diffraction pattern or a list of d-spacings and intensities (relative or absolute)? If the graphical representation of the diffraction is used to define the claim is use, then in the event of a litigation there will almost inevitably be contradictory views on the part of opposing expert witnesses of the comparison of the allegedly infringing material with that claimed in the patent.

On the other hand if the solid material is claimed using a list of peaks, then how many peaks should be included? Indeed how many peaks are required to uniquely define a crystal form for a well defined chemical entity? Should the claim(s) contain a maximum number of peaks, a minimum number of peaks, or is there some optimal number? Current U.S. case law suggests that the proof of literal infringement requires that every peak listed in a claim be identified in the allegedly infringing material. This would seem to argue for including a minimum number of peaks in the claim. (Zenith 1994) Examples covering the whole spectrum may be found in the patent literature. For instance, the first claim of US Patent 6,420,557 (Harris et al. 2002) lists 99 peaks and intensities in the first (independent) claim for a specific crystal form, while the first (independent) claim of US Patent 5,969,156 (Briggs 1999) lists *either* of only two peaks as defining the invention.

Another aspect of intellectual property protection in the pharmaceutical industry is the growing incidence of counterfeit medicines (WHO (2006); Fernandez et al.

(2008)). In addition to posing a threat to intellectual property, forged pharmaceutical products are not subject to regulatory supervision and at a minimum often lack therapeutic value or much worse may in fact threaten the health of the unwary or uninformed consumer. Thus health officials as well as the holders of patent rights on drugs are on the watch for counterfeit pharmaceutical products. This is very much a cat-and-mouse game with the regulators and industrial watchdogs constantly improving methods of detection while the counterfeiters attempt tomatch and outdo their sleuthing techniques with ever more sophisticated methods of copying. XRPD is an important part of the armory on this economic and scientific battleground and is being used extensively in the efforts to detect and prosecute forgeries (Maurin et al. 2007). A typical example is given in Figure 4.

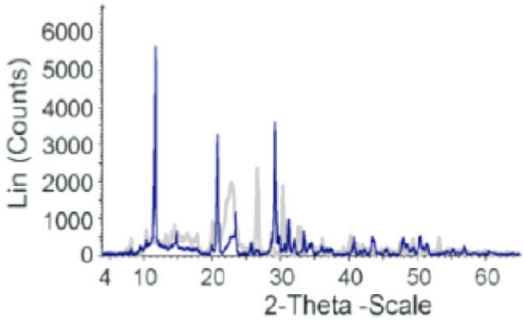

Fig 4. The comparison of diffraction patterns of a counterfeit "Viagra" tablet and the original drug (shown as the thick lines in grey) taken with the coatings
Removed (from Maurin et al. 2007).

Amorphous APIs and amorphous components of APIs

The amorphous state is playing an increasingly important role in the pharmaceutical industry (Petit and Coquerel 2006, Bates et al. 2006, Taylor and Shamblin 2009,). In general, manufacturers prefer to identify, develop and market the most stable crystalline form (Wieckhusen 2010). However, when a material fails to crystallize, the only choice may be to proceed with an amorphous form. In addition, the solubility of a crystalline form with otherwise advantageous properties may be so low that the material has little or no therapeutic value. Amorphous materials, sometimes stabilized to prevent crystallization, may be the only solution in such instances, since the less stable amorphous product will be more soluble than its crystalline congeners (Byrn et al. 1999, Hancock and Zografi 1997).

Due to the absence of long range order, amorphous solids do not exhibit sharp x-ray diffraction peaks but are characterized by a generally broad "halo" pattern reflecting the sum of all the short range order (Figure 1). The diffraction from a completely amorphous material will lack any sharp Bragg peaks, which are indicative of the presence of some long range order. The number and intensity of any Bragg peaks

superimposed on the halo can be used to asses the degree of crystallinity in a solid (Saleki-Gerhardt (1994)), while whole pattern fitting may be used to quantify the amount of amorphous material in a solid exhibiting a higher degree of crystallinity (Chen et al. (2001)).

References

Antonio SG, Benini FA, Ferreira FF, Rosa PC, Paiva-Santos C (2011) *J. Pharm. Sci.* DOI 10.1002/jps

Bates S, Zografi G, Engers D, Morris K, Crowley K, Newman A. (2006) *Pharm. Res.* 23, 2333-2349

Beckers D (2008) *Pharm. Manuf. Pack. Sources*, Spring 2008, pp. 82-85

Beckmann W, Nickish K, Budde U (1998) *Org. Process Res. Dev.* 3, 298-304

Beckmann W (2000) *Org. Process Res. Dev.* 4, 272-384

Beckmann W, Otto W, Budde U (2001) *Org. Process Res. Dev.* 5, 387-392

Bernstein J, Polymorphism in molecular crystals, Oxford University Press, Oxford, 2002

Bernstein J, "Polymorphism and patents from a chemist's point of view", in Hilfiker (2006), pp. 365-384

Bernstein J, Henck J-O, "Pharmaceuticals: Development and Formulation" in Chung FH and Smith DK (editors) Industrial applications of X-ray diffraction, Marcel Dekker, NY (2000), pp. 527-538

Birch M, Fussell SJ Higginson PD, McDowell N, Marziano I (2005) *Org. Process Res. Dev.* 9, 360-364

Braga D, Bernstein J, "Crystal polymorphism: Challenges at the crossroads of science and technology", in Braga D, Grepioni F (editors), Making crystals by design, Wiley-VCH Verlag GmbH Co. KGaA, Weinheim (2007), pp. 293-314

Briggs CA, Jennings RA, Wade R, Harasawa K, Ichikawa S, Minohara K, Nakagawa S (1999) U.S. Patent 5,969,156

Brittain HG, ed., Physical characterization of pharmaceutical solids, Marcel Dekker, NY (1995)

Brittain HG, ed., Polymorphism in pharmaceutical solids, Marcel Dekker, NY (1999)

Brittain HG. 2009. Polymorphism in pharmaceutical solids; 2nd ed. New York: Informa Healthcare Press

Brittain HG. 2011. Polymorphism and Solvatomorphism in 2009, *J. Pharm. Sci.* 100, 1260-1279 (2011)

Byrn SR, Pfeiffer R, Stowell JG, Solid state chemistry ofdrugs, 2nd edn., SSCI Inc., West Lafayette (1999)

Capes JS, Cameron RE (2007) *Cryst. Growth Des.* 7, 108–112

Chen XM, Bates S, Morris KR (2001) *J. Pharm.Biomed Anal.* 26, 63-72

Chipera SJ, Bish DL (2002) *J. Appl. Cryst.* 35, 744-749

Erice (2004). Although admittedly relatively inaccessible, the lecture notes for the 2004 Erice School "Diversity Amidst Similarity: A Multidisciplinary Approach to Polymorphs, Solvates and Phase Relationships" contains a number of contributions relevant to the topic of this lecture with applications to pharmaceuticals, and well as many useful references

Fernandez FM, Green MD, Newton PN (2008) *Ind. Eng. Chem. Res.* 47, 585-590

Food and Drug Administration (2007). Guidance for industry: ANDAs: Pharmaceutical solid polymorphism—chemistry, manufacturing, and controls information. Rockville, MD: US Department of Health and Human Services, Food and Drug Administration, Center for Drug Evaluation and Research

Giron D (2003) *Eng. Life Sci.* 3, 103-112

Giron, D, Mannier S, Mutz M, Peichon P, Buser T, Stowasser F, Schulze K, Bellus M (2007) *J. Therm Anal. Cal.* 89, 729-743

Hancock BC and Zograpfi G (1997) *J. Pharm. Sci.* 86, 1-12

Harris LJ, Storey R, Wood AS (2002) U.S. Patent 6,420,557

Griesser UJ," The importance of solvates", in Hilfiker (2006), pp. 211-234

Hilfiker R, ed., Polymorphism in the pharmaceutical industry, Wiley-VCH, Weinheim (2006)

Iyengar SS, Phadnis NV, Suryanaryyanan R (2001) *Powd. Diffr.* 16, 20-24

Jenkins R, Snyder RL, "Introduction to X-ray powder diffraction", Wiley-Interscience, New York (1996)

Klug HP, Alexander LE (1954) "X-ray diffraction procedures for polycrystalline and amorphous materials", John Wiley, New York

Kumar L, Amin A, Bansal AK (2007) *Drug Disc. Today* **12**, 1047-1052

Llinàs A, Goodman M (2008) *Drug. Disc. Today* 13, 198-210, and references therein

Mangin D, Puel F Veesler S (2009) *Org. Process Res. Dev.* 13, 1241-1253

Marti E (1988) *J. Therm. Anal. Cal.* 33, 37-45

Maurin JK, Pluci´nski F, Mazurek AP, Zbigniew F (2007) *J. Pharm. and Biomed Anal.* 43, 1514–1518

Meyerson AS (2002) (editor) Handbook of industrial crystallization, Butterworth-Heinemann, Woburn, MA

Morris KR, “Structural aspects of hydrates and solvates”, in Brittain (1999), pp.125-182
Morissette SL et al. (2004) *Adv. Drug Del. Rev.* 56, 275-300
Petit S, Coquerel G (2006) “The amorphous state” in Hilfiker (editor) (2006), pp. 259-285
Saleki-Gerhardt A, Ahlneck C, Zografi, G. (1994) Int. J.Pharm. 101, 237–247
Singhal D, Curatolo W (2004) *Adv. Drug Deliv. Rev.* 56, 335-347
Stahly GP (2007) *Cryst. Growth Des.* 7, 1007-1026
Suryanaryyanan R (1990) *Powd. Diffr.* 5, 155-159
Tanninen VP, Yliruusi L (1992) *Int. J. Pharm.* 81, 169-177
Taylor L, Shamblin SL (2009) in Brittain (ed.) (2009), pp. 587-629
Wieckhusen D *International School on Crystallization 2010: Foods, Drugs and Agrochemicals*, Granada, Spain, Abstracts of Lectures, May 26, 2010. http://www.iscgranada.org
WHO (2006) Declaration of Rome, Conclusions and Recommendations of the WHO International Conference on Combating Counterfeit Medicines, 18 Feb, 2006
Wirth DD, Stephenson GA (1997) *Org. Process Res. Dev.* 1, 55-60
Yamamura S, Momoe Y (2001) *Int. J. Pharm.* 212, 203-212
Yu LX, Lionberger RA, Raw AS, D’Costa R, Wu H, Hussain AS (2004) *Adv. Drug Deliv. Rev.* 56, 349-369
Zenith Laboratories v. Bristol-Meyers Squib, 19F.3d 1418, 30 U.S.P.Q.2d1285 (Fed. Cir.), cert denied, 523 U.S. 995, 115 S.Ct 500, 130 L.Ed.2d 409 (1994)
Zevin LS, Kimmel G (1995) ”Quantitative X-ray diffractometry”, Springer, New York

Parametric Powder Diffraction

William I. F. David[1] and John S.O. Evans[2]
[1]ISIS Facility, Science and Technology Facilities Council, Rutherford Appleton Laboratory, Harwell Science and Innovation Campus, Didcot, UK
[2]Dept of Chemistry, University of Durham, South Road, Durham, UK

Abstract The rapidity with which powder diffraction data may be collected, not only at neutron and X-ray synchrotron facilities but also in the laboratory, means that the collection of a single diffraction pattern is now the exception rather than the rule. Many experiments involve the collection of hundreds and perhaps many thousands of datasets where a parameter such as temperature or pressure is varied or where time is the variable and life-cycle, synthesis or decomposition processes are monitored or three-dimensional space is scanned and the three-dimensional internal structure of an object is elucidated. In this paper, the origins of parametric diffraction are discussed and the techniques and challenges of parametric powder diffraction analysis are presented. The first parametric measurements were performed around 50 years ago with the development of a modified Guinier camera but it was the automation afforded by neutron diffraction combined with increases in computer speed and memory that established parametric diffraction on a strong footing initially at the ILL, Grenoble in France. The theoretical parameterisation of quantities such as lattice constants and atomic displacement parameters will be discussed and selected examples of parametric diffraction over the past twenty years will be reviewed that highlight the power of the technique.

1. Parametric powder diffraction – the beginnings

While many papers before 1960 reported multiple powder diffraction measurements, it was the development of a modification to the Guinier camera (Figure 1a) by Lenné [1] that marks the beginning of parametric powder diffraction. Lenné's modification was profound but simple and involved translating a film cassette across a narrow aperture that defined the equatorial plane of scattering. Simon [2] developed a modified version for air-sensitive samples and these cameras were used extensively over the next two decades to monitor structural changes, principally as a function of temperature. An example of some early work on the ferroelastic phase transition in $LaNbO_4$ [3] is presented in Figure 1b which clearly shows the continuous transformation from monoclinic to tetragonal symmetry. While these photographs gave an excellent oversight into the behaviour of materials, extracting quantifiable data involved using microdensitometry where the transmission of light, pixel by pixel, through the photograph was digitised. Given the computing power and avail-

able memory, analysis of a single photograph of the complexity presented in Figure 1b was a major undertaking.

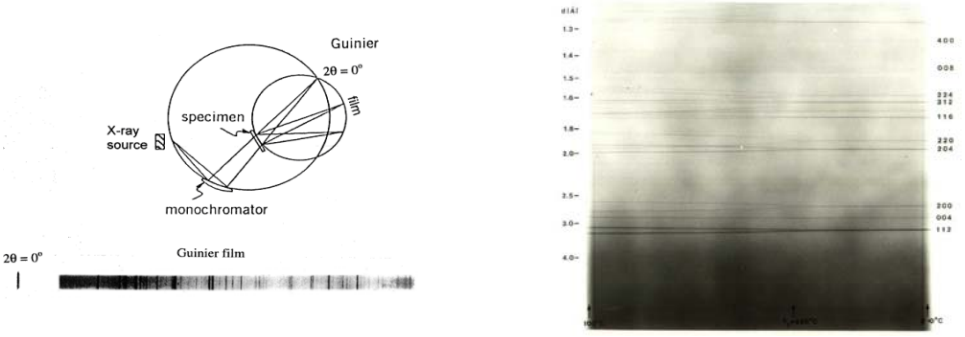

Fig. 1. (a) the Guinier camera geometry with the ribbon of illuminated film along the equatorial plane; (b) a Guinier-Simon photograph of ferroelastic $LaNbO_4$ covering the approximate temperature range from 100°C to 800°C [3]. The monoclinic-tetragonal transition is clearly visible at ~590°C and it is possible to see the anisotropic increase in line-broadening (particularly for the 220 reflection) around the phase transition.

The next major breakthrough in parametric powder diffraction was to occur with neutrons not X-rays. The Rietveld method [4, 5] was developed initially for neutron powder diffraction and its application to X-ray scattering came a decade later [6, 7].

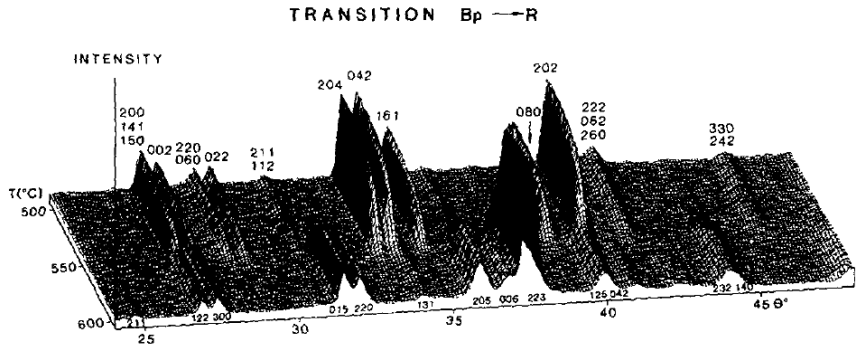

Fig. 2. A typical thermodiffractogram from D1b: the temperature dependence of the neutron powder diffraction pattern of $Sr_2Co_2O_5$ showing one of five phase transitions Bp and R refer to the paramagnetic brownmillerite-type and rhombohedral structures of $Sr_2Co_2O_5$. [9]

By the late 1970s, profile refinement was well-established for neutron powder diffraction and the Institut Laue et Langevin (ILL), Grenoble was at the forefront of the development of neutron scattering techniques. Two powder diffractometers were commissioned; the high resolution diffractometer, D1a, which was represented the state of the art in structural precision and accuracy from powder diffraction data and D1b, a medium resolution neutron powder diffractometer, with a large area position sensitive detector. In the late 1970s, a complete D1a dataset was collected in 6-12 hours, but D1b data could be collected in minutes. Jean Pannetier, the D1b instru-

ment scientist at the time, developed the technique of thermodiffractometry [8] which defines the beginning of parametric powder diffraction analysis. A typical mid-1980s example from D1b of the complex evolution of a crystal structure, that of $Sr_2Co_2O_5$ [9], is presented in Figure 2.

2. Crystal structure parameters: some equations

Parametric powder diffraction measurements yield a wealth of information about the variation of structural parameters as a function of an external variable such as temperature of pressure. In this section, we discuss the variation of crystallographic parameters such as lattice constants and displacement parameters as a function of temperature. Equations of state as a function of pressure have also been derived and applied to powder diffraction data [10] but these will not be discussed in this lecture. Perhaps the simplest temperature dependence to explore is associated with the thermal motion of an atom – the displacement parameter. Each atom in a crystal structure vibrates around a mean position defined its crystallographic coordinates. The potential around this equilibrium position is, to a good approximation, quadratic in nature. The temperature dependence of the mean square displacement, $\langle u^2 \rangle$, of such a quantum system, mass m, vibrating with frequency, ω, is given by $\langle u^2 \rangle = (\hbar/2m\omega) \coth(\hbar\omega/2kT)$ (see [11]). Strictly speaking, this argument, originally derived by Einstein, pertains not to individual atoms but to phonons but the assumption generally works well for displacement parameters. This is illustrated in Figure 3 which shows the difference in libration parameters between ND_3 and BD_3 rotation in ammonia borane, ND_3BD_3.

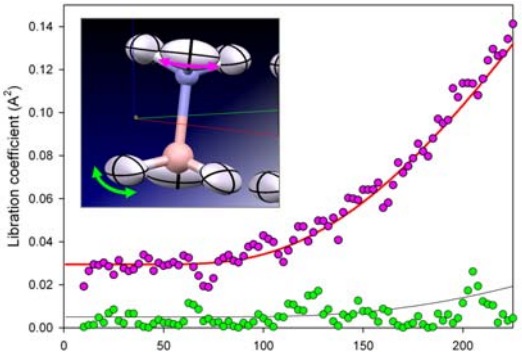

Fig. 3. The coefficients for ND_3 and BD_3 libration in ammonia borane. As observed by NMR, the ND_3 libration is larger and has a lower frequency than BD_3.

The approximate equations that determine thermal expansion may also be derived from a quantum-mechanical analysis. Thermal expansion is, however, a consequence of anharmonic potentials as it is easier for bonds to expand than contract. Following [11], the temperature dependence of the mean position, a, of a weak anharmonic potential of the form $V(x) = \frac{1}{2}mw^2x^2 + kx^3$ is given by the formula $a = 3k\hbar$

$\coth(\hbar\omega/2kT)/2m^2\omega^3$. In simpler terms, this Einstein oscillator behaviour may be expressed as

$$\frac{(a-a(T=0))}{T} = \frac{(\Theta_E/T)}{\exp(\Theta_E/T)-1}$$

One final caveat – basic modelling of specific heat data (see, for example, Kittel (1976) [12]) suggests that a more correct formulation is a low-frequency, quadratic density of states model originally formulated by Debye

$$\frac{(a-a(T=0))}{T} = \frac{3}{(\Theta_D/T)^3}\int_0^{\Theta_D/T}\frac{\xi^3}{\exp(\xi)-1}\,d\xi$$
$$= \left[\frac{\pi^4}{5(\Theta_D/T)^3} - \sum_{n=1}^{\infty}\left(3+\frac{9}{(n\Theta_D/T)}+\frac{18}{(n\Theta_D/T)^2}+\frac{18}{(n\Theta_D/T)^3}\right)\frac{\exp(n\Theta_D/T)}{n}\right]$$

This formulation is straightforward to implement in a least squares analysis. A good example of the use of this parametric fitting is solid C_{60} which we will use in this lecture to illustrate a number of different aspects of parametric powder diffraction. High resolution neutron powder diffraction data of solid C_{60} were collected on HRPD at ISIS using a 2.5g. sample [13]. After an initial long 3½ hr. run at 4K, the temperature was raised in 2K intervals from 10K to 272K. Each dataset was collected for 20 min. with 5 min. allowed for temperature equilibration. The resulting refined lattice parameters are presented in Figure 3a and have been precisely determined with a(4K)= 14.04212(2)Å, a(170K)= 14.07080(10)Å and a(272K)= 14.15425(20)Å. This high precision is important for the extraction of non-crystallographic information which will be discussed further in section 4.

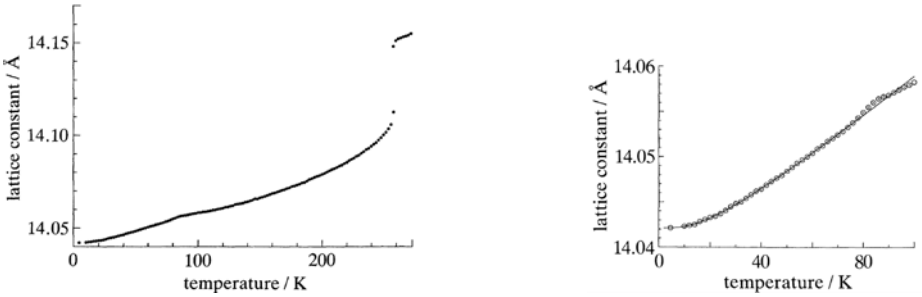

Fig. 3. (a) the cubic cell constant of C_{60} as a function of temperature from 4K to 272K and (b) observed (circles) and calculated (line) C_{60} lattice constant below the orientational glass transition. The data were fitted between 4K and 70K using a combined Debye and Einstein model.

The C_{60} lattice constant shows two significant features at ~80K and ~260K. The upper feature corresponds to an orientational melting of C_{60}. Above this transition temperature, T_c, the orientation distribution is close to isotropic; below T_c, C_{60} hops between two sets of distinct crystallographic orientations – the lower energy, major orientation is characterised by pentagonal face directed along the 110 direction while the higher energy, minor orientation is characterised by hexagonal face along 110. The lower feature in Figure 3a corresponds to an orientational glass transition. Above this temperature, C_{60} is rotating sufficiently quickly to maintain thermody-

namic equilibrium and the relative fractions of major and minor orientations follow a Boltzmann distribution. This will be discussed further in section 4.

Below the orientational glass transition, the fractions of major and minor orientations are quenched at the glass transition temperature value. The lattice constant behaviour is typical of substances at low temperature. The roughly linear dependence with temperature above *ca.* 50 K levels off to a constant value at the lowest temperatures. In specific heat data analysis, both the Debye and Einstein models described above can look superficially similar as the evaluation of the specific heat involves an integration, and consequent smoothing, over phonon frequencies. The same also holds for lattice constant analysis. With high precision data, however, the relative merits of a Debye, Einstein or approximate combination can be discriminated in both specific heat and lattice parameter quantities. This has been found to be the case in the analysis of C_{60}. Working with data between 4 K and 70 K, a 'Debye-only' model gave a significantly poorer fit (χ^2 = 12.1) to the data than an 'Einstein-only' model (χ^2 = 1.53). A single Debye + single Einstein model gave an improved fit (χ^2 = 1.20). No further parameters could be justifiably introduced to improve the fit. The fitted lattice constant is given by

$$a(T) = 14.042\,103(36) + 0.000\,157(8) \times a_{\mathrm{D}}(52.0(6)/T) + 0.000\,65(9) \times a_{\mathrm{E}}(93(8))/T)$$

The derived Debye and Einstein temperatures are 52(6) K and 93(8) K which are close to anticipated values obtained from specific heat data.

3. Refining a complete experiment – "surface" refinements

In the previous section, we discussed the parametric fitting of structural quantities such as lattice constants and displacement parameters as a function of an experiment variable such as temperature and pressure. In this section, we explore the possibility and advantages of going beyond the serial refinement of a set of diffraction data to the simultaneous refinement of all the diffraction data together [14, 15]. The simple idea behind this approach is that if one has an ensemble of data collected under evolving conditions of a variable such as time, temperature, pressure or chemical environment (a "surface" of diffraction data) many of the key parameters one extracts from a Rietveld refinement can be derived from the whole set of data rather than from a single (noisy) data set. A trivial example might be the zero-point of a diffractometer during a series of time resolved experiments. The physical instrumental misalignment leading to this correction is unlikely to change during the course of the experiment, and the variable is therefore best determined from all data sets simultaneously rather than from each individual set independently. In this way one can sometimes extract "good information" from individually "bad data". An additional key feature of the parametric approach to data analysis is that physically sensible conditions may be imposed on the refined parameters in a flexible manner.

This is extremely useful – and, indeed, essential, when the information content in individual data sets is sufficiently low (e.g. due to low data quality or a complex structural model) that a number of different models can provide an equivalent fit.

One area where this approach is potentially very powerful is in the quantitative phase analysis of materials with complex or closely related structures. For example, WO_3 undergoes a series of phase transitions on cooling as shown schematically in Figure 4 in which the material evolves from a hypothetical high-temperature, high-symmetry cubic form to a series of lower symmetry forms of increasing complexity. [16-21]

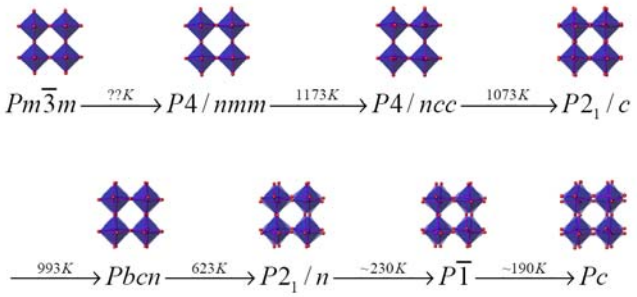

Fig. 4. The sequence of phase transitions in WO_3.

Figure 5a shows a two-dimensional "film plot" of powder diffraction data recorded on cooling a sample of monoclinic $P2_1/n$ WO_3 from 300 K to 90 K. Data were collected using a Bruker d8 diffractometer equipped with a pHeniX cryostat using Cu K_α radiation, with each dataset recorded for 20 minutes. The difficulty in performing a quantitative analysis of such diffraction data arises from the displacive nature of the transitions only resulting in small changes in atomic coordinates, which in turn leads to relatively minor changes in the diffraction pattern.

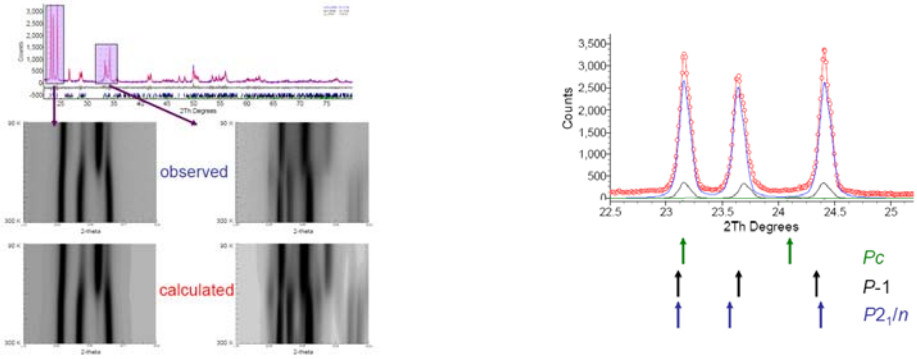

Fig. 5. (a) Surface "film plot" showing changes in two regions of the diffraction pattern of WO_3 on cooling. Observed and calculated surfaces from a parametric refinement are shown and (b) 300 K diffraction data showing predicted reflection positions for the {200} family of reflections. The 2θ range corresponds to that shown in left hand zoomed region of Figure 5a.

In fact, as shown by Figure 5b, if we consider a small region of the diffraction pattern around 24° 2θ all three phases of WO_3 have peaks in this 2θ region, with similar intensities. If one fits a single experimental dataset it is therefore possible for the "incorrect" structure to distort to fit the diffraction data. For example, even though the material is predominantly in the monoclinic $P2_1/n$ form at room temperature the $P1$ structural model, which has more degrees of freedom, can distort to fit the experimental data as well as a $P2_1/n$ model. This makes quantitative analysis of an evolving mixture of $P2_1/n$ and $P1$ phases extremely challenging. Figure 6 shows the implications of this on quantitative Rietveld refinement on the data in Figure 5a as a function of temperature. Here all 100 data sets have been fitted independently using three-phase Rietveld refinement. A total of 91 parameters were used to fit each data set, requiring 9100 refined parameters in total.

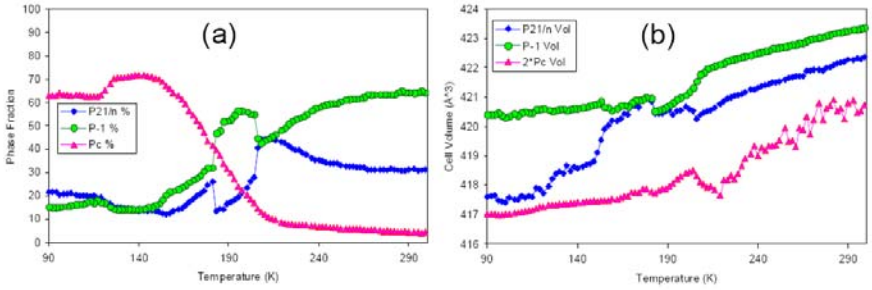

Fig. 6. (a) Phase fractions and (b) cell volumes of $P2_1/n$, $P1$ and Pc forms of WO_3 obtained by independent Rietveld refinement.

It is clear from Figure 6(a) that the evolution of refined phase fractions as a function of temperature makes little chemical sense. It is extremely unlikely, for example, that abrupt and reverse changes of the type apparently observed at 180 K and 200 K occur. This suggests that the refinements have found false minima. This occurs despite each refinement being set up as carefully as possible, with variables constrained to lie within sensible minimum and maximum ranges of ideal values. That these are false minima is further shown by Figure 6(b) where the apparent temperature dependence of refined cell volumes is clearly non-physical. Clearly independent Rietveld refinement of these data is not the optimal approach.

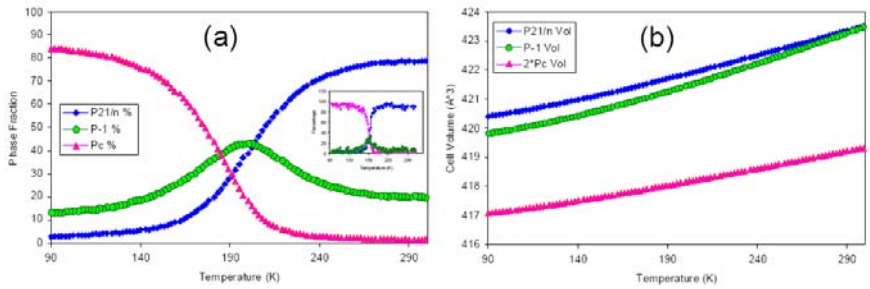

Fig. 7. (a) Phase fractions and (b) cell volumes of $P2_1/n$, $P\bar{1}$ and Pc forms of WO_3 obtained by parametric Rietveld refinement. Note that volumes extrapolate into temperature regions where individual phases no longer exist.

Figure 7 shows results from fitting the same data using a parametric approach in which all patterns were fitted simultaneously. To fit the data, three simple assumptions were made. Firstly, it was assumed that the cell parameters of each individual phase show a smooth variation with temperature. The specific variation was not imposed on the data, but cell parameters of the three phases were parameterised using the following expression, $a(T) - a(0) + c_1/(\exp(\theta/T) - 1)$ (see section 2) where coefficients $a(0)$, c_1 and θ were refined from the diffraction data. For variable unit-cell angles, a second-order polynomial was used. Secondly, it was assumed that the temperature factor refined for each atomic site should increase smoothly with temperature. The same Einstein functional form was used as for the lattice constants (see section 2). Finally, the peak shape description was set up such that each individual phase had an identical peak shape description at all temperatures. In this fashion, a single Rietveld refinement was performed with 1102 parameters fitted simultaneously to all 100 datasets. This led to the phase fractions and cell volumes shown in Figure 7. The extracted phase fractions make much more chemical sense and vary in a smooth fashion with temperature even though they were not constrained in any way. The values also agree well with those extracted from analysis of neutron data on a similar sample (inset to Figure 7(a)). The parametrically fitted cell parameters also make physical sense in that they give rise to comparable volume coefficients of expansion for each phase as expected.

The success of this approach has two basic origins. The most important influence is the fact that the three-phase model, with each phase constrained to have cell parameters which evolve with temperature in a physically sensible way, must simultaneously fit each experimental data set. This essentially prevents the $P\bar{1}$ phase, for example, distorting to fit the room temperature data, as the distortions required to do so would prevent accurate fitting of data recorded around 200 K, where more of the $P\bar{1}$ phase is present. Secondly, the parametric approach to modelling peak shapes means that the peak-shape parameters for an individual phase are dominated by the temperature regions of the diffraction surface when it is actually present. This prevents, for example, peak shapes for the Pc phase becoming infinitely broad in regions of

the data where the phase is not present, "mopping up" minor errors in fitting the experimental background and influencing the quantitative refinement. In essence the parameters modelling an individual phase are determined by regions of the data where the phase is present rather than regions where it is not.
The approach used to fit the data in this example is entirely general and the degree of complexity, in terms of which variables are parameterised and which functions are used, is the choice of the analyst. It is possible, for example, to parameterise atomic coordinates, peak shape parameters or background functions as required. One criticism of the approach is that one imposes a certain physical form on the evolution of variables which may not be correct. In fact, this objection can turn out to be a major strength. If an inappropriate parametric form is chosen for a given variable, or if the overall model is not sufficiently flexible to model all the features of the diffraction surface the inadequacy is often revealed in a plot of R-factor against data set number for the parametric refinement. Normally one would expect a smooth evolution in R-factor (e.g. as data quality improves slightly on cooling). If the parametric model is incorrect one sees unexpected variations (e.g. humps in certain temperature regions) with temperature. When data sets are refined independently these tell-tale variations can be lost as the Rietveld model can distort in non-physically sensible ways to fit an individual data set and the distinguishing power of the R-factor is reduced.

4. Parametric powder diffraction – beyond crystal structure

In this section, we illustrate the possibility of obtaining significant non-crystallographic properties from parametric diffraction. We use the example of solid C_{60} [13] and continue our discussion from section 2 focussing on the low-temperature ordered phase and, in particular, the orientational glass transition around 80K. Below this transition, the proportions of the two orientations are fixed. There is a slight rise around the glass transition temperature, T_g and this is attributed to the fact that the cooling rate (*ca*. 1 K min^{-1}) is substantially faster than the heating rate (i.e. the experiment duration). The re-orientational hopping thus unlocks at a lower temperature than the original 'quenching' temperature. This effect is more prominent in the lattice parameter and can be used to determine the relaxation rate and hence the re-orientational correlation. A model for this effect is developed later in this section. Above T_g, the decrease in major orientation fraction may be expressed in terms of a Boltzmann distribution since thermal equilibrium is achieved. The energy difference between major and minor orientations, ΔG, may be expressed by the equation

$$(p_{\mathrm{H}}/p_{\mathrm{P}}) = ([1/\mathrm{p_P}]-1) = \exp(-\Delta G/kT)$$

and thus

$$\Delta G = -kT\ln((1/p_{\mathrm{P}})-1).$$

A least squares fit assuming ΔG to be constant between 90 K and 200 K gives fair but not excellent agreement (Figure 8a). The derived value for the energy difference is 122(3) K. Above 200 K, there are clear precursor effects of the orientational order – disorder transition at 260 K. Evaluation of the energy difference, ΔG, calculated point by point from the above equation emphasises these precursor effects and clearly indicates that ΔG is not precisely constant between 90 K and 200 K and that there is therefore an additional entropic contribution (Figure 8b).

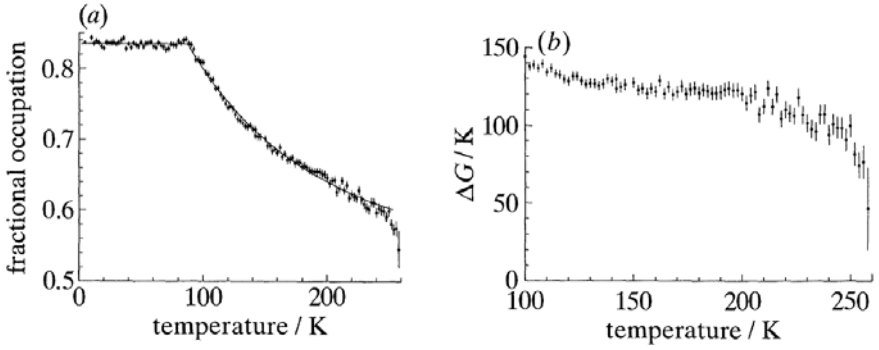

Fig. 8. (a) The fractional occupation, p_P, of the more energetically favourable, major orientation as a function of temperature. The sum of major, p_P, and minor, p_H, sums to unity. The quenching of the relative populations of major and minor orientation fractions at the glass transition of ~90K is clearly evident. The fitted line above 90K corresponds to a refined energy difference of 122(4)K (11.0(3)meV) between the two orientations. There are clear departures from this behaviour above 200K; (b) the free energy difference between the two orientations obtained the relative major and minor orientation populations.

Previously in this section, attention was drawn to the anomalous rise in the major orientation fraction at the glass phase transition temperature. This was explained in terms of the differing rates of initial cooling (*ca.* 1 K min^{-1}) and heating. The latter corresponds to the experimental time of *ca.* 25 min. (i.e. 12.5K min^{-1}). The slower rate of heating implies that the system will unquench at a lower temperature and that the approach to thermal equilibrium will be distinguishable when thermal relaxation rate (the inverse of the reorientational correlation time) is around an order of magnitude longer than the experimental time. This behaviour is particularly evident in the temperature variation of the lattice parameter as an anomalous rise in the vicinity of the glass transition. As an example of obtaining non-crystallographic data, a model is developed that explains the lattice parameter anomaly below T_g and enables relaxation rates to be determined and hence the reorientational activation energy to be derived.

Consider the information in Figure 9a below the orientational glass transition temperature, T_g. The plotted data provide a baseline that corresponds to a fixed major/minor orientation ratio. The dotted line represents the thermodynamically stable, but unattainable, population ratio. As T_g is approached, thermal relaxation begins to

occur. The lattice constant rises above the 'quenched' baseline. Relaxation does not approach completion, however, until T_g.

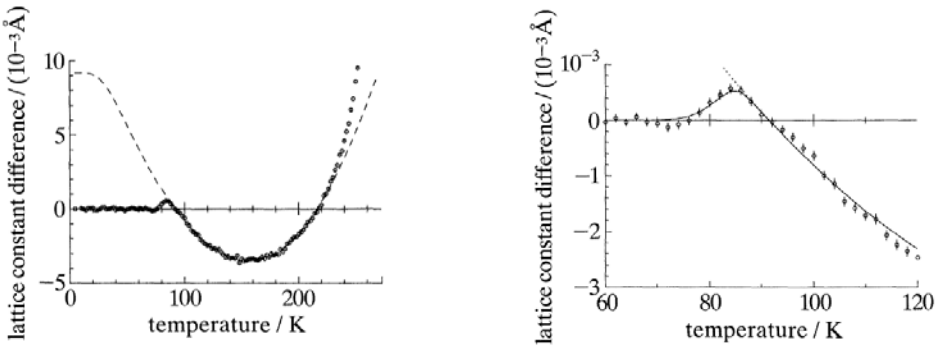

Fig. 9. (a) The lattice constant difference between the observed and calculated C60 lattice constant (see Figure 3). From this, the relative volumes of pentagonal and hexagonal orientations may be obtained; (b) the lattice constant difference fitter to a recursive function that model the return to thermal equilibrium arounf the glass transition temperature. Reorientation times extracted by the method lead to an accurate estimate of the reorientation activation energy.

The approach to thermal equilibrium is, however, a cumulative effect which, when accounted for, leads to the conclusion that the relaxation rate, $\tau(T_k)$, at the k^{th} temperature step may be obtained from the equation

$$\left(u_k \Big/ \left[1 - \sum_{r=1}^{k-1} u_r\right]\right) \approx [1 - \exp(-T_{exp}/\tau(T_k))]$$

where the experiment time, $T_{exp} \approx 25$min, $u_k = \Delta a_k / z_k$ is the deviation of the plotted data from the baseline and z_k is the difference between the theoretical equilibrium lattice constant and the baseline. The relaxation rate can thus be obtained in a recursive manner. A starting point of 70 K was found to be adequate. The relaxation rates obtained are listed in the following table:

temperature/ K	τ (derived) / sec	τ (calc) / sec
74	8.47×10^4	8.18×10^4
76	3.51×10^4	3.31×10^4
78	1.32×10^4	1.40×10^4
80	5.89×10^3	6.21×10^3
82	3.20×10^3	2.86×10^3

The functional form of this anomalous lattice parameter model is shown in Figure 9b where it can be seen to provide an excellent fit to the data. Note that the full lattice constant range in this figure is only 0.004Å. The variation in relaxation rate of more than an order of magnitude between 74 K and 82 K permits a precise Arhennius formulation to be obtained. Writing $\tau(T) = \tau_0 \exp(E_a/kT)$ yields τ_0 to be $10^{-10\pm1}$s and

a reorientational activation energy of 219(7) meV in excellent agreement with other techniques. This parametric powder diffraction study of C_{60} not only yields an accurate account of the temperature variation of the crystal structure of C_{60} through the orientational glass and order-disorder transitions but also provides detailed information about reorientation times and the relative energies of and the activation energy between the two crystallographically distinct orientations. Similar properties may be obtained from studying in-situ reactions and in operando processes.

5. Conclusions

Most modern X-ray and neutron powder diffractometers have the potential to collect datasets in a matter of minutes and indeed with synchrotron radiation the timescales can be significantly shorter [24]. Combining sophisticated sample environment, substantial computer memory and speed and advanced computer programs, it is possible with parametric powder diffraction not only to investigate the temperature and pressure evolution of a material through complex phase transitions but to perform a very wide range of more complex experiments. These include in-situ synthesis reactions, in-operando material systems such as batteries, hydrogen storage materials, hydration/dehydration and gas absorption/desorption and the pixel-by-pixel scanning of materials at the micron level. By performing advanced parametric analysis it can be possible to extract "non-crystallographic" information such as rate constants, activation energies, temperature and others from diffraction data. It also becomes possible to introduce physically meaningful constraints or restraints to an entire body of diffraction data and obtain "high quality" information from individually "low quality" data.

Acknowledgements

We would like to thank our colleagues, Richard Ibberson (ISIS, now NIST), Takasuke Matsuo (Osaka) and Graham Stinton (Durham, now Edinburgh) for their collaboration in the C_{60} and ZrP_2O_7 and WO_3 parametric diffraction studies discussed in these lecture notes. We particularly would like to thank and acknowledge the huge contribution that Alan Coelho has made that underpins this work. His computer program, Topas, is simply crucial in enabling the most complex parametric diffraction experiments to be analysed and understood.

References

1. H.-U. Lenné, "Die Böhmit-Entwässerung, verfolgt mit einer neuen Röntgenheizkamera" (Engl. translation: "The dehydration of Boehmite observed with a new X-ray heating camera"), *Z. Krist.* **116** 190-209 (1961)
2. A. Simon. “Eine Methode zur Untersuchung extrem luftempfindlicher Substanzen mit der. Guinier-Methode” *J. Appl. Cryst.* **3** 11-18 (1970)
3. W.I.F. David, “Structural studies of ferroic ABO_4 crystals, D. Phil thesis”, University of Oxford, (1981)
4. H.M. Rietveld “Line Profiles of Neutron Powder-Diffraction Peaks for Structure Refinement” *Acta Cryst.* **22** 151-152 (1967)
5. H.M. Rietveld "A profile refinement method for nuclear and magnetic structures", *J. Appl. Cryst.* **2** 65–71 (1969).

6. G. Malmros and J.O. Thomas, "Least-squares structure refinement based on profile analysis of powder film intensity data measured on an automatic microdensitometer" *J. Appl. Cryst*. **10** 7-11 (1977)
7. C.P. Khattak and D.E. Cox, "Profile analysis of X-ray powder diffractometer data: structural refinement of $La_{0.75}Sr_{0.25}CrO_3$" *J. Appl. Crystallogr.* **10** 405-11 (1977)
8. J. Pannetier, "Thermodiffractometry" *Chemica Scripta* **26A** 131-139 (1986)
9. J. Rodriguez-Carvajal, J.M Gonzalez-Calbet, J.C. Grenier, J. Pannetier and M. Anne, "Phase Transitions in $Sr_2Co_2O_5$: a Neutron Thermodiffractometry Study" *Solid State Comm*. **62** 231-234 (1987)
10. http://www.iucr.org/resources/commissions/crystallographic-computing/newsletters/1/fitting-equations-of-state (and references therein)
11. R.P. Feynman, "Statistical Mechanics: A Set of Lectures", pp. 52-55, W. A. Benjamin, Inc. Advanced Book Program, Reading, Massachusetts 1972
12. C. Kittel, "Introduction to Solid State Physics", John Wiley and Sons (1976)
13. W.I.F. David, R.M. Ibberson and T. Matsuo "High resolution neutron powder diffraction: a case study of C_{60}" *Proc. R. Soc. London A,* **442**, 129–146 (1993)
14. G.W. Stinton and J.S.O. Evans, "Parametric Rietveld refinement" *J. Appl. Cryst*. **40** 87-95 (2007)
15. J.S.O. Evans, "Advanced Input Files and Parametric Quantitative Analysis using Topas" *Materials Science Forum* **651** 1-9 (2010)
16. B.J. Campbell, J.S.O. Evans, F. Perselli, and H.T. Stokes, Rietveld refinement of structural distortion-mode amplitudes; http://iucrcomputing.ccp14.ac.uk/iucrtop/ comm/ ccom/ newsletters/2007nov/ (2007)
17. C.J. Howard, V. Luca, and K.S. Knight: *J. Phys.: Condens. Matter,* **14** 377-387 (2002)
18. E.K.H. Salje, S. Rehmann, F. Pobell, D. Morris, K.S. Knight, T. Herrmannsdorfer, and M.T. Dove, *J. Phys. Condens. Matter*, **9** 6563-6577 (1997)
19. T. Vogt, P.M. Woodward, and B.A. Hunter, *J. Solid State Chem*., **144** 209-215 (1999)
20. P.M. Woodward, A.W. Sleight, and T. Vogt, *J. Phys. Chem. Solids*, **56** 1305-1315 (1995)
21. P.M. Woodward, A.W. Sleight, and T. Vogt, *J. Solid State Chem*., **131** 9-17 (1997)
22. W.I.F. David, "Powder Diffraction: by Decades" The Power of Powder Diffraction, 44th International School of Crystallography, Erice (2011)
23. W.I.F. David, J.S.O. Evans and A.W. Sleight, "Direct evidence for a low-frequency phonon mode mechanism in the negative thermal expansion compound ZrW_2O_8" *Europhys. Lett.* **46**, 661–666 (1999)
24. A.N. Fitch, "Ultrafast Powder Diffraction" The Power of Powder Diffraction, 44th International School of Crystallography, Erice (2011)

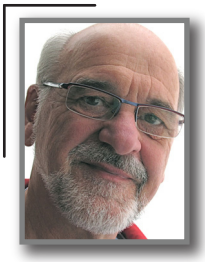

Combination of X-ray powder diffraction, electron diffraction and HRTEM data

Christian Baerlocher and Lynne B. McCusker
Laboratory of Crystallography, ETH Zurich, Switzerland

Introduction

X-ray powder diffraction and electron microscopy are probably the two most useful techniques for analyzing the structures of polycrystalline materials. While it is relatively easy to measure an X-ray powder diffraction pattern, a detailed interpretation of the data is not always straightforward because of the well known overlap of reflections with similar diffractions angles. This hinders structure elucidation by conventional (single-crystal) crystallographic methods, because the algorithms assume that the intensities are reliable. However, a wide variety of approaches have now been developed to deal with this overlap problem, and structures of moderate complexity can now be solved from powder diffraction data in an almost routine manner [1].

With an electron microscope, on the other hand, very tiny crystals (<100 nm) can be examined individually, because electrons interact much more strongly with matter than do X-rays. Furthermore, because electrons can be focussed easily, both diffraction patterns and high-resolution images can be obtained. These obvious advantages are offset by the fact that the operation of an electron microscope requires considerable expertise and the measured diffraction intensities are distorted by a number of effects that are not easy to control or correct for. Nonetheless, electron crystallography has been applied successfully to various classes of materials (e.g. [2,3, U. Kolb, this school).

These two techniques are remarkably complementary (see Table 1), and over the last few years, several ways of combining them have been developed to address structures that cannot be solved by either method alone. In this lecture, the relevant features of the two techniques, the algorithms used to combine the different kinds of data, and some recent examples taken from the world of zeolite structures are described.

Table 1. Comparison of X-ray Powder and Electron Diffraction Data

	X-ray Powder	Electron
Data collection	easy	difficult
Data set	complete (up to $2\theta_{max}$)	incomplete
Lattice parameters	precise	approximate
Intensities	kinematic	dynamical
Multiple diffraction	no	yes
Systematic absences	difficult	easy
Crystallite size	μm	nm
Reflection overlap	yes	no
Phase information	no	yes (from HRTEM images)

2. Structure determination from powder diffraction and electron microscopy data

Powder diffraction

As mentioned above, the main limitation of X-ray powder diffraction data is reflection overlap. In most cases, the total intensity measured for a group of overlapping reflections is simply equipartitioned over the contributing reflections. The problem can be reduced by collecting high-resolution data at a synchrotron facility, but it cannot be eliminated. It was soon recognized that single crystal methods could not be applied for diffraction patterns with severe overlap and alternative approaches would be required. Supplementing the powder diffraction data with chemical information (known bond distances and angles, coordination numbers, connectivity, etc.) was found to be a particularly effective approach [1]. This resulted in a number of automated model-building programs based on global optimization algorithms. While direct methods operate in reciprocal space (i.e. with reflection intensities and phases), the global optimization algorithms work in direct space. For more detailed information, the reader is referred to the book *Structure Determination from Powder Diffraction Data* [4], the special issue of *Z. Kristallogr*. devoted to the same topic [5] and of course to the lectures of this school.

A few algorithms, such as the shake-and-bake modification to direct methods [6], the charge-flipping algorithm that was introduced only recently [8], and the zeolite-specific program *Focus* [8], alternate between the two spaces and can therefore benefit from the individual strengths of both. On particular idea that can be used in this respect is the concept of a structure envelope [9]. A structure envelope defines regions within the unit cell that are most likely to contain atoms, and can be generated from just a few strong, low-index reflections [10].

Electron microscopy

All aspects of electron crystallography are of course extensively covered in the workshop on that topic. For the benefit of the "powder people" the problems and techniques relevant for this lecture are briefly mentioned here. Whereas the main problem with powder diffraction data is the reflection overlap, the main problem of electron diffraction is the strong interaction of the electron beam with the crystal. As a consequence the diffracted beams are also strong and can, in turn act as incident beams. Thus, the interaction between the incident beam and the crystal cannot be treated as a single-scattering event for each reflection as it is for X-rays (kinematical approximation). The thicker the sample, the more severe is this effect.

Selected area electron diffraction (SAED)

If the crystal in the electron beam is thin enough (~ 50nm or less), however, the dynamical effects are minimized and the diffraction intensities measured using a conventional selected area electron diffraction (SAED) technique can be treated as quasi-kinematical. In a typical SAED pattern, the incident beam is generally aligned along a zone axis, and the complete zero-order diffraction pattern for that zone (zero order Laue zone or ZOLZ) can be recorded out to a resolution of less than 1 Å in a single shot. However, because many reflections are excited simultaneously, multiple scattering effects can be severe, and the measured intensities are not very reliable.

Precession electron diffraction (PED)

In 1994, Vincent and Midgley [11] introduced the precession electron diffraction (PED) technique that partially solves this problem. The electron beam is deflected and then precessed around a stationary crystal, and with this tilted illumination, only a few reflections are excited at a time, so the possibilities for multiple scattering are reduced and the resulting diffraction intensities are more kinematical in nature. Although the PED intensities are still not ideal, they are significantly improved over typical SAED intensities [12], and have been used to solve several structures [13-16.

High-resolution transmission electron microscopy (HRTEM)

Because the electron beam can be focused, it is also possible to record a magnified image of the sample with an electron microscope. The advantages of having a high-

resolution transmission electron microscope (HRTEM) image for structure analysis are twofold. First, the image shows approximately where the atoms are in that projection of the unit cell even if atomic resolution is not attained, so the validity of a structure envelope can be evaluated by eye. Second, the Fourier transform of the image yields a list of structure factor amplitudes *and* phases for the reflections in the corresponding diffraction pattern. Before the Fourier transform is performed, the image is usually lattice and symmetry averaged to obtain a clearer and defect-free image. Then a contrast-transfer-function (CTF) correction is applied, which allows for the modulation of the amplitudes and phases caused by various parameters of the microscope. Fourier transform of this modified image then generates the desired phase information. The crystallographic image processing software package *CRISP* [17] can be used to perform these calculations.

3. Dual-space structure solution algorithms

It was mentioned earlier that a few structure determination algorithms work in both reciprocal and direct space, so information from different sources can in principle be added in either realm. Such algorithms are particularly well-suited for combining data from different sources. In the last few years, two of them, *Focus* [8] and powder charge flipping *pCF* [18], which is implemented in the program *Superflip* [19], have been used successfully to combine X-ray powder diffraction and electron microscopy data.

FOCUS

Focus is a zeolite-specific structure-solution program that uses chemical information (real space) to compensate for the ambiguities in the reflection intensities (reciprocal space) extracted from a powder diffraction pattern. Structure factor amplitudes are calculated from the extracted intensities, and are then assigned starting phases (usually random). These are used to generate a (random) electron density map. The program then interprets the map and calculates a (partial) model. It is primarily in this interpretation step that the chemical information about zeolite framework structures is exploited (4-connected, 3-dimensional network of corner-sharing TO_4 tetrahedra, where T is any tetrahedrally coordinated atom such as Si or Al). If a framework model is found, it is classified and written to a file. When a sufficient number of frameworks have been found, a histogram is generated, and in general, the framework found most frequently (from different starting phase sets) will be the correct one. The algorithm has now been applied by many different laboratories with considerable success. Its only drawback is that it is specific to zeolites.

Until 2006, the germanosilicate ITQ-22 [20] had the most complex zeolite framework structure, so it was used to test the value of including some initial phases in the *Focus* input [21]. These tests showed that by prescribing the phases of just 31 of the 992 strongest reflections, the time required for structure solution could be reduced

from 31 days to 44 hours. Doubling the number of phases to 62 resulted in 17 solutions within 11 hours. Obviously even a limited amount of phase information has a significant effect on the structure solution.

Powder charge flipping

In 2004, Oszlányi and Sütő introduced a more general algorithm for structure solution from single-crystal data, that they called charge flipping [22]. The details of this algorithm as applied to powder diffraction data is explained by L. Palatinus during this school. To start with, an electron density map is generated using random phases as in *Focus*, and therefore it is again simple to introduce already known phases in this step to help the solution process. How this and other combinations help this process is explained in the following chapters.

4. Combining X-ray powder diffraction data with HRTEM images

Data from high-resolution electron microscopy images can be supplied to the *Focus* and *pCF* algorithms in several different ways. For example, a structure envelope for a zeolite derived from one or more HRTEM images can be imposed in real space to limit the peak search in *Focus* or to set the electron density in the pore regions to zero in *pCF*. It is also possible to include all phases obtained from HRTEM images in the starting phase set in either program. Although it would be possible to keep these phases fixed, experience has shown that it is more prudent to allow them to change during the normal procedure, whether in *Focus* or *pCF*, to allow any incorrect phases to correct themselves. However, in *pCF*, it is critical that they be fixed for the initial 10-20% of the cycles if they are to be effective. A further option is to use an approximate or partial model that has been deduced from HRTEM images as a seed for generating sets of complete starting phase sets.

Different combinations of these options eventually led to the determination of the three most complex zeolite structures using powder diffraction data (TNU-9 [24], IM-5 [25] and SSZ-74 [26]). The relevant aspects of these structure solutions are given in the following sections to illustrate the procedure. Although all three are zeolites, only the first was solved using the zeolite-specific program *Focus*. The more generally applicable *pCF* algorithm was used for the other two, and the concepts applied in all three cases should be readily transferable to non-zeolite materials.

TNU-9

The first true test of the value of including phases in the *Focus* input was performed in the structure solution of the high-silica zeolite TNU-9 [24]. It's high-resolution synchrotron powder diffraction pattern could be indexed (*C*2/*m*, a = 28.2219 Å, b = 20.0123 Å, c = 19.4926 Å, β = 92.33°), but there were a few unindexed peaks, so

SAED data were used to confirm the unit cell. However, attempts to solve the structure with *Focus* using the powder diffraction data alone were not successful. From three high-quality HRTEM images of TNU-9 (along the [010], [001] and [$\bar{1}10$] zone axes), the phases of 258 reflections were estimated using the *CRISP* software package. Only when these phases were included in the *Focus* input along with a structure envelope to describe the pore system, could the structure, with 24 Si and 52 O atoms in the asymmetric unit, be solved.

IM-5

In the case of IM-5 [25], another high-silica zeolite, a slightly different approach was used. As for TNU-9, impurities were present, so SAED experiments were performed to verify the unit cell (*Cmcm*, a = 14.299 Å, b = 57.413 Å and c = 20.143 Å). Initially, the phases of 95 reflections were estimated from three HRTEM images (along the [100], [010] and [001] zone axes) and included in *pCF* runs, but the resulting electron density maps could not be interpreted on an atomic level. After careful corrections to the HRTEM images, a 3-dimensional potential map was generated in the space group *C*2*cm* and a model with 36 Si atoms in the asymmetric unit deduced. Although this structural model was geometrically strained and its calculated powder pattern did not fit the measured one very well, it was reasoned that it was probably at least partially correct (certainly more so than a random structure). Therefore it was used as a seed to generate 1000 different starting phase sets for 1000 *pCF* runs. To do this, the phase of each structure factor calculated from the geometrically optimized model was varied by up to 25% in a random manner. The 1000 electron density maps resulting from these *pCF* runs were symmetry averaged assuming the space group *C*2*cm*, and then the best five were combined. Interpretation of this map was almost trivial: 35 of the 36 Si atoms and 61 of the 79 O atoms could be located directly in the strongest 106 peaks. The position of the missing Si atom was derived from the positions of the four surrounding Si atoms and the missing bridging O atoms were added. Rietveld refinement of this model revealed that it could be described in the higher space group *Cmcm* with 24 Si atoms in the asymmetric unit. These HRTEM images of IM-5 were later used to test the limits of electron crystallography. By careful analysis, it proved to be possible to derive the positions of the 24 Si atoms from the HRTEM data alone (Sun *et al*., 2010).

SSZ-74

The *pCF* approach was also applied to synchrotron powder diffraction data collected on the high-silica zeolite SSZ-74 [26]. In this case, no impurities were present and the pattern could be indexed with confidence with a monoclinic unit cell (*C*2/*c* or *Cc*, a = 20.514 Å, b = 13.395 Å, c = 20.097 Å, β = 102.2˚). Unfortunately, only one HRTEM image of relatively low resolution was available, and only 29 structure factor amplitudes and phases could be derived from it. These were used to construct a

structure envelope that could be imposed in real space in the *pCF* algorithm to eliminate any electron density in the pores.

The best electron density maps generated from a series of *pCF* runs were examined by eye. Those judged to have realistic pores and at least a partial framework structure were averaged, and then used as a seed within the *Superflip* program to generate 100 new starting phase sets in a manner analogous to that used for IM-5 (but with a map in this case rather than a model). The ten best maps from these runs were then averaged, and the framework structure could be recognized easily. The space group symmetry had to be reduced to *Cc*, and the final structure, with 23 Si atoms in the asymmetric unit, proved to be a most unusual one with ordered Si vacancies.

5. Combining X-ray powder with precession electron diffraction data

Although it is readily apparent that HRTEM images can be extremely useful in the structure determination process, they are not always easy to obtain, especially if the sample is beam sensitive. To circumvent this problem, Xie *et al.* [27] investigated the possibility of using the less demanding precession electron diffraction (PED) technique in place of HRTEM. While PED and X-ray powder diffraction data have been used in combination by Dorset [28] to solve and refine the structure of the zeolite ZSM-10, in that case, the structure was solved from the PED data and then refined with the X-ray data. The question here is whether or not the two sets of data can be combined to facilitate structure solution. Two approaches have been developed: (1) PED data are used to identify weak reflections, and (2) PED data are used to estimate the phases of the reflections in the projection. Both strategies proved to have a significant and beneficial effect on the structure solution process. To keep things simple, the structure factors derived from the PED patterns were calculated assuming kinematical scattering and no geometric corrections were applied.

Weak reflection elimination

Although the scattering factors for X-rays and electrons are not identical, they do show the same general trend, so reflections that are weak in the electron diffraction pattern should also be weak in the corresponding X-ray diffraction pattern. Thus, if those reflections are eliminated during the X-ray intensity extraction process, the intensities of the remaining reflections in an overlap group should be better estimated (see Figure 1).

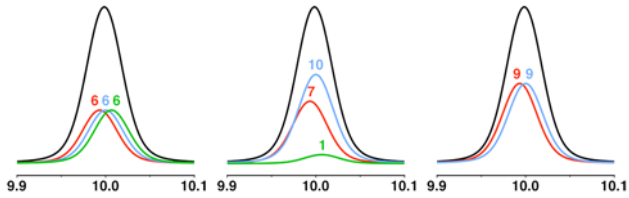

Fig. 1. The effect of weak reflection elimination on intensity extraction. The true intensities of three reflections (10, 7, 1) under a single peak are shown in the center. On the left is a conventional equipartitioning (6, 6, 6), and on the right, equipartitioning after the weak reflection has been eliminated (9, 9, 0).

Tests on the zeolite ZSM-5 (*Pnma*; $a = 20.022$Å, $b = 19.899$Å, $c = 13.383$Å) using just four projections ([010], $[01\bar{2}]$, $[02\bar{1}]$ and $[10\bar{1}]$ with a total of 594 reflections) showed that the electron density map generated by *pCF* with intensities derived using this weak reflection elimination (WRE) procedure improved significantly. Of the 3042 reflections in the powder diffraction pattern, 412 were defined to be weak and eliminated from the intensity extraction procedure. With the new set of intensities, the best maps produced by the powder charge flipping algorithm matched the correct one much better. The agreement factor R_{map}, which compares the *pCF* map with a reference map calculated from the true structure, decreased from over 55% without WRE to less than 25%.

Phase retrieval from PED data using charge flipping

Precession electron diffraction data have already been used in combination with direct methods and maximum entropy methods to determine two-dimensional structures [13-15]. This is an indication that the reflection intensities are reliable enough and have sufficient resolution for the phasing process to succeed. For three-dimensional structures, of course, a single projection is insufficient to solve the structure, but the phases for selected projections can be used in combination with X-ray powder diffraction data in the same way as those derived from 2-dimensional electron microscopy images.

Xie *et al*. [26] used the single-crystal charge-flipping algorithm implemented in the program *Superflip* [22] to estimate the phases. Using the same PED patterns for ZSM-5 as for the weak reflection elimination study, 100 charge-flipping runs were performed on each of the four two-dimensional datasets (289 reflections for [010], 162 for $[01\bar{2}]$, 124 for $[02\bar{1}]$ and 246 for $[10\bar{1}]$). The resolution for each of these datasets was *ca.* 0.8 Å.

For each projection, the five maps with the best *Superflip R*-values were averaged. Then a Fourier transform was applied to calculate the phases of the corresponding reflections. Even though the symmetry of the map at this stage was *P*1, the space group symmetry was imposed for this transformation to ensure that only phases consistent with a centrosymmetric space group were obtained. The total amplitude that

was correctly phased was more than 70% for each of the four zones. This number compares well with that obtained for the phases derived from HRTEM images.

Combining weak reflection elimination and phase retrieval.
It is to be expected that the combination of weak reflection elimination and phase retrieval will further improve the changes for a successful structure determination. This was tested with PED data recorded for the zeolite TNU-9. Five PED patterns were used to eliminate 323 reflections and to derive 176 phases. The best map showed the positions of 23 of the 24 Si atoms in the asymmetric unit and many of the O atoms. By "recycling" this map in a second series of *pCF* runs, more realistic electron densities for Si and O atoms were obtained and all 24 Si atom positions could be located.

6. Combining X-ray powder with selected area electron diffraction data

Selected area electron diffraction patterns can also be used to advantage in conjunction with X-ray powder diffraction. Not only can the unit cell dimensions be verified, but the intensities can also be used if sufficient care has been taken in recording them. In the case of the zeolite ITQ-26 (*I*4/*mmm*, a = 26.7769(8) Å, c = 13.2505(5) Å), Dorset *et al*. [29] used 41 and 17 SAED intensities taken along the [001] and [100] directions, respectively, as input to the maximum entropy program MICE [30] to produce low resolution electrostatic potential maps. These were not sufficiently detailed to allow direct interpretation, but could be used to screen the framework structures generated by *Focus* from the X-ray powder diffraction data.
Sun *et al*. [31] used SAED data in a somewhat different way to solve the structure of the germanosilicate zeolite ITQ-37 ($P4_132$, a = 26.5126(3) Å). Because the unit cell is cubic and rather large, many symmetry-unrelated reflections overlap exactly in the powder pattern (e.g. 511 and 333). SAED patterns were recorded along the [100], [110], [111] and [120] directions and their intensities extracted using the program *ELD* [32]. To get a better estimate of the relative intensities of the reflections in the overlap groups, the ratios of the corresponding SAED intensities were used to prepartition them. This improved set of intensities was then used as input for *Superflip*, and the resulting electron density maps could be interpreted in a straightforward manner.

7. Conclusions

The combination of X-ray powder diffraction and electron microscopy techniques is a powerful one for the determination of the structures of polycrystalline materials that resist solution by more conventional methods. Crystallographic phase information obtained from high-resolution electron microscopy images or from precession electron diffraction patterns has proven to be particularly useful. The powder dif-

fraction structure determination programs *Focus* and *pCF*, both of which operate in both direct and reciprocal space, use the phase information in the critical early stages of the structure solution procedure. Electron diffraction data, whether recorded using the conventional selected area or the newer precession technique, can also be exploited to get a better estimation of the relative intensities of overlapping reflections. By combining data from these two different sources, several complex zeolite structures have been solved. The concepts used for these zeolite structure solutions are generally applicable, and can also be applied to other classes of materials, whose structures cannot be solved by more traditional methods.

References

[1] David, W. I. F. and Shankland, K., Structure determination from powder diffraction data, *Acta Crystallogr. A*, 64, pp. 52-64 (2008), and references therein

[2] Dorset, D. L., *Structural Electron Crystallography*, Plenum Press, New York, (1995).

[3] Zou, X. D. and Hovmöller, S., Electron crystallography: imaging and single-crystal diffraction from powders, *Acta Crystallogr. A*, 64, pp.149-160 (2008).

[4] David, W.I.F., Shankland, K., McCusker, L.B. and Baerlocher, Ch., eds., *Structure Determination from Powder Diffraction Data*, OUP: Oxford (2002).

[5] Baerlocher, Ch. and McCusker, L.B., eds., Structure determination from powder diffraction data, *Z. Kristallogr. Special Issue*, 219, pp. 782-901, (2004).

[6] Miller, R., DeTitta, G. T., Jones, R., Langs, D. A., Weeks, C. M. and Hauptman, H. A. (1993). On the application of the minimal principle to solve unknown structures, *Science*, 259, pp. 1430

[7] Oszlányi, G. and Sütő, A. (2008). *Ab initio* structure solution by charge flipping, *Acta Crystallogr. A*, 64, pp. 123-134

[8] Grosse-Kunstleve, R. W., McCusker, L. B. and Baerlocher, Ch. (1997). Powder diffraction data and chemical information cmbined in an automated structure determination procedure for zeolites *J. Appl. Crystallogr.*, 30, pp. 985-995.

[9] Brenner, S., McCusker L. B. and Baerlocher, Ch. (1997). Using a structure envelope to facilitate structure solution from powder diffraction data, *J. Appl. Crystallogr.*, 30, pp. 1167-1172.

[10] Brenner, S., McCusker, L B and Baerlocher, Ch. (2002). The application of structure envelopes in structure determination from powder diffraction data, *J. Appl. Crystallogr.*, 235, pp. 243-252.

[11] Vincent, R. and Midgley, P.A. (1994). Double conical beam-rocking system for measurement of integrated electron diffraction intensities, *Ultramicroscopy*, 53, pp. 271-282

[12] Oleynikov, P., Hovmöller , S. and Zou, X. D. (2007). Precession electron diffraction: observed and calculated intensities, *Ultramicroscopy*, 107, pp. 523-533.

[13] Weirich, T. E., Portillo, J., Cox, G., Hibst, H. and Nicolopoulos, S. (2006). *Ab initio* determination of the framework structure of the heavy-metal oxide $Cs_xNb_{2.54}W_{2.46}O_{14}$ from 100 kV precession electron diffraction data, *Ultramicroscopy*, 106, pp. 164-175

[14] Dorset, D. L., Gilmore, C. J., Jorda, J. L. and Nicolopoulos, S. (2007). Direct electron crystallographic determination of zeolite zonal structures, *Ultramicroscopy*, 107, pp. 462-473.

[15] Gilmore, C. J., Dong, W. and Dorset, D. L. (2008a). Solving the crystal structures of zeolites using electron diffraction data. I. The use of potential-density histograms, *Acta Crystallogr. A*, 64, pp. 284-294. Gilmore, C. J., Dong, W. and Dorset, D. L. (2008b). Solving the crystal structures of zeolites using electron diffraction data. II. Density-building functions, *Acta Crystallogr. A*, 64, pp. 295-302.

[16] Boullay, P., Dorcet, V., Perez, O., Grygiel, C., Prellier, W., Mercey, B. and Hervieu, M. (2009). Structure determination of a brownmillerite $Ca_2Co_2O_5$ thin film by precession electron diffraction, *Phys. Rev. B*., 79, pp. 184108-1-184108-8.

[17] Hovmöller, S. (1992). CRISP: crystallographic image processing on a personal computer, *Ultramicroscopy*, 41, pp.121-135.

[18] Baerlocher, Ch., McCusker, L. B. and Palatinus, L. (2007). Charge flipping combined with histogram matching to solve complex crystal structures from powder diffraction data, *Z. Kristallogr*., 222, pp. 47-53.

[19] Palatinus, L. and Chapuis, G. (2007). SUPERFLIP - a computer program for the solution of crystal structures by charge flipping in arbitrary dimensions, *J. Appl. Crystallogr.*, 40, pp. 786-790.

[20] Corma, A., Rey, F., Valencia, S., Jorda, J. L. and Rius, J. (2003). A zeolite with interconnected 8- 10- and 12-ring pores and its unique catalytic selectivity, *Nature Mater*., 2, 493-497.
[21] Gramm, F. (2007). Kombination von Transmissions-Elektronenmikroskopie mit Pulver-Beugungsdaten zur Lösung von komplexen Zeolith-Strukturen, *Ph.D. Thesis*, ETH Zurich, Switzerland.
[22] Oszlányi, G. and Sütő, A. (2004). *Ab initio* structure solution by charge flipping, *Acta Crystallogr. A*, 60, pp. 134-141. Oszlányi, G. and Sütő, A. (2005). *Ab initio* structure solution by charge flipping II. Use of weak reflections, *Acta Crystallogr. A*, 61, pp. 147-152.
[23] Zhang, K. Y. J. and Main, P. (1990). Histogram matching as a new density modification technique for phase refinement and extension of protein molecules, *Acta Crystallogr. A*, 46, pp. 41-46.
[24] Gramm, F. Baerlocher, Ch., McCusker, L B., Warrender, S. J., Wright, P. A., Han, B., Hong, S. B., Liu, Z., Ohsuna, T. and Terasaki, O. (2006). Complex zeolite structure solved by combining powder diffraction and electron microscopy, *Nature*, 444, pp. 79-81.
[25] Baerlocher, Ch., Gramm, F., Massüger, L., McCusker, L.B., He, Z., Hovmöller, S. and Zou, X. (2007). Structure of the polycrystalline zeolite catalyst IM-5 solved by enhanced charge flipping, *Science*, 315, pp. 1113-1116.
[26] Baerlocher, Ch., Xie, D., McCusker, L. B., Hwang, S.-J., Chan, I. Y., Ong, K., Burton, A. W. and Zones, S. I. (2008). Ordered silicon vacancies in the framework structure of the zeolite catalyst SSZ-74, *Nature Mater.*, 7, pp. 631-635.
[27] Xie, D., Baerlocher Ch. and McCusker, L. B. (2008). Combining precession electron diffraction data with X-ray powder diffraction data to facilitate structure solution, *J. Appl. Crystallogr.*, 41, pp. 1115-1121.
[28] Dorset, D.L. (2006). The crystal structure of ZSM-10, a powder X-ray and electron diffraction study, Z. Kristallogr., 221, 260-265.
[29] Dorset, D. L., Strohmaier, K. G., Kliewer, C. E., Corma, A., Diaz-Cabanas, M. J., Rey, F. and Gilmore C. J. (2008). *Chem. Mater*., 20, 5325-5331.
[30] Gilmore, C., Dong, W. and Bricogne, G. (1999). A multisolution method of phase determination by combined maximization of entropy and likelihood. VI. The use of error-correcting codes as a source of phase permutation and their application to the phase problem in powder, electron and macromolecular crystallography, *Acta Crystallogr. A*, 55, pp. 70-83.
[31] Sun, J., Bonneau, C., Cantín, Á., Corma, A., Díaz-Cabañas, M. J., Moliner, M., Zhang, D., Li, M. and Zou, X. (2009). The ITQ-37 mesoporous chiral zeolite, *Nature*, 458, 1154-1158.
[32] Zou, X. D., Sukharev, Y. and Hovmöller, S. (1993). Quantitative measurement of intensities from electron diffraction patterns for structure determination - new features in the program system

Powder diffraction + Computational Methods

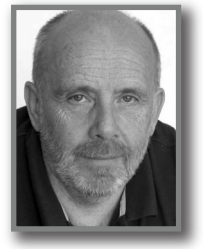

Ľubomír Smrčok
Institute of Inorganic Chemistry, Slovak Academy of Sciences, Bratislava, Slovak Republic

Abstract. It is proposed that application of computational methods provides an attractive route towards structures, whose accuracy is well-comparable to that typical for single crystal standards. Although theoretical calculations and powder diffraction seemingly represent completely disjunctive sets, it is demonstrated that they could meet at three stages of structure analysis from powders – initial model building, structure refinement and crystal chemical analysis.

Introduction

A restricted amount of structural information extractable from a powder diffraction pattern strongly limits the accuracy of structural data resulting from Rietveld refinement, which usually follows a structure solution step. If the information content of a powder pattern is insufficient and we are, this reality notwithstanding, interested in accurate structure, it is time to turn out our attention to other methods of refinement. Basically, there are two possible routes. The first one, introducing various improvements to the Rietveld method is the subject of other contributions to this School. In this place we will focus on the second direction and will point to the advantages of symbiosis of powder diffraction with several types of theoretical (quantum chemistry) calculations. Although theoretical calculations and powder diffraction seemingly represent completely disjunctive sets, we will show how they could meet at three stages of structure analysis from powders – initial model building, structure refinement and crystal chemical analysis based on the refined parameters.

Molecular calculations

The first occasion a crystallographer comes across a theoretical calculation during structure solution is, as a rule, preparatory step dedicated to building of a structural model to be used in *i*) a future structure solution in the direct space, or *ii*) for geometrical analysis of electron density maxima obtained by a calculation in reciprocal space. Seen from the quantum chemistry side "a model building" corresponds to optimization of the geometry of a molecule, starting either from a very approximate outline based on a combination of the fragments taken from a choice of databases, or even on the oracle nicknamed chemical intuition.
In case of organic molecules one is normally satisfied with relatively simple quantum chemistry molecular calculation, frequently referred to as “calculations in vacuum”. Both terms are equivalent and in fact only emphasize the fact, that the

geometry of the subject is not influenced by its environment. Such calculations can be easily accomplished by any standard quantum chemistry package (Gaussian, Turbomole, Gamess, NWChem, ADF, etc.…) as this path is the most used and hence the best tuned and debugged. For simple organic compounds reasonable results are normally obtained at DFT level of theory by making use of one from the family of hybrid functionals (e.g. B3LYP) combined with the split valence ("Popple") basis sets augmented by diffuse and polarization functions. For example, the 6-31+G* basis (the symbol stands for the basic 6-31G basis augmented with polarization denoted by * and diffuse functions denoted by +) will provide satisfactory results in the vast majority of the cases (Cramer, 2002; Szabo and Ostlund, 1989).

It should be however noted, that optimization of a flexible molecular geometry under the absence of any "environment" ("external field") is likely to provide the values of torsional angles disagreeing with the values obtained in the subsequent structure solution and refinement. If the differences are striking, one should, before accusing any of the method of its total or partial malfunction, carefully evaluate the impact of the external field and/or of formation of intra- and intermolecular hydrogen bonds. In any case, the shape of a flexible molecule ought to be optimized also during the direct space structure solution, of course only if the accuracy of the experimental data permits. A word of warning: semiempirical methods belonging to the NDO group (CNDO, INDO, MNDO, AM1,PM3,…) though fast, are known not giving very accurate molecular geometries.

While preparing the building blocks of a future organic structure usually does not pose any important problem worth explicitly mentioning, this need not be the case for metal-organic or inorganic compounds. Geometry of a representative cluster (a polyhedron) of the atoms (a central atom of a transition metal surrounded by medium sized organic ligands or water, for instance) playing the role of "molecule" can be to a certain degree influenced by a spin state of a transition metal.

Furthermore, presence of very heavy atoms in the structure could call for application of so called Effective Core Pseudopotential (ECP) in place of the basis functions approximating the inner (core) shells of the atoms. This approach not only saves the computational time due to the reduction of dimensionality of the problem, but modern relativistic pseudopotentials also take care about the important part of relativistic effect, which plays non-negligible role for atoms beyond the first transition metal row. Note that when using an ECP, the valence parts of the basis functions of all atoms in the molecule should be consistent and one is discouraged from mixing of principally different types of bases.

Solid state calculations

Inasmuch as structure solution process usually provides only approximate positions of atoms, an improvement of their accuracy is desirable. Standard "powder" refinements nowadays almost exclusively rely on a few variants of Rietveld idea,

that the parameters of a function approximating the diffraction profiles can be refined by a non-linear weighted least-squares procedure simultaneously with the atomic parameters. Due to the notorious problems with accurate and cheap description of powder diffraction profiles, with instrumental and sample effects and in particular with a low number of structure factors compared to the number of refined atomic parameters, the accuracy of the resulting structures is, more often than not, markedly inferior to that typical for the current single crystal standards. Although several improvements of this procedure have been already proposed (restrained and rigid body refinements, just among others; see e.g. Immirzi, 2009; Afonine et al., 2009 and the references cited therein), the problem with a low number of uncorrelated/inaccurate structure factors persists. As the elements of the Jacobian matrix related in Rietveld method to structural parameters are calculated considering the structure factors and not the individual profile intensities, any bias in the former is involuntarily transferred to the accuracy of the refined atomic parameters. In reality, accuracy of any powder refinement is smaller or at maximum identical to the accuracy of a single crystal refinement based on the same numbers of independently collected structure factors and refined parameters. Unfortunately, in a common practice this is the ideal point never reachable as the accuracy of structure factors from a powder pattern is always lower, especially due to overlap of the individual diffractions caused by collapse of 3D diffraction pattern to 1D or due to various sample effects.

A remedy to the chronic difficulty of standard powder refinements, which is the aforementioned lack of information extractable from a powder pattern, could be structure optimization by energy minimization in the solid state. If we (for the lack of space) restrict ourselves only to the solid-state DFT methods, we realize that the size of problems tractable on a laboratory computer nowadays reaches ~1000 atoms per unit cell - in dependence on the level of approximation used by the concrete computational method. This number greatly exceed the widely accepted limits for powder refinements, which frequently fail in providing accurate results even for the structures with much, much smaller numbers of atoms. Moreover, since theoretical calculations are frequently done in the *P*1 space group, simultaneous optimization of the geometries of possibly symmetrically equivalent units within a unit cell provides a good measure of internal consistency of structure optimization and/or solution. The main "crystallographic" advantage of this approach is that all atoms in a structure are on equal footing, i.e. not weighted by their scattering abilities. For organic structures (in fact, not only for them) it implies direct access to accurate geometry of hydrogen bonds, whose knowledge is in good deal of cases essential for understanding of physicochemical properties of a compound. Secondly, a shape of the molecule or of a fragment (polyhedron) in an "inorganic" structure is further optimized under the constraints imposed by a crystal field. Last but not least, by exploiting the resulting wavefunction several interesting quantities like electronic or

vibrational densities of states, distribution of the electron density in a crystal, stress tensors, etc. are easily accessible. The approach to handling of lattice parameters is twofold. Either they are refined in advance e.g. by LeBail technique and kept fixed in the course of optimization of the atomic coordinates, or their values are refined along with the atomic coordinates. Validity of both these approaches has been a subject of long discussions with many pros and cons. In short, the main argument of the "pros" group is that, that without the cell parameters "the optimized structure is not in the minimum" (...of total energy), while the second group proclaims that the accuracy of the lattice parameters obtained from a crystallographic experiment is as a rule much more accurate than that of those obtained by energy minimization and there is hence no need to make it worse.

Such a combined approach to powder structure solution and refinement was to our best knowledge pioneered by Dinnebier et al. (2001) in their study of a rigid ferrocene-based macrocycle, $C_{48}H_{44}B_4Fe_2N_8O_4$, crystallizing in a relatively large monoclinic ($C2/c$) cell (V=4152.8Å^3). In order to decrease the number of the optimized atom coordinates the calculation was done in the reduced cell with $V/2$. The initial structure models were generated by Monte Carlo method using the synchrotron data and the atomic coordinates were refined by energy minimization in the solid state. Refined structures were put to Rietveld refinement and the profile parameters were improved, while keeping the atomic coordinates fixed. This study was soon followed by the structure solution followed by the refinement by crystal energy minimization of the red polymorph of tetrahexylsexitiophene (Neumann et al., 2002). The powder pattern was collected with a laboratory diffractometer and the structure solved by Monte Carlo technique. Nearly identical solution in the space groups $C2/m$, $C2$ and P-1 were found, of which the first was at last chosen.

Since then, two different attitudes to co-existence of classic crystallographic Rietveld refinement and the refinement by crystal energy minimization have developed. The first and the more frequently used, gives more weight to standard Rietveld refinement and uses theoretical calculation only to refine positions of hydrogen atoms and/or for "validation" of a refined structure (see for example Bhattacharya et al., 2010, Brodski et al., 2004; Das et al., 2011; Kaduk, 2002a,b; 2004; Kaduk et al., 2010; Withfield et al., 2008, 2010). The second approach, on the contrary, is based on the presumption that it is unlikely that Rietveld refinement with all atoms relaxed can provide sufficiently accurate structural data for the structures built from more than few atoms. Rietveld refinement is therefore used only for estimation of isotropic displacement parameters and/or selected "profile" parameters, like preferred orientation correction (e.g. Florence et al., 2009; Jorík et al, 2008; Smrčok et al., 2007, 2008, 2009a, 2009b, 2010). Like the first approach, also the second has been successfully applied to both organic, metal-organic and inorganic compounds. Note, however, that the lists of the papers belonging to any of these groups are not claimed to be complete and the author apologizes for omissions.

The requirements for successful application of energy minimization in structure refinement are however stricter than those typical for a standard Rietveld refinement. First of all, the model must be complete, i.e. no dangling bonds resulting from omission of atoms (intentional or accidental) are allowed. Partial occupancies of atomic positions are not possible and must be modeled by a supercell simulating distribution of atoms and vacancies. The optimization path could depend on the initial configuration, as the optimization of atomic coordinates by energy minimization is not, in spite of his robustness, the method of global minima. Fortunately, in case of a configuration being rather far from a reasonable minimum, its accuracy can be improved by molecular dynamics approach. A way towards improvement of resulting accuracy is application of d-DFT method (e.g. van de Streek and Neumann, 2010). This pragmatic approach may, however, bring unwanted variability into energy calculations, unless the empirical correction terms ("d") are rigorously defined.

Although there is a variety of computer programs for theoretical calculation in the solid state available, two of them are probably at the leading edge: CASTEP (Milman et al, 2010) and VASP (Hafner, 2000)[1]. Both these codes employ pseudopotentials to approximate the inner (core) shells of atoms and plane waves as a basis set describing the valence charge density. In spite of the effort invested to construction of pseudopotentials of various flavors, the user should always carefully consider their quality, especially when dealing with the atoms from the opposite corners of the periodic table in one structure. Plane waves in place of the basis set have for the solid state calculations several advantages over the localized basis functions typical for molecular calculations. Using FFT procedure one can calculate the electronic structure using plane-waves basis set in reciprocal rather than in the direct space, making the calculation less computationally demanding. A good beginner's guide to the art of solid state calculations is provided in the review paper by Gillan (1997).

Post-optimization calculations

The last stage where theory meets experiment is post-optimization applications of theoretical methods not only for the molecules (fragments) cut from a structure, but also for "bulk". These applications are not by any means any by-products and require each a special attention. The first group in principle employs very similar methods as those used at the model building stage, but calculation of some derived quantities require a higher accuracy of the calculations and hence larger basis sets or even a higher level of theory. A very typical post-optimization application is detailed analysis of hydrogen bonds geometry including calculation of the relevant binding energies or vibration analysis. The next widely accepted "chemical" application,

[1] Because it is not the role of this contribution to provide a comprehensive list of all the approaches and of the relevant computer codes, a reader is asked to visit e.g. http://www.psi-k.org/codes.shtml.

which can prove useful especially when comparing properties of a series of structurally similar compounds, is estimation of the atomic charges followed by calculation of the dipole moment and, optionally, of its components. Sadly, importance of the atomic charges is in many cases overestimated and obvious arbitrariness in their calculation frequently ignored. Projected densities of electronic states obtained from a calculation in the solid state provide a good picture of bonding conditions in a crystal and are frequently correlated to the selected physical properties. Calculated vibrational densities of states can aid interpretation of vibrational (IR, Raman, INS) spectra by revealing significance of the individual modes.

Quite a prominent chemical application calculated at the molecular level is Natural Bond Orbitals (NBO) method, which transforms a given wave function into a localized form, corresponding to the one-center ("lone pairs") and two-center ("bonds") elements of the chemist's Lewis structure picture. In NBO analysis, the input atomic orbital basis set is transformed via natural atomic orbitals (NAOs) into natural bond orbitals (NBOs). Resulting NBOs correspond to the image, in which two-center bonds and lone pairs are localized (Reed et al., 1988; Weinhold and Landis, 2005). Examples of application of NBO in interpretation of the variations in bond distances in the crystal structures is e.g. in Smrčok et al. (2007) or in Langer et al. (2009). In the second case also the concept of inequivalent hybridization (Bent, 1961) was applied to explain variations in some bond angles in the aminoethylene substituent attached to flourophenyl from their expected ideal values. Another nice example of symbiosis of crystallography, though here single-crystal, and theoretical calculations is a combined structure solution of $[Ag_{26}In_{18}S_{36}C_{l6}(dppm)_{10}(thf)_4]$ $[InCl_4(thf)]_2$ (Ahlrichs et al., 2004). Although the structure was solved from X-ray single crystal data, the assignment of several atom positions solely on the basis of X-ray analysis was impossible due to close scattering factors of the pairs Ag/In and S/Cl and very similar bond lengths for Ag-S and In-S. The correct assignment was found by molecular DFT/TZVPP calculation.

Acknowledgement

This contribution was partially supported by Slovak Grant Agency VEGA under the contract 2/0150/09. My thanks are to P.Mach for his critical reading of a draft of the text and also to R.Skorczyk, whom I have never met, but whose paper (Skorczyk, 1976) has many years ago triggered my interest in the field of the solid state calculations.

References

Afonine, P.V, Grosse-Kunstleve, R.W., Urzhumtsev, A., Adams, P.D.: Automatic multiple-zone rigid-body refinement with a large convergence radius. Journal of Applied Crystallography 42:607–615 (2009)

Ahlrichs, R., Eichhőfer, A., Fenske, D., Hampe, O., Kappes, M.M., Nava, P., Olkowska-Oetzel, J.: Synthesis and structure of $[Ag_{26}In_{18}S_{36}C_{l6}(dppm)_{10}(thf)_4]$ $[InCl_4(thf)]_2$ – a combined approach of theory and experiment. Angewandte Chemie – International Edition 43:3823-3827 (2004)

Bhattacharya, A., Kankanala, K., Pal, S., Mukherjee, A.K. :A nimesulide derivative with potential anti-inflammatory activity: Synthesis, X-ray powder structure analysis and DFT study. Journal of Molecular Structure 975:40–46 (2010)

Bent, H.A.: An appraisal of valence-bond structures and hybridization in compounds of the first-row elements. Chemical Reviews 61:276–311 (1961)

Brodski, V., Peschar, R., Schenk, H., Brinkmann, A., Van Eck, E.R.H., Kentgens, A.P.M. , Coussens, B., Braam, A.: Structure of melaminium dihydrogenpyrophosphate and its formation from melaminium dihydrogenphosphate studied with powder diffraction data, solid-state NMR, and theoretical calculations. Journal of Physical Chemistry B108:15069-15076 (2004)

Cramer, C.J. Essentials of computational chemistry. John Wiley and Sons, Ltd. Baffins Lane, Chichester, West Sussex, PO19 1UD, England (2002).

Das, U., Chattopadhyay, B., Mukherjee, M., Mukherjee, A.K.:Crystal structure and electronic properties of three phenylpropionic acid derivatives: A combined X-ray powder diffraction and quantum mechanical study. Chemical Physics Letters 501:351–357 (2011)

Dinnebier, R.E., Ding, L., Kuangbiao, M., Neumann, M.A., Tanpipat, N., Leusen, F.J.L., Stephens, P.W., Wagner, M.: Crystal structure of a rigd ferocene-based macrocycle from high-resolution X-ray powder diffraction. Organometallics 20:5642–5647 (2001)

Florence, A.J., Bardin, J., Johnston, B., Shankland, N., Griffin, T.A.N., Shankland, K.: Structure determination from powder data: Mogul and CASTEP. Zeitschrift für Kristallographie Suppl. 30:215–220 (2009)

Gillan, M.J.: The virtual matter laboratory. Contemporary Physics 38:115–130 (1997)

Hafner, J.: Atomic-scale computational materials science. Acta Materialia 48:71:92 (2000)

Immirzi, A.: Constraints and restraints in crystal structure analysis. Journal of Applied Crystallography 42:362–364 (2009)

Jorík, V., Scholtzová, E., Segl'a, P.: Combined powder diffraction and solid-state DFT study of [Cu(2,6-dimethoxynicotinate)(2)(mu-ronicol)(2)](n) complex. Zeitschrift für Kristallographie 223:524-529 (2008)

Kaduk, J.A.: Terephthalate salts of dipositive cations. Acta Crystallographica B58:815–822 (2002a)

Kaduk, J.A.: Aromatic carboxylate salts. terephthalates Transactions of American Crystallographic Association 63–84 (2002b)

Kaduk, J.A.: Crystal structure of guaifenesin, 3-.2-methoxyphenoxy.-1,2-propanediol. Powder Diffraction 19:127–132 (2004)

Kaduk, J.A.., Toft, M.A., Golab, J.T.: Crystal structure of antimony oxalate hydroxide, $Sb(C_2O_4)OH$. Powder Diffraction 25:19–24 (2010)

Langer, V., Mach, P., Smrčok, Ľ., Milata, V.: (E)-Methyl 2-[(2-flourophenyl) aminomethylene- 3-oxobutanoate: X-ray and density functional (DFT) study. Acta Crystallographica C65:o183–o185 (2009)

Milman, V., Refson, K. , Clark, S.J., Pickard, C.J., Yates, J.R. , Gao, S.-P., Hasnip, P.J., Probert, M.I.J. , Perlov, A., Segall, M.D.: Electron and vibrational spectroscopies using DFT, plane waves and pseudopotentials: CASTEP implementation. Journal of Molecular Structure: THEOCHEM 954:22-35 (2010).

Neumann, M.A., Tedesco, C., Destri, S., Ferro, D.R., Porzio, W.:Bridging the gap – structure determination of the red polymprph of tetrahexylsexithiophene by Monte Carlo simulated annealing, first-principles DFT calculations and Rietveld refinement. Journal of Applied Crystallography 35:296–303 (2002)

Reed, A.E., Curtiss, L.A., Weinhold, F.: Intermolecular interactions from a Natural Bond Orbital, donor-acceptor viewpoint. Chemical Reviews 88:899–926 (1988)

Skorczyk, R.: The calculation of crystal energies as an aid in structural chemistry. I. A semi-empirical potential field model with atomic constants as parameters. Acta Crystallographica A32:447–452 (1976)

Smrčok, Ľ., Jorík, V., Scholtzová, E., Milata, V.: Ab initio structure determination of 5-anilinomethylene-2,2-dimethyl-1,3-dioxane-4,6-dione from laboratory powder data - a combined use of X-ray, molecular and solid-state DFT study. Acta Crystallographica B63:477–484 (2007)

Smrčok, Ľ., Brunelli, M., Boča, M., Kucharík, M.: Structure of K_2TaF_7 at 993 K: the combined use of synchrotron powder data and solid-state DFT calculations. Journal of Applied Crystallography 41:634–636 (2008)

Smrčok, Ľ., Bitschnau. B., Filinchuk, Y.: Low temperature powder diffraction and DFT solid state computational study of hydrogen bonding in NH_4VO_3. Crystal Research and Technology 44:978–984 (2009a)

Smrčok, Ľ., Kucharík, M., Tovar, M., Žižak, I.: High temperature powder diffraction and solid state DFT study of beta-cryolite (Na_3AlF_6). Crystal Research and Technology 44:834–840 (2009b)
Smrčok, Ľ., Černý, R., Boča, M., Macková. I., Kubíková, B.: K_3TaF_8 from laboratory X-ray powder data. Acta Crystallographica C66:I16–I18 (2010)
Streek, van de, J. Neumann, M.A.: Validation of experimental molecular crystal structures with dispersion-corrected density functional theory of calculations. Acta Crystallographica B66:544-558 (2010)
Szabo, A., Ostlund, N.S.: Modern Quantum Chemistry: Introduction to Advanced Electronic Structure Theory. McGraw-Hill (Tx); Revised edition. (1989)
Weinhold, F., Landis, C.: Valency and Bonding. A Natural Bond Orbital Donor-Acceptor Perspective. Cambridge University Press, Cambridge, New York, Madrid, Cape Town, Singapore, Sao Paulo (2005)
Whitfield, P.S., Le Page, Y., Davidson, I.J.: *Ab initio* structure determination of the low twmperature phase of succinonitrile from X-ray powder diffraction data – coping with potential poor quality using DFT *ab initio* methods. Powder Diffraction 23:292–299 (2008)
Whitfield, P.S., Mitchell, L.D., Le page, Y., Margeson, J., Roberts, A.C.: Crystal structure of the mineral strontiodresserite from laboratory powder diffraction data. Powder Diffraction 25:322–328 (2010)

Information on Imperfections

Matteo Leoni
University of Trento, Department of Materials Engineering and Industrial Technologies, Trento, Italy

Abstract. Line Profile Analysis is the common name given to those methods allowing microstructure information to be extracted from the breadth and shape of the peaks in a diffraction pattern. A fast analysis is always possible via traditional techniques such as the Scherrer formula, Williamson-Hall plot and Warren-Averbach method, but at the expenses of the physical meaning of the result. A more sound alternative is offered by the Whole Powder Pattern Modelling, allowing physical information to be extracted from diffraction data in a self-consistent way.

Introduction

Nanostructured materials are still a hot topic in current research. An obvious choice for the analysis of the microstructure of such systems would be microscopy, as the sub-nm resolution can be easily achieved on last generation Transmission Electron Microscopes (TEMs) and Scanning Probe Microscopes (SPMs). However, obvious does not always mean better. SPMs mainly provide morphological information, whereas the TEM, albeit accessing morphology and microstructure information, is limited to the analysis of a few grains, a too small range to guarantee a good statistical significance of the measurements.

A possible alternative is certainly offered by indirect methods such as powder diffraction. The microstructure information is contained, highly integrated, in a single powder diffraction pattern: already at the beginning of last century, in fact, it was observed a close relationship between e.g. the breadth of a diffraction peak and the microstructure of the scattering domains. In the years, several techniques have been proposed for the so-called Line Profile Analysis (LPA), mainly grouped into two broad classes characterised by a totally different approach to the problem:

- pattern decomposition (PD) i.e. fitting of the individual peaks in the pattern using some bell-shaped function and *a posteriori* analysis of the parameters of the fit
- pattern modelling (PM) i.e. fitting of a set of microstructure models to the entire diffraction pattern.

Most of the traditional techniques of LPA, still widely employed by the scientific community, fall in the first category. They are e.g. the well known Scherrer formula (SF), Williamson-Hall (WH) plot and Warren-Averbach (WA) method [1-8].

They all pretend to give some microstructure information under the form of *average domain size* and *microstrain*: in most practical cases, however, the true meaning of

those terms and the theory behind those methods are highly overlooked. Pattern modelling is the modern answer to most of the limitation of traditional LPA. The information provided e.g. by the Whole Powder Pattern Modelling [9-11] is in fact tightly bound to the physics of the material (e.g. a domain size distribution is refined, and a quantitative account of the sources of microstrain is given) and the model is refined directly on the data for full consistency. A brief account for traditional and advanced models is here given. For further details, an extensive account is provided in the old and recent literature [5,6,12-15].

Integral breadth methods

Scherrer formula relates the Full-Width at Half-Maximum (FWMH) of a diffraction peak in Bragg position $2\theta_B$ with a so-called *average crystallite size* $\langle D \rangle$. To render the approach independent of the actual shape of the $\{hkl\}$ peak, the FWHM is usually replaced with the so-called Integral Breadth (IB) $\beta_{\{hkl\}}$ i.e. the ratio between peak area and peak maximum. With this definition, SF reads:

$$\beta_{\{hkl\}}(2\theta) = \lambda K_\beta \Big/ \left(\langle D \rangle \cos\theta_{\{hkl\}} \right) \qquad (0.1)$$

where λ is the wavelength, K_β is the so-called Scherrer constant for the given shape and $\theta_{\{hkl\}}$ is Bragg angle. In reciprocal space, we can analogously write $\beta_{\{hkl\}}(d^*) = K_\beta / \langle D \rangle$ being d^* the reciprocal space variable. The Scherrer constant in eq. (0.1) can be calculated for any given domain shape and in general depends on *hkl* (see e.g. [8]).

The meaning of the *average crystallite size* obtained from the SF is not obvious. In fact, applying the idea of Bertaut [16,17], $\langle D \rangle$ is an average of the length of the columns in which the shape can be subdivided along the scattering direction. Therefore it does not represent the average size of a physical object, the quantity of usual interest. For non-spherical sizes, the average crystallite size depends on the *hkl* and the same value can be obtained with different shapes.

In order to compare the broadening corresponding to different directions and try to increase the level of information that can be extracted, Williamson and Hall [2] proposed to plot the FWHM or the IB in reciprocal space. For an isotropic domain (direction-independent size), this plot is expected to be constant in reciprocal space. An increase in the integral breadth with the distance from the origin of the reciprocal space is observed, and the following model is employed:

$$\beta(d^*) = K_\beta \Big/ \langle D \rangle + 2 \cdot \left\langle \varepsilon^2 \right\rangle^{1/2} \cdot d^* \qquad (0.2)$$

being the combination of Scherrer formula with the differential of Bragg's law. The first term in (0.2) is again named *average crystallite size* (extrapolation of the integral breadth to the origin of the reciprocal space), whereas the second is the so-

called *microstrain* or *root mean strain*. The true meaning of this approach and of the corresponding results is seldom considered.
In fact, even if the WH formalism seems straightforward, there is no physical reason for summing the two contributions up. As breadths are additive only for Lorentzians, the Williamson-Hall formalism is strictly valid only for Lorentzian peaks, condition seldom met in practice. Alternatives have been proposed to cover all Gauss/Lorentz-type combinations [18,19], being complete from a mathematical point of view but poor from a physical one.
The meaning of the size term in eq. (0.2) is that of the Scherrer formula. In the real case of polydispersed domains, the *average crystallite size* provided by the SF and WH plot is different from the first moment of the size distribution. If we assume a certain shape for the domains, we can see that this size is in fact the ratio between two high order moments of the size distribution [20].
Quoting the result of the SF or WH as "average size" may thus lead to confusion or misinterpretation.
The microstrain contribution is quite an abstract concept as it provides an evidence for the presence of defects, but it does not identify their source. It should also be borne in mind that the microstrain term accounts for the breadth of the local strain distribution: should the microstrain be constant or average to a non-zero value, a residual strain (leading to shift in peak position) would be present.

Fourier methods
A first step towards the use of the full information contained in a diffraction peak was the introduction of the Warren-Averbach method [3-6], the father of all Fourier methods of LPA. If $x = s - s_{\{hkl\}}$ is the distance in reciprocal space with respect to Bragg position $s_{\{hkl\}}$, then the peak profile $h(x)$ in the powder diffraction pattern of a polycrystalline material results from the folding of an instrumental profile $g(x)$ with sample-related effects $f(x)$ (microstructure) [5,6]:

$$h(x) = \int f(x)\, g(y-x)\, dy = f(x) \otimes g(x) \qquad (0.3)$$

The Fourier Transform (FT) allows an easier handling of this expression: the convolution theorem, in fact, states that the FT of a convolution can be obtained as the product of the Fourier transforms of the functions to be folded. In synthesis:

$$H(L) = FT\left[h(x)\right] = FT\left[f(x)\right] \cdot FT\left[g(x)\right] \qquad (0.4)$$

where L is the variable conjugate to x. The original h(x) function can be obtained by inverse Fourier transform of $H(L)$. In traditional Fourier methods, the $f(x)$ is obtained by inverting equation (0.4) and is further split into size ($A^S(L)$) and a strain or distortion ($A^D(L)$) components:

$$C(L) = FT\left[f(x)\right] = FT\left[h(x)\right] / FT\left[g(x)\right] = A^S(L)\,A^D(L) \qquad (0.5)$$

The separation becomes trivial if size effects are considered as isotropic and thus independent of the diffraction order (true for spherical domains). Strain effects, in fact, depend on the diffraction order (and thus the reciprocal space variable) and can be expressed, in a first order approximation, as: $A^D(L) = \langle \cos 2\pi L n \varepsilon_L \rangle = 1 - 2\pi^2 L^2 n^2 \langle \varepsilon_L^2 \rangle$ where ε_L is the strain averaged over the length L. A suitable plot of $\ln(FT[f(x)]) = \ln(A^S(L)) + \ln(A^D(L))$ as a function of n^2 is the practical tool for Warren-Averbach analysis. A size term, with meaning similar to that of the SF, can be obtained in this case by taking the intercept of the initial slope of $A^S(L)$ [5]. The chain of operations leading to the result is quite long and several approximations are made: the consistency between data and result cannot be readily verified.
A few extensions of the WA method have been proposed. In the Multiple Whole Profile Fitting (MWP) [21,22], for instance, simple models for the size and strain terms $A^S(L)$ and $A^D(L)$ are fitted to the Fourier coefficients extracted from the experimental data. Arbitrary data pre-processing is necessary to separate the peaks and to extract their Fourier transform. Even if transforms of multiple peaks are simultaneously used, the method is nowadays scarcely employed, as fitting in Fourier space leads to results that cannot be easily checked on the measured data.

Whole Powder Pattern Modelling

A leap forward in LPA was the introduction of reciprocal-space full pattern techniques such as the Whole Powder Pattern Fitting (WPPF) [9,23-25] and the Whole Powder Pattern Modelling (WPPM) [9-11,20,23-45] or variants of it [21,22,46-48]. In those techniques, model parameters are directly refined on the entire pattern as in the Pawley [49] and Rietveld methods (RM [50-52]). We can somehow consider the WPPM as the dual of the Rietveld method as they have common bases, but complementary targets: structural refinement in RM, microstructural refinement in WPPM. The major differences lay in the generation of the peak profiles (Fourier plus reciprocal space in WPPM, angular in the RM) and in the treatment of the peak shape (peaks from microstructure models in WPPM, and Williamson-Hall or effective models in the RM).
Using some microstructure model in the Rietveld method to improve the fit and to extract extra information is certainly an advancement over traditional LPA, as the whole pattern is employed. The structural constraint on peak intensities can however pose serious problems, as it can bias the microstructure extraction. It would be ideal to model structure and microstructure simultaneously, but it is advised to perform the microstructure studies with the least degree of biasing to correctly take into account the subtle features of each profile.
The WPPM starts from the Fourier approach of eq. (0.3) and (contrary to traditional methods) works in a convolutive way. Each peak in the pattern is built as:

$$I_{hkl}\left(s-s_{hkl}\right)=k\left(s\right)h\left(s-s_{hkl}\right)=k\left(s\right)\int C(L)\,\mathrm{e}^{2\pi iL\cdot\left(s-s_{hkl}\right)}\,dL \qquad (0.6)$$

where $k(s)$ groups all geometrical and structural factor that are constant or known functions of s (e.g., structure factor, Lorentz-polarization factor). This equation is not fully general, as it implicitly assumes that the broadening contributions act on the entire $\{hkl\}$ reflection family and thus that a multiplicity term (included in $k(s)$) can be used. Certain defects (e.g. faults), can however act independently on each member of the reflection family, leading to:

$$I_{\{hkl\}}\left(s-s_{\{hkl\}}\right)=\sum_{hkl}w_{hkl}I_{hkl}\left(s-s_{\{hkl\}}-\delta_{hkl}\right) \qquad (0.7)$$

where w_{hkl} is a weight function, $(s - s_{\{hkl\}} - \delta_{\mathrm{hkl}}) = (x - \delta_{\mathrm{hkl}})$ is the reciprocal-space distance from the centroid of the (hkl) component and δ_{hkl} is the shift from the reciprocal-space point $s_{\{hkl\}}$ corresponding to the Bragg position in the absence of defects. The sum in eq. (0.7) is over independent profile sub-components, selected on the basis of the specific defects (e.g. 4 for {111} when faults are present in the *fcc* case: selection is based on the value of h+k+l that can be ±3 or ±1).
The whole pattern is synthesised as sum of peaks obtained by means of eq. (0.6) and (0.7) plus background and aberrations. The desired parameters are then refined by fitting the model to the measured data using a nonlinear least squares routine. Full consistency between data and model is thus preserved.
Any broadening contribution can enter the convolution chain and can therefore be included in eq. (0.6). The most common broadening sources in a real case are certainly those related to the non-ideal nature of the instrument, the finite size of the coherently diffracting domain (size effect) and to the presence of defects such as e.g. dislocations and faults. Taking this into account, the $C(L)$ reads:

$$C\left(L\right)=T^{IP}\left(L\right)A_{hkl}^{S}\left(L\right)\left\langle \mathrm{e}^{2\pi i\cdot\psi_{hkl}(L)}\right\rangle \left\langle \mathrm{e}^{2\pi i\cdot\phi_{hkl}(L)}\right\rangle \qquad (0.8)$$

where $T^{IP}(L)$ and $A^{S}{}_{hkl}$ are the FT of the instrumental profile (IP) and domain size components, respectively, and the terms in brackets (<>) are average phase factors related to lattice distortions (ψ) and faulting (ϕ). A plug and play behaviour is thus envisaged: new broadening sources can be considered by including the corresponding complex FT in the product of equation (0.8). Expressions are available for a wide selection of cases of practical interest [10-15,20,23-35,53,54] including a size distribution of domains with given shape, the effects of dislocations and stacking faults, grain surface relaxation, antiphase boundaries, distribution of cell parameters, just to cite some. The method is conveniently implemented in a flexible and freely available software [31] allowing the analysis of X-rays, synchrotron, neutron or electron diffraction patterns.

A warning should be given here: the physical bases of the approach should always be considered. The WPPM is certainly valid if the broadening sources are diluted and independent, i.e. if the correlation between defects can be neglected. If this does not apply, then cross terms start playing a role: errors can arise if this is not properly done and therefore the WPPM needs being revised. For example, in the case of extended faulting and heavy interaction between structure and microstructure, a possible alternative to traditional models has been proposed in [55].

Example of analysis

The analysis of a nanocrystalline ceria specimen produced by sol-gel (details are given in [36]) is proposed using traditional and advanced techniques of LPA. The diffraction pattern collected on a laboratory instrument over ca. 24h is shown in fig. 1.1a. TEM shows spherical domains with a distribution of diameters approximately lognormal (cf. bar plot in fig. 1.1b, evaluated on 800 isolated grains [36]).

The application of Scherrer formula to the most intense {111} peak is proposed in fig. 1.1c: no fitting, no background and no peak overlapping were considered. From the FWHM of the peak, it is possible to estimate an average $<D>/K_\beta$ of 5.8 nm. The actual size value depends on the Scherrer constant K_β and therefore on the domain shape.

To improve the result, all peaks were simultaneously fitted using pseudo-Voigt functions, properly considering the instrumental profile contribution. The corresponding IB was employed for the WH analysis (cf. Figure 1.1d). Linear fitting leads to $\beta(d^*) = 0.019 + 0.008d^*$. Despite the clear presence of a microstrain ($<\varepsilon^2>^{1/2} = 0.004$), the size is 5.3 nm, i.e. smaller than the SF result. This is a caveat that instrumental effects *must* always be considered in the analysis.

Residual anisotropic broadening is clear in the WH plot (errors are small and points do not lie on the line), and can be ascribed to the presence of dislocations. The WPPM analysis was conducted assuming the presence of a lognormal distribution of spherical domains (compatible with TEM) and of dislocations. The modelled pattern is shown in fig. 1.1a together with the experimental data: the residual is flat and the GoF is close to 1 [36], witnessing the perfect match of data and model.

The resulting WPPM size distribution is proposed in fig. 1.1b superimposed to the TEM result. The mean size is 4.4 nm, quite far from SF and WH results. A better agreement (3.98 nm) is obtained if the correcting factor ¾ (valid of a lognormal distribution of spheres [20]) is applied to the WH result to extract the first moment of the distribution. What is clear, however, is that or a well behaving specimen (narrow monomodal distribution), the breadth of the peaks gives at least an order of magnitude estimate of the size. Considering that CeO_2 is a ceramic, a high dislocations density is also obtained (1.4×10^{16} m^{-2}): the value corresponds to ca. 1 dislocation every few grains, in agreement with TEM observations [26].

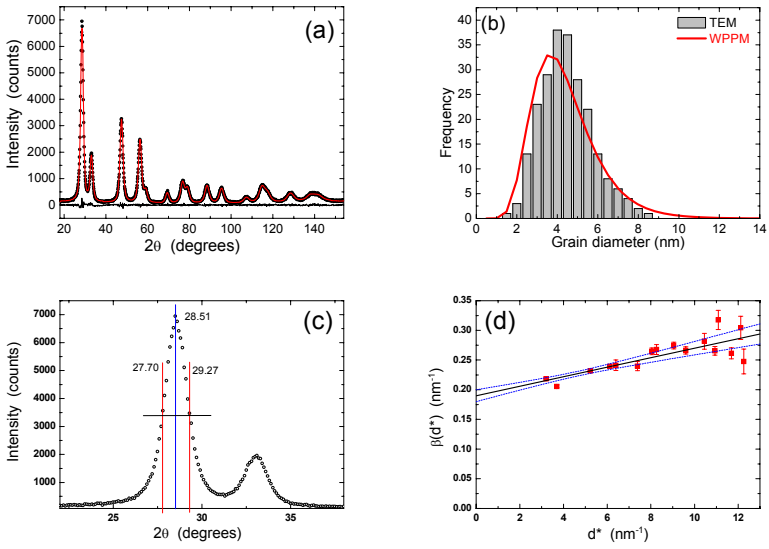

Fig. 1. (a) Experimental pattern (dots), WPPM result (line) and difference curve (line below). Comparison between TEM and WPPM size distributions is proposed in (b). The analysis using Scherrer formula and Williamson-Hall plot are shown in (c) and (d) respectively.

A final word should be dedicated to the number of parameters employed in the analysis: excluding Scherrer formula, clearly inappropriate here, the WH plot involved the use of 67 parameters (4 parameters for each of the 16 peaks +3 for the background). Conversely just 26 were necessary for the WPPM (16 intensities, 1 cell parameter, 2 size, 3 dislocations, 3 background, 1 specimen displacement). A higher quality result is thus obtained with less model parameters, further suggesting that modern LPA methods are mature enough for a more frequent use.

Acknowledgments The author wish to thank prof. P. Scardi for continuous support, critical reading and useful discussions. The PM2K software implementing the WPPM method and the DIFFaX+ code for the analysis of systems with heavy faulting are both available on request from the author. A free license is granted for academic and non-profit use.

References

[1] Scherrer P.: Bestimmung der Grösse und der inneren Struktur von Kolloidteilchen mittels Röntgenstrahlen. Nachr. Ges. Wiss. Göttingen. **26 September**, 98-100 (1918)
[2] Williamson G.K., Hall W.H.: X-ray line broadening from filed aluminium and wolfram. Acta Metall. **1**, 22-31 (1953)
[3] Warren B.E., Averbach B.L.: The effect of cold-work distortion on X-ray patterns. J. Appl. Phys. **21**, 595-600 (1950)
[4] Warren B.E., Averbach B.L.: The separation cold-work distortion and particle size broadening in X-ray patterns. J. Appl. Phys. **23**, 497-512 (1952)
[5] Warren B.E.: X-ray Diffraction. Addison-Wesley, Reading, MS (1969)
[6] Klug H.P., Alexander L.E.: X-ray Diffraction Procedures for Polycrystalline and Amorphous Materials, 2nd ed. Wiley, New York (1974)
[7] Langford J.I., Louër D.: Powder diffraction. Rep. Prog. Phys. **59**, 131-234 (1996)
[8] Langford J.I., Wilson A.J.C.: Scherrer after sixty years: A survey and some new results in the determination of crys-

tallite size. J. Appl. Cryst. **11**, 102-113 (1978)
[9] Scardi P., Leoni M., Dong Y.H.: Whole diffraction pattern-fitting of polycrystalline fcc materials based on microstructure. Eur. Phys. J. B **18**, 23-30 (2000)
[10] Scardi P., Leoni M.: Whole Powder Pattern Modelling: theory and application, in: Diffraction Analysis of the Microstructure of Materials, edited by Mittemeijer E. J. & Scardi P., Springer-Verlag, Berlin. p. 51-91 (2004)
[11] Scardi P., Leoni M.: Whole powder pattern modelling. Acta Cryst. A **58**, 190-200 (2002)
[12] Snyder R.L., Fiala J., Bunge H.J. (eds.): Microstructure Analysis from Diffraction. Oxford University Press, Oxford (1999)
[13] Mittemeijer E. J., Scardi P. (eds.): Diffraction Analysis of the Microstructure of Materials, Springer-Verlag, Berlin (2004)
[14] Guagliardi A., Masciocchi N. (eds.): Diffraction at the nanoscale. Nanocrystals, defective & amorphous materials. Insubria University Press, Como (2010)
[15] Scardi P., Dinnebier R. (eds.): Extending the Reach of Powder Diffraction Modelling. Trans Tech Publications Ltd, Zurich (2010)
[16] Bertaut E.F.: X-ray study of the distribution of crystallite dimensions in a crystalline powder [in French]. CR Acad. Sci. Paris **228**, 492-494 (1949)
[17] Bertaut E.F.: Raies de Debye-Scherrer et répartition des dimensions des domaines de Bragg dans les poudres polycristallines. Acta Cryst. **3**, 14-18 (1950)
[18] Scardi P., Leoni M., Delhez R.: Line-broadening analysis using integral breadth methods: a critical review. J. Appl. Cryst. **37**, 381-390 (2004)
[19] Balzar, D.: Voigt-function model in diffraction line-broadening analysis in: Microstructure Analysis from Diffraction, edited by Snyder R.L., Fiala J., Bunge H.J., Oxford University Press, Oxford (1999)
[20] Scardi P., Leoni M.: Diffraction line profiles from polydisperse crystalline systems. Acta Cryst. A **57**, 604-613 (2001)
[21] Ungár T., Gubicza J., Ribárik G., and Borbély A.: Crystallite size distribution and dislocation structure determined by diffraction profile analysis: principles and practical application to cubic and hexagonal crystals. J. Appl. Cryst. **34**, 298-310 (2001)
[22] Ribárik G.: Modeling of diffraction patterns properties, PhD thesis, Eötvös University, Budapest (2008)
[23] Scardi P., Dong Y.H., Leoni M.: Line profile analysis in the Rietveld method and whole-powder-pattern fitting. Mat. Sci. Forum **378-381**, 132-139 (2001)
[24] Scardi P.: Profile Modelling versus Profile Fitting in Powder Diffraction. Z. Kristallogr. **217**, 420-421 (2002)
[25] Scardi P., Leoni M.: Line profile analysis: pattern modelling versus profile fitting. J. Appl. Cryst. **39**, 24-31 (2006)
[26] Leoni M.. Scardi P.: Surface Relaxation Effects in Nanocrystalline Powders, in: Diffraction Analysis of the Microstructure of Materials, edited by Mittemeijer E.J. & Scardi P., Springer-Verlag, Berlin. p. 413-454 (2004)
[27] M. Leoni: Grain surface relaxation and grain interaction in powder diffraction. Mat. Sci. Forum **443-444**, 1-10 (2004)
[28] Scardi P., Leoni M.: Diffraction whole-pattern modelling for the study of anti-phase domains in Cu_3Au. Acta Mater. **53**, 5229-5239 (2005)
[29] Leoni M., Scardi P.: Nanocrystalline domain size distributions from powder diffraction data. J. Appl. Cryst. **37**, 629-634 (2004)
[30] Armstrong N., Leoni M., Scardi P.: Some considerations concerning Wilkens' theory of dislocation line-broadening. Z. Kristallogr. Suppl. **23**, 81-86 (2006)
[31] Leoni M., Confente T., Scardi P.: PM2K: a flexible program implementing Whole Powder Pattern Modelling. Z. Kristallogr. Suppl. **23**, 249-254 (2006)
[32] Scardi P., Leoni M., Faber J.: Diffraction line profile from a disperse system: a simple alternative to Voigtian profiles. Powder Diffraction **21**, 270-277 (2006)
[33] Leoni M., Martinez-Garcia J., Scardi P.: Dislocation effects in powder diffraction. J. Appl. Cryst. **40**, 719-724 (2007)
[34] Estevez-Rams E., Leoni M., Scardi P., Aragon-Fernandez B., Fuess H.: On the powder diffraction pattern of crystals with stacking faults. Phil. Mag. 83 [36], 4045-4057 (2003)
[35] Martinez-Garcia J., Leoni M., Scardi P.: A general approach for determining the diffraction contrast factor of straight-line dislocations. Acta Cryst. A **65**, 109-119 (2009)
[36] Leoni M., Di Maggio R., Polizzi S., Scardi P.: An X-ray diffraction methodology for the microstructural analysis of nanocrystalline powders: application to cerium oxide. J. Am. Ceram. Soc. **87**, 1133-1140 (2004)
[37] Scardi P.: Microstructure and lattice defects in highly deformed metals by X-ray Diffraction Whole Powder Pattern Modelling. Z. Metall. **96**, 698-702 (2005)
[38] De Giudici G., Biddau R., D'Incau M., Leoni M., Scardi P.: Reactivity of nanocristalline fluorite powders: defect density threshold. Geochimica et Cosmochimica Acta **69** [16], 4073-4083 (2005)

[39] Scardi P., Leoni M., Lamas D.G., Cabanillas E.D.: Grain size distribution of nanocrystalline systems. Powder Diffraction **20** [4]. 353-358 (2005)
[40] Leoni M., De Giudici G., Biddau R., D'Incau M., Scardi P.: Analysis of polydisperse ball-milled fluorite powders using a full pattern technique. Z. Kristallogr. Suppl. **23**, 111-116 (2006)
[41] Scardi P., Leoni M., D'Incau M.: Whole Powder Pattern Modelling of cubic metal powders deformed by high energy milling. Z. Kristallogr. **222**, 129-135 (2007)
[42] Scardi P., Leoni M., Straffelini G., De Giudici G.: Microstructure of Cu-Be alloy triboxidative wear debris. Acta Mater. **55**, 2531-2538 (2007)
[43] Scardi P., D'Incau M., Leoni M.: Full pattern methods for the analysis of plastically deformed materials. Solid State Phenomena **130**, 27-32 (2007)
[44] D'Incau M., Leoni M., Scardi P.: High energy grinding of FeMo powders. J. Mat. Research **22**, 1744-1753 (2007).
[45] Pesenti H., Leoni M., Scardi P.: XRD Line Profile Analysis of calcite powders produced by high energy milling. Z. Kristallogr. Suppl. **27**, 143-150 (2008)
[46] Ungár T.: Microstructure Parameters from X-ray Diffraction Peak Broadening. Scripta Mater. **51**, 777-781 (2004)
[47] Ribárik G., Gubicza J., Ungár T.: Correlation between strength and microstructure of ball-milled Al–Mg alloys determined by X-ray diffraction. Mat. Sci. Eng. A **387-389**, 343–347 (2004)
[48] Balogh L., Ribárik G., Ungár T.: Stacking faults and twin boundaries in *fcc* crystals determined by X-ray diffraction profile analysis. J. Appl. Phys. **100**, 023512 (2006)
[49] Pawley G.S.: Unit-cell refinement from powder diffraction scans. J. Appl. Cryst. **14**, 357-361 (1981)
[50] Rietveld H.M.: Line profiles of neutron powder-diffraction peaks for structure refinement. Acta Cryst. **22**, 151-152 (1967)
[51] Rietveld H.M.: A profile refinement method for nuclear and magnetic structures. J. Appl. Cryst. **2**, 65-71 (1969)
[52] Young R.A. (ed.): The Rietveld Method. Oxford University Press, Oxford (1993)
[53] Leineweber A., Mittemeijer E.J.: Diffraction line broadening due to lattice-parameter variations caused by a spatially varying scalar variable: its orientation dependence caused by locally varying nitrogen content in ε-$FeN_{0.433}$. J. Appl. Cryst. **37**, 123-135 (2004)
[54] van Berkum J.G.M.: Strain Fields in Crystalline Materials, PhD Thesis, Technische Universiteit Delft, Delft, The Netherlands (1994)
[55] Leoni M., Gualtieri A., Roveri N.: Simultaneous refinement of structure and microstructure of layered materials. J. Appl. Cryst. **37**, 166-173 (2004)

Characterization of the microstructure in random and textured polycrystals and single crystals by diffraction line profile analysis

Tamás Ungár and Gábor Ribárik

Department of Materials Physics, Eötvös University Budapest, Hungary

Abstract

X-ray or neutron diffraction patterns are simulated by convoluting defect specific profile functions based on continuum theory of elasticity. The defect related profile functions are controlled by the physically mandatory minimum number of parameters: the dislocation density, ρ, the dislocation arrangement parameter, M, one or more parameters describing strain anisotropy where their number depends on the crystal symmetry, the median, m and the logarithmic variance, σ of the log-normal size distribution function, and finally the density of stacking faults, α or the frequency of twin boundaries, β. These parameters are, at the same time, among the most relevant physical parameters describing the microstructure of crystalline materials. The theoretical diffraction patterns are produced by the convolution of the defect related, physically based profile functions in the "extended Convolutional Multiple Whole Profile" (eCMWP) software package. The usage of the software package is demonstrated by the microstructure determination in randomly-textured and textured polycrystalline and single crystals specimens of different materials.

Keywords: *dislocation structure, planar defects, texture, strain anisotropy, X-ray line broadening*

1. Introduction

Line profile analysis is an indirect method for determining the microstructure of crystalline materials. In that sense it can be considered as the counterpart of the different electron microscopy methods which in turn are fundamentally imaging procedures. Despite the indirect nature of line profile analysis it proves to be a valuable and powerful method providing information complementary about several microstructure properties. In the present work the basic principles of line profile analysis are summarized and the practical use of the software package, the extended Convolutional Multiple Whole Profile (eCMWP) method is presented [1-4]. The program is freely accessible via: http://www.renyi.hu/cmwp. After an easy registration the latest version can be downloaded or it can be used interactively through a web frontend. The software package allows to evaluate different diffraction patterns measured on different crystalline materials: powders, bulk polycrystals, single crystalline samples or textured specimens. The different parts of the software package offer different ways of the evaluation which can be optimally adapted to the particular problem. For example, in the case of single crystals, the individual diffraction profiles of different Bragg reflections can be analyzed in terms of individual dislocation contrast factors. Or, in the case of an ideally random powder specimen, the whole measured powder pattern can be evaluated with the same philosophy as the structure refinement by the Rietveld method. In this case the whole

measured pattern is fitted by a theoretically constructed diffraction pattern which is expressed in terms of dislocation structures by average dislocation contrast factors, crystallite size and size-distribution functions and densities of different planar defects. The theoretical diffraction patterns are constructed by different defect related profile functions. Strain profiles are derived for dislocated crystals by using the theoretical results of Krivoglaz [5], Wilkens [6] and Groma [7]. Size profiles are calculated by using fundamental optical principles [8] and the concept of column length [9]. Size distribution is taken into account by assuming the log-normal size distribution density function [10]. The profiles of planar defects are shown to be the sum of symmetrical and anti-symmetrical Lorentzian functions [3,4,11-13]. The defect related profile functions derived on the basis of well established physical principles are given by the absolutely necessary, fewest possible number of parameters. These parameters are used for matching the theoretically constructed diffraction pattern with the measured diffraction spectrum in the extended convolutional multiple whole profile (eCMWP) procedure [1-4]. The principles of constructing the defect related profile functions and fundamentals of the application of the eCMWP method are discussed by presenting a few typical examples, along with the accuracy and reliability of the values of the physical parameters provided by the software package.

2. The principles of line profile analysis based on defect related profile functions

The method of line profile analysis discussed here is a *bottom-up* approach. The correct interpretation of diffraction line profile analysis is substantiated, when possible, by the simultaneous application of imaging and other physical methods, especially transmission and scanning electron microscopy, TEM and SEM, and electrical resistivity and different calorimetric methods. The defects are classified according to the type of lattice distortion or lattice imperfection they produce.

Microstrain, which is heterogeneous on the length scale of atomic distances, is produced by one-dimensional linear defects and is described by the mean square strain $\langle\varepsilon^2\rangle$ [5-7]. The prototype of such defects are dislocations, but non-equilibrium triple junctions of grain boundaries are also of this type of defects. The corresponding profile function, I^D_{hkl}, is given by its Fourier transform (FT) [6]:

$$\mathrm{FT}(I^D_{hkl}) = A^D_{hkl} = \exp(-2\pi^2 g^2 L^2 \langle\varepsilon_{g,L}{}^2\rangle) = \exp[-\rho \left(\frac{\pi b}{2}\right)^2 g^2 C L^2 f(\eta)] \,, \qquad (1)$$

where ρ, b and C are the density, the absolute value of the Burgers vector and the contrast factor of dislocations, respectively. g is the absolute value of the diffraction vector, $|g|=2\sin\theta_B/\lambda$ (θ_B is the Bragg angle and λ wavelength of the radiation), L is Fourier variable, $f(\eta)$ is the L dependence of $\langle\varepsilon^2\rangle$ for linear lattice defects, especially dislocations, and $\eta=L/R_e$, where R_e is the effective outer cut-off radius of dislocations. Since the value of R_e depends on the actual value of the dislocation density, Wilkens introduced a dimensionless parameter, M for characterizing the effective outer cut-off radius of dislocations [6]:

$$M = R_e\sqrt{\rho} \quad . \qquad (2)$$

For randomly distributed dislocations M is larger than unity and the tails of the strain profiles decay relatively fast, the profiles are closer to "bell-shape" or Gaussian functions. For narrow dislocation dipoles M is smaller than unity and the strain profiles have long tails, the profiles are closer to Lorentzian shape functions. It is noted here, in accordance with the fact that the

functional form of strain profiles varies with the dipole character of dislocations, that the strain profiles are usually neither of Gaussian nor of Lorentzian and nor of pseudo-Voigtian functions. But, they are the inverse Fourier transform of A^D_{hkl}, which is a function of the number density and the arrangement parameter of dislocations: ρ and M, i.e. $A^D_{hkl}=A^D_{hkl}(\rho,M)$. It is noted further that for dislocated crystals the mean square strain is a function of both, g and L [6]:

$$\langle\varepsilon_{g,L}^2\rangle=(b/2\pi)^2\pi\rho Cf(\eta), \quad (3)$$

where the g dependence is within the dislocation contrast factors C [6,8]. This functional nature of $\langle\varepsilon_{g,L}^2\rangle$ is the physical background for why it is physically not appropriate to characterize the *microstrain* by a bald number.

Size broadening is an X-ray optical effect. When the coherently scattering domains decrease the diffraction spots in reciprocal space blow up [9]. If the coherently scattering domains are equiaxed the blow-up is isotropic and therefore the corresponding line broadening is independent of the scattering order, or uniform in reciprocal space. If, however, the coherently scattering domains are oblate or elongated, or simply non-equiaxed, the blow-up in reciprocal space will become (1) *hkl* dependent and (2) anisotropic around each particular reciprocal lattice point [10,11]. Bertaut has shown that the profile of a size broadened peak is the sum of the intensities diffracted by parallel columns constituting the diffracting crystallites. These columns have unit cross sectional area are parallel to the diffracting vector [12]. The diffraction peak corresponding to one particular column is the squared Fourier transform of the form function of that column length. The size-broadened peak is the volume-weighted sum of the individual peaks corresponding to the individual columns. The *measured* size broadened peak is thus related to the area or volume weighted *column-length distribution* in the specimen. The *column-length distribution*, on the other hand, depends on the size, the shape and the size distribution of the crystallites. In order to obtain the area or volume weighted mean size of crystallites or their size-distribution specific assumptions about the shape and the size-distribution have to be made [13]. A large number of experiment has evidenced that the log-normal size distribution function, $f(x)$, given by the median m and the logarithmic variance σ, describes the size distribution of crystallites in a wide range of bulk or loose powder materials [14-17]. Another possibility would be to "fit" the size distribution of crystallites, cf. [18]. Hinds has shown that the arithmetic-, area- and volume-weighted mean crystallite diameters are [19]:

$$\langle x\rangle_{arithm}=m\exp(0.5\sigma^2)\,, \quad (4a)$$

$$\langle x\rangle_{area}=m\exp(2.5\sigma^2)\,, \quad (4b)$$

$$\langle x\rangle_{vol}=m\exp(3.5\sigma^2)\,. \quad (4c)$$

The size profile, I^S_{hkl} and its Fourier transform, A^S_{hkl} are [1,16]:

$$I^S(s)_{hkl}=\int_0^\infty M\cdot\frac{\sin^2(\pi Ms)}{2(\pi s)^2}\cdot erfc\left[\frac{\ln(M/m)}{\sqrt{2}\,\sigma}\right]dM\,, \quad (5)$$

$$A^S(L)_{hkl} \sim \frac{m^3 \exp(4.5\sigma^2)}{3} erfc\left[\frac{\ln(|L|/m)}{\sqrt{2}\,\sigma} - 1.5\sqrt{2}\sigma\right] -$$

$$- \frac{m^2 \exp(2\sigma^2)|L|}{2} erfc\left[\frac{\ln(|L|/m)}{\sqrt{2}\,\sigma} - \sqrt{2}\sigma\right] + \frac{|L|^3}{6} erfc\left[\frac{\ln(|L|/m)}{\sqrt{2}\,\sigma}\right], \quad (6)$$

where s=2sinθ/λ and *erfc* is the complementary error function.

Twin boundaries or stacking faults are infinite planar defects, at least on the atomic length scale. They are a specific type of boundary breaking down the coherency of scattering, and produce a specific type of size broadening with specific *hkl* dependence. Stacking faults, on top of that, can change the local crystal symmetry thus producing an *hkl* dependent *homogeneous* strain, where this strain is manifested by shifts of the corresponding sub-profiles [3,4,20-23]. Twin boundaries, however, do not cause peak shifts. The small peak shifts produced by twinning at relatively high densities of twin boundaries are related to the interference of overlapping Bragg reflections close to each other in reciprocal space [4]. The profile functions of twinned or stacking faulted crystals has been shown to be the sum of sub-profiles corresponding to the signed *hkl* values, where the sub-profiles are the sum of a symmetrical and anti-symmetrical Lorentzian function [3,4,22]. Based on theoretical considerations and the numerical application of the DIFFaX [23] software a numerical procedure has been developed in which the breadths and shifts of the symmetrical and anti-symmetrical Lorentzian profile functions of the sub-profiles are given by 5th order polynomials as a function of the densities of twin boundaries, β, or stacking faults, α for cubic and hexagonal crystals [3,4].

Point defects or point-defect type defects like precipitates or inclusions cause short range lattice distortions [5]. In correlation with the reciprocity between the crystal space and reciprocal space the short range distortions produce scattering at long distances from the Bragg reflections. This type of diffraction is known as Huang scattering [5,23,25]. The measurement and determination of Huang scattering is not easy because it appears together with the background scattering [26].

The *hkl* dependence of strain broadening is known as *strain anisotropy* [27-32]. The determination of dislocation types, Burgers vector populations and dislocation densities can done in line profile analysis on the basis of the dislocation model of strain anisotropy [1-4,16,17,33]. From eq. (3) it is seen that the *hkl* dependence of $\langle\varepsilon_{g,L}^2\rangle$ and the dislocation contrast factor C are identical. The strain parallel to the diffraction vector $\boldsymbol{g}$ is:

$$\varepsilon_g = \frac{\partial}{\partial\xi}(\boldsymbol{gu})/g\,, \quad (7)$$

where $\boldsymbol{u}$ is the displacement field and ξ is parallel to $\boldsymbol{g}$. For the *hkl* dependence of C the following can be written [8]:

$$C \propto \langle[\frac{\partial}{\partial\xi}(\boldsymbol{gu})/g]^2\rangle = \langle(\boldsymbol{g\beta g})^2/g^2\rangle\,, \quad (8)$$

where $\boldsymbol{\beta}=grad\mathbf{u}$ is the distortion tensor. The pointed brackets indicate averaging over the crystal volume. The above equation shows that Cg^4 is a fourth order polynomial of hkl [8]:

$$Cg^4 = P_4(hkl) \, . \tag{9}$$

In a texture free polycrystal or a powder specimen the contrast factor can be averaged over the permutations of *hkl*. For cubic and hexagonal systems the *hkl* dependence of the average contrast factors is [8]:

$$\overline{C} = A + B\mathrm{H}^2 \, , \tag{10}$$

$$\overline{C} = A' + \frac{[B'(h^2+k^2+i^2)+C'l^2]l^2}{[h^2+k^2+i^2+\frac{3}{2}(\frac{a}{c})^2 l^2]^2} \, , \tag{11}$$

where the constants A, B, A', B' and C' depend on the elastic constants of the crystal and the type of dislocations, and $H^2=(h^2k^2 + h^2l^2 + k^2l^2)/(h^2+k^2+k^2)^2$. If A or A' are non-zero the average contrast factors can be given as [16]:

$$\overline{C} = \overline{C}_{h00}(1-qH^2) \, , \tag{12}$$

$$\overline{C}_{hk.l} = \overline{C}_{hk.0} \, [1 + q_1 x + q_2 x^2] \, , \tag{13}$$

where $\overline{C}_{h00}$ and $\overline{C}_{hk.0}$ are the average contrast factor of the *h00* and *hk.0* reflections in cubic and hexagonal crystals, and $x =(2/3)(l/ga)^2$, l and a are the lattice constants of a hexagonal crystal. The q and q_1, q_2 parameters depend on the elastic constants of the crystal and the type of dislocations, and can be evaluated numerically [34,35]. In cubic crystals for screw dislocations with <001> Burgers vectors the value of A in eq. (10) is zero. In such a case eq. (12) cannot be applied [36], the evaluation has to be done by applying eq. (10).

Based on the above discussion the physically modeled diffraction pattern, $I^{PM}(2\theta)$ is:

$$I^{PM}(2\theta) = \sum_{hkl} I^S_{hkl} * I^D_{hkl} * I^{PD}_{hkl} * I^{INST}_{hkl} + I_{BG} \, , \tag{14}$$

where the defect related profile functions are the size, I^S_{hkl}, the strain I^D_{hkl} and the planar defect profiles, I^{PD}_{hkl}. The corresponding physical profile is given by convolution:

$$I^P_{hkl}(2\theta) = I^S_{hkl} * I^D_{hkl} * I^{PD}_{hkl} \, . \tag{15}$$

At the core of the eCMWP procedure the Fourier transforms of the defect related profiles are evaluated and the Fourier transform of $I^P_{hkl}(2\theta)$ is constructed as the product of these:

$$A^P_{hkl}(L) = A^S_{hkl} \cdot A^D_{hkl} \cdot A^{PD}_{hkl} \, . \tag{16}$$

The inverse Fourier transform of $A^P_{hkl}(L)$ provides $I^P_{hkl}(2\theta)$ which in eq. (14) is convoluted with the instrumental pattern, $I^{INST}_{hkl}(2\theta)$.

Two options are available to determine the background. (a) Fix points can be determined in the patterns interactively and a spline is fitted to these base-points. Once the modeled pattern has been calculated there is further option to alter the base-points. This procedure allows the adjustment of the modeled pattern and the background in a selfconsistent manner. (b) The background can also be given by Legendre polynomials where the coefficients are fitted.

The measured and physically modeled patterns are matched by the Marquard-Levenberg non-linear least squares method [1-4]. The quality of the fitting procedure can (i) either be observed visually by inspecting the differences between the measured and calculated patterns or (ii) determined quantitatively by checking the value of the "R-weighted pattern", i.e. R_{wp}, used as the definition in [37]. The R_{wp} values are also listed in the tables below.

3. Non-textured powder pattern of single phase materials: ball-milled PbS (Galena)

PbS (Galena) has the B1 NaCl structure. It is a stable mineral crystal which can be crushed into a powder with very different grain size either in a mortar or by ball milling. Depending on the grain size it appears either as shiny or as matt deep-black powder. Thanks to this property it has been widely used as the base material for different make-ups in ancient Egypt and is still in use, for the same purpose, in some Southeast Asian countries. The microstructure of laboratory specimens of PbS ball-milled and subsequently heated at different temperatures and different durations was used to trace back the fabrication technology for producing make-ups in ancient Egypt [38]. Specimens of make-up found in ancient Egyptian tombs were acquired from the museum of the Louvre in Paris, France. The dislocation densities and crystallite size-distributions were determined by line profile analysis in the archaeological and the laboratory specimens. It was concluded that most of the archaeological specimens were fabricated by gentle to not-too-strong crushing and some of the specimens were heated, but never to a higher temperature than about 3 to 400 ^{o}C [38]. The diffraction patterns were recorded at the high-resolution powder diffraction beam line of the ESRF synchrotron in Grenoble, France. Two typical diffraction patterns are shown in Fig. 1. One corresponds to a laboratory specimen ball-milled for 12 h, the other one to one of the archaeological specimens (E14455 [38]). The pattern of the archaeological specimen shows that though PdS was the major component in ancient Egyptian make-up it contained more components [39]. Fig. 2 shows the measured (open circles) pattern of the 12 h ball-milled laboratory specimen, the pattern fitted by the eCMWP method (red line) and the difference between the measured and fitted data at the bottom of the figure. The inset is an enlarged part between 2θ=27 and 35^{o}.

The diffraction patterns corresponding to the ball-milled and heat treated patterns are texture free powder patterns. The application of the eCMWP procedure is simple, it does not require any special caution. Nevertheless, the careful choice of the initial parameter values can be useful for obtaining reliable results within foreseeable short time. For example, the elastic anisotropy, i.e. $A_z=2c_{44}/(c_{11}-c_{12})$, of PbS is $A_z\cong0.31$ [40]. The corresponding value of the q parameter in eq. (12) is definitely negative. The fitting procedure can be started therefore, e.g. with q=-2. The software finds within a few steps the final values of q=-6.5 ($\pm$1). Ball milling for 12 h will probably produce submicron grain size powder with a not too narrow size distribution. This means the *m* value will be in the 100 nm range and σ, the logarithmic variance of the log-normal size distribution, will probably be between 0.5 and 1. The dislocation density is expected to be not too low, however, since PbS is a brittle ionic crystal it will probably not be as large as in metallic materials. $\rho\cong10^{14}$ m^{-2} is a good starting value. The *M* parameter is most critical since it is determined by the tail region of the diffraction

profiles. The tail regions, on the other hand, are most sensitive to the subtraction of the background. A good guide for the realistic values of the *M* parameter can be found in the actual values of the dislocation density. At dislocation densities smaller than about 10^{14} m^{-2} or larger than about 5×10^{15} m^{-2} the *M* value cannot be smaller than unity or larger than 2, respectively. These thumb rules are related to the collective behavior of dislocations which means that the dipole character is weaker or stronger at smaller or larger dislocation densities [6,41]. The physical parameter values provided by the eCMWP method for two ball-milled laboratory specimens and the E14455 archaeological specimen are listed in Table 1. The values of the dislocation densities suggest that the E14455 specimen was ball milled and heated. The crystallite size values would suggest that the E14455 specimen was in the "as-received" state. Latter, however, is very unlikely, and the $\langle x \rangle_{area}$ values of the 2 h ball-milled and heated specimens are not too far from each other. It can be concluded, therefore, that the E14455 specimen was most probably "gently crushed" and heated between 3 and 400 ^{o}C [38]. It is noted here that in [38] the evaluation was done by the multiple whole profile (MWP) [1] procedure, which is part of the eCMWP software package, and in which the instrumental effect is deconvoluted from the measured patterns. In the present work the diffraction patterns are revisited by the eCMWP method, as shown in Fig. 2 and listed in Table 1, and the physical parameter values provided by the MWP and eCMWP procedure are identical within the experimental errors.

4. Determination of planar defects

The density of planar defects was determined by the eCMWP method in Cu, Cu-10%Zn and Cu-30%Zn specimens prepared by the method of high pressure torsion (HPT) [42,43]. The diffraction experiments were carried out in a special high-resolution double-crystal diffractometer with negligible instrumental effect. The $K\alpha_2$ component of the Cu fine-focus rotating anode (Nonius, type FR 591) was selected by the symmetrical (220) reflection of the primary Ge monochromator. The cross-section of the beam on the specimen was estimated as ~0.1×0.5 mm^2. The diffraction profiles were registered the linear position-sensitive gas flow detector (OED 50 Braun, Munich). The specimen was observed by a short depth-sharpness microscope of the magnification of approximately 20× and the magnified image was inspected on a video monitor. The X-ray peak was located within an accuracy of better than 0.1 mm. The position of the specimen was located in the beam during the X-ray operation to a precision of approximately ±0.1 mm. The diffraction patterns were recorded on each specimen in three different positions: in the center of the disk, R=0, at the half-radius position, R=1/2R_o and near the edge of each disk, R=R_o, where R_o is the radius of the disc-shape specimen . The distance between the detector and specimen was selected so that the complete diffraction profiles fitted into the gauge length of 50 mm of the position-sensitive detector. With this setting the 111/200, 220, 311/222, 400 and the 331/420 profiles or profile-pairs were measured separately. Two typical diffraction patterns corresponding to the Cu-10%Zn specimen measured at the centre and the periphery are shown in Fig. 3. The open symbols are the measured intensities and the red lines are the patterns calculated by the eCMWP procedure. The qualitative features of the microstructure can be read from a typical Williamson-Hall plot of the FWHM values in Fig. 4 corresponding to the centre regions of the three investigated specimen. Note that the FWHM of the 311 reflection in the Cu-30%Zn specimen is almost equal to the 200 FWHM value. This behavior is typical for the presence of planar defects, in the present case twin boundaries. The m, σ, $\langle x \rangle_{area}$, ρ, β, q and R_{wp} values for the three specimens at the three different position are listed in Table 2.

The contribution of planar defects to line broadening is evaluated by using the parameter files corresponding either to twin boundaries, β, or to intrinsic, α_{intr} or extrinsic, α_{extr}, stacking faults, respectively. It is suggested that in the first steps the patterns are evaluated without planar defects. Once the best fits are achieved, the 3 possible planar defects can be allowed consecutively. The type of planar defect is determined by the lowest values of the weighted-sum-of-squared-residual (WSSR). For the 3 investigated specimens these values are listed for the 3 fault types in Table 2. It can be seen that in all cases the WSSR values corresponding to twin boundaries are the smallest. It is noted that if there is evidence for the concomitant presence of two or three fault types, the parameter files can be modified accordingly, as it was done in the case of twinning in hexagonal CP-Ti specimens [4].

5. Determination of the dislocation structure in textured materials

When the material is strongly textured and the different texture components may have different dislocation densities with different dislocation types, eqs. (10) to (13) do not hold, and both the experiment and the evaluation has to be conducted in a different manner as described in paragraph 3.

Polycrystalline NiAl specimens were prepared with three different major textures: <100>, <110> and <111>, respectively [44]. The samples were uniaxially compressed either under atmospheric or hydrostatic pressure. The X-ray beam and detector system was the same as described in paragraph 4. Two surfaces were cut on the specimens: one perpendicular, and one parallel to the loading direction, denoted axial- and side-case, respectively [36]. The specimens were mounted in an Eulerian cradle in order to orient the major texture component into diffraction condition for each measured reflection. This facility was used, especially for the axial-case measurements, since in the side-case the texture was almost random [44]. The Williamson-Hall plot of the FWHM values of the <100> textured specimen deformed to 6 % in compression is shown in Fig. 5. The axial and size-case plots are considerably different. In the side-case (open triangles) the 200 reflection has a large broadening in correlation that this reflection has the largest average contrast factor in NiAl. However, in the axial-case (open circles) the 200 reflection shows a much smaller broadening, indicating that these two reflections sample two different grain populations.

The evaluation is continued by considering the plastic response and the slip systems in the different texture components. The Schmid factors were evaluated and listed in Table 3 [45,46]. In the NiAl alloy with the B2 ordered structure primary slip takes place on the {110}<100> slip system, while secondary slip changes from {110}<111> to {110}<110> at about 550K coinciding with the brittle-to-ductile transition temperature. In Table 3 it can be seen that in the <100> oriented grains the most probable one is the secondary {110}<111> slip system type. In this system the Burgers vector is large, glide is difficult and TEM indicates overwhelmingly screw dislocations. In the other two grain populations all possible slip system types can be activated. Plastic deformation of the <100> oriented grains is much more difficult than the other populations, therefore the <100> and the other populations are denoted as *hard* and *soft* grains, respectively [36].

The 200 and all other reflections in the axial-case patterns correspond to two different grain populations with fundamentally different dislocation structure, therefore in this case eqs. (10) to (13) do not hold, the average dislocation contrast factors are not coupled to each other by the equation containing the fourth order invariant of *hkl*. The strain contribution in these patterns can only be evaluated by determining individual dislocation contrast factors, C_{ind}, to

each diffraction profile. The side-case patterns, however, since in this case all the grain populations are random, can still be evaluated by using the average contrast factors, as in eqs. (10) to (13). The average dislocation density is therefore determined from the side-case patterns. The eCMWP software package offers the option to evaluate the strain contribution to line broadening by assigning individual dislocation contrast factors, C_{ind}, to each diffraction profile. The measured individual dislocation contrast factors, $C_{ind,measured}$, for the 200 reflections in the axial-case patterns are: 0.151, 0.028 and 0.042 for the <100>, <110> and <111> texture specimens, respectively, where the formal dislocation density is $\rho^*=10.1\times10^{14}$ m^{-2}. In accordance with eq. (3) the formal and true dislocation densities, ρ^* and ρ, and the formal and theoretical contrast factors, C^* and C_{Th} are related as [36]:

$$\rho=\rho^* C^*/C_{Th} . \qquad (17)$$

In the <100> oriented hard grains only screw dislocations are activated in the {110}<111> slip system [45,46]. For these dislocation the theoretical contrast factors were calculated by the ANIZC freely available software [34]: C_{Th}=0.7123 [36]. With the above listed formal contrast factor values the true dislocation densities in the hard grains of the 6 % deformed samples are: 2.1, 0.4 and 0.53×10^{14} m^{-2} for the <100>, <110> and <111> texture specimens, respectively.

The dislocation types were determined from the side-case patterns by using eq. (10) instead of (12). This was necessary because for the <100> Burgers vector screw dislocations, which are an important contribution in the hard grains, the constant A in eq. (10) is zero. The strain anisotropy was analyzed in terms of Burgers vector types and it was found that in the <100> textured specimen about 10 % of the dislocations are of edge and screw mixed character with <100> Burgers vector and 90 % <111> screw dislocations: $0.1\langle100\rangle_{screw+edge}+0.9\langle111\rangle_{screw}$. In the other two textured specimens the same dislocations appear with about equal weight: $0.5\langle100\rangle_{screw+edge}+0.5\langle111\rangle_{screw}$. The volume fractions of the hard, f_{Hard} and soft, $(1-f_{Hard})$ grains can be obtained from the quantitative evaluation of the texture measurements [36]. The average dislocation densities, ρ_{Av} along with the dislocation densities in the hard and soft grains, ρ_{Hard} and ρ_{Soft}, the f_{Hard} values and the fractions of ρ_{Hard} to ρ_{Av}: ρ_{Hard}/ρ_{Av}, are given in Table 4. This last column in the table shows that in the <100> textured specimen the hard grains deform strongly and contribute substantially to the strength of the material. In the other two samples the hard grains act as hard inclusions which almost do not deform plastically.

The present example shows that the appropriate combination of strain anisotropy and individual line profile analysis carried out for single textured grain populations can provide detailed characterization of the microstructure in different texture components of the same material.

6. Extension of the method of line profile analysis to patterns obtained by neutron diffraction

High angular resolution and relatively small instrumental broadening are advantageous requirements for the successful application of line profile analysis. With X-ray diffraction in both, laboratory and synchrotron experiments, these two conditions can be well satisfied. With neutron diffraction this is not easy and not trivial, mainly because the neutron flux would be extremely diminished if the beam cross-section was reduced to less than a few mm. At least, this was the case with neutron diffractometers staged at reactor sources. With the

establishment of spallation sourced, however, the flux of neutrons has been raised to such an extent that the angular resolution could be improved considerably.

The evolution of the microstructure in the 6061-T6 aluminum alloy during friction-stir-welding (FSW) was in-situ followed by neutron diffraction in the sample stage of the Materials Research at Temperature and Stress (SMARTS) at the Los Alamos Neutron Science Center [47]. The neutron-diffraction patterns were analyzed by the GSAS Rietveld code [48] and the FWHM values of the physical profiles were plotted in a *modified* Williamson-Hall plot [31] as shown in Fig. [6]. The strongly enlarged slope in the case of the FSW state indicates the large increase in the dislocation density. As listed in Table 1. in [47] the dislocation density in the as received base-materials and in the FSW materials was determined as: 4.5× and 32×10^{14} m^{-2}, respectively.

Beryllium specimens were plastically deformed by compression in the Los Alamos Neutron Science Center and the diffraction patterns were measured by neutron diffraction [49]. The instrumental effect was measured on the SRM-640 silicon standard specimen. A typical time-of-flight diffraction spectrum transformed to θ-2θ pattern by using the fictive wavelength λ=0.0578 nm is shown in Fig. 7. The open circles are the measured intensity values, the red line is the patterns simulated by the eCMWP [3,4] procedure and the line in the bottom of the figure is the difference between the measured and fitted patterns. The dislocation density, ρ, the twin density, β, the q_1 and q_2 parameter values and the R_{wp} values are given in Table 5 for an annealed and two specimen deformed to 20 % reduction by compression, one at a quasi-static low speed (Q.-stat.) and one at the deformation rate of 5 %/s. In all three specimens the coherently scattering domain size was larger than the detection limit by line broadening. The dislocation densities are rather low. Even in the sample deformed at the rate of 5 %/s the dislocation density is only 0.6×10^{14} m^{-2}. No twinning has been observed in the quasi statically deformed specimen, whereas β=0.23±0.02 twin density was observed on the {10.2} twin planes in the fast deformed sample. Latter means that the average distance between the twin boundaries is about 60 nm. The q_1/q_2 parameter values substantiate mainly ***<a>*** type dislocations. More details of these studies will be published in [49].

7. Microstructure of single grains extracted from polycrystalline specimen

The dislocation model of strain anisotropy proved to be a powerful method to obtain qualitative and quantitative data about the dislocation type, arrangement and density in single- and polycrystalline materials, especially when mainly one Burgers vector type is present in the crystal [50]. In hexagonal materials three Burgers vector types, <*a*>, <*c*> and <*c*+*a*> and about 11 dislocation types are conceivable [51]. In a polycrystal the dislocation structure can vary from grain-to-grain depending on the orientation of the particular grain related to applied stress direction and to the stress state exerted by the neighborhood of the grain [51-55]. In the diffraction pattern of bulk polycrystalline materials the diffraction experiment carries out automatic averaging over a large ensemble of grains. This type of averaging obscures the detailed information about dislocation type, arrangement and density, and most probably provides only a messy mismatch about the prevailing dislocation structure in hexagonal materials. In recent endeavor single grain diffraction was carried out on bulk polycrystalline specimens to obtain detailed microstructure data on the grain scale [56]. The method is the extension of the synchrotron experiment designed for single crystal orientation and structure determination from bulk polycrystalline samples [57,58]. The thin rod-shape specimen is rotated at a slow rate in the monochromatic X-ray beam over a large ω range while the diffraction pattern is recorded a few hundred times by a fast detector. In the method described

in [57,58] the sample to detector distance is about 200 mm which enables to obtain the diffracted image in a wide reciprocal space range within a relatively short period of time. The specimen diameter and the beam cross-section are adjusted to acquire well separated diffraction spots at one time corresponding to individual grains in the specimen [58]. While the specimen is rotated over the ω axis the diffraction spots are coming-and-going. From the correlation between the ω settings of the specimen and the appearance of the diffraction spots the spots are correlated to specific grains and the grain orientations and positions in the specimen are determined [57-59]. The method was extended by placing the detector into an additional positions far from the specimen in order to expand the angular resolution for the purpose of line profile analysis [56]. In the far position the detector was moved into several adjacent positions in order to cover a large enough reciprocal space volume. The specimen rotation was repeated for the close and each far detector position.

The evaluation of the diffraction data was carried out in several steps. In the first step the diffraction patterns in the close detector position were indexed and the grain orientations determined. In this procedure the ImageD11 [60] software was used. A typical image provided by this software, once the indexing is successful, is shown in Fig. 8. The Debye-Scherrer rings are straightened. The positions of the Ti reflections according to the 44-1294 ASTM card are indicated by small red + signs. The corresponding indices are given in the figure caption.

The diffraction spots are 3-dimensional intensity distributions in reciprocal space: $I_{hkl}=I(\eta,\omega,2\theta)$, where η is the azimuth coordinate along the Debye-Scherrer arc, ω is the "rocking-curve" direction and 2θ is the "radial-direction" along the diffraction vector. The microstrain, i.e. the mean square strain $\langle\varepsilon_{g,L}^2\rangle$, produced by dislocations is provided by $I(2\theta)=\int I(\eta,\omega,2\theta)d\eta d\omega$ [5-7]. In the following we call $I(2\theta)$ the *line profile*. The line profile is obtained by integrating the total intensity distribution corresponding to one diffraction spot over η and ω. This procedure was carried out by producing an image recognizing software package which is (i) searching for the cohesive intensity maxima within the consecutive ω frames and (ii) determines the η ranges for the same diffraction maxima in the same ω frames. Once these ω frames and the corresponding η ranges are determined the integration is carried out numerically. Four typical ω frames selected from a cohesive series consisting of altogether 12 frames is shown in Fig. 9. The gray scale images show that the intensity is increasing and decreasing as the corresponding grain comes into and goes out of diffraction orientation. The integration over η is performed within the regions assigned by the black border lines and these results are summed up for each relevant ω frame. A typical diffraction pattern with 6 line profiles is shown in Fig. 10 for one of the grains, #47. Note that some of the line profiles correspond to the same $|\boldsymbol{g}|$ value but to different orientations. The qualitative feature of line broadening can be well seen in the Williamson-Hall (WH) plot of the FWHM values of line profiles. A typical WH plot for grain #44 is shown in Fig. 11a. The data show that the breadths are different for different orientations even for the same $|\boldsymbol{g}|$ values. The diffration profiles were evaluated by the eCMWP method for obtaining the *measured* individual dislocation contrast, $C_{individ}^{Meas}$ factors for each reflection. The last step was to find the dislocation type and Burgers vectors prevailing in the investigated individual grains. This step was carried out by finding the best accordance between the measured and theoretically conceivable, $C_{individ}^{Meas}$ and C_{Theor} dislocation contrast factors. The theoretical contrast factors were determined by using the ANIZC [35] software. The best correlation between the measured and theoretical contrast factors for the grain #44 was found for <*c*+*a*> screw dislocations with the Burgers vector type: <2113> [56]. The qualitative cross-check of the

prevailing dislocation type is provided by the *modified* WH plot [31] in which the breadth values are plotted versus $KC^{1/2}$ instead of K, as shown in Fig. 11b.

8. Conclusions

The *bottom-up* approach to line profile analysis is based on physically well established theoretical profile functions deduced from specific models of different lattice defect types: (i) heterogeneous microstrains, (ii) the dislocation model of strain anisotropy, (iii) size and size-distribution of coherently scattering domains, (iv) planar defects in cubic and hexagonal crystals and (v) defect structures in single crystals. The comprehensive software package eCMWP is designed for dealing with very different complex microstructure characterization problems. The fundamental theoretical equations used in the software package are listed in eqs. (1) to (16). The different parameters together and the physical meanings have been discussed by reviewing specific problems, especially (a) the dislocation density and crystallite size-distribution in ball-milled PbS (Galena), (b) the evolution of the frequency of twin densities in Cu and Cu-Zn alloys, (c) the dislocation types and dislocation densities in plastically deformed, strongly textured NiTi shape memory alloys (d) neutron diffraction of a friction-stir-welded aluminum alloy and compression deformed Be, and (e) the extraction of single crystal dislocation data from bulk polycrystalline CP-Ti specimens. The method of X-ray or neutron diffraction line profile analysis provides quantitative numbers for the density or size of the different types of lattice defects. The concomitant analysis by electron microscopy methods, especially TEM and/or SEM offers a most comprehensive and reliable characterization of the substructures of structural materials.

Acknowledgements

The authors are grateful to the Hungarian National Science Foundation, OTKA T-71594, T-80772 & T-67692. Thanks are due to Dr D. W. Brown and coworkers for using some of their results prior to publication in [49]. G.R. is grateful for the support of the Magyary Zoltán Fund and to the EEA Grants and Norway Grants.

References

[1] T. Ungár, I. Dragomir, Á. Révész, A. Borbély, J. Appl. Cryst. 32 (1999) 992-1002.
[2] G. Ribárik, J. Gubicza, T. Ungár, Mater. Sci. Eng. A, 387-389 (2004) 343-347.
[3] L. Balogh, G. Ribárik, T. Ungár, J. Appl. Phys. 100 (2006) 023512.
[4] L. Balogh, G. Tichy, T. Ungár, J. Appl. Cryst. 42 (2009) 580-591.
[5] M.A. Krivoglaz, Theory of X-ray and Thermal Neutron Scattering by Real Crystals, Plenum Press, New York, 1996.
[6] M. Wilkens, in: J.A. Simmons, R. de Wit, R. Bullough (Eds.), Fundamental Aspects of Dislocation Theory, vol. II., Nat. Bur. Stand. (US) Spec. Publ. No. 317, Washington, DC, USA, 1970, p. 1195.
[7] I. Groma, Phys. Rev. B 57 (1998) 7534-7542.
[8] T. Ungár, G. Tichy, Phys. Stat. Sol. (a), 171 (1999) 425-434.
[9] R.W.James, The optical principles of the diffraction of X-ray, G. Bell and Sons, Ltd., London, 1965.
[10] J.I. Langford, A. Boultif, J.P. Auffrédic, D. Louër, J. Appl. Cryst. 26 (1993). 22-33.
[11] P. Scardi, M. Leoni, R.J. Delhez, J. Appl. Cryst. 37 (2004) 381-390.

[12] E.F. Bertaut, Acta Cryst. 3 (1950) 14-18.
[13] J.I. Langford, D. Louër, Rep. Prog. Phys. 59 (1996) 131-234.
[14] Ch.D. Terwilliger, Y.M. Chiang, Acta Metall. Mater. 43, (1995) 319-328.
[15] C.E. Krill, R. Birringer, Philos. Mag. A 77 (1998) 621-640.
[16] T. Ungár, J. Gubicza, G. Ribárik, A. Borbély, J. Appl. Cryst. 34 (2001) 298-310.
[17] P. Scardi, M. Leoni, Acta Cryst. A, 58 (2002) 190-200.
[18] Leoni, M. & Scardi, P, J. Appl. Cryst., 37 (2004) 629-634.
[19] W.C. Hinds, Aerosol Technology: Properties, Behavior and Measurement of Airbone Particles, Wiley, New York, 1982.
[20] B.E. Warren, B.L. Averbach, J. Appl. Phys. 21 (1950) 595-597.
[21] E. Estevez-Rams, M. Leoni, P. Scardi, B. Aragon-Fernandez, H. Fuess, Philos. Mag. 83 (2003) 4045-4057.
[22] L. Velterop, R. Delhez, Th.H. de Keijser, E.J. Mittemeijer, D. Reefman, J. Appl. Cryst. 33 (2000) 296-306.
[23] M.M.J. Treacy, J.M. Newsam, M.W. Deem, Proc. R. Soc. London Ser. A, 433 (1991) 499-520.
[24] R.I. Barabash, J.S. Chung, M.F. Thorpe, J. Phys.: Condens. Matter, 11 (1999) 3075-3090.
[25] Th. Michelitsch, A. Wunderlin, Phys. Stat. Sol. 198 (2006) 615-620.
[26] B. Schönfeld, G. Kostorz, Elastic diffuse scattering of alloys: status and perspectives, in Diffuse Scattering and the Fundamental Properties of Materials, Eds. R.I. Barabash, G.E. Ice, P.E.A. Turchi, Momentum Press, 2009, pp. 119-137.
[27] G.A. Caglioti, A. Paoletti, F.P. Ricci, Nucl. Instrum. 3 (1958) 223-228.
[28] A.R. Stokes, A.J.C. Wilson, Proc. Camb. Phil. Soc. 38 (1942) 313-322.
[29] P. Klimanek, R.L. Kuzel Jr. Appl. Cryst. 21 (1988) 59-66.
[30] R.L. Kuzel Jr., P.J. Klimanek, J. Appl. Cryst. 22 (1989) 299-307.
[31] T. Ungár, A. Borbély, Appl. Phys. Lett. 69 (1996) 3173-3175.
[32] T. Ungár, J. Powder Diffraction, 23 (2008) 125-132.
[33] P. Cordier, T. Ungár, L. Zsoldos, G. Tichy, Nature, 428 (2004) 837-840.
[34] I.C. Dragomir, T. Ungár, J. Appl. Cryst., 35 (2002) 556-564.
[35] A. Borbély, I.C. Dragomir, G. Ribárik, T. Ungár, J. Appl. Cryst., 36 (2003) 160-162.
[36] T. Ungár, K. Nyilas, W. Skrotzki, Int. J. Mater. Res. 99 (208) 725-733.
[37] R. A. Young, *in The Rietveld Method*, Ed. R.A.Young, IUCr, Oxford University Press, 1993, pp. 22.
[38] T. Ungár, P. Martinetto, G. Ribárik, E. Dooryhée, Ph. Walter, M. Anne, J. Appl. Phys. 91 (2002) 2455-2465.
[39] Ph. Walter, P. Martinetto, G. Tsoucaris, R. Bréniaux, M.-A. Lefebvre, G. Richard, J. Talabot, E. Dooryhée, Nature, 397 (1999) 483-486.
[39] L. Wei, C. Junfang, W. Teng, Physica B, 405 (2010) 1279-1282.
[40] F.F. Csikor, I. Groma, Phys. Rev. B, 70 (2004) 064106.
[42] T. Ungár, L. Balogh, Y.T. Zhu, Z. Horita, C. Xu, T. G. Langdon, Mat. Sci. Eng. A 444 (2007) 153-156.
[43] L. Balogh, T. Ungár, Y. Zhao, Y.T. Zhu, Z. Horita, C. Xu, T. G. Langdon, Acta Mater. 56 (2008) 809-820.
[44] W. Skrotzki, R. Tamm, C.-G. Oertel, B. Beckers, H.-G. Brokmeier, E. Rybacki, Mater. Sci. Eng. A, 329-331 (2002) 235-240.
[45] R.D. Noebe, R.R. Bowman, M.V. Nathal, in Physical Metallurgy and Processing of Intermetallic Compounds, Eds. N.S. Stoloff, V.K. Sikka, Chapman & Hall, New York (1996) pp. 212.

[46] W. Skrotzki, R. Tamm, C.-G. Oertel, B. Beckers, H.-G. Brokmeier, E. Rybacki, Mater. Sci. Eng. A, 319-321 (2001) 364-367.
[47] W. Woo, T. Ungár, Z. Feng, E. Kenik, B. Clausen, Met. Trans. A, 41A (2010) 1210-1216.
[48] A.C. Larson, R.B. Von Dreele, General Structure Analysis System (GSAS), Los Alamos National Laboratory Report LAUR 86-748 (2004).
[49] D. W. Brown, B. Clausen, T.-A. Sisneros, D. C. Donati, L. Balogh, Met. Trans. A, in preparation.
[50] T. Ungár, J. Powder Diffraction, 23 (2008) 125-132
[51] I.P. Jones, W.B. Hutchinson, Acta Metall. 29 (1981) 951-968.
[52] P.G. Partridge, Metallurgical reviews, 118 (1968) 169-193.
[53] M.P. Miller, J.S. Park, P.R. Dawson, T.S. Han, Acta Mater. 56 (2008) 3927-3939.
[54] S. Merkel, C.N. Tomé, H.R. Wenk, Phys. Rev. B, 79, 064110 (13) (2009).
[55] R.A. Lebensohn, C.N. Tome, P. Castaneda, P. Phil. Mag. 87 (2007) 4287-4322.
[56] T. Ungár, G. Ribárik, L. Balogh, A. A. Salem, S. L. Semiatin, G. Vaughan, Scripta Mater., 63 (2010) 69-72.
[57] E.M. Lauridsen, S. Schmidt, R.M. Suter, and H.F. Poulsen, J. Appl. Cryst., 34 (2001) 744-750.
[58] D. Juul Jensen, E. M. Lauridsen, L. Margulies, H. F. Poulsen, S. Schmidt, H. O. Sørensen, G. B. M. Vaughan, Materials Today, 9 (2006) 18-25.
[59] X. Fu, H.F. Poulsen, S. Schmidt, S.F. Nielsen, E. M. Lauridsen and D. Juul Jensen, Scripta Mater., 49, (2003) 1093-1096.
[60] J. Wright, ImageD11, http://sourceforge.net/projects/fable/files/ImageD11/

Table 1. The median and logarithmic variance, *m* and σ of the log-normal size distribution function, the area average mean crystallite size, $\langle x \rangle_{area}$ and the average dislocation density, ρ for the ball-milled (BM) laboratory specimens. R_{wp} in the last row gives the reliability of the fit, cf. [37]. The as-received material was obtained from a source in the USA (U) [38]. E14455 denotes one of the archaeological specimens acquired from the Louvre museum, Paris, France [38]. The R_{wp} values varied between 0.35 and 0.55 and the M values were between 1.8 and 3, where the smaller values correspond to the larger dislocation densities in correlation with the screening effect of dislocations [6].

Specimen	m [nm]	σ	$\langle x \rangle_{area}$ [nm]	ρ [10^{14} m^{-2}]
U as-received	99 (±10)	0.67 (±0.1)	305 (±30)	3.3 (±1)
U 12h-BM	8 (±1)	0.8 (±0.15)	40 (±5)	40 (±5)
U 2h-BM +2h at 300 °C	96 (±10)	0.56 (±0.1)	210 (±20)	2.6 (±1)
U 2h-BM +2h at 400 °C	84 (±8)	076 (±0.15)	260 (±30)	1.3 (±0.8)
U 10m-BM	25 (±2)	0.85 (±0.15)	150 (±25)	7.3 (±2)
E14455	76 (±7)	0.73 (±0.15)	290 (±30)	2.4 (±1)

Table 2. The median and variance, *m* and σ, of the log-normal size distribution of sub-grains, the area average mean crystallite size, $\langle x \rangle_{area}$, the average dislocation density, ρ, the average density of twin boundaries, β and the q parameter values for the dislocation contrast factors, for the three materials, Cu, Cu-10%Zn and Cu-30%Zn at positions of 0*R*, (1/2)*R* and 1*R*, respectively [40,41]. R_{wp} in the last row gives the reliability of the fit, cf. [37]. The M values are between 1.4 and 2, where the smaller values correspond to the larger dislocation densities in correlation with the screening effect of dislocations [6].

position	*m* [nm]	σ	$\langle x \rangle_{area}$ [nm]	ρ [10^{14} m^{-2}]	β %	q	R_{wp}
Cu							
0 R_o	51 (5)	0.25 (0.05)	60 (5)	17.5 (3)	0.0 (0.02)	2.4 (0.2)	0.025
(1/2) R_o	42 (5)	0.38 (0.05)	60 (5)	14.2 (3)	0.0 (0.02)	2.2 (0.2)	0.034
1 R_o	45 (5)	0.33 (0.05)	59 (5)	19.2 (3)	0.0 (0.02)	2.2 (0.2)	0.034
Cu-10%Zn							
0 R_o	55 (5)	0.28 (0.05)	67 (5)	9.4 (2)	0.16 (0.02)	2.2 (0.2)	0.021
(1/2) R_o	50 (5)	0.27 (0.05)	60 (5)	34 (5)	0.82 (0.02)	2.1 (0.2)	0.014
1 R_o	39 (5)	0.33 (0.05)	51 (5)	43 (5)	1.36 (0.02)	2.2 (0.2)	0.014
Cu-30%Zn							
0 R_o	25 (3)	0.3 (0.05)	31 (3)	97 (7)	1.82 (0.02)	2.4 (0.2)	0.014
(1/2) R_o	29 (3)	0.25 (0.05)	34 (3)	81 (7)	2.88 (0.02)	2.3 (0.2)	0.016
1 R_o	24 (3)	0.29 (0.05)	30 (3)	117 (10)	3.73 (0.02)	2.5 (0.2)	0.02

Table 3. The largest Schmid factors of the three different possible slip systems [44,45] for the three different main texture components [36].

Slip system	<100> Texture	<110> Texture	<111> Texture
{100}<100>	0	0.50	0.34
{110}<100>	0	0.36	0.48
{110}<111>	0.45	0.43	0.28

Table 4. Dislocation densities in the hard, ρ_{Hard} and soft, ρ_{Soft} grains and the average value, $\rho_{Average}$, the volume fraction of hard grains, f_{Hard}, the true stress, σ_{True} at 6 % compression and the weighted fraction of dislocation densities in the hard grains, $f_H\rho_H/\rho_{Av}$ for the differently textured specimens [36].

Texture	f_{Hard}	ρ_{Hard} [10^{14} m^{-2}]	ρ_{Soft} [10^{14} m^{-2}]	$\rho_{Average}$ [10^{14} m^{-2}]	σ_{True} [MPa]	$f_H\rho_H/\rho_{Av}$
<100>	0.66	2.15	1.1	3.25	940	0.45
<110>	0.23	0.4	1.3	1.7	490	0.053
<111>	0.21	0.53	2	2.5	530	0.044

Table 5. Dislocation densities, ρ, twin boundary frequencies, β, the q_1/q_2 values for the dislocation contrast factors and the R_{wp} values for compression deformed Be specimens measured by neutron diffraction [49].

Be	ρ [10^{14} m^{-2}]	β	q_1/q_2	R_{wp}
Annealed	0.02 (0.01)	-	-	0.5
Deformed Q.-Stat.	0.2 (0.05)	-	0.2/0.2 (0.2)	0.52
Deformed 5 %/s	0.6 (0.1)	0.23 (0.02)	0.43/-0.63 (0.2)	0.52

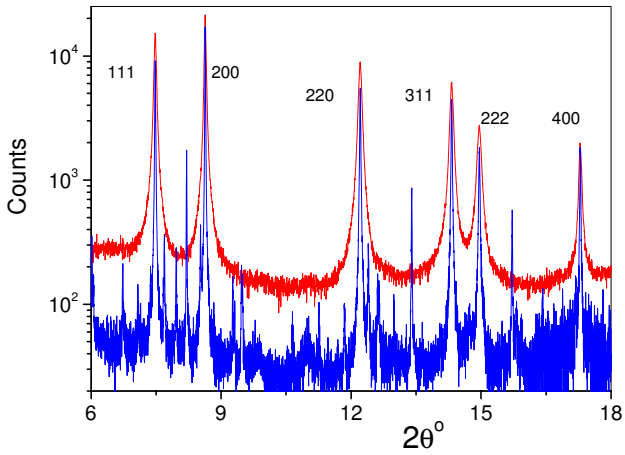

Figure 1. The sections between 2θ=6° to 18° of two typical diffraction patterns, one of a laboratory specimen ball-milled for 12 h (upper red line) and the other one of the E14455 [38] archaeological specimens. The pattern of the archaeological specimen shows that though PdS was the major component in ancient Egyptian make-up, they contained more components [39].

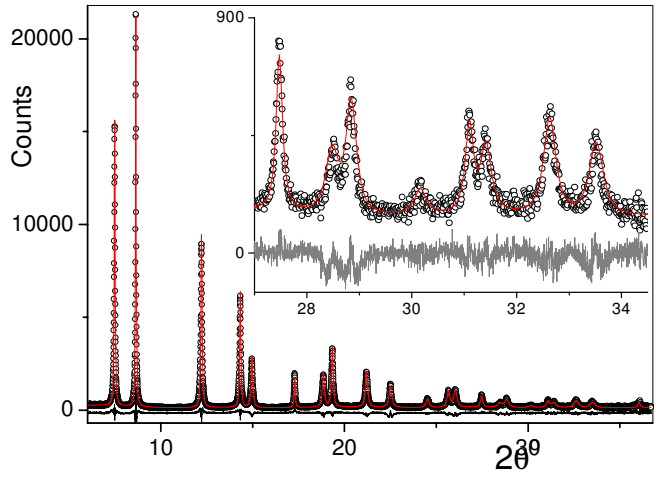

Figure 2. The measured (open circles) pattern of the 12 h ball-milled laboratory specimen of PbS (Galena) and the pattern fitted by the eCMWP method (red line). The inset is an enlarged part between 2θ=27 and 35°. The difference between the measured and fitted data are shown below the measured and fitted patterns.

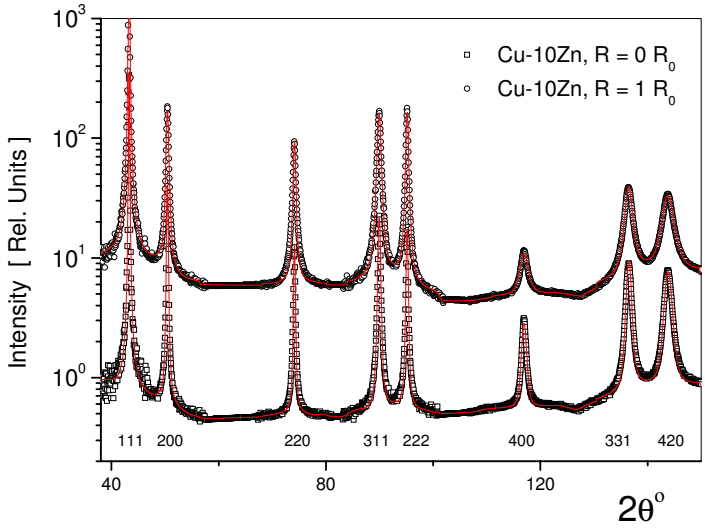

Figure 3. Two typical diffraction patterns of the Cu-10%Zn specimen measured at the centre, $R=0R_0$, and the periphery, $R=R_0$, of the high-pressure-torsion deformed disk-shape specimen [42,43]. The open symbols are the measured intensities and the red lines the patterns calculated by the eCMWP procedure.

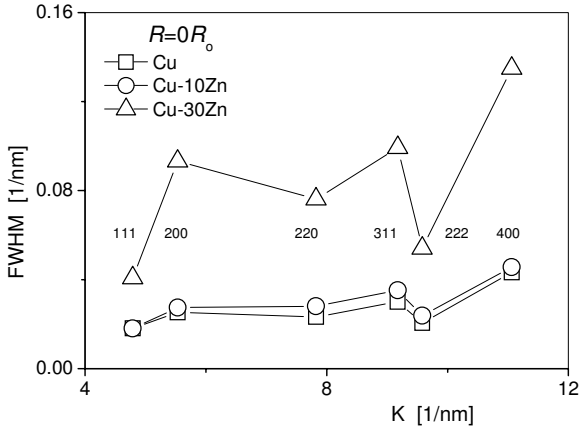

Figure 4. Williamson-Hall plots of the FWHM values of the high-pressure-torsion deformed disk-shape Cu, Cu-10%Zn and Cu-30%Zn specimen measured at the centre regions of the discs [42,43].

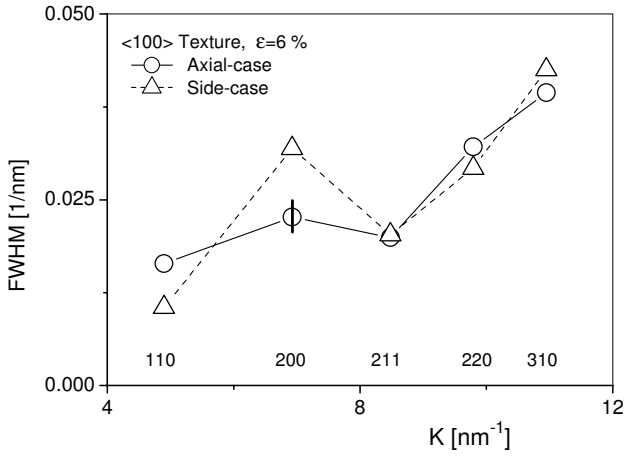

Figure 5. The Williamson-Hall plot of the FWHM values of the <100> textured specimen deformed to 6 % in compression measured on the axial (open circles) and the side (open triangles) surfaces, respectively [36].

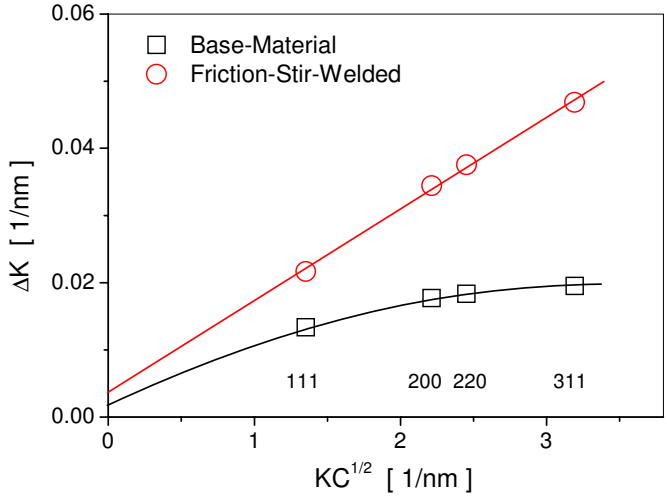

Figure 6. The values FWHM, ΔK, of the physical profiles of the 6061-T6 aluminum alloy in the as-received state, Base-Material, (open black squares) and during friction-stir-welding, FSW, close to the edge of the FSW tool (open red circles) in a *modified* Williamson-Hall plot [31,47].

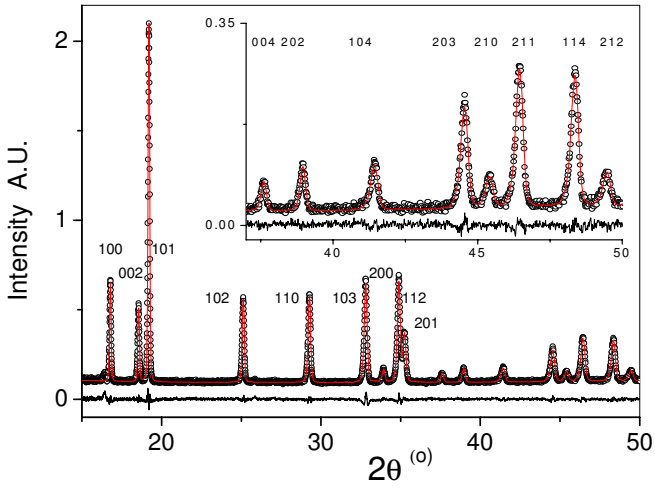

Figure 7. The neutron diffraction pattern of the 5 %/s compression deformed Be measured in the SMARTS diffractometer (open circles) and the spectrum calculated by the eCMWP procedure (solid red line) [3,4].The difference between the measured and fitted data are shown in the bottom of the figure. (By courtesy of Dr D. W. Brown and coworkers [49].)

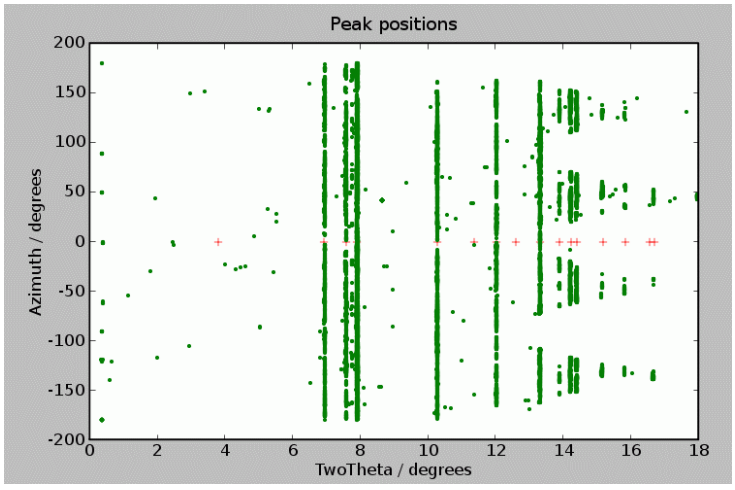

Figure 8. Typical output of the indexing software: ImageD11 [55] once the Debye-Scherrer rings have been straightened. Each spot in the image corresponds to a diffraction maximum. The stray dots are noise which is eliminated in further evaluations. The indices starting from $2\theta=6.9^{o}$ are: 10.0, 00.2, 10.1, 10.2, 11.0, 10.3, 20.0, 11.2, 20.1, 00.4, 20.2, 10.4, 20.3, 21.0 and 21.1. The small red + signs from $2\theta=6.9^{o}$ onward correspond to the first 15 reflections of Ti identified and indexed [56,60].

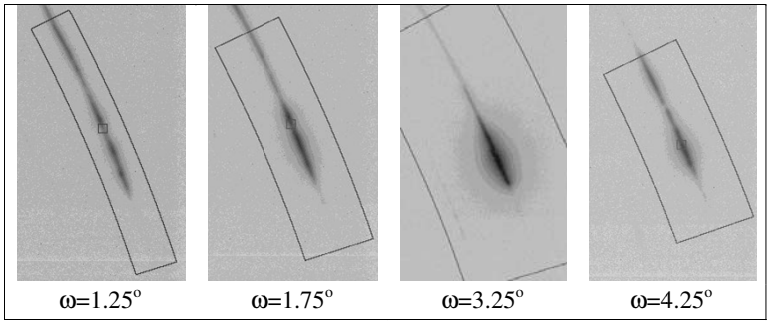

Figure 9. Portions of four typical far-detector frames showing the integration procedure along the Debye-Scherrer arcs in the η direction. The large crosses mark the highest intensity positions in the frames and the lines circumventing the diffraction spots are placed at distances of ±6-times and ±15-times the full-width-at-half-maximum (FWHM) of the peaks in the radial, i.e. 2θ, and in the η directions, respectively. Integration over the ω direction is done by summing up the frames over an ω range where the intensity falls off to 1% of the maximum intensity. For the peak shown here 12 subsequent ω frames have been summed up [56].

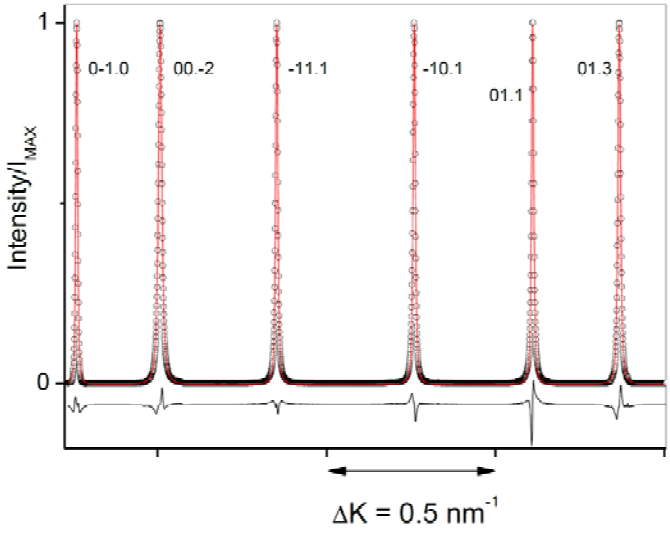

Figure 10. A typical diffraction pattern with 6 line profiles of the grain #47 in a CP-Ti specimen [56]. Note that some of the line profiles correspond to the same |**g**| value but to different orientations.

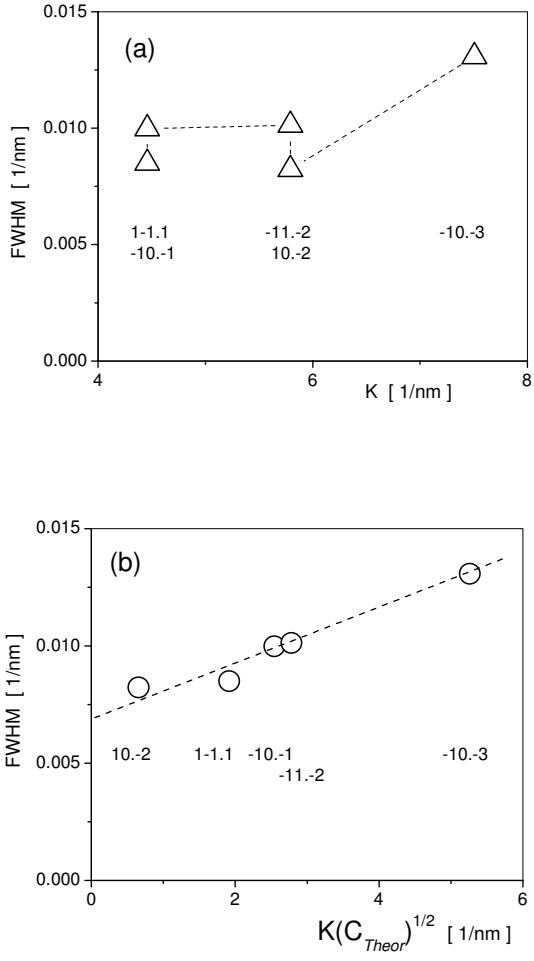

Figure 11. Typical Williamson-Hall (a) and *modified* Williamson-Hall (b) plots for grain #44. The data show that the breadths are different for different orientations even for the same $|\boldsymbol{g}|$ values. In the *modified* Williamson-Hall plot the theoretical dislocation contrast factors correspond to <*c*+*a*> type screw dislocations [56].

Pair Distribution Function Technique: Principles and Methods

Simon J.L. Billinge
Dept of Applied Physics and Applied Mathematics, Columbia University, New York, NY, and Condensed Matter Physics and Materials Science Dept, Brookhaven National Laboratory, Upton, NY (USA)

One of the frontiers when studying complex and nanostructured materials is the characterization of structure on the nanoscale. We describe how the atomic pair distribution function analysis of powder diffraction data can be used to this end, and what kind of structural information can be obtained in different situations.

Introduction

This presentation is adapted from a description of the PDF method described in Chapter 16 of "*Powder Diffraction: Theory and Practice*" [1].
Increasingly, materials that are under study for their interesting technological or scientific properties are highly complex. They are made of multiple elements, have large unit cells and often low dimensional or incommensurate structures [2]. Increasingly also, they have aperiodic disorder: some aspect of the structure that is different from the average crystal structure. In the case of nanoparticles the very concept of a crystal is invalid as the approximation of infinite periodicity is no longer a good one. Still we would like to study the structure of these materials. Powder diffraction is an important method for characterizing these materials, but we have to go beyond the Bragg equation and crystallographic analysis.
The "total scattering" approach treats both the Bragg and diffuse scattering on an equal basis [3]. Powder diffraction data are measured in much the same way as in a regular powder measurement. However, explicit corrections are made for extrinsic contributions to the background intensity from such things as Compton scattering, fluorescence, scattering from the sample holder, and so on. The resulting coherent scattering function *I(Q)* is a continuous function of *Q*, the magnitude of the scattering vector, $Q = |\boldsymbol{Q}| = 2k\sin\theta = \frac{4\pi\sin\theta}{\lambda}$, with sharp intensities where there are Bragg peaks, and broad features in between, the diffuse scattering. In general we like to work with a normalized version of this scattering intensity, *S(Q)*. This is the intensity normalized by the incident flux per atom in the sample. S(Q) is the total-scattering structure function. It is a dimensionless quantity and the normalization is such that the average value, $\langle S(Q)\rangle = 1$. Despite the tricky definition, it is worth remembering that *S(Q)* is nothing other than the powder diffraction pattern that has been corrected for experimental artifacts and suitably normalized.

To get a good resolution in real-space, the *S(Q)* must be measured over a wide range of *Q*-values. The coherent intensity (the features) in *S(Q)* die out with increasing *Q* due to the Debye-Waller factor which comes from thermal and quantum zero-point motion of the atoms, as well as any static displacive disorder in the material. By a *Q*-value of 30-50 $Å^{-1}$ (depending on temperature and stiffness of the bonding) there are no more features in *S(Q)* and there is no need to measure it to higher-*Q*. Still, this is much higher than conventional powder diffraction experiments using laboratory x-rays or reactor neutrons. The maximum *Q* attainable in back-scattering from a copper-K_α tube is around 8 $Å^{-1}$ and from a Mo-K_α tube 16 $Å^{-1}$. Routine total-scattering measurements can be made using laboratory sources with Mo or Ag tubes; however, for the highest real-space resolution, and the smallest statistical uncertainties, synchrotron data are preferred. In the case of neutron scattering, spallation neutron sources are ideal for this type of experiment.

Total scattering *S(Q)* functions appear different to standard powder diffraction measurements because of the *Q*-range studied, but also because of an important aspect of the normalization: the measured intensity is divided by the total scattering cross-section of the sample. For neutrons, this scattering cross-section is simply $\langle b \rangle^2$, where *b* is the coherent neutron scattering length of the atoms of the material in units of barns. The angle brackets denote an average. The scattering length, *b*, is constant as a function of *Q* and so is just part of the overall normalization coefficient. However, in the case of x-ray scattering, the sample scattering cross-section is the square of the atomic form-factor, $\langle f(Q) \rangle^2$, which becomes very small at high-*Q*. Thus, during the normalization process the data at high-*Q* are amplified (by being divided by a small number). This has the effect that even rather weak intensities at high-*Q*, which are totally neglected in a conventional analysis of the data, become rather important in a total-scattering experiment. Because the signal at high-*Q* is weak it is important to collect the data in that region with good statistics. This is illustrated in Fig. 1.

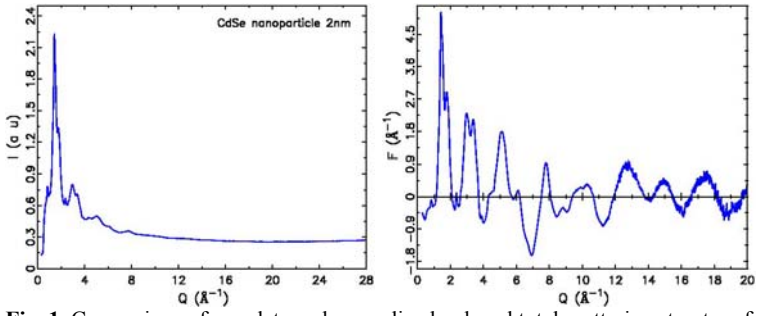

Fig. 1. Comparison of raw data and normalized reduced total scattering structure function F(Q)=Q[S(Q)-1]. The sample is a powder of 2nm diameter CdSe nanoparticles and the data are x-ray data from 6ID-D at the Advanced Photon Source at Argonne National Laboratory. The raw data are shown in the left panel. The high-Q data in the region Q>9 appear smooth and featureless (left panel). However, after normalizing and dividing by the square of the atomic form-factor, important diffuse scattering is evident in this region of the diffraction pattern (right panel).

Thus, the value added of a total scattering experiment over a conventional powder diffraction analysis is the inclusion of diffuse scattering as well as Bragg peak intensities in the analysis, and the wide range of Q over which data are measured. In fact, the total scattering name comes from the fact that *all* the coherent scattering in *all* of Q-space is measured.

Total scattering data can be analyzed by fitting models directly in reciprocal-space (i.e., the $S(Q)$ function is fit). However, an interesting and intuitive approach is to Fourier transform the data to real-space to obtain the atomic pair distribution function (PDF), which is then fit in real-space. The reduced pair distribution function, $G(r)$, is related to $S(Q)$ through a Sine Fourier transform according to

$$G(r) = \frac{2}{\pi} \int_{Q\,\mathrm{min}}^{Q\,\mathrm{max}} Q[S(Q) - 1]\sin(Qr)dQ \cdot \quad (1)$$

Examples of a $G(r)$ functions are shown in Fig. 2.

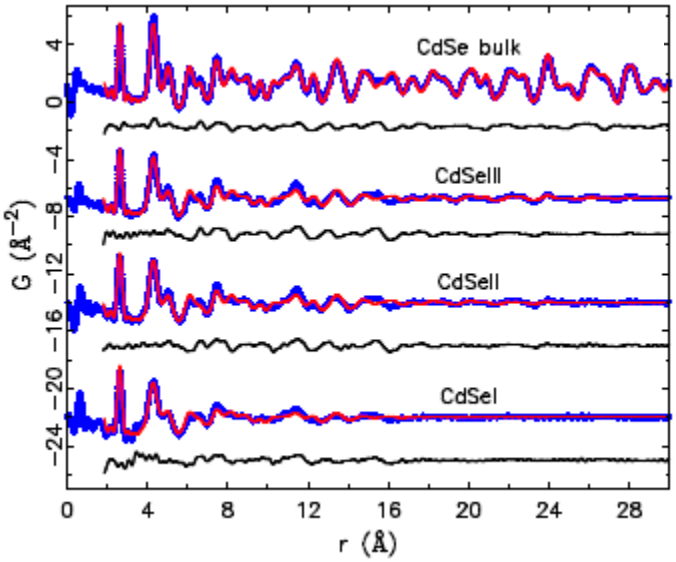

Fig. 2. PDFs in the form of G(r) from bulk CdSe, and from a series of CdSe nanoparticles. The blue curve at the bottom is the PDF obtained from the data shown in Figure 1. The thick lines are from the data, with thin lines on top from models of the local structure in these nanoparticles. Offset below are difference curves between the model and the data. Figure adapted from [4].

It has peaks at positions, r, where pairs of atoms are separated in the solid with high probability. For example, there are no peaks below the nearest neighbor peak at ~2.5 Å which is the Cd-Se separation in CdSe [4]. However, in addition to the nearest-neighbor information, valuable structural information is contained in the pair-correlations extending to much higher values of r. In fact, with high Q-space resolution data, PDFs can be measured out to tens of nanometers (hundreds of angstroms) and the structural information remains quantitatively reliable.

There are now many classes of problems that have been studied using total scattering analysis. Traditionally it was used for liquids [5] and amorphous materials, more recently for the study of disorder in crystalline materials, and now with increasing popularity it is used to study nanostructured materials. A number of recent reviews [3,6,7] give examples of modern applications of the PDF method.

Theory

The basis of the total scattering method is the normalized, measured, scattering intensity from a sample, total scattering structure function, $S(\boldsymbol{Q})$ [3,8,9]. The wavevector, $\boldsymbol{Q}$, is a vector quantity and in general the intensity variation, $S(\boldsymbol{Q})$, will depend on which direction one looks in Q-space. However, when the sample is isotropic, for example, a powder, it depends only on the magnitude of Q and not its direction.

Similarly, the Fourier transform of the scattered intensity, in the form of $S(Q)$, yields the reduced atomic pair distribution function, $G(r)$, defined by Eqn. 1. This is strictly correct when the sample is made of a single element. We will discuss an approximate extension that works excellently in practice, to the more interesting case of multiple elements.

The inverse transformation of Eqn. 1 can be defined and it yields the structure function $S(Q)$ in terms of $G(r)$,

$$S(Q) = 1 + \frac{1}{Q}\int_0^\infty G(r)\sin(Qr)dr. \qquad (2)$$

There are a number of similar correlation functions related to $G(r)$ by multiplicative and additive constants. They contain the same structural information but are subtly different in some detail. $G(r)$ is the function obtained directly from the Fourier transform of the scattered data. The function oscillates around zero and asymptotes to zero at high-r. It also tends to zero at $r = 0$ with the slope $-4\pi\rho_0$, where ρ_0 is the average number density of the material. From a practical point of view $G(r)$ is attractive because the random uncertainties on the data (propagated from the measurement) are constant in r [3]. This means that fluctuations in the difference between a calculated and measured $G(r)$ curve have the same significance at all values of r. Thus, for example, if the observed fluctuations in the difference curve decrease with increasing r this implies that the model is providing a better fit at longer distances (perhaps it is a model of the average crystallographic structure). This inference cannot be made directly from a difference curve to $\rho(r)$ or $g(r)$. A further advantage of the $G(r)$ function is that the amplitude of the oscillations gives a direct measure of the structural coherence of the sample. In a crystal with perfect structural coherence, oscillations in $G(r)$ extend to infinity with a constant peak-peak amplitude [10]. In the $G(r)$ from a real crystal the peak-peak amplitude of the signal gradually falls off due to the finite Q-resolution of the measurement, which is then the limitation on the spatial coherence of the measurement rather than the structural

coherence itself. A higher *Q*-resolution results in data extending over a wider range of *r*. In samples with some degree of structural disorder, the signal amplitude in *G*(*r*) falls off faster than dictated by the *Q*-resolution and this becomes a useful measure of the structural coherence of the sample. For example, it can be used to measure the diameter of nanoparticles.

Another function often denoted *g*(*r*) is called the pair distribution function. It is normalized so that, as $r \to \infty$, $g(r) \to 1$ and has the property that for *r* shorter than the distance of closest approach of pairs of atoms $g(r)$ becomes zero. It is closely related to the pair density function, $\rho(r) = \rho_0 g(r)$. Clearly, $\rho(r)$ oscillates about, and then asymptotes to, the average number density of the material, ρ_0 at high-*r* and becomes zero as $r \to 0$. The relationship between these correlation functions is given by

$$G(r) = 4\pi r\left(\rho(r) - \rho_0\right) = 4\pi\rho_0 r(g(r) - 1) \quad (3).$$

Finally we describe the radial distribution function, *R(r)* given by

$$R(r) = 4\pi r^2 \rho(r) \quad (4),$$

which is related to *G(r)* by

$$G(r) = \frac{R(r)}{r} - 4\pi r\rho_0 \quad (5).$$

The *R(r)* function is important because it is the most closely related to the physical structure since $R(r)dr$ gives the number of atoms in an annulus of thickness *dr* at distance *r* from another atom. For example, the coordination number, or the number of neighbors, N_C, is given by

$$N_C = \int_{r_1}^{r_2} R(r)dr \quad (6),$$

where r_1 and r_2 define the beginning and ending positions of the RDF peak corresponding to the coordination shell in question. This suggests a scheme for calculating PDFs from atomic models. Consider a model consisting of a large number of atoms situated at positions $\mathbf{r}_\nu$ with respect to some origin. Expressed mathematically, this amounts to a series of delta functions, $\delta(\mathbf{r} - \mathbf{r}_\nu)$. The RDF is then given as

$$R(r) = \frac{1}{N}\sum_{\nu}\sum_{\mu}\delta(r - r_{\nu\mu}) \quad (7),$$

where $r_{\nu\mu} = |\mathbf{r}_\nu - \mathbf{r}_\mu|$ is the magnitude of the separation of the ν-th and μ-th ions and the double sum runs twice over all atoms in the sample. Later we address explicitly samples with more than one type of atom, but for completeness we give here the expression for *R(r)* in this case:

$$R(r) = \frac{1}{N}\sum_{\nu}\sum_{\mu}\frac{b_\nu b_\mu}{\langle b\rangle^2}\delta(r - r_{\nu\mu}) \quad (8),$$

where the b's are the Q-independent coherent scattering lengths for the ν^{th} and μ^{th} atoms and $\langle b \rangle$ is the sample average scattering length. In the case of x-rays the b's are replaced with atomic number, Z.

Experimental Methods

Total scattering measurements have basically the same requirements as any powder diffraction measurement. Special requirements for high-quality total scattering data are the following:

1) Data measured over a wide Q-range. This requires wide scattering angles and/or short-wavelength incident radiation.

2) Good statistics, especially at high-Q where the scattering signal is weak.

3) Low background scattering. It is important to measure weak diffuse scattering signals accurately which is difficult on top of high backgrounds.

4) Stable set-up and accurate incident intensity monitoring. The data are normalized by incident intensity. It is important that the incident beam and detector characteristics do not change in an uncontrolled way during the course of the experiment, or that this can be corrected, for example, by monitoring the incident beam intensity as is done at synchrotron x-ray and spallation neutron measurements.

X-ray experiments can be carried out using laboratory diffractometers with Mo or Ag sources which give Q-ranges up to $Q_{max} \sim 14$ Å^{-1} and 20 Å^{-1}, respectively. These are less than optimal values for Q_{max}, but acceptable for straightforward characterization of nanostructured materials at room temperature. Optimally, x-ray experiments are carried out at x-ray synchrotron sources using high incident energy x-rays. These can be done with incidence energies in the vicinity of 30-45 keV in conventional Debye-Scherrer geometry (for instance using be beamlines such as X31 at ESRF or 11BM at APS that are constructed for regular powder diffraction). However, more common these days is to use the rapid acquisition PDF mode (RAPDF) in which data for a PDF is collected in a single-shot using a planar 2D detector [11]. This is illustrated in Figure 3.

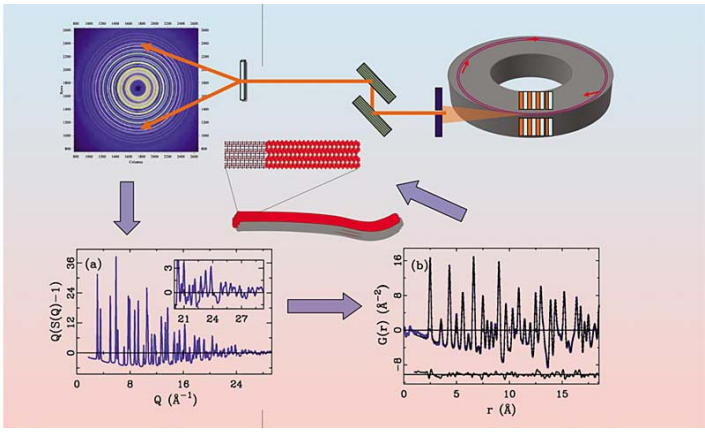

Figure 3: Schematic of the rapid acquisition RAPDF x-ray data collection method.

Dedicated beamlines have been constructed at APS for this purpose (11ID-B and 11ID-C) with similar beamlines under construction at NSLS (X17A), ESRF and NSLS-II. In this geometry, incident x-rays of energy 60-150 keV are fired through a sample and collected on a large area image-plate detector placed behind the sample. The experiment consists of ensuring the incident beam is perpendicular and centered on the detector and the sample, then exposing the image plate. Depending on the strength of scattering and the sensitivity of the detector, exposures for good PDFs in excess of Q_{max}=30 Å^{-1} can be obtained in as little as 100 ms, and typically a few seconds to minutes. This compares to data collection times of 8 – 12 hours with conventional non-parallel counting approaches, even at the synchrotron. The RAPDF measurement is ideal for time-resolved and parametric measurements, of local structure through phase transitions for example. The *Q*-resolution of these measurements is very poor because of the geometry, and this limits the *r*-range of the resulting data from crystalline materials. However, most modeling is carried out over rather narrow ranges of *r* and this represents a very good tradeoff. Where a wide *r*-range is necessary for the measurement (to study some aspect of intermediate range order on length-scales of 5-10 nanometers for, example) the Debye-Scherrer geometry diffractometers can be used.

In the case of neutron measurements, the requirement of short-wavelenths really limits experiments to time-of-flight spallation neutron sources. Reactor sources with hot moderators would give good quality data for PDF studies, but are in short supply. The requirements for a spallation neutron powder diffractometer are laid out in the list of experimental requirements above. Normal time-of-flight powder diffractometers can be used provided the length of the flight-path and frequency of operation are such to allow good fluxes of neutrons with short wavelength (0.2 - 0.4 Å). Currently neutron guides do not propagate these short-wavelength neutrons effectively so shorter flight-path diffractometers with or without guides give the best

data. Currently the instruments of choice are NPDF at the Lujan Center at Los Alamos National Laboratory in the USA and GEM at ISIS, Rutherford Laboratory, in the UK. The former was upgraded with PDF experiments in mind and has excellent stability on a water moderator and low backgrounds, though data collection time is not quite at the level of GEM. New powder diffractometers are coming on line at the Spallation Neutron Source at Oak Ridge National Laboratory (NOMAD and POWGEN) that will give unprecedented data-rates and will be suitable for PDF studies.

A number of data correction programs are available for free download and these take care of the corrections and normalizations needed to obtain PDFs from raw data. These can be browsed at the ccp14 software website [12]. Commonly used, and generally easy to use, programs are Gudrun [13] and PDFgetN [14] for spallation neutron data and PDFgetX2 [15, 16] for x-ray data. PDFgetX2 has the corrections implemented for accurate analysis of RAPDF data. Details of the corrections are beyond the scope of this article, but can be found in some detail in "*Underneath the Bragg peaks: structural analysis of complex materials"* by Egami and Billinge [3].

Extracting structural information from total scattering

Here we confine ourselves to real-space modeling whereby the PDF of the model is calculated and compared to an experiment. Fitting the PDF is generally done with models described by a small number of atoms in a unit cell (which may or may not be the crystalline unit cell) and yields information about the very local structure. Information can be extracted directly from the PDF in a model-independent way because of its definition as the atom-pair correlation function. The position of a peak in the PDF indicates the existence of a pair of atoms with that separation. There is no intensity in $R(r)$ for distances less than the nearest-neighbor distance, $r < r_{nn}$ and a sharp peak at r_{nn}. This behavior is very general and true even in atomically disordered systems such as glasses, liquids and gasses. In crystals, because of the long-range order of the structure, all neighbors at all lengths are well defined and give rise to sharp PDF peaks. The positions of these peaks give the separations of pairs of atoms in the structure directly and the width contains information about thermal motion of the atoms, or static disorder. In general, it is not possible to tell directly from the data whether a PDF peak broadening is static or dynamic in nature, though this can sometimes be inferred by fitting a temperature dependence to a dynamical model such as the Debye model.

When a well-defined PDF peak can be observed, we can determine information about the number of neighbors in that coordination shell around an origin atom by integrating the intensity under that peak, as shown in Eqn. 6. In the case of crystalline Ni there are four Ni atoms in the unit cell (fcc structure). Each nickel ion has 12 neighbors at 2.49 Å [17]. When we construct our PDF we will therefore place 48 units of intensity at position r=2.49 Å (the weighting factor, $b_m b_n / \langle b \rangle^2$, is

unity since there is only one kind of scatterer) and divide by N=4 since we put 4 atoms respectively at the origin. Thus, integrating the first peak will yield 12 which is the coordination number of Ni. The same information can be obtained from multi-element samples if the chemical origin of the PDF peak, and therefore the weighting factor, is known. If, as is often the case, PDF peaks from different origins overlap this process is complicated. Information can be extracted by measuring the chemical specific differential or partial-PDFs directly [18], by fitting the peaks with a series of Gaussian functions, or better, by full-scale structural modeling.

Atomic disorder in the form of thermal and zero-point motion of atoms, and any static displacements of atoms away from ideal lattice sites, give rise to a distribution of atom-atom distances. The PDF peaks are therefore broadened resulting in Gaussian shaped peaks. The width and shape of the PDF peaks contain information about the real atomic probability distribution. For example, a non-Gaussian PDF peak may suggest an anharmonic crystal potential.

Modeling the data reveals much more information that straight model independent analysis. The most popular approach for real-space modeling is to use PDFfit, and its replacement PDFfit2 and PDFgui [19, 20], a full-profile fitting method analogous to the Rietveld method [21] but where the function being fit is the PDF.

Parameters in the structural model, and other experiment-dependent parameters, are allowed to vary until a best-fit of the PDF calculated from the model and the data derived PDF is obtained, using a least-squares approach. The sample dependent parameters thus derived include the unit cell parameters (unit cell lengths and angles), atomic positions in the unit cell expressed in fractional coordinates, anisotropic thermal ellipsoids for each atom and the average atomic occupancy of each site.

We highlight here the similarities and differences with conventional Rietveld. The main similarity is that the model is defined in a small unit cell with atom positions specified in terms of fractional coordinates. The refined structural parameters are exactly the same as those obtained from Rietveld. The main difference from conventional Rietveld is that the *local* structure is being fit which contains information about short-range atomic correlations. There is additional information in the data, which is not present in the average structure, about disordered and short-range ordered atomic displacements. To successfully model these displacements it is often necessary to utilize a "unit cell" which is larger than the crystallographic one. It is also a common strategy to introduce disorder in an average sense without increasing the unit cell. For example, in the example where an atom is sitting in one of two displaced minima in the atomic potential, but its probability of being in either well is random, can be modeled as a split atomic position with 50% occupancy in each well. This is not a perfect, but a very good, approximation of the real situation and is very useful as a first order attempt at modeling the data.

This "Real-space Rietveld" approach is proving to be very useful and an important first step in analyzing PDFs from crystalline materials. This is because of two main reasons. First, its similarity with traditional Rietveld means that a traditional Rietveld derived structure can be compared *quantitatively* with the results of the PDF modeling. This is an important first step in determining whether there is significant evidence for local distortions beyond the average structure. If evidence exists to suggest that local structural distortions beyond the average structure are present, these can then be incorporated in the PDF model. The second strength of the real-space Rietveld approach is the simplicity of the structural models making it quick and straightforward to construct the structural models and making physical interpretations from the models similarly quick and straightforward. The most recent version of the PDFfit code comes with a user-friendly graphical user interface facilitating many tasks in the data analysis, called PDFgui and PDFfit2 [19]. PDFfit was originally designed to study disorder and short-range order in crystalline materials with significant disorder such as nanoporous bulk materials. It has also found extensive use in studying more heavily disordered materials such as nanocrystalline materials and nanoporous materials and this looks set to increase in the future.

Conclusions

This chapter contains a brief account of the theory behind the PDF method and the basic methods for obtaining suitable data, analyzing it and extracting nanostructural information from it. Interest in the technique is growing rapidly as the quality of structural information obtainable from it improves due to methodological advances, and as more and more researchers seek to make and characterize materials on the nanoscale.

Acknowledgements

Work in the Billinge group is supported by the US-Department of Energy, Office of Science, through grant DE-AC02-98CH10886 and by the US National Science Foundation through grant DMR-0703940.

References

[1] R. E. Dinnebier and S. J. L. Billinge, *"Powder Diffraction: Theory and Practice"*, **2008**, The Royal Society of Chemistry, Cambridge, UK.
[2] S. J. L. Billinge and I. Levin, *Science* **2007**, *316*, 561-563.
[3] T. Egami and S. J. L. Billinge, "*Underneath the Bragg peaks: structural analysis of complex materials"*, **2003**, Pergamon Press, Elsevier, Oxford, England.
[4] A. S. Masadeh, E. S. Bozin, C. L. Farrow, G. Paglia, P. Juhás, A. Karkamkar, M. G. Kanatzidis and S. J. L. Billinge, Phys. Rev. B **2007**, *76*, 115413.
[5] A. K. Soper, *Chem. Phys.* **1996**, *202*, 295.
[6] S. J. L. Billinge and M. G. Kanatzidis, *Chem. Commun.* **2004**, *2004*, 749.
[7] T. Proffen, S. J. L. Billinge, T. Egami, and D. Louca, *Z. Kristallogr.* **2003**, *218*, 132.

[8] B. E. Warren, "*X-ray diffraction",* **1999**, Dover, New York.
[9] H. P. Klug and L. E. Alexander, "*X-ray diffraction procedures for polycrystalline and amorphous materials"*, 2nd edition, **1974**, Wiley, New York.
[10] V. A. Levashov, S. J. L. Billinge, and M. F. Thorpe, *Phys. Rev. B* **2005**, *72*, 024111.
[11] P. J. Chupas, X. Qiu, J. C. Hanson, P. L. Lee, C. P. Grey, and S. J. L. Billinge, *J. Appl. Crystallogr.* **2003**, *36*, 1342.
[12] URL: http://www.ccp14.ac.uk
[13] Information can be found at the ISIS disordered materials group website: http://www.isis.rl.ac.uk/disordered/dmgroup_home.htm
[14] URL: http://pdfgetn.sourceforge.net/
[15] X. Qiu, J. W. Thompson, and S. J. L. Billinge, *J. Appl. Crystallogr.* **2004**, *37*, 678.
[16] URL: http://www.pa.msu.edu/cmp/billinge-group/programs/PDFgetX2/
[17] R. W. G. Wyckoff, "*Crystal Structures"*, 2nd edition, volume 1, **1967**, Wiley, New York.
[18] D. L. Price and M-L. Saboungi, in "*Local Structure from Diffraction"*, S. J. L. Billinge and M. F. Thorpe Eds., **1998** page 23, Plenum, New York.
[19] C. L. Farrow, P. Juhas, J. W. Liu, D. Bryndin, E. S. Bozin, J. Bloch, T. Proffen, and S. J. L. Billinge, *J. Phys: Condens. Matter* **2007**, *19*, 335219.
[20] URL: http://www.diffpy.org
[21] R. A. Young, "*The Rietveld Method"*, volume 5 of International Union of Crystallography Monographs on Crystallography, **1993**, Oxford University Press, Oxford.

Debye Analysis

Yuri G. Andreev
School of Chemistry, University of St Andrews, St Andrews, Scotland

Introduction

The arrival of Rietveld method manifested the renaissance of powder diffraction methodology as a tool for structure refinement [1]. It took another 25-30 years after that for the powder method to end the dominance of single-crystal diffraction as the technique for *ab initio* structure determination [2-5].

Despite the mentioned advances in powder methodology, single-crystal diffraction remains the technique of choice if a single crystal of adequate quality and size of the solid in question is available. At modern synchrotron sources diffraction data, sufficient for establishing the crystal structure, can be collected from a micron-size single crystal. However, when the crystal size is in the nanometer range or the structure lacks translational symmetry due to disorder, powder diffraction remains the only option on hand.

Full-profile analyses of powder diffraction patterns, *e.g.* Rietveld method, utilise empirical peak-shape functions which work reasonably well when long-range translational symmetry is not violated by small and anisotropic crystallite size, non-uniform deformation of the crystal lattice, loss of structural registry in 1 or 2 dimensions, *etc*. Such crystal structure imperfections are common in a number of materials of current interest, which include graphene and nanoparticles. More often than not, the shape of diffraction peaks from such disorded materials, cannot be adequately described by analytical functions, rendering the application of established powder methods difficult or impossible [6]. The arrival of total scattering approach [7,8] circumvents the use of such methods by employing basic x-ray diffraction theory which uses Fourier transforms. Based on the early methodologies of Kitaigorodsky and Guinier [9,10] originally used to interpret diffuse scattering data, the total scattering approach takes full advantage of the modern powerful synchrotron radiation sources to collect high quality diffraction data in a wide range of values of the modulus of the wave vector, Q. The extended Q range greatly reduces the truncation errors, caused by performing a Fourier transform within a finite interval, and produces an atomic pair distribution function which takes into account both diffuse and Bragg scattering data.

In this presentation a different approach is used to interpret diffraction data from imperfect structures. The method utilises the fundamental equation of Debye [11] which allows to calculate a powder pattern by considering diffraction/interference contributions from each pair of atoms in the scattering domain. Thus calculated

powder profile from a trial direct-space structural model can be directly compared to the experimental diffraction pattern.

Debye formula

In 1915 Debye derived an equation that relates directly the inter-atomic distances between each pair of atoms in the scattering volume to the observed X-ray diffraction pattern, without recourse to symmetry (crystallography) [11]. The equation is exact in the first Born, or kinematic, approximation and deals explicitly with Bragg and diffuse scattering as well as the small-angle scattering from a powder. The intensity of X-ray radiation diffracted by an array of atoms, allowing all orientations of the array to have equal probability, is

$$I(\theta) = \sum_n f_n^2(\theta) + 2\sum_i \sum_j f_i(\theta) f_j(\theta) \left[\sin\left(4\pi r_{ij} \sin\theta/\lambda\right) \Big/ \left(4\pi r_{ji} \sin\theta/\lambda\right) \right],$$

where $f_n(\theta)$ is the atomic form-factor of the n^{th} atom in the array, λ is the wavelength and r_{ij} is the distance between atoms i and j.

To account for the effect of preferred orientation a multiplier, T_{ij}, can be added into the double sum of the above equation [12].

$$T_{ij} = \left(T^2 \cos^2 \alpha_{ij} + \frac{1}{T} \sin^2 \alpha_{ij} \right)^{-3/2}$$

The correction is similar to the March-Dollase formulation [13], however, in this case α_{ij} is the angle between r_{ij} and the preferred orientation vector.

Applications

Layered structures with dimensional disorder

Layered materials with loose coupling between sheets (layers) in the structure are prone to losing the inter-layer registry (ordering) on mechanical impact (*e.g.* ball-milling) or during intercalation/deintercalation of host atoms or molecules between the layers. The classic examples of such materials are graphite and hexagonal boron nitride. Under normal circumstances both solids have a highly symmetrical hexagonal structure with only a few atoms in the asymmetric unit. Atoms in these structures are arranged in honeycomb layers, with the latter stacked in registry, forming a 3D-ordered array which gives a powder pattern with sharp symmetric peaks, Fig.1a.

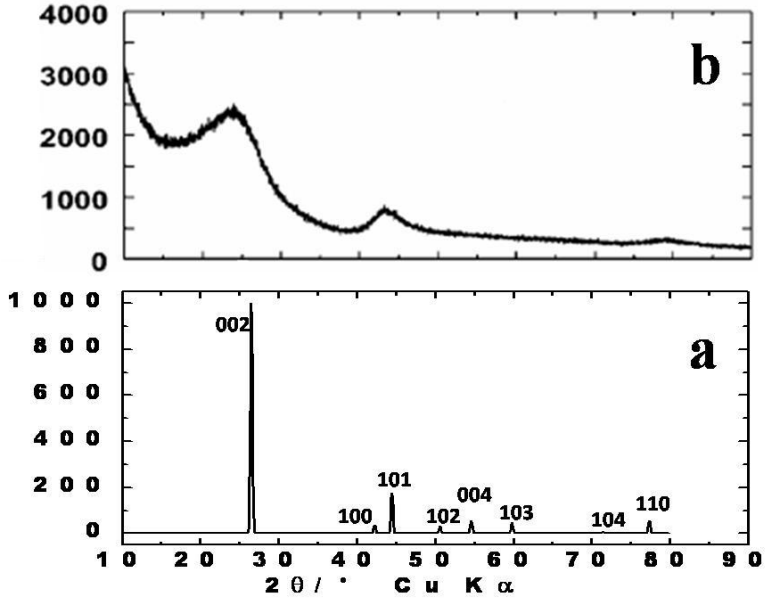

Fig. 1. X-ray diffraction patterns of 3D-ordered (a) and turbostratically disordered (b) graphite

When such layered materials are synthesised *via* a disorder-inducive route or subjected to mechanical or chemical treatments mentioned above, the size of the in-plane ordered regions tend to decrease along with the degree of the inter-layer registry. This type of disorder is often referred to as turbostratic distortions. Such distortions have dramatic effect on the powder diffraction pattern, Fig. 1b. All reflections that are not of the *00l*, *h00* or *hk0* type disappear. The *00l* peaks broaden and shift to lower *2θ* (higher *d*-spacing) values, while the shape of the in-plane *h00* and *hk0* reflections, in addition to broadening and shifting of the position of the maximum count towards higher *2θ*, becomes highly asymmetric, with significantly slower intensity decay from the peak maximum on the lower *d*-spacing side. The latter peak shape in some cases can be adequately described by the function derived by Warren and Bodenstein for diffraction reflections from a single circular honeycomb layer (or a collection of randomly oriented layers of this type) [14]. The profile, $Y_{hk}(2\theta)$, of such 2D reflection is defined as follows

$$Y_{hk}(2\theta) = mMD\lambda^{3/2}F^2R^{5/2}\Omega\left[2\pi A_a^2 \sin\theta\left(\sin\theta + \sin\theta_0\right)^{1/2}\right]^{-1},$$

where

$$\Omega = \int_0^1 \left\{\left[\arccos S - S\left(1-S^2\right)^{1/2}\right] \Big/ S^{1/2}\right\}\left(\cos 2\pi\gamma S + \sin 2\pi\gamma S\right) dS,$$

$$A_a = a^2\sqrt{3}/2,\ \gamma = \left(4R/\lambda\right)\left(\sin\theta - \sin\theta_0\right),$$

m is the multiplicity of the *hk* reflection; *M* is the number of randomly oriented layers in the sample; *D* is the distance to the receiving surface; λ is the wavelength; *F*, *R* and *a* are the in-plane structure factor, layer radius and lattice parameter, respectively; θ_0 is the position of the *hk0* reflection in the case of 3D ordering. Note that, unlike for 3D reflections, the position of the 2D peak maximum is a function not only of the in-plane lattice parameter but also of the layer size!
The peak-shape function of Warren and Bodenstein has been successfully applied to determine the in-plane crystallite size and lattice in a turbostratically disordered hexagonal BN, Fig. 2 [15].

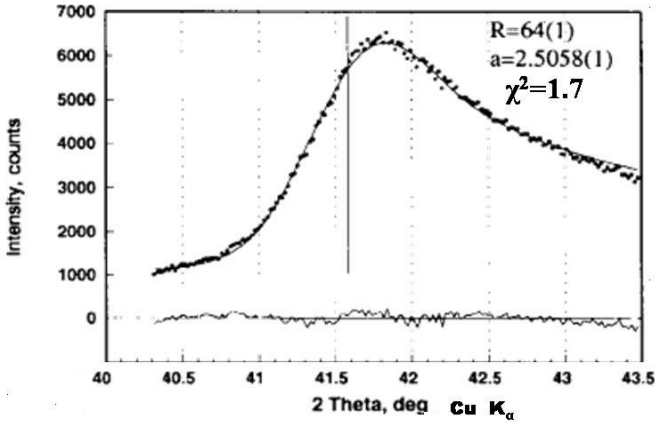

Fig. 2. Exprimental (dots), calculated using the formulation of Warren and Bodenstein [14] (solid line) and difference (solid line around y=0) X-ray diffraction profile of *10* peak of turbostratically disordered hexagonal BN. Vertical solid line indicates the position of *100* reflection in 3D-ordered hex-BN, *R*, and *a* (both in Å) are the in-plane radius of the ordered region and lattice parameter, respectively.

However, modelling of 2D diffraction peak shapes from single honeycomb layers of different size, Fig. 3, and ensembles of parallel, but not in complete crystallographic registry, layers (to produce *00l* reflections, in addition to *h0* and *hk*) using Debye equation clearly demonstrates that the analytical formulation would fail in some cases [16].

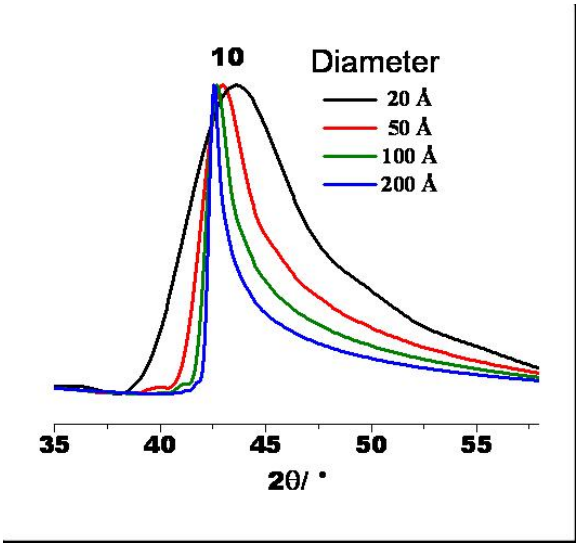

Fig. 3. Calculated using Debye equation X-ray diffraction profiles of *.10* reflection from single circular graphene layers of different size.

Thus, when the radius of a layer is reduced to 10 Å deviations from perfect circular shape become more evident and the 2D profile shape suggested by Warren and Bodenstein provides a poor match to the true profile obtained by using the equation of Debye. Similarly, even for larger layer size, when turbostratic distortions are caused by random rotations of the layers, the single-layer peak shape fails to adequately describe the 2D reflection profile, Fig. 4.

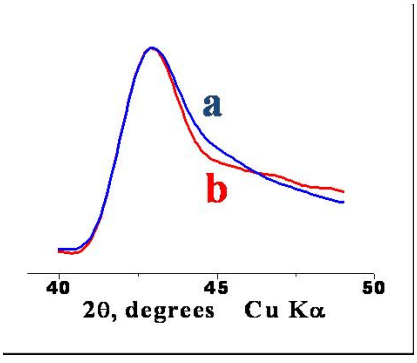

Fig. 4. Calculated using Debye equation X-ray diffraction profiles of *.10* reflection from (a) single circular graphene layer (50 Å in diameter) and (b) 16 such layers first stacked in the *ABAB* registry of graphite and then rotated by a randomly chosen angle around their centres.

Oxidation of Ni nanoparticles

In the course of neutron diffraction study of oxygen insertion into spherical Ni nanoparticles, 160 Å in diameter, a pronounced peak asymmetry, Fig. 5, has been

detected at early stages of oxidation, when the oxygen content is several atomic percents and the NiO phase is not yet formed [17].

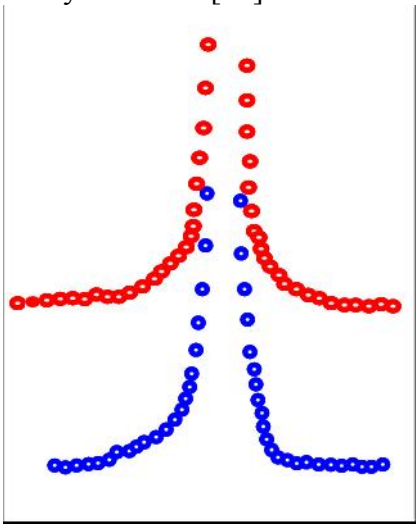

Fig. 5. Fragments of the experimental neutron diffraction profile of the *400* reflection from oxygen-free (top) 160 Å Ni particles and the same particles at an early oxidation stage (bottom).

The true diffraction profiles, *I(θ)*, of the *400* reflection from the oxidised and oxygen-free powders, which have been extracted by solving the convolution equation

$$H(\theta) = \int I(\theta) G(\theta - \theta') d\theta'$$

[*H(θ)* and *G(θ)* are experimental profiles from the nanoparticular and micron-size Ni powders, respectively], reveal that on oxidation the intensity of the left satellite of the main peak becomes greater than that of the right satellite, Fig. 6.

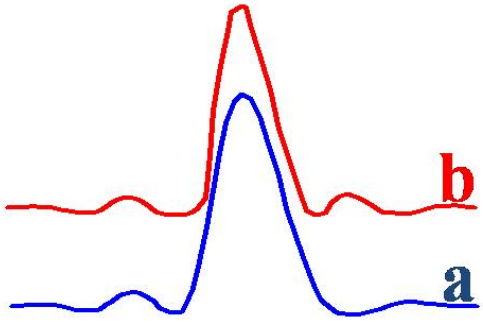

Fig. 6. True neutron diffraction profiles, *I(θ)*, of the *400* reflection from 160 Å Ni particles (a) at an early oxidation stage and (b) oxygen-free.

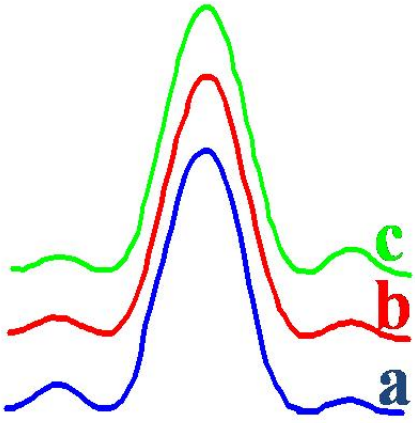

Fig. 7. Calculated using Debye equation neutron diffraction profiles of the *400* reflection from (a) non-uniformly expanded, (b) ideal and (c) non-uniformly contracted spherical Ni nanoparticles.

In order to explain the changes in the peak shapes the profile of the *400* reflection was calculated using Debye equation. A spherical Ni particle with the ideal and non-uniformly deformed *fcc* structure was used as a model. The deformation was introduced through the components of the deformation tensor implying that the greatest distortion of the ideal lattice is observed on the surface of the particle and gradually reduces towards the centre. The calculated profiles show that the satellites of the main diffraction peak are of equal height for the ideal particle (Fig. 7b) while non-uniform deformation causes considerable redistribution of their intensities. The left-hand side satellite is higher for the expanded particle (Fig. 7a) and is lower for the non-uniformly contracted particle (Fig. 7c). The $I(\theta)$ profile from the oxidised powder is similar to that of the expanded particle (compare Fig.6a and Fig. 7a). It is natural to assume that the observed deformation is caused by the presence of oxygen atoms in the nickel particle which form a coherent solid solution with the metal. The non-uniformity of the deformation can be explained by the concentration gradient of oxygen within the particle, with the higher oxygen content in the surface area.

Deformations in TiO_2-B nanotubes

According to TEM data internal and external diameters of TiO_2-B nanotubes are ~50 and ~100 Å respectively, and the length can be up to tens of microns. A powder X-ray diffraction pattern for the nanotubes is presented in Fig. 8 along with the ideal monoclinic TiO_2-B crystal structure and a simulated powder X-ray diffraction pattern based on the latter.

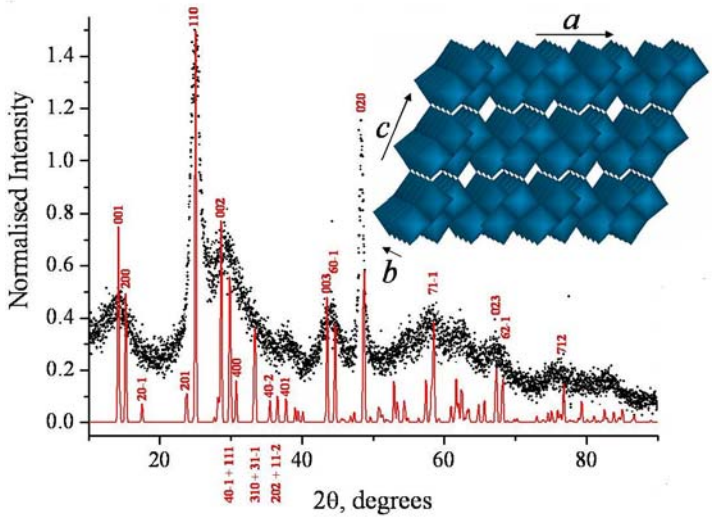

Fig. 8. Dots - observed X-ray diffraction pattern of TiO_2-B nanotubes; red line – simulated pattern based on the ideal TiO_2-B structure. Numbers are Miller indices. Inset shows ideal TiO_2-B crystal structure with crystallographic axes.

Comparison between the simulated and observed powder patterns highlights the severe *hkl*-dependent peak broadening/distortion of the latter, features that reflect the limited dimensions of the tube walls, the anisotropy of the nanotubes and the structural distortions (deviations from the ideal crystal structure) which are expected to occur on bending a layered crystal structure into a nanotube.

The *020* reflection in Fig 8 is noticeably narrower than other peaks in the experimental pattern and by application of the Scherrer formula a coherence length in the *b* direction is estimated at 144 Å. This exceeds the diameter of the tubes and implies that the *b*-axis lies along the axial direction of the nanotubes.

Many materials have been formed as nanotubes, the vast majority are based on layered structures in which the layers fold to form the tubes. Since the layers of the TiO_2-B structure lie in the *ab* plane and since *b* lies along the axial direction, a tube may be formed by folding the *ab* plane along *a*, as shown in Fig 9 (middle pattern).

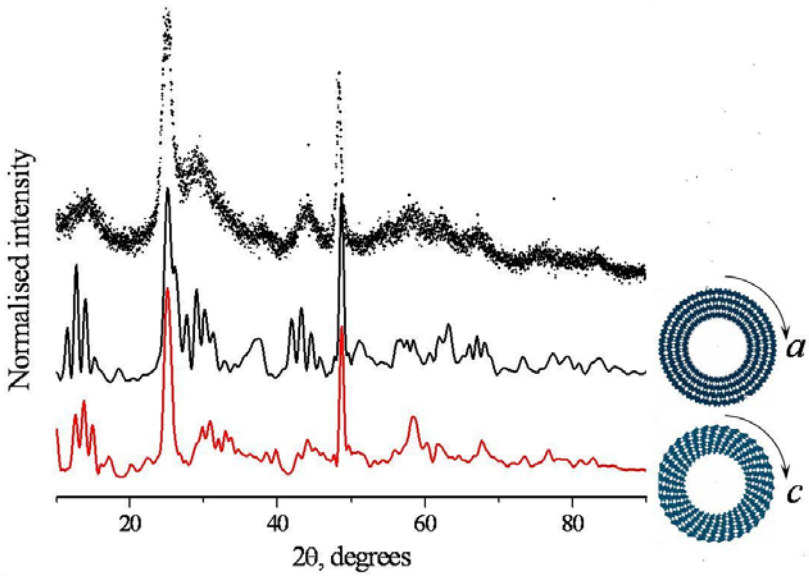

Fig. 9. Dots - observed X-ray diffraction pattern of TiO_2-B nanotubes; black line – simulated pattern based on folding the *ab* plane of the ideal TiO_2-B structure along *a* into a tube; red line - simulated pattern based on folding the *bc* plane of the ideal TiO_2-B structure along *c* into a tube. Views along the tube axis for each model are also shown.

Such a structure is consistent with the TEM image which indicates that the walls are composed of 4 layers, consistent with the wall thickness of ~25 Å. Hence, the first structural model to be constructed was based on folding 4 layers of the crystal structure in the *ab* plane, as just described. The length of the tube was set at 142 Å (equivalent to 38 unit cells along *b* in the ideal structure), consistent with the coherence length along *b*, and the internal diameter at 23 Å, consistent the TEM data. Bending a slab of the ideal TiO_2-B structure into a tube inevitably leads to distortions of the TiO_6 octahedra along the annulus of the tube.

A powder diffraction pattern generated from this model using Debye equation is compared with experiment in Fig 9, from which it is clear that the model does not adequately describe the nanotubes. The peaks of the simulation are narrower and more abundant than in the observed powder diffraction pattern, suggesting that the model possesses more symmetry than is the case in practice. Similar problems are noted for an alternative model in which the tubes are formed by folding the *bc* plane along *c*, Fig 9 (bottom pattern). Despite the inadequacies of both models, comparison between them and the observed powder diffraction pattern suggests that folding along *a* better describes the nanotubes. Also, as discussed above, folding along *a* is more physically reasonable than folding along *c*.

Recognising that a model involving order throughout the entire nanotube does not adequately describe the observed data, segments of this structure were considered, all retaining 4 layers in the radial direction and extending 142 Å along *b* but extend-

ing to different degrees along the circumference. A segment of dimension 32 Å best represents the observed data, Fig. 10.

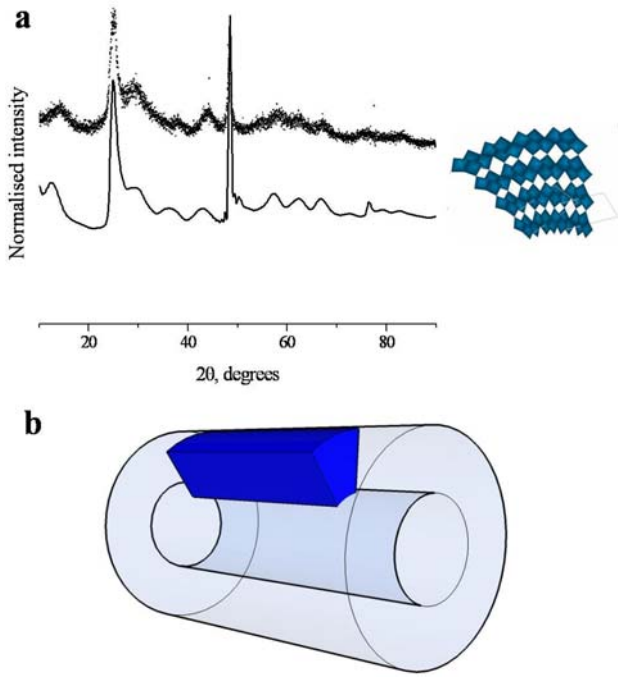

Fig. 10. (a) Dots - observed X-ray diffraction pattern of TiO_2-B nanotubes; black line –simulated pattern of a 3.2 nm tube segment with a view of the model along *y*. (b) Schematic representation of an ordered segment within a nanotube.

A schematic representation of a segment within the tube is also shown in Fig. 10; the segments are not in registry with each other but are aligned along the axial direction of the tubes. Further details about this investigation can be found in [12].

Structure refinement of TiO_2-B nanoparticles

In all of the above examples of Debye analysis only visual comparison of calculated and experimental powder diffraction data has been used to arrive at the conclusions about the structural imperfections. Ultimately a full-profile structure refinement procedure based on Debye equation is required.

An algorithm and a computer code for such Debye refinement have been recently developed. The algorithm utilises a simulated annealing procedure, with a protocol similar to that described in reference [18], to find the minimum of the conventional, in structure refinements, figure-of-merit function, χ^2. The code is written for computers with multiple processors working in parallel.

The refinement procedure has been successfully applied to refine the shape and structural parameters of TiO_2-B nanoparticles. Based on the TEM data, these nanoparticles were originally characterised as 30 Å spheres with the structure of the bulk TiO_2-B phase. However, a powder pattern calculated from the reported model using Debye equation provides a rather poor fit to the experimental data, Fig. 11a,

while the latter reveals an anisotropic peak broadening (albeit less pronounced than in the case of the nanotubes), suggesting less symmetrical shape of the coherently

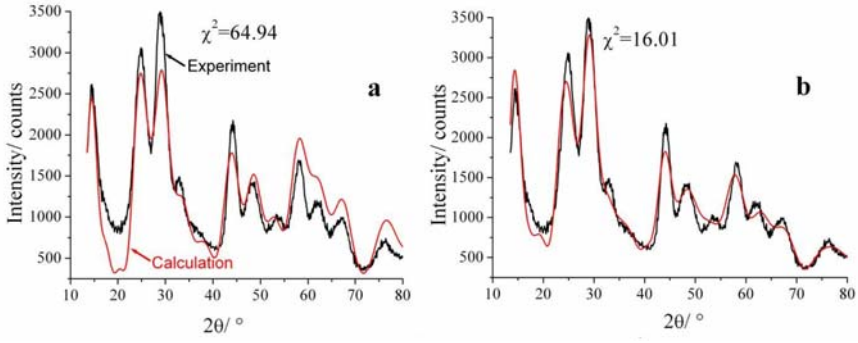

scattering regions.

Fig. 11. Observed and calculated using Debye equation X-ray diffraction patterns of TiO_2-B nanoparticles in the beginning (a) and at the end (b) of structure refinement.

During the refinement, the crystallites were described as ellipsoids, with variable axes lengths In addition, 4 lattice parameters of the monoclinic cell and the amplitudes of isotropic mean-square displacements,$<U^2>^{1/2}$, for Ti and O atoms were varied. The refinement was performed on a 12-core workstation and converged after 24 hours, producing a significantly better fit to the experimental pattern, Fig. 11b.
The axes of the elliptical particles turned out to be 24, 25 and 39 Å, $<U^2>^{1/2}$ values close to 0.5 Å, for both Ti and O.

References

1. H. M. Rietveld, *J. Appl. Cryst.* 1969, **2**, 65.
2. A. Altomare, M. C. Burla, M. Camalli, G. Cascarano, C. Giacovazzo, A. Guagliardi, A. G. G. Moliterni, G. Polidori and R. Rizzi, *Materials Science Forum* 1998, **278**, 284
3. Y. G. Andreev, P. Lightfoot and P. G. Bruce, *J. Chem. Soc. Chem. Comm* 1996, 2169.
4. B. M. Kariuki, H. Serrano-Gonzalez, R. L. Johnston and K. D. M. Harris, *Chem. Phys. Lett.* 1997, **280**, 189.
5. W. I. F. David, K.Shankland and N. Shankland, *J. Chem. Soc. Chem. Comm.* 1998, 931.
6. S. J. L. Billinge and I. Levin,. *Science* 2007, **316**, 561.
7. R. L. McGreevy and L. Pusztai,. *Molecular Simulation* 1988**, 1**, 359.
8. V. Petkov, S. J. L. Billinge, S. D. Shastri and B. Himmel,. *J. Non-Crystalline Solids* 2001, **293**, 726
9. A. I. Kitaigorodsky X-ray Structural Analysis of Microcrystalline and Amorphous. Substances Gostekhizdat, Moscow, 1952 (in Russian).
10. A. Guinier. (1963). X-ray Diffraction in Crystals, Imperfect Crystals and Amorphous Bodies. W. H. Freeman and Co., San Francisco:, 1963 (first published in French in 1956)
11. P. Debye,. *Annalen der Physik* 1915, **351**, 809.
12. Y. G. Andreev and P. G. Bruce, *J. Am. Chem. Soc.* 2008, **130**, 9932.
13. W. A. Dollase,. *J. Appl. Cryst.* 1986, **19**, 267.
14. B. E. Warren and P. Bodenstein, *Acta Cryst.* 1966, **2**, 602.
15. Y. G. Andreev and T. Lunström, *J. Appl. Cryst.* 1994, **27**, 767.
16. Y. G. Andreev and T. Lunström, *J. Appl. Cryst.* 1995, **28**, 534.
17. Y.G. Andreev, A.V. Burkhanov, A.G. Ermolaev, F. M. Zelenyuk, V. N. Lapovok, V. F. Petrunin, E. P. Sukhovich and L. I. Trusov, *Phys. Chem. Mech. Surfaces* 1990, 5, 2560. (first published in Russian in 1986).
18. Y. G. Andreev, P. Lightfoot and P. G. Bruce, *J. Appl. Cryst.* 1997, **30**, 294

Quantitative Phase Analysis

Ian C. Madsen, Nicola V.Y. Scarlett and Nathan A.S. Webster
CSIRO Process Science and Engineering, Clayton Sout, Victoria, Australia

1. Introduction [i]

The most common use of powder diffraction in analytical science is the identification of crystalline components, or phases, present in a sample of interest. The near universal applicability of the method for this purpose is derived from the fact that a diffraction pattern is produced directly from the components' crystal structure. However, for multi-phase samples, once the nature of phases present has been established, the next question usually asked of the diffractionist is “how much of each phase is there ?”

The mathematical basis of quantitative phase analysis (QPA) from diffraction data is well established and, in an ideal world, QPA should be a relatively straightforward science. However, there are a significant number of factors, most of them experimental, which serve to decrease the accuracy which can be obtained. Some of these, such as accuracy in measurement of peak position and intensity, resolution of overlapping peaks and counting statistics, relate to instrument geometry and data collection conditions, while other sources of error derive from sample related issues. This latter group includes effects such as preferred orientation (which distorts the observed relative intensities from those expected for a randomly oriented powder), crystallite size and strain broadening (leading to increased peak overlap) and microabsorption (where phases which strongly absorb the incident and diffracted beams are underestimated with respect to weakly absorbing phases). Microabsorption remains the largest impediment to accurate QPA and is more pronounced in X-ray diffraction than neutron based studies.

This paper provides some of the background to methods of QPA from diffraction data. The round robin on quantitative phase analysis run under the auspices of the International Union for Crystallography (IUCr) Commission on Powder Diffraction (CPD) [1-2] demonstrated that 87% of participants collected laboratory-based X-ray diffraction data, while the majority (75%) used whole pattern, especially Rietveld [3] based, methods for the analysis of their data.

Rietveld-based methods have the potential to produce more accurate and precise results than those obtained from conventional single peak methods. The improvement derives from the fact that (i) all of the peaks in the pattern contribute to the analysis, regardless of the degree of overlap, and (ii) the impact of some sample related effects, such as preferred orientation, are minimised by the inclusion of all reflections.

The application of models for correction of other residual aberrations, serves to further improve the analysis.
While the Rietveld technique was initially developed for the refinement of crystal structure, other parameters, which must be refined to ensure best fit between the observed and calculated patterns, contain useful, non-structural information which can be of interest to the analyst. These include peak width and shape which can be related to crystallite size and strain or preferred orientation parameters which can be related to crystal morphology. However, it is the Rietveld scale factor which, in a multiphase mixture, is related to the amount of the phase present that is interesting in the current context.
There is extensive coverage of traditional 'single-peak' methods in earlier literature [4-8] plus a thorough review of the field by Zevin and Kimmel [9] to which the reader is directed for more detailed explanations. Due to the wide-spread use of the Rietveld method in QPA, this chapter will focus only on the use of whole-pattern, Rietveld based approaches. The mathematical basis will be described along with detailed discussion of various modifications which aim to produce absolute, rather than relative phase abundances. A number of case studies and applications, which serve to illustrate selected issues in QPA, are also presented.

2.Mathematical Basis

2.1. Rietveld-Based Methods

The Rietveld method uses a model to calculate a diffraction pattern which is then compared with observed data. The difference between the two patterns is then reduced through least squares minimisation. The refinable parameters used in the models provide the analyst with information regarding the crystal structure of the component phases, the crystallite size and strain and, importantly, their relative proportions. The Rietveld scale factor, which is a multiplier for each component's contribution to the pattern, is related to the relative abundance of that phase and can be used in the quantification of phases.
The integrated intensity I of the hkl reflection for phase α in a multi-phase mixture measured on a flat-plate sample of infinite thickness using a diffractometer with Bragg-Brentano geometry is given by:-

$$I_{(hkl)\alpha} = \left[\frac{I_0 \lambda^3}{32\pi r}\frac{e^4}{m_e^2 c^4}\right]\cdot\left[\frac{M_{hkl}}{2V_\alpha^2}\left|F_{(hkl)\alpha}\right|^2\cdot\left(\frac{1+\cos^2 2\theta\cos^2 2\theta_m}{\sin^2\theta\cos\theta}\right)\cdot Exp\left(-2B\left(\frac{\sin\theta}{\lambda}\right)^2\right)\right]\cdot\left[\frac{W_\alpha}{\rho_\alpha \mu_m^*}\right] \quad (1)$$

where I_0 is the incident beam intensity, e is the charge on an electron, m_e is the mass of an electron, r is the distance from the scattering electron to the detector and c is the speed of light. M_{hkl} and F_{hkl} are the multiplicity and structure factor of the hkl reflection respectively, V is the unit cell volume and θ and θ_m are the diffraction angles for the hkl reflection and the monochromator respectively. B is the mean atomic displacement parameter (ADP). W_α and ρ_α are the weight fraction and density of phase α respectively, while μ_m^* is the mass absorption coefficient of the entire sample.

Many of the terms in Equation 1 can be grouped together and defined as a constant K. Equating $I_{(hkl)\alpha}$ with the overall Rietveld scale factor S_α for each phase, Equation 1 reduces to :-

$$S_\alpha = \left[\frac{K}{V_\alpha^2}\right] \cdot \left[\frac{W_\alpha}{\rho_\alpha}\right] \cdot \frac{1}{\mu_m^*} \qquad (2)$$

Since this expression inherently contains the weight fraction information it can be rearranged to derive W_α :-

$$W_\alpha = \frac{S_\alpha \rho_\alpha V_\alpha^2 \mu_m^*}{K} \qquad (3)$$

The value K is an 'experiment constant' that can be used to put W_α on an absolute basis. O'Connor and Raven [10] have shown that K is dependant only on the instrumental conditions and is independent of individual phase and overall sample-related parameters. A single measurement therefore is sufficient to determine K for a given instrumental configuration.
For each phase, the density ρ_α can be calculated from :-

$$\rho_\alpha = 1.6604 \cdot \frac{ZM_\alpha}{V_\alpha} \qquad (4)$$

where ZM is the mass of the unit cell contents (Z is the number of formula units in the unit cell and M is the molecular mass of the formula unit) and V is the unit cell volume [1].

Substitution and rearrangement of Equation 4 in Equation 3 shows that:-

$$W_\alpha = \frac{S_\alpha (ZMV)_\alpha \mu_m^*}{K} \qquad (5)$$

[1] The value $1.6604 = 10^{24} / 6.022 \times 10^{23}$ is needed to convert ρ in AMU/Å^3 to g/cm^3

In this context, $(ZMV)_\alpha$ is the 'calibration constant' for phase α and can be calculated from published or refined crystal structure information alone. Determination of K may be carried out by :-

(i) Measurement of a standard pure phase or mixture separately from the measurement of the actual unknown mixture in question, or

(ii) Using a phase which is present in the sample in known amount.

The value of K calculated in this way will be appropriate for the calibration of subsequent measurements as long as all instrumental conditions remain the same as those used in its determination. This methodology is important in many applications in that it produces, within the limits of experimental error, absolute phase abundances and is referred to hereafter as the external standard approach. While the use of a phase within the sample to determine K may be considered as an internal standard approach, in some applications, including *in situ* studies, that phase may be removed from the system through, for example, decomposition or dissolution. However, the value of K remains valid for subsequent determination of phase abundances as the reaction proceeds.

Equation 5 is directly applicable for the analysis of those phases for which detailed crystal structure information is available. For phases where only a partial structure (for example, an indexed unit cell but no atom coordinates or site occupation factors) is available, an empirical ZMV can be derived using mixtures of the phase of interest with known amounts of a well characterised standard [11]. QPA of phases with partial structure is also possible through the use of Equation 3 but an estimate of the phase density, obtained through direct measurement, is required.

The limitations of the approach embodied in Equations 3 and 5 derive from the need to (i) conduct a measurement of K and (ii) estimate the value of the mass absorption coefficient μ_m^* for the sample(s) used to determine K, as well as each sample of interest. The benefits which can be derived however, namely the ability to extract the absolute, rather than relative, phase abundances, make it worth pursuing in many analytical situations.

The value of μ_m^* can be calculated from the sum of the products of the theoretical mass absorption coefficient (μ_j^*) of each element (or phase) and the weight fractions (W_j) of all n elements (or phases) in the sample. Elemental composition may be determined, for example, by X-ray fluorescence (XRF) measurement and use of this is more accurate than the use of phase composition as it takes into account any amorphous material not represented by peaks in the diffraction pattern but which still contributes to μ_m^*.

$$\mu_m^* = \sum_{j=1}^{n} \mu_j^* W_j \qquad (6)$$

The need to measure K and measure, or calculate, μ_m^* serves to increase the overall experimental difficulty and can be eliminated in a number of ways. For a simple two phase mixture where both phases, α and β, are fully crystalline, the sum of their weight fractions W_α and W_β equals unity and can be expressed as [12]:-

$$W_\alpha = \frac{W_\alpha}{\left(W_\alpha + W_\beta\right)} \tag{7}$$

Substitution of Equation 5 for phases α and β in Equation 7 results in:-

$$W_\alpha = \frac{S_\alpha \left(ZMV\right)_\alpha}{S_\alpha \left(ZMV\right)_\alpha + S_\beta \left(ZMV\right)_\beta} \tag{8}$$

Alternatively, in a multi-phase sample, the addition of an internal standard s in known amount W_s and taking the ratio of Equation 5 for analyte and standard phases provides the relationship:-

$$W_\alpha = W_s \cdot \frac{S_\alpha \left(ZMV\right)_\alpha}{S_s \left(ZMV\right)_s} \tag{9}$$

The method embodied in Equation 9 also serves to produce absolute phase abundances $W_{\alpha(absolute)}$ and is referred to hereafter as the internal standard approach. One of the benefits accruing from the use of absolute phase abundances is the ability to estimate the presence and amount of any amorphous and/or unidentified phases $W_{(unknown)}$ present through :-

$$W_{(unknown)} = 1.0 - \sum_{k=1}^{n} W_{k(absolute)} \tag{10}$$

The so-called matrix flushing method of Chung [13-14] uses the additional constraint that all phases are known and included in the analysis. The consequence of this constraint is that the analysed weight fractions are summed to the assumed concentration of the crystalline components (usually unity). Hill and Howard [15] and Bish and Howard [12] have applied the matrix flushing approach to the Rietveld analysis context and shown that the weight fraction of phase α in an n phase mixture is given by the relationship :-

$$W_\alpha = \frac{S_\alpha (ZMV)_\alpha}{\sum_{k=1}^{n} S_k (ZMV)_k} \tag{11}$$

The use of Equation 11 in QPA once again eliminates the need to measure the instrument calibration constant and estimate the sample mass absorption coefficient. However, the method normalizes the sum of the analysed weight fractions to unity. This approach, while it is the most widely used in Rietveld based QPA and is almost universally coded into Rietveld analysis programs, only produces the correct relative phase abundances. If the sample contains amorphous phases, and/or minor amounts of unidentified crystalline phases, the analysed weight fractions will be overestimated. Where absolute phase abundances are required in, for example, the derivation of reaction kinetics in *in situ* studies, then one of the methods which produces absolute phase abundances must be used.

3. QPA applications in minerals research

3.1. Crystallisation from hydrothermal solutions

The strengths and weaknesses of some of the methods described in Section 2.1 are highlighted in the recent work of Webster et al. [16] in a study of the mechanism and kinetics of nucleation and crystal growth in the context of the Bayer process for the extraction of aluminium from bauxite ores. Specifically, the experiments utilise synthetic Bayer liquors, consisting of Al-loaded caustic solutions to which a variety of seed material is added. Several polymorphs of $Al(OH)_3$ (gibbsite, bayerite and nordstrandite) crystallise from solution onto the seed material. The rate of crystallisation, and the ratio of the phases, depends on the sample conditions used, including the Al and caustic concentration in solution, as well as sample temperature.

The mechanism and rate of crystallisation were followed by collecting X-ray diffraction data at the powder diffraction beamline of the Australian Synchrotron over a period of about 3 hours. The diffractometer incorporates a Mythen detector [17] which allows for the simultaneous collection of 80º 2θ of the diffraction pattern. A wavelength 0.826 Å was used to ensure adequate penetration of the beam in the sample. The sample environment (described in Madsen et al. [18]) consisted of a 1 mm quartz glass capillary heated to temperatures between 60 and 75º C using a hot air blower.

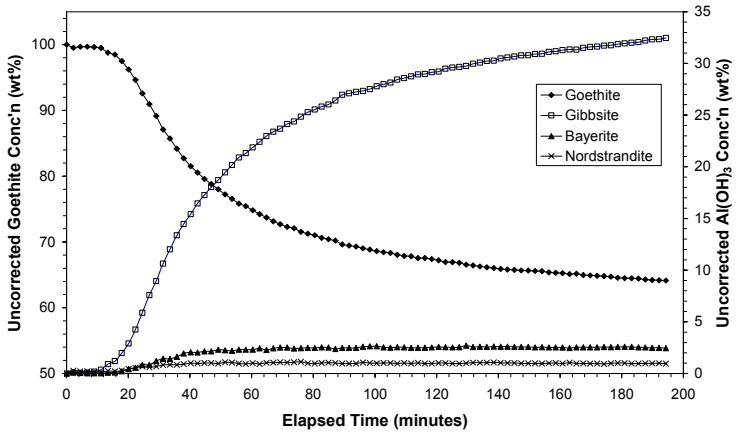

Fig. 1. The results of quantitative phase analysis from the seeding experiments of Webster *et al.* [16]. The values were derived using the Hill/Howard [15] relationship in Equation 11. Note the decrease in apparent goethite concentration (left axis) as the polymorphs of $Al(OH)_3$ (right axis) crystallise from solution.

The data were analysed using the TOPAS software [19]. A fundamental parameters approach [20] was used with an empirical instrument width and shape contribution determined using the NIST SRM660 LaB6 profile standard. For the samples in the study, refined parameters included 2θ zero offset, pattern background and, for each phase, the Rietveld scale factor, crystallite size and strain and unit cell dimensions. A number of different approaches were used to extract the phase abundances at each stage of the reaction. Initially, QPA was derived using Equation 11; the value that many Rietveld analysis programs output as their first estimate of phase abundance. Figure 1 shows the output from an *in situ* run in which goethite (FeOOH) was added as the seed.

At the start of the run, prior to the crystallisation of any of the $Al(OH)_3$ polymorphs, Figure 1 shows that the reported concentration of the goethite seed is 100 wt% since it is the only phase represented in the analysis at that time. On formation of gibbsite, bayerite and nordstrandite, the goethite concentration decreases progressively to about 65 wt% and the total $Al(OH)_3$ concentration reaches about 35 wt% at the end of the run. However, these figures are in disagreement with (i) the fact that goethite is unlikely to dissolve or otherwise be consumed in this system, (ii) the known addition of goethite to the sample and (iii) the total amount of Al available from solution. The problem with the QPA in this case arises from the fact that only the crystalline components are considered in the analysis and that Equation 11 normalises the sum of their analysed weight fractions to unity. However, aluminium, which is in solution at the start of the run, forms crystalline phases continuously throughout the reaction after an initial incubation period. In order to overcome the anomalies in the QPA results, it is necessary to consider the sample as a whole; that is, the concentra-

tion of both the solid and liquid components in the X-ray beam for the duration of the experiment.

In this sample, the goethite seed was added at a concentration of 14.13 wt% in the slurry injected into the sample capillary. If the assumption is made that, in this environment, goethite is unreactive and hence will not change its concentration during the reaction, it can effectively be used as an internal standard to put the $Al(OH)_3$ concentrations on an absolute basis. The QPA results derived using the internal standard or 'spiked' approach in Equation 9 are shown in Figure 2.

The goethite concentration is now fixed at the known addition at the start of the run. The concentrations of the $Al(OH)_3$ polymorphs are put on an absolute scale, thus allowing derivation of relative rates of formation for runs conducted at different temperatures.

If, however, there is residual doubt about the reactivity of the goethite, it may be necessary to use the external standard approach embodied in Equation 5. In this case the value for the instrument constant, K, can be derived using the Rietveld scale factor, ZMV and the known addition of goethite in a rearranged Equation 5. For this determination, the goethite scale factor from the first few data sets was averaged to minimise any errors which may be introduced by counting statistics. The value of the sample mass absorption coefficient μ_m^* has been set to an arbitrary value of unity for both the determination of K and all subsequent analyses since the overall chemical content of the capillary, and hence the attenuation of the X-ray beam, does not change during the reaction.

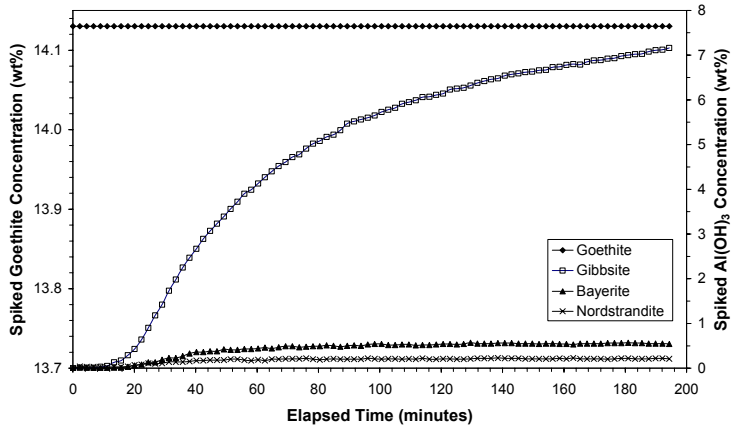

Fig. 2. The results of quantitative phase analysis from the seeding experiments of Webster *et al.* [16]. The values are absolute phase abundances derived using the relationship in Equation 9. The goethite concentration (left axis) is now fixed at the known addition at the start of the run (14.13 wt%).

This experimental work was conducted at the Australian Synchrotron where the ring current is boosted every 12 hours. In between these times the current, and hence the incident beam intensity, decays resulting in what amounts to a change in the 'in-

strument configuration'. This requires a modification of the *K* value and subsequent calculation of concentration to compensate for the changing incident intensity in a modified Equation 5 :-

$$W_{\alpha i} = \frac{S_{\alpha i}(ZMV)_{\alpha}\,\mu_m^*}{K} \cdot \frac{I_0}{I_i} \qquad (12)$$

where I_0 and I_i are the monitor count (or ring current) at the start of the run and during data set *i* respectively.

Figure 3 now shows the results of QPA derived from Equation 12. In this case the concentrations of the $Al(OH)_3$ polymorphs are similar to those in Figure 2. However, since the phase abundances are derived using an external standard approach, any changes in the goethite concentration can now be monitored. Figure 3 shows a small, but systematic, decrease in the goethite concentration as the run progresses. At the end of the run, the goethite concentration appears to be lower by about 1% relative than the concentration at the start.

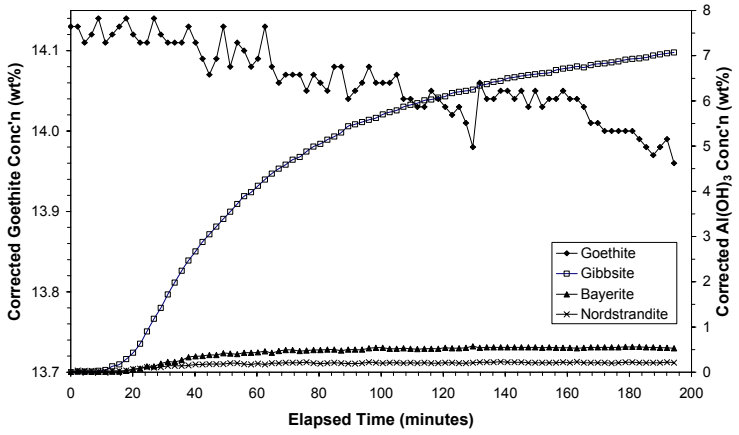

Fig. 3. The results of quantitative phase analysis from the seeding experiments of Webster *et al.* [16]. The values are absolute phase abundances derived using the relationship in Equation 12. Note the slight decrease in the goethite concentration (left axis) during the run.

This apparent decrease has been attributed to the 'shielding' of the goethite from the X-ray beam by the $Al(OH)_3$ phases as they form and coat the goethite nuclei. This decrease in intensity from the goethite could then be used to obtain an average thickness of the $Al(OH)_3$ phases. This layer was calculated to be about 5.5 μm (assuming a linear absorption coefficient of 9.5 cm^{-1} for gibbsite) resulting in an overall particle size of about 11 μm at the end of the run (the goethite particles are about 0.2 x 2 μm and hence do not contribute significantly to the overall particle size). This is in good agreement with independent SEM measurements.

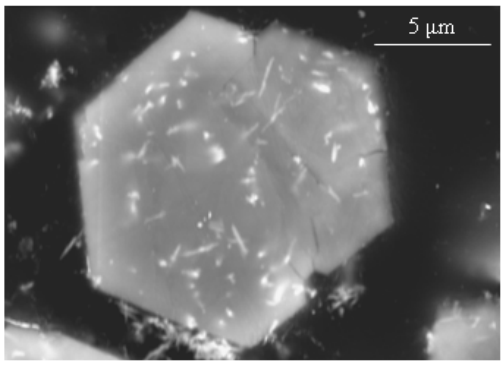

Fig. 4. SEM image of a gibbsite particle (grey) which has grown on the goethite seed (white inclusions).

4. Precision, Accuracy & Calculation of Error [ii]

The question of precision and accuracy in QPA via XRD is a difficult one. It is simple enough to calculate errors on the basis of replication or precision in the mathematical fit. However, determination of the actual accuracy of the analysis is no trivial task in a standardless method. In fact, it cannot be achieved without recourse to some other measure of the sample which does incorporate standards. Too often, analysts will report Rietveld errors calculated in the course of refinement as the errors in the final quantification. These numbers relate purely to the mathematical fit of the model and have no bearing on the accuracy or otherwise of the quantification itself.

Consider, for example, a three phase mixture of corundum, magnetite and zircon. Such a sample was presented as Sample 4 in the IUCr CPD Round Robin on quantitative phase analysis [2]. Its components were chosen with the deliberate aim of creating a sample in which severe microabsorption occurs. Table 1 shows the weighed amounts of each component and the results of replicate analyses of three different sub-samples of this material.

In this context, the Rietveld error represents the uncertainty in the mathematical fit between the observed and calculated patterns and is the value most often quoted as the error in the phase abundance. Contrasting with this is the standard deviation of the mean abundances which represents the expected precision in the analysis and is 3 to 4 times greater than the Rietveld derived errors. The good level of fit achieved in conducting these analyses (evidenced in the low R-factors) could lead the analyst to conclude that the mean value +/- the standard deviation of the mean is an adequate measure of the phase abundances and their errors.

Table 1. Comparison of errors generated during the analysis of XRD data (Cu Kα) from three sub-samples of Sample 4 from the IUCr CPD round robin on quantitative phase analysis [2]. The bias values are (measured – weighed) while the values denoted "XRF" are the phase abundances generated from elemental concentrations measured by X-ray fluorescence methods.

		Phase	
n = 3	**Corundum**	**Magnetite**	**Zircon**
Weighed	50.46	19.46	29.90
Mean measured wt%	56.52	17.06	26.42
Mean of Rietveld errors	0.15	0.11	0.11
S.D. of measured wt%	0.63	0.41	0.35
Mean of bias	6.06	-2.58	-3.48
XRF	50.4(2)	19.6(1)	29.5(1)

However, the Rietveld errors and the replication errors are at least an order of magnitude smaller than the bias (measured – weighed). The bias, due to the presence of severe microabsorption, represents the true accuracy which can be achieved in this system if the analyst takes no further steps are taken to identify the cause and minimize the effect of absorption contrast or other aberrations which may affect accuracy.

In the example above, the phases are such that the chemistry is unambiguous and the phase quantification could have been derived by normative calculation from bulk elemental analysis (XRF). This is not often the case, but it is frequently possible to establish the composition of each phase within a system via electron probe microanalysis or similar and conduct the inverse of a normative calculation to derive the bulk chemistry from the XRD QPA. This can then be compared with the results of a standards based technique such as XRF to obtain a measure of the accuracy of the XRD analysis. Where this is not possible or practical, it is better to consider XRD QPA as a "semi-quantitative" technique at best.

5. References

1. Madsen, I.C., et al., Outcomes of the International Union of Crystallography Commission on Powder Diffraction Round Robin on Quantitative Phase Analysis: samples 1a to 1h. Journal of Applied Crystallography, 2001. 34(4): p. 409-426.
2. Scarlett, N.V.Y., et al., Outcomes of the International Union of Crystallography Commission on Powder Diffraction Round Robin on Quantitative Phase Analysis: samples 2, 3, 4, synthetic bauxite, natural granodiorite and pharmaceuticals. Journal of Applied Crystallography, 2002. 35(4): p. 383-400.
3. Rietveld, H.M., A Profile Refinement Method for Nuclear and Magnetic Structures. Journal of Applied Crystallography, 1969. 2: p. 65-71.
4. Cullity, B.D., Elements of X-Ray Diffraction. 2nd ed. 1978: Addison-Wesley Publishing Company. 555.

5. Klug, H.P. and L.E. Alexander, X-ray diffraction procedures: for polycrystalline and amorphous materials. 1974, New York: Wiley. 966.
6. Jenkins, R. and R.L. Snyder, Introduction to X-ray powder Diffractometry. 1996: Wiley-Interscience.
7. Chung, F.H. and D.K. Smith, Chapter 2 - The Practice of Diffraction Analysis, in Industrial Applications of X-ray Diffraction, F.H. Chung and D.K. Smith, Editors. 2000, Marcel Dekker.
8. Madsen, I.C. and N.V.Y. Scarlett, Quantitative Phase Analysis, in Powder Diffraction: Theory and Practice, R.E. Dinnebier and S.J.L. Billinge, Editors. 2008, The Royal Society of Chemistry: Cambridge, UK. p. 298-331.
9. Zevin, L.S. and G. Kimmel, Quantitative X-ray Diffractometry. 1995: Springer-Verlag New York, Inc.
10. O'Connor, B.H. and M.D. Raven, Application of the Rietveld Refinement Procedure in Assaying Powdered Mixtures. Powder Diffraction, 1988. 3(1), 2-6.
11. Scarlett, N.V.Y. and I.C. Madsen, Quantification of phases with partial or no known crystal structures Powder Diffraction, 2006. 21(4): p. 278-284.
12. Bish, D.L. and S.A. Howard, Quantitative phase analysis using the Rietveld method. Journal of Applied Crystallography, 1988. 21(2): p. 86-91.
13. Chung, F.H., Quantitative interpretation of X-ray diffraction patterns of mixtures. I. Matrix-flushing method for quantitative multicomponent analysis. Journal of Applied Crystallography, 1974. 7: p. 519-525.
14. Chung, F.H., Quantitative interpretation of X-ray diffraction patterns of mixtures. II. Adiabatic principle of X-ray diffraction analysis of mixtures. Journal of Applied Crystallography, 1974. 7: p. 526-531.
15. Hill, R.J. and C.J. Howard, Quantitative Phase Analysis from Neutron Powder Diffraction Data using the Rietveld Method. Journal of Applied Crystallography, 1987. 20: p. 467-474.
16. Webster, N.A.S., , Madsen Ian C., Loan Melissa J., Knott Robert B., Naim Fatima, Wallwork Kia S. and Kimpton Justin A. An Investigation of Goethite-Seeded Al(OH)3 Precipitation Using in situ X-ray Diffraction and Rietveld-based Quantitative Phase Analysis. Journal of Applied Crystallography, 2010. 43: p. 466-472.
17. Schmitt, B., et al., Mythen detector system. Nuclear Instruments and Methods in Physics Research Section A, 2003. 501: p. 267-272.
18. Madsen, I.C., N.V.Y. Scarlett, and B.I. Whittington, Pressure acid leaching of nickel laterite ores: an in situ diffraction study of the mechanism and rate of reaction. Journal of Applied Crystallography, 2005. 38(6): p. 927-933.
19. Bruker AXS, TOPAS V4.2: General Profile and Structure Analysis Software for Powder Diffraction Data, B.A. Karlsruhe, Editor. 2009.
20. Cheary, R.W. and A.A. Coelho, A Fundamental Parameters Approach to X-ray Line-profile Fitting. Journal of Applied Crystallography, 1992. 25(2): p. 109-121.

[i] Sections 1 to 3 have been extracted from Chapter 4, *Quantitative Phase Analysis using the Rietveld Method* by Ian C. Madsen, Nicola V.Y. Scarlett, Daniel P. Riley and Mark D. Raven in the forthcoming book Modern Diffraction Methods (Wiley-VCH) eds Mittemeijer and Welzel. Reprinted by kind permission of Wiley-VCH.

[ii] Section 4 above has been extracted from a Chapter 11, *Quantitative Phase Analysis* by Ian C. Madsen and Nicola V.Y. Scarlett in Powder Diffraction: Theory and Practice (Royal Society of Chemistry) eds Dinnebier and Billinge ISBN 978-0-85404-231-9. Reprinted by kind permission of Royal Society of Chemistry.

Further details of, and extensive references to, quantitative phase analysis methodology and its application to a wide range of materials and mineralogical systems can be found within the two books.

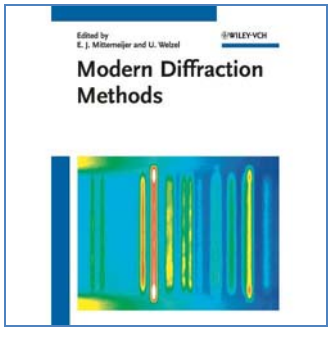

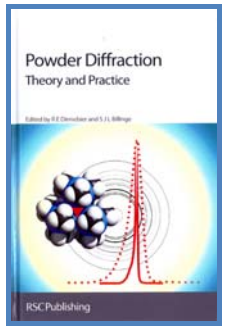

Quantifying amorphous phases

Arnt Kern[1], Ian C. Madsen[2] and Nicola V.Y. Scarlett[2]
[1]Bruker AXS GmbH, Karlsruhe, Germany
[2]CSIRO Process Science and Engineering, Clayton South, Victoria, Australia

1 Introduction

X-ray powder diffraction (XRPD) is (i) the most direct, (ii) the only truly phase sensitive, and thus (iii) the most commonly used analytical technique for quantitative analysis of crystalline and amorphous phases in mixtures. The fundamental relationships between diffracted peak intensity in a powder diffraction pattern and the quantity of a phase in a mixture are well established. Both single peak and full pattern methods for quantitative phase analysis (QPA) are mature and extensively covered in literature, e.g. [1-5]. Recently, thorough reviews of the field have been given in [6, 7], with emphasis on current methods, sources of error, as well as accuracy and precision. This chapter builds on chapter "Quantitative Phase Analysis" by Madsen, Scarlett and Webster (p. 292), dealing with quantification of amorphous materials as a special case.

More often than not, polycrystalline materials contain amorphous or poorly crystalline phases. In many cases, the presence of amorphous or poorly crystalline phases is undetected or simply ignored. While information about amorphous phase amounts is frequently not sought-after, this is also a result of the preferred (and sometimes indiscriminate) use of the classical Rietveld method [8, 9], as one of the most convenient methods for QPA available. It is, however, frequently overlooked, that the classical Rietveld method only delivers relative phase amounts by default; in the presence of amorphous and/or any amount of unidentified crystalline phases, the analyzed crystalline weight fractions may be significantly overestimated. Most phase abundances reported in literature, obtained via Rietveld analysis, are provided in a manner suggesting absolute values. However, where no allowance of amorphous and/or unidentified phases has been made/reported, it is actually reasonable to assume relative phase abundances instead. While knowledge of relative phase amounts may be sufficient for many analyses, e.g. for monitoring of trends, there is a rapidly increasing number of applications in industry and materials science, where it is essential to know absolute phase amounts including amorphous component(s). Important examples include pharmaceuticals, (geo)polymers, cements, among others, where the absolute crystalline and amorphous fractions are critical for their usefulness.

Limitations of QPA have already been discussed in chapter "Quantitative Phase Analysis" by Madsen, Scarlett and Webster (p. 292) and are principally the same for analysis of amorphous phases. There are some instances which require special con-

sideration, mostly due to differences in the way X-rays are scattered by crystalline and amorphous phases. This is complicated by the fact that there is often no sharp dividing line between crystalline and amorphous materials.
Crystalline materials are frequently characterized as solids with fixed volume, fixed shape, and *long-range order* bringing about structural anisotropy, producing sharp diffraction peaks (e.g. [5]). Amorphous (or non-crystalline) materials are thus solids with fixed volume, fixed shape, characterized by *short-range order*, which, however, may also have loose long-range order (e.g. [5]). This therefore embraces disordered materials possessing only one- or two-dimensional, or lesser, degrees of order [1]. Scattering by an amorphous material produces broad diffraction bands (or halos), which may extend to some ten's of degrees 2θ. Note that terms like "short"- and "long"-range order", as well as "sharp" and "broad" diffraction maxima clearly show the ambiguity of these definitions, and why there cannot be a sharp dividing line between crystalline and amorphous materials.
A more strict definition for amorphous solids has been given by [1]: "*The term, amorphous solid, must be reserved for substances that show no crystalline nature whatsoever by any of the means available for detecting it*". In other words: The ability to detect and characterize ordering is dependent upon the principles of the analytical method and models being used. Conventional X-ray diffraction loses its power for crystalline material structures on the nano-scale, diffraction patterns become broad and features are less defined. Frequently, resulting ambiguities are paraphrased in literature by the term "X-ray amorphous" to highlight the limitations of X-ray diffraction.
Recently it has been shown by several authors, that so-called "total scattering" analysis techniques, based on pair distribution functions (PDF) obtained from Fourier transformed XRPD data, allow the extraction of structural information from amorphous materials, also providing for "finger-printing" (amorphous phase identification) and quantitative analysis [e.g. 10-13]. In this technique, all information of the powder pattern, that is Bragg-peaks as well as background (diffuse scattering) is equally used. This is in contrast to conventional XRPD methods, where the background is treated independently and frequently discarded from the analysis.
The scope of this paper is limited to conventional powder diffraction methods for quantitative analysis of amorphous phases. Total scattering is not discussed here, due to a) the intrinsic limitation of the Q ($4\pi\sin\theta/\lambda$) range accessible in the vast majority of currently installed laboratory equipment and b) the current lack of both dedicated and mature software tools.

2 Analytical techniques

Quantification of crystalline and amorphous phase amounts relies on the determination of the intensity contribution of each component phase in a mixture to the diffraction pattern; the mathematical base is detailed in chapter "Quantitative Phase Analysis" by Madsen, Scarlett and Webster (p. 292). For this reason, the same

methodology can be used for quantitative analysis of crystalline and amorphous phase amounts. Analysis of the latter, however, can be made difficult by the fact that the intensity contribution of amorphous phases to the diffraction pattern is not always evident, especially at low concentrations. Accordingly, available evaluation methods can be grouped into two categories:

1. Indirect methods are based on the use of internal or external standards. Only crystalline components are analyzed and subsequently put on an absolute scale. The amorphous fraction is then calculated by difference, that is indirectly. Most importantly, unidentified and amorphous phases cannot be distinguished, only the sum of these phases can be estimated. Indirect methods are suited for amorphous phases without clearly evident intensity contribution to the diffraction pattern.
2. Direct methods provide a direct measure of an amorphous compound by analyzing the amorphous intensity contribution to the diffraction pattern. Individual unidentified and amorphous phases may be distinguished, and some approaches allow the quantification of more than one amorphous phase if data quality is sufficient. Direct methods rely on the ability to observe the intensity contribution of amorphous phases to the diffraction pattern.

In the following a survey of the most commonly used conventional laboratory XRPD techniques is presented, adapted from [14]. Benefits and limitations of the methods are compared and recommendations made accordingly. Successful analysis requires careful considerations in choosing the best suited evaluation method for a given sample.

2.1 Single peak method

Single peak methods are direct methods based on the measurement of one or more peaks, for each phase of interest, and assume that the intensity of these peaks are representative of the amount of the individual phases. They rely on the availability of a suite of standard samples from which calibration constants may be determined, and on the direct estimation of the amorphous intensity contribution to the diffraction pattern. This can be done using profile fitting or simple numerical methods. The general procedure is:

1. Prepare a series of standards containing the amorphous phase at known concentrations
2. Obtain a measure of the amorphous component's intensity which may be related to its concentration
3. Generate a calibration curve, e.g.

$$W_a = A * I_a + B \quad (1)$$

where W_a is the fraction of the amorphous phases and I_a is the measure of the intensity of the amorphous phase (determined in (1)).
The term *measure* has been chosen to highlight the fact that single peak methods do not necessarily require background determination; i.e. I_a is not required to solely represent the amorphous band intensity, it can also represent the sum of the amorphous band intensity plus background. This in an advantage in those cases where the distinction between background and amorphous band intensity is difficult and therefore unreliable. Note: If the background intensity is included, the calibration function will not go through the origin of the plot. At first glance this may be deemed to be an unconventional approach, it nevertheless can allow for very accurate analyses.
Profile fitting has the definite advantage over numerical methods in dealing better with peak overlap in the presence of crystalline phases. Numerical methods are based on some sort of numerical integration of step intensities within one or more selected 2θ ranges and are in widespread use, most notably in X-ray fluorescence analysis. The distinct advantage of numerical methods is the possibility of choosing small measurement ranges (usually optimized to regions with no or negligible peak overlap). These may include complete peaks / bands but may be limited to a single data point.
Benefits:
Single peak methods can be limited to one or a few phases, and there is no need to characterize all phases in the mixture. They generally allow for significantly longer measurement times per data point, compared to whole pattern methods. This will lead to a significant improvement in counting statistics, and thus allow for quantitative analysis at higher levels of precision and improved lower limits of detection. The method has the potential to minimize errors related to microabsorption as this aberration is included in the calibration function. When profile fitting is used, more than one amorphous phase can be analyzed.
Limitations:
At higher degrees of overlap, the distinction between amorphous band intensities and crystalline phase peaks (tails!) can become difficult and unreliable, particularly if the latter are broad. The methods also require access to relatively pure or well-described materials for preparation of standards, and are thus only applicable to mixtures similar to the calibration suite. Neither sample properties nor the instrument setup must change between the calibration and unknown measurements, and tube ageing must be monitored, otherwise the calibration function is invalidated.

2.2 Whole pattern methods

Whole pattern methods rely on the comparison of observed wide range diffraction data with a) calculated patterns (Rietveld methodology) or b) measured patterns (e.g. [15, 16]). In the Rietveld methodology patterns are calculated using structure factors calculated from (i) crystal structure information, or (ii) measured from actual samples, or (iii) both. Measured pattern approaches use measured diffraction data ac-

quired from pure phase data libraries, which need to accurately represent all phases in the mixture. Although this methodology has distinct advantages specifically if crystal structures are unknown (e.g. for disordered or amorphous materials), it is a niche approach as it does not allow for structure refinement (e.g. lattice parameters in the case of solid solutions) or preferred orientation corrections.
In the following the 6 most commonly used methods for the characterization of amorphous phase amounts within the Rietveld methodology are described, based on [14].

Method 1: Internal Standard Method
The Internal Standard Method is an indirect method, where the sample is "spiked" with a known mass of standard material and the QPA normalized accordingly. In this method, the weight fraction W_α of the crystalline phases present in each sample is estimated using the algorithm of Hill and Howard [9],

$$W_\alpha = \frac{S_\alpha (ZMV)_\alpha}{\sum_{j=1}^{n} S_j (ZMV)_j} \quad (2)$$

where S, Z, M and V are, respectively, the Rietveld scale factor, the number of formula units per unit cell, the mass of the formula unit and the unit-cell volume, and n is the number of phases in the analysis.
This is the basis of QPA via the Rietveld method assuming that all phases in the sample are crystalline and have been included in the model and thus Equation (2) sums the analyzed concentrations to unity. In the presence of amorphous or non-included phases, these values will be overestimated with respect to the true concentrations. The presence of a known weight fraction of an internal standard material in the sample allows these reported concentrations to be corrected proportionately according to:

$$Corr(W_\alpha) = W_\alpha \frac{STD_{known}}{STD_{measured}} \quad (3)$$

where $Corr(W_\alpha)$ is the corrected weight percent, STD_{known} the weighed concentration of the standard in the sample and $STD_{measured}$ the analyzed concentration derived from Equation (1).
The amount of amorphous material $W_{amorphous}$ can then be derived from:-

$$W_{amorphous} = 1 - \sum_{j=1}^{n} Corr(W_j) \quad (4)$$

Obviously, the Internal Standard Method can also be used, if the concentration of one phase in a mixture is known (e.g. via complimentary methods such as elemental analysis or others) and thus can be defined as the internal standard.

Benefits:

The Internal Standard Method is enabled in many Rietveld analysis packages.

Limitations:

The approach is reliant upon obtaining a standard of appropriate absorption contrast to prevent the introduction of errors into the analysis via the creation of a microabsorption problem. Only the sum of all amorphous and unidentified phases can be reported. The standard addition process is laborious (weighing, mixing), and not feasible in industrial, automated sample preparation environments. Furthermore, and most significantly, the sample is contaminated.

Method 2: External Standard Method

The External Standard Method [17] is an indirect method and closely follows the approach in the Internal Standard Method in that it attempts to put the determined crystalline components on an absolute scale and derives the amorphous content by difference. An external standard - either a pure material or a mixture in which the chosen standard is present in known quantity - is used to determine a normalization constant (K) which allows the calculated weight percentages to be placed on an absolute scale,

$$W_\alpha = \frac{S_\alpha (ZMV)_\alpha \cdot \mu_m^*}{K} \quad (5)$$

where μ_m^* is the mass absorption coefficient of the entire sample.

K is dependent only on the instrumental conditions and is independent of individual phase and overall sample-related parameters. Therefore, a single measurement should be sufficient to determine K for a given instrumental configuration.

Benefits:

The External Standard Method uses an external standard, the sample is not contaminated. As good laboratory practices require regular instrument monitoring (alignment, tube aging) anyway, the choice of an appropriate standard enables to put all QPA results on an absolute basis and thus enables the calculation of the amorphous fraction, without any additional experimental effort.

Limitations:

Only the sum of all amorphous and unidentified phases can be reported. The normalization constant K is dependent on the instrumental conditions and needs redetermination to compensate for tube ageing and any instrument configuration changes.

Method 3: PONKCS Method

The PONKCS method is a direct method, its background and application is described in detail in [18]. In this method, phases with partial or no known crystal structure are characterized by measured rather than calculated structure factors. Most importantly, this overcomes the requirement of the traditional Rietveld method that the crystal structures of all phases must be known. Intensity contributions of crystalline as well as amorphous phases to the diffraction pattern may be characterized via single line or Pawley [19] or Le Bail fitting [20] methods.

The PONKCS Method follows the same general form as that used in the Internal Standard Method but now includes all crystalline and amorphous phases characterized by either calculated or empirical structure factors in Equation (2). However, for all phases using empirically derived structure factors (i.e. those with no defined crystal structure), ZMV "calibration constants" must be derived. This can be achieved by using a known mixture of a respective crystalline or amorphous phase α and an internal standard s,

$$(ZMV)_\alpha = \frac{W_\alpha}{W_s}\frac{S_s}{S_\alpha}(ZMV)_s \quad (6)$$

A one time calibration per phase with a single standard mixture is usually sufficient. It is highly recommended to create a database with "PONKCS phases"; such a database can be used in full analogy to crystal structure databases.

Benefits:

The PONKCS Method includes amorphous phase(s) in the analysis model. It has the potential to model more than one amorphous phase. It may be used simultaneously with classical Rietveld methodology for phases in the system with known crystal structures. When ZMVs have been calibrated for all phases, microabsorption will be eliminated, as this aberration is included in the calibration. Thus, where microabsorption potentially leads to significant errors, it should be considered to use the PONKCS methodology also for all crystalline phases of which the crystal structures are known, i.e. replacing their calculated ZMVs by calibrated ZMVs.

Limitations:

This method requires availability of a standard mixture to derive an empirical ZMV.

Method 4: Linear Calibration Model (LCM) Method

The Linear Calibration Model (LCM) Method is a direct method and similar to the previous approaches, however, the information pertaining to the crystalline phases is discarded. Similar to the PONKCS Method, the intensity contribution of an amorphous phase to the powder pattern is modeled via single line or Pawley or Le Bail fitting methods, but only the refined scale factor is used in subsequent analysis. This allows the derivation of a simple linear calibration model from a suite of standard

mixtures, which relates the refined scale factor, *S,* to the amorphous phase concentration, W_{amorph},

$$W_{amorph} = A \cdot S - B \quad (7)$$

where A and B are the slope and any residual offset of the calibration, respectively.

Benefits:

The LCM Method has the potential to model more than one amorphous phase. It is convenient to use when there is minimal variation of absorption contrast between the phases. For systems where there is significant variation in absorption between phases, then a sample absorption correction must be included. Errors related to microabsorption can be minimized as this aberration is included in the calibration function.

Limitations:

The approach requires preparation of a series of standards for calibration and is only applicable to mixtures similar to the calibration suite. Neither sample properties nor the instrument setup must change between the calibration and unknown measurements, and tube ageing must be monitored, otherwise the calibration function is invalidated.

Method 5: Full Structure Method

The Full Structure Method is a direct method and relies on finding a crystal structure which adequately models the positions and relative intensities of the observable bands of a amorphous component in a diffraction pattern. Allowance for extreme peak broadening provides peak widths and shapes which represent those of the amorphous bands in the observed data. Since this method treats all components as crystalline and includes them in the analysis, the amorphous phase abundance can be obtained using the traditional Rietveld method, applying the algorithm of Hill and Howard [9], Equation 1.

Benefits:

The Full Structure Method has the potential to model more than one amorphous phase, and requires no standards or calibration.

Limitations:

Some amorphous material will not have a representative crystal structure, i.e. available crystal structures (with long-range order) may not accurately represent material which only has short-range order (e.g. glasses).

Method 6: Degree of Crystallinity Method

The Degree of Crystallinity (DOC) Method is a direct method, which is relatively straightforward but different from the methods discussed earlier. For a detailed description refer to e.g. [21]. This method is based on the estimation of the total intensity or area contributed to the overall diffraction pattern by each component in the

analysis. The degree of crystallinity (in literature also referred to as "crystalline index"), DOC, is then calculated from the total areas under the defined crystalline and amorphous components from

$$DOC = \frac{Crystalline\ Area}{Crystalline\ Area + Amorphous\ Area} \quad (8)$$

The weight fraction of the amorphous material, W_{amorph}, can be calculated from

$$W_{amorph} = 1 - DOC \quad (9)$$

This approach can only be used, if the crystalline phase has the same chemical composition of the whole sample. Where this requirement is not fulfilled, absolute values can be obtained via calibration based on a suite of standard materials.

Benefits:

The DOC Method is enabled in many software packages and has the potential to model more than one amorphous phase. The method does not require application of calibration constants, if the crystalline phase has the same chemical composition of the whole sample.

Limitations:

Difficulties arise in defining intensity contributions as "crystalline" or "amorphous". If the chemistry of the crystalline phase is different from the whole sample then an additional calibration step is required to obtain absolute phase amounts.

3 Summary

All of the methods discussed in this paper are principally capable of determining amorphous phases in mixtures with the same accuracy (and precision) as for crystalline phases, in ideal cases even down to 1% absolute or better. Limitations are the same as for QPA of crystalline phases and are dictated by sample properties and the analytical technique used. Table 1 gives an overview about important properties of the latter.

Table 1. Important properties of the analytical techniques discussed.

Method	Calculation of amorphous content	Requires calibration suite or standard	Can correct for microabsorption errors	Can deal with more than one amorphous phase
Single Peak	Direct	Calibration suite	Yes	Yes
Internal Standard	Indirect	Internal standard	No	No
External Standard	Indirect	External standard	No	No
PONKCS	Direct	Single mixture	Yes	Yes
LCM	Direct	Calibration suite	Yes	Yes
Full Structure	Direct	No	No	Yes
DOC	Direct	Case dependent	No	Yes

Benefits and limitations of the individual analytical techniques are to be thoroughly considered when choosing the best method for a given mixture; some basic principles can be summarized as follows:

- Intensity contributions of amorphous phases to the diffraction pattern are not always evident, especially at low concentrations. In this case amorphous bands will be difficult to model and indirect methods (Internal or External Standard Method) will usually perform better.
- Where intensity contributions of amorphous phases are evident, any method based on modeling amorphous bands provides improved accuracy. These methods will usually require a sample of pure amorphous material, or a sample where the amorphous content is high, to establish an accurate model.
- For indirect methods, any errors in the structural models for the crystalline phases have the potential to decrease the overall accuracy. This is especially true when structure models for amorphous materials are selected.
- Calibration based methods usually have the potential to achieve the highest accuracy, as many aberrations, most notably microabsorption, are included in the calibration function.

- Any method based on calibration suites or standards have issues with the availability of suitable calibration samples and standards. Where single samples are to be analyzed, it is generally not practical to make a calibration suite.
- Any calibration sample and standard will contain amorphous materials which, if not accounted for, will decrease accuracy. This is also true for materials deemed to be perfectly crystalline, as any material possesses a non-diffracting surface layer with some degree of disorder due to relaxation of the crystal structure and inclusion of surface reaction products and adsorbed species (water, hydrocarbons, ...) Such a layer can easily account for a mass fraction of several percent in a finely divided solid.

4 References

1. Klug, H.P. and Alexander, L.E., X-ray Diffraction Procedures: For Polycrystalline and Amorphous Materials. 1974, New York: Wiley.
2. Jenkins, R. and Snyder, R.L., Quantitative Analysis, in Reviews in Mineralogy Vol 20: Modern Powder Diffraction, Bish, D.L. and Post, L.E., Editors. 1996, Mineralogical Society of America.
3. Zevin, L.S. and Kimmel, G., Quantitative X-ray Diffractometry. 1995, Springer.
4. Whitfield, P. and Mitchell, L., Phase Identification and Quantitative Methods, in Principles and Applications of Powder Diffraction, Clearfield, A., Reibenspiess, J. and Bhuvanesh, N., Editors. 2008, Blackwell Publishing.
5. Pecharsky V.K. and Zavalij, P.Y., Fundamentals of Powder Diffraction and Structural Characterization of Materials. 2009. Springer.
6. Madsen, I.C. and Scarlett, N.V.Y., Quantitative Phase Analysis, in Powder Diffraction: Theory and Practice, Dinnebier, R.E. and Billinge, S.J.L., Editors. 2008, The Royal Society of Chemistry: Cambridge, UK.
7. Madsen, I.C. and Scarlett, N.V.Y., Riley, D.P. and Raven, M.D., Quantitative Phase Analysis using the Rietveld Method, in Modern Diffraction Methods, Mittemeijer, E.J. and Welzel, U., Editors. 2011, Wiley-VCH. (in press)
8. Rietveld, H.M. (1969):, A Profile Refinement Method for Nuclear and Magnetic Structures. Journal of Applied Crystallography, 2, 65-71.
9. Hill, R.J. and C.J. Howard (1987): Quantitative Phase Analysis from Neutron Powder Diffraction Data using the Rietveld Method. Journal of Applied Crystallography, 20, 467-474.
10. Egami, T. & Billinge, S.J.L., Underneath the Bragg Peaks: Structural Analysis of Complex Materials. 2003: Pergamon.
11. Billinge, S.J.L., Local Structure from Total Scattering and Atomic Pair Distribution Function (PDF) Analysis, in Powder Diffraction: Theory and Practice, Dinnebier, R.E. and Billinge, S.J.L., Editors. 2008, The Royal Society of Chemistry: Cambridge, UK.
12. Proffen, T., Page, K.L., McLain, S.E., Clausen, B., Darling, T.W., TenCate, J.A., Lee, S., and Ustundag, E. (2005): Atomic pair distribution function analysis of materials containing crystalline and amorphous phases. - Z. Kristallogr., 220, 1002–1008.
13. Billinge, S.J.L., Dykhne, T., Juhàs, P., Bozin, E., Taylor, R., Florence, A.J., and Shankland, K. (2010): Characterization of amorphous and nanocrystalline molecular materials by total scattering. - CrystEngComm, 12, 1366–1368.
14. Madsen, I.C. and Scarlett, N.V.Y. (2011): A survey of methodologies for the determination of amorphous content via X-ray powder diffraction. In preparation.
15. Chipera, S.J. and Bish, D.L. (2002): FULLPAT: A full-pattern quantitative analysis program for X-ray powder diffraction using measured and calculated patterns. - J. Appl. Cryst., 35, 744-749.
16. Cressey, G. & Schofield, P.F. (1996): Rapid whole-pattern profile-stripping method for the quantification of multiphase samples. - Powder Diffr. 11, 35-39.
17. O'Connor, B.H. and Raven, M.D. (1988): Application of the Rietveld Refinement Procedure in Assaying Powdered Mixtures. Powder Diffraction, 3, 2-6.
18. Scarlett, N.V.Y. and Madsen, I.C. (2006): Quantification of phases with partial or no known crystal structures Powder Diffraction, 21, 278-284.
19. Pawley, G.S. (1981): Unit-cell refinement from powder diffraction scans. - J. Appl. Cryst., 14, 357-361.
20. Le Bail, A., Duroy, H. & Fourquet, J.L. (1988): Ab-initio Structure Determination of LiSbWO6 by X-Ray Powder Diffraction. - Mat. Res. Bull., 23, 447-452.

21. Riello, P., Quantitative Analysis of Amorphous Fraction in the Study of the Microstructure of Semi-crystalline Materials, in Diffraction Analysis of the Microstructure of Materials, Mittemeijer, E.J. and Scardi, P., Editors. 2004, Springer.

5 Additional Reading

The following papers, categorized by subject and in alphabetical order, can be summarized as "Good Powder Diffraction Practice" and should be memorized by everybody working in this field:

Rietveld structure refinement and quantitative analysis:

Hill, R.J. (1992): Rietveld refinement round robin. I. Analysis of standard X-ray and neutron data for $PbSO_4$. - J. Appl. Cryst., 25, 589-610.

Hill, R.J. & Cranswick, L.M.D (1994): Rietveld Refinement Round Robin. II. Analysis of Monoclinic ZrO_2. J. Appl. Cryst., 27, 802-844

Madsen, I.C., Scarlett, N.V.Y., Cranswick, L.M.D. and Lwin, T. (2001): Outcomes of the International Union of Crystallography Commission on Powder Diffraction Round Robin on Quantitative Phase Analysis: samples 1a to 1h. - J. Appl. Cryst., 34, 409-426.

Scarlett, N.V.Y., Madsen, I.C., Cranswick, L.M.D., Lwin, T., Groleau, E., Stephenson, G., Aylmoree, M. and Agron-Olshinaa, N. (2002): Outcomes of the International Union of Crystallography Commission on Powder Diffraction Round Robin on Quantitative Phase Analysis: samples 2, 3, 4, synthetic bauxite, natural granodiorite and pharmaceuticals. - J. Appl. Cryst., 35, 383-400.

Data acquisition - general:

Hill, R.J. & Flack, H.D. (1987): The Use of the Durbin-Watson d Statistic in Rietveld Analysis. - J. Appl. Cryst., 20, 356-361.

Hill, R.J. & Madsen, I.C. (1984): The Effect of Profile Step Counting Time on the Determination of Crystal Structure Parameters by X-ray Rietveld Analysis. - J. Appl. Cryst., 17, 297-306

Hill, R.J. & Madsen, I.C. (1986): The Effect of Profile Step Width on the Determination of Crystal Structure Parameters and Estimated Standard Deviations by X-ray Rietveld Analysis. - J. Appl. Cryst. ,19, 10-18

Hill, R.J. & Madsen, I.C. (1988): Effect of Divergence and Receiving Slit Dimensions on Peak Profile Parameters in Rietveld Analysis of X-ray Diffractometer Data. - J. Appl. Cryst., 21,398-405

Data acquisition - variable counting time (VCT):

Cockcroft, J.K. (2002): Variable Count Time Data Collection in Powder X-ray Diffraction. - IUCr CPD Newsletter No. 27, 23-24.

David, W.I.F. (1992): Accuracy in Powder Diffraction: Optimization of data collection strategies. - Abstract P2.6, NIST Special Publication No. 846, Page 210.

David, W.I.F. (2004): Powder Diffraction: Least-Squares and Beyond. - J. Res. Natl. Inst. Stand. Technol. 109, 107-123

Madsen, I.C. & Hill R.J. (1992): Variable step-counting times for Rietveld analysis or getting the most out of your experiment time. Adv. X-ray Anal., 35, 39-47

Madsen, I.C. & Hill R.J. (1994): Collection and analysis of powder diffraction data with near-constant counting statistics. J. Appl. Cryst., 27, 385-392

Quantitative phase analysis: method developments

Luca Lutterotti
Dipartimento di Ingegneria dei Materiali e Tecnologie Industriali, Università degli Studi di Trento, Trento, Italy

Abstract
During the years several methods have been developed to identify and quantify the phases in our samples. The newly developed methods respond to precise needs like increasing accuracy, lowering detection limits, automatize and speed-up the process or overcome errors and limitations. Most of the last developments are based on the use of large set of data and full pattern analyses like the Rietveld method. The progresses have been stimulated by the need to analyze new and complex materials with the help of advanced hardware to collect quickly and reliably our data. Refinement of old and new methods will be presented for the quantification of phases as well as some examples. Particular cases will be treated for layered materials and thin films, bulk amorphous, textured samples and clay materials. The last frontier appears to be the combination of the diffraction with other techniques to improve the final analysis.

Introduction

In the quantitative analysis of our samples we may identify two principal cases that it is worth to consider. The first case is when the sample is a powder or was a bulk reduced to a powder; this is quite a common case. There is also a second important case when the sample is a bulk not reducible to a homogeneous powder or it has a special structure/distribution of phases for which it is necessary to analyze it in the original form. In the first case we can just utilize the usual methods for quantitative analysis, provided we take every precaution to fulfill the requisites for a good analysis: homogeneous sample, a sufficient number of small grains and randomly oriented.
When the sample is a bulk or a sample is not fulfilling all these requisites, we need to employ special methodologies and measurement techniques to perform the quantitative analysis. In this chapter we will cover this second case showing some of the methods developed to quantify the phases amount and distribution through diffraction and the help of other techniques when necessary.

Layered materials and thin films

There are several cases in which the material is structured in more layers. Each layer may have different phases and a phase may be present in more than one layer. If the

sample is analyzed the traditional way, by assuming an homogeneous volume, this may lead to two problems:

- The phase fraction we obtain does not really represent the composition of the sample and their quantification depends on the beam penetration.
- The absorption factor in the formula for the quantitative analysis is no more a constant value and this also will result in increasing the inaccuracy of the analysis.

In such cases it is necessary to use a model for the layered material to take into account thicknesses of the layers, absorption factors and phases distribution. The absorption factor depends on the phase content and thickness in each layer and this cause a circular dependency in the quantification method. The Rietveld method as a multi parametric fitting technique can solve the problem by including a suitable model. This has been done and demonstrated for the analysis of the oxidation of some super-alloys[1]. Following that work we can compare an analysis made assuming a homogeneous sample and subsequently adopting the correct model. In this example an Inconel 738 has been oxidized at high temperature (for details we remind to the original work) and the phases have been identified and quantified using an X-ray diffraction pattern collected in Bragg-Brentano geometry, copper radiation. Table 1 reports the phase quantification by the Rietveld method assuming a homogeneous sample and the layered model.

It is immediately clear how much informative is the correct model. Determining a phase fraction for the substrate using the homogeneous model does not make sense. A first indication that the sample has a layered structure is given by the B factors (a overall B factor for each phase has been used). Looking at the third row of table 1 phases on top of the layers show much higher intensity at low angle respect to high angle and this is corrected in the Rietveld by a higher B factor. Instead for phases down in the sequence the reverse is observed. The correct layered model has been constructed by trial and error, observing the B factor value. This has been compared and validated using EDXS elemental maps in a cross section.

To correctly compute the absorption factor in a layered model we point the reader at the excellent formulation in [2] (see equation 23) that include also the case of a general orientation of the sample surface respect to the incident and diffracted beam.

Table 1. Rietveld phases quantification for the oxidized Inconel 738 assuming a homogeneous sample and a layered model [1].

Rietveld homogeneous	Cr_2O_3	TiO_2	$CrNbO_4$	Al_2O_3	Alloy matrix	Ni_3Al	
Volume fraction	0.49	0.011	0.353	0.055	0.086	0.005	
B factor	0.297	-1.77	5.72	4.76	-4.75	-3	
Rietveld layered model	Volume fraction						Layer thickness (μm)
Layer #	Cr_2O_3	TiO_2	$CrNbO_4$	Al_2O_3	Alloy matrix	Ni_3Al	
1	-	-	1	-	-	-	0.089
2	0.952	0.048	-	-	-	-	2.2
3	-	-	-	0.973	0.026	0.001	0.36
4	-	0.11	-	-	0.845	0.045	5
5	-	-	-	-	0.95	0.05	∞
B factor	-0.19	0.73	-0.45	1.98	0.51	0.6	

The procedure can be used successfully also for textured thin films provided a sufficient number of pattern/data is collected to characterize quantitatively the texture [3-5]. This is necessary when the texture is strong as it happens often in the thin film production. Otherwise, for the errors connected to the adoption of a simplified texture models and only one pattern, we remind at a subsequent paragraph.

Clay materials and turbostratic disorder

The quantification of clay materials or in general of phases having stacking faults like turbostratic disorder (e.g. graphitic materials) has been always a big problem as the traditional Rietveld method is not able to fit the pattern with the same accuracy as for other phases. Indeed, also other methods (internal standard, RIR or PONKCS; see the work of Madsen in this book), if they can ameliorate the analysis, they do not provide a satisfactory solution, most of the time. In 2004 Ufer et al. [6, 7] have introduced an elegant way to treat the turbostratic disorder as encountered in many clay materials. This permits a good fitting of the diffraction pattern using a simple to setup model where it is only necessary to identify the faulting axis and fit the anisotropic crystallite size broadening. This has been used to successfully quantify clay materials [8] as you can see in figure 1 and carbon-carbon composites. This kind of modeling is present in both BGMN and Maud Rietveld software.

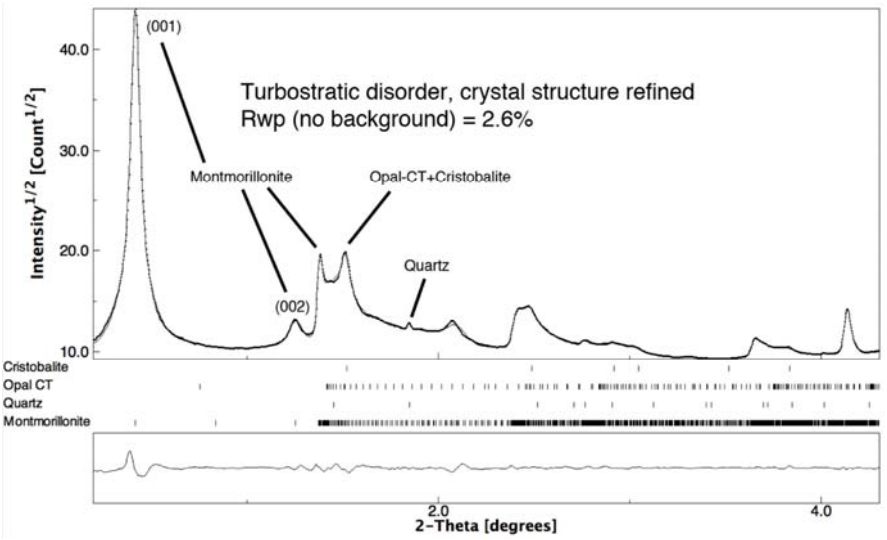

Fig. 1. Rietveld phases quantification of clay minerals using the model of Ufer et al. [6] for both the Ca-montmorillonite and the Opal-CT.

Texture and preferred orientation

Preferred orientations are one of the main causes of errors in phase quantification by diffraction as enlightened in another part of this book. The best method in such case is to try to avoid them by changing the experiment or re-preparing the sample. Not always this is successful or can be done, as for example in the case of a bulk or a film. When the texture of the sample cannot be eliminated completely by the experimental procedure, we need to choose an analysis strategy to get the phase quantities as much accurate as possible. We have ideally 3 choices:

- Not apply any correction for preferred orientations
- Apply the texture factors computed from the Orientation Distribution Function (ODF) for this sample
- Fit and apply some corrections based on a simplified texture model.

To examine the effect of each method we have constructed a simple case with a known amount of phases and ODF. We can test the different corrections and their effect on the quantitative phase results. The test is based on a Cu-Fe bulk sample where the two phases were co-laminated for a certain extent. The original content is 1/3 in volume of Fe and 2/3 of Cu. The sample in cube form has been analyzed at the IPNS neutron TOF source in Argonne. A sufficient number of TOF pattern covering different orientation of the sample has been collected in order to obtain the true ODF for both phases. The complete analysis has been done on all patterns using the Rietveld method with the EWIMV texture model [5]. This full analysis confirmed the 1/3 – 2/3 volume fraction for the Fe and Cu phases (0.667(2) % vol. Cu and R_{wp} = 18%) and the overall fitting for only one bank is reported in figure 2. The EWIMV

method provides us the ODF from which some pole figures have been calculated and are shown in figure 2 along with the measurement points in the orientation space. As we can see the texture is the typical one for such laminated phases. It is not a strong texture and nearly orthorhombic.

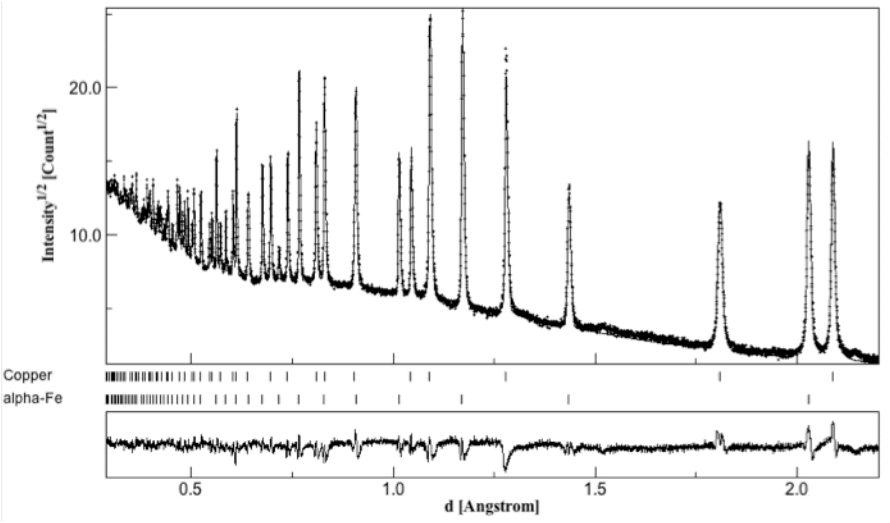

Fig. 2. Rietveld fit of all patterns of bank 2. Rwp = 18 %.

For our test we will use the Rietveld method for the phase analysis but with only one pattern in the center of the pole figure to be in the same usual conditions of a Bragg-Brentano experiment. In Bragg-Brentano the usual measurement only covers the center of the pole figure and consequently even if we spin the sample this does not decrease the texture and only improves the statistic. Moreover measuring only one point in the pole figures, even if for more reflections, it does not permit to discriminate the kind of texture or measure the complete ODF and in general the normalization cannot be done. All the texture models we can apply in this case are based on a fiber texture with the axe in the center of the pole figure. In table 1 the results for different models are summarized. Also two different ranges in d-space were used to check the effect of the number of reflections. Not always the best fit correspond to the best result in the quantitative analysis. Obviously correcting for the true ODF should give a good result even if only one pattern is used. But when this is not possible the test shows that using no correction at all gives the worse fit but the results are acceptable. Not always this is true for the other models. The March-Dollase produces a better fit but a wrong quantitative analysis. For the harmonic method this depends on the range and expansion used even if the texture is not strong. This is due to the fact that we suppose a certain fiber texture when it is not. The advice is that when we do not know the texture type, applying no corrections for the texture has more probability of giving a good result even if the fit is worse.

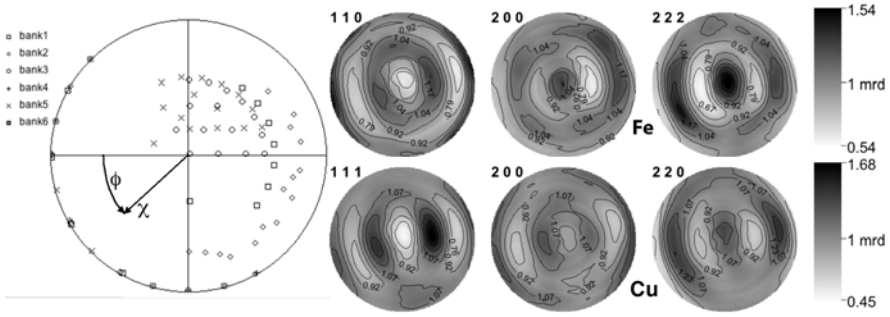

Fig. 3. Pole figures (recalculated from ODF, on the right) for the Fe-Cu sample as obtained from the full refinement of all patterns by Rietveld + EWIMV; on the left the measurement point of each pattern is reported as texture measurement angles (so-called pole figure coverage). Different symbols indicate patterns coming from different banks (detectors).

If the texture is stronger the use of the wrong model (and no simplified models, harmonic included, are correct in this case) will cause a worse result.

Table 1. Result of quantitative analysis on Fe-Cu sample by refinement of a single pattern using different preferred orientation correction models.

	0.3-2.2 Å range		0.79 – 2.2 Å range	
Type of P.O. correction	% vol. Cu	R_{wp} (%)	% vol. Cu	R_{wp} (%)
ODF corrected	67.8(14)	14.5	66.5(19)	15.6
No correction	65.5(25)	31.5	63.3(37)	35
March-Dollase	58.3(20)	25	57.3(38)	29
Fiber harmonic, L_{max} = 4	67.4(23)	27.5	62.7(41)	30.5
Fiber harmonic, L_{max} = 6	70.0(13)	13	66.0(25)	14.5
Fiber harmonic, L_{max} = 8	71.4(14)	12.7	70.2(40)	14.4

Microabsorption

Microabsorption or absorption contrast affects the quantitative analysis when we have large grains of a highly absorbing phase with other low absorbing phases. In such cases we have few alternatives to avoid or reduce absorption contrast effects:

- Grind the powder to reduce the grain size below a certain level (usually 1 micron).
- Change the wavelength or radiation to a more penetrating one.
- Apply a model to correct the absorption contrast in the analysis (this requires the knowledge of the grain sizes of the phases).

Most of the time only the third option is feasible and the most used correction is the so-called Brindley microabsorption model [9-10]. Applying it to the formula for quantitative analysis by the Rietveld method [10, 14-15] we get for a mixture of N phases:

$$w_i = \frac{I_i \rho_i}{\tau_i \sum_{j=1}^{N} \frac{I_j \rho_j}{\tau_j}}$$

where I is the scale factor from the Rietveld fitting, w_i is the weight fraction for phase i, ρ_i the density and τ_i the absorption contrast effect. Brindley has reported some tables for the absorption contrast effect from which we can extrapolate a function of a form similar to the absorption characteristic [11]. For spherical particles the Brindley table can be fitted well by [11]:

$$\tau_i = -0.00229 + 2.054 e^{-\frac{(\mu_i - \bar{\mu}) R_i + 0.50356}{0.69525}}$$

where μ_i is the linear absorption coefficient for phase i, $\bar{\mu}$ the mean linear absorption coefficient of the mixture and R_i the mean particles radius. Similar formulas can be obtained also for other shapes correction.

Amorphous and polymer crystallinity determination

Le Bail in 1995 [12] published how by diffraction it is impossible to distinguish between a real amorphous and a nanocrystalline structure without any long range order. So there is always the possibility to reproduce an amorphous diffraction pattern using a so-called pseudo-amorphous model in which the short range order is simulated by a particular crystal structure and the long range order is loosed by small crystallite sizes and/or high value of r.m.s. microstrain. The advantage of the description is that the short range order can be refined much better in the Rietveld framework instead of relying uniquely on Monte Carlo techniques. In 1998 Lutterotti et al. [13] demonstrated how this pseudo-amorphous model can be used in the Rietveld to accurately measure the amorphous content without any internal or external standard. The classical formula developed for Rietveld phase analysis [13-14] works perfectly to give the amorphous content as a normal phase if the model is sufficiently accurate in describing the short range order. The benefits of this method are that no calibration, internal or external standard are needed and it can be applied also to bulk samples. Limitations are that it requires a model for the pseudo-amorphous and the background level should be estimated correctly. For the last problem it is advisable to use a monochromator in the diffracted beam to lower the background as much as possible.

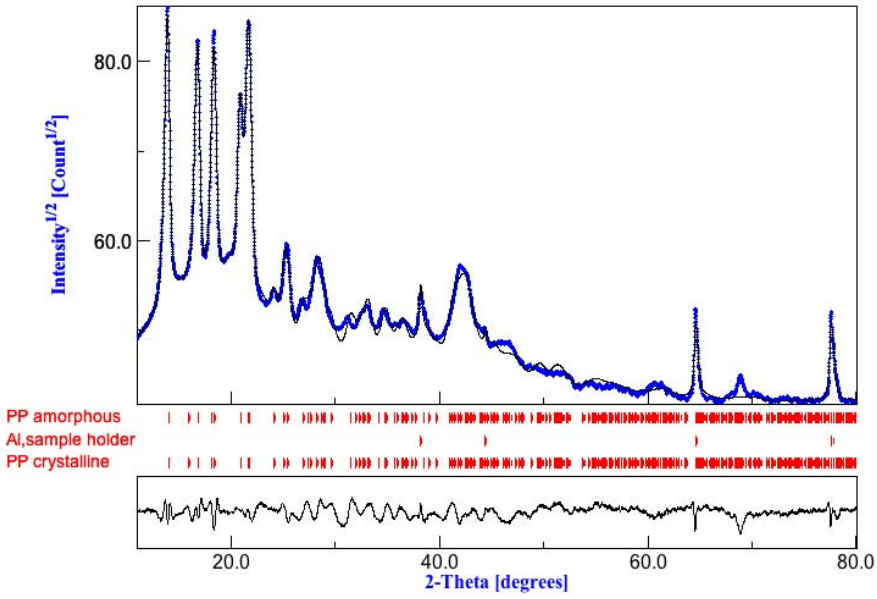

Fig. 4. Crystallinity determination on polypropylene by Rietveld fitting.

The methodology can be used for crystallinity determination in polymers. An example is shown in figure 4 for polypropylene where the same crystal structure is assumed for both the amorphous part and the crystalline part. This assumption is quite reasonable in the polymer case and it gives results in agreement with DSC measurements. The same hypothesis do not work always in the case of ceramics or alloys, the silica glass structure by Le Bail is an example. The method requires that the pseudo-crystal structure is known. Up to now very few of them have been found or tested [12, 16, 17] but in the case the pseudo-structure is unknown and a pure sample is available the same procedure as in the PONCKS can be used to calibrate the intensities. This last methodology has been used to determine the phase quantities with the presence of two different amorphous structures [18]. Two examples are reported in figures 5 and 6 and table 4. In both examples an incipient (griseofulvine and nifedipine) in crystalline form is amorphized by ball milling with the help of a polymer (PVP) to stabilize the amorphous form. In such case the procedure has been able to quantify the incipient crystallinity with the presence of a second amorphous, the PVP polymer by the fact that the two amorphous phases have a different pattern. Those last examples are a further proof of how flexible is the Rietveld method and how a correct quantification can be reached using the appropriate model.

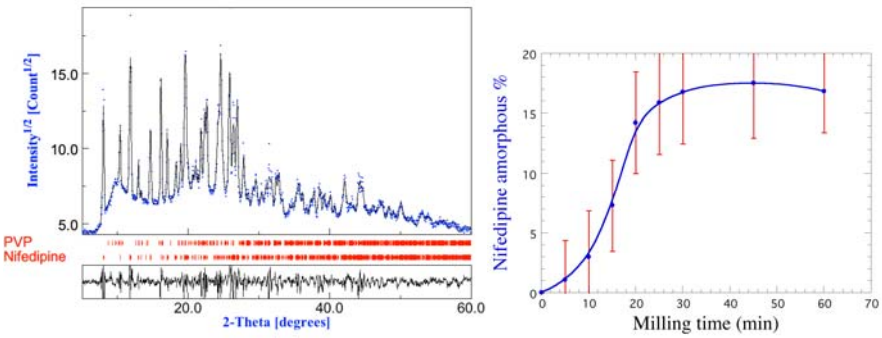

Fig. 5. Quantification of the nifedipine amorphization inside the PVP matrix by ball milling. On the left the Rietveld fit using the PVP modeled using the cell of the crystalline PVP with the PONCKS method and the pseudo-structure of the nifedipine for the amorphous part; on the right the nifedipine amorphous content as determine by the Rietveld fit.

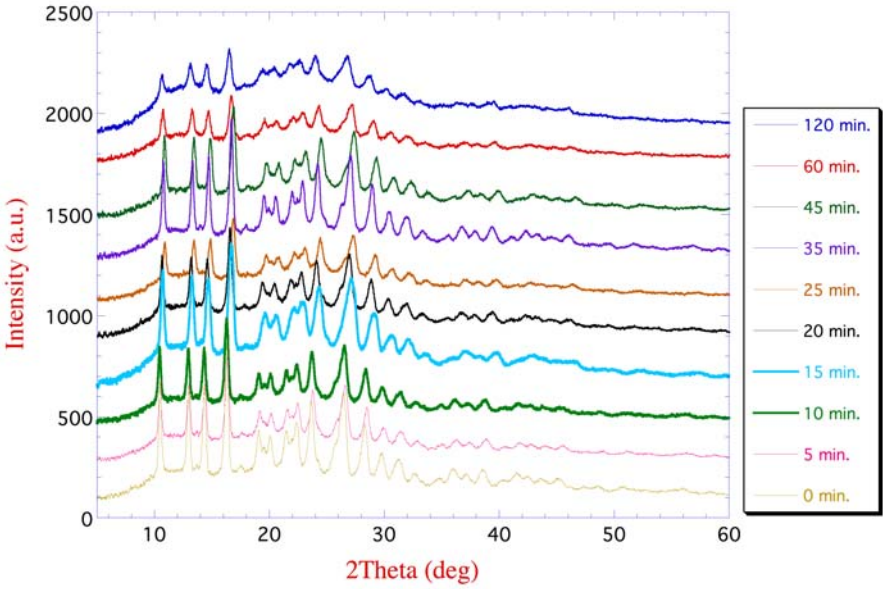

Fig. 6. Amorphization of the griseofulvine in the PVP matrix for different milling times. The values of griseofulvine crystallinity are reported in table 4.

Table 4. Griseofulvine crystallinity after milling at different times.

Crystallinity (%)	100	70	60	51	50	40	46	50	35	32	17
Milling time (min)	0	5	10	15	20	25	35	45	60	90	120

References

[1] Lutterotti L., Scardi P., Tomasi A.: Application of the Rietveld method to phase analysis of multilayered systems. Mat. Science Forum **133-136**, 57-62 (1993)

[2] Simek D., Kuzel R., Rafaja D.: Reciprocal-space mapping for simultaneous determination of texture and stress in thin films. J. Appl. Cryst. **39**, 487-501 (2006)

[3] Ferrari M., Lutterotti L.: Method for the simultaneous determination of anisotropic residual stresses and texture by X-ray diffraction. J. Appl. Phys. **76** (11), 7246-7255 (1994)
[4] Cont L., Chateigner D., Lutterotti L., Ricote J., Calzada M. L., Mendiola J.: Combined X-ray texture-structure-microstructure analysis applied to ferroelectric ultrastructures: a case study on Pb0.76Ca0.24TiO3. Ferroelectrics **267**, 323-328 (2002)
[5] Lutterotti L.: Total pattern fitting for the combined size-strain-stress-texture determination in thin film diffraction. Nuclear Inst. and Methods in Phys. Res. B **268**, 334-340 (2010)
[6] Ufer K., Roth G., Kleeberg R., Stanjek H., Dohrmann R., Bergmann J.: Description of X-ray powder pattern of turbostratically disordered layer structures with a Rietveld compatible approach. Zeitschrift für Kristallographie, **219**, 519–527 (2004)
[7] Ufer K., Kleeberg R., Bergmann J., Curtius H., Dohrmann R.: Refining real structure parameters of disordered layer structures whitin the Rietveld method. Zeitschrift für Kristallographie Supplements, **27**, 151–158 (2008)
[8] Lutterotti L., Voltolini M., Wenk H.-R., Bandyopadhyay K., Vanorio T.: Texture analysis of a turbostratically disordered Ca-montmorillonite. Amer. Miner. **95**, 98-103 (2010)
[9] Brindley G. W.: A theory of X-ray absorption in mixed powders. Philos. Mag. **36**, 347-369 (1945)
[10] Taylor J. C., Matulis C. E.: Absorption contrast effects in the quantitative XRD analysis of powders by full multiphase profile refinement. J. Appl. Cryst. 24, 14-17 (1991)
[11] Elvati G., Lutterotti L.: Avoiding surface and absorption effects in XRD quantitative phase analysis. Mater. Sci. Forum **278-281**, 69-74 (1998)
[12] Le Bail A.: Modelling the silica glass structure by the Rietveld method. J. Non-Cryst. Solids **183** (1-2), 39-42 (1995)
[13] Lutterotti L., Ceccato R., Dal Maschio R., Pagani E.: Quantitative analysis of silicate glass in ceramic materials by the Rietveld method. Mater. Sci. Forum, **278-281**, 87-92 (1998)
[14] Hill R. J., Howard C. J.: Quantitative phase analysis from neutron powder diffraction data using the Rietveld method. J. Appl. Cryst, **20**, 467-474 (1987)
[15] Bish D. L., Howard S. A.: Quantitative phase analysis using the Rietveld method. J. Appl. Crystallography **21**, 86-91 (1988)
[16] Le Bail A.: Reverse Monte Carlo and Rietveld modeling of the NaPbM2F9 (M=Fe,V) fluoride glass structures. J. Non-Cryst. Solids **271**, 249-259 (2000)
[17] Lutterotti L., Campostrini R., Di Maggio R., Gialanella S.: Microstructural characterization of amorphous and nanocrystalline structures through diffraction methods. Mat. Sci. Forum **343-346**, 657-664 (2000)
[18] Lutterotti L., Bortolotti M., Magarotto L., Deflorian C., Petricci E.: Rietveld structural and microstructural characterization of pharmaceutical products using the program Maud. Presented at PPXRD-4, 21-24 February 2005, Barcelona, Spain

Texture – An Overview

R.B. Von Dreele
Advanced Photon Source, Argonne National Laboratory, USA

Introduction

By definition, an ideal microcrystalline powder consists of a very large number of small crystals that are randomly oriented with respect to each other and to the macroscopic dimensions of the sample. Ignoring macroscopic effects of absorption, the diffraction intensity for any Bragg reflection from this sample is independent of its orientation in the beam because there is an equal probability of crystallites being in the diffracting condition for all sample orientations. In this circumstance, the observed intensities are proportional to the crystal structure diffraction intensities (F_{hkl}^2) after applying simple geometric corrections (e.g. Lorentz-polarization and absorption) and the appropriate reflection multiplicity.

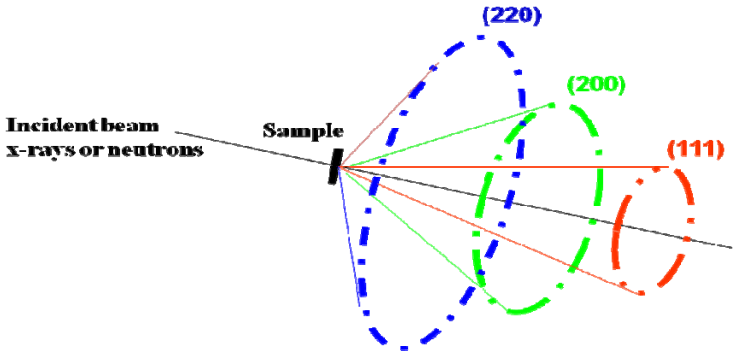

Fig. 1. Cartoon view of the effect of texture or preferred orientation on the diffracted intensities from a sample. Note that in general the intensity pattern around each ring will change as the sample is rotated in the beam.

However, the process of producing the sample by packing microcrystals in a holder (flat plate or cylinder) can force the crystal grains into a non-random orientation. For example, if the crystallites have a strong platy habit, then they will preferentially pack so that their plate normal aligns perpendicular to the sample surface. Conversely, crystallites with a needle-like habit will pack so that the needle axis preferentially lies in the sample surface plane. In either case the diffraction intensities are not independent of sample orientation and some intensities will be enhanced while others are suppressed for a particular sample orientation as shown in Figure 1. It is important to note that this "preferred orientation" not only describes how the crystal-

lites align with respect to each other but also with respect to the macroscopic sample dimensions.
Samples that are polycrystalline solid objects (e.g. a metal bar, wire or plate) are usually produced by some mechanical process (e.g. rolling, drawing or pressing) that frequently forces a non-random orientation of the crystallites in response to plastic deformation of the material during the forming operation. The resulting crystallite orientations ("texture") can be more complex that those obtained from packing of powders and due to anisotropy in physical properties (elasticity, conductivity, etc.) the details of the orientation can have an impact on the formed object's material properties.
In the course of crystal structure analysis from powder diffraction data, these changes in the Bragg intensities from preferred orientation can strongly degrade the quality of the result of a Rietveld refinement and can prevent a structure solution for an unknown. This nuisance factor is generally most severe for Bragg-Brentano x-ray diffraction experiments, particularly for highly absorbing materials. It is less a problem for Debye-Scherrer experiments where powders are packed in thin capillaries and frequently use is made of high energy synchrotron radiation. Neutron powder diffraction experiments with large samples and almost no absorption rarely show preferred orientation effects.

Fig. 2. Obverse and reverse view of a silver Roman coin; is it a fake?

On the other hand, the crystallite orientation ('texture') within a formed, polycrystalline object can be of considerable technological interest. For example, the texture can be used to infer the history of the piece – "was that piece of metal cast, rolled or drawn to give that shape?" The answer to this question might be of great interest to a museum curator of Roman artifacts looking for fakes (Fig.2). Significantly, the macroscopic properties of materials (strength, stress/strain, thermal expansion, magnetization, superconductivity, thermal conductivity, etc.) are frequently dependent on direction within a crystal structure and therefore dependent on the texture in a

polycrystalline object made of these materials. For example, the steel plates that make up a common electrical transformer must be produced with a very strong alignment of the steel crystal grains to have the desired magnetization properties for an efficient transformer. In another example, the formation of cuprate high-T_c superconductors into wires requires that the crystallographic c-axis be perpendicular to the wire axis because the superconductivity is largely confined to the basal plane. Reducing the impact of preferred orientation on powder diffraction data can be done in a variety of ways. For Bragg-Brentano samples, one can use either "back mounting" or "side mounting" which attempt to prevent the alignment of the crystal grains against the surface exposed to x-rays. The samples can also be prepared by "spray drying" which agglomerates the crystallites into spherical particles which are then loaded in the sample holder; the presumption is that the crystallite grains are more randomly oriented within these particles. Additionally, a sample spinner is often used. Note that this does not eliminate preferred orientation; it simplifies it by making the distribution have cylindrical symmetry. Note that in Debye-Scherrer geometry, the sample generally is spun about the cylinder axis to remove the effect of sample grittiness and thus improve the powder average; it also makes any preferred orientation have cylindrical symmetry.

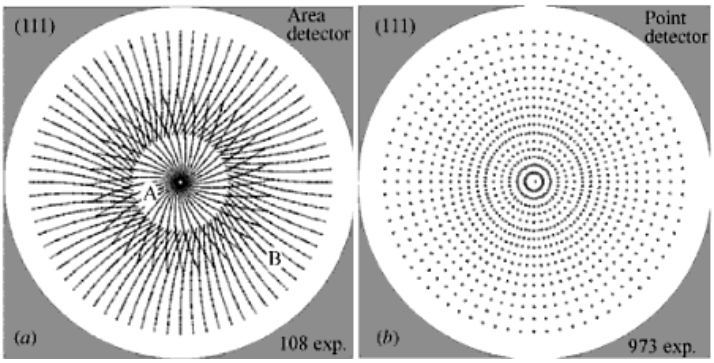

Fig. 3. Typical sample orientation grid for pole figure measurement at nominally 5° orientation resolution using (a) an area detector and (b) a point detector. (Taken from "Two-dimensional x-ray diffraction", Bob B. He, 2009, Wiley,New York, p 230.)

The measurement of texture requires the determination of how individual reflection intensities change as the sample is placed in a suite of orientations in the x-ray (or neutron) beam. The classical approach as done in the laboratory is to sample a few reflections in a grid of orientations (typically 5deg steps on two angles – cf Fig. 3b). After applying absorption, geometric and normalization corrections, the intensities are then displayed in a polar plot ("pole figure") of the two angles for each reflection sampled in the experiment. This measurement can be time consuming requiring 12-24hrs on a laboratory diffractometer equipped with a special pole figure measuring device. Instruments equipped with area detectors can use fewer sample orientations

and thus can obtain the required data in less time (cf Fig. 3a). The observed intensities must arise from cleanly separated peaks; note that the geometry used in this data collection is not optimized for peak resolution.
An alternative approach is to use "whole pattern fitting" of full diffraction patterns from a small subset of sample orientations; a model is used to represent the texture and the coefficients are obtained via Rietveld techniques. This approach can take advantage of high energy synchrotron x-rays with area detectors or spallation neutrons and time-of-flight data collection techniques and be much faster than the classical measurement of pole figures.

Texture models:
Modern Rietveld refinement programs will frequently allow inclusion of a texture model to describe the change in Bragg intensity for each reflection from that expected for an ideally random powder. The simplest is that of March (1932) as simplified by Dollase (1986)

$$O_h = \frac{1}{M}\sum_{j=1}^{n}\left(R_o^2 \cos^2\phi + \frac{\sin^2\phi}{R_o}\right)^{-\frac{3}{2}} \qquad (1)$$

This expression is essentially a modifier of the reflection multiplicity, M, for all equivalent h depending on the ratio, R_o, of the major and minor axes of a cylindrically symmetric ellipsoid and on the angle, ϕ, each equivalent reflection, h, makes with some user specified direction, H. The sum is over all the equivalent reflections, n. This description is suitable for either a cylindrical sample spun about its axis as in a Debye-Scherrer experiment or a flat sample spun about its normal in a Bragg-Brentano experiment.
A more complex description derives from a representation of the orientation distribution function (ODF). The ODF gives the probability of finding a particular crystallite orientation with respect to some defined sample coordinate system and is an average over all locations within the sample volume. A further elaboration not considered here is to describe the ODF(xyz) as it varies over the sample volume; this may be of interest in, for example, comparing the bulk texture of a manufactured object with its surface texture. The properties of the ODF are that it must be a real and positive function for which the integral over all orientations is unity. It may also have certain symmetries arising from both the manufacturing process used to make the sample and the crystal symmetry of material. If there is more than one crystalline phase, each will have its own ODF. An ODF has two parts; one is symmetric to inversion ("even" part) and the other is not ("odd" part). Due to Friedel's Law only the even part of the ODF will affect the diffracted intensities and the odd part is thus invisible.

Projections of the ODF are used to represent the texture. If a particular reciprocal crystal direction is chosen as hkl and a projection is made along one sample axis, the result is a "pole figure" and is plotted as a function of two sample orientation angles (ϕ,ψ) as in Figure 3. Conversely, one can choose a particular sample direction (xyz) and then make a projection along some reciprocal crystal direction, and plot the projection as a function of two crystal orientation angles (μ,ν) to obtain an "inverse pole figure". These pole figures also have certain mathematical properties. They must be real and positive everywhere and their integral over all orientations must be unity. Their magnitudes are usually expressed as "multiples of random distribution" (MRD).

As noted above, a diffraction experiment is sensitive to the ODF of a crystalline phase within a solid object in that reflection intensities can differ depending on the fraction of crystallites with a particular orientation. A way of representing this effect on intensities is with the General Axis Equation (Bunge, 1993; Von Dreele, 1997)

$$A(h,y) = 1 + \sum_{l=2}^{L} \frac{4\pi}{2l+1} \sum_{m=-l}^{l} \sum_{n=-l}^{l} C_l^{mn} K_l^m(h) K_l^n(y) \qquad (2)$$

which is dependent on both a direction in the sample coordinates, $y(\phi,\psi)$, and a direction in the crystal reciprocal space, $h(\mu,\nu)$, and is thus 4-dimensional in (ϕ,ψ,μ,ν). The outer summation is over the only even indices, l, to some maximum, L, thus representing the even part of the ODF that can affect the diffracted intensities. Recall that the odd part has no impact on the diffracted intensities. The two sets of terms, $K_l^m(h)$ and $K_l^n(y)$, are spherical harmonics symmetrized according to the crystal and sample symmetries, respectively. The forms of the spherical harmonics are identical to those used for the angular part of the atomic orbitals, and form an orthogonal set of functions. The C_l^{mn} coefficients are determined by Rietveld refinement and are restricted according to both the crystal and sample symmetries; the orthogonality properties of the functions confer great stability to this refinement. If all C_l^{mn} are zero, then clearly the diffraction is the same in all directions as from an ideally random powder. By selecting either a specific h or y direction and then computing A(h,y) over the remaining orientation angles, one can produce either a pole figure for the selected h or an inverse pole figure for the selected y. The texture index, J, can be obtained from the coefficients via

$$J = 1 + \sum_{l=2}^{L} \frac{1}{2l+1} \sum_{m=-l}^{l} \sum_{n=-l}^{l} \left| C_l^{mn} \right|^2 \qquad (3)$$

If the texture is random then J=1, otherwise J>1. J is very large for strongly textured materials; $J=\infty$ for a single crystal.

Applications

In this talk a few applications of the spherical harmonic model will be presented. One is the original test case study (Von Dreele, 1997) of a calcite sample used in an earlier round robin study (Wenk, 1991) and the other is a combined texture/microstrain study of a 3-layer hot rolled stainless/carbon steel sandwich (obtained from H. Priesmeyer, 1995). Both were performed using neutron time-of-flight (TOF) diffraction data collected at LANSCE, Los Alamos National Laboratory on the High Intensity Powder Diffractometer (HIPD). In a neutron TOF experiment, the detectors are in fixed locations as is the sample, thus in the general axis equation the sample direction, y, is fixed and each powder pattern is in essence an inverse pole figure scaled by the magnitudes of the crystal structure factors. A complete texture measurement for the calcite was thus obtained from 13 sample orientations in 4 sets of detectors, comprising 52 inverse pole figure measurements. Similarly, 24 sample orientations and 3 detectors were used for the steel sample resulting in 72 inverse pole figures (Fig.4)

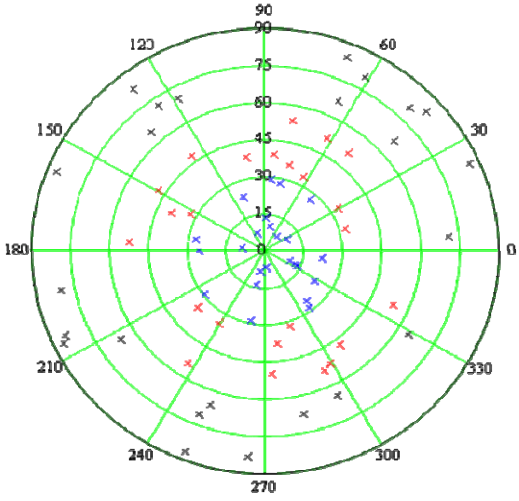

Fig. 4. The 72 ϕ,ψ orientations obtained in 24 settings for the steel sample on HIPD.

The Rietveld refinement on the steel sandwich required two texture descriptions, one for each phase. The stainless steel texture model had 18 C_l^{mn} and the carbon steel model had 12 C_l^{mn} coefficients. These were then used in the general axis equation to generate pole figures (Fig. 5)

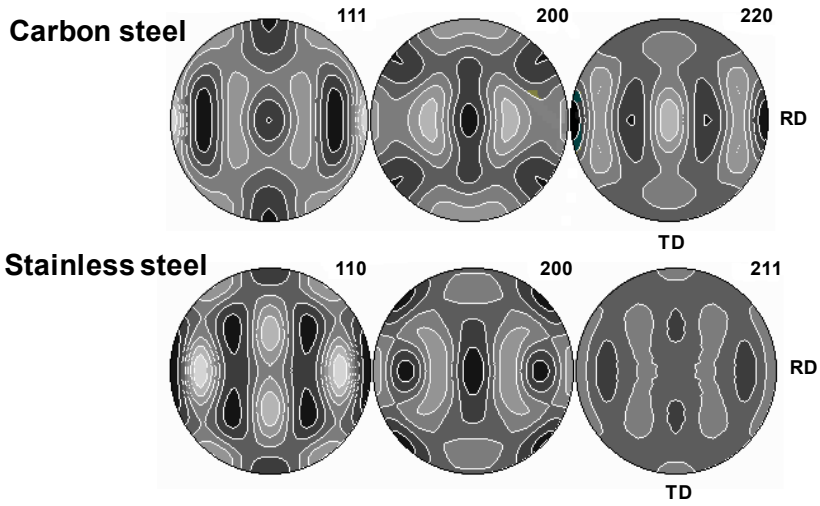

Fig. 5. Pole figures for carbon steel (top) and stainless steel (bottom) obtained from the hot rolled steel sandwich. They are both examples of (100)[110] rolling texture.

Acknowledgments. This work was supported by the US Department of Energy, Office of Basic Energy Sciences, Office of Science, under contract No. DE-AC-02-06CH11357.

References

Bunge, H.-J. (1993). *Texture Analysis in Materials Science*, Gottingen: Cuviller Verlag.
Dollase, W.A. (1986). *J. Appl. Cryst*. **19**, 267-272.
March, A. (1932). *Z. Kristallogr*. **81**, 285-297.
Priesmeyer, H. (1995), private communication
Von Dreele, R.B. (1997). *J. Appl. Cryst*. **30**, 517-525.
Wenk, H.-R. (1991*). J. Appl. Cryst*. **24**, 920-927.

Using Texture for Structure Solution

Christian Baerlocher and Lynne B. McCusker
Laboratory of Crystallography, ETH Zurich, Switzerland

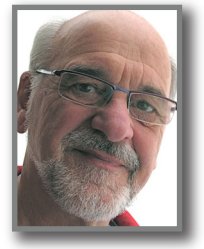

Introduction

In a conventional powder diffraction pattern, reflections with similar *d*-spacings overlap and their individual intensities cannot be measured. It is only the ambiguity in the relative intensities of these overlapping reflections that hinders the determination of the structures of polycrystalline materials. A number of methods have been developed to circumvent this problem [1], but if the ambiguity could be resolved from the outset, it would be possible to take advantage of the powerful techniques that have already been developed for single-crystal data and apply them directly. One way of addressing the overlap problem experimentally is to adopt a more elaborate data collection strategy in which several different, but related, data sets are collected on the same polycrystalline sample [2]. For example, a material that exhibits anisotropic thermal expansion can be measured at several different temperatures, and the changes in the overlap pattern caused by the changes in the lattice parameters exploited to obtain better estimates of the individual reflection intensities [3]. Alternatively, a sample with a preferred orientation of the crystallites, which will yield powder diffraction patterns that are dependent upon the orientation of the sample in the X-ray beam, can be used. It is this second option that is the subject of this contribution.

Much of the background material presented in the following sections can also be found in an overview of the method by Baerlocher et al. [4], along with a more comprehensive list of references.

Concept

The idea behind the 'texture method' is illustrated for a two-dimensional case in Figure 1, where the diffraction pattern of an "ideal" powder with randomly oriented crystallites is shown together with that of a textured powder sample. In both cases, the corresponding single-crystal pattern has been superimposed. Because not all crystallite orientations are equally represented in the textured sample, the reflections are concentrated in certain regions of reciprocal space, so by measuring the diffraction pattern along different radial directions (e.g. by orienting the sample differently in the X-ray beam), additional intensity information can be extracted. For example, the four reflections marked with arrows in Figure 1 overlap in the normal powder diffraction pattern, but can be separated in the pattern from the textured sample. The

sample orientations yielding the desired information depend upon how the crystallites are oriented in the sample. For simplicity, only two dimensions are shown in Figure 1, but extension to three dimensions is straightforward: circles become spheres and a third dimension is added to the single crystal diffraction pattern. In the two-dimensional case, the sample is simply rotated to the desired orientation. In three dimensions, the sample can also be tilted.

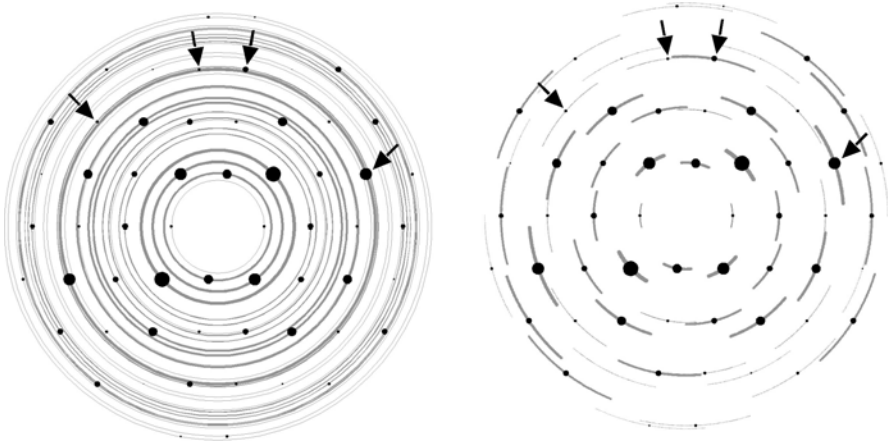

Fig. 1. 2-dimensional diffraction pattern for a powder with randomly oriented crystallites (left) and for a textured powder (right). The corresponding single crystal pattern is superimposed in both cases. Four symmetrically non-equivalent reflections that overlap in the normal powder pattern are marked with arrows

Analysis of the data from such a textured sample is based on the equation:

$$y(2\theta,\chi,\phi) = \sum_{hkl} I_{hkl} P_{hkl}(\chi,\phi) G(2\theta - 2\theta_{hkl}) \qquad (1)$$

where $y(2\theta,\chi,\phi)$ is the intensity measured at diffraction angle 2θ for sample orientation (χ (tilt), ϕ (rotation), I_{hkl} is the single crystal intensity, $P_{hkl}(\chi,\phi)$ is the fraction of the intensity of the reflection *hkl* that is observed at the sample orientation (χ,ϕ), and *G* is the standard Rietveld peak-shape function. The key to the method lies in the $P_{hkl}(\chi,\phi)$-values, which depend upon the orientations of the crystallites in the sample. Once these values have been determined, the resulting set of linear equations can be solved for I_{hkl}.

Reflection Geometry

To apply this approach practically, a textured sample has to be prepared and data collected. The original experiments were performed in reflection mode, and a schematic diagram of the setup is shown in Figure 2. A texture goniometer that allows the sample to be oriented in a controlled manner (tilt χ and rotation ϕ) is re-

quired. As the sample is tilted in χ, parts of it are displaced from the focusing circle of a normal Bragg-Brentano geometry, causing severe broadening of the diffraction peaks. By using a parallel X-ray beam and a pre-detector analyzer crystal, this effect can be eliminated, and sharp diffraction patterns collected for all sample orientations.

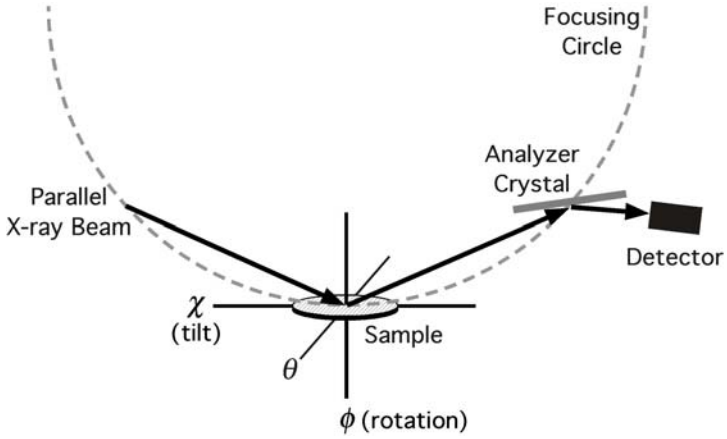

Fig. 2. Schematic diagram of the reflection geometry setup showing the sample tilt (χ) and rotation (ϕ) axes, and the pre-detector analyzer crystal. The focusing circle for a laboratory Bragg-Brentano geometry with a divergent X-ray beam is also indicated.

The orientation of the crystallites in the sample can be determined by measuring how the intensities of a set of selected reflections vary as the sample is tilted and rotated. These reflections must be non-overlapping and have sufficient intensity to be measured accurately. The number and *hkl*-type required depends upon the symmetry of the sample and of the crystal structure. For each reflection, the detector is set at the appropriate 2θ angle and the sample at θ, and then for each 5˚ tilt in χ (usually up to 80˚), the sample is rotated 360˚ in ϕ in 5˚ steps. The intensity is thereby measured for (16 x 72) +1 = 1153 sample orientations for each of the selected reflections.

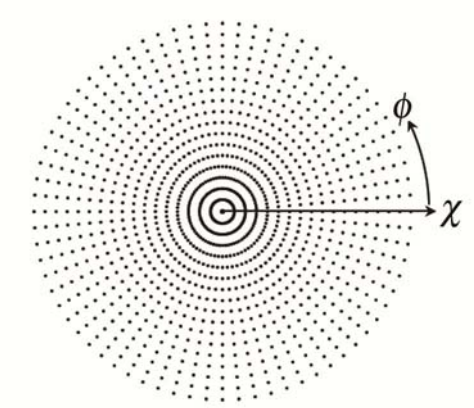

Fig. 3. A schematic drawing of the pole figure sampling using a 5° x 5° grid in χ and ϕ. Each point represents an intensity measurement for the sample orientation (χ,ϕ).

The results of such measurements are generally plotted in the form of pole figures (see Figure 3). For a sample with completely randomly oriented crystallites, the pole figure will show no variation with sample orientation (i.e. the values for all orientations are 1.0). For a textured sample, however, some orientations will have values higher than 1.0 while others will be lower. The values in a pole figure are usually given in terms of "multiples of random distribution" (m.r.d.).

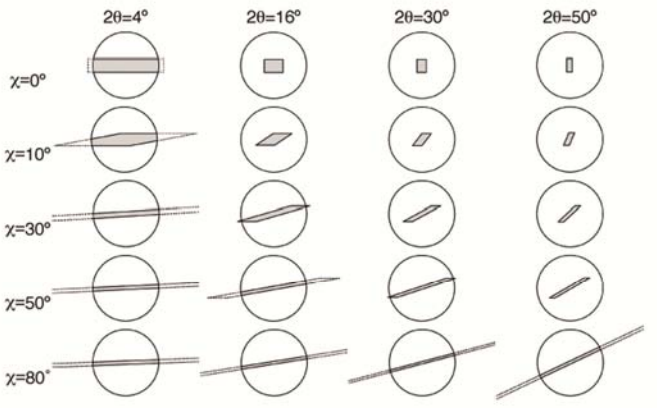

Fig. 4. Change of the footprint of the X-ray beam on the sample as a function of diffraction angle 2θ and sample tilt χ.

Once the pole figures have been measured for a few reflections and the orientation of the crystallites in the sample (orientation distribution function or ODF) determined using a standard texture program such as MAUD [5], a few sample orientations are selected for full θ-2θ data collection. Those orientations likely to yield the highest intensity contrasts for different directions in reciprocal space are chosen.

These data are then used in conjunction with the *P*-values calculated from the ODF and equation (1) to refine a single set of I_{hkl} values.

One of the problems with the reflection geometry is that the footprint of the X-ray beam on the sample changes as a function of both diffraction angle 2θ and sample tilt χ. As can be seen in Figure 4, the X-ray beam overshoots the sample at low 2θ and high χ. Furthermore, the size of the analyzer crystal and of the receiving slit of the detector can limit the fraction of the diffracted beam that is actually measured, and, depending on the absorption characteristics of the sample, the asssumption of "infinite thickness" may not be met for all reflections and sample orientations.

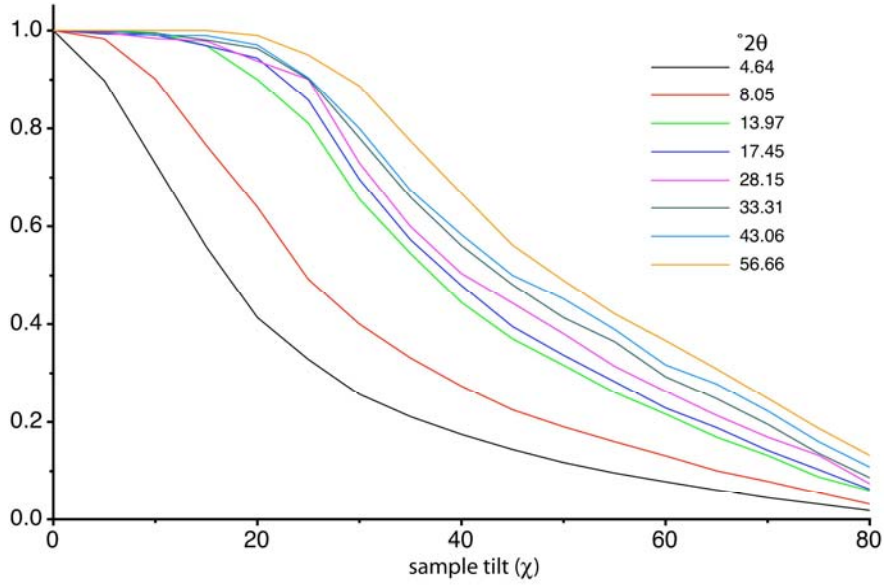

Fig. 5. The variation in the intensities recorded for an untextured sample of zeolite A as a function of sample tilt (χ) and diffraction angle (2θ). All curves have been normalized to the reflection intensity at $\chi = 0$

The effect of all of these factors on the measured data must be taken into account during data analysis. To do this, the diffracted intensity of an untextured sample (with an absorption similar to that of the sample of interest) is measured as a function of 2θ and χ to obtain intensity calibration curves (Figure 5). These curves are then used to correct the data collected on the sample of interest. This correction is a significant one, involving a factor of five or more at higher tilt angles. Any errors in the measurement at high tilt angles (e.g. arising from an inhomogeneity in the sample) will be magnified.

To align the texture goniometer, to collect data for the tilt correction, to collect pole figure data for 5-10 reflections, and to collect full data sets for 5-10 different sample orientations, a minimum of 3 days of synchrotron beamtime is required.

Transmission Geometry

By adapting the experiment to a transmission mode setup (Figure 6), several of the problems encountered with the reflection mode experiment can be solved. With the transmission geometry, the entire sample (*ca* 0.2-0.3 mm ball) is bathed in the X-ray beam for all sample orientations, so the problem of sample inhomogeneity is eliminated and no tilt calibration curves are needed. A 2-dimensional area detector rather than a 0-dimensional point detector is used, so the data collection is more efficient. Furthermore, full diffraction patterns are collected automatically for all sample orientations (i.e. not just a few selected ones), so the data are more complete.

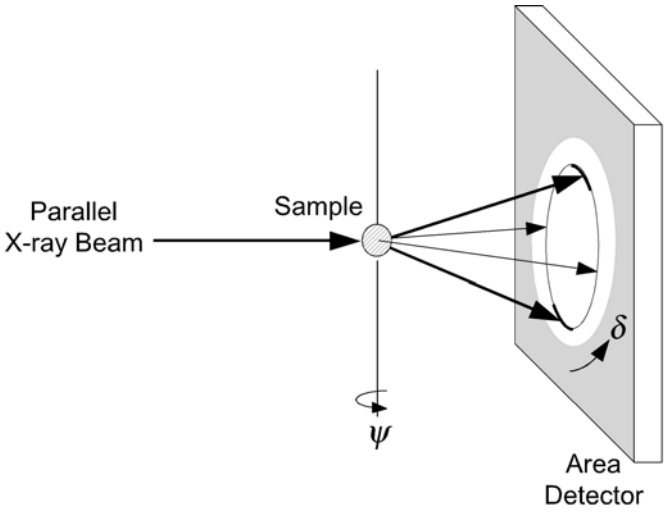

Fig. 6. Schematic diagram of the transmission mode setup showing the sample rotation axis (ψ) and the sample tilt (δ).

The price to be paid for the faster data collection is a loss of resolution, both in peak sharpness (FWHM-resolution) and in 2θ range (d_{min}-resolution). The FWHM-resolution is determined by the size of the sample, the sample-detector distance, and the resolution of the detector. The larger the sample-detector distance, the better the resolution. Unfortunately, the larger this distance, the smaller the 2θ range. For comparison, a typical FWHM in reflection mode is *ca*. 0.02˚2θ and in transmission mode *ca*. 0.05˚2θ, and the 2θ range accessible with the area detector is limited to ca. 35˚2θ.

A typical dataset consists of 36 imaging plate frames, each corresponding to a sample rotation of 5˚ in ψ. The data on each frame are then divided into radial wedges of 5˚, which are integrated to give 72 diffraction patterns, each corresponding to a different sample tilt δ. This yields a total of 36 frames x 72 wedges = 2592 full diffraction patterns, corresponding to 1296 unique sample orientations (ψ,δ). Pole-

figure data are therefore measured automatically for all reflections. Typicallly, 3-6 hours of synchrotron beamtime are required per dataset.
Because of the inversion symmetry inherent to diffraction data, only one half of the 72 radial wedges are actually unique. It is also possible to rotate the sample 360˚ instead of 180˚ and to use only one quadrant of data per frame. Such a data collection obviously takes twice as long (72 frames instead of 36), but by repositioning the imaging plate to cover just one quadrant, the 2θ range can be increased by a factor of $\sqrt{2}$.
The sample rotation and tilt in transmission mode (ψ,δ) do not correspond exactly to those in reflection mode (ϕ,χ), because a θ-2θ diffraction geometry is not used in the former [6]. This difference has to be taken into account in the data analysis. Because more data are collected, more reflections can be used to determine the ODF, and more patterns can be used to derive the intensities using equation (1). However, the low resolution of the data limits their effectiveness. For samples with a low to medium degree of reflection overlap, the setup is adequate, but for the more complex problems, which are those of interest, it is not.

Transmission Geometry with a Linear Detector

By adapting the experiment to take advantage of the unique features of the linear Si-microstrip detector installed on the Materials Science Beamline at the Swiss Light Source [7] (Figure 7), the problems encountered with the area detector could be resolved. This linear detector offers a larger angular range than does the imaging plate setup (60 vs. 35 ˚2θ) and sharper peaks (0.03 vs 0.05 ˚2θ). However, because it is a 1- rather than a 2-dimensional detector, each of the 1296 sample orientations has to be measured separately, so data collection requires a Eulerian cradle and more beamtime (ca 12h), and the resulting statistics are poorer. Fortunately, with the new edition of the Si-strip detector (Mythen II), improved focusing of the beam to yield a high intensity, homogeneous beam, and an optimized data collection strategy, these problems could be overcome.

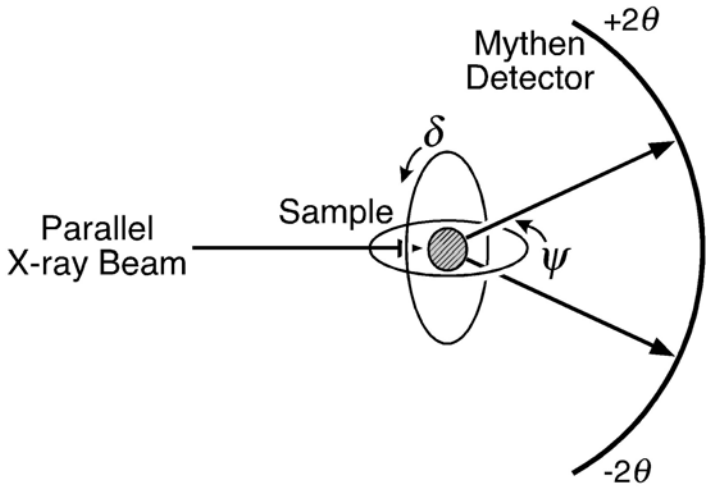

Fig. 7. Schematic diagram of the transmission mode setup with the linear Si-strip detector and the sample rotation (ψ) and tilt (δ) circles of the Eulerian Cradle

Unlike other texture determination programs, MAUD [5] does not require a 5˚ x 5˚ grid of data points for the individual pole figures, so a more efficient coverage of orientation space can be used (e.g. fewer points at lower tilt angles - see Figure 3). In this way, the number of orientations measured can be reduced from 1296 to 302 with almost no loss of information. Furthermore, the 120˚2θ range of the detector can be exploited to measure two patterns at once (0 - 60˚2θ and 0 - -60˚2θ) (see Figure 7).

Examples

An example for each of the experimental setups described above is described briefly below.

Reflection Geometry

The zeolite UTD-1F has a large monoclinic unit cell (a = 14.970 Å, b = 8.476 Å, c = 30.028 Å, β = 102.65˚), so the degree of reflection overlap is high [8].

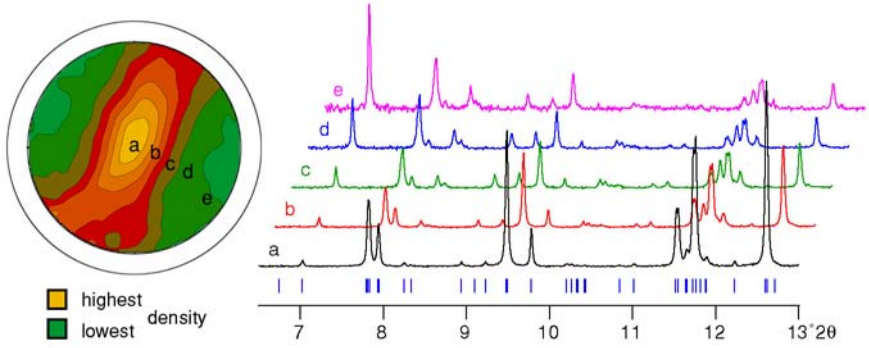

Fig. 8. As synthesized UTD-1F. The pole figure for the $10\bar{2}$ reflection showing the orientations selected for collection of full diffraction patterns (left) and sections of these patterns (right). Note the changes in the intensities as a function of sample orientation..

The crystals have a needle-like morphology, and a textured sample was prepared in a polystyrene matrix. The experimental setup was calibrated using an untextured zeolite A sample (Figure 3). Then pole figure data for seven non-overlapping reflections were collected on the textured UTD-1F sample. From these, the ODF was determined. Full diffraction patterns were measured for five different orientations, and these were used to extract a set of single-crystal-like reflection intensities for input to a direct methods program. The complex structure, with 117 atoms in the asymmetric unit, was then determined. One of the pole figures and sections of the five patterns are shown in Figure 8.

Transmission Geometry with an Imaging Plate

Attempts to solve the structure of the aluminophosphate $AlPO_4$-M (*Pbca*, a = 9.749 Å, b = 29.167 Å, c = 9.353 Å) from conventional powder diffraction data had failed, so it was thought to be a suitable candidate for testing the transmission setup [4]. The crystallites were needle-like, so a procedure similar to that used for UTD-1 was used to prepared a textured sample. In this case though, a *ca.* 0.3 mm cube was cut from the polystyrene preparation for data collection. A typical imaging plate frame from this measurement is shown in Figure 9.

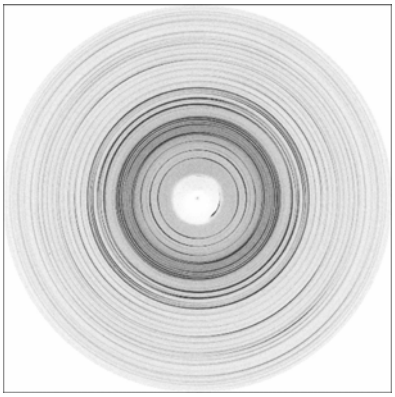

Fig. 9. Imaging plate frame for the orientation $\psi = 30^{\circ}$ collected on the textured sample of AlPO-M. Note the differences in intensity around the rings.

Ten reflections were used to determine the ODF, and then all 1296 datasets were used to extract a single set of reflection intensities. In this case, the data from the textured sample were supplemented with high-resolution data collected on an untextured sample. In this way, a set of I_{hkl} consistent with both measurements could be extracted. With these data, direct methods revealed an aluminophosphate layer structure. The location of the organic cations and water molecules between the layers were then easily determined using conventional difference Fourier syntheses.

References

[1] David, W.I.F., Shankland, K., McCusker, L.B., Baerlocher, Ch. (eds.) Structure Determination from Powder Diffraction Data, Oxford University Press, 2002.
Baerlocher, Ch., McCusker (eds.) *Z. Kristallogr*. **219**, 782-901, 2004

[2] Wessels, T., Baerlocher, Ch., McCusker, L.B. and David, W.I.F. In: *Structure Determination from Powder Diffraction data* (Eds. W.I.F. David, K. Shankland, L.B. McCusker, Ch. Baerlocher), Oxford University Press, 2002, pp. 162-178.

[3] Shankland, K., David, W.I.F., Sivia, D.S. *J. Mater. Chem*. **7**, 569-572 (1997).
Brunelli, M., Wright, J.P., Vaughan, G.R.M., Mora, A.J. and Fitch, A.N. *Angew. Chem. Int. Ed.* **42**, 2029-2032 (2003).
Wright, J.P.: *Z. Kristallogr*. **219**, 791-802 (2004).

[4] Baerlocher, Ch., McCusker, L.B., Prokic, S. and Wessels, Th. *Z. Kristallogr*. **219**, 803-812.

[5] Lutterotti, L., *http://www.ing.unitn.it/~maud/*.

[6] Heidelbach, F., Riekel, C. and Wenk, H.-R. *J. Appl. Crystallogr*. **32**, 841-849 (1999).

[7] Schmitt, B., Bronnimann, C., Eikenerry, E.F., Gozzo, F., Hormann, C., Horisberger, R. and Patterson, B. *Nucl. Instr. Methods A* **501**, 267-272 (2003).

[8] Wessels, T., Baerlocher, Ch. and McCusker, L.B. *Science* **284**, 477-479 (1999).
Wessels, T., Baerlocher, Ch., McCusker, L.B. and Creyghton, E.J. *J. Am. Chem. Soc.* **121**, 6242-6247 (1999).

Old ideas - new opportunities

Lynne B. McCusker and Christian Baerlocher
Laboratory of Crystallography, ETH Zurich, Zurich, Switzerland

Abstract. Techniques for structure analysis that were slowly abandoned by single-crystal crystallographers as computer programs became increasingly powerful, are enjoying a rebirth in the world of powder diffraction. In particular, introducing non-diffraction information into the structure analysis procedure in different ways to supplement the powder diffraction data has proven to be remarkably effective. Model building algorithms have been devised, chemical information is used in the automatic interpretation of electron density maps, and geometric restraints have been implemented in Rietveld refinement programs. The traditional Patterson method has also been exploited in novel ways to improve both the partitioning of overlapping reflections and structure solution. Macromolecular crystallography is another rich source of techniques that can help the powder diffractionist overcome the problem of too few data for the number of structural parameters. Protein methods that have been adapted to the powder diffraction case include the generation of structure envelopes and the use of two density modification technqiues (solvent flattening and histogram matching).

1. Introduction

Many of the techniques used by crystallographers over 50 years ago for structure solution have fallen into disuse, because single-crystal computer programs have become so powerful that they are no longer necessary. However, with the increasing interest in using powder diffraction data for structure analysis, some of these old ideas are enjoying a rebirth. Model building, which was the prime method of structure determination before the age of Patterson and direct methods [1], has taken on new meaning in the context of real-space global-optimization approaches to structure solution [2]. Indeed these methods also take advantage of well-established mathematical algorithms. The Patterson function itself was first introduced in 1934 [3], and has been exploited in various ways by powder diffractionists [4]. Chemical information gleaned from non-diffraction experiments, which has become almost irrelevant for single-crystal structure analyses, is being used again, not only to check the validity of structural models, but also to guide structure solution. Finally, as in the early days of structure refinement, when experimental data could not be measured with high accuracy, known bond distances and angles and/or chemical composition are now being used to stabilize Rietveld structure refinements [5,6].

The world of macromolecular crystallography is another source of techniques that has been exploited by powder diffractionists. Powder diffraction data suffer from

the same problem as protein diffraction data: there are too few data for the number of parameters needed to describe the structure of the material. Many of the techniques originally developed for macromolecular structure analysis can be adapted to the powder case. For example, just as low resolution data can be used to derive a protein molecular envelope, which describes the approximate shape of a protein molecule and its position in the unit cell [7], a structure envelope ("structure envelope", because the structure may not consist of molecules and therefore may not have a closed form) can be derived from low-resolution powder diffraction data [8]. Density modifications like histogram matching [9] and solvent flattening [10] proved to be valuable techniques along the way to solving the phase problem in macromolecular crystallography, and similar ideas have been transferred with some success to powder charge flipping (pCF) [11].
The classic crystallographic literature is a treasure trove of ideas and techniques waiting to be explored. It has not yet been fully exploited, but some gems have been recovered, and these are the subject of this contribution.

2. Model building

To construct a structural model that is consistent with all the data that has been gathered on a material is usually a difficult undertaking, especially if the structure is complex. Nonetheless, innumerable crystal structures have been solved in exactly this manner. By using information such as the size and shape of the unit cell, its symmetry, the chemical composition and density of the material, bond distances and angles in related structures, connectivity information from spectroscopy, and/or adsorption properties, a structure whose diffraction pattern agrees with the measured one can often be derived. This is a very powerful approach, because its only limit is the imagination of the model builder. However, if done by hand, it requires time, experience, perseverence and intuition.
Fortunately, for the less talented among us, computers have now been trained to do a good portion of the work [12]. The crystallographer still has to recognize the correct solution, and perhaps make small corrections to it, but the computer happily builds innumerable models according to whatever scheme the programmer/crystallographer has devised, and can check these against the measured diffraction pattern in seconds. This approach has proven to be particularly well-suited to small organic molecules, whose connectivity is known (e.g. pharmaceuticals). The molecule can be described fairly easily in terms of its bond distances and angles, and then allowed to twist around any of the bonds that do not have fixed torsion angles, and to move around the unit cell with any orientation until its diffraction pattern matches the measured one. Global optimization algorithms have been adapted to control the generation and optimization of such models. The two most common of these are the simulated annealing and evolutionary algorithms. With the help of a computer, the old-fashioned model-building technique has become a powerhouse in the determination of the crystal structures of organic molecules. Algorithms that ad-

dress the specific needs of other types of materials, where the connectivity may not be known in detail (e.g. coordination compounds, hydrides [2] or framework structures [13]) have also been devised.

The idea of incorporating non-diffraction information into the structure solution process has not stopped with model building. There are now methods of structure solution that operate in both real (model building) and reciprocal (diffraction) space, using both chemical and diffraction data. The first of these hybrid approaches was probably the *Shake-and-Bake* algorithm introduced in 1993 [14] for single-crystal data. The first for powder diffraction data was the zeolite-specific program *Focus* [15], which combines an electron density map generation in reciprocal space with an automatic interpretation of the map in real space. The key to the program lies in the interpretation step, which looks specifically and exhaustively for a 4-connected 3-dimensional framework structure. The combination has been demonstrated to be a powerful one, and *Focus* has now been used to solve a large variety of zeolite-type framework structures.

The advantages of incorporating real-space information into the structure determination process have been recognized, and the more recent versions of the direct methods program *EXPO* also actively use chemical information such as coordination geometry in the automatic structure determination procedure [16]. The third hybrid method is charge flipping [17,18,9], which combines electron density map generation in reciprocal space with a density modification in real space. This approach will be discussed in more detail in section 6.

3. Patterson methods

The autocorrelation function of a crystal structure that was derived by Patterson in 1934 [3] has proven to be a remarkably useful one in powder diffraction. The function itself is relatively robust with respect to the ambiguity in reflection intensities, and that has advantages for heavy atom structures, but that is not its only attraction. The function has also been exploited to improve the partitioning of overlapping reflections [19,20] and to improve direct methods applied to powder diffraction data [21]. By applying the symmetry minimum function, another gem from the crystallography archives based on the superposition of Patterson maps [22,23], the location of atomic positions can also be automated [4,24].

4. Restraints

Crystallographers are fortunate to have large databases of crystal structures at their disposal. The two most useful to powder diffractionists are the Cambridge Structural Database (CSD: http://www.ccdc.cam.ac.uk/products/csd/) for organic and organometallic compounds and the Inorganic Crystal Structure Database (ICSD: http://icsd.fiz-karlsruhe.de/icsd/) for inorganic materials. These databases hold a wealth of information, and in particular they make it easy to look for fragments and/or to check the value and range of bond distances and angles found in structures

related to the one of interest. This information can, of course, be quite useful in model building and in checking the validity of a solution, but it can also be used directly to stabilize a structure refinement [6].

Poor quality diffraction patterns are sometimes unavoidable, whether it is because it is from a fast *in situ* measurement, e.g. to follow a phase transition, a high-pressure experiment involving a tiny sample and a complicated environment, or simply a material that does not crystallize well. In such cases, it is often advantageous to supplement the diffraction data with non-diffraction information. By specifying well-known interatomic distances and/or angles, for example, a refinement can be stabilized without adding undue bias to the structure. The refined structure still has to satisfy the requirement that its diffraction pattern matches the measured one, but at the same time its bond distances and angles have to fall into a chemically acceptable range. This restrained refinement approach is almost always used in the refinement of protein structures, where the data are also insufficient to support the number of structural parameters. Interatomic distances and angles gleaned from the databases can also be put to use in the global optimization routines mentioned in the previous section. Similarly, potential energy calculations can be used as supplementary information for structure solution [25].

5. Structure envelopes

Establishing the approximate shape of a protein molecule and its position in the unit cell has been found to be quite useful at the beginning of the phasing process in protein crystallography. This molecular envelope is basically a very low-resolution estimation of where most of the electron density is concentrated in the unit cell. With the phases of just a few hundred low-resolution (high *d*-value) reflections the envelope can be calculated. A very similar approach has been developed for powder diffraction data. There are two differences: (1) only a handful of reflections (1-10) are required, because the unit cells are much smaller than those of macromolecules, and (2) the envelope does not necessarily have a closed form, because the structure may be extended rather than molecular. These structure envelopes have been used to advantage in combination with several structure determination algorithms that work in real space.

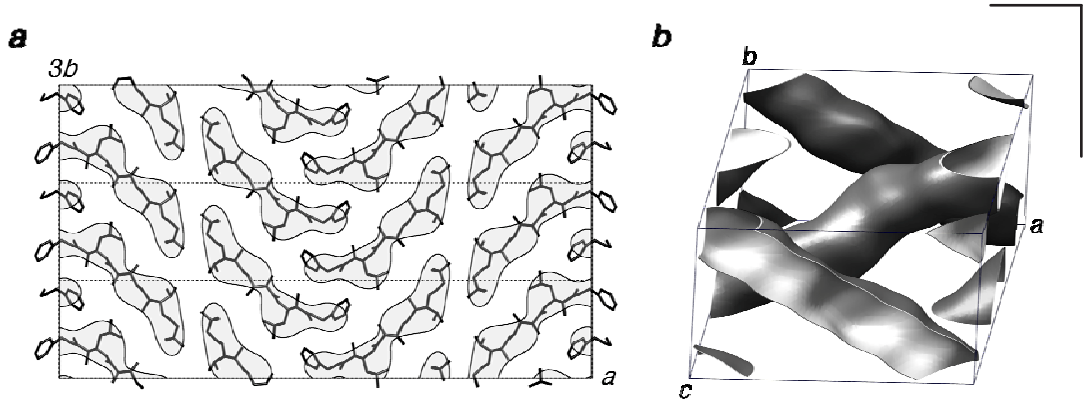

Fig. 1. Examples of structure envelopes. (a) The 2-dimensional envelope derived for a tri-β-peptide with the final refined structure superimposed [26]. (b) The partial channel system of the zeolite SSZ-74 (derived from a single HRTEM image) that was used in conjunction with a powder charge-flipping algorithm to solve the structure [28b].

The first application of a structure envelope in a true structure solution was in the elucidation of the crystal structure of a tri-β-peptide molecule with 17 degrees of freedom [26]. A 2-dimensional envelope was calculated for the projection along the short axis (centrosymmetric projection), and then used to filter the starting structural models for simulated-annealing optimization (Figure 1a). Three-dimensional structure envelopes have also been used to define a zeolite's pore system (Figure 1b) in conjunction with both *Focus* [27] and powder charge flipping [28]. The latter were calculated using phases derived from high-resolution transmission electron microscopy (HRTEM) images.

6. Density modification

Solvent flattening is a standard density modification technique used in macromolecular crystallography to reduce the noise in the electron density map and thereby improve the phases [10]. The assumption is that the solvent region should be basically featureless, so the regions outside the molecular envelope are set to a small constant value, and then new phases calculated. A similar approach has been used for zeolite structures in conjunction with powder charge flipping. If the channel system of the zeolite (or even part of it) is known (e.g. as in Figure 1b), the density in those regions of the unit cell can be set to zero during the pCF run and this improves the solutions.

Histogram matching is another density modification technique used in protein crystallography [9] that has been exploited by the powder diffractionists. Given the chemical composition of a material per unit cell, the size and number of peaks expected in the electron density map are known. We just do not know where these peaks will be. This means that it is possible to estimate the histogram of the electron density map from the chemical composition, and this histogram can be imposed in real space upon any generated electron density map. This density modification pro-

cedure has been implemented in the powder charge flipping algorithm in the program *Superflip* [29] as a second kind of perturbation of the map. It is applied just before the overlapping reflections are repartitioned, and has proven to improve the solutions considerably [11].

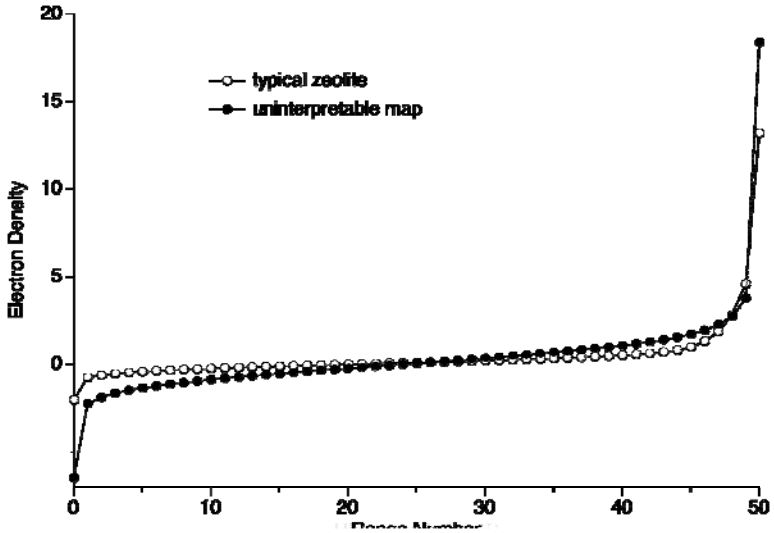

Figure 2. Electron density histogram arranged in order of increasing electron density for a typical zeolite (o) and for an uninterpretable map after a few charge-flipping cycles (•). Note the large number of zero density ranges.

7. Conclusions

Many of the approaches to structure solution used in the early days of X-ray crystallography can be applied successfully to powder diffraction data, when more conventional methods fail. Similarly, many of the concepts originally developed for macromolecular crystallography are also valid in the powder diffraction case, and can be applied to advantage. In some cases, these techniques just facilitate solution, but in others, they make the difference between solving and not solving a structure.

References

[1] (a) Bragg, W.L. 1933, *The Crystalline State*, vol. 1, Bragg, W.H. & Bragg, W.L., eds., G. Bell & Sons, Ltd., London.
(b) Bunn, C.W. 1946, *Chemical Crystallography*, Clarendon Press, Oxford, UK.

[2] Favre-Nicolin, V. and Cerny, R. 2004, A better FOX: using flexible modelling and maximum likelihood to improve direct-space *ab initio* structure determination from powder diffraction, *Z. Kristallogr*. **219**, 847-856.

[3] Patterson, A.L. 1934, A fourier series method for the determination of the components of interatomic distances in crystals, *Phys. Rev*., **46**, 372-376.

[4] Estermann, M.A. and David, W.I.F. 2002, Patterson methods in powder diffraction: maximum entropy and symmetry minimum function techniques, in *Structure Determination from Powder Diffraction Data*, W.I.F. David, K. Shankland, L.B. McCusker and Ch. Baerlocher, eds., Oxford University Press, Oxford, pp. 202-218.

[5] Waser, J. 1963, Least-squares refinement with subsidiary conditions, *Acta Crystallogr*. **16**, 1091-1094.

[6] Baerlocher, Ch. 1993, Restraints and constraints in Rietveld refinement, in *The Rietveld Method*, R.A. Young, ed., Oxford University Press, Oxford, pp. 186-196.

[7] Bragg, W.L. and Perutz, M.F. 1952, The external form of the haemoglobin molecule. I, *Acta Crystallogr*. **5**, 277-283.
[8] Brenner, S., McCusker, L.B. and Baerlocher, Ch. 1997, Using a structure envelope to facilitate structure solution from powder diffraction data, *J. Appl. Crystallogr*. **30**, 1167-1172.
[9] Zhang, K.Y.J. and Main, P. 1990, Histogram matching as a new density modification technique for phase refinement and extension of protein molecules, *Acta Crystallogr*. *A***46**, 41-46.
[10] Bhat, T.N. and Blow, D.M. 1983, A method for refinement of partially interpreted protein structures including a procedure for scaling between a model and an electron-density map, *Acta Crystallogr. A***39**, 166-170.
[11] Baerlocher, Ch., McCusker, L.B. and Palatinus, L. 2007, Charge flipping combined with histogram matching to solve complex crystal structures from powder diffraction data, *Z. Kristallogr*. **222**, 47-53.
[12] (a) Shankland, K. 2011, this conference.
(b) David, W.I.F. and Shankland, K. 2008, Structure determination from powder diffraction data, *Acta Crystallogr. A***64**, 52-64.
[13] Deem, M.W. and Newsam, J.M. 1989, *Nature* **342**, 260-262.
[14] Miller, R., DeTitta, G.T., Jones, R., Langs, D.A., Weeks, C.M. and Hauptman, H.A. 1993, *Science* **259**, 1430-1433.
[15] Grosse-Kunstleve, R.W., McCusker, L.B. and Baerlocher, Ch. 1997, Powder diffraction data and crystal chemical information combined in an automated structure determination procedure for zeolites, *J. Appl. Crystallogr*. **30**, 985-995.
[16] Altomare, A., Caliandro, R., Cuocci, C., Giacovazzo, C., Moliterni, A.G.G., Rizzi, R. and Platteau, C. 2008, Direct methods and simulated annealing: a hybrid approach for powder diffraction data, *J. Appl. Crystallogr*. **41**, 56-61.
[17] Oszlányi, G. and Sütő, A. 2004, *Ab initio* structure solution by charge flipping, *Acta Crystallogr. A***60**, 134-141.
[18] Wu, J., Leinenweber, K., Spence, J.C.H. and O'Keeffe, M. 2006, *Ab initio* phasing of X-ray powder diffraction patterns by charge flipping, *Nature Mater*. **5**, 647-652.
[19] David, W.I.F. 1987, The probabilistic determination of intensities of completely overlapping reflections in powder diffraction patterns, *J. Appl. Crystallogr*. **20**, 316-319.
[20] Estermann, M.A., Gramlich, V., 1993, Improved treatment of severely or exactly overlapping Bragg reflections for the application of direct methods to powder data, *J. Appl. Crystallogr.* **26**, 396-404.
[21] Rius, J., Torreles, X., Miravitlles, C., Ochando, L.E., Reventos, M.M. and Amigo, J.M. 2000, A tangent formula derived from Patterson-function arguments. VII. Solution of inorganic structures from powder data with accidental overlap, *J. Appl. Crystallogr*. **33**, 1208-1211.
[22] Kraut, J. 1961, The crystal structure of 2-amino-ethanol phosphate, Acta Crystallogr. 14, 1146-1152.
[23] Simpson, P.G., Dobrott, R.D. and Lipscomb, W.N. 1965, The symmetry minimum functiuon: high order image seeking functions in X-ray crystallography, Acta Crystallogr. 18, 169-179.
[24] Estermann, M.A. 1995, Solving crystal structures with the symmetry minimum function, *Nucl. Instr. Methods A* **354**, 126-133.
[25] Putz, H., Schoen, J.C. and Jansen, M. 1999, Combined method for ab initio structure solution from powder diffraction data, *J. Appl. Crystallogr*. **32**, 864-870 (1999).
[26] Brenner, S., McCusker, L.B. and Baerlocher, Ch. 2002, The application of structure envelopes in structure determination from powder diffraction data, *J. Appl. Crystallogr*. **35**, 243-252.
[27] Gramm, F., Baerlocher, Ch., McCusker, L.B., Warrender, S.J., Wright, P.A., Han, B., Hong, S.B., Liu, Z., Ohsuna, T. and Terasaki, O. 2006, Complex zeolite structure solved by combining powder diffraction and electron microscopy, *Nature* **444**, 79-81.
[28] (a) Baerlocher, Ch., Gramm, F., Massüger, McCusker, L.B., He, Z., Hovmöller, S. and Zou, X. 2007, Structure of the polycrystalline zeolite catalyst IM-5 solved by enhanced charge flipping *Science*, **315**, 1113-1116.
(b) Baerlocher, Ch., Xie, D., McCusker, L.B., Hwang, S.-J., Chan, I.Y., Ong, K., Burton, A.W. and Zones, S.I. 2008, Ordered silicon vacancies in the framework structure of the zeolite catlyst SSZ-74, *Nature Mater*. **7**, 631-635.
[29] Palatinus, L. and Chapuis, G. 2007, SUPERFLIP - a computer program for the solution of crystal structures by charge flipping in arbitrary dimensions, *J. Appl. Crystallogr*. **40**, 786-790.

The future of powder diffraction is 2-D

R.E. Dinnebier and B. Hinrichsen
Max-Planck-Institute for Solid State Research, Stuttgart, Germany

Abstract. The growing attractiveness of two-dimensional detectors in powder diffraction does brings with it one severe drawback – the 2D to 1D data reduction. This can be a most time consuming and error prone operation, especially when the artefacts of the sample environment affect the intensities. Some developments in the field of calibrating, filtering and evaluation are presented. A selection of applications will be given throughout the oral presentation.

Introduction

The combination two-dimensional detectors, powder diffraction and synchrotron light sources has been staggeringly successful, opening doors to many new experiments [1-5]. The great advantages of such data collection lie in the short exposure times as well as in the huge redundancy. A large angular region of the Bragg cone is recorded in a single exposure; indeed most detectors are set up perpendicular and centrally to the primary beam, intercepting the Bragg cone over the entire azimuthal range. The standard practice is to integrate the image along the ellipses described by the intersection of the cone with the planar detector to a conventional powder pattern [6]. This commonly reduces the amount of information by the square root of the number of pixels. Does this represent the gamut of information contained in a powder diffraction image? A glance at an image from a calibration standard might lend itself to such a conclusion. Less perfect samples, as well as sample environments leave distinctive artefacts on images. How can they be extracted, filtered or interpreted? Methods offering answers to some of these questions are introduced.

Experimental geometry

The experimental geometry of a plane detector used for powder diffraction has been explained in detail by others [6]. We will therefore merely give a short outline of the most important points.

Each diffraction (Bragg) cone intersecting a plane detector results in an elliptical projection (see figure 1). This projection is described most palpably using the experimental parameters of the beam centre, the sample to detector distance, the tilt of the detector out of the normal of the primary beam and finally the azimuthal rotation of the tilt with respect to an arbitrarily selected position.

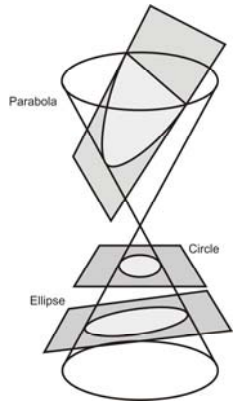

Fig. 1. Conic sections. The planes represent the detector plane at various angles to the primary beam. The projections of the Bragg cone trace a circle, an ellipse or a parabola on the detector.

In the course of the calibration of the experimental geometry a high quality image of a standard sample is used to determine and refine the required five parameters.

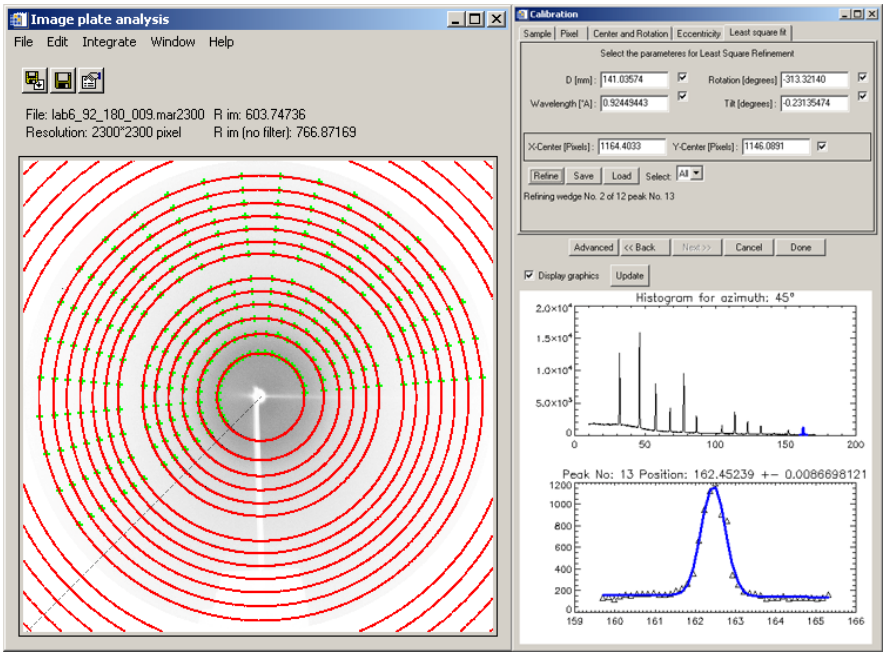

Fig. 2. Conventional calibration refinement method. On the left the radial lines are traced from the centre to the edge. The intensity profile is traced and the various peaks are fitted using a Gaussian profile function. The successfully refined peak positions are utilized to refine the five calibration parameters.

The standard method for refining the calibration parameters can be separated into two parts. Initially a number of radial lines are drawn from the common focus of the ellipses to the edge of the image. The profile along these lines is plotted, and the peak positions refined using a Gaussian profile. To ensure that an acceptable number

of pixels are selected to contribute to the individual histograms the radial lines need to be of an acceptable width, in our case a width of five pixels for these lines returned good results. The peak positions, or rather the positions of the intersection of the radial lines with the ellipses, are now known. Each point can be uniquely associated to a given lattice spacing. The requirement that points belonging to the same lattice spacing should have an identical diffraction angle is sufficient for the refinement of the calibration parameters. A Levenberg-Marquard least squares minimization using the positions weighted by the statistical uncertainty of the initial peak refinement procedure leads to the final calibration values. This method leads to good results if enough radial lines are chosen and the initial six starting values, the five calibration parameters and the wavelength, are sufficiently close to the true values. To ensure this we have developed pattern recognition techniques which very successfully estimate these parameters [7,8]. These have been described elsewhere. Recently an alternative calibration method has been proposed [9] which appears to have a high degree of automation.

Whole image refinement

The question poses itself, especially in view of the great computing power available to us currently, why image analysis is always synonymous with data reduction? Could not far more information be gleaned from diffraction images than a distilled I(2θ) plot? As a first step along the path of full pattern appreciation this holistic approach was applied to the calibration refinement with surprising results.
Calibration, as described earlier, is commonly a two step process. The initial step is the determination of the intersections of any number of radial lines with the Bragg ellipses. The second is the refinement of the ellipse (calibration) parameters along those points (see figure 2).

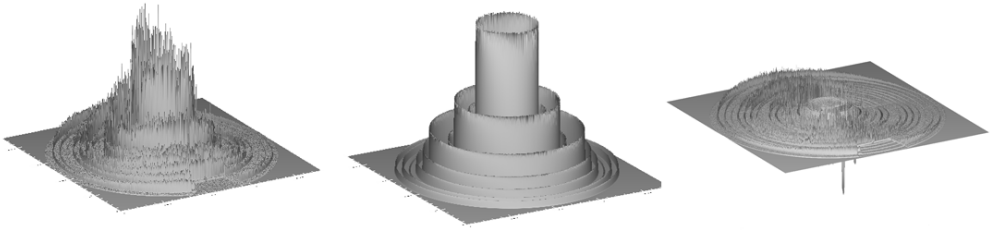

Fig. 3. Whole image refinement. The observed intensities (I_{obs}) are shown in the left image. In the central image the simulated images (I_{calc}) are shown. The difference is shown on the right. The calibration parameters are refined to minimize the difference between I_{obs} and I_{calc}.

The approach chosen here was to refine the sought after parameters against the difference of the observed and computed *images* (figure 3). The number of data points in such a refinement is of course rather large, a couple of million against what would normally be a couple of hundred. As ellipses furthest from the centre are most susceptible to the calibration quality, the FWHM of the highest angle peak of a from the integrated pattern was chosen to give an idea of the calibration results. The material

used was the common calibration standard finely ground LaB_6. Whole image refinement showed an improvement over the conventional method of 15%, reducing the FWHM from 0.122° to 0.106°.

Filtering techniques

Experimental artefacts are a continual nuisance in the analysis of *in-situ* experiments. These generally result from the experimental environment, can however stem directly from the sample. Data becoming to powder diffraction analysis originates from an ideal sample, having all the positive attributes: random orientation, narrow size dispersion and an improved statistical distribution by sample rotation. In some cases this ideal cannot be achieved, this is especially valid for high-pressure powder diffraction experiments. Sample rotation, if any, is limited to a small angular range because of the diamond diffraction peaks and the deleterious effects of gasket shadowing. An X-ray beam that has a diameter in the order of a few micrometers further worsens the already poor statistics of such an experiment. The general image obtained is filled with single grain spikes looming over the intensity of the Debye-Scherrer ring by at least an order of magnitude. A few peaks on a ring can cause the normal averaging process used during integration to produce data misrepresents the true powder intensities.

When estimating the most representative value for the intensity of a single bin generally only the mean of the intensities within the bin was calculated. This of course leads to great aberrations when outlier intensities are within the bin. One way of dealing with such data would be to select the median value as a more robust estimator of the true intensity. This however still leads to variances which do not portray the true data quality. The sigmas of the intensities, which are generally used to weight the least squares refinements are completely meaningless and of no use in the refinement process.

An alternative method is to filter out the aberrant values. As a rule only very few highly deviant values cause the averaging problems. A method which can be looked upon as the inverse of the aforementioned median intensity estimation is that of fractile filtering. Here a highest or lowest intensity fraction of the data is removed. As this method has no real intensity based cut-off criteria it is very robust. An additional advantage is that it does not skew normally distributed data. The effects of this computationally cheap filter can be seen in figure 4, an example of a high temperature image.

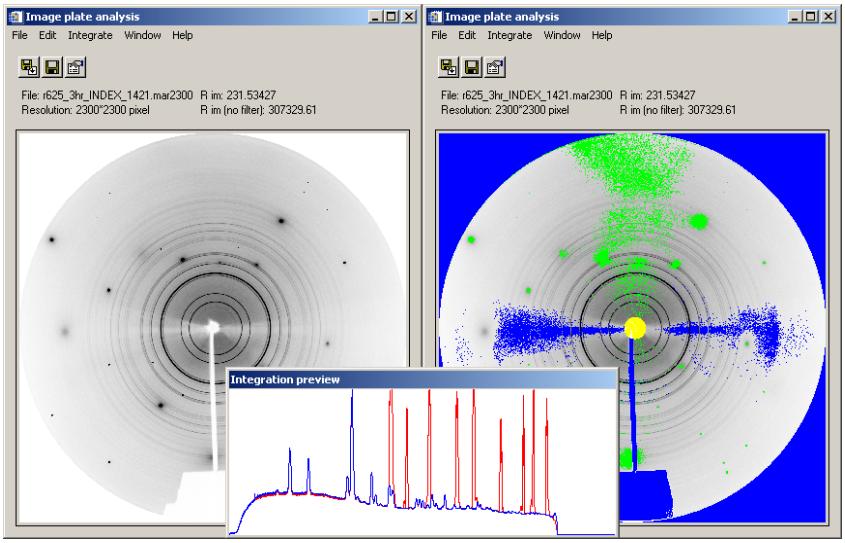

Fig. 4. Results of fractile filtering on an image from a high temperature experiment. Top left: before filtering, top right: after filtering. The spots of high intensity result from the sapphire capillary. The lower image is a preview of the finally integrated diffractogram, red is the unfiltered pattern, blue is the filtered pattern.

Reliability values

The visual appreciation of a two-dimensional diffraction image can sometimes give an idea of the quality of the data gathered. No quantitative measure of the quality of such a data collection has yet been proposed. In lieu of appraising the effectiveness of the presented filtering algorithms an unbiased estimation of the data quality seemed opportune. A measure that has shown itself to be of good use is shown in equation (1).

$$R_{im} = \frac{\frac{1}{n}\sum_{i=1}^{n}\left(\frac{1}{m-1}\sum_{j=1}^{m}(I_j - \bar{I})^2\right)}{\frac{1}{l}\sum_{k=1}^{l} I_k - I_b} \qquad (1)$$

Where l is the total number of pixels in the image, n is the number of bins used to integrate the image and m is the number of pixels within each bin. I_k is the intensity of the kth pixel and I_b the background intensity of that pixel. This is a very simple measure of the average bin variance, normalized to the background corrected total intensity.

The value is intensity and consequently detector independent. It is intentionally very sensitive to azimuthal variations in intensity. This leads to an extremely good indica-

tor of not only the uniformity of the Bragg peaks but also of a successful calibration, as can be seen in table 1.

Table 1. Image reliability values for some typical examples.

LaB_6	R_{im}(filter applied)*100	R_{im} (no filter)*100
good calibration	0.414	25.9
bad calibration	10.1	45.9
Experimental data		
sapphire tube	1.12	4512
DAC	15.3	7532

Concluding remarks

Some aspects in the analysis of two-dimensional powder diffraction patterns have been presented. The effectiveness of filtering methods dealing with outlier intensities has been shown, as has been a holistic approach to the calibration question. Finally an image reliability factor has been proposed to quantify the quality of a diffraction image. All the functionality has been implemented in a freely available software package, Powder3D [10].

References

Hanfland, M., Schwarz, U., Syassen, K. and Takemura, K., 1999, *Physical Review Letters* **82** 1197.
Knapp, M., Baehtz, C., Ehrenberg, H. and Fuess, H., 2004, *J. Synchrotron Rad.* **11** 328-334.
Norby, P. 1997, *J. Appl. Cryst.* **30** 21-30.
Meneghini, C., Artioli, G., Balerna, A., Gualtieri, A. F., Norby, P. and Mobiliob, S., 2001, *J. Synchrotron Rad.* **8** 1162-1166
Wenk, H. R. and Grigull, S., 2003, *J. Appl. Cryst.* **36** 1040-1049
Hammersley, A. P., Svensson, S. O., Hanfland, M., Fitch, A. N. and Häusermann, D., 1996, *High Pressure Research* **14** 235-248
Hinrichsen, B., Dinnebier, R. E., Rajiv, P., Hanfland, M., Grzechnik, A. and Jansen, M., 2006, *J. Phys.: Cond. Mat.* **18** 1021-1037
Rajiv, P., Hinrichsen, B., Dinnebier, R. E., Joswig, M., Jansen, M., 2007, *Powder Diffraction* 22(1), 3-19
Cervellino, A., Giannini, C., Guagliardi, A. and Ladisab, M., 2006, *J. Appl. Cryst.* **39** 745-748
Hinrichsen, B., Dinnebier, R.E., and Jansen, M., 2006, *Z. Krist.* **23** 231-236

Future role of computing

Kenneth Shankland
School of Pharmacy, University of Reading, Whiteknights, Reading, UK

Abstract. Advances in computing have underpinned developments in crystallography since programmable computers first became available. It is impossible to predict accurately how computers will develop, even in the relatively short term, but there are general trends that can be inferred. Here, we examine some of these trends and speculate how they may impact upon crystallography and in particular, powder diffraction.

In the mid 50s, a team of researchers led by Dorothy Hodgkin published the molecular and crystal structure of Vitamin B12 [1], work which along with her determination of the structure of penicillin [2], won her the Nobel Prize in Chemistry in 1964. It is interesting to contrast the ways in which these two structures were elucidated. Key to the first solution was a set of Beevers-Lipson strips (purchased by Hodgkin at a cost of £5), later augmented by a Hollerith machine, whilst key to the second was access (provided via Kenneth Trueblood) to the SWAC computer at UCLA. In 1950, with some 2,300 vacuum tubes, it was the fastest computer in the world. Access to computing power was a major enabler in the structure determination process, allowing the rapid calculation of 3D Patterson and Fourier maps. In the subsequent decades, this enabling role has continued; one cannot imagine techniques such as Shake-n-Bake, multi-solution direct methods or maximum entropy without the underlying computational power to make their implementation feasible on anything approaching sensible timescales. Of course, raw number-crunching power alone is only one aspect of computing, with issues such as storage and data transfer also having a significant impact. Nevertheless, for many crystallographic purposes, it remains the most important and our consideration shall begin here.

Processing power: Moore's law [3] has often been used to describe the approximate doubling every year of the number of components present in integrated circuits. This does not *necessarily* equate to a doubling of available computing power, though for many years it has. It is only relatively recently that CPU speeds have plateaued in response to heat dissipation problems and a desire to create CPUs that are more energy efficient. In order to maintain onward development in terms of overall available CPU power 'per unit area', manufacturers have moved towards multi-core models which, in effect, have multiple CPUs embedded in a single package. In order to take advantage of these packages, code has to be re-written and the writing of such multi-threaded applications remains largely the domain of the specialist coder. Until

such time as programming tools and libraries make coding of threaded applications much easier, it is difficult to see how the majority of existing crystallographic applications are going to be adapted to run efficiently on multiple cores. That said, for those applications that exhibit coarse-grained parallelism (i.e. ones where substantial computational chunks can be executed independently of each other) the re-coding process is much simpler and can frequently be achieved simply by invoking several copies of a single executable from a wrapper script. Each copy typically operates on a different data set or on the same data set with a different set of controlling parameters. With desktop computers frequently shipping with quad-core processors, the speed gains to be had are significant and the trend towards higher core densities means that these gains are set to increase.

For coarse-grained applications of the type just outlined, it is a relatively straightforward step to the adapt the scripting process still further such that the multiple program copies can be executed not only on the multiple cores of a single computer, but also on the multiple CPUs of discrete networked computers. This is an area where a number of well-developed applications make the code adaption process easy [4]. Such a *distributed computing* model works extremely well at the 'departmental' level, where tens to hundreds of personal computers can be easily brought to bear on problems that require large amounts of CPU power. For a powder diffraction related exemplar, see [5].

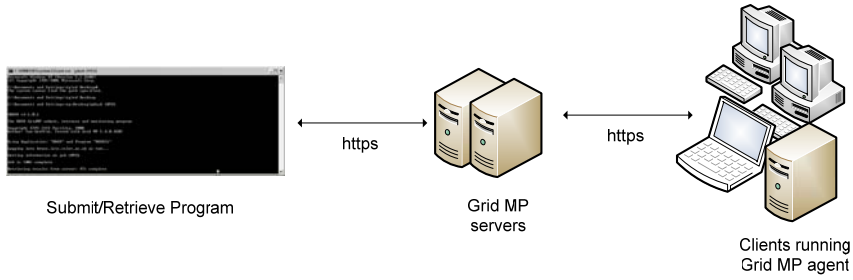

Fig. 1. A high level overview of the operation of a coarse grained problem running under the Grid MP system [4]. The user runs a program on a desktop PC to submit a job (which consists of a series of independently executable workunits) to the Grid MP servers, which then take care of distributing workunits to individual PCs that are participating in the Grid MP system i.e. PCs that are running the so-called agent program and are capable of running the assigned workunit.. As each workunit is completed, a result is returned to the servers. When all workunits are complete, the overall 'result' is returned to the user's desktop PC.

Distribution of calculations on an even bigger level can be achieved with 'grid' or' cloud' computing models where multiple sites (potentially worldwide) participate[1].

[1] The distinction between grid and cloud computing is a fine one and not one that need concern us here. Both concepts embody the notion of providing on-demand compute resources without the need to invest in dedicated hardware.

In these computing models, the user does not necessarily know (or care!) the resources that are being allocated to their computational problem - they simply 'submit' their job to the grid / cloud from their own PC and wait for the results to be returned once the calculations are complete. Once one's intrinsic distrust of distributing hard-earned experimental data to essentially unknown sites is overcome, the advantages of leveraging such a system, in terms of scale, are obvious.

With CPUs available on such a large scale, can the desktop ever compete? For certain applications, in the short-to-medium term, the answer appears to be yes, using not the modest number of multiple cores of a CPU but the multiple cores of a graphics processing unit (GPU). By way of example, the Nvidia GeForce GTX 580 graphics processor has 512 cores that can be accessed from high-level computer languages using the CUDA toolkit [6]. Such processors can be operated in parallel, and indeed dedicated hardware such as the Nvidia TESLA (where multiple CUDA-enabled chips are contained in a single cabinet) offers remarkable processing power for relatively little expense. Of course, such low-cost, high-performance dedicated solutions have existed in the past (see, for example, the Transputer [7] of the late 1980s) but they have usually been linked with highly-specialised hardware and (more importantly) specialised software and / or programming languages (Occam, in the case of the Transputer). GPUs differ in that, as an integral part of a PC, there is no barrier to adoption other than the fact that specific programming toolkits are still required and more importantly, programming parallel operations is an intrinsically difficult task and not all programs will benefit. Nevertheless, there are those who feel that GPUs are simply the latest in a very long line of "next big things" and that advances in CPUs will make them irrelevant - only time will tell.

Finally, the market for dedicated hardware remains intact - specialist computers such as the Cray CX1 continue to provide solutions for those with particular stand-alone requirements.

Memory: The ca. 4GB of RAM available to applications running under 32-bit operating systems is now sufficient for the vast majority of crystallographic applications operating on a single data set to be performed with ease, with no resort to swapping data to disk during processing. As 64-bit operating systems become the norm, this address space jumps to into the terabyte range (e.g. Windows Server 2008 R2 has a maximum physical address space of 2TB i.e. 2000GB), meaning that it will become possible to operate quickly and efficiently on multiple data sets or even on raw data sets (as opposed to processed images) if desired.

Storage: In the last 30 years, the cost of hard-disk storage has fallen by a factor of 200, with a megabyte of storage now costing less than US 10¢. As such, long term storage of data for the typical crystallography lab is not an issue. For central facilities, where data rates and volumes are much larger, long-term storage remains an issue as the *true* cost of data storage (or, more accurately, curation) is much greater

than the cost of the physical media, as it must include factors such as redundancy, off-site copies, integrity, access etc. Nonetheless, as the limits of magnetic media storage continue to be pushed, it seems likely that long-term storage of raw data will soon no longer be a cost concern. Of course, the question arises, is it necessary to store (for example) raw image files taken from a diffractometer? Often, the answer will be "no", as the data can frequently be re-collected from the same or another sample[2]. However, if cost is no longer a particular consideration, then it is likely that long-term storage will become the default situation. Optical data storage options (CDs, DVDs) have been somewhat sidelined by the pace of change in magnetic storage, but holographic data storage [8] may finally break through, with DVD-sized disks capable of holding ca. 300GB of data. Such storage solutions have been promised for many years, but they may have arrived too late to compete seriously with hard-disk based storage, either in terms of price or performance.

Networking It is not immediately obvious how such a low-level element as networking impacts upon the ability of the crystallographer to perform useful work, but there are two areas where increased networking speeds will certainly bring benefits. Firstly, low-latency networking plays a crucial role in cluster computing, enabling data to be transferred rapidly between CPUs (it is not sufficient to simply connect computers with conventional network protocols, even when gigabit network cards are used). These low-latency networking components constitute a significant percentage of the cost of dedicated compute clusters. As network speeds increase and the cost of these components falls, then we will see clusters of the type required to run (for example) intense crystal structure prediction calculations [9] become more widely used, with obvious benefits. Secondly, with conventional gigabit networking increasingly the norm, remote-desktop-type (or VNC-type) access to PCs is an increasingly workable option within institutions. This way of working is particularly useful where licensed software is tied to a particular piece of hardware and the hardware can be accessed remotely, but it will require much faster, more reliable and pervasive internet connections if the model is to be extended outside of institutions to homes and other workplaces.
Improved networking, combined with long-term data storage, may also obviate the need for (for example) users of central facilities having to copy data in order to return with it to their home institution; it may in fact be much simpler to either leave the data at the facility, or copy it upon returning to a home institution.

Virtual machines Increasingly, conventional desktop PCs in departmental setups are likely to be replaced by virtual machines i.e. PCs that are created and destroyed as required in computer memory, executing as 'applications' on servers running a

[2] Contrast this with, for example, the situation where time is an integral element of the observation and therefore the observation can never be repeated e.g. astronomical or seismic. In such cases, effective data curation is critical.

base operating system with a hypervisor [10]. These PCs are accessed over the network using remote-desktop-type mechanisms and have several clear advantages. For example, virtual PCs can be setup with appropriate software as required and then copied to create multiple instances of this setup for people to access simultaneously. Or, if particular applications have particular computing requirements, the capabilities of the virtual machine can be specified to match these requirements e.g. large amounts of RAM when computing high-resolution Fourier maps. Virtual PCs also have great potential in teaching e.g. one can setup a PC and provide students with access, secure in the knowledge that the PC can be destroyed at the end of the tutorial and then re-created instantly.

Mobile applications A typical 'smartphone' now has more processing power than is actually needed to perform many crystallographically useful operations. However, it is debatable whether (with current display sizes / resolutions and very limited input options) one would want to perform complex crystal structure refinements on anything smaller than a tablet-sized device with an associated physical keyboard. However, there are certain applications that lend themselves well to coding for small mobile devices. For example, when calculating molecular volumes to see if they are consistent with a determined unit cell volume, the method of Hofmann [11] is much more accurate than the commonly used 18Å^3 rule, but requires that one has access to a table of elements and their corresponding molecular volume contributions. As such, the temptation is to go with the quick and easy-to-calculate 18Å^3 rule. However, the limited amount of information required for the method of Hofmann is very easily coded into a simple application, and a GUI can be added using native toolkits, depending upon the particular platform being used. Users of Android phones can take advantage of the Google AppInventor system [12] to rapidly create and test an application on a PC before deploying it on a phone. One such very simple example is shown in Figure 2. One can conceive of many other simple tools that could be developed to aid the crystallographer e.g. energy to wavelength convertor, variable count time scheme calculator, scattering factor tables etc.

Fig. 2. Screensnap of a prototype Android application for molecular volume calculations, running on an HTC Desire mobile phone.

Web-based applications There is an increasing trend towards applications that do not actually reside on a computer, but are accessed via the web and execute within web browsers e.g. Google Docs. Sitting somewhere between these two extremes are applications that download on demand from the web, but then execute as if they were normal installed applications (which, to some extent, they are). The recently released powder pattern display program *JPowder* is written in Java and uses Java Webstart technology to provide such behaviour [12]. The first time the program is run from the *JPowder* web site, it downloads and then installs (even on computers that are relatively tightly locked-down e.g. beamline PCs) before executing. It is then able to display powder diffraction data present on the computer. When run subsequently, it first checks for an updated version of the code and downloads / installs / runs it automatically if one exists. If there is no update, or there is no network access, the currently installed copy still runs. Such mechanisms decrease one's dependence upon any one particular location or computer, allowing 'favourite' programs to be run anywhere.

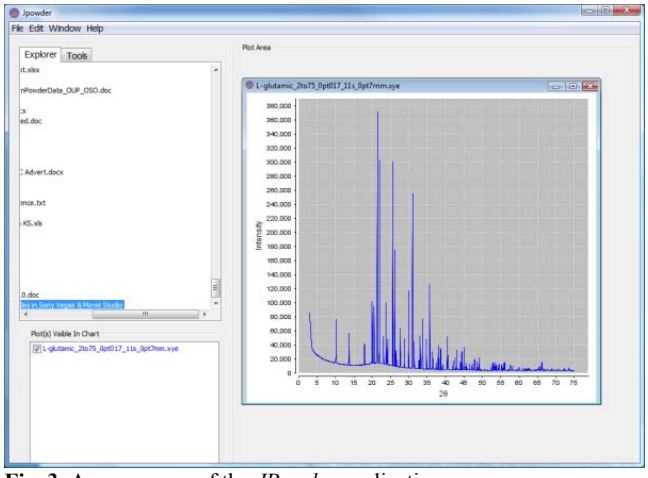

Fig. 3. A screensnap of the *JPowder* application.

Access Increased disk storage, http communication and web-type access to SQL databases have combined to make it relatively simple for almost anyone to provide online access to searchable information that previously remained hidden away in drawers in laboratories. By way of example, crystal structures that may be of no *particular* structural interest but may have value as part of the general ensemble of crystal structures, can now easily be made publically accessible. There is a wide range of initiatives, such as the Crystallography Open Database [14], CrystalEye [15] and eCrystals [16]. The numbers of structures deposited is still relatively small, though growing in the case of the Crystallography Open Database, largely as a result of contributions from the AMCSDthe decision by the IUCr Executive Committee in 2007 that CIFs associated with structural papers published in IUCr journals should

be made freely available to databases. As a result, it is easier than ever to retrieve structural information and to develop 'value-added' services on top of these.

Summary The only confident prediction one can make in respect of the future impact of computing on crystallography is that it will continue to enable and ease the execution of the underlying science. Recently, a massively parallel IBM computer ('Watson') took part in a US quiz show, Jeopardy, and beat two human opponents. As such, it comes close to passing the Turing test [17], doing so by leveraging processing power (some 2880 Power7 cores), massive amounts of stored information (> 15TB of text), high-speed access to the information (500GB/s) and advanced software designed specifically to answer questions presented in natural language. When such technology inevitably reaches the laboratory, it will be most interesting to see how it can be applied in a crystallographic context.

Acknowledgements
I am extremely grateful to both Chris Gilmore and Bill David, for teaching me that computers can never be fast enough. My thanks also to Tony Csoka, Anders Markvardsen, Tom Griffin and Damian Flannery whose coding skills have played a crucial role in unlocking the speed of the computer hardware I've used over the years.

References

1. D. C. Hodgkin, J. Kamper, M. Mackay, J. Pickworth, K. N. Trueblood and J. G. White. "Structure of Vitamin B12". *Nature*, (1956), 178,64.
2. D. C. Hodgkin, C. Bunn, B. Rogers-Low, and A. Turner-Jones. "X-ray Crystallographic Investigation of the Structure of Penicillin," in *Chemistry of Penicillin*, Princeton University Press, Princeton, NJ (1949).
3. G. E. Moore. "Cramming more components onto integrated circuits". *Electronics* (1965) 8.
4. See, for example, GridMP (http://www.univa.com/products/grid-mp.php) or Condor (http://www.cs.wisc.edu/condor/)
5. T. A. N. Griffin, K. Shankland, J. V. van de Streek & J. Cole, GDASH: a grid-enabled program for structure solution from powder diffraction data. *Journal of Applied Crystallography*, (2009), 42,356.
6. CUDA, http://www.nvidia.com/object/cuda_home_new.html
7. http://en.wikipedia.org/wiki/Transputer
8. http://www.inphase-tech.com/products/default15b9.html?tnn=3
9. http://www.avmatsim.eu/
10. http://www.xen.org/products/xenhyp.html
11. D. W. M. Hofmann. "Fast estimation of crystal densities". *Acta Cryst. B.* (2002) B57, 489-494
12. http://appinventor.googlelabs.com/about/
13. A. J. Markvardsen, K. Puphaiboon, M. Arjeneh, K. Shankland, H. L. Guest, T. A. N. Griffin, D. R. Badham & D. W. Flannery, Jpowder: a Java-based program for the display and examination of powder diffraction data. *Journal of Applied Crystallography*, (2010) 43, 1532.
14. http://www.crystallography.net/
15. http://wwmm.ch.cam.ac.uk/crystaleye/
16. http://ecrystals.chem.soton.ac.uk/
17. http://en.wikipedia.org/wiki/Turing_test

Poster Abstracts

Structural topology of phases in the Bi2O3-P2O5-MOy systems: towards the deduction of new functional materials

A. Aliev, M. Colmont, D. Endara, M. Huvé, O. Mentré
UCCS, Lille1 University, France

POSTER 1

The possibility for rational prediction of new inorganic Bi-based phosphates by intergrowth of versatile building units (BU) is concerned in the poster. In the whole series of compounds predicted/prepared up today, the concerned BUs are infinite 2D-polycationic ribbons formed of oxygen centered $O(Bi,M)_4$ tetrahedra. The width of the ribbons is tuneable, according to the number N of connected tetrahedra. The connection between them is achieved by isolated PO_4 groups, sometimes surrounding 1D-channels hosting Mn^+ cations. The versatility of these chemical systems arises from the possibility of partial occupancy of these tunnels, while edges of BUs can host M/Bi mixed positions. It is such that a number of new compounds with N ranging from 1 to infinte are stable with respect to the electro neutrality.
From the crystal structure point of view, these systems present the possibility for predicting in a rational manner novel complex intergrowths according to "empirical rules" deduced from known parent-members. In addition, we have shown that for great N values, several BUs are polar. Then, the prediction/formulation/preparation of non-centrosymmetric materials is possible. Examples of efficient second harmonic generators will be given. Other striking features concern the strong disorder that exist in the PO4-rich inner space, due to local faults within the rigid BU-based framework.
From the experimental point of view, our finding for new materials is often helped by High Resolution Electron Microscopy in complementarity with diffraction techniques. Here, it is worth arguing that due to the strong contrast between Bi rich-BU's and their surrounding PO_4 , a particular image code is associated with each BU, helpful for the crystal structure determination from HREM images only. The precise crystal structure has been deduced from powder XRD after formulation and synthesis. SHG is comparable to those of KDP.
From the point of view of their electric and magnetic particularities, it is remarkable that depending on the main topology between BUs several properties can be targeted and reached. Particularly, a number of different magnetic behaviour have been evidenced in these series of compounds when M is a paramagnetic cation.

POSTER 2

Comparative In Situ Synthesis Studies of CuSICON: $CuM_2P_3O_{12}$ [M = Ti, Zr, Sn and Hf]

D.G. Billing and R.P. Forbes
Molecular Science Institute and DST-NRF Centre of Excellence in Strong Materials, School of Chemistry, Univ. of the Witwatersrand, Johannesburg, South Africa

The NaSICON (Na Super Ionic Conductor) structural family with formula $AxMyP_3O_{12}$ [$0 \le x \le 1$; $1 \le y \le 3$] crystallize with rhombohedral symmetry [space group R-3c (No. 167)] and are composed of a three dimensional corner sharing framework of PO_4 tetrahedra and MO_6 octahedra connected to form a chain like structure with two dimensional channels extending throughout the structure [1]. Owing to the flexibility of this structure towards ionic substitutions at various lattice sites, these materials have enjoyed consistent scientific interest due to the various useful physical properties that they posses. CuSICON (Cu super ionic conductor), with general formula $CuZr_2P_3O_{12}$ is an example of a material that is isostructural with the NaSICON parent structure [2]. TGA and EPR studies have previously indicated the presence of a reversible oxidation-reduction reaction in which Cu(I) is oxidized to Cu(II) along with the formation of CuO [3]. This reaction is followed by the partial auto-reduction of Cu(II) to Cu(I). As a result of these observations, this study is directed towards gaining further understanding of the structural characteristics of members of the CuSICON family with general formula $CuM_2P_3O_{12}$ (M =Ti, Zr, Hf, Sn). Thus far in situ laboratory XRPD studies have shown that the oxidation-reduction reaction in question is the cause of a reversible 2nd order phase transformation. For example, the heating of $CuSn_2P_3O_{12}$ (S.G.:167 R-3cH) results in the oxidation of the material to $Cu_{0.5}Sn_2P_3O_{12}$ (S.G.:148 R-3), a Cu(II) compound, which then through continued heating is reduced back to $CuSn_2P_3O_{12}$ (S.G.:167 R-3cH). In each case small quantities of CuO was observed indicating that the reduction reaction does not continue to completion. Furthermore, it was found that quenching experiments conducted on the Cu(II) phase isolated this stable material which is distinct from the parent phase. This result has implications on any future applications that may be envisaged for this material and indeed similar results were obtained with all of the members that have been studied. Selected results will be presented.

[1] Hong, H.; Mat. Res. Bull., 1976, 11, 173
[2] Yao, P.C.; and Fray, D.J. Solid State Ionics, 1983, 8, 35
[3] Schaffer, R.J.; Kumar, R.V. et al; Mat. Res. Bull., 1999, 34, 1153

Keywords: in-situ powder diffraction, investigating phase changes during firing, thermal studies

Electron density study of $NaGaH_4$ from maximum entropy method

N. Bindzus, H. Svendsen, M. Christensen, T.R. Jensen, B.B. Iversen
Dept of Chemistry, Aarhus University, Aarhus, Denmark

POSTER 3

The search for hydrogen storage materials has received massive attention during the past decade in hope that hydrogen, in the future, may replace fossil fuels as energy carrier. Among the considered compound, it is worth mentioning $NaGaH_4$ that is formed of almost isolated GaH_4^- anions and spherical Na^+ moieties. It has about 4.2 wt% hydrogen, therefore not fulfilling the requirements for being a candidate hydrogen storage material for mobile applications. However, the compound reveals peculiar structural features that deserve further examination. In particular, a phase transition around 280 K has been pointed out by an anomaly in heat capacity measurements. A NMR study has implied that the phase transition can be attributed to changes in the orientation state of the distorted tetrahedron. Despite all the hints of a phase transition, structural knowledge is still lacking. We studied $NaGaH_4$ in the temperature range 90 K – 390 K by synchrotron X-ray powder diffraction data and by complementary synchrotron neutron powder data measured on the deuterated sample, $NaGaD_4$. For each of the considered temperatures, the Maximum Entropy Method (MEM) is utilised to maximise the information contained in the extracted structure factors and to determine the corresponding electron density. The MEM charge density at 90 K is analysed within the quantum theory of atoms in molecules and compared to theoretical charge density obtained from periodic ab initio DFT calculations. The Rietveld refinements as well as MEM densities of $NaGaH_4$ and $NaGaD_4$ do not provide any apparent, structural explanation of the expected phase transition. Most likely this is due to a symmetry reduction, which is indicated by NMR and Raman scattering. Therefore, starting from the recognised space group of $NaGaH_4$, *Cmcm*, we explored its subgroups through refinements of the 300 K neutron and X-ray data. Of the symmetry reduced space groups, $P2_1/m$ is the only one capable of describing the structural NMR results.

Structural characterization of semiconductor nanocrystalline materials produced by mechanical alloying

C.E.M. de Campos
Dept de Física, Universidade Federal de Santa Catarina UFSC, Florianópolis, SC, Brazil

POSTER 4

This presentation is devoted to show the last advances on use of powder diffraction to the understanding the structure of mechanically alloyed nanomaterials and their behavior with ageing and other thermodynamic parameters. Rietveld data analysis of several structures identified in the mechanical alloyed samples are being refined routinely, viewing to explore facilities of GSAS+EXPGUI program package to determine phases fraction, mean crystallite size and microstrains. Anisotropic models are also been used when necessary, as the case of nanometric ZnO. Several TM-VI samples were produced and characterized by powder diffraction and other techniques, where TM represents transition metals (Fe, Co, Ni, Zn) and V represents S, Se and Te. The evolution of the structure(s) of the mechanical alloyed samples was(were) followed as a function of processing time, annealing temperature, ageing, etc. using powder diffraction and Rietveld method.

Solid-state synthesis and crystal structures of chiral co-crystals and salts of serine and dicarboxilyc acids

L. Chelazzi, F. Grepioni, D. Braga
Dipartimento di Chimica "G. Ciamician", Università di Bologna, Bologna

POSTER 5

Co-crystallization provides a new strategy for altering the chemical and physical properties of molecular solid forms. The possibility of co-crystallization has to take into account the competition with kinetic factors associated with the nucleation stage of the crystallization processes. A way to overcome the thermodynamic-kinetic dualism is the "solvent-free" condition. It as also been shown that, in some systems, chiral recognition can affect solid state reactions just as it does in solution chemistry, and that products of grinding and solution experiments can be different[1,2]. In the present work we make use of solution experiments and mechano-chemical techniques to obtain co-crystals or salts of chiral compounds3. For this purpose, serine(-), serine(+), serine-(+/-), succinic and oxalic acids were chosen as starting materials. Salts and co-crystals obtained were studied by single-crystal and powder X-ray diffraction methods, showing the formation of different polymorphs depending on the synthetic method (crystallization from solution, grinding or kneading). The new salts were also studied by variable-temperature X-ray powder diffraction to check their thermal stability.

1 Kuroda R., Imai Y. and Sato T., Chirality, 2001, 13,588;
2 Chen S., Xi H., Henry R. F., Marsden I. and Zhang G. G. Z., CrystEngComm, 2009, 11,427.
3 D. Braga, F. Grepioni and G. I. Lampronti, CrystEngComm, 2011, Advance Article DOI: 10.1039/C0CE00576B, Communication

POSTER 6

A nanoscale molecular switch triggered by thermal, light, and guest perturbation

M.B. Duriska[1], S.M. Neville[1], B. Moubaraki[1], J.D. Cashion[2], G.J. Halder[3], K.W. Chapman[4], C. Balde[5], J.F. Létard[5], K. S. Murray[1], C.J. Kepert[6], S.R. Batten[1]

[1]School of Chemistry, Monash Univ., Vic, Australia
[2]School of Physics, Monash Univ., Australia
[3]Materials Science Division, Argonne National Laboratory, USA
[4]X-ray Science Division, Argonne National Laboratory, USA
[5]Laboratoire des Sciences Moléculaires ICMCB, CNRS UPR 9048, France
[6]School of Chemistry, Univ. of Sydney, Australia

Molecule-based magnetic materials, such as those that display magnetic ordering or spin crossover (SCO) are attractive candidates for components in the data storage and electronics industries. Miniaturization of next-generation advanced magnetic materials to the nanometer scale is required for their use in electronic devices. Recent efforts to produce nano-scale molecular switching materials have been focused on the 'top-down' approach. Herein we report the assembly, by using a 'bottom-up' approach, of a nanoscale metal-organic switching nanoball, which shows a magnetic response to a range of external stimuli.
X-ray single crystal and powder diffraction techniques were used to characterise the material. Furthermore, the structural consequence of the electronic switching was followed using a purpose built setup at the APS Chicago to monitor the change in lattice parameters as a function of temperature.

Correlation between magnetic properties and crystalline structure in non stoichiometric cobalt ferrite nanoparticles

POSTER 7

E. Fantechi[1], F. Pineider[1], C. Innocenti[1], L. Lartigue[1,2], C. Sangregorio[1,3], D. Gatteschi[1]
[1]INSTM and Dip. di Chimica, Univ. di Firenze, Sesto F.no, Italy
[2]CNRS-UM2, C.M.O.S.- Univ. Montpellier II, Place E. Bataillon, Montpellier, France
[3]CNR-ISTM, Milan, Italy

Magnetic nanoparticles (MNP) have been the subject of increasing interest in different fields of research due to their remarkable properties. In biomedicine, these materials can be used as contrast agents for MRI and as mediators in hyperthermia therapy. Up to now, the most studied materials are iron oxides, thanks to their biocompatibility. However, there is an increasing interest to investigate other kind of materials in order to improve the hyperthermic efficiency and decrease the size of the inorganic core. Among the different types of MNP, cobalt ferrites are promising candidates but their use for actual treatment is hampered by the high toxicity of Co. Within this framework, we investigated the structural and magnetic properties of a series of non-stoichiometric cobalt ferrite MNP to find the conditions for reducing the toxicity while preserving the hyperthermic efficiency.
We present here the synthesis and the structural, magnetic and hyperthermic properties of highly monodisperse MNP with average size of few nm containing different amounts of cobalt ($Co_xFe_{3-x}O_4$, 0.1<x6 nm) to obtain a significant heating, independently of the Co content. For larger particles size, but well below those required for iron oxides, very high hyperthermic efficiency is observed even for low Co content. This opens the possibility to strongly reduce the metal oxide content, and keeping low the potential toxicity of the inorganic core.
The analysis of the magnetic behaviour shows an unusual dependence of the effective magnetic anisotropy on the Co content, which is ascribed to a composition dependent distribution of divalent ions among tetrahedral and octahedral sites in the spinel structure. In order to verify this hypothesis a detailed structural investigation, by EXAFS, Magneto-Optic Spectroscopy and HR-TEM is in progress.</x

In-situ XRD studies of kinetic processes of cement-based materials

M. Favero, M. C. Dalconi, L. Valentini, G. Artioli
Univ. di Padova, CIRCe Center and Dipartimento di Geoscienze, Padua, Italy

POSTER 8

Cement material plus water is a complex system undergoing critical chemical and physical changes in time during the hydration, setting and hardening. The number of involved physico-chemical parameters is so large that a unique hydration model able to explain mechanisms controlling the processes is far from being understood. To partly overcome the chemical complexity of real cement materials like Ordinary Portland Cement (OPC), simplified cement systems are often used for research purposes.
Three simplified cement systems formed by calcium silicates (C3S - Ca3SiO5 and C2S - Ca2SiO4), tricalcium aluminate (C3A - Ca3Al2O6) and a varying amount of Gypsum were considered. In-situ x-ray diffraction measurements were performed in order to monitor phase evolution during hydration. A methodological approach, considering different instrumental setups ¬– focusing transmission flat-sample, focusing transmission capillary and reflection flat-sample – has been applied to test the feasibility of using a laboratory instrument. The obtained experimental data are needed to proof the effectiveness of software modelling (HydratiCA), which is still under a development stage.
Preliminary results indicate the presence of Ettringite, Portlandite, AFm-14 and an hydration product whose main diffraction peak is at 8.2 Å (10.75° 2θ, CuKα1), which we suppose to be hemicarboaluminate. Hydration kinetics derived from XRD data were used to interpret calorimetric data obtained on the same samples.

In situ X-ray powder diffraction of the formation of inorganic-organic hybdrid compounds based on phosphonosulfonic acids

M. Feyand and Norbert Stock
Institut für Anorganische Chemie Kiel, Germany

POSTER 9

Inorganic-organic hybrid compounds are recently under intensive investigations due to their enormous structural variety and the potential application in the areas of gas storage, catalysis or charge storage materials.[1, 2] A suitable route to synthesize such compounds are solvothermal reactions. Such reactions are so called black-box systems and no information regarding the crystallization process is obtained. Therefore, we are using energy-dispersive X-ray diffraction (EDXRD) to obtain information on the crystallization process. From these studies possible intermediate phases can be observed and kinetic parameters can be established. The in situ EDXRD investigations are carried out in glass reactors using white synchrotron radiation (beamline F3, HASYLAB, Germany) to achieve a time resolution below one minute per spectrum. In addition to conventional heating methods we were also able to implement a microwave reactor system.
Here we report the results of our recent investigations on metal phosphonatosulfonates. Both heating methods are used to study the formation of $Sm(O_3P\ C_4H_8\ SO_3)(H_2O)$ (**1**) During the first five minutes intermediate phase was observed which transforms completely into **1**. Temperature dependent measurements allowed the extraction of rate constants and determination of the Arrhenius activation energy by using the model of Sharp and Hancock.[3]
In a second study the synthesis of the literature known compound $Cu_2[(O_3P\text{-}C_2H_4\text{-}SO_3)(H_2O)2(OH)]\bullet 3\ H_2O$ (2)[4] was investigated by EDXRD methods. A crystalline intermediate phase was observed during the first two minutes and the crystal structure was determined from high resolution powder diffraction data. (beamline G3, HASYLAB, Germany) This data allowed us to establish a possible reaction mechanism for the formation of **1**, which proceeds through the hydrated compound $Cu_2[(O_3P\text{-}C_2H_4\text{-}SO_3)(H_2O)2(OH)]\bullet 4\ H_2O$.

[1] A. Clearfield, In Progress in Inorganic Chemistry 1998, 47, 371.
[2] A. Cheetham, G. Férey, T. Loiseau, Angew. Chem. Int. Ed. 1999, 38, 3268.
[3] M. Feyand, C. Na?ther, A. Rothkirch, N. Stock, Inorg. Chem. 2010, 49, 11158.
[4] A. Sonnauer, N. Stock, Eur. J. Inorg. Chem. 2008, 2008, 5038.

POSTER 10

A new generation x-ray powder diffraction facility at NSLS-II

S. Ghose, E. Dooryhee, X. Shi, M. Rehak
Photon Sciences Directorate, Brookhaven National Laboratory, Upton, USA

An X-ray Powder diffraction (XPD) beamline is being designed at the new synchrotron X-ray source (NSLS II) at Brookhaven National Laboratory, USA. This powder diffraction beamline will become a multi-instrument facility with the ability to collect diffraction data at high x-ray energies (30 keV-80 keV), offering rapid acquisition (milli-second) as well as high angular resolution capabilities. XPD addresses future scientific challenges in *e.g.*, hydrogen storage, CO_2 sequestration, advanced structural ceramics, catalysis, and materials processing. Such materials of high technological value often are complex, nanostructured and heterogeneous. The scientific grand challenge is to obtain robust and quantitative (micro)structural information, not only in the ground state at ambient conditions, but also in *situ* or in *operando* with varying temperature, pressure, magnetic, electric or stress field, chemical environment, etc. The beam size is adjustable to match the graininess and heterogeneity scales of the samples above the micron scale. The beamline is of novel optical design, making use of techniques and instrumentation pioneered or under development at the NSLS (*e.g.,* Laue optics and Ge strip array detectors). The optical layout is optimized for taking full advantage of the high flux of a 7m long 1.8T damping wiggler. XPD is designed to combine sample-limited Q-space-resolution diffraction measurements and sample-limited real-space-resolution Pair Distribution Function measurements. Full user operation mode begins June 2015.

In situ characterization of crystallization processes applying synchrotron X-ray diffraction and Raman spectroscopy

T. Gnutzmann[1], M. Klimakow[1], K. Rademann[2], F. Emmerling[1]
[1]BAM Federal Institute for Materials Research and Testing, Berlin, Germany
[2]Dept of Chemistry, Humboldt-Universitaet, Berlin, Germany

POSTER 11

Polymorphism is the property of many inorganic and especially organic molecules to crystallize in more than one crystal structure. This feature causes problems whenever only a distinct modification is demanded. On the other hand polymorphic systems are useful for the investigation of structure-property-relationships. In this context *in situ* methods permit the detection and identification of transient metastable polymorphs and the elucidation of their crystallization mechanisms. However, *in situ* studies require techniques providing a sufficient time resolution. X-ray diffraction using synchrotron radiation allows high time resolution of the crystallization process due to the brilliance of the radiation. Combining this method with optical spectroscopy enables further insight. Raman spectroscopy renders information about the molecular structure and intermolecular interactions between the molecules in solutions, amorphous, and crystalline state. Therefore, the spectroscopic data perfectly complete the results of diffraction methods. An ultrasonic levitator as sample holder avoids measurement artefacts due to the container walls and enables monitoring of crystallization processes uninfluenced by any surfaces. The possibilities of the approach mentioned above are exemplarily shown for the investigation of the polymorphic substance nifedipine. This Ca antagonist exhibits one amorphous and at least three crystalline modifications. The existence of more metastable polymorphs is assumed.[1,2] Only the crystal structure of the most stable form has been solved yet. The crystallization process is followed with synchrotron XRD at the µSpot-Beamline at BESSY II and Raman spectroscopy in lab using different solvents and varying the ambient conditions especially humidity.

(1) Klimakow, M.; Leiterer, J.; Kneipp, J.; Rossler, E.; Panne, U.; Rademann, K.; Emmerling, F. Langmuir 2010, 26, 11233-11237.
(2) Grooff, D.; De Villiers, M. M.; Liebenberg, W. Thermochimica Acta 2007, 454, 33-42.

POSTER 12

More reliable intensity extraction from powders using texture

J. Grässlin[1], L.B. McCusker[1], C. Baerlocher[1], F. Gozzo[2], B. Schmitt[2], L. Lutterotti[3]
[1]Laboratory of Crystallography, Dept of Materials, ETH Zürich, Switzerland
[2]Swiss Light Source, PSI, Villigen, Switzerland
[3]Dept of Materials Engineering and Industrial Technology, Univ. of Trento, Italy

The intensity variation in the XRD pattern obtained from a textured sample as a function of sample orientation (tilt and rotation) can be applied to resolve the relative intensities of overlapping reflections. With the new Si-microstrip detector (Mythen II) on the MS Beamline at SLS and the new features in the program *Maud*, both the experimental and the data analysis procedures could be redesigned. Thereby, a significant improvement in the quality of the extracted reflection intensities was achieved.
To test this modified method, two samples of a Zr-phosphate with a known crystal structure were measured: a textured sample using the revised experimental setup and data collection strategy, and an untextured sample in a 0.5mm capillary. Both datasets were collected at the SLS using the Mythen detector. For the analysis, reflections up to d_{min} = 1.0 Å were considered, and a reflection separation factor of 0.5*FWHM was used to define the overlap groups. Comparison of the structure factors extracted from conventionally measured powder diffraction data with those derived from a textured sample indeed shows the latter to be significantly better. The agreement between the amplitudes obtained with a LeBail extraction using *Maud* for the untextured data and those calculated from the refined crystal structure can be expressed as an *R* value of 0.547 for overlapping reflections. Amplitudes derived in a joint extraction using 32 powder patterns (different orientations) collected on a textured sample yielded an *R* value of 0.408 for overlapping reflections.
The quality of the extraction could be further improved by combining the amplitudes derived from the textured sample with those derived from the untextured one. This combination results in an *R* value of 0.385. If the remaining difficulties with the estimation of the background and the description of the peak shapes can also be solved, the results will become even better.

POSTER 13

Characterization of monazite-type-ceramics used for nuclear waste management

J. Heuser, H. Schlenz, D. Bosbach
Institute of Energy and Climate Research, Safety Research and Reactor Technology (IEK-6), Forschungszentrum Jülich GmbH, Jülich, Germany

The conditioning of nuclear waste from nuclear power plants and from nuclear weapons is an important issue according to science and society. Therefore the research on an appropriate matrix for the immobilization of e. g. actinides is of great interest. Beyond the widely used borosilicate glasses, ceramics are promising materials for conditioning. Monazite-type ceramics with compositions $Ln PO_4$ (Ln = La, Ce, Nd, Sm, Eu, Gd), e. g., represent an important material in this field. To obtain a suitable host matrix for radionuclides, the characterization of monazites of different chemical composition and their thermal and structural behaviour is a promising option. Monazite was chosen because of its outstanding properties according to radiation resistance and chemical durability.

Our aim is to find a composition with a minimum melting point or an eutectic mixture in order to improve the production design for future industrial synthesis. We synthesized Samarium-Cerium-monazites $Sm_x Ce_{1-x} PO_4$ (x = 0-1) that can be used as a simulation for radionuclide-doped matrices. Different compositions of the aforementioned solid solution were prepared by hydrothermal synthesis at T = 220 °C, $p \sim 25$ bar.

The sample properties were analysed chemically by EDX, structurally by XRD and Raman spectroscopy and thermally by TG-DSC. By means of our characterizations we could show that the system with the endmembers $SmPO_4$ and $CePO_4$ does not behave like an ideal solid solution. Accordingly we assume a minimum of melting point in the compositional range around $Sm_{0.6}Ce_{0.4}PO_4$. First results of this work will be presented.

POSTER 14

In-situ synchrotron diffraction studies of halide substitution in $Mg(BH_4)_2$

S. Hino, J.E. Fonneløp, M.H. Sørby, B.C. Hauback
Physics Dept, Institute for Energy Technology, Kjeller, Norway

The mixture of $Mg(BH_4)_2$ and MgX_2 (X= Cl, Br) has been studied by in-situ synchrotron powder X-ray diffraction (PXD). $Mg(BH_4)_2$ which contains large amount of hydrogen with 14.9 mass % is one of the most promising hydrogen storage materials for mobile use. The material undergoes a polymorphic phase transition from **α phase to β phase** at around 190 °C and desorbs hydrogen at around 300 °C. In order to reduce the temperature for hydrogen release, substitution of $(BH_4)^-$ by halide anion has been studied to change stability and thermodynamics of mixed phase $Mg(BH_4)_{2-x}X_x$. We investigated the generation of the mixed phase by using PXD. In-situ PXD patterns shows **α-$Mg(BH_4)_2$** in the mixture of $Mg(BH_4)_2$ and $MgCl_2$ milled for 12 h with 500 rpm transforms to an unknown intermediate phase at around 120 °C. After that, the unknown phase changed to **β-$Mg(BH_4)_2$**. In addition, **β-$Mg(BH_4)_2$** in the mixtures of $Mg(BH_4)_2$ and $MgCl_2$/$MgBr_2$ milled for 12 h with 280 rpm and then annealed at 200 °C shows smaller unit cell compared to pure beta phase. It could be due to possible substitution of $(BH_4)^-$ by halide ions, because ionic radius of Cl^-/Br^- are smaller than that of $(BH_4)^-$.

In situ studies of apatite formation in water

POSTER 15

C.J.S. Ibsen, H. Birkedal
Dept of Chemistry and iNANO, Aarhus Univ., Aarhus, Denmark

The formation of crystals is still not understood despite over a hundred years of research[1]. In situ diffraction studies are very promising tools as they allow studying the formation kinetics, time dependent crystal size and strain in detail[2]. However, studies of crystallization of low-Z compounds in water is particularly challenging due to the low diffraction contrast and the very large water wide angle scattering background. Such compounds include key minerals of biological relevance such as apatite, Ca10(PO4)6(OH)2 , and the calcium carbonates. Here we present a setup allowing such studies at 2nd generation synchrotrons with ~10 s time resolution. We apply the setup to studies of the crystallization formation of apatite under the influence of the organic molecule alizarin red S, which binds strongly to Ca2+. We have previously shown that alizarin red S influence the apatite nanocrystal size and induces an alizarin red S concentration dependent lattice deformation[3]. We find that alizarin red S changes the nucleation time of apatite. Comparison with other systems shows that each organic additive may influence crystallization in a specific way thus illustrating the complexity of the crystallization problem.

[1]M. A. Lovette et al. Ind. Eng. Chem. Res. 2008, 47, 9812-9833.
[2]H. Jensen et al. Angew. Chem. Int. Ed. 2007, 46, 1113-; P. Norby Curr. Opin. Colloid Interface Sci. 2006, 11, 118; G. V. Jensen et al. Chem. Mater. 2010, 22, 6044-6055.
[3]C. J. S. Ibsen & H. Birkedal Nanoscale 2010, 2, 2478-2486

POSTER 16

SU-63 and SU-64: Novel germanates by varying HF and water contents

A.K. Inge[1], B. Guo[2], C. Bonneau[1,3], J. Sun[1], K.E. Christensen[4], Z. Yuan[2], X. Zou[1]
[1]Dept Materials and Environmental Chemistry, Stockholm Univ., Stockholm, Sweden
[2]College of Chemistry, Nankai Univ., Tianjin, China
[3]Inst. for Integrated Cell-Material Science, Kyoto University, Kyoto, Japan
[4]Diamond Light Source Ltd., Diamond House, Oxfordshire, United Kingdom

Porous crystalline oxides such as zeolites and related open-frameworks are of interest for their ability to selectively accommodate guest species in their pores and channels. Applications include shape and size selective ion exchange, catalysis, separation, and adsorption. Many of the properties of the material are dependent on features such as framework composition, ring size, and channel dimensions. Our work focuses on the synthesis, structure determination by single crystal and powder XRD, and characterization of novel framework materials. Germanium has been used as a framework element to construct numerous framework architectures with extra-large-rings (>18-membered rings). Composite building units (CBU) of germanium oxides in various coordination geometries promotes the formation of open-framework with large rings. Germanium often takes form tetrahedral, trigonal bipyramidal, and octahedral coordination geometries. Recent results show that water and HF contents in the starting mixture of reagents play significant roles in directing the formation of specific building units. ASU-21,[1] SU-63,[2] and SU-64[2] are three structures that have resulted by tuning these parameters. 1,6-dimainohexane was used as a structure directing agent and each of the structures contain 18-membered rings. The structures however are constructed of different CBUs. Higher concentrations of HF in the synthesis mixture tend to result in frameworks with four or five connected Ge_7 clusters as in SU-63, while Ge_{10} phases such as ASU-21 form in the absence of HF. SU-64 forming in a region of the phase diagram with intermediate HF concentration is constructed of both Ge_7 and Ge_9 clusters. Control over the formation of specific CBUs is expected to aid in the design of novel framework materials. In addition to 3D frameworks we have also developed 0D cages, 1D nanotubular structures, and 2D layers and slabs.

[1] *Inorg. Chem.* **2009**, *48*, 9962 [2] *Inorg. Chem.* **2011**, *50*, 201

Phase transition in CdSe quantum dots

F. Kanodarwala[1] ,J. Stride[1,2]
[1]School of Chemistry, Univ. of New South Wales, Sydney, Australia
[2]Bragg Institute, Australian Nuclear Science and Technology Organisation, Sydney, Australia

POSTER 17

Quantum dots (QDs) are nanocrystalline semiconductors which exhibit extraordinary quantum confinement phenomenon [1] - which provides them with distinctly different optical, electronic, and magnetic properties from their bulk counterparts. These properties have enabled their application to many different technological areas including biological labelling and diagnostics, light-emitting diodes [2] and electroluminescent devices, photovoltaic devices, lasers, and even as single-electron transistors.
Although extensive research has been conducted on nanocrystals of group II–VI, III–V, and IV–VI and metal oxide nanocrystals but still CdSe remains the most thoroughly studied nanocrystal system.
Our aim is to synthesis high-quality CdSe nanocrystals through benchtop colloidal synthesis whilst analysing the effects of varying the reaction temperature, solvent and reaction time on the size, shape and crystallinity of the quantum dots.
CdSe exists in two crystal structures, namely the hexagonal wurtzite (WZ) structure and the cubic zinc- blende (ZB) structure. Mainly all the synthetic techniques currently employed usually produces NCs in WZ structure. Very recently, ZB-CdSe NCs have been successfully obtained [3] but there is lack of any systematic or comparative study in relation to conventional WZ system.
Powder X-ray diffraction (Fig.1) shows the phase transition of the crystallite phases from cubic zinc-blende to hexagonal wurtzite and back to cubic as a function of reaction time. We believe this is due to the rapid growth along the {111} facets of the cubic unit cell and then finally the other facets 'catch-up' to result in a particle with cubic symmetry once again. The only reported phase transition in CdSe has been the one from cubic to hexagonal phase, induced due to annealing of the product at high temperatures.
The results obtained by XRD are in conformity with those deduced through high resolution transmission electron microscopy.
In conclusion we have successfully synthesized the less common cubic CdSe quantum dot and demonstrated through XRD the phase transition in CdSe quantum dot from cubic to hexagonal and back to cubic phase as a function of reaction time.
References:
[1] B. O. Dabbousi et al., J. Phys. Chem. B, 101, 9463-9475, 1997
[2] Aurora Rizzo et al., ACS Nano, 1506–1512, 2009
[3] Y.A. Yang et al., Chem. Int. Ed. 44, 6712, 2005

Coordination chemistry in the solid state: reactivity of metal chlorides with imidazole, pyrazole and their hydrochlorides

M.A. Kurawa[1], C. J. Adams[2], A. G. Orpen[2]
[1]Dept of Pure and Industrial Chemistry, Bayero Univ. Kano, Kano Nigeria
[2]School of Chemistry, Univ. of Bristol, Cantocks Close, Bristol, UK

POSTER 18

The state of the art in crystal engineering was exploited to synthesize crystalline coordination compounds $[MCl_2L_2]$ (M= Co, Zn, Cu, Cd, Mn, Pd and Pt; L = Him or Hpz) by simple grinding of the appropriate metal chloride and the neutral ligands in the solid state. Similarly, mechanochemical treatment of imidazolium chloride $[H_2im]Cl$ with metal chlorides MCl_2 produce imidazolium tetrachlorometallate salts $[H_2L]_2[MCl_4]$. Solid pyrazole reacts with HCl gas to form pyrazolium chloride $[H_2pz]Cl$, which also reacts in the solid state under grinding with MCl_2 to produce the pyrazolium analogues of the tetrachlorometallate salts. Mechanochemical reaction of $[H_2L]_2[MCl_4]$ salts with bases such as KOH, K_2CO_3 (or Ag_2O for M = Pd, Pt) or thermal elimination of HCl also affords the coordination compounds $[MCl_2(HL)_2]$ which were also obtained via grinding $[H_2L]Cl$ with basic metal salts. On the other hand exposure of the crystalline coordination compounds to HCl as vapour or dry gas results in the formation of the perhalometallate salts.

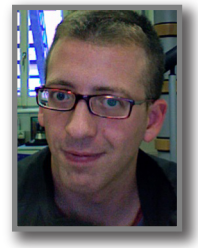

POSTER 19

Ionic co-crystals of calcium chloride: possible applications of ICC in the pharmaceutical industry

G.I. Lampronti, A. Turrina, L. Maini, F. Grepioni, D. Braga
Dept Chemistry "G. Ciamician", Univ. of Bologna, Italy

The use of electrostatic interactions such as those present in ionic co-crystals containing alkali metals and alkaline earth metals compounds has never been systematically explored in the field of Crystal Engineering. In this type of structures the interaction between inorganic ions and organic molecules (and water molecules, if any) must be seen as a special case of solvation, with the organic molecules acting as a solvent molecules (in competition with 'water) for ions.[1] In the case of primary and secondary amides, N-H and C=O dipoles act respectively as donor and acceptor for hydrogen bonds, thus with the possibility of solvating inorganic salts. In this context we have chosen to investigate the behaviour of the following few, selected molecules: barbituric acid, diacetamide, malonamide, oxamide and urea. As for the inorganic counterpart, $CaCl_2$ salt was chosen because of its non-toxicity and potential applications in the pharmaceutical field. Synthetic methods for this study vary from classical crystallization from solution, to slurry, mechanochemical solid state techniques (grinding and kneading), and solid-gas techniques (vapor-diffusion). Crystal structures were solved from single crystal data, or by powder diffraction using simulated annealing procedures when no single crystal was available. Calcium coordination polyhedra fragments (CaO_{water}) taken from known ICC structures were inserted as rigid bodies in the simulated annealing procedure to minimize calculation times. All compounds were analyzed with DSC, TGA and variable temperature XRD.

REFERENCES

1: Braga D, Grepioni F, Maini L, Prosperi S, Gobetto R, Chierotti MR, Chem Commun, 2010, 46(41):7715-7717

POSTER 20

Epitaxis vs. solid solution of isostructural coordination polymer

M. Lusi, L.J. Barbour
Dept of Chemistry, Univ. of Stellenbosch, Stellenbosch, Italy

Different synthetic conditions often afford different products and this is more evident for complex structures (i.e. solvates, polymorphs, cocrystals, solid solutions, etc). We show how solution growth of a given set of components produces an epitaxial heterocrystal while mechanochemical synthesis yields a solid solution.

Isomorphous structures convert into non-isostructural anhydrous phases. Crystal structure determinted by powder diffraction

L. Maini, G. I. Lampronti, S. Prosperi, D. Braga
Dip. Chimica "G. Ciamician", Università di Bologna, Italy

POSTER 21

Hydrated ionic –cocrystal of Barbituric acid BA•MBr•2H_2O (M=Na, K, Rb) are found to be isomorphic, however upon dehydration they convert to anhydrous ionic cocrystal which are not isomorphic neither isostructural. The stability of the anhydrous phase is inverse proportional to the cation radii, and only BA•RbBr is stable in air and it was possible to determine its crystal structure from single crystal X-ray diffraction. BA•MBr (M=Na, K) rapidly absorb water form air and convert to the hydrated form. The crystal structures of the anhydrous forms were determined by X-ray powder diffraction collected in a capillary. BA•NaBr was solved although the powder pattern contains some extra-peaks due to the presence of NaBr and BA•NaBr•2H_2O. The crystal structure of BA•NaBr is characterized by two independent molecules in the asymmetric unit which is in agreement with the SSNMR. The dehydration process was characterized by variable temperature X-ray powder diffraction and thermal analysis as DSC and TGA.

POSTER 22

Reversible isomer conversion of $[CuI(PPh_3)]_4$ by organic solvents

D. Braga[1], F. Grepioni[1], L. Maini[1], P.P. Mazzeo[1], B. Ventura[2]
[1]Dipartimento di Chimica "G.Ciamician", Università di Bologna, Bologna, Italy
[2] Istituto per la Sintesi Organica e la Fotoreattività (ISOF) – CNR, Bologna, Italy

Reactions between copper(I) iodide and triphenylphosphine have been explored in solution and in solid state and six luminescent coordination complexes have been obtained and characterized via X-ray diffraction and UV-Vis spectroscopy. Solid-state reactions of CuI with PPh_3 in different conditions (kneading, vapour digestion) and stoichiometries resulted in the formation of high ratio ligand:metal compounds while tetrameric structures could be obtained only by solution. Crystal structures were determined by single crystal X-ray diffraction while purity of the bulk product was checked by XRPD.

Three different tetrameric structures with 1:1 stoichiometry have been synthesized: two closed cubane type polymorphs $[Cu_4I_4(PPh_3)_4]$Iα and $[Cu_4I_4(PPh_3)_4]$Iβ and an open step-like isomer $[Cu_4I_4(PPh_3)_4]$II. The conversions between the polymorphs and isomer have been studied and characterized by XRPD. The most stable form $[Cu_4I_4(PPh_3)_4]$Iα can convert into the open step-like isomer $[Cu_4I_4(PPh_3)_4]$II in slurry experiment with EtOH, CH_2Cl_2, AcCN and converts back into $[Cu_4I_4(PPh_3)_4]$Iα when exposed to vapour of toluene.

At room temperature all compounds exhibit a bright emission in the solid state that markedly shifts bathochromically or ipsochromically on cooling to 77K according to the nature of the transition (CC or XLCT). Theoretical calculations on tetrameric cubane clusters have also been performed to justify the differences in UV-VIS emission spectra between polymorphs.

Main features and last advances in *EXPO2011*

A. Moliterni[1], A. Altomare[1], C. Cuocci[1], C. Giacovazzo[1,2], R.Rizzi[1]
[1]IC, Sede di Bari, Bari, Italy
[2]Dipartimento Geomineralogico, Università di Bari, Campus Universitario, Bari, Italy

POSTER 23

Advances on experimental devices and computing methods have made *ab-initio* crystal structure solution by powder data more and more popular, even if it can be still a challenge due to peak overlap, background definition and/or preferred orientation. Traditional approaches like Direct Methods (DM) or Patterson Methods (PM), based on structure factor moduli, may fail owing to the uncertainty on the integrated intensity estimates. On the contrary, direct space techniques are independent on the integrated intensities, even if they need additional *prior* information on molecular geometry.
EXPO2011, the heir of *EXPO2009* [1], is a package able to solve *ab-initio* inorganic, metallorganic and organic compounds. It can carry out all the traditional steps of the structure solution process: 1) indexation; 2) space group determination; 3) integrated intensities estimation; 4) crystal structure solution (DM or PM); 5) crystal structure refinement (Rietveld method).
In addition, it can work on direct space (Simulated Annealing) and can exploit hybrid approaches, by combining reciprocal and direct space procedures.
The structure solution process has been strengthened by new methods, particularly powerful in case of low resolution data and/or organic compounds, able to: a) improve the phasing process; b) optimize the structure model correcting the truncation effects on the electron density (in direct space or in reciprocal space or in both of them [2]).
The main features of *EXPO2011* and some applications to experimental data are described.

[1] Altomare, A., Camalli, M., Cuocci, C., Giacovazzo, C., Moliterni, A., Rizzi, R. (2009). *J. Appl. Cryst.* **42**, 1197-1202.
[2] Altomare, A., Cuocci, C., Giacovazzo, C., Moliterni, A., Rizzi, R. (2010). *J. Appl. Cryst.* **43**, 798-804.

POSTER 24

Crystal forms of two potential foldamers

E. Nauha, A. Suhonen, K. Helttunen, K. Salorinne, J. Ollikka, M. Nissinen
Dept of Chemistry, Nanoscience Center, Univ. of Jyväskylä, Finland

Foldamers[1] are chain like molecules that adopt specific secondary structures with the help of noncovalent interactions. Synthetic foldamers could mimic the structures and functions of biological molecules or show interesting properties for new applications. Two novel molecules[2], that could form a helical structure around halogen anions and work as a starting point for foldamers, were synthesized and the properties of these examined in solution and the solid state. The difference between the two molecules is the identity of the central ring, which is either benzene (N^1,N^3-bis(2-benzamidophenyl)benzene-1,3-dicarboxamide) or pyridine (N^2,N^6-bis(2-benzamidophenyl)pyridine-2,6-dicarboxamide). Evaporation crystallization experiments were prepared to study the complexation and possible polymorphism in the solid state. Crystal structures were measured of crystals suitable for single crystal X-ray diffraction, but the primary analysis methods were powder X-ray diffraction and ATR-IR spectroscopy.

The benzene variant was found to crystallize in at least 5 crystal forms, one of which has been identified as a dimethyl sulfoxide solvate by way of single crystal X-ray diffraction. Two structures where a fluoride anion is complexed by the molecule have also been identified. The benzene variant has so far shown no indication of folding as was expected. The pyridine variant was found to crystallize in at least 4 crystal forms and crystal structures of three have been solved. The solved structures are a loosely packed pure form, and isostructural methanol and ethanol solvates. In the crystal structures the molecule is folded into itself with the aid of three hydrogen bonds.

1 S. H. Gellman, *Acc. Chem. Res.*, **1998**, 31, 173-180.
2 E. Nauha, A. Suhonen, K. Helttunen, K. Salorinne, J. Ollikka, M. Nissinen. Manuscript in preparation.

Structure solution with long flexible chains present – test of a method with FOX

M. Oszajca, W. Lasocha
Faculty of Chemistry, Jagiellonian Univ., Kraków, Poland

POSTER 25

Molecules with long carbon chains present themselves as a challenge for global optimization techniques. Their torsional flexibility introduces many degrees of freedom in optimized objects additional to the basic positional and rotational parameters. Introduction of these parameters to calculations shows a significant complexity jump for the problems solved in structure solution. Studies by Zhou et al[1,2] showed that a redefinition of solution space by dividing molecules into shorter fragments simplifies the searching process due to relatively easier determination of positional and rotational coordinates compared to torsional ones. Their approach used a genetic algorithm based program to test their hypothesis. In their study they introduced three paths of splitting the optimized moieties. Here, we tried to apply the proposed strategy to structure solution of DMAN-glutaric acid and DMAN-suberic acid complexes. Both structures were solved using a rigid body approach with FOX[3] and later refined by Rietveld method with Jana2006[4]. These refined structures were later used as reference for testing the effects of different definitions of dicarboxylic acids molecules in the structure solution step. Series of calculations were performed for non-split moieties and for each of the strategies proposed in [1] and [2]. The results of this study show that using this approach, with structures containing flexible fragments, results in smoother and faster Rietveld refinement. This is due to the starting points being much closer to the final values as compared to the whole fragment approach.

References

[1] Zhou Z., Siegler V., Harris K. D. M., Cheung E. Y., Habershon S., Johnston R. L., Chem Phys Chem, 2007, 8, 650-653
[2] Zhou Z., Harris K. D. M., Comp. Mater. Sci., 2009, 45, 118-121
[3] Favre-Nicolin V., Cerny R., J. Appl. Cryst. , 2002, 35, 734-743
[4] Petricek V., Dusek M., Palatinus L., (2006) Jana2006. The crystallographic computing system. Inst. of Physics, Praha, Czech Rep.

POSTER 26

Structure and microstructure of Sn-doped indium oxide (ITO)

J. Popovic[1], B. Grzeta[1], E. Tkalcec[2], C. Goebbert[3], V. Ksenofontov[4], A. M. Tonejc[5] M. Bijelic[5]
[1]Rudjer Boskovic Institute, Zagreb, Croatia
[2]Faculty of Chemical Engineering and Technology, Univ. of Zagreb, Zagreb, Croatia
[3]CWT Clean Tec AG, Halberstadt, Germany
[4]Johannes Gutenberg-Universität, Mainz, Germany
[5]Faculty of Science, University of Zagreb, Zagreb, Croatia

Tin doped indium oxide (ITO) is a transparent conductive oxide (TCO) with excellent electrical and optical properties [1]. Both indium oxide (In^2O_3) and ITO crystallize in a cubic bixbyite-type structure, space group Ia-3[2]. The unit cell contains 80 atoms, where 32 sites are occupied by cations in two non-equivalent six-fold coordinated sites (B and D sites, respectively).
Structural changes in indium oxide lattice due to tin doping were studied by XRD. The local environment of Sn inside a host lattice was investigated by ^{119}Sn Mössbauer spectroscopy. Microstructure was studied by means of TEM and XRD line broadening analysis. Nanocrystalline ITO samples containing 0-14 at% Sn were prepared by a sol-gel technique. Unit-cell parameter a of samples was determined by UNITCELL program [3] and refined by WPPF program [4]. The unit-cell parameter increased with tin doping level up to 7.8 at% Sn and decreased at higher levels. This suggested that Sn substitution for In on B and D sites of the original In_2O_3 structure is non-uniform and dependant on Sn content. Rietveld refinement showed the presence of interstitial oxygen in the ITO samples. The position of interstitial oxygen indicated on D site preference for Sn at low doping level and subsequent increase in B site occupancy with the increase in Sn content, which agreed well with the ^{119}Sn Mössbauer spectroscopy results. Simultaneously with the Rietveld structure refinement, the analysis of diffraction line broadening was carried out using Si powder as a standard for instrumental line broadening. The crystallite size decreased and lattice strain increased with the increase in Sn doping level. The particle sizes as determined by TEM followed the behavior of crystallite sizes obtained by XRD line broadening analysis.

1. Chopra, K.L. et all., Thin Solid Films. 102 (1983) 1
2. Marezio, M., Acta Crystallogr. 20 (1966) 723
3. Toraya, H., J. Appl. Crystallogr. 26 (1993) 583
4. Toraya, H., J. Appl. Crystallogr. 19 (1986) 440

50 mol% Sc doped BaTiO3: characterization of structure and conductivity

S.M.H. Rahman[1], I. Ahmed[1,2+], C.S. Knee[3], S.G. Eriksson[1]
[1]Chalmers Univ. of Technology, Sweden
[2]The ISIS facility, Rutherford Appleton Laboratory, U.K.
[3]Univ. of Gothenburg, Sweden
[+]Currently working at Volvo Technology, Gothenburg, Sweden

POSTER 27

Keywords: perovskite, ionic/proton conductivity, X-ray diffraction, Impedance spectroscopy.

$BaTiO_3$ has been extensively studied due primarily to its ferroelectric and positive temperature coefficient of resistance properties. Moreover, it has been shown that acceptor-doped $BaTiO_3$ exhibits considerable proton conductivity [1-3] but so far the majority of these studies have included materials with low (5~10%) doping levels only. Recent study shows high (50%~80%) In doped $BaTiO_3$ demonstrates significant proton conductivity [4, 5]. In this study we aim to characterize the structural and functional properties of 50 mol% Sc doped $BaTiO_3$, $BaTi_{0.5}Sc_{0.5}O_{3-\delta}$ (BTS) with an emphasis on the proton conductivity.
The material was prepared by solid state synthesis route and the phase purity was examined by powder X-ray diffraction. Rietveld analysis on X-ray powder diffraction data on as-prepared (cell parameter, a=4.1354(1) Å), vacuum dried (a=4.1344(1) Å) and hydrated sample (a=4.1361(1) Å) showed to be a cubic crystal system with space group Pm-3m. Upon protonation of the vacuum dried sample, an increment of 0.04% on cell parameter was observed. TGA revealed that ~ 42 % of the theoretical maximum protonation were achieved when the materials were exposed to humid environment in a hydration furnace. Electrical conductivity was measured on pre-hydrated pellet by ac impedance spectroscopy (IS) as a function of temperature under wet and dry Ar. The materials showed significantly higher total conductivity up to 600 °C in the wet Ar cooling run than that of dry Ar, along with a plateau in the temperature range of 250°C to 600 °C. BTS shows **σtotal value of $1.31*10^{-4}$** and $2.68*10^{-4}$ Scm^{-1} at 300 °C and 600 °C respectively in wet Ar.
References
1) T. Schober and A. Magrez, Ionics 10 (2004), 17-19.
2) K. D. Kreuer, Solid State Ionics, 97 (1997) 1.
3) K.D. Kreuer, et al., Solid State Ionics, 145 (2001) 295-306.
4) Eric Quarez et al., Journal of Power Sources, 195 (2010) 1136-1141.
5) S.M.H. Rahman, et al.50 mol% In doped BaTiO3: Characterization of structure and conductivity, in manuscript.

Thermal phase evolution of $Ca(BH_4)_2$ studied by SR-PXD

M.D. Riktor[1], Y. Filinchuk[2], M.H. Sørby[1], B.C. Hauback[1]
[1]Physics Dept., Institute for Energy Technology, Kjeller, Norway
[2]Institute of Condenced Matter and Nanosciences, Univerité Catholique de Louvain, Louvain-la-Neuve, Belgium

POSTER 28

Future increase in demand for energy requires development of alternative methods to store and convert energy. Regarding road transportation fuel, the use of hydrogen as an energy carrier is considered a very attractive solution. A major challenge for the introduction of hydrogen as an energy carrier for mobile applications is safe and efficient storage of hydrogen. The conventional ways are to store hydrogen either as pressurized gas in high pressure tanks or as cryogenic liquid. However, both these methods suffer from major drawbacks concerning i.e. energy consumption and safety.
A method which can store hydrogen very efficiently is storage in solid compounds, e.g. metal hydrides. The complex hydride $Ca(BH_4)_2$ is a compound potentially very suitable for hydrogen storage purposes due to high volumetric and gravimetric capacity for hydrogen as well as suitable thermodynamic properties according to the predicted decomposition reaction. However, experimental work done so far shows a more complex decomposition pathway including formation of several intermediate phases, as well as high decomposition temperature and severe reversibility. In order to be able to improve sorption properties and to clarify suitability as hydrogen storage material, detailed knowledge about decomposition mechanisms and reaction pathway is of crucial importance.
We have studied the decomposition of $Ca(BH_4)_2$ by in-situ synchrotron x-ray diffraction (SR-PXD) and high resolution SR-PXD measurements. The data provides detailed information on the phase transformations during decomposition, and two of the unknown intermediate phases have been identified and structure models proposed.

POSTER 29

Structural research on phosphate and phosphosilicate ceramics, which are used for nuclear waste management

S. Schmitz, H. Schlenz, D. Bosbach
Institute of Energy and Climate Research, Safety Research and Reactor Technology (IEK-6), Forschungszentrum Jülich GmbH, Jülich, Germany

The further development of the conditioning and disposal of nuclear waste poses a major challenge in the near future. In this context, monazite ($LnPO_4$, *Ln* = La, Ce, Nd, Sm, Eu, Gd) appears to be a promising alternative matrix to borosilicate glasses for the immobilization of actinides like U, Th and Pu.

Monazite is a natural thorium ore, chemically variable and highly radiation resistant. The eldest known monazites including thorium are determined up to 3.2 Ma in age. The high melting temperatures of about 2000°C are a clear disadvantage of monazite phases and at a first glance this seems to be a drawback.

However, our initial phase is $NdPO_4$ with a melting temperature of 1975±20°C. Our intention is to reduce the melting and sintering temperatures of this particular monazite phase, but maintaining the positive properties of monazite simultaneously.

In order to include tetravalent actinides (e.g. Th, U, Pu), a second phase is used for charge balance. We used cheralite ($CaTh(PO_4)_2$) and huttonite ($ThSiO_4$) as end-members for solid solutions. Both phases are isostructural to monazite. Two series of solid solutions in the systems $NdPO_4$-$CaTh(PO_4)_2$ and $NdPO_4$-$ThSiO_4$ were synthesized by solid state reactions at T=1400°C and atmospheric pressure for several hours.

The sample properties were analyzed chemically by EDX, structurally by XRD and Raman spectroscopy and thermally by TG-DSC. Complete solid-solution along the $NdPO_4$-$CaTh(PO_4)_2$ join and along the NdPO4-ThSiO4 join does exist.

POSTER 30

A low temperature charge ordered phase of the 6H-perovskite Ba3NaRu2O9

M.S. Senn[1], S.A.J. Kimber[2,3], A.H. Hill[3], J.P. Attfield[1]
[1]Centre for Science at Extreme Conditions and School of Chemistry, Univ. of Edinburgh, King's Buildings, Edinburgh, United Kingdom
[2]Helmholtz-Zentrum Berlin für Materialien und Energie, Berlin, Germany
[3]European Synchrotron Radiation Facility, Grenoble, France

Perovskite-related ruthenates have been extensively studied due to their technological applications which range from dielectric resonators for mobile phones to fuel cell membranes. Whilst much is understood about the electronic and structural properties of cubic-type perovskites e.g. SrRuO3, less is known about the related hexagonal perovskites.
A 6-layer hexagonal perovskite form of BaRuO3 can be stabilised by doping the Ba site such that the formal stoichiometry is Ba3ARu2O9. This 6-H perovskite structure is stabilised by a wide range of dopants, A+ to A4+ cations with ionic radii of 0.68-1.17Å. Of the 28 known derivatives all bar three (A= Sr, Bi and Cu) are reported to crystallise in the aristotypical space group P63/mmc at ambient conditions. This apparent homogeneity across the series of compounds is surprising considering the range in oxidation states, ionic radii and the electronic configuration of A. In addition only three derivatives of the series are known to undergo any low temperature structural transition (A= Na, Nd and Co).
The structure of Ba3NaRu2O9 has been determined using powder x-ray diffraction data from ESRF instrument ID31. At room temperature the structure has P63/mmc symmetry but at 110K, a monoclinic distortion is observed (P2/c, a= 5.83995(2)Å, b= 10.22171(4)Å, c=14.48491(6)Å, β = 90.2622(3)o). The 110K structure contains two inequivalent Ru sites which display Ru5+/Ru6+ charge order.

POSTER 31

Superflip parameter optimization for solving structures of complex organic and inorganic compounds

D. Sisak, L.B. McCusker, C. Baerlocher
Dept of Material Science ETH Zurich, Switzerland

A variety of structures have been solved using the powder charge flipping algorithm (Superflip), but as the program is relatively new, the selection of the values for the input parameters has been rather arbitrary. The systematic study answering the questions about the effect of the different input parameters on structure solution; minimum data resolution which can be used and use of the information obtained from the other sources was undertaken.

Combination of parameters which deal with: establishing the groups of overlapped reflections; repartitioning the overlapped reflections; isotropic displacement factor and threshold for charge flipping were varied within the sensible range. The data collected for inorganic (1) and organic (2) compound were used for the tests.

(1) The original solution (Superflip) of zirconium phosphate structure lacked the correct symmetry, some of the oxygen atoms in Zr-O-P layers and the quinolinium ions between the layers. With optimized input parameters, the centro-symmetric space group was recognized and complete layers could be found. Diffuse electron density clouds between the layers (quinolinium ions) were apparent.

(2) For ribose, exhaustive tests on Superflip input parameters did not provide the structure solution. Reasoning that starting with more realistic set of phases might help, possible models were generated using the direct-space program (FOX). None of these were correct, but by using the phases calculated from a flexible model to generate starting phase sets, and varying the input parameters once again, a set of optimal parameters could be found, and easily interpretable electron density maps with the correct symmetry generated.

In both cases, optimization of the input parameter set was repeated for the lower resolution data. For zirconium phosphate, parameter change did not affect the solution quality. For ribose, optimization of parameter set resulted in complete solutions down to the resolution of 1.18 Å.

POSTER 32

"Jumping crystals" – new materials for clean conversion of light and thermal energy into mechanical motion

Ž. Skoko[1] and P. Naumov[2]
[1]Dept of Physics, Faculty of Science, Univ. of Zagreb, Zagreb, Croatia
[2]Dept of Material and Life Science, Graduate School of Engineering, Osaka Univ. 2–1 Yamada-oka, Suita, Osaka, Japan

The **thermosalient solids**, which are colloquially also referred to as **"jumping crystals"**,[1–4] are promising materials for fabrication of *actuators* – mechanical devices capable for conversion of thermal energy into motion or mechanical work at a macroscopic level. If heated or cooled these materials usually undergo sharp phase transitions with strongly anisotropic change of their structure. As a result, the crystals undergo large change in their cell volume (~12% in some inositols)[3] causing such crystals to jump to heights of up to several times their length. With less than ten existing reports,[1–4] the thermosalient effect is a very poorly understood phenomenon. The origin of the effect, however, is the key question to be answered, if the mechanism responsible for this unusual, and potentially very useful behavior is to be explained.

As part of our study of thermosalient materials, we investigated *oxitropium bromide* (OXTB),4 a pharmaceutical compound which is being used as an anticholinergic drug. When heated, OXTB crystals undergo endothermic phase transition at 330.95 K. The transition is accompanied by highly anisotropic cell expansion of 4%, whereupon the *b* axis stretches 11% and the *c* axis shrinks 7%. The phase transition is reversible, and it shows thermal hysteresis.

We succeeded, for the first time, in determining the structure of the high-temperature phase of OXTB. Our results showed that the thermosalient behavior of OXTB is casued mainly by intramolecular changes in its structure. The process was completely characterized by means of single crystal X-ray diffraction, IR and NMR spectroscopy, and DSC.

References:

1. Etter, M. C.; Siedle, A. R. J. Am. Chem. Soc. 1983, 105, 641-643.
2. Gigg, J.; Gigg, R.; Payne, S.; Conant, R. J. Chem. Soc., Perkin Trans. I 1987, 2411-2414.
3. Steiner, T.; Hinrichs, W.; Saenger, W. Acta Cryst. 1993, B49, 708-718.
4. Zamir S.; Bernstein, J.; Greenwood, D. J. Mol. Cryst. Liq. Cryst. 1994, 242, 193-200.

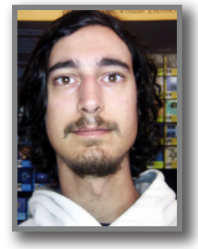

POSTER 33

Building models of post-synthetically pillared MOFs for structure solution from XRPD data

P. Smart and L. Brammer
Univ. of Sheffield, Sheffield, England

Metal organic Frameworks (MOFs) are a class of porous materials, with potential applications in the areas of gas storage, separation and heterogenous catalysis. They have advantages over other porous materials as the size, surface area and chemical nature of the pores and channels can be readily designed through selection of the organic component. As MOFs are traditionally synthesized in a one-pot self assembly process, the range of functional groups available to decorate the interior surfaces is limited to those that will not disrupt formation of the desired framework topology.

Our strategy to overcome this limitation involves the post-synthetic pillaring of 2D layered MOFs. We have shown that this technique can provide access to otherwise unobtainable MOF structures, however the products obtained are often polycrystalline. Due to the disordered nature of the guests contained within the pores of the product, the XRPD pattern is not usually of sufficient quality to solve the structures directly through real or reciprocal space methods. In these cases we have shown that through modification of related single crystal structures, sufficiently accurate models of the product crystal structures can be built which can be used as starting models for Rietveld refinement.

POSTER 34

Structural investigations of 2,3,4-tri-O-acethyl-β-D-xylopyranosides and 2,3,4-tri-N-acethyl-β-D-xylopyranosides

D.K. Stepien[1], T. Gubica[2], A. Temeriusz[1], K. Paradowska[2], E. G?owacka[1], M.K. Cyra?ski[1], A. Ostrowski[3]
[1]Faculty of Chemistry, Univ. of Warsaw, Warsaw, Poland
[2]Dept of Physical Chemistry, Faculty of Pharmacy, Medical Univ. of Warsaw, Warsaw, Poland
[3]Faculty of Chemistry, Warsaw Univ. of Technology, Poland

p-Nitrophenyl β-D-xylopyranoside is an invaluable substrate in enzyme studies focused on the activity of β-xylosidases.[1-4] This compound has found many applications in enzymology due to its chromogenic properties and as a effective antithrombotic drugs[7-10] because they induce the biosynthesis of glycosaminoglycans in cell culture.[5,6] The nitrogen analogue of the *p*-nitrophenyl β-D-xylopyranoside is *N*-*p*-nitrophenyl-β-D-xylopyranosylamine, which can be classified to *N*-xylosides. The derivatives of *N*-phenyl-β-D-xylopyranosylamine are the inhibitors of the porcine trehalase enzyme and have the fungicidal activity toward *Rhizoctonia solani*.[7]

Complex structural analysis (single crystal and powder X-ray diffraction) were performed for *N*-o-, *N*-*m*-, and *N*-*p*-nitrophenyl-2,3,4-tri-*O*-acetyl-β-D-xylopyranosylamines and for o-, *m*- and *p*-nitrophenyl 2,3,4-tri-*O*-acetyl-β-D-xylopyranosides. Moreover, solid-state 13C CP MAS NMR spectra were recorded for all powdered samples. Temperature scans for single crystals made on the goniometer head revealed phase transitions at c.a. 180 K and c.a. 210 K for *N*-*o*-nitrophenyl-2,3,4-tri-*O*-acetyl-β-D-xylopyranosylamine (1) and at c.a. 125K for *m*-nitrophenyl 2,3,4-tri-*O*-acetyl-β-D-xylopyranoside (5).

References:

1. Han, Y.; Chen, H. J. Mol. Catal. B: Enzym. 2010, 63, 135–140.
2. Eneyskaya, E.V.; Ivanen, D.R.; Bobrov, K.S.; Isaeva-Ivanova, L.S.; Shabalin, K.A.; Savel'ev, A.N.; Golubev, A.M.; Kulminskaya, A.A. Arch. Biochem. Biophys. 2007, 457, 225–234.
3. Kiss, T.; Erdei, A.; Kiss, L. Arch. Biochem. Biophys. 2002, 399, 188–194.
4. Gomez, M.; Isorna, P.; Rojo, M.; Estrada, P. Biochimie 2001, 83, 961–967.
5. Okayama, M.; Kimata, K.; Suzuki, S. J. Biochem. 1973, 74, 1069–1073.
6. Schwartz, N.B. J. Biol. Chem. 1977, 252, 6316–6321.
7. Qian, X.; Li, Z.; Liu, Z.; Song, G.; Li, Z. Carbohydr. Res. 2001, 336, 79–82.

Synthesis and structure characterization of a silicogermanate with -CLO framework

POSTER 35

J. Su[1,2], Y. Wang[2], J. Lin[2*], J. Sun[1], X. Zou[1*]
[1]Berzelii Center EXSELENT on Porous Materials and Inorganic and Structural Chemistry, Dept of Materials and Environmental Chemistry, Stockholm Univ., Stockholm, Sweden
[2]Beijing National Laboratory for Molecular Sciences, State Key Laboratory for Rare Earth Materials Chemistry and Applications, College of Chemistry and Molecular Engineering, Peking University, Beijing, China

Introduction

Cloverite (-CLO) is one of the most interesting types in zeolite frameworks, because of its extra-large pore defined by 20 TO_4 tetrahedra and the supercage with a body-diagonal of about 30 Å. Much work has been done to synthesize new materials with this topology. However, all the reported compounds are phosphates. Here, we report the synthesis and structure determination of a new silicogermanate with –CLO type framework. To our best knowledge, this is the first silicogermanate cloverite.

Experimental

The silicogermanate was synthesized hydrothermally from a mixture of GeO2, fumed silica, a solution of SDA and HF solution at 110 °C for 15-30 days.
The powder X-ray diffraction data used for structure refinement was collected on a PANalytical X'Pert Pro. The final structure model was refined by Rietveld refinement using TOPAS 3.0.

Results and discussion

From the elemental analysis and ICP result, we conducted the formula for GeSi-CLO to be $(Si_{0.45}Ge_{0.55})_{192}O_{372}(OH)_{24}F_{24}(C_9H_{22}N)_{24}(H2O)_x$.
We found that the powder XRD pattern is similar to the pattern of the –CLO structure. Therefore, the –CLO structure was used as an initial model, with the space group *Pm*-3*m*. The final framework structure was refined by Rietveld refinement (Rp=0.0516 Rwp=0.0680 and Rexp=0.0322). All the bond distances and angles are reasonable in the refined structure. Due to the very large cavities, many water molecules can reside in the channels. It was difficult to locate the templates. Instead, some disordered atoms were added at random positions inside the pores and refined subsequently.

Conclusion

A new silicogermanate, GeSi-CLO, with the -CLO framework was synthesized. As a silicogermanate, the framework structure of GeSi-CLO has been confirmed to be isostructural to -CLO by Rietveld analysis.

Acknowledgements

This work was supported by the Natural Science Foundation of China and Berzelii Center EXSELENT on Porous Materials and Inorganic and Structural Chemistry.

POSTER 36

Stress characteristics of steel microstructure disturbed by a laser-remelting process

L. Tarkowski[1], H.-G. Brokmeier[2, 4], N. Schell[4]., S. Pawlak[1], K. Dutka[3] J.T. Bonarski[1]

[1]Institute of Metallurgy and Materials Science, Polish Academy of Sciences, Kraków, Poland

[2]Institute of Materials Science and Engineering-Department TEXMAT-Clausthal Univ. of Technology, Clausthal-Zellerfeld, Germany

[3]Univ. of Warmia and Mazury, Olsztyn, Poland

[4]Helmholtz Zentrum Geesthacht, Outstation at Hasylab, Hamburg Germany

Efficiency of commonly applied laser-welding technology is determined to a large extent by stress-texture characteristics of microstructure of the joined materials modified during the process. The work presents selected variant of generating the intended microstructure changes in the area of constructional steel plate by means of a laser beam remelting. Due to relative sharp gradient of the residual stresses and the necessity of its identification in the individual microstructure-zones of the remelted steel, a high energy synchrotron beam was applied to the measurement of the lattice strains. Transmission geometry of the diffraction experiment delivered experimental data to the procedure of stress calculation. The obtained results revealed a spatial configuration of the residual stress field generated in microstructure of the steel around the laser-remelting path. The performed stress analysis indicates the most crucial areas of the laser-modified material which make possible to predict it exploitation behaviour.

Crystal structure analysis from crystalline powders of metal-organic lanthanide-containing networks prepared by solid-state reactions

L. Vella-Zarb and U. Baisch
School of Chemistry, Newcastle Univ., Newcastle upon Tyne, United Kingdom

POSTER 37

Rare earth crystal engineering is a challenging field in chemistry due to the high number of parameters to be considered when developing a synthetic bottom-up approach in which both crystallographic and rare earth chemical knowledge are required for the design and construction of inorganic tectons. These tectons may then be used to prepare new materials in a controlled manner with specific optical or magnetic properties.[1,2] In this work, crystalline oxalatolanthanide complexes (Ln = Ce, Eu, Gd, Dy, Ho, Yb) were used as inorganic tectons. Combining them with protonated melamine enabled us to engineer crystals consisting of a layered coordination salt structure.
The compounds were synthesised by simple ball milling of the reagents with a catalytic amount of water, but due to the low solubility of both the lanthanide anion and the melaminium nitrate, crystallization of the products proved problematic. In most cases only microcrystalline powders could be obtained.
Two types of crystal structures have been determined so far: In Type I (Yb-derivative) the chelating oxalate ligands of the anionic building block $[Yb(C_2O_4)_4]^{5-}$ act as hydrogen bond acceptors linking the melaminium layers while simultaneously saturating the coordination sphere of the lanthanide ion, whereas in the Type II (Gd-derivative) $[Gd(C_2O_4)_2]$- systems, a two dimensional framework linked by hydrogen bonding to isolated melaminium molecules is formed.
Powder diffraction has been a very powerful and useful technique in determining which lanthanide metal forms which type of structure, and/or whether a new structure was discovered. The results of these studies are compared and discussed with the data obtained from single-crystal data known from the Ytterbium and Gadolinium derivative.

[1] G. R. Desiraju, Angew. Chem., Int. Ed., 2008, 46, 8342-8356.
[2] U. Baisch, D. Braga, CrystEngComm, 2009, 11, 40-42.

POSTER 38

Gas-solid reactions in non-porous cristalline materials

L. Brammer[1], G. Minguez Espallargas[2], A. Florence[3], R. Sullivan[1], I. Vitorica Yrezabal[1]
[1]Univ. of Sheffield, Sheffield, United Kingdom
[2]CSIC, Valencia, Spain
[3]Univ. of Strathclyde, Glasgow, United Kingdom

Chemical reactions in the organic solid state are uncommon but well-established. In this work a class of crystalline reactions within nonporous materials of a coordination network and an organometallic salt will be presented, wherein bonds are broken and formed in a ligand substitution reaction at silver (I) and copper (II) centre. It has been shown that the behaviour of the Ag^{+} ions in these networks show structural similarities to the hydrogen "ions" in the carboxylic acid structures. We have extended this equivalence by inclusion of an alcohol molecule in the $[Ag_2(O_2CR)_2]$ dimer. A series of compounds of general formula $[Ag_4(TMP)_3(O2CRf)_4(ROH)_2]$ (TMP = 2,3,5,6-tetramethylpyrizine, R_f = perfluoroalkyl group, ROH = alcohol) have been prepared and crystallographically characterised. The release of the alcohol molecules from the expanded dimer and their extrusion from the crystals of the coordination network material $[Ag_4(TMP)_3(O2CR_f)_4(ROH)_2]$ yielding the alcohol-free network $[Ag_4(TMP)_3(O_2 CR_f)_4]$ has been investigated using X-ray powder diffraction studies. In the study of halogen bonding, especially bonds formed by M–X•••X–C (X= Cl, Br and I). A series of compounds with the generic formula (nX-pyH)(MX_4) (n = 3,4) (X = Cl, Br, I) (M = Co, Zn, Cu) were synthesised. It has been shown that under ambient conditions $(3ClpyH)_2CuCl_4$ releases two molecules of HCl forming the coordination compound $Cu(3Cl\text{-}py)_2Cl_2$. Here we present an extended study of this reaction where the $Cu(nXpy)_2X_2$ was reacted *in situ* with HX (n = 3,4; X= Cl and Br) at ESRF synchrotron source.

Structural study of nanocrystalline Ti-doped gahnite

M. Vrankic[1], B. Gržeta[1], J. Popovic[1], E. Tkalcec[2], S. Kurajica[2]
[1]Rudjer Boskovic Institute, Zagreb, Croatia
[2]Faculty of Chemical Engineering and Technology, Univ. of Zagreb, Zagreb, Croatia

POSTER 39

Titanium doped materials with spinel-type structure have been interesting as the active media for solid-state lasers [1]. Among them, Ti-doped spinel ($MgAl_2O_4$:Ti) was found to have strong blue luminescence at ~490 nm [2], while Ti-doped **α-$ZnAl_2S_4$** spinel-type crystals exhibit luminescence in the IR spectral range 0.8-1.4 μm [1]. In both described cases, the emission bands arose from Ti^{4+} on spinel octahedral cation site. We have studied titanium incorporation in gahnite, $ZnAl_2O_4$. Gahnite is cubic with the normal spinel structure, space group *Fd-3m*. When doped with Co^{2+}, Mn^{2+} or rare-earth ions it exhibits luminescence and can be used as a cathodoluminescent material [3]. There is no literature data on titanium doped gahnite.

Powder samples of gahnite doped with titanium were prepared by a sol-gel technique using zinc nitrate hexahydrate, aluminum-*sec*-butoxide and titanium(IV) butoxide as starting components. The excess of zinc component was used for the purpose of charge balance in the prepared samples. Samples could be described by formula $Zn(Al_{2-2x}Ti_xZn_x)O_4$, with $0.25 \geq x \geq 0.04$. XRD patterns indicated that all samples had the characteristic spinel-type structure. Unit-cell parameter a was refined by WPPF program [4]. The unit cell increased with the increase of Ti-doping level. Rietveld structure refinement confirmed that Ti^{4+} was incorporated on octahedral cation site in the normal spinel-type structure of gahnite with Zn excess. The prepared samples exhibited luminescence at ~470 nm.

1. S. Anghel, G. Boulon, A. Brenier, E. Fortin, S. Klokishner, D. Koshchug, L. Kulyuk, K. Sushkevich, J. Phys.: Condens. Mater. 22 (2010) 055903.
2. T. Sato, M. Shirai, K. Tanaka, Y. Kawabe, E. Hanamura, J. Lumin. 114 (2005) 155.
3. G. Müller, Electroluminescence II. Semiconductors and Semimetals, Academic Press, New York, 2002, 60.
4. H. Toraya, J. Appl. Cryst. 19 (1986) 440.

POSTER 40

Mid-infrared, powder diffraction, and ab-initio study of anion substitution in $LiBH_4$

O. Zavorotynska[1], M. Corno[1], P. Ulegno[1], G. Spoto[1], L.H. Rude[2], L.M. Arnbjerg[2], L.M. Jensen[2], M. Baricco[1]
[1]Dip. di Chimica I.F.M. and NIS, Università di Torino, Torino, Italy
[2]Center for Materials Crystallography (CMC), Interdisciplinary Nanoscience Center (iNANO) and Dept of Chemistry, Aarhus Univ., Aarhus, Denmark

Solid solutions of alkaline metal borohydrides with the corresponding halides have a range of interesting properties. Recently these compounds were found to form solid electrolytes with high ion conductivity. Apart from that, adding halide to the borohydride can destabilize the latter leading to improved hydrogen storage properties of these compounds.
The structure of metal borohydrides has been successfully studied with diffraction methods over decades. Vibrational spectroscopy has also often been utilized as an informative characterization tool. In mid-infrared spectra of metal borohydrides the internal stretching and bending modes of $[BH_4]^-$ tetrahedra are observed. These modes are strongly influenced by the site symmetry of the $[BH_4]^-$ tetrahedra and by the surrounding cations. Hence, in principle they can be used to characterize the modifications in the structure of borohydrides.
In this study we have utilized mid-infrared spectroscopy to characterize ion solutions of $LiBH_4$ with corresponding halides. To predict the vibrational spectra of new halogen substituted compounds, and also the thermodynamics of solid-solution formation, calculations with CRYSTAL code, developed at the University of Torino, have been performed. Finally, the crystal structure of potential new compounds has been characterized by x-ray powder diffraction to validate the solid solutions formation.

Additional Participants

Angelo Agostino

Angela Altomare

Ulrich Baisch

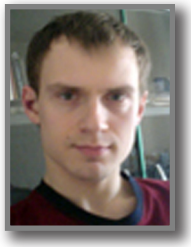

Ivan Bobrikov

Christian Butterhof

Hong Chen

Spoorthi Dharmayat

Pierrick Durand

Henrik Fahlquist

Yaroslav Filinchuk

Christoph Frommen

Terry Humphries

Danielle Kennedy

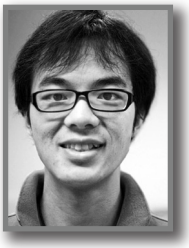

Leifeng Liu

Ahmed Mabied

Thomas Wolfgang Martin

William Rickard

Keisuke Saito

Talitha Santini

Moritz-C. Schlegel

Marcin Stachowicz

Alex Ulyanenkov

Yaroslav Yakimov

Presenting author index

Pages 1-206 are in *volume 1*; pages 207-412 are in *volume 2*.

A

Aliev, A. 365
Andreev, Yuri G. 281

B

Baerlocher, Christian 220, 333
Bernstein, Joel 198
Billing, D.G. 366
Billinge, Simon J.L. 270
Bindzus, N. 367

C

Černý, Radovan 62
Chelazzi, L. 369

D

David, William I. F. 19, 207
de Campos, C.E.M. 368
Duriska, M.B. 370

F

Fantechi, E. 371
Favero, M. 372
Feyand, M. 373
Fitch, Andy 103

G

Ghose, S. 374
Giacovazzo, Carmelo 121
Gnutzmann, T. 375
Gozzo, Fabia 86
Grässlin, J. 376

H

Heuser, J. 377
Hino, S. 378

I

Ibsen, C.J.S. 379
Inge, A.K. 380

J

J.Gilmore, Chris 142

K

Kanodarwala, F. 381
Kern, Arnt 304
Kolb, Ute 30
Kurawa, M.A. 382

L

Lampronti, G.I. 383
Leoni, Matteo 239
Lusi, M. 384
Lutterotti, Luca 316

M

Madsen, Ian C. 292
Maini, L. 385
Margiolaki, Irene 187
Mazzeo, P.P. 386
McCusker, Lynne B. 55, 343
Moliterni, A. 387

N

Nauha, E. 388

O

Oszajca, M. 389

P

Palatinus, Lukáš 160
Popovic, J. 390
Pulham, Colin R. 113

R

Rahman, S.M.H. 391
Riktor, M.D. 392

S

Schmitz, S. 393
Senn, M.S. 394
Shankland, Kenneth 37, 70, 170 356
Sisak, D. 395
Skoko, Ž. 396
Smart, P. 397
Smrčok, Ľubomír 231
Stephens, Peter W. 43
Stepien, D.K. 398
Su, J. 399

T

Tarkowski, L. 400

U

Ungár, Tamás 248

V

Vella-Zarb, L. 401
Vitorica Yrezabal, I. 402
Von Dreele, R.B. 326
Vrankic, M. 403

W

Whitfield, Pamela 77
Wright, Jonathan P. 177

Z

Zavorotynska, O. 404